



**The University of  
Nottingham**

**HIGH TEMPERATURE  
ANISO-THERMO-MECHANICAL  
ANALYSIS OF SUPERPLASTIC  
FORMING TOOLS**

GEORGE GREEN LIBRARY OF  
SCIENCE AND ENGINEERING

**BY**

**Aditya A. Deshpande, B.E., M.Sc.**

**Thesis submitted to the University of Nottingham for the  
degree of Doctor of Philosophy**

**August 2009**

# CONTENTS

|  |           |
|--|-----------|
| <b>ABSTRACT .....</b>  | <b>4</b>  |
| <b>ACKNOWLEDGEMENTS .....</b>  | <b>6</b>  |
| <b>NOMENCLATURE .....</b>  | <b>7</b>  |
| <br>   |           |
| <b>CHAPTER 1 INTRODUCTION .....</b>  | <b>11</b> |
| 1.2 FAILURE MODES AND LIFE PREDICTION OF SPF TOOLS .....                         | 14        |
| 1.3 FINITE ELEMENT MODELLING OF SPF PROCESS AND TOOLS .....                      | 17        |
| 1.4 SCOPE OF THE THESIS .....  | 18        |
| <b>CHAPTER 2 LITERATURE REVIEW .....</b>   | <b>24</b> |
| 2.1 INTRODUCTION.....  | 24        |
| 2.1.1 <i>Fatigue</i> .....   | 25        |
| 2.1.2 <i>Creep</i> .....   | 28        |
| 2.1.3 <i>Fatigue-creep interaction</i> .....                                     | 29        |
| 2.1.4 <i>Ratchetting</i> .....   | 30        |
| 2.2 THERMO-MECHANICAL/ISOTHERMAL FATIGUE.....                                    | 32        |
| 2.2.1 <i>Introduction</i> .....  | 32        |
| 2.2.2 <i>TMF and IF testing of high temperature materials</i> .....              | 33        |
| 2.2.3 <i>Effect of hold time period in high temperature cyclic loading</i> ..... | 36        |
| 2.3 LOW CYCLE FATIGUE AND RATCHETTING.....                                       | 38        |
| 2.3.1 <i>Interaction of LCF and ratchetting</i> .....                            | 38        |
| 2.3.2 <i>Mechanisms of material ratchetting</i> .....                            | 40        |
| 2.3.3 <i>Structural ratchetting</i> .....  | 42        |
| 2.3.4 <i>Time dependent ratchetting</i> .....                                    | 43        |
| 2.4 MATERIAL BEHAVIOUR MODELLING.....  | 44        |
| 2.4.1 <i>Introduction</i> .....  | 44        |
| 2.4.2 <i>Cyclic plasticity</i> .....   | 46        |
| 2.4.3 <i>Uncoupled elastoplasticity-creep</i> .....                              | 51        |
| 2.4.4 <i>Elasto-viscoplasticity</i> .....  | 52        |
| 2.5 TMF LIFE PREDICTION METHOD .....   | 55        |
| 2.5.1 <i>Introduction</i> .....  | 55        |
| 2.5.2 <i>Life prediction models</i> .....  | 56        |
| 2.6 WORK DONE ON SPF TOOLS.....  | 61        |
| 2.7 SUMMARY.....   | 65        |
| <b>CHAPTER 3 HIGH TEMPERATURE MATERIAL TESTING.....</b>                          | <b>86</b> |
| 3.1 INTRODUCTION.....  | 86        |
| 3.2 TMF TEST RIG AND TESTING.....  | 88        |
| 3.2.1 <i>Test set-up</i> .....   | 88        |
| 3.2.2 <i>Testing procedure</i> .....   | 91        |
| 3.3 ISOTHERMAL MULTI STRAIN RANGE FATIGUE TESTS.....                             | 93        |
| 3.3.1 <i>SS-316 stainless steel</i> .....  | 93        |
| 3.3.2 <i>XN40F alloy</i> .....   | 94        |

|   |   |            |
|---|---|------------|
| 3.4   | FATIGUE LIFING TESTS FOR SS-316 STAINLESS STEEL .....       | 95         |
| 3.4.1   | <i>Isothermal LCF testing</i> .....                         | 95         |
| 3.4.2   | <i>TMF testing</i> .....                                    | 95         |
| 3.4.3   | <i>Fatigue life evaluation</i> .....                        | 96         |
| 3.5   | FATIGUE LIFING TESTS FOR XN40F ALLOY .....                  | 96         |
| 3.5.1   | <i>Isothermal LCF testing</i> .....                         | 97         |
| 3.5.2   | <i>TMF testing</i> .....                                    | 97         |
| 3.5.3   | <i>Fatigue life evaluation</i> .....                        | 98         |
| 3.6   | STRESS CONTROLLED RATCHETTING TESTS FOR XN40F ALLOY .....   | 99         |
| 3.7   | STRESS RELAXATION TESTS FOR XN40F ALLOY .....               | 100        |
| 3.8   | SUMMARY AND CONCLUSIONS .....                               | 101        |
| <b>CHAPTER 4 MATERIAL CHARACTERISATION AND MODELING .....</b> |   | <b>139</b> |
| 4.1   | INTRODUCTION .....  | 139        |
| 4.2   | MATERIAL MODELS .....                                       | 140        |
| 4.2.1   | <i>Isotropic hardening model:</i> .....                     | 140        |
| 4.2.2   | <i>Linear kinematic hardening model:</i> .....              | 141        |
| 4.2.3   | <i>Nonlinear isotropic/kinematic hardening model:</i> ..... | 143        |
| 4.2.4   | <i>Power law creep model</i> .....                          | 144        |
| 4.2.5   | <i>Two-layer viscoplastic model</i> .....                   | 145        |
| 4.3   | IDENTIFICATION OF MATERIAL CONSTITUTIVE CONSTANTS .....     | 148        |
| 4.3.1   | <i>Non-linear kinematic hardening model</i> .....           | 148        |
| 4.3.2   | <i>Combined isotropic/kinematic hardening model</i> .....   | 150        |
| 4.3.3   | <i>Power law creep model</i> .....                          | 151        |
| 4.3.4   | <i>Two-layer viscoplastic model</i> .....                   | 152        |
| 4.4   | VALIDATION OF MATERIAL MODELS .....                         | 153        |
| 4.5   | SUMMARY AND CONCLUSIONS .....                               | 154        |
| <b>CHAPTER 5 LIFE PREDICTION METHODOLOGY .....</b>            |   | <b>180</b> |
| 5.1   | INTRODUCTION .....  | 180        |
| 5.2   | REVIEW OF TMF LIFE PREDICTION MODELS .....                  | 181        |
| 5.2.1   | <i>Linear Damage summation model</i> .....                  | 181        |
| 5.2.2   | <i>Ductility exhaustion model</i> .....                     | 182        |
| 5.2.3   | <i>Frequency separation model</i> .....                     | 184        |
| 5.2.4   | <i>Strain range partitioning model</i> .....                | 184        |
| 5.2.5   | <i>Ostergren strain energy model</i> .....                  | 186        |
| 5.2.6   | <i>Zamrik strain energy model</i> .....                     | 186        |
| 5.2.7   | <i>Strain energy partitioning model</i> .....               | 187        |
| 5.3   | TMF LIFE PREDICTION .....                                   | 187        |
| 5.4   | SUMMARY AND CONCLUSION .....                                | 190        |
| <b>CHAPTER 6 FINITE ELEMENT MODELING .....</b>                |   | <b>200</b> |
| 6.1   | INTRODUCTION .....  | 200        |
| 6.2   | TOOL GEOMETRIES AND MATERIAL .....                          | 202        |
| 6.3   | THEORY OF HEAT TRANSFER .....                               | 203        |
| 6.3.1   | <i>Introduction</i> .....                                   | 203        |
| 6.3.2   | <i>Heat transfer mechanisms</i> .....                       | 203        |
| 6.4   | HEAT TRANSFER TEST ON XN40F BLOCK .....                     | 206        |
| 6.4.1   | <i>Introduction</i> .....                                   | 206        |
| 6.4.2   | <i>Test results</i> .....                                   | 208        |

|  |  |            |
|--|--|------------|
| 6.5  | VALIDATION OF HEAT TRANSFER MODEL .....                    | 208        |
| 6.5.1  | <i>Thermal properties</i> .....                            | 208        |
| 6.5.2  | <i>Validation of heat transfer model</i> .....             | 211        |
| 6.6  | FE MODELING OF SPF THERMAL CYCLES .....                    | 213        |
| 6.6.1  | <i>Description of SPF thermal cycles</i> .....             | 213        |
| 6.6.2  | <i>Boundary conditions</i> .....                           | 216        |
| 6.6.3  | <i>FE predicted SPF thermal cycles</i> .....               | 217        |
| 6.7  | FE MODELING OF THERMO-MECHANICAL ANALYSES OF SPF TOOL..... | 218        |
| 6.7.1  | <i>Introduction</i> .....                                  | 218        |
| 6.7.2  | <i>Contact modeling</i> .....                              | 219        |
| 6.7.3  | <i>Boundary conditions</i> .....                           | 220        |
| 6.7.4  | <i>Loading conditions</i> .....                            | 221        |
| 6.7.5  | <i>Meshing</i> .....                                       | 221        |
| 6.8  | SUMMARY AND CONCLUSION .....                               | 223        |
| <b>CHAPTER 7 THERMO-MECHANICAL ANALYSES OF SPF TOOL.....</b> |  | <b>244</b> |
| 7.1  | INTRODUCTION.....  | 244        |
| 7.2  | EFFECT OF MAJOR CYCLES WITHOUT MINOR CYCLES .....          | 246        |
| 7.2.1  | <i>Effect of thermal cycle 'A'</i> .....                   | 246        |
| 7.2.2  | <i>Effect of thermal cycle 'B'</i> .....                   | 248        |
| 7.2.3  | <i>Comparison of thermal cycle 'A' and 'B'</i> .....       | 249        |
| 7.3  | EFFECT OF HEATING AND COOLING RATES .....                  | 249        |
| 7.4  | EFFECT OF MINOR CYCLES.....                                | 252        |
| 7.4.1  | <i>Uncoupled plasticity-creep model</i> .....              | 252        |
| 7.4.2  | <i>Two-layer viscoplasticity model</i> .....               | 256        |
| 7.5  | EFFECT OF BATCH SIZE.....                                  | 259        |
| 7.6  | TOOL LIFE PREDICTIONS .....                                | 262        |
| 7.7  | SUMMARY AND CONCLUSION .....                               | 266        |
| <b>CHAPTER 8 CONCLUSIONS AND FUTURE WORK.....</b>            |  | <b>295</b> |
| 8.1  | INTRODUCTION.....  | 295        |
| 8.2  | MATERIAL CHARACTERISATION AND MODELLING.....               | 296        |
| 8.3  | ISOTHERMAL AND TMF-CREEP RATCHETTING LIFING TESTS .....    | 297        |
| 8.4  | THERMO-MECHANICAL ANALYSES OF SPF TOOL .....               | 299        |
| 8.5  | SPF TOOL LIFE PREDICTIONS .....                            | 302        |
| 8.6  | FUTURE WORK RECOMMENDATIONS.....                           | 303        |
| <b>REFERENCES .....</b>                                      |  | <b>306</b> |
| <b>APPENDIX A.....</b>                                       |  | <b>319</b> |
| <b>APPENDIX B .....</b>                                      |  | <b>321</b> |
| <b>APPENDIX C.....</b>                                       |  | <b>322</b> |
| <b>APPENDIX D.....</b>                                       |  | <b>326</b> |

## ABSTRACT

The main objective of the thesis is to establish a methodology to analyse the aniso-thermo-mechanical behaviour of a representative large industrial Superplastic Forming (SPF) tool made of XN40F material (40% Ni, 20% Cr, Balance Fe) to identify and evaluate different failure mechanisms to improve and predict the tool life. Sequentially coupled thermo-mechanical analyses under realistic loading conditions are developed within a general purpose non-linear Finite Element (FE) code, ABAQUS to predict and analyse the complex temperature-stress-strain cycles of the SPF tool.

The temperature dependent cyclic plasticity and creep material data is established for the tool material performing the multi-strain range isothermal cyclic tests and the stress relaxation tests for a range of temperatures. Various strain controlled thermo-mechanical fatigue-creep and stress controlled ratchetting tests are designed and performed based on the preliminary FE analyses of the tool. The strain controlled and the stress controlled representative tests are carried out to capture the most damaging phase of the SPF thermo-mechanical cycle. In addition to above tests, heat transfer tests are also carried out on the rectangular block of tool material to validate the employed heat transfer methodology.

Material constants are identified for different material behaviour models such as combined non-linear kinematic/isotropic hardening model for the cyclic plasticity, power law creep model for secondary creep and the two-layer viscoplastic model to address the combination of plasticity and creep. The identified constants are validated against the isothermal and thermo-mechanical fatigue tests. The FE

modelling of the heat transfer tests using the calculated convective heat transfer coefficients and other thermal properties is carried out and the predicted thermal histories are compared with the experimental results.

The validated heat transfer methodology is employed to simulate the realistic thermal cycles of the SPF tool. In addition to thermal loading, the tool gravity and the clamping pressure to counteract the forming gas pressure are employed in the thermo-mechanical analyses of the tool. The tool platen contact is also modelled where the platen is considered as analytically rigid surface. Various thermo-mechanical analyses are performed to investigate the effect of different thermal cycles, heating and cooling rates and the batch sizes, i.e. number of parts formed in a forming campaign, on the tool damage.

Different strain and strain energy based thermo-mechanical fatigue life prediction methodologies are explored and evaluated using the isothermal and thermo-mechanical fatigue-creep lifing tests. The simple ductility exhaustion method is also developed to predict the ratchetting life of the specimen and the tool. The tool life predictions are performed employing the FE predicted stress-strain results into the identified stress-strain-life equations from the isothermal lifing tests. The predicted thermo-mechanical behaviour and tool lives are compared against the representative test and the industrial experience.

From all thermo-mechanical fatigue-creep and ratchetting test results and thermo-mechanical analyses of the tool, the fatigue-creep interaction is found to be the most important factor in the tool failure.

## ACKNOWLEDGEMENTS

It is a pleasure to thank all the people who made this thesis possible.

First of all, I seize this opportunity to express my sincere feelings of gratitude towards my supervisor, Professor Sean Leen. I am grateful for his scholastic guidance and encouragement during my study and constructive comments during the preparation of this thesis. My heartfelt thanks also go to Professor T H Hyde for his valuable suggestions and knowledge during the course of this research work.

I am extremely thankful to Mr. Thomas Buss for his genuine help and guidance in performing material testing on the thermo-mechanical fatigue test rig. I also thank Mr. Keith Dinsdale for his kind support in the experimental work of this project. I am also grateful to Dr. Jin Shang for his guidance in the beginning of this project.

I am indebted to Mr. Ian Leaver and Mr. John Chippendale from BAE SYSTEMS UK for sponsoring my PhD and providing me with important industrial information to achieve my research objectives successfully. I am also very thankful to the International office and the School of Mechanical Materials and Manufacturing of the University of Nottingham for giving me scholarship to undertake my PhD.

I also mention my special thanks to my wife Saloni for being there for me always and motivating me towards the completion of this thesis.

Lastly, and most importantly, I thank my adored parents and sister who always supported and encouraged me to pursue my ambition. For this and much more, I will forever remain in their debt. I dedicate this thesis to them.

## NOMENCLATURE

|                     |  |
|---------------------|--|
| $a$                 | Basquin material constant                                    |
| $a$                 | Crack length   |
| $A$                 | Area of facet  |
| $A$                 | Secondary creep constant                                     |
| $b$                 | Coffin-Manson material constant                              |
| $b$                 | Isotropic hardening constant                                 |
| $c$                 | Specific heat  |
| $C$                 | Hardening modulus  |
| $C$                 | Material constant  |
| $C_{SB}$            | Stefan-Boltzmann constant                                    |
| $D$                 | Damage   |
| $e$                 | Emissivity   |
| $f$                 | Two-layer viscoplasticity constant                           |
| $E$                 | Young's modulus  |
| $g$                 | Gravity  |
| $h$                 | Convective heat transfer coefficient                         |
| $k$                 | Thermal conductivity   |
| $k$                 | Cyclic yield stress  |
| $K_p, \mathbf{K}_p$ | Elastic modulus of the plastic part (tensor)                 |
| $K_v, \mathbf{K}_v$ | Elastic modulus of the viscous part (tensor)                 |
| $L$                 | The characteristic length of the geometry                    |
| $m$                 | Material constant  |
| $n$                 | Secondary creep exponent                                     |
| $N$                 | Number of cycles to failure                                  |
| $Nu_L$              | Nusselt number   |
| $p_{SWT}$           | Smith-Watson-Topper damage parameter                         |
| $q$                 | Heat transfer energy   |
| $Q_\infty$          | Asymptotic value defining maximum expansion of yield surface |

|               |   |
|---------------|---|
| $R$           | Stress or strain ratio  |
| $R$           | Isotropic hardening variable                                      |
| $Ra_L$        | Rayleigh number   |
| $S$           | Surface area  |
| $S$           | Deviatoric stress   |
| $S$           | Deviatoric stress tensor  |
| $t$           | Time  |
| $T$           | Temperature   |
| $T^0$         | Sink temperature  |
| $T_s$         | Surface temperature   |
| $T_\infty$    | Ambient temperature   |
| $U$           | Internal energy   |
| $U$           | Nodal displacement  |
| $V$           | Volume of material  |
| $X$           | Co-ordinate axial   |
| $X$           | Kinematic hardening variable (back stress)                        |
| $X$           | Back stress tensor  |
| $Y$           | Co-ordinate axial   |
| $Z$           | Co-ordinate axial   |
| $\alpha$      | Constant for bi-linear strain range partitioning                  |
| $\alpha$      | Thermal diffusivity ( $m^2/s$ )                                   |
| $\alpha$      | Back stress   |
| $\alpha$      | Back stress tensor  |
| $\beta$       | Constant for bi-linear strain range partitioning                  |
| $\beta$       | Volumetric thermal expansion                                      |
| $\gamma$      | Recall term (material constant) of non-linear kinematic hardening |
| $\delta_{ij}$ | Kronecker delta   |
| $\epsilon$    | Strain  |
| $\epsilon$    | Strain tensor   |
| $\phi$        | Angle   |
| $\Delta$      | Range   |
| $\nu$         | Frequency   |

|          |                     |
|----------|---------------------|
| $\nu$    | Kinematic viscosity |
| $\nu$    | Poisson's ratio     |
| $\rho$   | Density             |
| $\sigma$ | Stress              |
| $\sigma$ | Stress tensor       |

### **SUPERSCRIPTS**

|       |                         |
|-------|-------------------------|
| $e$   | Elastic                 |
| $eq$  | Equivalent              |
| $in$  | Inelastic               |
| $me$  | Mechanical              |
| $p$   | Plastic                 |
| $pl$  | Plastic                 |
| $r$   | Ratchet                 |
| $t$   | Total                   |
| $tot$ | Total                   |
| $th$  | Thermal (Equation 4.12) |
| $vp$  | Visco-plastic           |
| $v$   | Viscous                 |
| $Z$   | Absolute zero           |

### **SUBSCRIPTS**

|           |   |
|-----------|---|
| $a$       | Amplitude   |
| $c$       | Creep   |
| $f$       | Fatigue failure or fracture                                   |
| $i, j, k$ | Equation variables  |
| $m$       | Mean  |
| max       | Maximum   |
| min       | Minimum   |
| $p$       | Plastic   |
| $pp$      | Tensile plastic strain reversed by compressive plastic strain |
| $pc$      | Tensile plastic strain reversed by compressive creep strain   |

|           |   |
|-----------|---|
| <i>cp</i> | Tensile creep strain reversed by compressive plastic strain |
| <i>cc</i> | Tensile creep strain reversed by compressive creep strain   |
| <i>u</i>  | Ultimate  |
| <i>R</i>  | Rupture failure   |
| <i>y</i>  | Yield   |

### **ABBREVIATIONS**

|             |                                |
|-------------|--------------------------------|
| <b>FE</b>   | Finite element                 |
| <b>HCF</b>  | High cycle fatigue             |
| <b>IF</b>   | Isothermal fatigue             |
| <b>LCF</b>  | Low cycle fatigue              |
| <b>NLKH</b> | Non-linear kinematic hardening |
| <b>SPF</b>  | Superplastic forming           |
| <b>TMF</b>  | Thermo-mechanical fatigue      |

Note: – The meaning of each symbol and abbreviation is also explained in the text.

- Tables, figures and photographs are placed at the end of the text in each chapter.

# Chapter 1

## INTRODUCTION

### 1.1 Superplastic forming process and tooling

The superplastic forming (SPF) process is an important manufacturing process in the aerospace and automotive industries because of its capability to produce highly complex sheet components in a single operation. The application of this process has been extending to other industries manufacturing medical implants and sports equipments. The SPF process is generally used to form geometrically complex components and hence requires complex shaped tools. Superplasticity is a term used to describe exceptional ductility that certain metals exhibit when deformed under specific conditions such as high temperature (greater than one half the absolute melting point of sheet metal), controlled strain rate, usually 0.0001 to 0.01/sec and a very fine grain size material (of the order of 10  $\mu\text{m}$ ) [1]. The tensile ductility of superplastic materials ranges from 500% to 1000% in a certain range of temperature and strain rate [2]. In order to successfully produce complex sheet metal component using the SPF process, it is important to determine the optimum superplastic temperature, sensitivity of the flow stresses and the elongation with temperature using numerical simulation [3]. Fig. 1.1 shows the schematic diagram of the superplastic forming process.

The superplastic forming process has significant advantages over conventional forming methods. The SPF process is generally completed in a single step. It provides products with an excellent structural integrity, light weight and superior

strength which are essential qualities for aerospace components. The weakness of the process includes the need for tight control of temperature and strain rate [1, 4]. Because of long forming times due to slow strain rates, the SPF process is not suitable for high volume production. However, the advantages such as maximum structural efficiency, light weight structures, less part counts and the ability to manufacture complex geometry parts, make this process an integral part of the aerospace industry.

There are various forming processes such as blow forming, vacuum forming, thermoforming, deep drawing, forging, extrusion and superplastic forming-diffusion bonding (SPF-DB). Of these processes, blow forming, vacuum forming and SPF-DB are widely used in the aerospace industry. The SPF-DB process combines the two processes due to same temperature requirement; also the application of gas pressure is common in both. Figs. 1.2 and 1.3 show the complex shape aerospace components formed by the SPF and SPF-DB processes. Titanium, aluminium and nickel based superplastic metallic alloys are broadly used in the aerospace industry to form complex shaped components. The low densities of aluminium and titanium alloys make these materials highly suitable for aerospace applications. Moreover the ability of titanium to easily diffusion-bond facilitates the combined SPF-DB process, which provides extremely efficient and highly utilised structures [5].

Due to increased titanium forming in the aerospace industry, new superior and expensive low oxidation tool materials such as nickel base alloys have been developed. However, quality and durability problems of specially designed tools limit the growth of titanium SPF forming [6]. In addition to the development of

specialised SPF tool alloys, large heating presses have been developed over the years with large platen sizes of 2x3 m and clamping capability of 1250 tons to counteract the forming gas pressure up to 500 Psi (Fig. 1.4 ) [7]. These large presses have mainly been developed to accommodate large SPF tools used broadly in the aerospace applications. The large SPF tools primarily suffer from distortion due to thermal cycling and high temperature creep in addition to the creep-fatigue cracking. A high temperature environment also affects the surface quality of tooling due to oxidation. Moreover, distortion and oxidation affect the quality of formed parts. Tools are vital for the success of most manufacturing processes including SPF. The requirements of satisfactory tooling are (i) the ability to continuously form components within required dimensional tolerance and surface quality, (ii) efficient operation, continuously at high temperature with no damage and (iii) ability to produce high output and capability to manufacture parts at minimum cost for optimized forming conditions [8].

The superplastic forming tools need to withstand a high temperature cyclic loading and a steady mechanical loading for extended durations and therefore are manufactured (by casting) using specialized alloys having low thermal expansion coefficients and high oxidation resistance and they must not undergo phase transformations during heating and cooling cycles of the SPF process. A wide range of materials have been used for the SPF tooling such as ceramics, graphite, metals and alloys. Metal and alloy tools are generally employed for large production applications. Nickel base alloys are widely used in the aerospace industry, especially for titanium forming since they have excellent properties at high temperature, such as high temperature strength, creep rupture strength and fatigue and oxidation

resistance. These specially designed materials are very expensive and therefore the cost of tool failure is significant which makes the tool life an important limiting aspect in the SPF process.

## **1.2 Failure modes and life prediction of SPF tools**

Due to severe loading conditions of high temperature thermal cycling and mechanical loading such as clamping pressure and forming gas pressure, the SPF tools may undergo various modes of failure such as permanent distortion, thermal fatigue, fatigue-creep interaction, ratchetting and oxidation. The tool damage can mainly be attributed to one of the following factors: 1) the tool and billet temperature or temperature cycles, 2) thermal, physical and mechanical properties of the tool material, 3) surface finish of the SPF tool, 4) heating press and tonnage, 5) the magnitude of contact stresses developed during the forming [9]. The occurrence of high temperature results in a nonlinear material behaviour due to low yield stresses and creep deformation. Creep relaxation during the constant temperature forming cycle induces plastic deformation and distortion of the tool after ambient cooling [4].

SPF tools experience one or more of the following three damages

- **Permanent distortion:** The heating and cooling cycles develop temperature gradients and thermal stresses within the tools. Thermal and mechanical stresses can result in cyclic plasticity and creep deformation which further leads to dimensional inaccuracy in the formed components. In addition to cyclic plasticity and creep, microstructure changes in the material at high temperatures may affect the dimensions of the tool [10].

- Cracking: The cyclic thermo-mechanical loading of tools leads to thermo-mechanical fatigue and creep which may develop cracks. The thermal cyclic loads at high temperature result into the creep-fatigue interaction which may lead to progressive deformation of tools, with number of cycles causing cracks to propagate.
- Oxidation: The high temperature operating conditions lead to oxidation of forming surfaces. This causes damage to the surface of the tool and affects the surface quality of the formed parts [11, 12].

A number of different SPF tools for various structures in the aerospace industry have been developed in last three to four decades. The regions and the types of failure are different for different SPF tools due to complicated geometries and sizes. The SPF loading conditions (thermal cycles, clamping and forming gas pressure) change with different tools and the components formed. The BAE systems company, the current world leaders in SPF technology, has experienced unique problems with their individual tools. Tools made up of Armco 22.4.9 wrought material have never failed due to cracking but suffered from poor surface finish on the formed parts mainly due to oxidation at high temperature. Alternatively, the tools made of Esco cast 22.4.9 have often cracked around the periphery in early stages of manufacture but the cracks do not propagate with further forming campaigns. Cronite 25/20 tools have been used for a single forming batch and they crack significantly.

The XN40F tool employed in this project as a case study represents the large SPF tools used in the aerospace industry. This tool and the material are relatively new for the BAE systems. The tool is cast from XN40F material by Aubert & Duval (40%

Ni, 20% Cr, and 0.35% C, Balance Fe). The density of the material at room temperature is  $7920 \text{ Kg/m}^3$ . The temperature dependent mechanical and creep properties of the material are summarised in Tables 1.1 and 1.2 [13]. Fig. 1.5 shows the geometry of XN40F tool which is approximately  $1.5 \times 2 \text{ m}$  in size. According to industrial experience, such tools often crack after 30 to 40 forming campaigns where approximately 20 to 40 components form in a forming campaign. The major cracks tend to occur along the free edges of the long sides of the tool (Fig 1.5). To date the XN40F tool has not cracked but has undergone re-machining to produce components within the tolerance.

The distortion and premature failure due to cracking of SPF tools limits the expansion of the SPF process. A premature failure of tools made of expensive materials significantly affects the economics of the process in today's commercial world. Improving the tool life and tool life prediction is a challenging task. The life of various different SPF tool alloy materials is difficult to predict due to lack of knowledge of the effect of temperature on crack initiation and propagation behaviour [1].

The SPF tool life prediction is a primary concern for today's aerospace industry to reduce the costs associated with the process. A thorough understanding of the thermo-mechanical behaviour of tool materials along with numerical analyses of the actual SPF tools is essential for predicting the SPF tool life and its performance under different loading conditions. A comprehensive thermo-mechanical fatigue and fatigue-creep data is required for detailed thermo-mechanical analyses of SPF tools. The life prediction of SPF tools forms one of the most complicated topics in the

material research as it involves high temperature fatigue, fatigue-creep interaction along with environmental corrosion. Very little research [14-16] has been carried out on the thermo-mechanical failure analysis of real industrial SPF tools.

### **1.3 Finite element modelling of SPF process and tools**

Due to advancement in the computing technology, the finite element method has become a powerful tool in simulating superplastic forming processes [2, 3, 17-22]. The FE simulation of sheet metal forming has been extensively used in the aerospace applications to minimise the cost and time involved in a component development process. It generates accurate prediction of deformation of the sheet metal and the final thickness distribution of formed parts. The finite element method is also used for optimising the superplastic forming parameters such as optimum load and pressure-time curves [23].

Research from the last few years has shown that FE simulation is a feasible approach to model a non-linear material behaviour and contact friction between the tool and the sheet; moreover it is valuable to predict the deformation especially for complex shapes. However, there has not been enough research on thermo-mechanical analysis of the SPF tool as they are commonly considered as rigid bodies [4]. Few researchers have explored FE modelling to analyse high temperature forming tools such as hot forging, casting and extrusion tools. Gao [4] and Shang [16] performed FE modelling for the SPF tool analysis.

Finite element based simulation of realistic thermo-mechanical conditions is the only effective method for predicting and analysing complex temperature-stress-strain

cycles of the SPF tools [24]. This method facilitates optimisation of the process parameters such as thermal cycle, heating and cooling rates and batch sizes of forming campaigns to improve the tool life. However, an accurate prediction of the thermo-mechanical behaviour of the tool requires accurate material behaviour models and material characterisation data.

## 1.4 Scope of the thesis

The primary objectives of this project are to

- Establish a methodology to analyse thermo-mechanical behaviour of a large industrial SPF tool (XN40F - 40% Ni, 20% Cr, Balance Fe) under realistic loading conditions using FE modeling, material characterization and testing.
- Identify and analyse tool failure mechanisms.
- Identify the factors affecting the tool life.
- Optimize process parameters to improve the tool life.
- Establish the SPF tool life prediction methodology

Secondary objectives to accomplish the primary objectives are; (i) establish temperature dependent cyclic plasticity and creep material data to model the cyclic elastic-plastic-creep thermo-mechanical behaviour of the tool material, (ii) identify material constants for material behaviour models and validate them against the experimental results, (iii) perform uniaxial isothermal and thermo-mechanical fatigue-creep and ratchetting lifing tests, (iv) perform thermal and thermo-mechanical FE analyses of a realistic 3D SPF tool under realistic loading conditions using the identified material behaviour constants, (v) identify stress-strain life equations from the lifing tests for different thermo-mechanical fatigue-creep life

prediction methodologies and (vi) develop a representative test, capturing the thermo-mechanical loading of the tool to estimate its life.

Chapter 2 provides a through background for research work presented in this thesis.

Chapter 3 describes the material testing carried out on the SS-316 stainless steel and the XN40F alloy. Isothermal multistrain-range cyclic tests for a range of temperatures are carried out to characterise the material for non-linear kinematic and combined non-linear kinematic/isotropic hardening material models. Stress relaxation tests are also performed on the XN40F alloy to identify creep constants for Norton's power law for secondary creep. Various thermo-mechanical fatigue (TMF)-creep and isothermal fatigue tests are carried out to obtain TMF and isothermal fatigue life data. Stress controlled isothermal and thermo-mechanical ratchetting tests are also carried out on the XN40F alloy to study its ratchetting behaviour.

Chapter 4 explains the identification and validation of material constants obtained for the material behaviour models such as combined non-linear kinematic hardening model for cyclic plasticity, power law creep model for secondary creep and the two-layer viscoplastic model. The identified constants are employed in material behaviour models and the predicted stress-strain loops are compared with the isothermal and thermo-mechanical fatigue-creep experimental loops.

Chapter 5 summarises the different thermo-mechanical fatigue-creep and ratchetting life prediction methodologies explored in this project. The stress-strain life equations are obtained from isothermal fatigue lifing test data for different life prediction

approaches. These equations are employed to predict TMF lives of various TMF and TMF-creep tests carried out.

Chapter 6 describes FE modelling of the SPF tool and the process. The FE modelling of the heat transfer process using calculated convective heat transfer coefficients is validated against the heat transfer tests that were carried out on a rectangular block of XN40F material at the University of Nottingham. The realistic SPF thermal cycles are simulated in the ABAQUS commercial FE package using the uncoupled heat transfer analysis. In addition to thermal loading, mechanical loading conditions such as tool gravity and clamping pressure during the forming cycle are employed in the thermo-mechanical FE models of the SPF tool. The tool-platen contact with friction is also modelled to employ the realistic boundary conditions.

Chapter 7 describes the results of numerous thermo-mechanical FE analyses of a representative BAE SPF tool. Sequentially coupled thermo-mechanical analyses are carried out to understand thermo-mechanical behaviour of the SPF tool. Two different material models; the uncoupled plasticity-creep and the two-layer viscoplasticity are employed separately to model the temperature dependent material behaviour. The predicted results by each model are analysed and compared. The stress-strain loops are plotted for the critical elements of the tool to investigate different failure mechanisms. The SPF tool life predictions are also performed by employing the FE predicted stress and strain in the experimentally obtained stress-strain-life equations using different life prediction methodologies. The predicted tool behaviour and tool lives are compared with the representative test and industrial

experience. Chapter 8 presents the conclusions of the thesis and the recommendations for future work.

Table 1.1 Mechanical properties of BAE Systems SPF tool material XN40F [13]

| Temperatures<br>°C | Young's<br>Modulus<br>GPa | 0.2% Yield<br>strength<br>MPa | UTS<br>MPa | Elongation<br>% |
|--------------------|---------------------------|-------------------------------|------------|-----------------|
| 20                 | 162                       | 215                           | 375        | 3               |
| 500                | 130                       | 140                           | 230        | 5               |
| 850                | 105                       | 110                           | 185        | 20              |
| 950                | 92                        | 75                            | 120        | 32              |

Table 1.2 Creep rupture strength of BAE Systems SPF tool material XN40F [13]

| Temperature<br>°C | Stress<br>MPa | Failure time<br>hour |
|-------------------|---------------|----------------------|
| 925               | 32            | 100                  |
| 925               | 24            | 1000                 |

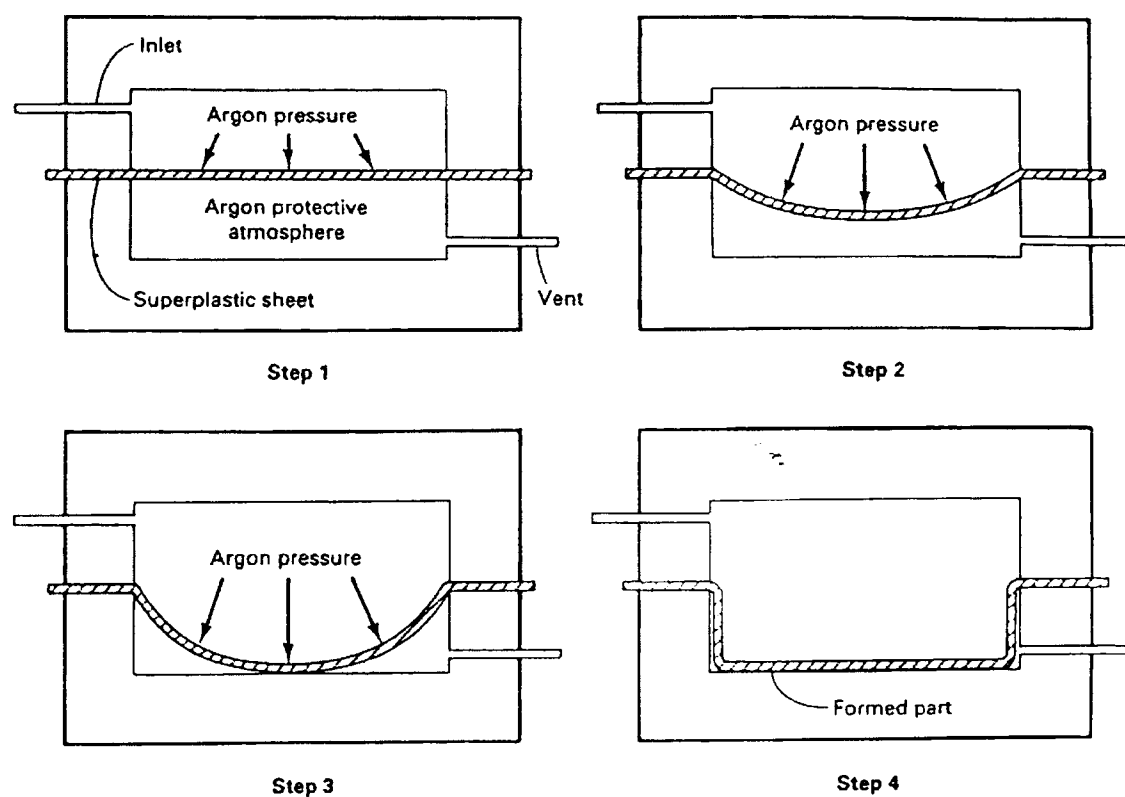


Figure 1.1 Schematic diagram of the superplastic forming process [1].

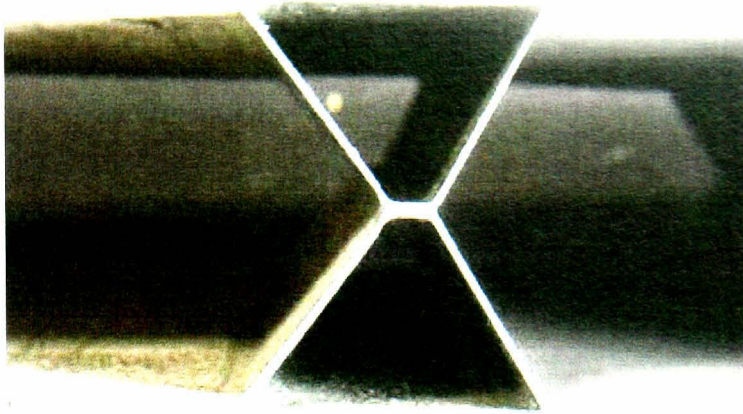


Figure 1.2 A segment of four sheet core configuration of SPF/DB Typhoon foreplane  
(Image BAE Systems) [5]



Figure 1.3 Wide-chord fan blade of an aero engine (Image Rolls Royce Plc) [5]

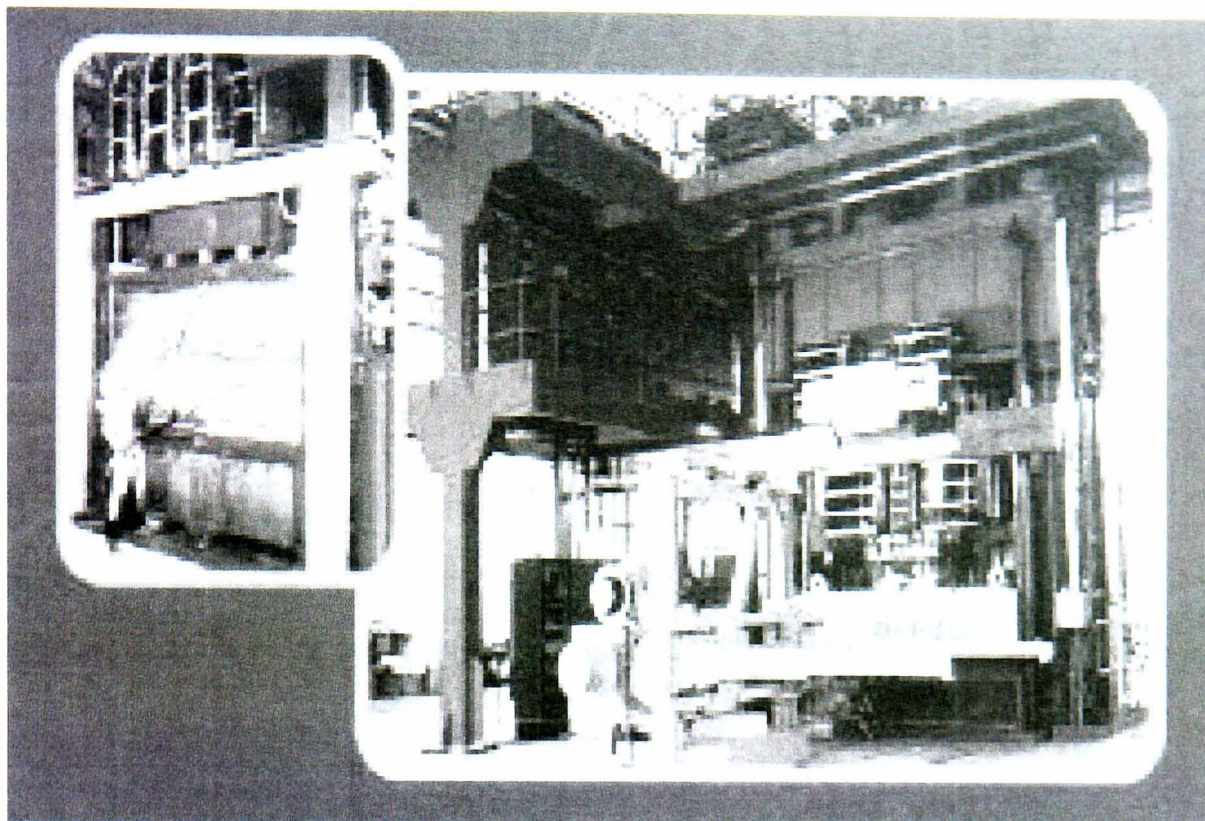


Figure 1.4 A modern SPF press with material handling equipment and a technician loading the blank sheet [7].

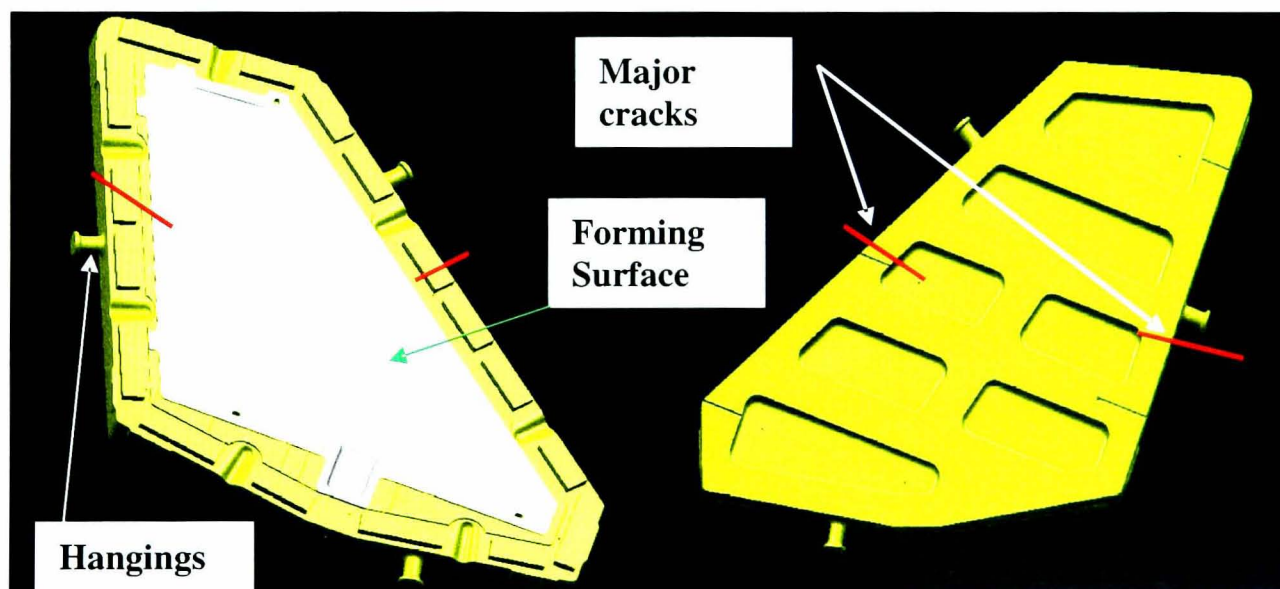


Figure 1.5 One half of a typical British Aerospace systems SPF tool (top and bottom views) [25].

## Chapter 2

### LITERATURE REVIEW

#### 2.1 Introduction

Superplastic forming is an important manufacturing process in the aerospace industry and is used to form many complex aircraft structures with tight tolerances. Superplastic forming tools need to withstand high temperature cyclic loading and steady mechanical loading for extended durations and therefore are manufactured from specialized alloys. Hence the cost of tool failure is significant and the tool life is an important limiting aspect in the SPF process. SPF tools may fail due to a combination of one or more modes of failure such as fatigue, creep, fatigue-creep interaction, ratchetting and oxidation.

In many engineering structures such as pressure vessels, nuclear reactors, gas turbines, aero engines and hot working tools such as forging and SPF, cyclic thermal loads are superimposed on sustained mechanical loads. Under such loading conditions, a structure experiences different responses such as elastic shakedown, plastic shakedown and ratchetting. In elastic shakedown, a structure shakes down to elastic behaviour after an initial elastic-plastic response and may fail after a finite number of cycles due to high cycle fatigue. Structural behaviour exhibiting stable reverse or alternating plasticity over each cycle is referred to as plastic shakedown. In plastic shakedown, the structure can be expected to fail due to low cycle fatigue. Alternatively, structural behaviour exhibiting an accumulation of (plastic) strain with each loading cycle is referred to as ratchetting and the structure may fail due to an

incremental plastic collapse. At high temperature the viscosity of the material and the time dependence of ratchetting becomes important and should be addressed for the safety of components [26]. At high temperature, creep and stress relaxation mechanisms are involved in the process along with thermal fatigue, which leads to complex creep-fatigue interaction.

## **2.1.1 Fatigue**

Under the application of repeated stress or strain cycles, a structure may fail at stresses below the tensile strength and often below the yield strength of the material. This mode of failure is called fatigue. Fatigue failure is divided into three regimes; crack initiation, crack propagation and final failure as shown in Fig. 2.1 [27]. There are two main types of fatigue failure: high cycle fatigue and low cycle fatigue.

### **2.1.1.a High cycle fatigue**

In case of high cycle fatigue, stresses are below the yield strength of the material and cycles to fracture are generally  $\geq 10^4$ . This is also called stress-controlled fatigue. According to Wohler [28], who initially investigated stress controlled cyclic loading effects on railroad wheel axles, the fatigue life of an axle increases with decreasing stress levels and it also appeared to have infinite life below a certain stress level. At the same time fatigue life was significantly reduced in the presence of a notch as shown in Fig. 2.2 [28].

Fatigue tests are generally performed by cycling the material either in tension-compression or in rotation and bending. The stress generally varies in sinusoidal form with time as shown in Fig. 2.3 [27].

From Fig. 2.3:

$$\Delta\sigma = \sigma_{\max} - \sigma_{\min}, \sigma_a = \frac{\sigma_{\max} - \sigma_{\min}}{2}, R = \frac{\sigma_{\min}}{\sigma_{\max}} \quad (2.1)$$

where  $\Delta\sigma$ ,  $\sigma_m$  and,  $\sigma_a$  are stress range, mean stress and stress amplitude respectively.

For high cycle fatigue, the fatigue life based on crack initiation can be determined by fitting the experimental data to the equation form given below (Fig. 2.4) [29].

$$\Delta\sigma N_f^a = C_1 \quad (2.2)$$

This empirical equation is called Basquin's law where  $a$  and  $C_1$  are constants and  $N_f$  is the number of cycles to failure.

#### 2.1.1.b Effect of mean stress on fatigue life

For completely reversible cycles ( $\sigma_m = 0$ ;  $R = -1$ ), the mean stress is zero. However, in realistic loading conditions, a non zero mean stress occurs and plays an important role in the evolution of a material's fatigue behaviour. Fatigue life decreases with increase in mean stress for a given stress amplitude [30]. Empirical relations were developed by Goodman, Gerber and Soderberg to incorporate mean stress effects on fatigue life. These relations are given below.

$$\text{Goodman equation } \sigma_a = \sigma_{\text{fat}} \left( 1 - \frac{\sigma_m}{\sigma_{\text{ts}}} \right) \quad (2.3)$$

$$\text{Gerber equation } \sigma_a = \sigma_{\text{fat}} \left( 1 - \left( \frac{\sigma_m}{\sigma_{\text{ts}}} \right)^2 \right) \quad (2.4)$$

$$\text{Soderberg equation } \sigma_a = \sigma_{\text{fat}} \left( 1 - \frac{\sigma_m}{\sigma_{\text{ys}}} \right) \quad (2.5)$$

where  $\sigma_a$  is the stress amplitude at  $\sigma_m \neq 0$ ,  $\sigma_{\text{fat}}$  is the fatigue strength in terms of stress amplitude when  $\sigma_m = 0$  and  $\sigma_{\text{ts}}$  and  $\sigma_{\text{ys}}$  are the tensile and the yield strength

of the material respectively. The above relations are shown in Fig. 2.5 [27]. Most of the materials give behaviour which lies between the Gerber and the Goodman lines.

### **2.1.1.c Low cycle fatigue**

Low cycle fatigue occurs when the stresses are above the yield strength of the material and cycles to fracture are generally  $\leq 10^4$ . This failure mode is also called strain controlled fatigue. Therefore low cycle fatigue damage occurs only when cyclic plastic strains are generated. Fig. 2.6 [29] shows the stabilized stress-strain hysteresis loop in the low cycle fatigue regime with a plastic strain range. The material hardens or softens under the application of cyclic loading and the material response changes until cyclic stability occurs.

For low cycle fatigue, Basquin's equation is not appropriate and therefore the empirical formula obtained by plotting the stabilized plastic strain range against number of cycles to failure (Fig. 2.7) was developed by Coffin and Manson to predict the low cycle fatigue life [29].

$$\Delta\epsilon^{pl} N_f^b = C_2 \quad (2.6)$$

where  $b$  and  $C_2$  are Coffin-Manson constants.

### **2.1.1.d Thermal fatigue**

The fatigue behaviour of materials is influenced by temperature, especially when the temperature is higher than half the melting point. The importance of high temperature fatigue arises because many components in the aerospace, automotive and power industries operate under high temperature conditions with high thermal gradients. This leads to the occurrence of cyclic plastic strains which incurs fatigue damage in the component. The temperature variations occurring during high

temperature operations of constructions and their components give rise to thermal stresses and strains, which usually result in crack initiation and growth, and final failure of highly stressed components is called thermal fatigue [31].

### **2.1.2 Creep**

Creep is a time dependent deformation of the material under the application of constant load or stress. It accelerates with increases in stress or temperature. Creep deformation in metals usually arises when the operating temperature is greater than  $0.4T_m$  where  $T_m$  is the absolute melting temperature of the material. The deformation due to creep and time to rupture depends on the operating temperature, applied stress and the material itself.

Creep deformation of a material is commonly studied by performing uniaxial tension or compression test where the strain history at constant temperature and stress is recorded until the specimen fails by rupture. Fig. 2.8 shows a typical creep curve which is divided into three regimes: primary, secondary and tertiary [31]. The creep curve shows initial elastic strain due to the applied load followed by primary creep in which the creep strain rate decreases due to material hardening. Primary creep is followed by a steady state or secondary creep in which strain increases steadily with time. Most materials spend a considerable fraction of their creep life in this regime. After secondary creep, the tertiary regime occurs in which the creep deformation accelerates due to material damage resulting in a rapid increase in strain rate followed by creep rupture.

Time dependent deformation at elevated temperatures also comprises creep recovery and stress relaxation phenomena. Creep recovery (Fig. 2.9) occurs when the stress is suddenly removed during the creep test where the part of the total strain is recovered in terms of instantaneous elastic strain and creep strain which later becomes asymptotic. Stress relaxation occurs when the strain is held constant. Creep strain replaces elastic strain and causes the stress to relax with time. Fundamental information about time dependent phenomena at elevated temperature is captured in the creep and relaxation curves [31].

### **2.1.3 Fatigue-creep interaction**

Fatigue-creep interaction occurs in high temperature cyclic loading. It is also called high temperature fatigue. At elevated temperature, creep and stress relaxation influence the fatigue process which leads to fatigue-creep interaction. In realistic loading cycles, deformation due to cyclic load and the creep deformation during hold times exist. Hold times during stress controlled cycling leads to creep deformation whereas hold time during strain controlled cycling causes stress relaxation. Fatigue-creep interaction during strain controlled cycling is shown in Fig. 2.10 [31]. From Fig 2.10, it can also be seen that the cyclic life for SS-304 stainless steel reduces with hold periods in the tensile part and there appears to be a saturation point beyond which not much change in life occurs. Similarly with stress controlled cycling, the hold period again reduces the life of SS-304 steel; however without any saturation point [31].

#### **2.1.4 Ratchetting**

An incremental plastic strain accumulation during each cycle which leads to unacceptable changes in the dimensions of the parts is called ratchetting. There could be incremental growth or shrinkage of the component depending upon the loading cycles. This phenomenon was first analysed by Miller [32] who studied the effect of a cyclic heat flux through the wall thickness of a pressure vessel subjected to sustained internal pressure. It was shown that an incremental growth will occur with each cycle of heat flux if the thermal strains and membrane stress resulting from pressure are sufficiently high. Later on Edmunds and Beer [33], Burgreen [34] and Bree [35] studied the ratchetting behaviour of structures under cyclic thermal and mechanical loadings. According to Bree [36], at elevated temperatures under certain loading combinations, only two types of responses are possible which are either elastic or some kind of ratchetting. Ratchetting can occur during the interaction between sustained tensile load and alternating bending load. It can also occur due to thermal cycling alone as a result of differential yield strength in the hot and cold regimes of the cycle.

The ratchetting phenomenon is also called cyclic creep. Benham, Ford and Coffin produced a typical curve of ratchetting strain against number of cycles up to the point of fracture (Fig. 2.11) [37, 38]. The curve is divided into three sections similar to the creep curve where the primary phase comprises the first few cycles in which the ratchetting rate is large and dropping. A secondary phase consists of a constant ratchetting rate and the tertiary phase comprises of large strain proceeding to rupture of the specimen [39].

Ratchetting appearing in material tests is called material ratchetting where a homogeneous distribution of stress is assumed in the structure (tension bars) [40]. Ratchetting which does not occur in material tests but requires inhomogeneous distribution of the stress is referred to as structural ratchetting [40].

Hubel [40] described various phenomena of plastic ratchetting and provided an overview of different features and types of ratchetting under cyclic loading below the creep range. The term ratchetting was described in several ways where structural analysts define ratchetting as an increase in strain by a constant amount in each loading cycle [40]. Material researchers described ratchetting as any accumulation of strain even if the rate of accumulation decreases and reaches a steady state after a finite number of cycles. This phenomenon was termed plastic shakedown or transient ratchetting [40]. The situation where the accumulation of strain is not bounded until the fracture is called infinite ratchetting. It was also stated by the author that the ratchetting (Progressive deformation) is said to occur when a structure is subjected to cyclic loading and the mean strain during one loading cycle changes from the previous loading cycle even at a single point in the structure. A stress-strain diagram of finite and infinite ratchetting under uniaxial stress controlled loading is shown in Fig. 2.12 [40]. The strain accumulation was shown by plotting mean strain  $\bar{\epsilon}$  versus number of cycles under the stress controlled loading. It is not possible to accumulate strain in strain controlled loading and therefore the ratchetting will then only be apparent in the strain controlled tests with changes in the mean stress from cycle to cycle [40].

## 2.2 Thermo-mechanical/isothermal fatigue

### 2.2.1 Introduction

Thermomechanical fatigue (TMF) is the combined damage mechanism caused by cyclic thermal and mechanical loading in which the fatigue-creep interaction commonly occurs. The TMF lives of materials are observed to be quite different from their isothermal fatigue lives. Thomas et al. [41] showed that for the same strain amplitude, the creep-fatigue damage of Inconel 738 material for temperature cycles of 500 to 850°C was more severe than for isothermal testing at 850°C. Similarly, for the nickel base superalloy MAR-M-200, Bill et al. [42] observed that TMF in phase; (IP) i.e. maximum strain in a cycle corresponds to maximum temperature lives, for temperature variations from 450 to 1000°C were significantly shorter than their isothermal counterparts. Therefore they concluded that the life time estimation for actual gas turbine components should be predicted using TMF rather than isothermal conditions.

Thermo-mechanical fatigue testing is crucial in the design and reliability of critical components used in the power generation, aerospace and automotive industries. Since the last decade, TMF testing has been a focus of attention where thermo-mechanical fatigue behaviour is compared against isothermal fatigue for various materials in high temperature applications. Previously isothermal fatigue tests were commonly used for thermo-mechanical loading conditions and life cycle management of critical components were carried out by applying a large factor of safety.

## 2.2.2 TMF and IF testing of high temperature materials

Liu et al. [43] investigated the TMF behaviour of a cast K417 nickel-based superalloy under in-phase (IP) and out of phase; (OP) i.e. maximum strain in a cycle corresponds to minimum temperature loading conditions in the temperature range of 400 to 850°C. Tests were carried out under total strain control ( $R_\epsilon=-1$ ) using the MTS 810 servo hydraulic TMF machine. The failure life of the specimen was defined as the number of cycles to promote specimen breakage or tensile stress drop to a quarter of the maximum value. A triangular waveform was used for both strain and temperature cycling for about 200 sec. Isothermal fatigue tests were also carried out at 850°C with the mechanical strain cycling of triangular waveform. The total strain during the TMF tests is given by

$$\Delta\epsilon_t = \Delta\epsilon_{mech} + \Delta\epsilon_{th} \quad (2.7)$$

where  $\Delta\epsilon_t$  is the total strain range,  $\Delta\epsilon_{mech}$  is the mechanical strain range and  $\Delta\epsilon_{th}$  is the thermal strain range. The thermal strain profile was set under zero load control before the testing. Mechanical strain is expressed as the addition of elastic and plastic strain ranges

$$\Delta\epsilon_{mech} = \Delta\epsilon_e + \Delta\epsilon_p \quad (2.8)$$

The strain at 400°C was negative (compressive) under IP TMF cycling and positive (tensile) during OP TMF cycling. The hysteresis loops are shown in the Fig. 2.13 and Tables 2.1 and 2.2 summarize the TMF experimental results under in-phase and out of phase testing [43].

In the case of an OP cycling, a tensile mean stress was observed and the mean stress decreased monotonically with increasing mechanical strain range. In the case of a IP cycling, a compressive mean stress was observed where the mean stress increased

and then reduced as applied mechanical strain range was increased. The TMF cyclic stress response was dependent on the strain range as well as the phase between temperature and strain (Fig. 2.14). The IF, TMF IP and OP stress-strain curves were found to be above the static tensile curve which suggested that the K417 alloy exhibits cyclic hardening during thermo-mechanical and isothermal fatigue. The hardening tendency under IF is higher than under TMF (Fig. 2.15). At the same strain amplitude, the fatigue life for the OP condition was longer than for IP and fatigue life for IF is longer than for IP and OP (Fig. 2.16) [43].

Shi et al. [44] studied the high temperature fatigue behaviour of TZM molybdenum alloy under mechanical and thermo-mechanical cyclic loads. High temperature isothermal mechanical fatigue and IP TMF tests were carried out using load control. The stress-strain response and fatigue life of the material were measured. In phase TMF tests with a temperature range of 350 to 500°C and isothermal fatigue tests at 350°C and 500°C were performed. The ratchetting phenomenon was observed during all of the tests with the hysteresis loops moving in the tensile direction with increasing creep rate, which is dependent on temperature and load amplitude (Fig.2.17) [44]. It was observed that the isothermal fatigue lives at 350°C are slightly higher than at 500°C. However, IP TMF life was lower than the IF lives and ratchetting occurred during the tests with an increasing creep rate [44].

Roth and Biermann [45] analyzed the thermo-mechanical fatigue behaviour of the  $\gamma$ -TiAl alloy TNB-V5 (Ti-45-Al-5Nb-0.2C-0.2B at. %) with the help of TMF and IF tests in the temperature range of 400 to 800°C under total strain control. Cyclic deformation, stress-strain loops and fatigue lives were evaluated for different strain-

temperature cycles. The results showed that the OP loading showed a high positive mean stress whereas IP loading showed a high negative mean stress. Also the OP fatigue lives were found to be shorter than the IP ones. This contradicts the TMF behaviour of a cast K417 nickel-based superalloy [43] where the OP lives are longer than the corresponding IP lives however the loading conditions were different for both the materials.

Similarly, Jiang et al. [95] worked on understanding the thermomechanical fatigue behaviour of Cr-Ni-Mo (with wt %, C-0.18, Cr-3.0, Mo-2.0, Ni-2.0, Balance Fe) cast hot work die steel. Stress controlled thermomechanical and isothermal fatigue tests were carried out using a closed loop electro-hydraulic machine with specimens heated by high frequency induction coil and cooled by compressed air. Infrared rays were used to measure the temperatures. For both TMF and IF conditions, the cyclic creep phenomenon was observed. The TMF tests gave the tensile cyclic creep and the IF tests showed compressive cyclic creep as shown in Fig. 2.18. Cyclic creep in the tensile direction is more damaging than in the compressive direction as the tensile cyclic creep increases the crack opening and accelerates the fatigue damage accumulation (Fig 2.19).

TMF IP and TMF OP tests were performed on a single crystal nickel based superalloy DD8 (Cr-15.61, Co-8.40, W-5.85, Al-3.91, Ti-3.98, Ta1.03 and balance Ni) by Liu et al. [96] under mechanical strain control with temperature variation from 450 to 900°C. Cyclic hardening and softening occurred within the first ten cycles and saturation was observed until failure of the specimen. The OP TMF life was found to be shorter than the IP TMF life at lower strain ranges. However the IP

life was shorter than the OP life at higher strain ranges (Fig. 2.20). This occurred due to the dominant creep deformation at high temperature and high strain range for IP loading.

Nagesha et al. [88] studied the thermo-mechanical fatigue behaviour of nitrogen alloyed type 316L austenitic stainless steel under different temperature regimes. A few TMF tests were also carried out in vacuum to analyse environmental effect on life. Creep and oxidation were observed to be important mechanisms in the damage under IP cycling when the peak temperature and peak stress are in the creep range (above 600°C). Isothermal cycling at the peak temperature of TMF showed lower lives than the IP and OP cycling. However, the difference in isothermal and TMF life decreases with increase in peak temperature of TMF cycling. It was also observed that the testing under vacuum resulted in an increase in life significantly for OP cycling [88].

### **2.2.3 Effect of hold time period in high temperature cyclic loading**

High temperature low cycle fatigue (LCF) is always influenced by time dependent processes such as creep, oxidation, phase transformations and dynamic strain ageing (DSA). Mannan and Valsan [46] discussed the high temperature LCF behaviour of 316L (N) stainless steel and modified 9 Cr-1Mo steel and their welds. DSA was observed to increase the stress response and reduce ductility. High temperature oxidation was observed to accelerate fatigue cracking in modified 9Cr-1Mo steel. TMF tests were performed on 316L (N) and lives under out of phase cycling were found to be lower than in-phase cycling in the low temperature conditions, whereas

at higher temperatures, in-phase life was found to be lower than the out of phase life. Creep was found to be the dominant factor during high temperature regime [46].

The effect of hold time was quantified by applying strain hold at the peak strain in tension/compression. The hold time caused the stress to relax and creep-fatigue interaction was observed. The creep-fatigue lives of the 316(N) base metal, 316 weld metal and a 316L (N)/316 weld joint as a function of length of hold time is shown in Fig. 2.21. It was observed that the effect of hold time is dependent on the position as well as duration of hold time. At lower strain rates and long holding periods at high temperatures, oxidation was found to influence the fatigue life. Isothermal tests conducted at peak temperatures of TMF cycling showed a lower life than TMF tests. TMF damage was influenced by creep as extensive intergranular cracking occurred during 400-650°C IP test [46]. Tensile hold was observed to be more damaging than the compressive hold. Compared to continuous cycling, the imposition of hold period was found to decrease the fatigue life.

Under some specific working conditions, high temperature materials used in gas turbine engines and power plants are subjected to OP TMF. Zhou et al. [47] investigated OP TMF of two nickel based single crystal superalloys, TMS-75 and TMS-82+, used in gas turbine blades and vanes for power plants and aero engines. The temperature was cycled between 400 and 900°C in OP waveform with hold time in compression (Fig. 2.22). Experimental results showed that the TMF property of TMS-82+ is better with a hold time than without a hold time (Table 2.3). It suggested that the TMS-82+ showed a greater stress relaxation resistance at 900°C and a

greater tensile strength at 400°C than TMS-75, which led to a smaller plastic strain in tension and a longer rupture life for TMS-82+ with hold time periods in the cycle.

## **2.3 Low cycle fatigue and ratchetting**

The damage mechanism under the LCF regime which leads to the accumulation of inelastic strain in the presence of non zero mean stress is called ratchetting which increases fatigue damage and shortens the life of engineering components [48]. According to Weiß et al. [49] in LCF, ratchetting is a secondary phenomenon of cyclic plasticity which can accelerate the fatigue damage or can act as a failure mechanism itself.

### **2.3.1 Interaction of LCF and ratchetting**

Kapoor [39] evaluated damage mechanisms for ductile metals under cyclic loading. Experiments were carried out on thin tubular copper specimens with strain cycles similar to those under rolling or sliding contact. It was observed that the failure takes place by LCF when a strain cycle is closed. On the other hand with an open strain cycle, failure was observed to occur by ratchetting with accumulation of plastic strain reaching the critical value of strain, comparable to failure strain under monotonic tension test. According to Kapoor [39], LCF and ratchetting are independent and competitive mechanisms and the failure occurring by either of them leads to a shorter life. Kapoor reassessed the results of uniaxial and biaxial tests reported in the literature along with new data from bi-axial tests on copper and found the results to be in agreement with the above hypothesis. The number of cycles to failure by LCF

was given by the Coffin-Manson equation whereas the ratchetting life was given by a ductility exhaustion approach [39].

Rider et al. [50] analysed fatigue-ratchetting interactions for low carbon steel (En3) and low alloy steel (En19). Thin walled tubular specimens were subjected to a range of constant twist amplitude in combination with a range of axial loads. The experiments were carried out to investigate the influence of accumulation of ratchet strain on fatigue life. It was concluded that the specimen life was not controlled by ratchet strain accumulation however the life was mainly controlled by fatigue crack growth [50].

Kang and Liu [51] showed that the ratchetting and fatigue failure behaviours of annealed and tempered 42CrMo steel were different from each other due to different cyclic hardening and softening feature resulted from heat treatments. The important observations from this work were the ratchetting strain increases monotonically with mean nominal stress and the nominal stress amplitude. It was also seen that the effect of stress amplitude on ratchetting was greater than the mean stress. When the applied nominal stress level is relatively low, the failure of the material is mainly controlled by the low-cycle fatigue with constant strain amplitude whereas with high nominal stress; the material fails due to ratchetting. The fatigue life in cyclic stressing is lower than in cyclic straining due to ratchetting strain produced under the cyclic stressing [51].

Kang et al. [52] analysed the multiaxial ratchetting-fatigue interactions of annealed and tempered 42CrMo steels. Proportional and non-proportional multiaxial stress and

strain controlled cyclic loading tests were performed on 42CrMo steel. The effect of mean stress, stress amplitude and loading path was evaluated through a set of experiments. The key experimental observations from this paper were (i) the fatigue life in non-proportional multiaxial strain cycling is lower than that in the proportional one and all multiaxial fatigue lives are shorter than the corresponding uniaxial lives and (ii) that the fatigue life of multiaxial stress cycling is lower than that in strain cycling for the same strain amplitude due to the occurrence of ratchetting and (iii) that multiaxial ratchetting-fatigue interaction should be taken into account while predicting the fatigue life in the stress cycling with non-zero mean stress.

Satyadevi et al. [53] proposed a failure criterion for materials exhibiting ratchetting during very low cycle fatigue (VLCF) based on stress control. The failure criterion proposed was based on the initiation of plastic instability. It was proposed that when the true stress in the specimen during ratchetting reaches the true ultimate strength of the material, the specimen fails due to initiation of plastic instability. The proposed model was validated by experimental observations made from stress controlled VLCF tests with tensile mean stresses and different combinations of fatigue loading.

### **2.3.2 Mechanisms of material ratchetting**

In the case of isotropic hardening, cyclic yield strength increases with the number of cycles (expansion of the yield surface without translation) which leads to an increase in mean strain under stress controlled loading. However in real materials, isotropic hardening does not carry on after finite number of cycles [40].

In the presence of mean stress (  $\sigma_{\min} \neq -\sigma_{\max}$  ) and stress controlled loading, strain may accumulate during each cycle [54]. This can occur even if unloading produces only elastic strains and reloading provides plastic strains (Fig. 2.23) [40]. Material models incorporate mean stress effect by introducing restraint on the movement of yield surface or by applying dynamic recovery term in the evolution law of kinematic hardening [55].

Under temperature dependent inelastic material properties, a temperature path history may cause ratchetting if the material responds slowly under isothermal conditions at a given temperature following inelastic forays at other temperatures [56, 57]. Strength differential phenomenon is observed if the yield strength in tension is different from yield strength in compression. This effect leads to ratchetting, which may be infinite, even if the material hardens kinematically [40].

Non-proportional loading in which stress components do not change proportionally may lead to ratchetting. From Fig. 2.24, the strain increments at maximum and minimum values of the loading cycle have a common component normal to the loading path and produces an increase in strain in the same direction with each cycle [40]. According to Hubel [40], this ratchetting mechanism is incorporated by all material models. Ratchetting will be infinite with no hardening or with isotropic hardening, provided the stress range is large enough to exceed the Von Mises circle. In the case of kinematic hardening, strain accumulation gradually slows down depending on the load level and material parameters [40].

### 2.3.3 Structural ratchetting

This type of ratchetting occurs due to in-homogeneity of the state of stress in a structure [40]. This type of ratchetting can be assessed by simplified inelastic methods or by detailed inelastic analyses. The interaction diagrams established by Bree [35] were based on constant primary stress  $\sigma_p$  and maximum secondary stress  $\sigma_s$ , which were normalized to the yield stress. Elastic-perfectly plastic material models used in simplified inelastic analyses of structure predicts infinite ratchetting. Alternatively, if hardening is involved, elastic or plastic shakedown may eventually occur after a finite number of cycles leading to finite ratchetting [40].

Among several types of ratchetting, Bree type ratchetting was predicted by several researchers addressing different engineering structural problems where the ratchet strain occurs in the combination of steady primary stress and cyclic secondary stress. Du Preez [58] studied the effect of thermal stresses and steady primary stresses on ratchetting in reactor vessels and investigated the stresses caused by localized hot spots in the shell of a reactor vessel using finite element analysis. Elastic-plastic analyses were performed using temperature dependent material properties and a linear kinematic hardening model with a constant hardening slope. The author assessed the occurrence of ratchetting based on Bree diagram as shown in Fig. 2.25. The Bree diagram proposed that the certain combination of stresses such as steady mechanical (primary) stresses and cyclic thermal (secondary) stresses causes incremental growth of strain per cycle. This incremental growth of strains may lead to distortion or fracture unless the accumulated strain is kept below the acceptable limits [58].

Hyde [59] analysed the effect of transverse pressure loading on thermal ratchetting of circular plates. A temperature independent elastic-perfectly plastic material model was used for lead alloy at room temperature 20°C. The results were compared with the Miller-Bree uniaxial model where bi-axial loading was simplified into uniaxial by neglecting the axial stress in the reactor vessels [32, 35]. According to Hyde [59], the Miller-Bree uniaxial model accurately predicts the ratchetting boundaries but gives inaccurate radial and hoop ratchet strains. To predict transverse deflections accurately, a complete inelastic finite element analysis is required [59].

#### **2.3.4 Time dependent ratchetting**

According to Kang et al. [26], the ratchetting behaviour is influenced by many factors such as temperature, loading history, loading path, loading rate and so on. For high temperature application, temperature is a key factor as the viscosity of the material and its effect on time dependent ratchetting plays an important role in the failure mechanism and which needs to be addressed carefully.

Kang et al. [26] studied the time dependent ratchetting by performing time dependent uniaxial/multiaxial cyclic loading tests on SS-304 stainless steel at room and elevated temperatures. The effects of loading rates, peak/valley stress and strain holds, and non-proportional loading paths on the low cycle fatigue and ratchetting behaviour of the material were discussed. It was observed that the different stress response occurred for different strain rate; hold time, load cycle and loading paths. Stress amplitude increased with increase in strain rate and decreased with increase in hold time. The ratchetting strain occurred at slow stressing rate or with peak/valley stress hold period was larger than at fast stressing rate and without hold periods. The large

ratchetting strain resulted from large creep strain produced during the hold or at slow stressing rate. A multiaxial ratchetting strain was less than the corresponding uniaxial ratchetting strain due to non-proportional additional hardening. Also the effect of hold period on multiaxial ratchetting was not greater than uniaxial [26]. This implies that creep deformation plays a crucial role in the ratchetting behaviour of materials.

## **2.4 Material behaviour modelling**

### **2.4.1 Introduction**

Finite element simulation requires constitutive models to be able to depict the macroscopic behaviour of materials accurately. The macroscopic approach allows the development of material behaviour laws from appropriate low cycle fatigue testing and can reproduce complex thermo-mechanical and non proportional cyclic loadings. Macroscopic or phenomenological models for cyclic loading commonly employ two additional components; back and drag stresses, describing the cyclic hardening and softening of material behaviour [60]. Additional effects such as stress relaxation during the dwell time can be included in models taking into account the static and thermal recovery.

Prager, Armstrong-Frederick and Chaboche developed classical constitutive equations for simulating material behaviour under cyclic loading. The invention of these models was mainly driven by the needs of the aeronautical and nuclear industries. Time independent cyclic plasticity deformation was reasonably addressed by various classical rules such as isotropic, non linear kinematic and combined isotropic/kinematic hardening [61].

In high temperature cyclic loading, time dependent deformation is influenced by viscous effects, which occur simultaneously with time-independent deformation. In order to consider the plastic and viscous behaviour at low and high temperatures, elastic-viscoplastic material models have been developed [55, 62]. Phenomenological unified elasto-viscoplastic models based on internal state variables are used for modelling the macroscopic behaviour of materials [63]. The Chaboche unified viscoplastic model provides a coupled viscous-plastic dissipation mechanism to model the material behaviour for a range of temperatures. However, the uncoupled plasticity-creep approach was also considered by many researchers such as Hossein Mahbadi et al. [73], Kawashima et al. [74], Shang et al. [16] due to its simplicity, where at lower temperatures and higher strain rates, material behaviour is modelled using the cyclic plasticity laws and at high temperature, creep behaviour was modelled by time dependent equations such as Norton's power law. This approach can give a reasonable agreement with experimental results for specific materials under specific loading conditions.

In the last two decades, various advanced material models were developed based on classical material models to take into account elastoviscoplasticity and creep-fatigue-interaction in the damage process. Constitutive models for ratchetting deformation were also formulated and verified. However, they were limited to specific applications. Many researchers such as Chaboche [64], Ohno and Wang [65] Ohno and Wang [66], Bari and Hassan [67], Yaguchi and Takahashi [68] and Kan et al. [69] have worked on improving the modelling of uniaxial-multiaxial and time dependent ratchetting for various different materials.

According to Kang [112], many phenomenological constitutive models were built by many researchers to simulate uniaxial and non-proportional multiaxial ratchetting of materials at room and elevated temperatures with reasonable accuracy by modifying the dynamic recovery term of the Armstrong-Frederick non-linear kinematic hardening rule. However due to complexity of ratchetting, the prediction capability of the proposed models is limited to specific cases based on macroscopic experimental results. Also these proposed models require many material parameters which limit its engineering applications. Therefore, Kang [112] suggested that the simplification of the proposed models with fewer material parameters should be a focus for future work.

#### **2.4.2 Cyclic plasticity**

Bernhart et al. [61] studied the high temperature low cycle fatigue behaviour of 55NiCrMoV8 martensitic forging tool steel. Isothermal tests were carried out on in the range of 200 to 550°C. The elasto-plastic non linear kinematic and isotropic hardening model constants were identified using isothermal tests. A strain path history variable was introduced to evaluate the dependence between the total strain amplitude and extent of material softening. Material parameter identification methodology was discussed and the model was validated by comparing experimental and predicted hysteresis loops during symmetrical and non symmetrical total strain LCF testing [61].

Zhang et al. [63] worked on modelling of anisothermal cyclic plasticity of martensitic steels. Tempered martensitic steel (X38CrMoV5) was investigated under isothermal and thermomechanical fatigue conditions. The model was devised

considering the theory of irreversible processes on the basis of experimental characteristics observed in isothermal fatigue. A cyclic anisothermal elasto-viscoplastic constitutive model with kinematic hardening, Bauschinger effect, continuous cyclic softening, strain rate dependence and plastic strain memorization was developed. A numerical computer program (TEVP: Thermo-elasto-viscoplastic) was developed in FORTRAN to compare the model with the experimental results. Two back stresses were applied in constitutive model to describe non saturating softening feature of such steels. TMF tests (temperature range 300-500°C) were carried out to plot hysteresis loops over a few hundreds of cycles to support the validation of anisothermal constitutive model [63]. The model showed a small discrepancy in the tensile part of the TMF IP loops where the model predicted a maximum stress for lower strain values than experimental results. Larger discrepancies were observed in stress-strain loops of the TMF OP tests.

Lee et al. [70] predicted ratchetting behaviour of 304 SS cylindrical shell using the Chaboche combined non-linear kinematic-isotropic hardening model implemented as an ABAQUS user subroutine UMAT. A thin wall cylinder under axially moving temperature distribution was studied numerically. Plastic ratchetting was predicted and the validity of the user subroutine was verified with the exact solutions of uniaxial loading cases and test results available in the literature for the cylinder. The effects of creep and relaxation were not considered in the model which is essential for creep ratchetting analysis. It was shown that the elastic-plastic analysis using the Chaboche constitutive theory is able to predict the ratchetting behaviour under secondary cyclic loads i.e. thermal stresses due to axially moving temperature

distribution. However, more than 50% error was observed on predicted cylinder expansion against the experimental results [70].

Weiβ et al. [49] studied the evolution of combined ratchetting and low cycle fatigue failure mechanisms in welded and non-welded pressure vessel components using the non-linear kinematic model of Ohno and Wang [65, 66]. A local strain approach with ratchetting evaluation using the above model was proposed. The evolution law of kinematic hardening with a variable back stress ( $\alpha_{ij}$ ), which is a function of plastic strain increment  $d\varepsilon_{ij}^{pl}$  and the equivalent plastic strain  $dp$  and the material constants  $c_1$  and  $c_2$  based on Armstrong and Frederick model was as follows [62]:

$$d\alpha_{ij} = c_1 d\varepsilon_{ij}^{pl} - c_2 \alpha_{ij} dp \quad (2.9)$$

Ohno and Wang [66] used the additive composition of total back stress  $\alpha_{ij}$  by  $M$  separate components  $\alpha_{ij}^{(k)}$  postulated by Chaboche [62]

$$\alpha_{ij} = \sum_{k=1}^M \alpha_{ij}^{(k)} \quad (2.10)$$

The same evolution equation as eq. (2.9) was used for each component  $\alpha_{ij}^{(k)}$  as follows:

$$d\alpha_{ij}^{(k)} = c_1^{(k)} d\varepsilon_{ij}^{pl} - c_2^{(k)} \alpha_{ij}^{(k)} dp \quad (2.11)$$

Ohno and Wang applied a threshold  $\bar{\alpha}^{(k)}$  for each component into the final term of equation 2.11 for its activation. This improves the simulation of ratchetting [49]. The modified evolution equation with the accumulated plastic strain increment results in

$$d\alpha_{ij}^{(k)} = h^{(k)} \left[ \frac{2}{3} d\varepsilon_{ij}^{pl} - \left( \frac{\bar{\alpha}^{(k)}}{r^{(k)}} \right)^{m^{(k)}} \frac{\alpha_{ij}^{(k)}}{r^{(k)}} dp \right] \quad (2.12)$$

$$\text{with } \bar{\alpha}^{(k)} = \sqrt{\left( \frac{3}{2} \alpha_{ij}^{(k)} : \alpha_{ij}^{(k)} \right)} \quad (2.13)$$

where  $h^{(k)}, r^{(k)}$  are parameters of the Ohno-Wang model. The material parameters  $h^{(k)}$  and  $r^{(k)}$  can be identified from the uniaxial stress-strain curve.

According to Weiß et al.[49], a non-linear activation of the dynamic recovery term from the Ohno-Wang model improves the simulation of ratchetting. The material parameter  $m^{(k)}$  controls the non-linearity of ratchetting. For  $m^{(k)} = \infty$ , a closed stress-strain loop (no ratchetting) is predicted and for  $m^{(k)} = 1$ , the equation 2.11 is turned into the Chaboche enhanced non-linear kinematic hardening model [49].

Kramer et al. [71] investigated the ratchetting behaviour of austenitic pipes using a non-linear kinematic hardening with superimposed isotropic cyclic hardening. Uniaxial monotonic and cyclic loading tests with and without zero mean stress were performed for characterizing the material parameters. The material model used a set of 13 parameters and was based on the Armstrong -Frederick and Chaboche constitutive theories (hence abbreviated as AFC model), implemented in an ABAQUS UMAT subroutine. Uniaxial tests with non zero mean stresses are required to describe ratchetting under multiaxial stress conditions. Reverse bending tests were performed at room temperature with and without internal pressure on austenitic pipes. Ratchetting was observed under internal pressure in the circumferential direction [71]. It was observed that the model over estimated the ratchet strains when uniaxial non zero mean stress tests were not considered for

identifying the constitutive parameters. When non zero mean stress tests were additionally considered in the parameter evolution, the predicted ratchetting behaviour was in good agreement with the experimental data [71].

Kulkarni et al. [72] also studied the ratchetting behaviour of piping materials such as SA-333 grade 6 carbon steel and SS-304 stainless steel through experiments and analysis. The authors evaluated the Chaboche kinematic hardening model to predict the ratchetting behaviour for uniaxial and biaxial loading histories. The parameters of the model were identified from the uniaxial strain controlled stabilized hysteresis loops.

The non-linear kinematic hardening model proposed by Chaboche was applied with incorporation of three Armstrong-Frederick kinematic hardening variables. The evolution equation for the back stress,  $\alpha$  proposed by Armstrong and Frederick is:

$$\dot{\alpha} = \frac{2}{3} C \dot{\epsilon}^P + \gamma \alpha \dot{p} \quad (2.14)$$

where  $\gamma$  is the recall term which incorporates the fading memory of strain path and makes the rule non-linear and  $C$  is the hardening modulus. The three decomposed rules of the Chaboche model were given by superposing the back stress term in equation 2.15.

$$\{\alpha\} = \sum_{i=1}^3 \{\alpha\}_i \quad (2.15)$$

The evolution of back stress for each decomposed rule was given by

$$\{\dot{\alpha}\}_i = \frac{2}{3} C_i \{\dot{\epsilon}^P\} + \gamma_i \{\alpha\}_i \dot{p} \quad (2.16)$$

The three decomposed rules divide the hysteresis loop into three parts where the first rule  $\alpha_1$  should correspond to the initial steep part of the stable stress-strain curve with a very large modulus, the second rule  $\alpha_2$  should correspond to the transient hardening portion of the stable loop and the third rule  $\alpha_3$  should depict the linear part of the loop at high strain values. The values of parameters  $C$  and  $\gamma_{i=1,2}$  were identified from uniaxial strain controlled tests whereas the parameter  $\gamma_3$  was determined from uniaxial ratchetting experiments to produce the best possible fit. The performance of the Chaboche model was evaluated by comparing the predicted results with experiments as shown in Figs 2.26 and 2.27. From Fig. 2.27, for the value of  $\gamma_3 = 0$ , ratchetting saturated completely and shakedown was predicted. Alternatively,  $\gamma_3 = 9$  showed a good agreement with both the strain controlled stabilized loop from Fig. 2.26 and the stress controlled ratchetting experiment shown in Fig. 2.27 [72].

### 2.4.3 Uncoupled elastoplasticity-creep

Mahbadi and Eslami [73] investigated elastic-plastic-creep cyclic loading of a thick pressure vessel based on the Frederick-Armstrong kinematic hardening model. Prager model was modified by Frederick and Armstrong so that the transformation of yield surface in the stress space is different during loading and unloading. Therefore a different hardening modulus in loading and unloading conditions was assumed.

The Von-Mises yield criterion was written in the form as follows.

$$f(\sigma_{ij} - \alpha_{ij}) = \left[ \frac{3}{2} (s_{ij} - \alpha_{ij})(s_{ij} - \alpha_{ij}) \right]^{1/2} = \sigma_0 \quad (2.17)$$

Where  $\sigma_{ij}$  and  $\alpha_{ij}$  are the stress and back stress tensors, and  $s_{ij}$  and  $\alpha_{ij}$  are the stress and back-stress deviatoric tensors in the stress space and the flow rule for Armstrong and Frederick kinematic hardening model is

$$d\varepsilon_{ij}^p = \frac{3dp}{2\sigma_0} (s_{ij} - \alpha_{ij}) \quad (2.18)$$

where  $\varepsilon_{ij}^p$  is the plastic strain.

Steady state creep was employed to analyse the creep deformation of the vessels. Mechanical and thermal loads were employed for the analyses of pressure vessels and creep was considered at elevated temperatures. When creep was considered, the Frederick-Armstrong model predicted ratchetting for the stress controlled cyclic loading, and predicted reverse plasticity for the strain controlled cyclic loading [73].

Kawashima et al. [74] studied the ratchetting deformation of 316 steel under the creep-plasticity interaction. A simple estimation of the accumulation of ratchet strain was proposed by using uncoupled plasticity-creep approach where experimental data at a very high strain rate was used for plasticity analysis and steady creep rate calculated by Norton's equation was superimposed on it. Even if the plasticity and creep are separated and experimental test data is used to avoid plasticity analysis, the calculated results showed good agreement with experimental results as shown in Fig.2.28 [74].

#### **2.4.4 Elasto-viscoplasticity**

Bernhart et al. [15] applied the Chaboche unified elastic-viscoplastic material behaviour model for modelling the thermo-mechanical behaviour of a simple

axisymmetric SPF die for assumed steady state thermal conditions. The material model was verified against high temperature anisothermal uniaxial cyclic tests and showed good agreement with the experimental stress-strain loops. However no hold periods (representing forming cycles) were applied in cyclic tests and therefore long term static recovery effects were not addressed during the model verification.

Charkaluk et al. [101] studied the fatigue design of a cast iron exhaust manifold under thermo-mechanical loadings where two material models were applied to compute the stress-strain behaviour under thermo-mechanical loadings; one was the classical unified viscoplastic model with linear kinematic hardening and the other one was the two layer visco-plastic model where the stress is partitioned into viscous and plastic components. The temperature dependent material parameters were determined from isothermal tension-compression and relaxation tests and were linearly extrapolated over a range of temperatures. This hypothesis was verified against LCF tests and showed a reasonable agreement. Charkaluk et al. [101] proposed a global approach to design structures under thermo-mechanical loading which was based on a 3D thermal computation, an elasto viscoplastic constitutive model and the dissipated energy per cycle as a damage indicator. It was stated that the problems regarding the choice of simple constitutive models and their effect on 3D structural computation of structures in the TMF context are still unresolved.

A two-layer viscoplastic model was also used for modelling behaviour of polymers. A two-layer viscoplastic model was used comprising elastic-plastic network in parallel with elastic viscous network based on the Maxwell model. This model is in-built in the ABAQUS commercial FE software and is argued to be capable of

modelling materials in which significant time dependent behaviour as well as plasticity occurs. Solasi et al. [75] employed this model to analyse polyelectrolyte membranes in fuel cells. Earlier Kichenin and Dang [115] applied this model to account for non-linear visco-elasticity of bulk medium density polyethylene.

Kan et al. [69] argued that the unified viscoplastic models can simulate the time dependent ratchetting at room temperature but are incapable of simulating time-dependent ratchetting at high temperatures, such as 700°C, due to lack of a static recovery term in the viscoplastic flow rule to describe the high viscous effects. The static recovery occurs in long-term stress relaxation and steady state creep rates. A new unified viscoplastic model was proposed with a static recovery term used to describe the significant time dependence of ratchetting of SS-304 stainless steel especially at high temperatures[69]. The kinematic hardening rule adopted is the same as the Abdel-Karim-Ohno model. The back stress equation for the proposed model is

$$\alpha = \sum_{i=1}^M r_i b_i \quad (2.19)$$

where  $\alpha$  is the total back stress divided into M components denoted as the product  $r_i b_i$ . The critical state of dynamic recovery is reflected by a surface

$$f_i = \bar{\alpha}_i^2 - r_i^2 = 0 \quad (2.20)$$

where  $\bar{\alpha}_i = \sqrt{\left(\frac{3}{2} \alpha_i : \alpha_i\right)}$  is the equivalent back stress and  $r_i$  is the radius of the critical surface.

The back stress evolution equation with static recovery term is:

$$\dot{b}_i = \frac{2}{3} \xi_i \dot{\epsilon}^{\text{in}} - \xi_i \left[ \mu_i \dot{p} + H(f_i) < \dot{\epsilon}^{\text{in}} : \frac{\alpha_i}{\bar{\alpha}_i} - \mu_i \dot{p} > \right] b_i - \chi(\bar{\alpha}_i)^{m-1} b_i \quad (2.21)$$

where  $\xi_i$  and  $r_i$  are temperature dependent material parameters,  $(:)$  specifies the inner product between second rank tensors;  $H(f_i)$  is the Heaviside function where if  $f_i \geq 0$ ,  $H(f_i) = 1$  and if  $f_i \leq 0$ ,  $H(f_i) = 0$ .

$\mu_i$  is the ratchetting parameter which allows Equation 2.21 to represent slight opening of the hysteresis loop (ratchetting), if  $0 < \mu_i \ll 1$ .  $\mu_i$  is identical for all the parts of the back stress and is determined by trial and error from uniaxial ratchetting test results [69]. The static recovery term  $\chi(\bar{\alpha}_i)^{m-1} b_i$  was applied to simulate the static recovery effect of the material produced in peak/valley stress hold and at high temperature. The parameters  $m$  and  $\chi$  were used to control the degree of static recovery and were assumed to be temperature dependent. The proposed model was implemented in ABAQUS and verified by numerical samples. The simulated results were in reasonable correlation with the experimental results. However the simulated hysteresis loops at 700°C were wider than the experiments, shown in Fig. 2.29.

## 2.5 TMF life prediction method

### 2.5.1 Introduction

Accurate TMF life prediction for high temperature critical components requires advanced life modelling techniques. A number of damage models have been proposed by many researchers to take into account complex TMF damage involving creep-fatigue interaction. TMF life can be predicted based on crack initiation as well as crack propagation models. Damage, stress, strain and energy based criteria were

used in predicting TMF lives. The advanced models need a number of different variables and associated parameters in the life equations to characterize the primary damage mechanism [76]. The required variables used in life equations are generally identified from stabilized cycles. The variables comprise of elastic, inelastic, and total strain ranges as well as dissipated energy, frequency, hold time, mean stress and strain rate [77]. Well known and advanced TMF models include the damage summation model [78], the frequency separation model [79], ductility exhaustion [80], strain range partitioning [81],[82]. These models were applied by many researchers around the globe for various different materials and applications. However, according to Zhuang and Swansson [76], who carried out a critical review on TMF life prediction, all the above models are capable of predicting TMF life with a reasonable accuracy for certain groups of materials and test conditions. However no model can consistently predict life accurately for all materials under numerous service conditions.

### 2.5.2 Life prediction models

Liu et al. [43] carried out thermo-mechanical fatigue life calculations based on the Ostergren strain energy method [83] and the Coffin-Manson pure inelastic strain method [84]. The Ostergren equation is given as

$$C = N_f^\beta \Delta \epsilon_p \sigma_T \quad (2.22)$$

where  $C$  and  $\beta$  are material constants,  $\sigma_T$  is the maximum stress in the cycle, and  $\Delta \epsilon_p$  and  $N_f$  are plastic strain range and the number of cycles to failure respectively.

The Coffin-Manson strain life is

$$\frac{\Delta \epsilon_p}{2} = \epsilon_f' (2N_f)^c \quad (2.23)$$

where  $\frac{\Delta \epsilon_p}{2}$  is the plastic strain amplitude  $\epsilon'_f$  is the fatigue ductility coefficient and  $c$  is the fatigue ductility exponent. Fig. 2.30 shows the correlation between predicted and observed life under TMF by the Ostergren and Coffin-Manson equation. Fig. 2.30 suggests that the TMF fatigue life is dependent upon both stress and strain rather than pure inelastic strain range and hence the Ostergren energy approach gave a better fatigue life prediction than the Coffin-Manson pure inelastic strain method [43].

Roth and Biermann [45] determined TMF lives using the Smith-Watson Topper damage parameter. The damage parameter  $P_{SWT}$  [85], takes the mean stress into account and was applied for general life prediction of TMF test results as follows:

$$P_{SWT} = \sqrt{\sigma_{\max}} \epsilon_a E \quad (2.24)$$

where,  $\sigma_{\max}$  is the maximum tensile stress,  $\epsilon_a$  is mechanical strain amplitude and  $E$  is the Young's modulus.  $P_{SWT}$  was plotted in a double logarithmic diagram versus the fatigue life for TMF tests on TNB-V5 material under various mechanical strain amplitudes, different temperature ranges and temperature strain cycles shown in Fig. 2.31.  $P_{SWT}$  shows a reasonable correlation against life for a general life prediction [45].

Nagesha et al. [88] predicted TMF life for 316L(N) stainless steel using an isothermal database and reasonable predictions were obtained by applying the Ostergren frequency modified damage function approach. The Tomkins crack growth model was also evaluated for TMF life prediction. The cyclic life based on the Ostergren fatigue life prediction model was given by

$$N_f = L(\sigma_{\max} \Delta \epsilon_p)^n \quad (2.25)$$

where  $n$  and  $L$  are material parameters which are determined from isothermal LCF tests.  $\sigma_{\max}$  and  $\Delta \epsilon_p$  are peak tensile stress and plastic strain range respectively.

In order to consider time dependent processes during non-isothermal cycling, Equation 2.25 was modified by Maier et al.[86] as follows

$$N_f = L(\sigma_{\max} \Delta \epsilon_p)^n \times (\nu^*)^{(1-k)} \quad (2.26)$$

where  $\nu^*$  is the effective frequency, which was calculated as  $\nu^* = \frac{1}{\tau + \Delta \tau}$ , where

$\tau$  is the cycle time and  $\Delta \tau$  is the time per cycle during which creep damage occurs and  $k$  is a material constant. The parameters  $n$ ,  $L$  and  $k$  were identified using the isothermal low cycle fatigue data.

The Tomkins crack growth material model [87] was also employed to predict the TMF life. The Tomkins model assumed that in the case of high strain cycling, the time spent in crack initiation is small and the damage occurs on a 45° shear plane at the crack tip during the tensile half of each cycle [88]. The crack growth equation is given as follows

$$\frac{da}{dN} = Ba \quad (2.27)$$

$$B = \Delta \epsilon_p \left[ \frac{1}{\cos \left[ \frac{\pi}{2} \cdot \frac{\sigma}{R_m} \right]} - 1 \right] \quad (2.28)$$

where  $\sigma$  and  $R_m$  are the maximum stress response and the UTS at the temperature at which peak tensile stress occurs. An initial crack length of 75 $\mu$ m was used for life

prediction and final crack growth to 1.2 mm was assumed. A conservative life prediction within a scatter band of two was obtained as shown in Fig.2.32 [88].

Jeong et al. [89] have proposed a creep-fatigue life prediction model based on energy dissipation during hold time. The relaxed stress range was assumed to be the creep fatigue damage function. The Creep-fatigue lives of high temperature materials with various hold times are shown in Fig. 2.33 [89]. A similar correlation was suggested by Yoon and Nam [90] and is expressed by a power law dependence as follows.

$$N_f = C't^m \quad (2.29)$$

where  $N_f$  is the creep fatigue life,  $t$  is the hold period and  $C'$  and  $m$  are constants.

A general stress relaxation model [91] in terms of holding time is given as

$$\Delta\sigma(t) = \sigma(0) - \sigma(t) = \alpha \ln(\beta t + 1) \quad (2.30)$$

where  $\alpha$  and  $\beta$  are constants capturing thermal energy and activation volume effects and  $\sigma(0)$  is the instantaneous stress at the beginning of stress relaxation at  $t=0$ .

For very long holding times, Equation 2.30 was modified to:

$$\Delta\sigma(t) = \alpha \ln(\beta t) \quad (2.31)$$

By combining Equations 2.30 and 2.31, the relation between the relaxed stress and creep fatigue life was expressed as follows:

$$\Delta\sigma(t) = \frac{2.303}{m} (m \log \beta - \log C') + \frac{2.303}{m} \log N_f \quad (2.32)$$

The proposed life model was validated as shown in Fig. 2.34

Park et al. [48] used three mean stress models to correlate isothermal fatigue lives of Inconel 718 at 649°C, namely 1) the Goodman equation [92], 2) the Smith-Watson-

Topper approach [85] and 3) the Walker parameter [93]. The SWT parameter was modified to include the ratchetting effect. The Equations for three models are:

$$\text{Goodman equation } \sigma_a^{eq} = \frac{\sigma_a}{1 - \sigma_m / \sigma_u} \quad (2.33)$$

$$\text{SWT } \sigma_a^{eq} = \sqrt{\sigma_{\max}} \sigma_a = \sigma_{\max} \sqrt{\frac{1-R}{2}} = \sigma_a \sqrt{\frac{2}{1-R}} \quad (2.34)$$

$$\text{Walker } \sigma_a^{eq} = \sigma_{\max}^{1-\gamma} \sigma_a^\gamma = \sigma_{\max} \left( \frac{1-R}{2} \right)^\gamma = \sigma_a \left( \frac{2}{1-R} \right)^{1-\gamma} \quad (2.35)$$

where  $\sigma_u$  is the ultimate tensile strength,  $R$  is the stress ratio ( $R = \sigma_{\min} / \sigma_{\max}$ ),  $\sigma_m$  is the mean stress,  $\gamma$  is a material constant and  $\sigma_{\max}$  and  $\sigma_{\min}$  are the maximum and minimum stresses respectively. The above models were used to predict fatigue life using Basquin's relation  $\sigma_a^{eq} = \sigma'_f (2N_f)^b$  and compared with experimental data. It was observed that the Goodman and SWT parameter did not show good agreement with the experimental data whereas Walker's parameter showed a reasonable correlation with experiments but still within a factor 2. Therefore authors modified the SWT parameter by incorporating ratchetting strain in the equation. The ratchetting strain was defined as:

$$\varepsilon_r = (\varepsilon_{\min} + \varepsilon_{\max}) / 2 \quad (2.36)$$

where  $\varepsilon_{\max}$  and  $\varepsilon_{\min}$  are the maximum and minimum strains in the cycle. The modified SWT equation was given by

$$\sigma_a^{eq} = \sqrt{\left( \frac{1}{2} \varepsilon_r \sigma_m + \sigma_a \right)} \sigma_a \quad (2.37)$$

The modified parameter was described via a linear relation between the ratchet strain and stress ratio as follows:

$$\varepsilon_r = A + B \frac{\sigma_m}{\sigma_a} \quad (2.38)$$

where A and B are material constants. The modified SWT parameter showed reasonable correlation with the test data as shown in Fig. 2.35 [48].

## 2.6 Work done on SPF tools

Comparatively little research has been carried out in the area of thermo mechanical analysis of SPF tools. Gao et al. [4] presented thermo-mechanical FE analyses of a simple axisymmetric cylindrical shaped (high Ni-Cr-Fe heat resistant cast steel) SPF tool (Fig. 2.36). The effects of residual stress and distortion were investigated in order to analyse the damage effects of the thermo-mechanical loading on the tool. A steady state heat transfer analysis was employed with thermal gradients; using non-isothermal boundary conditions. The power-law creep model was used for modelling the steady state creep. Two types of contacts were modelled: one was deformable to deformable between the sheet and the tool and another was deformable to rigid between the tool and the platen. Furthermore the clamping pressure and forming gas pressure were also considered in FE modelling.

However Gao et al. [4] did not consider the effect of temperature gradient and cyclic plasticity during sheet loading and unloading and therefore the inelastic strain was comprised of only creep strain. The results from this work suggested that a small thermal gradient was sufficient to cause geometrical distortion which induced high stresses after the application of the clamping load. It was observed that the effect of forming load (gas pressure) is negligible compared to that of clamping load and

hence simulation of sheet forming can be neglected. It was also found that the residual geometrical distortion increases with the production cycles and can impair the dimensional tolerances of formed components as shown in Figs. 2.36-2.38 [4].

Furthermore, Bernhart et al. [15] worked on investigating advanced material behaviour models for SPF dies to improve FE predictions. The unified elastic-viscoplastic material behaviour model of Chaboche was applied to model the material behaviour of heat resistant cast steel and die. This model required extensive experimental results on material properties up to the forming temperature. Experimental fatigue testing at different temperatures; were carried out on high Ni Cr alloy to obtain material parameters. In this model the strain is divided into elastic and viscoplastic parts and two stress components are used to describe the non-linear kinematic hardening  $X_i$  and to consider true limit of elasticity  $R_0$ . The equations in uniaxial form are:

$$f = \left| \sigma - \sum_{i=1}^2 X_i \right| - R_0 \quad (2.39)$$

$$\dot{p} = |\dot{\epsilon}_{vp}| = \left\langle \frac{f}{K} \right\rangle^n, \dot{\alpha}_i = \dot{\epsilon}_{vp} - \frac{D_i}{C_i} X_i \dot{p}, i = 1, 2 \quad (2.40)$$

$$\sigma = E \epsilon_{el}, X_i = C_i \alpha_i \quad (2.41)$$

Equation (2.39) describes the von-Mises yield criterion whereas equation (2.40) shows the Norton type visco-plastic strain evolution and non-linear internal strain variable  $\alpha_i$  evolution. The experimental stress-strain loops were compared with those obtained by the constitutive model for five different strain rates and found to be in reasonable agreement with experiments with approximately 10% error on stress range.

Bernhart et al. [14], performed thermo-mechanical simulations on a Ni-Cr-Fe heat resistant SPF die using a cyclic elasto-visco-plastic material model. The constitutive equations were implemented in the Abaqus software using UMAT and UVARM user subroutines and were used to analyse the stress-strain evolutions in SPF dies during a SPF cycle for an assumed steady-state thermal condition. The FE-predicted results showed that several locations in the die were subjected to high stresses and plastic deformation due to local thermal gradients during the mould pull out and forming [14].

Shang et al. [16] studied the elastic-plastic and creep behaviour of a large SPF tool using a sequential, three-dimensional, finite element heat transfer and mechanical stress analysis approach. Measured temperature-dependent monotonic stress-strain data was employed to define an anisothermal linear kinematic hardening model. An uncoupled plasticity-creep material model was employed. However, no experimental verification of the model was done. The author used simplified boundary conditions, i.e. constraining all the nodes of the bottom surface of the die in the vertical direction. The die contact with the platen was therefore not modelled and the effects of die gravity and clamping pressure during the forming cycle were not considered [16].

Shang et al. [94] characterised the high temperature behaviour of the 40%Ni-20% Cr, XN40F die material using isothermal fatigue and creep-fatigue interaction tests at 700 and 900°C to estimate the strain-life relationships. Short-term creep properties were approximately determined by monotonic tensile tests at two low strain rates of

$8 \times 10^{-5}$  and  $8 \times 10^{-4} \text{ s}^{-1}$  at  $900^\circ\text{C}$ . It was argued that that the Ni-Cr alloy investigated in this project is generically similar to stainless steel 304 which does not follow a straight-line creep-fatigue failure interaction locus. Based on this argument, a bilinear strain range partitioning approach was developed incorporating cyclic plasticity and creep damage together to predict the creep-fatigue life of the die. It was shown from finite element modeling, that the SPF die experiences both  $\Delta\epsilon_{pp}$  and  $\Delta\epsilon_{pc}$  cyclic inelastic strain ranges, i.e. cyclic strain ranges with plastic strain reversed by plastic strain ( $\Delta\epsilon_{pp}$ ) and cyclic strain ranges with plastic strain reversed by creep strain ( $\Delta\epsilon_{pc}$ ). Associated with these, were two damage components,

$D_{pc} = \frac{N_f}{N_{pc}}$  and  $D_{pp} = \frac{N_f}{N_{pp}}$ . The bi-linear damage summation equations, as shown in

Fig. 2.39 were described as,

$$\frac{N_f}{N_{pp}} + \beta \frac{N_f}{N_{pc}} = 1 \text{ for } \frac{N_f}{N_{pc}} < \frac{N_f}{N_{pp}} \quad (2.42)$$

$$\alpha \frac{N_f}{N_{pp}} + \frac{N_f}{N_{pc}} = 1 \text{ for } \frac{N_f}{N_{pp}} < \frac{N_f}{N_{pc}} \quad (2.43)$$

where  $N_{pp}$  is the number of cycles of  $\Delta\epsilon_{pp}$  to failure and  $N_{pc}$  is the number of cycles of  $\Delta\epsilon_{pc}$  to failure and where  $\alpha$  and  $\beta$  are constants, both greater than 1.

Additional tests at  $900^\circ\text{C}$ , devised to simulate the interaction between the  $\Delta\epsilon_{pp}$  and

$\Delta\epsilon_{pc}$  strain ranges for the die, were employed to show that  $\frac{N_f}{N_{pp}} < \frac{N_f}{N_{pc}}$  for the die

material and to identify the relevant value of  $\alpha$  for Equation 2.46, as shown in Fig.

2.39 The FE predicted strain ranges were used to predict the die life [94]. However,

no direct experimental validation of the predicted die life was possible. Comparisons

were made against other failure models such as Coffin-Manson and Smith Watson Topper (SWT) approach.

## **2.7 Summary**

The literature review chapter summarises different possible failure mechanisms of SPF tools such as low cycle fatigue, fatigue-creep interaction and time independent and dependent ratchetting. A review of stress- and strain-controlled thermo-mechanical fatigue-creep and ratchetting experiments, constitutive modelling, FE modelling and life prediction methodologies has been carried out to provide the reader with a thorough background for the research work presented in this thesis.

It was shown that no one else has worked on optimising the overall SPF process to improve the SPF tool life using FE modelling and thermo-mechanical fatigue-creep- and ratchetting experiments. In this research work, a large SPF tool from aerospace industry was investigated under realistic loading conditions specified by industry. Different failure mechanisms such as thermo-mechanical fatigue, fatigue-creep interaction and ratchetting were identified and evaluated using FE modelling and representative experiments, simulating representative SPF tool loading.

In this thesis, a significant amount of work has been carried out on a) validation of identified heat transfer coefficients and thermal properties using an inverse heat transfer analysis method, b) identification of material parameters for different cyclic elastic-plastic-creep material models, c) validation of materials parameters and models against experimental results, d) FE analysis of the realistic large SPF tool, e) optimisation of the SPF process parameters such as thermal history, heating and

cooling rates and batch size, f) TMF and IF life assessment tests on the SPF tool material g) representative thermo-mechanical fatigue-creep and ratchetting tests, designed to represent the temperature and stress-strain cycling associated with the most damaging phase of the SPF tool cycle and h) SPF tool life predictions.

Table 2.1 Summary of TMF IP test results [43].

| $\Delta\epsilon_r$ | $N_f$ (cycles) | $\Delta\epsilon_{max}$ | $\Delta\epsilon_p$ | $\sigma_{max}$ (MPa) | $\sigma_{min}$ (MPa) | $\sigma_m$ (MPa) |
|--------------------|----------------|------------------------|--------------------|----------------------|----------------------|------------------|
| 0.012              | 1573           | 0.003                  | 0.00036            | 155                  | -280                 | -62              |
| 0.014              | 183            | 0.0049                 | 0.000526           | 192                  | -631                 | -219             |
| 0.016              | 89             | 0.0076                 | 0.001714           | 379                  | -758                 | -224             |
| 0.020              | 28             | 0.0115                 | 0.0044             | 515                  | -820                 | -153             |
| 0.024              | 8              | 0.0157                 | 0.00694            | 647                  | -878                 | -116             |

Table 2.2 Summary of TMF OP test results [43].

| $\Delta\epsilon_r$ | $N_f$ (cycles) | $\Delta\epsilon_{max}$ | $\Delta\epsilon_p$ | $\sigma_{max}$ (MPa) | $\sigma_{min}$ (MPa) | $\sigma_m$ (MPa) |
|--------------------|----------------|------------------------|--------------------|----------------------|----------------------|------------------|
| 0.0042             | 1140           | 0.0048                 | 0.00013            | 742                  | -113                 | 315              |
| 0.0022             | 284            | 0.0068                 | 0.001              | 759                  | -310                 | 224              |
| 0.002              | 128            | 0.011                  | 0.00188            | 821                  | -601                 | 110              |
| 0.004              | 74             | 0.013                  | 0.00381            | 831                  | -659                 | 86               |
| 0.006              | 19             | 0.0152                 | 0.00722            | 842                  | -663                 | 89               |

Table 2.3 Thermomechanical fatigue results for two Ni based single crystal superalloys [47].

| Thermal-mechanical fatigue results |                  |             |       |                  |                  |                |                  |                  |
|------------------------------------|------------------|-------------|-------|------------------|------------------|----------------|------------------|------------------|
|                                    | $\epsilon_t$ (%) | $t^*$ (min) | $N_f$ | $\epsilon_p$ (%) | $\epsilon_e$ (%) | $\sigma$ (MPa) | $\sigma_t$ (MPa) | $\sigma_c$ (MPa) |
| TMS-75                             | 0.97             | -           | 5355  | 0.00             | 0.97             | 958            | 595              | 364              |
|                                    | 0.99             | 60          | 311   | 0.06             | 0.93             | 1034           | 718              | 316              |
|                                    | 1.28             | -           | 985   | 0.00             | 1.28             | 1322           | 878              | -443             |
|                                    | 1.28             | 10          | 158   | 0.13             | 1.15             | 1300           | 843              | -457             |
|                                    | 1.31             | 60          | 48    | 0.19             | 1.12             | 1326           | 768              | -558             |
|                                    | 1.28             | 600         | 22    | -                | -                | -              | -                | -                |
| TMS-82+                            | 1.01             | -           | 1994  | 0.00             | 1.01             | 1143           | 761              | -382             |
|                                    | 1.24             | -           | 710   | 0.00             | 1.24             | 1361           | 928              | -433             |
|                                    | 1.28             | -           | 450   | -                | -                | -              | -                | -                |
|                                    | 1.27             | 10          | 308   | 0.03             | 1.24             | 1391           | 956              | -435             |
|                                    | 1.29             | 60          | 70    | 0.09             | 1.20             | 1364           | 891              | -473             |
|                                    | 1.28             | 60          | 86    | -                | -                | -              | -                | -                |
|                                    | 1.28             | 600         | 29    | 0.23             | 1.05             | 1470           | 957              | -513             |

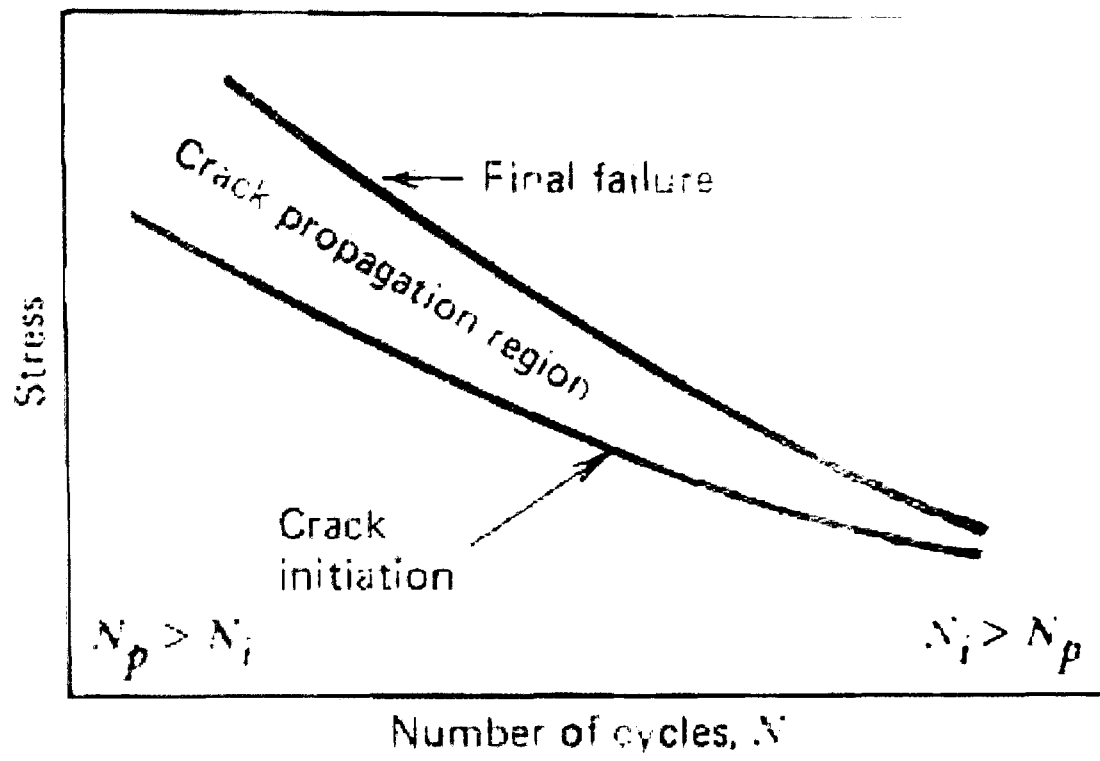


Fig. 2.1 Fatigue life criterions [27].

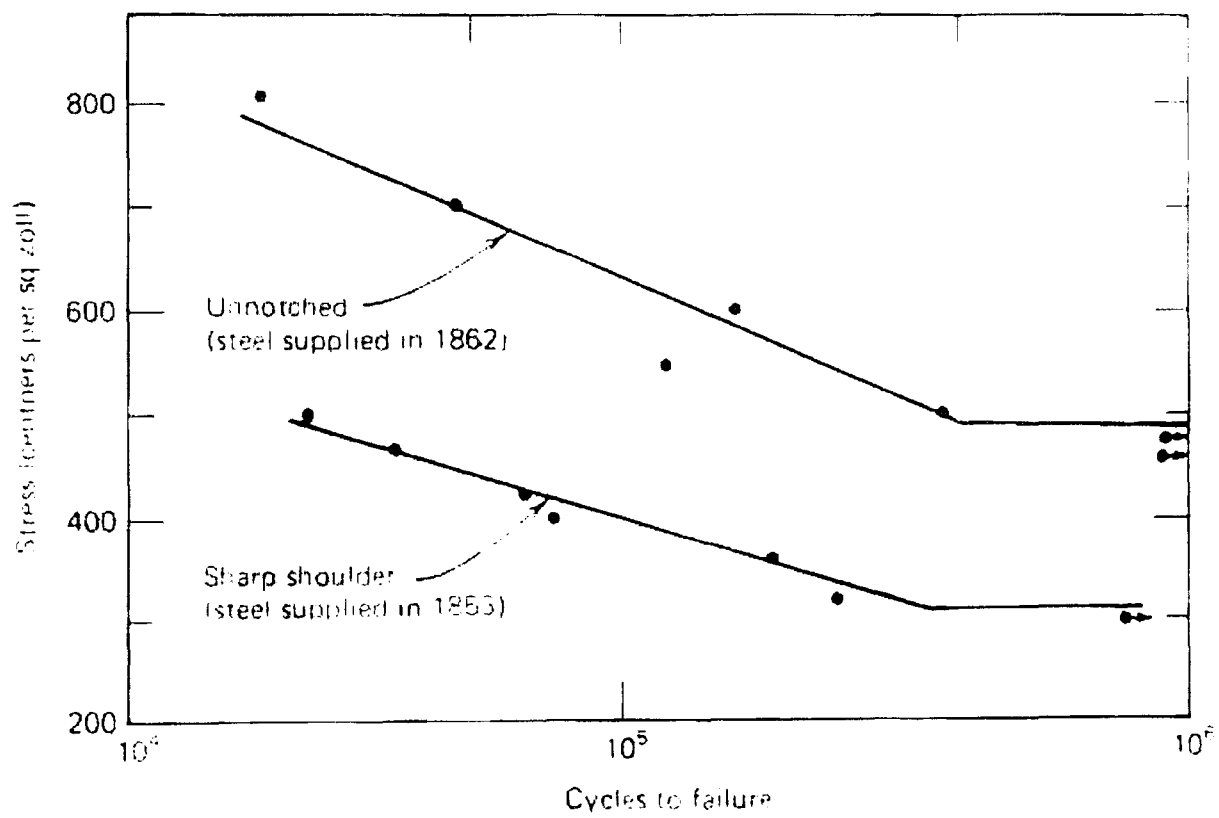


Fig. 2.2 Wohler's S-N curves for Krupp axle steel [28].

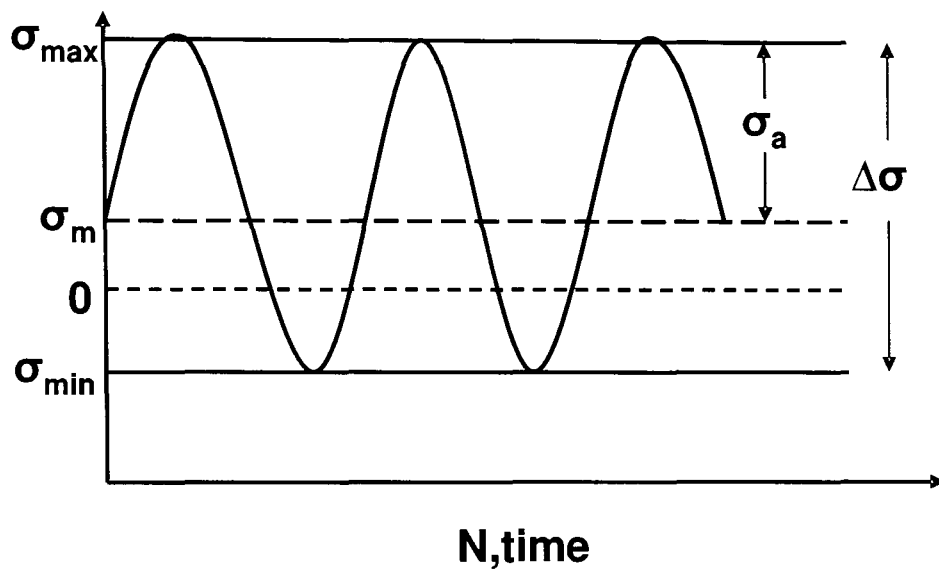


Figure 2.3 Cyclic stress controlled test nomenclature to define test parameters [27].

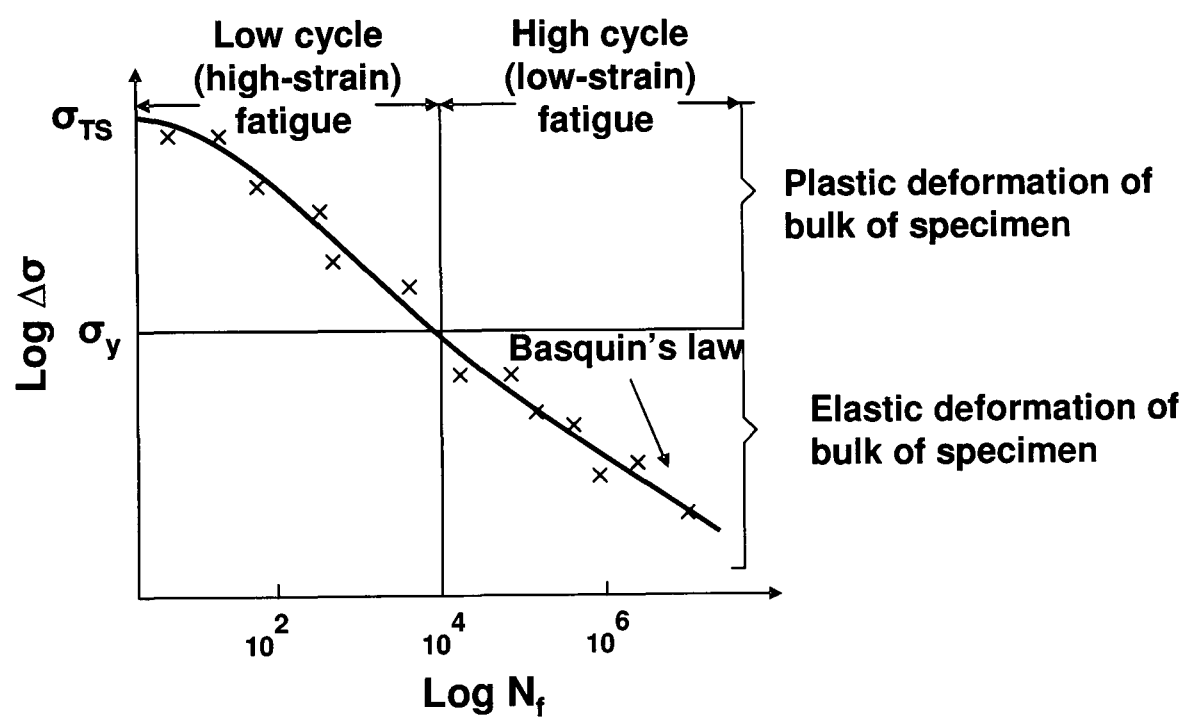


Figure 2.4 Initiation controlled high cycle fatigue representing Basquin's law [29].

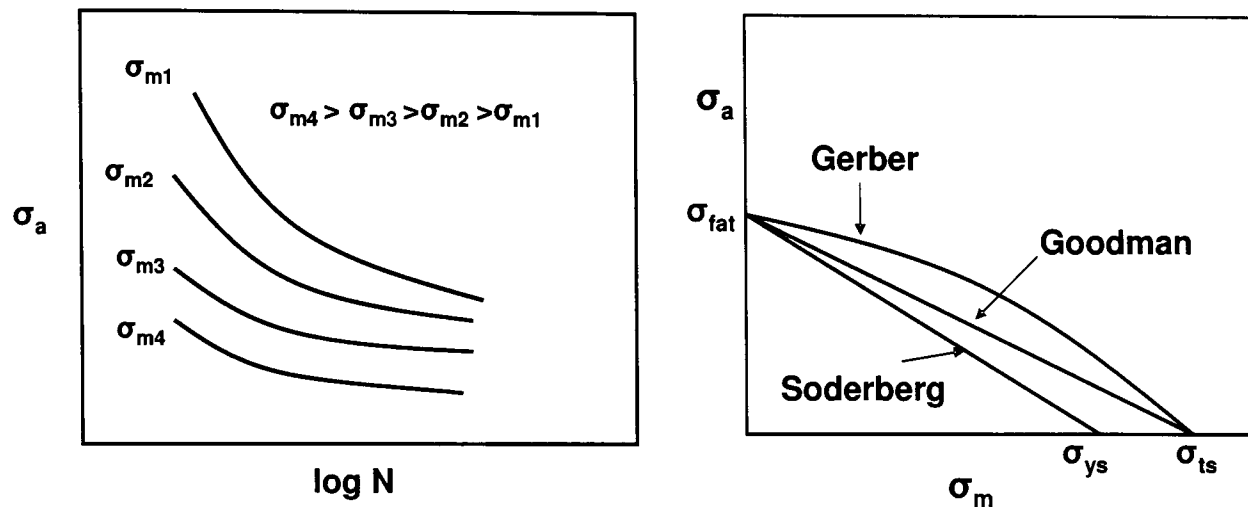


Figure 2.5 Representative plots of data showing effect of stress amplitude and mean stress on fatigue life (a) Typical S-N diagrams with different  $\sigma_m$  values (b) Gerber, Goodman and Soderberg diagrams depicting combined effect of alternating and mean stress on fatigue endurance [27].

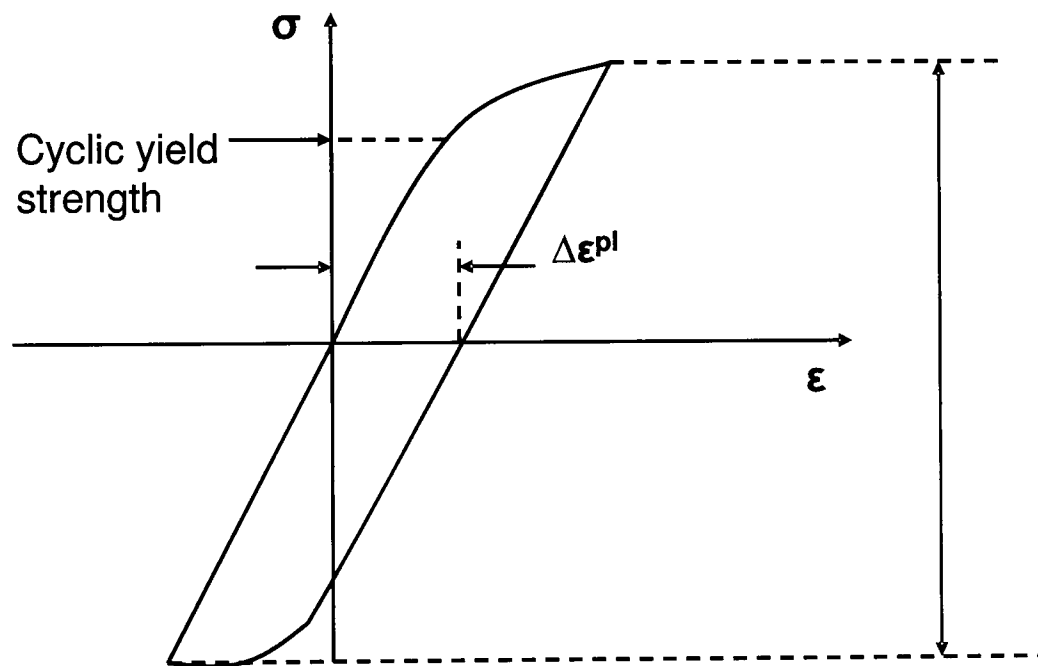


Figure 2.6 Stabilized hysteresis stress-strain loop in low cycle fatigue [29].

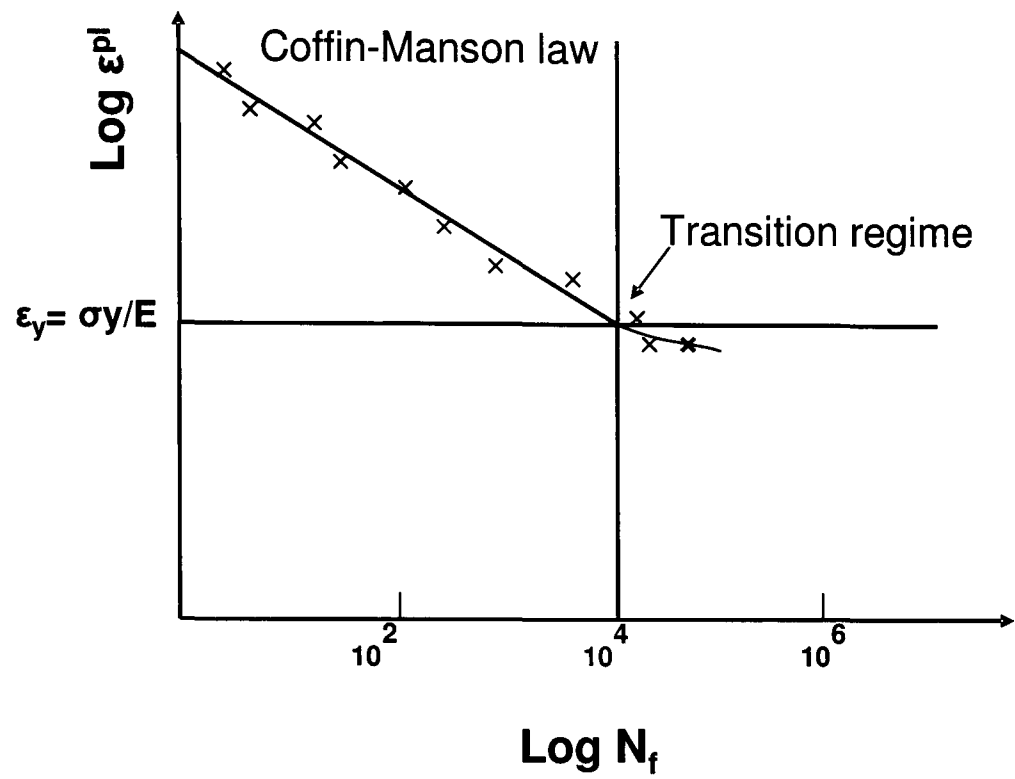


Figure 2.7 Initiation controlled low cycle fatigue representing Coffin-Manson Law [29].

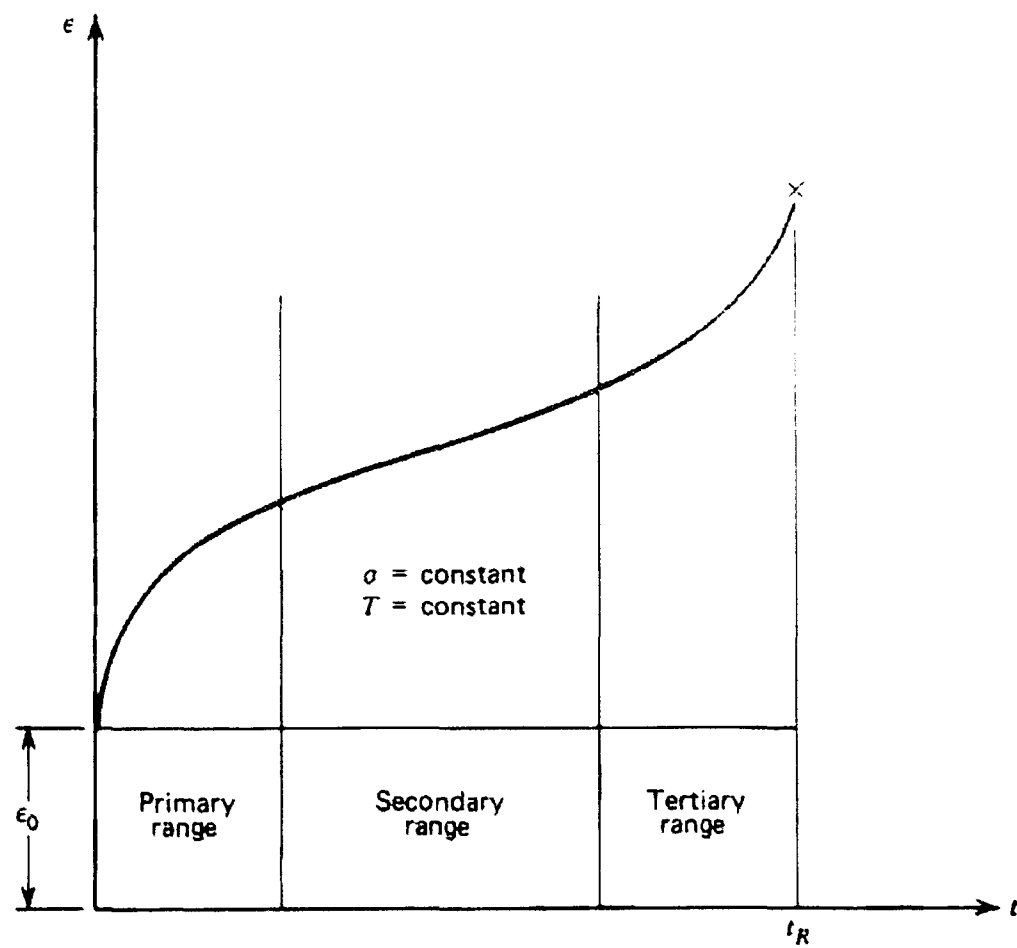


Figure 2.8 Typical creep curve showing the strain accumulation with time [31].

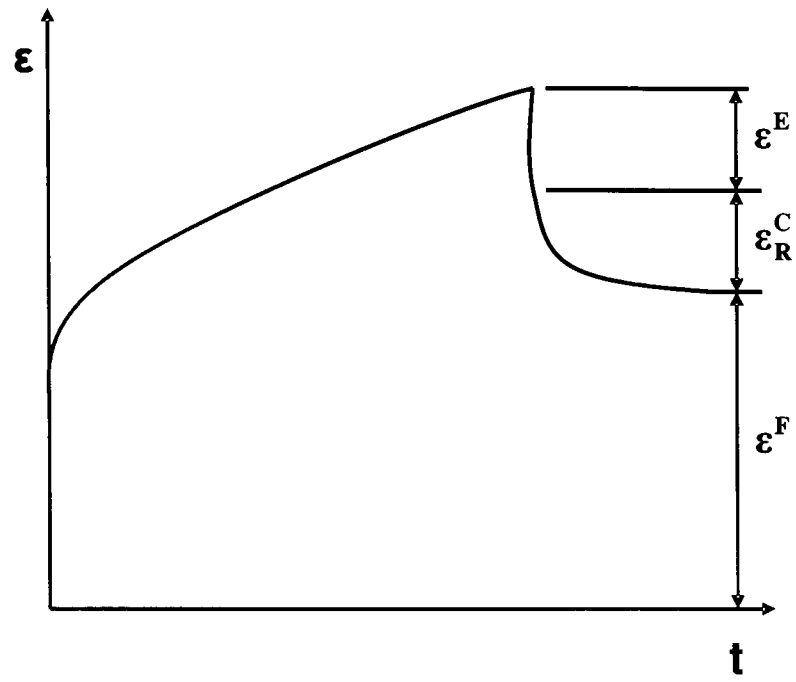
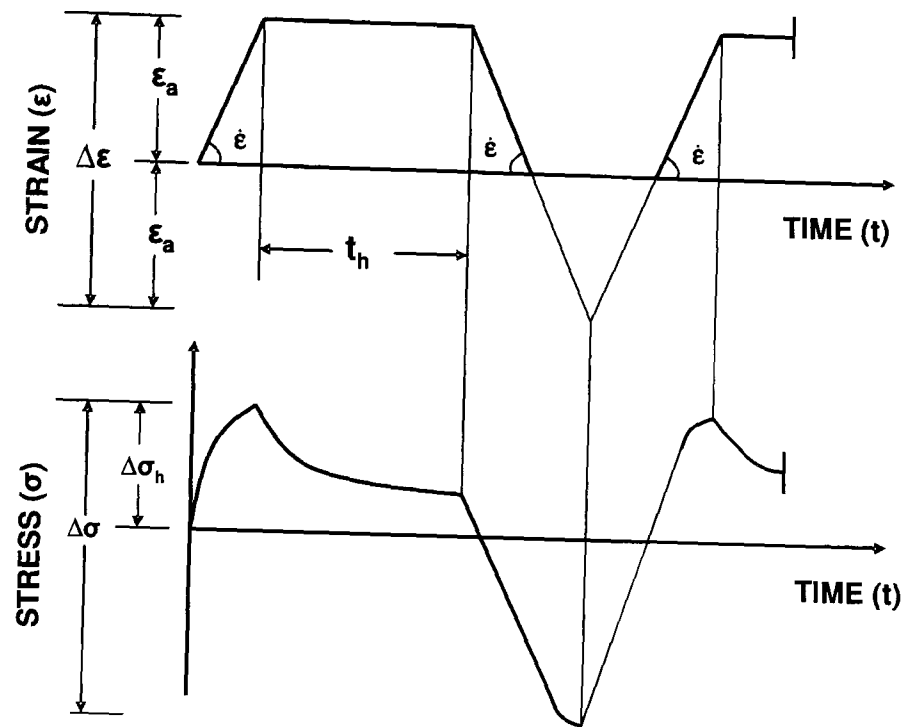


Figure 2.9 Typical strain versus time plot showing Creep recovery [31].



$\dot{\epsilon}$  = STRAIN RATE  
 $\Delta\epsilon$  = TOTAL STRAIN RANGE  
 $\pm\epsilon_a$  = CONTROLLED STRAIN AMPLITUDE =  $\Delta\epsilon/2$   
 $\Delta\sigma_h$  = MAXIMUM TENSILE STRESS  
 $t_h$  = HOLD-PERIOD  
 $\Delta\sigma$  = STRESS RANGE

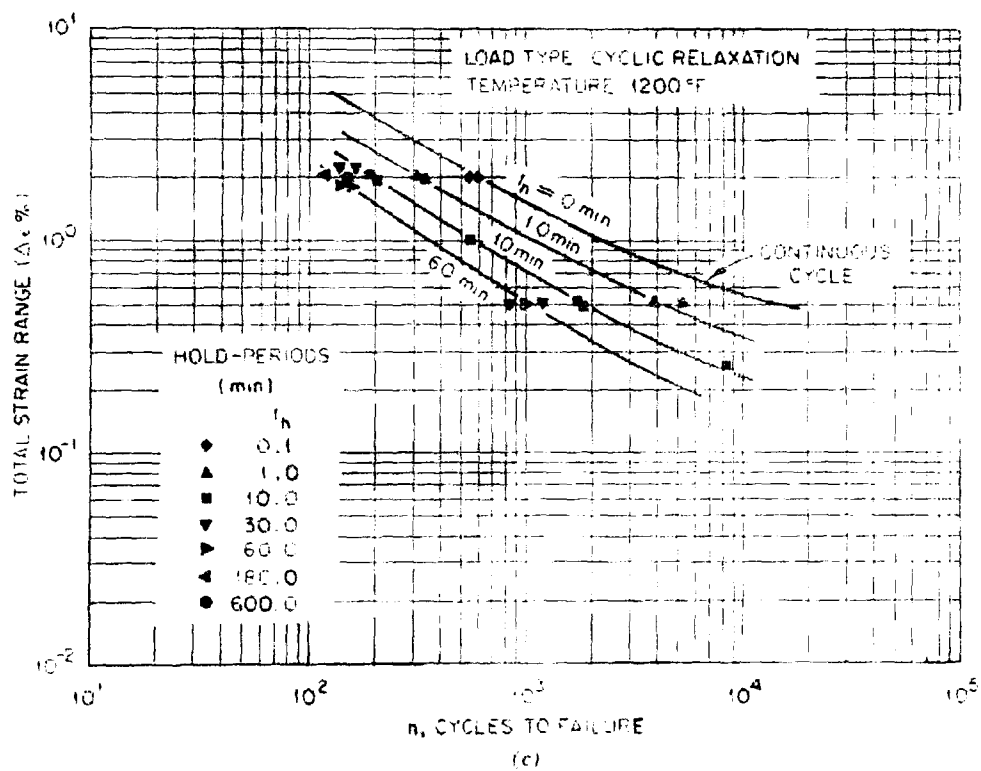


Figure 2.10 Cyclic relaxation data for 304 stainless steel at 1200°F (from Oak Ridge National Laboratory) [31].

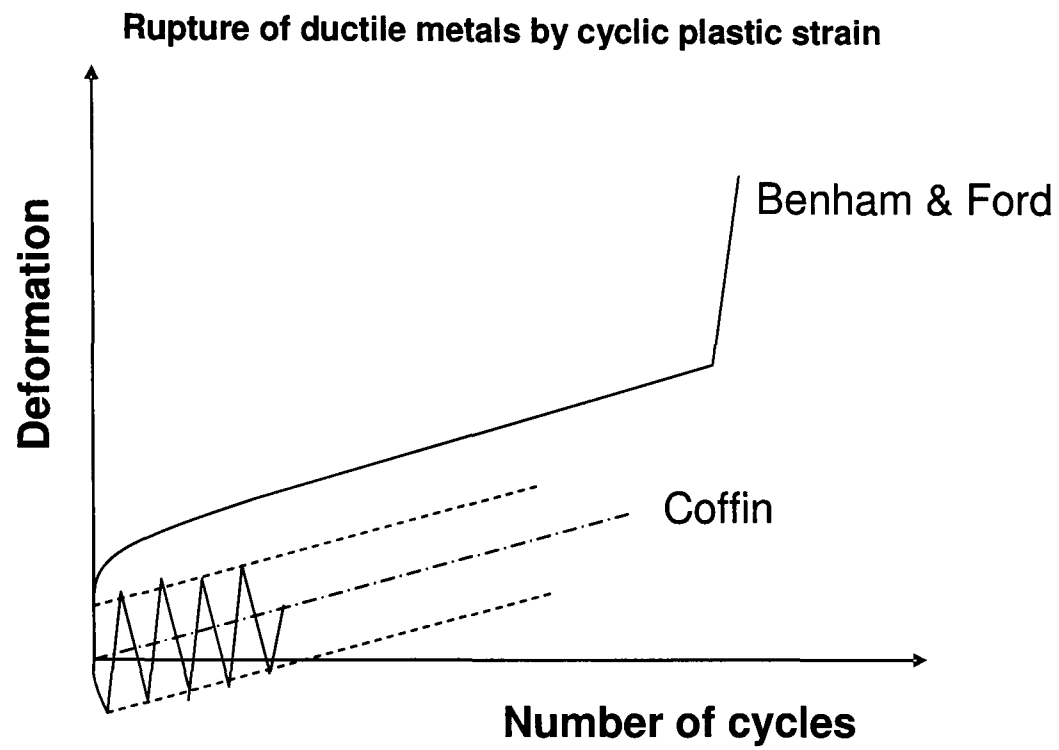


Figure 2.11 Results of ratchetting tests: Load controlled, mild steel from Benham and Ford; strain controlled, copper from Coffin [37] [38]. [39].

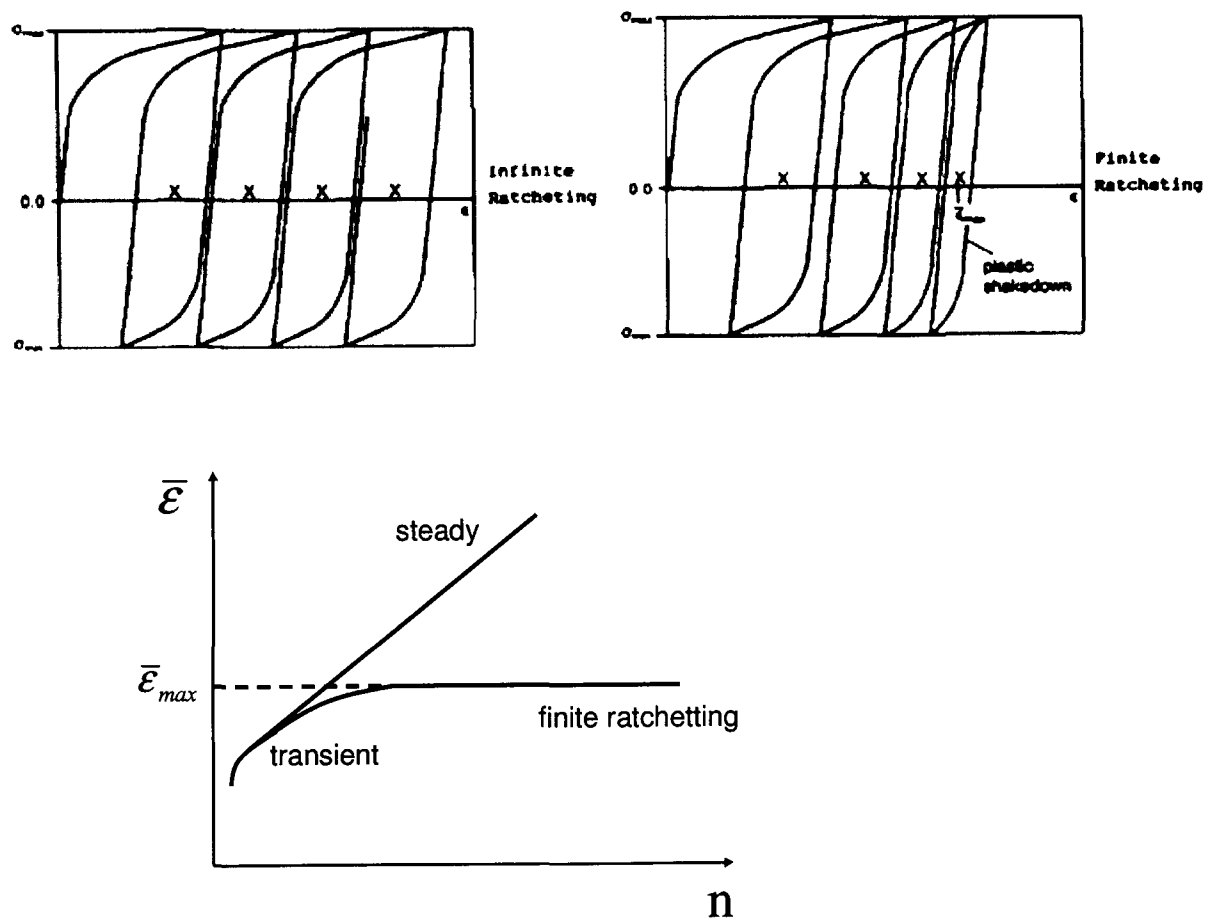


Figure 2.12 Distinction between infinite and finite ratchetting [40].

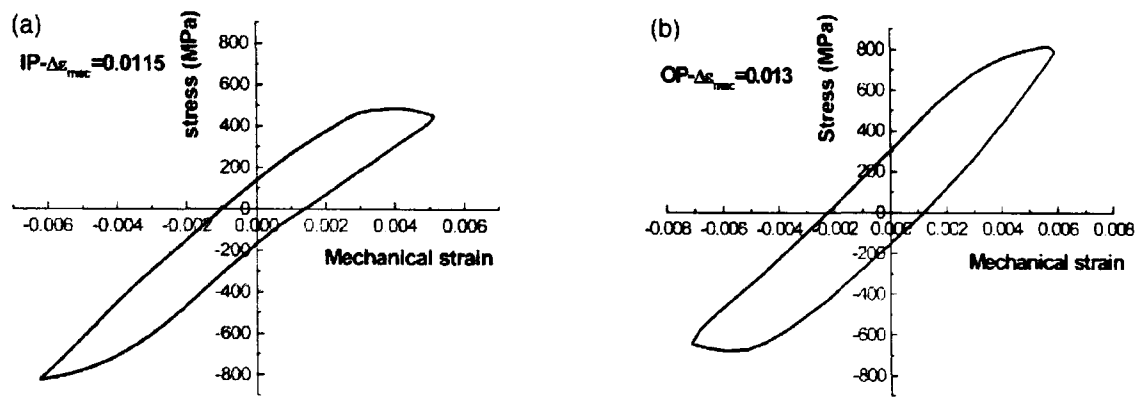


Figure 2.13 Typical hysteresis loops: (a) IP (b) OP for K417 superalloy [43].

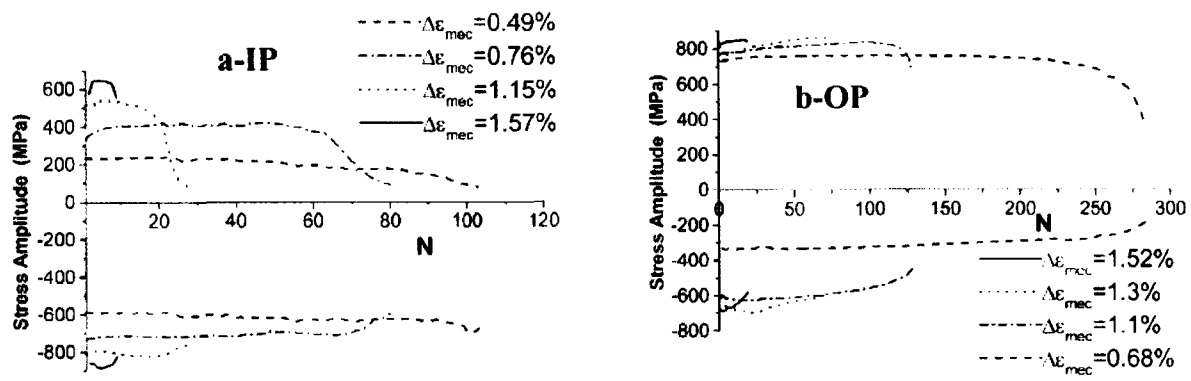


Figure 2.14 Cyclic stress response curves of TMF in K417 alloy: (a) IP; (b) OP [43].

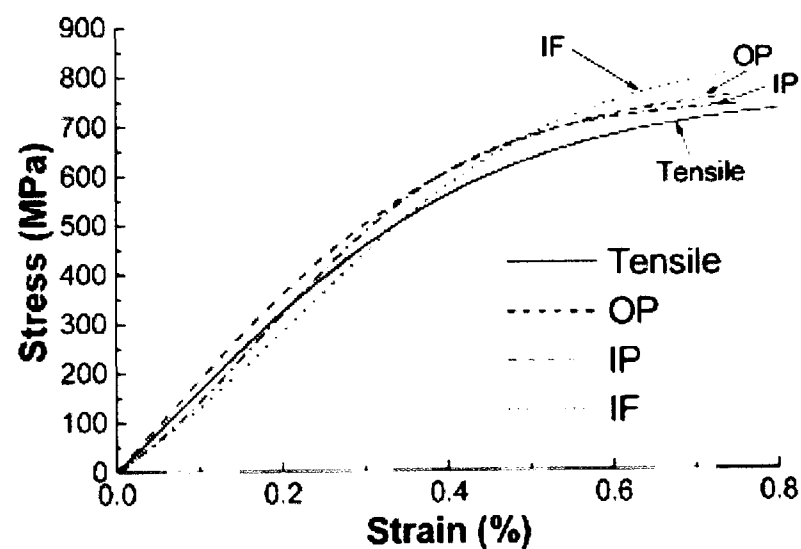


Figure 2.15 Stress-strain curves of TMF, IF and static-state tension at 850°C for K417 superalloy [43].

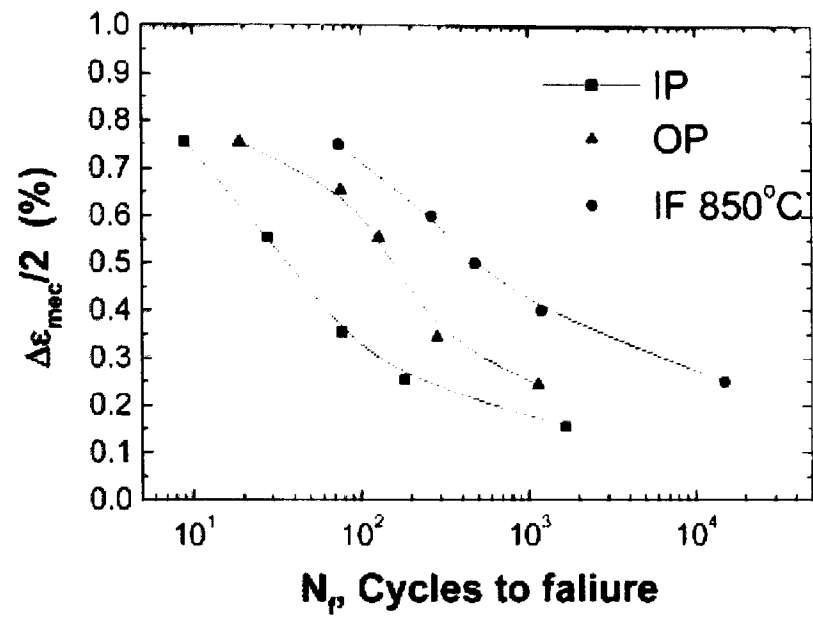


Figure 2.16 Mechanical strain amplitude versus life for TMF and IF at 850°C for K417 superalloy [43].

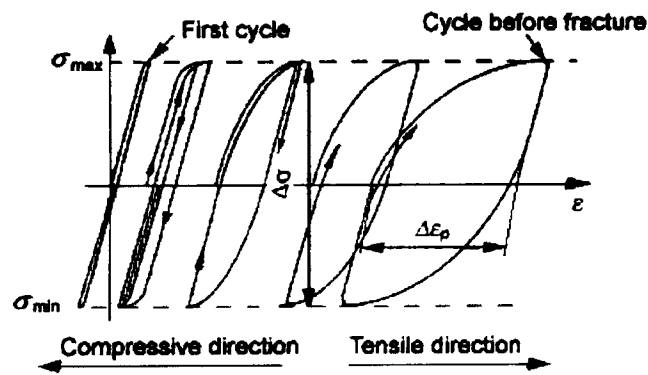


Figure 2.17 Schematic diagram of ratcheting phenomenon in load control fatigue [44].

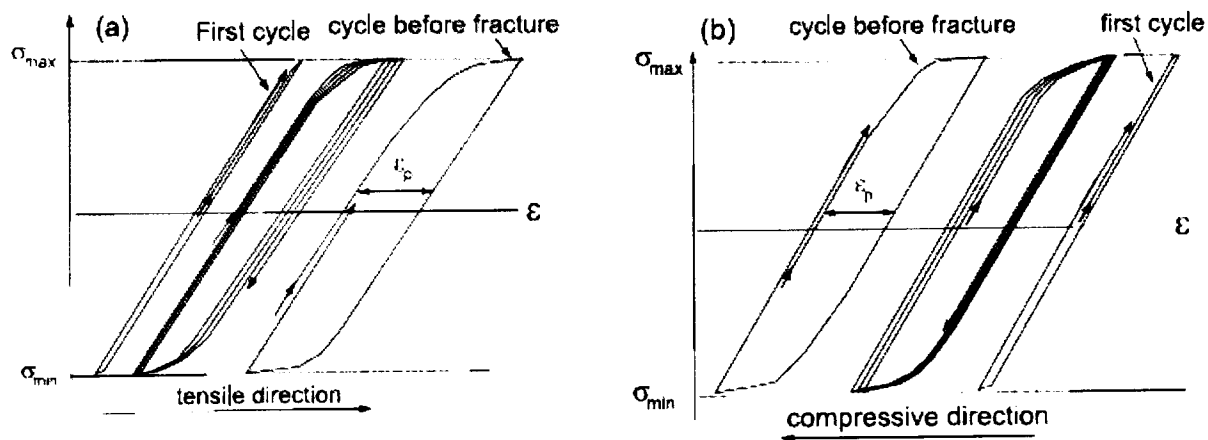


Figure 2.18 Schematic representation of creep and softening phenomenon a) TMF b) IF [95].

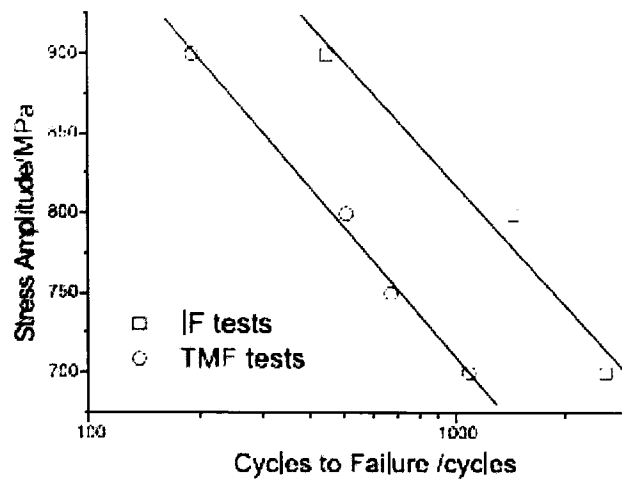


Figure 2.19 Experimental S-N curves for IF and TMF [95].

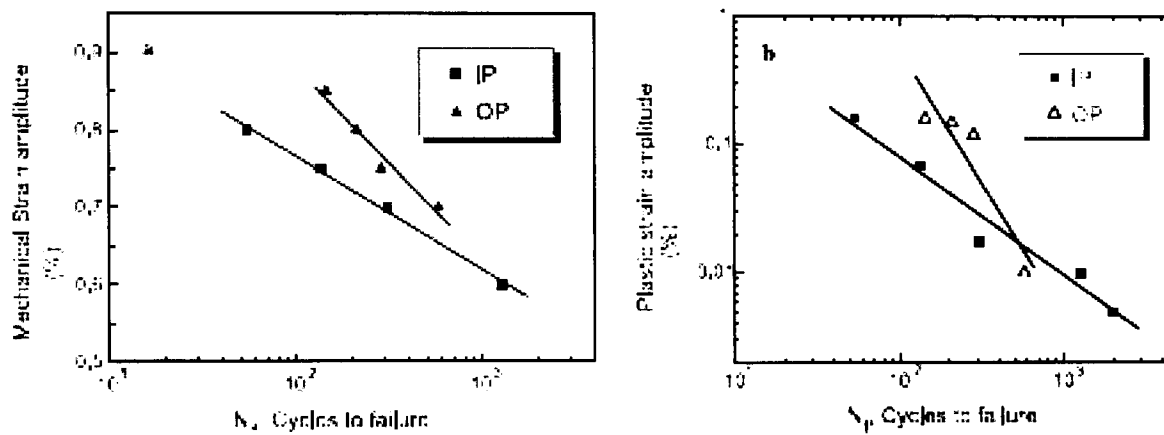


Figure 2.20 TMF lives on the basis of a) mechanical strain b) plastic strain [96].

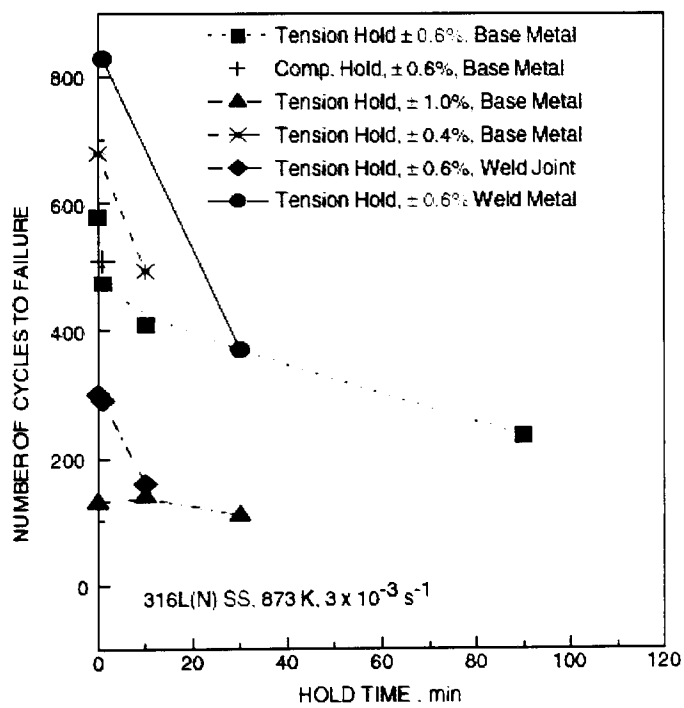


Figure 2.21 Fatigue life as a function of hold time [46].

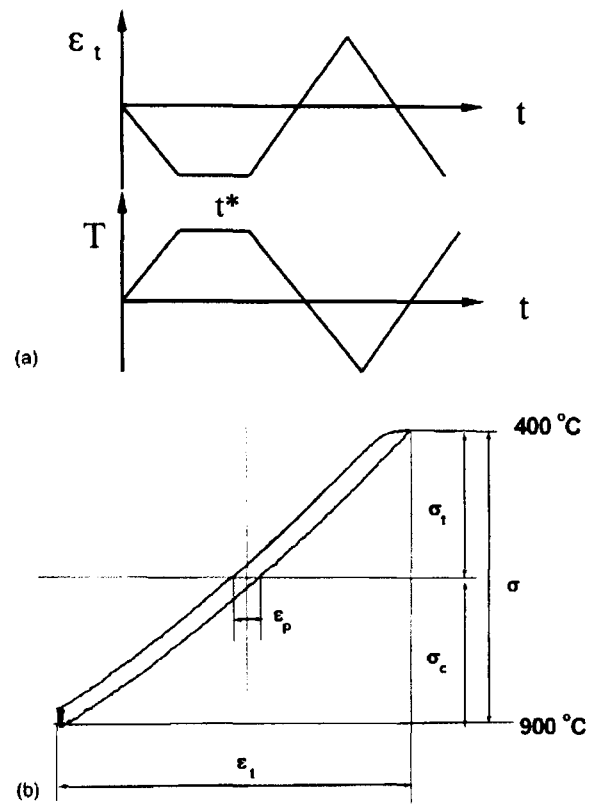


Figure 2.22 A schematic diagram of out of phase TMF cycling; a) Total strain, temperature vs time b) typical stress-strain hysteresis loop [47].

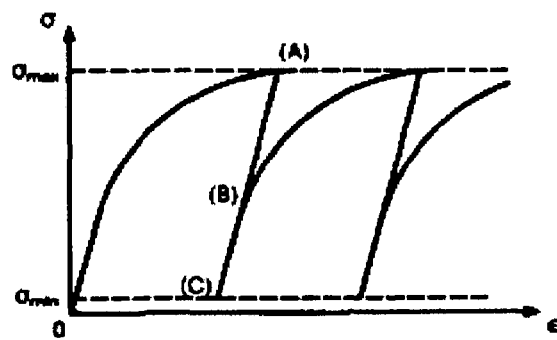


Figure 2.23 Ratchetting due to mean stress effect [40].

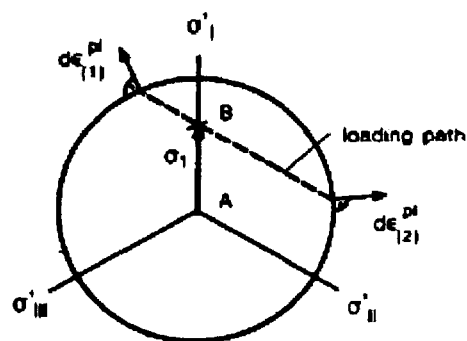


Figure 2.24 Non-proportional loading in stress space (Von-Mises yield surface) [40].

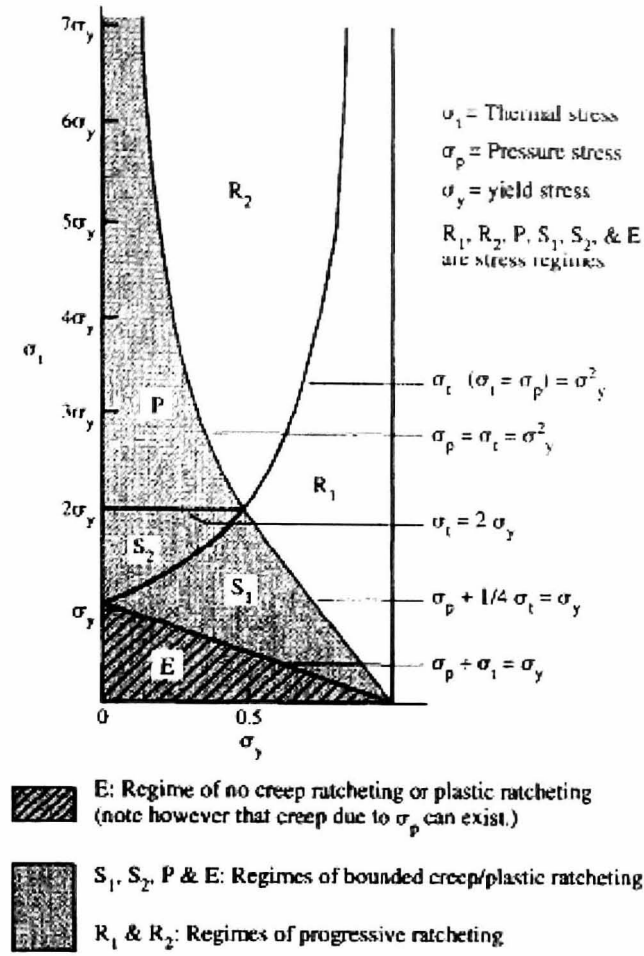


Figure 2.25 Stress regimes of Bree diagram [35, 36, 58].

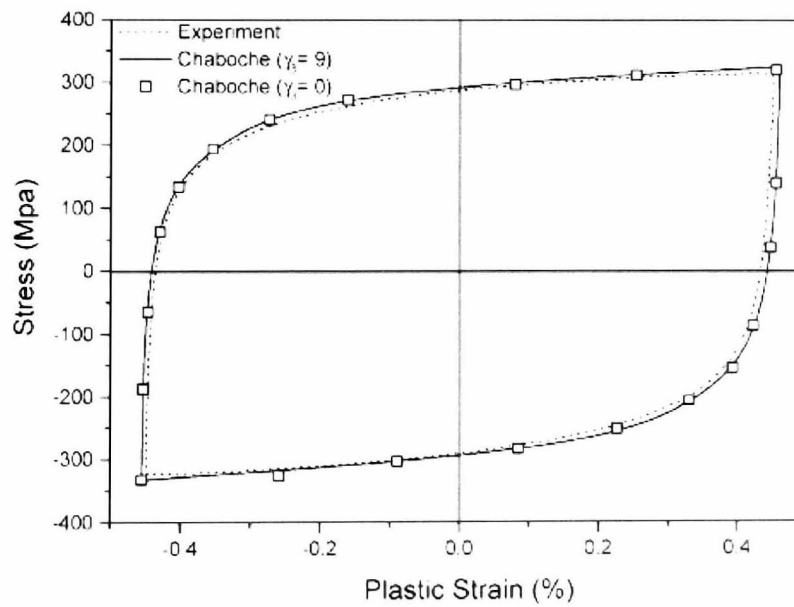


Figure 2.26 Prediction from the Chaboche model with three decomposed rule for stable hysteresis loop under strain controlled test [72].

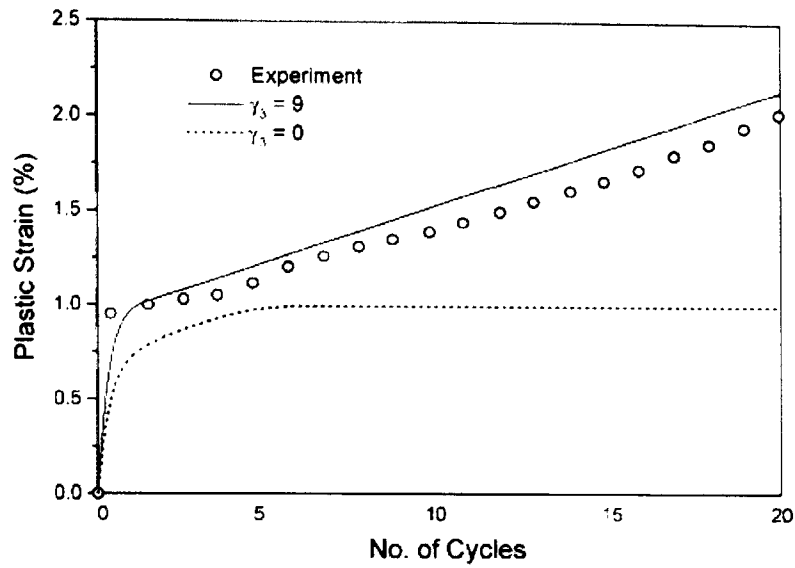


Figure 2.27 Prediction from the Chaboche model with three decomposed rule for stable hysteresis loop under stress controlled test with mean stress [72].

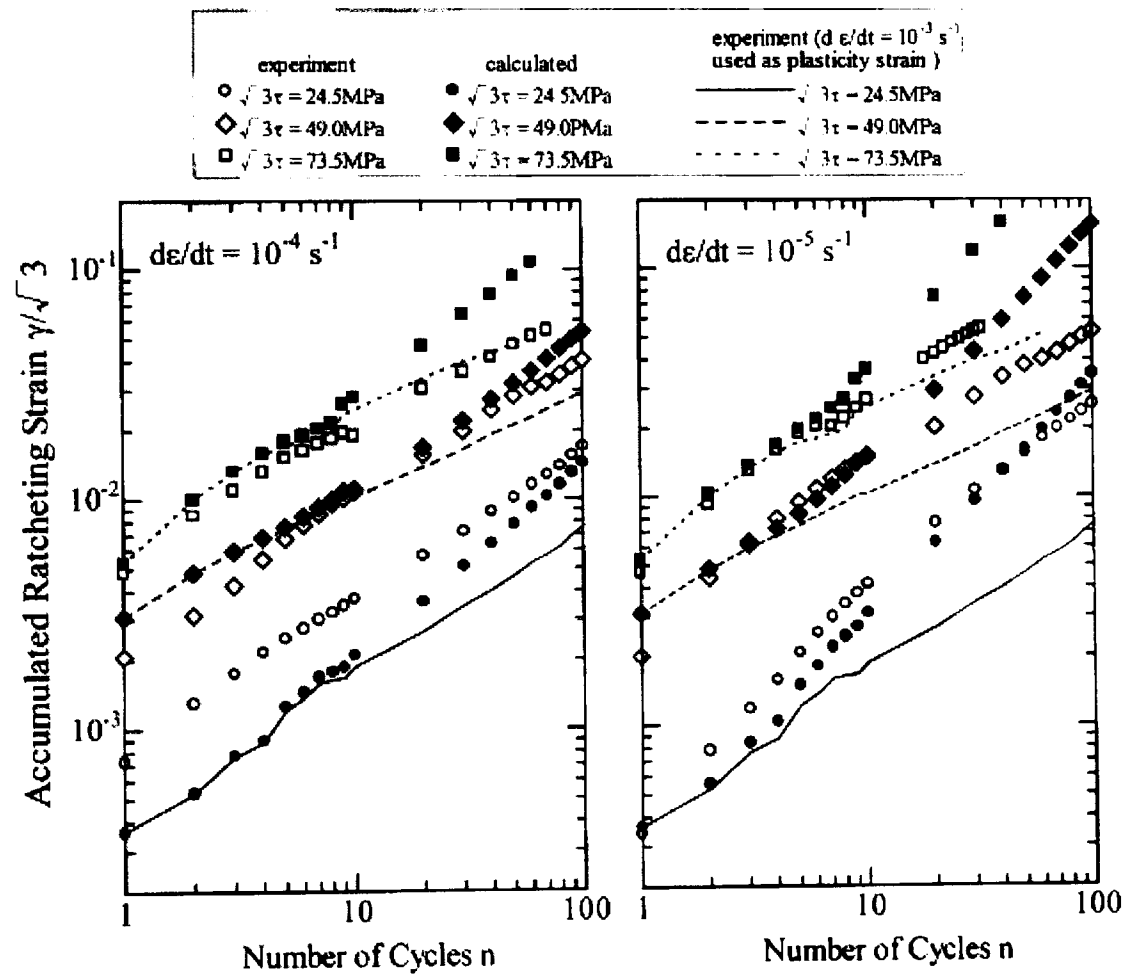


Figure 2.28 Predictions and experiments on creep-plasticity interaction (steady creep analysis,  $\epsilon_{tr} = 0.01$ ) [74]

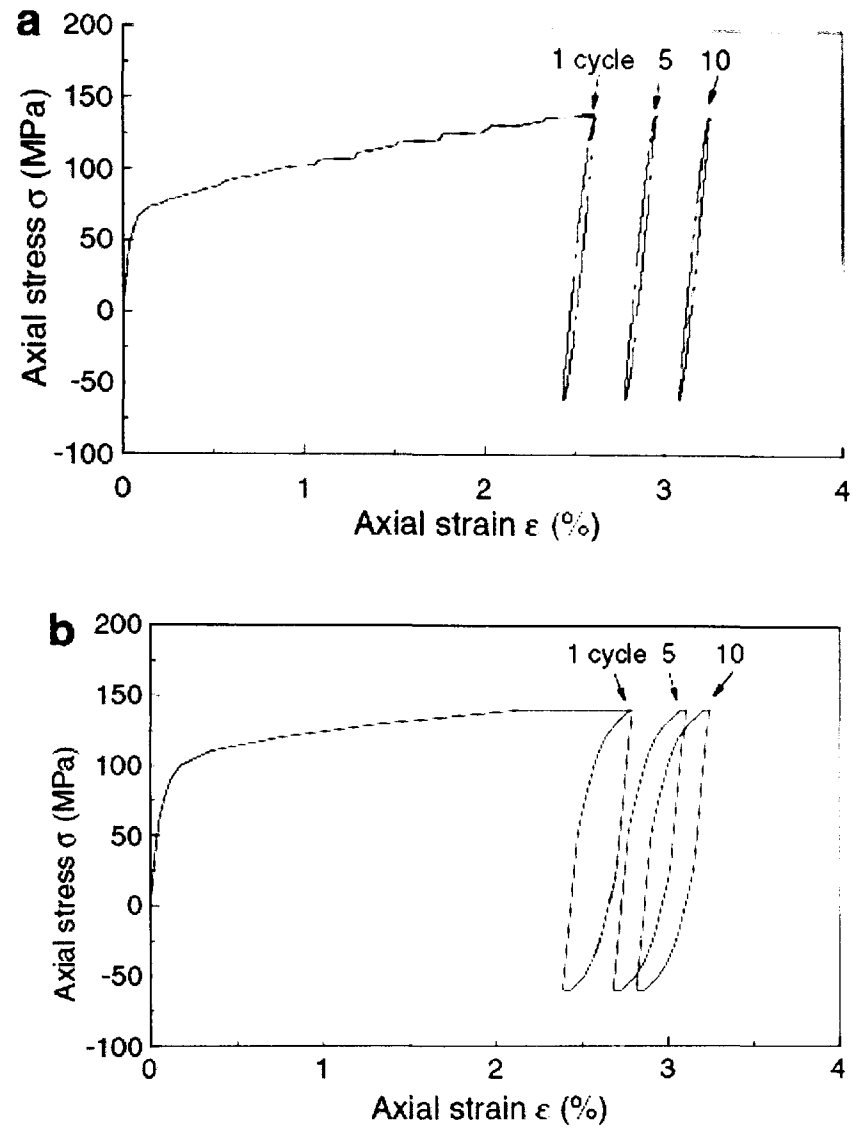


Figure 2.29 Results of ratchetting ( $40 \pm 100$  MPa) with peak/valley stress hold at 973 K and stressing rate of  $10 \text{ MPa S}^{-1}$ : (a) experiment ;(b) Simulation by ABAQUS [69]

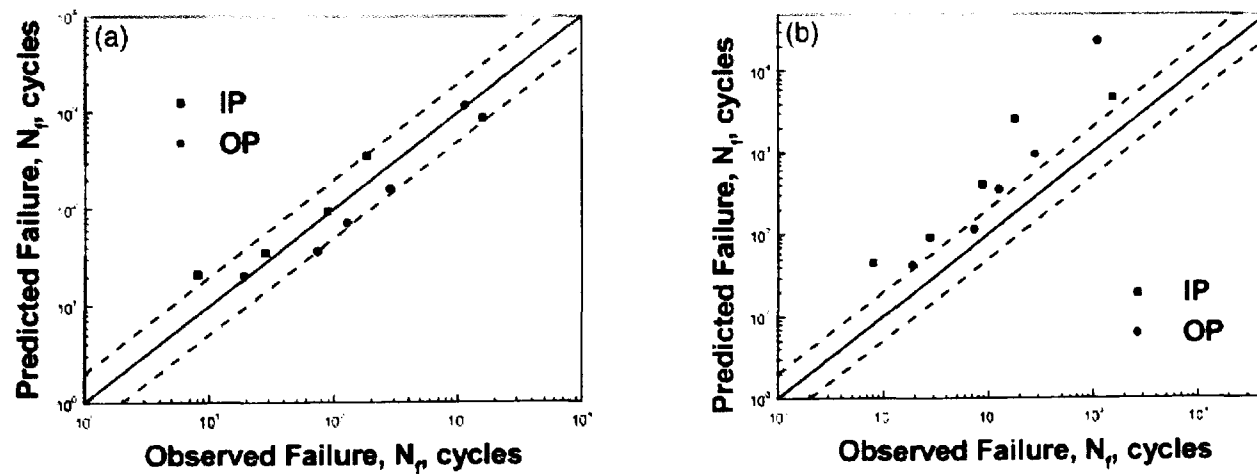


Figure 2.30 Predicted and observed life under TMF by (a) the Ostergren and (b) Coffin-Manson methods [43].

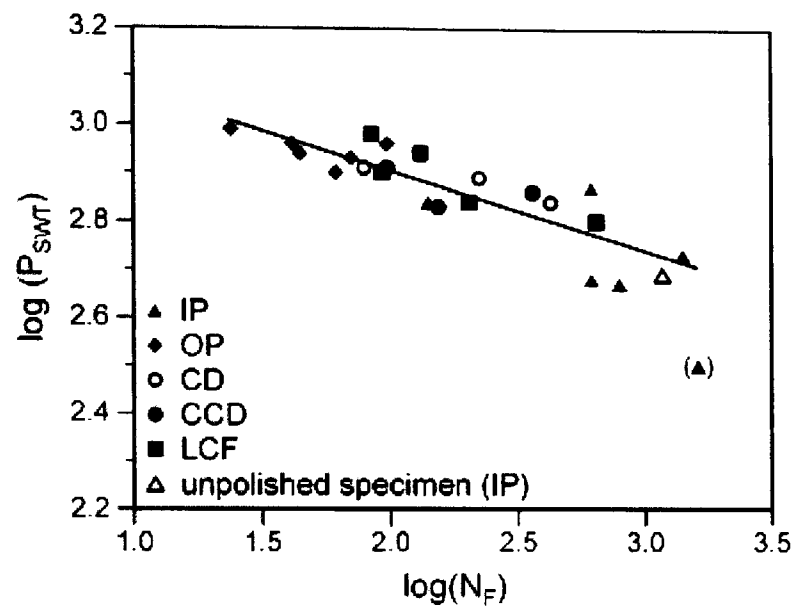


Figure 2.31 Double-logarithmic plot of the damage parameter  $P_{swt}$  vs. fatigue life for TMF tests under various mechanical strain amplitudes, temperature ranges and temperature-strain cycles and for LCF tests at 400°C, 600°C and 800°C and different mechanical strain amplitudes [45].

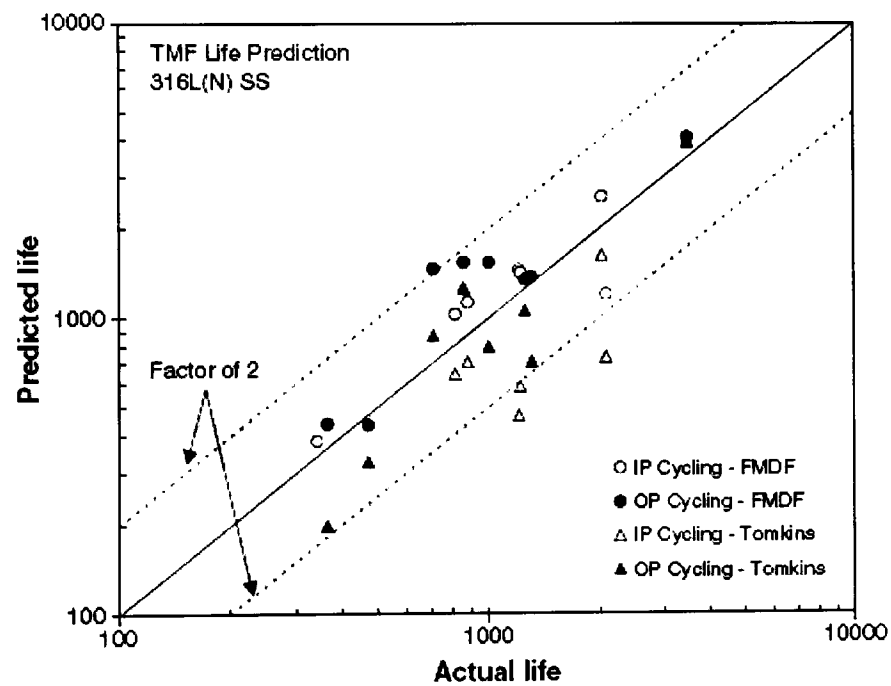


Figure 2.32 Comparison between the experimental and calculated TMF lives using FMDF and Tomkins crack growth approaches [88].

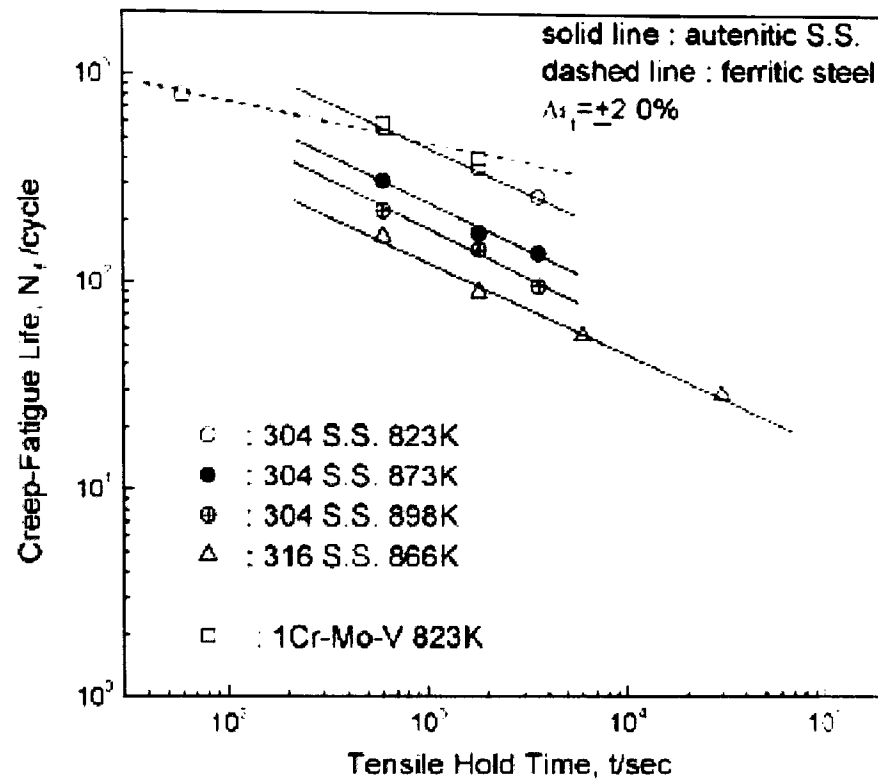


Figure 2.33 Creep-fatigue lives for high temperature materials with various hold times [89].

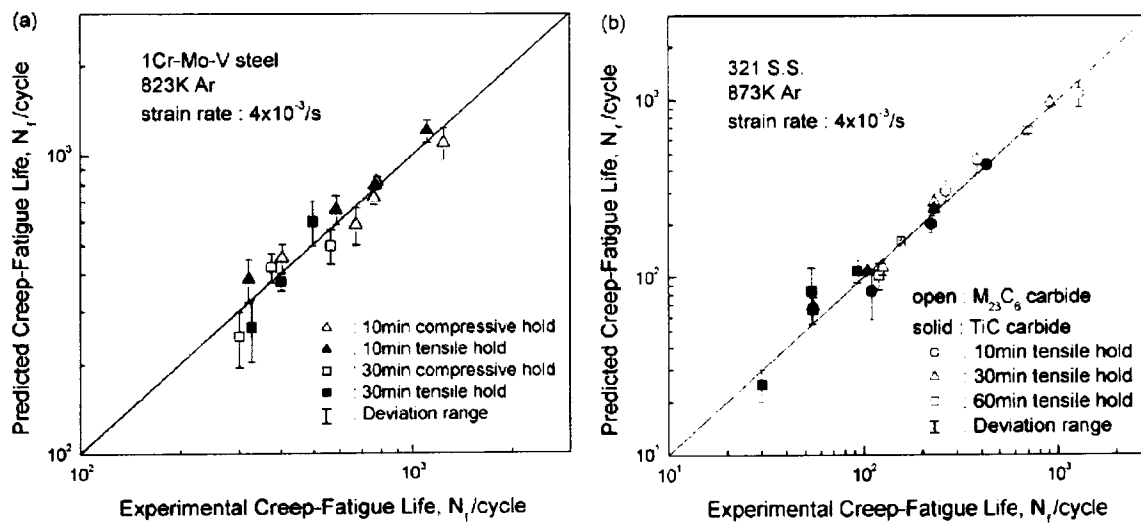


Figure 2.34 Comparison between predicted creep-fatigue lives and experimental creep-fatigue lives: (a) 1Cr-Mo-V steel (b) AISI 321 stainless steel at 873K [89].

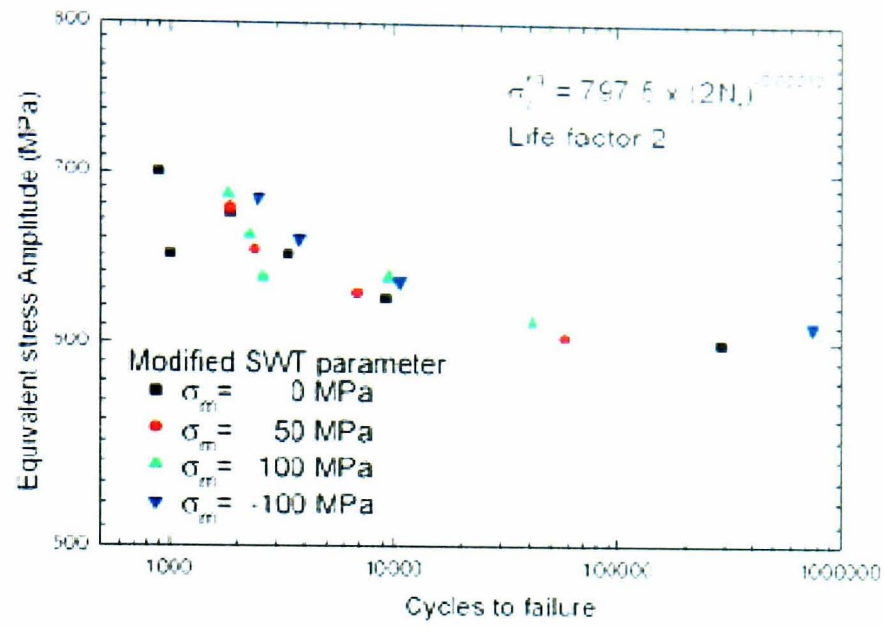


Figure 2.35 Correlation of fatigue data with and without mean stress using the modified SWT parameter for Inconel 718 at 649°C [48].

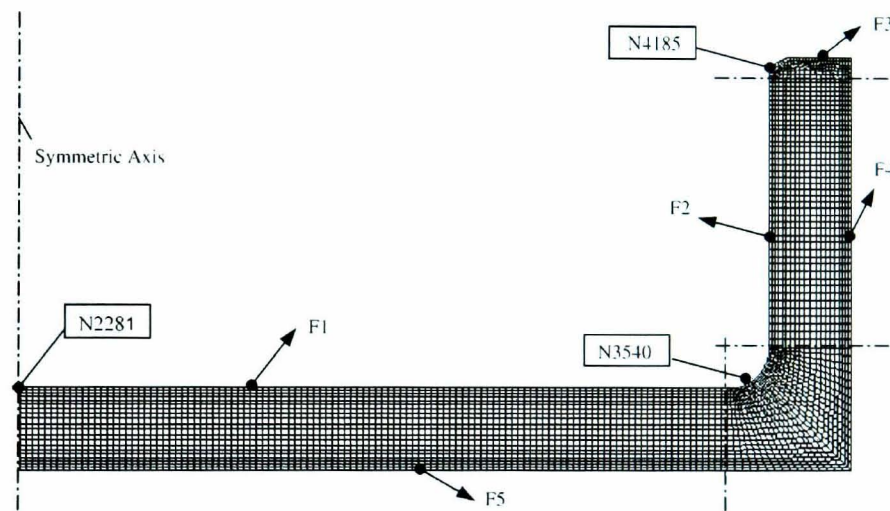


Figure 2.36 Finite element model of axisymmetric die [14].

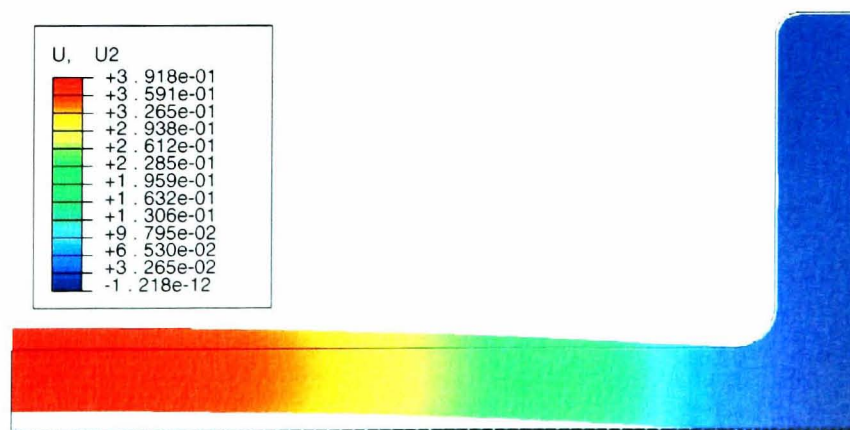


Figure 2.37 Deformation of the die after unloading period [14].

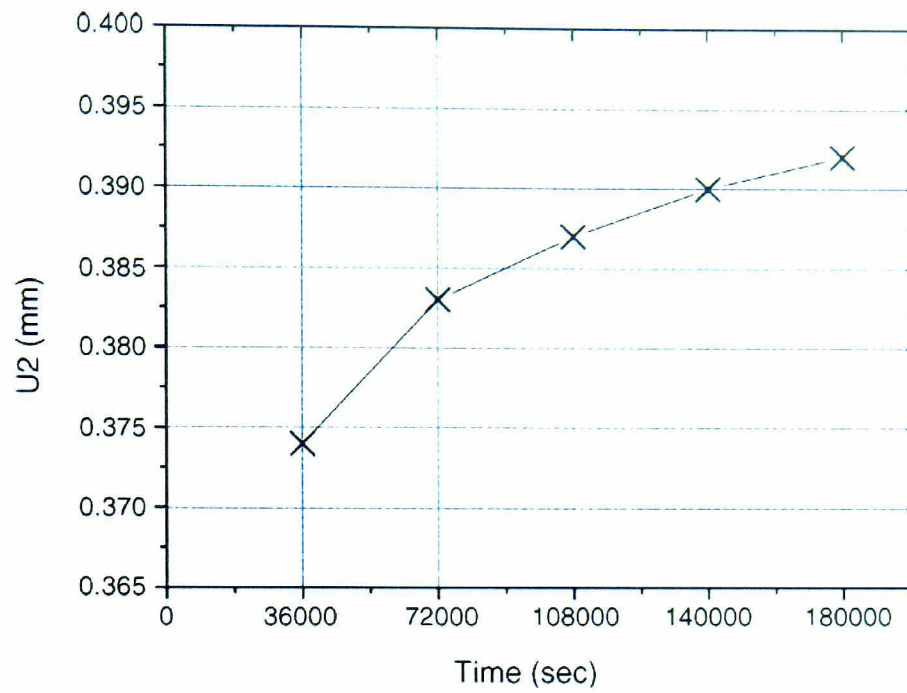


Figure 2.38 Axial residual displacement U2 at N2281 for five cycles [14].

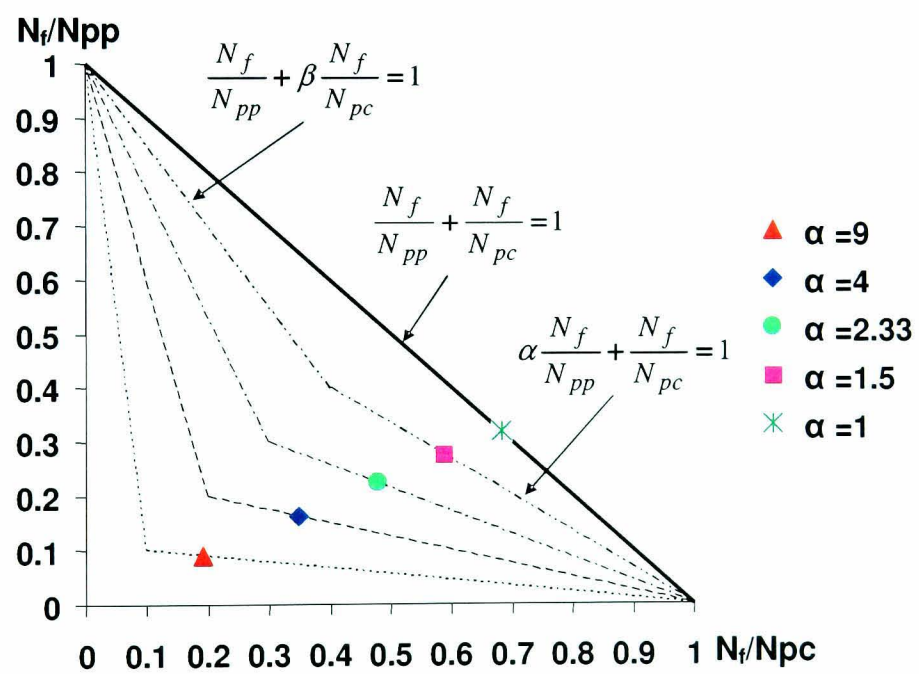


Figure 2.39 Schematic plot of the non-linear damage assumption approach [94].

## Chapter 3

### HIGH TEMPERATURE MATERIAL TESTING

#### 3.1 Introduction

Material testing is important to understand material behaviour under different loading conditions, experienced by components in real life. A good understanding of material behaviour is crucial in material modelling. Material testing is also required to predict material life under applied loading conditions. Two materials investigated in this thesis are; annealed SS-316 stainless steel and high nickel-chromium XN40F alloy.

A series of high temperature experiments were carried out on SS-316 stainless steel and XN40F alloy. Low cycle fatigue (LCF) tests were employed to obtain cyclic material data for a range of temperatures and strain amplitudes. Constant strain amplitude low cycle fatigue tests were also carried out to determine the isothermal fatigue life. Strain controlled thermo-mechanical fatigue tests (TMF) were performed to identify the TMF life and to understand thermo-mechanical behaviour under aniso-thermo-mechanical loading conditions.

Initially high temperature isothermal and TMF cyclic tests were carried out on SS-316 stainless steel. The test program for SS-316 stainless steel is summarized in Table 3.1. Then the actual SPF tool material XN40F (40% Ni, 20% Cr) was investigated through a series of experiments designed with consideration of the FE predicted SPF tool thermal and mechanical loading conditions. The test program for

XN40F alloy is shown in Table 3.2. In addition to strain controlled LCF and TMF tests, uniaxial stress controlled isothermal and thermo-mechanical ratchetting tests were carried out on XN40F material to study material ratchetting behaviour observed in preliminary FE analyses of the SPF tool. The effects of hold periods, representing the SPF forming cycle, were also employed in strain controlled thermo-mechanical fatigue and stress controlled ratchetting tests. Furthermore Stress relaxation tests were also carried out to identify the creep constants for modeling time dependent deformation in the FE tool analyses.

An Instron thermo-mechanical fatigue test rig was employed to carry out the high temperature material testing. The validated code of practice for Strain controlled TMF testing by European Commission Joint research centre (EUR 22281 EN) [97] was employed as guidance while performing TMF testing.

Thermo-mechanical fatigue testing plays an important role in the design, reliability and life-cycle management of critical components used in the power generation, aerospace and automotive industries where components are subjected to combined thermal and mechanical loadings. TMF testing facilitates study of the behaviour of material under combined thermal and mechanical loading by simultaneously varying uniform temperature and mechanical strain over a uniform gauge length of a TMF specimen with certain phase relationship, representing the loading conditions of a critical material element of a component.

The prime requirement of a TMF test is the optimisation of specimen geometry and heating system with respect to temperature field which should be as uniform as

possible over the gauge section of the specimen at every instant of the cycle [97]. Therefore the temperature uniformity over the gauge length of  $\pm 10^\circ\text{C}$  for  $200^\circ\text{C}$  to  $900^\circ\text{C}$  was achieved using careful design of the induction coil [98]. Another important aspect of TMF testing is the thermal strain compensation where the mechanical strain cycle can only be realized by controlling the total strain,  $\epsilon_{tot}$ , applied to the specimen, with thermal strain compensation to achieve a given mechanical strain,  $\epsilon_m = \epsilon_{tot} - \epsilon_{th}$ .

An arbitrary phase shift  $\phi$  between temperature  $T$  and mechanical strain  $\epsilon_m$  makes TMF testing extremely flexible where this additional degree of freedom generates a wide range of test combinations. The two basic relationships between temperature and mechanical strain are in-phase cycling ( $\phi = 0^\circ$ ) where the maximum mechanical strain occurs at the maximum temperature of the cycle and out of phase cycling ( $\phi = 180^\circ$ ) where the maximum mechanical strain occurs at the minimum temperature of the cycle as shown in Fig. 3.1 [97].

## **3.2 TMF test rig and testing**

### **3.2.1 Test set-up**

The 8862 machine from Instron with an axial servo electric dynamic testing system was used carry out all LCF, TMF and stress relaxation tests. The system comprises the load frame, servo electric actuator, power amplifier, load cell and control electronics. Figure 3.2 shows the TMF test rig with all accessories. The machine frame consists of a two column floor standing unit with adjustable crosshead position

using hydraulic crosshead lift and manual clamping. A servo electric screw driven actuator is supplied with the system with  $\pm 100$  kN axial load rating. The minimum speed of the actuator is approximately 1 micron/hr under strain control only whereas the maximum speed is 360 mm/minute.

A fatigue rated load cell of 100 kN is installed to the cross head with a central thread interface to the frame. The load accuracy of the system is  $\pm 0.5\%$  of the indicated load or  $\pm 0.005\%$  of load cell capacity. Hydraulically operated button head collet grips rated at  $\pm 35$  kN are used for clamping the specimen. The grips also allow cooling air to flow into the specimen through the hollow grip drivers. The upper grip is attached to the load cell whereas the lower grip is connected to the actuator as shown in Fig. 3.2. A high temperature ( $1200^{\circ}\text{C}$ ) strain gauged extensometer is used to measure strain during the test. The extensometer has a gauge length of 12.5 mm which is the distance between the two ceramic rods of the extensometer. The extensometer is mounted on the test rig using a spring mount kit shown in Fig.3.3.

The 8800, two axis controller, from Instron is provided with one integrated axis control board with position and load sensor conditioners. The first axis controls the test machine and is referred to as the mechanical axis and is configured for load frame. The second axis controls the heating/cooling system and is configured for the temperature control.

A water cooled variable frequency induction generator rated at 10 kW with a frequency range of 150-450 kHz is used in the system. The temperature of the RF coil is maintained at room temperature using a closed loop water chiller. The RF coil

with a specimen installed is shown in Fig. 3.3. A solid round specimen geometry (Fig. 3.4) with; gauge diameter 6 mm, parallel length 15 mm and shoulder diameter 16 mm was used for testing of the SS-316 steel and the XN40F alloy. A temperature control system provided with a high specification Eurotherm 2404 is integrated to provide temperature control. K-type thermocouples were used to measure and control the temperature during the testing. The induction heating system controller is interfaced to the Instron controller and communicates temperature demand set point from the Instron controller using 0-10V analogue input and temperature signal using a 0-10V analogue output. The system is also provided with an over temperature alarm using a separate thermocouple to shut down the heating system. The emergency stop on the RF heating system is integrated with the Instron 8862 machine emergency stop circuit.

The RF heating system heats the specimen with a maximum heating rate of 50°C/sec and a cooling rate of up to 25°C/sec with a forced air cooling; applicable to hollow specimens. Solid specimens are cooled by natural cooling. The temperature specifications over the 15 mm gauge length of the specimen are: test range- 200°C to 1100°C; temperature stability: (+/-) 15°C and temperature uniformity: (+/-) 10°C. An internal air cooling system is provided and operated from the laboratory air supply. A control is given from the Eurotherm on the above heating system and when cooling is required, a proportional valve controls the air flow to be passed through the specimen to generate cooling.

The system is also provided with Align pro software to check and adjust the load string alignment by adjusting the alignment fixture. The PC is installed with general

purpose interface bus (GPIB) for use with the Instron Fast Console and TMF software.

### **3.2.2 Testing procedure**

Spot welding was used to instrument thermocouples on the specimen surfaces of a gauge length. Thermocouple wires were spot welded to the specimen without contacting each other and keeping the distance between the two wires less than 1mm. Fig. 3.5 shows the standard practice for thermocouple welding [97]. At least two K-type thermocouples were welded on the specimen during every test with one thermocouple acting as a command thermocouple controlling the temperature set point and the other as the guide thermocouple.

After spot welding of thermocouples, the specimen was installed on the test rig between the hydraulically operated Button head collet grips. The axial extensometer was then installed using a spring mount kit as shown in Fig. 3.3. The mount kit was positioned such that not more than 300g contact force is exerted on the specimen through the ceramic rods. The extensometer was calibrated using the calibration kit and the calibration module in the TMF software. Then the total strain was set to zero.

Before starting any test, the evaluation of elastic modulus was carried out at room, maximum and minimum temperature of the test to ensure the correct operation of the stress, strain and temperature measurement systems. This also helps to verify the correct positioning of the sample. The measured values were compared with reference data and also checked for reproducibility before carrying out the actual test.

The TMF software divides the test into four separate stages, out of which the first three are preparatory stages that serve to perform an accurate TMF main test stage. Fig. 3.6 shows the schematic diagram of the TMF test stages. The first stage is the stabilisation stage where the specimen is held at zero load and the temperature is cycled according to the temperature waveform defined by the user for TMF testing. This allows thermal cycles to stabilise before running the later stages. The second stage is called thermal strain measurement in which the TMF software runs the temperature waveform again at zero load. The same waveform will be used in the main stage. The resultant thermal strain is measured by the extensometer and saved at the base time interval for next stages. The next stage is called the thermal strain verification. The Instron TMF software uses the time based thermal strain compensation method for correcting the effects of temperature cycling in which the measured thermal strain as recorded during the thermal strain measurement stage is applied on the specimen in synchronisation with the running temperature waveform. In this case the resultant stress is supposed to be close to zero. This is verified by measuring the stress and ensuring that it remains within the user defined limits. This is called the zero stress test. The last stage is the main test stage where the mechanical strain waveform is applied on the specimen in synchronisation with the temperature waveform.

In the cases of isothermal or low cycle fatigue tests, the temperature of the specimen was maintained constant by selecting the constant temperature option in TMF software. A soak time of 5 minutes was applied before carrying out all high temperature LCF tests. Only the main test stage was used in LCF testing by applying and running mechanical strain waveform. In the case of strain controlled TMF tests,

the temperature was cycled in synchronisation with the mechanical strain. All the four test stages were selected for all strain controlled TMF tests. Five cycles were carried out during stabilisation and verification test stages whereas ten cycles were performed under thermal strain measurement test stage. The first two stages can be optional if the thermal strain for a particular temperature waveform is measured and stored earlier which can be retrieved for the verification stage directly during TMF testing.

For stress controlled TMF testing, only the stabilisation and the main stage were carried out as there is no need for thermal strain compensation under stress control. Depending on the test type, the test stages were selected in the TMF software and performed in the same order.

### **3.3 Isothermal multi strain range fatigue tests**

Strain controlled multi strain range LCF tests were carried out by applying multiple strain amplitudes in steps on a single specimen. The tests were performed by maintaining a constant temperature across the specimen gauge length throughout the test. A soak time of 5 minutes was employed for every test before running the mechanical strain waveform. A fixed number of cycles were carried out at every strain range before running the next strain amplitude waveform.

#### **3.3.1 SS-316 stainless steel**

Isothermal, multi-strain range fatigue tests were carried out at three temperatures of 20°C, 300°C and 600°C. Strain ranges of 0.4%, 0.6%, 0.8% and 1% were employed for all the three temperature tests. Thirty cycles were carried out at every strain range

before applying the next strain amplitude. Triangular mechanical strain waveforms were used using ( $R_\epsilon = \epsilon_{\min}/\epsilon_{\max} = -1$ ) strain ratio and  $2 \times 10^{-4} \text{ s}^{-1}$  strain rate. The stress-strain loops stabilized in approximately 20 cycles. Fig. 3.7 shows the measured stabilized stress-strain loops obtained for all strain ranges and different temperatures. The backbone curve depicting the cyclic stress-strain data for three different temperatures is shown in Fig. 3.8. Fig. 3.8 shows that the cyclic stress decreases with increasing temperature.

### **3.3.2 XN40F alloy**

Similar to the SS-316 steel, fully reversed isothermal multi-strain range LCF tests were performed on XN40F alloy at four different temperatures of 20°C, 500°C, 700°C and 900°C, spanning the range of temperatures for the SPF process. Five strain ranges of 0.6%, 0.8%, 1.0%, 1.2% and 1.4% were applied in steps for every individual temperature. However the tests at 20°C and 500°C were ended during 1.2% strain range due to breaking of specimen and the data up to 1.0% strain range was obtained. Two strain rates of  $5 \times 10^{-3} \text{ s}^{-1}$  and  $5 \times 10^{-4} \text{ s}^{-1}$  were employed in order to quantify the cyclic strain rate effect. Thirty cycles were performed at every strain range; where the XN40F alloy stabilized in approximately 15 cycles. Fig. 3.9 and 3.10 show the stabilized stress-strain loops of XN40F alloy for the strain rates of  $5 \times 10^{-3} \text{ s}^{-1}$  and  $5 \times 10^{-4} \text{ s}^{-1}$  respectively. The backbone curves representing the cyclic material data for the two strain rates are shown in Fig. 3.11. Again the stabilized stress response decreases with increasing temperature for both strain rates.

### **3.4 Fatigue lifing tests for SS-316 stainless steel**

Strain controlled isothermal and TMF tests (Table 3.1) were carried out to identify the isothermal and the thermo-mechanical fatigue life of SS-316 stainless steel. Unlike the multi strain range LCF tests, a single strain range was applied on a specimen using a triangular mechanical strain waveform. Specimen failure was assumed to correspond to 15% drop in maximum load.

#### **3.4.1 Isothermal LCF testing**

Isothermal LCF tests at 600°C were carried out for three strain ranges of 1.0%, 1.2% and 1.4% using a fully reversed triangular mechanical strain waveform with a constant strain rate of  $2 \times 10^{-4} \text{ s}^{-1}$  as shown in Fig. 3.12. From the cyclic stress response curves (Fig. 3.13), it can be seen that the cyclic hardening occurred within the first 20 cycles. After initial hardening, a saturation stage was observed until the specimen failure (15% load drop).

#### **3.4.2 TMF testing**

Both in-phase and out of phase TMF tests (Table 3.1) were conducted under mechanical strain control with a temperature variation from 450 to 600°C. In-phase TMF tests were carried out for the same three strain ranges used in the IF testing with fully reversed triangular waveform and a strain rate of  $2 \times 10^{-4} \text{ s}^{-1}$  whereas only one out of phase TMF test was performed for a strain range of 1.0% (Figure 3.14). Again, cyclic hardening occurred within the initial 20 cycles (Figure 3.15) followed by saturation until the specimen failure. From Figure 3.15, it can be seen that a

compressive mean stress of 10 MPa occurred in IP TMF whereas tensile mean stress 18 MPa observed in OP TMF.

### **3.4.3 Fatigue life evaluation**

The IF and TMF lives of SS-316 stainless steel were evaluated and compared by plotting mechanical strain ranges, inelastic strain ranges, stress ranges and total strain energy as a function of fatigue life as shown in Fig. 3.15 to 3.18. The inelastic strain and stress ranges at half life were considered while plotting them as a function of fatigue life. The IF and TMF lives with respect to different damage parameters are summarised in Table 3.3. Fig. 3.16 shows that the fatigue life under in-phase TMF condition is shorter than IF at higher strain ranges of 1.2% and 1.4% whereas the TMF IP life at the lower strain range of 1.0% is longer than the corresponding IF life. It can also be seen from Fig. 3.16 that the fatigue life from the only out of phase TMF test carried out is shorter than the corresponding IF and TMF IP lives. Fig. 3.17 showed the similar trend with inelastic strain ranges as a function of fatigue lives. From Fig. 3.18, it can be concluded that the stress ranges from IF tests are shorter than for TMF tests. The total energy parameter ( $W=\Delta\sigma \times \Delta\varepsilon^{in}$ ) was also plotted as a function of fatigue life (Fig. 3.19) and showed a similar trend to that of IF and TMF test results.

## **3.5 Fatigue lifing tests for XN40F alloy**

The fatigue life tests for XN40F alloy were designed on the basis of the thermo-mechanical loading predictions of a realistic large SPF tool as discussed in chapters 6 and 7. Table 3.2 lists the strain controlled isothermal and TMF tests carried out to

determine the fatigue life. In the TMF testing only the OP condition was investigated as it is the predicted thermo-mechanical behaviour at critical locations of the tool. Strain hold periods were also employed in the TMF testing to mimic the dwell period of the SPF forming cycle. A ‘representative’ test with tensile mean strain was designed and performed. The representative test replicates the stress-strain-temperature behaviour of the tool across the front and back edges (critical locations) exposed to ambient when press front and back doors opened for blank insert and part removal operations of the tool from FE predictions.

### **3.5.1 Isothermal LCF testing**

Two isothermal LCF tests at 900°C were carried out for strain ranges of 0.8% and 1.2%. A fully reversed triangular mechanical strain waveform (Fig. 3.20) was applied with a strain rate of  $2.5 \times 10^{-4} \text{ s}^{-1}$ . The specimen was soaked for 5 minutes at 900°C before running the mechanical strain waveform. A cyclic stress response obtained from IF tests is shown Fig. 3.21.

### **3.5.2 TMF testing**

OP TMF tests were conducted using mechanical strain control with varying temperature from 750-900°C for fully reversed mechanical strain ranges (Fig. 3.22) of 0.8%, 1.0% and 1.2%. A strain rate of  $2.5 \times 10^{-4} \text{ s}^{-1}$  was employed based on the natural cooling rate of the specimen from 900 to 750°C. Three additional TMF tests were performed with a strain hold of 120 seconds (Fig. 3.24) in compression at 900°C dwell. The cyclic stress responses (Fig. 3.23 and Fig. 3.25) showed that cyclic hardening occurred for the initial 20 cycles which followed by a steady stabilized

response until the specimen failure. A tensile mean stress resulted for both the cases, i.e. with and without the hold period.

A representative SPF tool test was designed based on the FE analyses of the tool described in Chapters 6 and 7. Mechanical and temperature strain waveform is shown in Figure 3.26. A tensile mechanical strain of 0.3% was applied whilst varying the temperature from 900°C to 750°C (strain rate of  $1 \times 10^{-4} \text{ s}^{-1}$ ). This was followed by a complete mechanical strain recovery with temperature varying from 750 to 900°C at the same strain rate. A hold period of 120 seconds at zero strain and at 900°C temperature was employed to represent the forming cycle of the SPF process. An average tensile mean stress of 36 MPa resulted during the test as seen in Fig. 3.27. The test ended after 2086 cycles with a brittle fracture of the specimen (Fig. 3.28). The stabilized stress-strain loop is shown in Fig. 3.29. From Fig. 3.29, the compressive stress was relaxed during the strain hold from 42 MPa to 13 MPa in 120 seconds. The stabilised stress-strain loop showed an inelastic strain range ( $\Delta \epsilon^{\text{in}}$ ) of 0.19 %.

### 3.5.3 Fatigue life evaluation

As for the SS-316 stainless steel, the IF and TMF lives of the XN40F tool material were evaluated and compared by plotting various damage parameters such as mechanical strain ranges, inelastic strain and stress ranges and total energy ( $W = \Delta \sigma \times \Delta \epsilon^{\text{in}}$ ) as a function of fatigue life in Fig. 3.30 to 3.33. It can be seen that the TMF OP life is shorter than IF life which is consistent with the trend of SS-316 stainless. Furthermore the TMF OP life with a hold period is consistently shorter than that without a hold period. The inelastic strain ranges (Fig. 3.31) obtained at the half life

are not significantly different for IF and TMF tests but the IF stress ranges are significantly smaller as shown in Fig. 3.32. Total energy parameter  $W$  (Fig. 3.33) showed a similar relationship between IF and TMF lives.

### **3.6 Stress controlled ratchetting tests for XN40F alloy**

Stress controlled ratchetting tests were performed to study the material ratchetting behaviour of XN40F alloy under asymmetrical cyclic loading conditions with and without temperature cycling and with and without a stress hold. The peak stresses obtained from the strain controlled 'representative' test were used in the stress controlled ratchetting tests.

A 'representative' test was again carried out this time under stress control using the same cycle times as employed in the strain controlled 'representative' test (Fig. 3.26). The mechanical stress and temperature waveforms are shown in Fig. 3.34 with the stress is cycled from -42 MPa to 114 MPa in the OP condition and the temperature varying from 900-750°C. A stress and temperature hold at -42 MPa and 900°C was applied for 120 seconds. The temperature cycle stabilizes during the stabilization test which is followed by the main test stage where the mechanical stress is cycled in synchronisation with the temperature. Significant strain accumulation in compression occurred as shown in Figs. 3.35 and 3.36. The test was ended when the specimen started buckling after 297 cycles. The mean strain of 9.91% was accumulated in 297 cycles.

The second stress controlled TMF test was carried out without the stress and temperature hold period as shown in Fig. 3.37. Similar to the representative test, the

stress was cycled in the OP condition. The mean strain versus number of cycles is shown in Fig. 3.38. Here a strain accumulated in the tensile direction. A mean strain of 4.25% was accumulated in 7151 cycles.

Two isothermal stress controlled tests were also performed at 900°C and 700°C to analyse the effect of constant temperature on ratchetting behaviour. No stress hold period was applied in these isothermal tests. Fig. 3.39 shows the stress waveform where the temperature is constant during the test at 900°C. A mean tensile strain accumulated as shown in Fig. 3.40. The specimen broke with a ductile fracture with 39 % strain accumulated in 32 cycles (Fig. 3.41). The same test was performed at 700°C for 10 cycles to understand the ratchetting behaviour at lower temperature. A plastic shakedown occurred after initial transient ratchetting during the first 5 cycles (Fig. 3.42).

### **3.7 Stress relaxation tests for XN40F alloy**

Stress relaxation tests were carried out to identify the secondary creep constants for Norton's creep power law. Tests were performed at constant temperatures of 500, 700 and 900°C by applying and holding 0.15% strain in tension. However no stress relaxation was observed for the test at 500°C. Figs. 3.43 and 3.44 showed the stress relaxation that occurred during the strain hold period of 360 seconds for 900°C and 700°C temperatures respectively. For 900°C, the stress was relaxed from 83 MPa to 5 MPa whereas for 700°C the stress relaxation was from 155 MPa to 72 MPa.

### 3.8 Summary and conclusions

Isothermal multi strain range cyclic tests were successfully carried out on two materials, SS-316 stainless steel and XN40F alloy. The stabilized stress strain loops were obtained for a range of temperatures to determine the cyclic material data. This cyclic material data is presented as backbone curves and can be used to characterize material parameters to define various material models. The cyclic material data obtained is used in Chapter 4 to identify material parameters for non-linear kinematic, combined kinematic and isotropic and the two layer viscoplastic material models.

Strain controlled isothermal and TMF lifing tests were also performed on both the materials. From the test results, it can be concluded that the prediction of TMF life based on isothermal fatigue test data is not always safe especially for critical components working at high temperatures. Therefore TMF testing is very important in predicting the life of critical components operating under thermo-mechanical loading conditions. From TMF tests of both materials, the in phase TMF testing showed a compressive mean stress whereas the out of phase condition showed a tensile mean stress. However a negligible mean stress was observed in the IF tests.

In the case of SS-316 steel, the shortest life was observed for the TMF OP test comparing to the corresponding IF and TMF IP tests. The tensile mean stress is more damaging than the compressive mean stress. However, it can not be generalized that TMF OP life is always shorter than TMF IP life. The relationship between TMF IP and TMF OP differs from material to material and depends on material properties with respect to temperature [43, 44, 45, 95, 96].

For XN40F, TMF OP tests with a strain hold in compression showed the shortest life in comparison with IF and TMF OP tests. This suggests that the stress relaxation during strain hold is an important additional damage parameter for XN40F alloy. A strain controlled 'representative' SPF tool test was successfully performed on XN40F alloy. The representative test mimics the FE predicted critical damaging phase of part removal and insertion of the SPF process along with the forming cycle hold period for the critical locations of the tool based on FE analyses. A brittle fracture resulted after 2086 cycles and the representative SPF tool life was obtained.

Stress controlled TMF and IF tests were carried out to study the ratchetting behaviour of XN40F alloy. In the 'representative' stress controlled TMF test, ratchetting occurred in compression which is opposite to the direction of the mean stress, due to larger compressive creep strains occurring during the compressive stress hold period. However ratchetting in the tensile direction occurred for the remaining stress controlled tests without hold periods. The stress controlled TMF test without a hold period showed a slow ratchetting rate where a mean strain of 4.25% was accumulated in 7151 cycles. In contrast, for the isothermal test at 900°C, the mean strain of 39% was accumulated in only 32 cycles, test ending with ductile fracture of the specimen. The stress controlled isothermal test at 700°C showed plastic shakedown after initial transient ratchetting for the first 5 cycles. Stress relaxation tests at 500°C, 700°C and 900°C were also carried out to identify the secondary creep constants for FE modeling of the time dependent cyclic deformation of the SPF tool. These test results are used in Chapter 4 to identify the creep constants.

From XN40F test it is inferred that the XN40F material is very ductile at 900°C and the creep strain during the stress hold and the stress relaxation during the strain hold plays an important role in the tool failure.

Table 3.1 Test programme summary for SS-316 stainless steel

| Test No. | Test type                                   | Temperature       | Test Specifications  | Material parameters                                    |
|----------|---|-------------------|--|--|
| 1        | Isothermal multi-strain range fatigue tests | 20°C,300°C, 600°C | $R_{\epsilon}=-1$<br>Triangular waveform<br>$\Delta\epsilon=$<br>0.4%,0.6%,0.8% and 1%<br>Strain rate $=2 \times 10^{-4} \text{ s}^{-1}$ | Stabilized Stress-strain loops<br>(k, C and $\gamma$ ) |
| 2        | Isothermal strain controlled fatigue tests  | 600°C             | $R_{\epsilon}=-1$<br>Triangular waveform<br>$\Delta\epsilon=$ 1%,1.2% and 1.4%<br>Strain rate $=2 \times 10^{-4} \text{ s}^{-1}$         | IF life based on 15% drop in maximum stress            |
| 3        | Strain control TMF In-phase tests           | 450-600°C         | $R_{\epsilon}=-1$<br>Triangular waveform<br>$\Delta\epsilon=$ 1%,1.2% and 1.4%<br>Strain rate $=2 \times 10^{-4} \text{ s}^{-1}$         | TMF IP life based on 15% drop in maximum stress        |
| 4        | Strain control TMF Out of phase tests       | 450-600°C         | $R_{\epsilon}=-1$<br>Triangular waveform<br>$\Delta\epsilon=$ 1%<br>Strain rate $=2 \times 10^{-4} \text{ s}^{-1}$                       | TMF OP life based on 15% drop in maximum stress        |

Table 3.2 Test programme summary for XN40F alloy

| Test No. | Test type  | Temperature                  | Test Specifications   | Material parameters                               |
|----------|--|------------------------------|---|---|
| 1        | Isothermal multi-strain range fatigue tests                    | 20°C, 500°C, 700°C and 900°C | $R_\epsilon = -1$<br>Triangular waveform<br>$\Delta\epsilon = 0.4\%$<br>0.6%, 0.8%, 1.2%, 1.4%<br>Strain rates 1) $5 \times 10^{-3} \text{ s}^{-1}$<br>2) $5 \times 10^{-4} \text{ s}^{-1}$ | Stabilized Stress-strain loops<br>C and $\gamma$  |
| 2        | Isothermal strain controlled fatigue tests                     | 900°C                        | $R_\epsilon = -1$<br>Triangular waveform<br>$\Delta\epsilon = 0.8\%, 1.2\%$<br>Strain rate $2.5 \times 10^{-4} \text{ s}^{-1}$  | IF life based on 15% drop in maximum stress       |
| 3        | TMF OP strain controlled tests                                 | 750-900°C                    | $R_\epsilon = -1$<br>Triangular waveform<br>$\Delta\epsilon = 0.8\%, 1.0\%, 1.2\%$<br>Strain rates 1) $2.5 \times 10^{-4} \text{ s}^{-1}$<br>Hold period=0                                  | TMF life based on 15% drop in maximum stress      |
| 4        | TMF OP strain controlled tests with hold period in compression | 750-900°C                    | $R_\epsilon = -1$<br>$\Delta\epsilon = 0.8\%, 1.0\%, 1.2\%$<br>Strain rate $= 2.5 \times 10^{-4} \text{ s}^{-1}$<br>Hold period=120 Sec   | TMF life based on 15% drop in maximum stress      |
| 5        | Strain controlled TMF OP representative SPF tool test          | 750-900°C                    | $R_\epsilon \neq -1$<br>$\Delta\epsilon = 0.3\%$<br>Strain rate $= 1 \times 10^{-4} \text{ s}^{-1}$<br>Hold period=120 sec in compression   | TMF life based on 15% drop in maximum stress      |
| 6        | Stress control TMF OP representative SPF tool test             | 750-900°C                    | $R_\sigma \neq -1$<br>$\sigma_{\min} = -42 \text{ MPa}$<br>$\sigma_{\max} = 114 \text{ MPa}$<br>Hold period=120 sec in compression<br>Cycle time=180 sec                                    | Ratcheting life and material Ratcheting behaviour |
| 7        | TMF OP stress controlled test without hold period              | 750-900°C                    | $R_\sigma \neq -1$<br>$\sigma_{\min} = -42 \text{ MPa}$<br>$\sigma_{\max} = 114 \text{ MPa}$<br>Cycle time=60 sec<br>No hold period   | Material Ratcheting behaviour                     |

|   |  |                    |   |   |
|---|--|--------------------|---|---|
| 8 | Stress controlled isothermal tests without hold period | 700°C, 900°C       | $R_\sigma \neq -1$<br>$\sigma_{\min} = -42$ MPa<br>$\sigma_{\max} = 114$ MPa<br>Cycle time=60 sec<br>No hold period | Ratcheting life and material ratcheting behaviour |
| 9 | Stress relaxation tests                                | 500, 700 and 900°C | $\epsilon = 0.15\%$<br>Hold period=360 sec  | Secondary Creep constants                         |

Table 3.3 Summary of fatigue life test results of SS-316 stainless steel

| Test Specifications       | Mechanical strain range<br>$\Delta\epsilon$ | Inelastic strain range at half life<br>$\Delta\epsilon_{in}$ | Stress range at half life<br>$\Delta\sigma$ MPa | Number of cycles to failure<br>$N_f$ |
|---------------------------|---|--|---|--------------------------------------|
| IF test<br>600°C          | 0.01  | 0.0057   | 632   | 921                                  |
| IF test<br>600°C          | 0.012                                       | 0.0076   | 667   | 460                                  |
| IF test<br>600°C          | 0.014                                       | 0.0092   | 701   | 321                                  |
| TMF IP test<br>450-600 °C | 0.01  | 0.0048   | 700   | 1136                                 |
| TMF IP test<br>450-600 °C | 0.012                                       | 0.0068   | 736   | 414                                  |
| TMF IP test<br>450-600 °C | 0.014                                       | 0.0086   | 803   | 193                                  |
| TMF OP test<br>450-600 °C | 0.01  | 0.0053   | 712   | 700                                  |

Table 3.4 Summary of fatigue life test results of XN40F alloy

| <b>Test Specifications</b>                               | <b>Mechanical strain range</b><br>$\Delta\varepsilon$ | <b>Inelastic strain range at half life</b><br>$\Delta\varepsilon_{in}$ | <b>Stress range at half life</b><br>$\Delta\sigma$ MPa | <b>Number of cycles to failure</b><br>$N_f$ |
|--|---|--|--|---|
| IF test<br>900°C   | 0.008   | 0.0064   | 110  | 1202  |
| IF test<br>900°C   | 0.012   | 0.0105   | 168  | 366   |
| TMF OP test<br>750-900 °C                                | 0.008   | 0.0066   | 242  | 833   |
| TMF OP test<br>750-900 °C                                | 0.01  | 0.0078   | 239  | 733   |
| TMF OP test<br>750-900 °C                                | 0.012   | 0.0097   | 236  | 337   |
| TMF OP test<br>with hold in<br>compression<br>750-900 °C | 0.008   | 0.0067   | 236  | 453   |
| TMF OP test<br>with hold in<br>compression<br>750-900 °C | 0.01  | 0.0087   | 240  | 315   |
| TMF OP test<br>with hold in<br>compression<br>750-900 °C | 0.012   | 0.0102   | 271  | 226   |

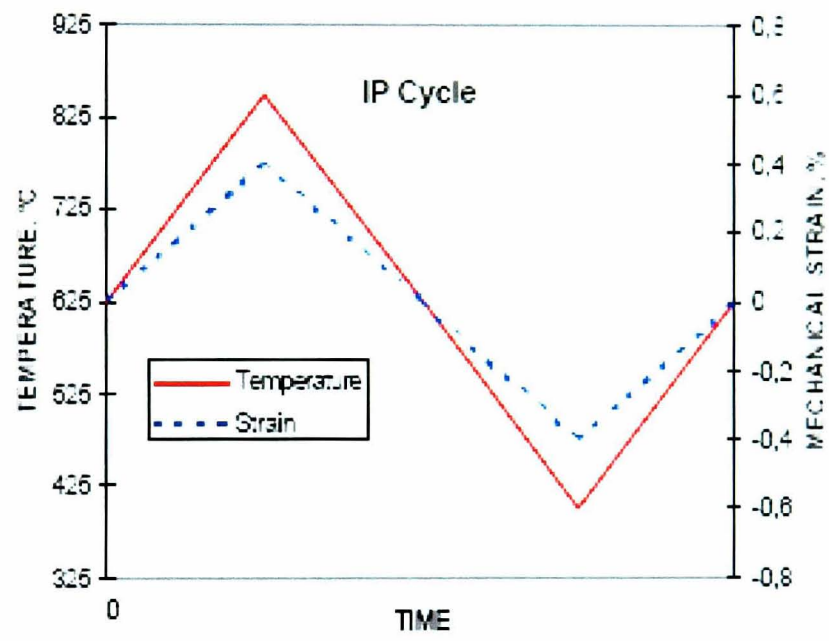
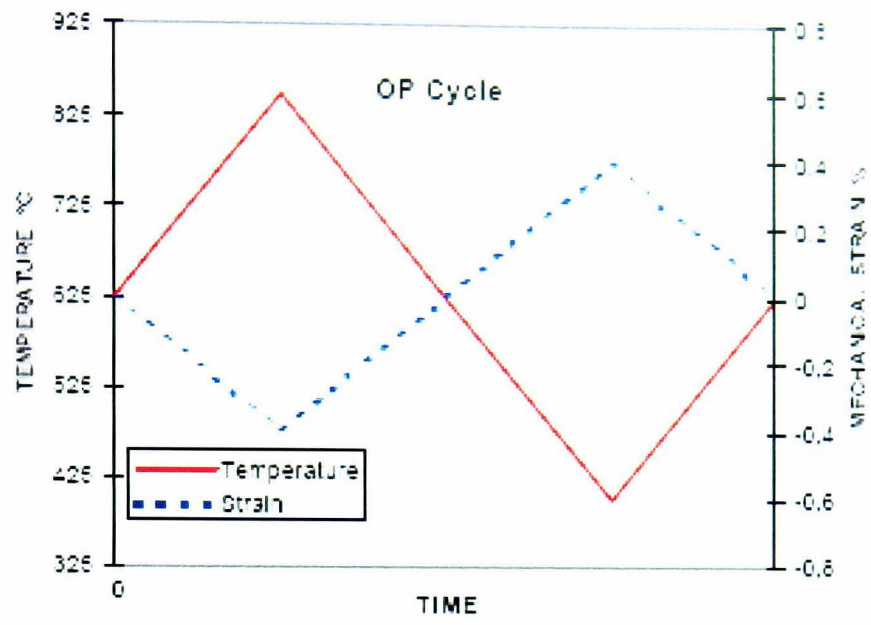
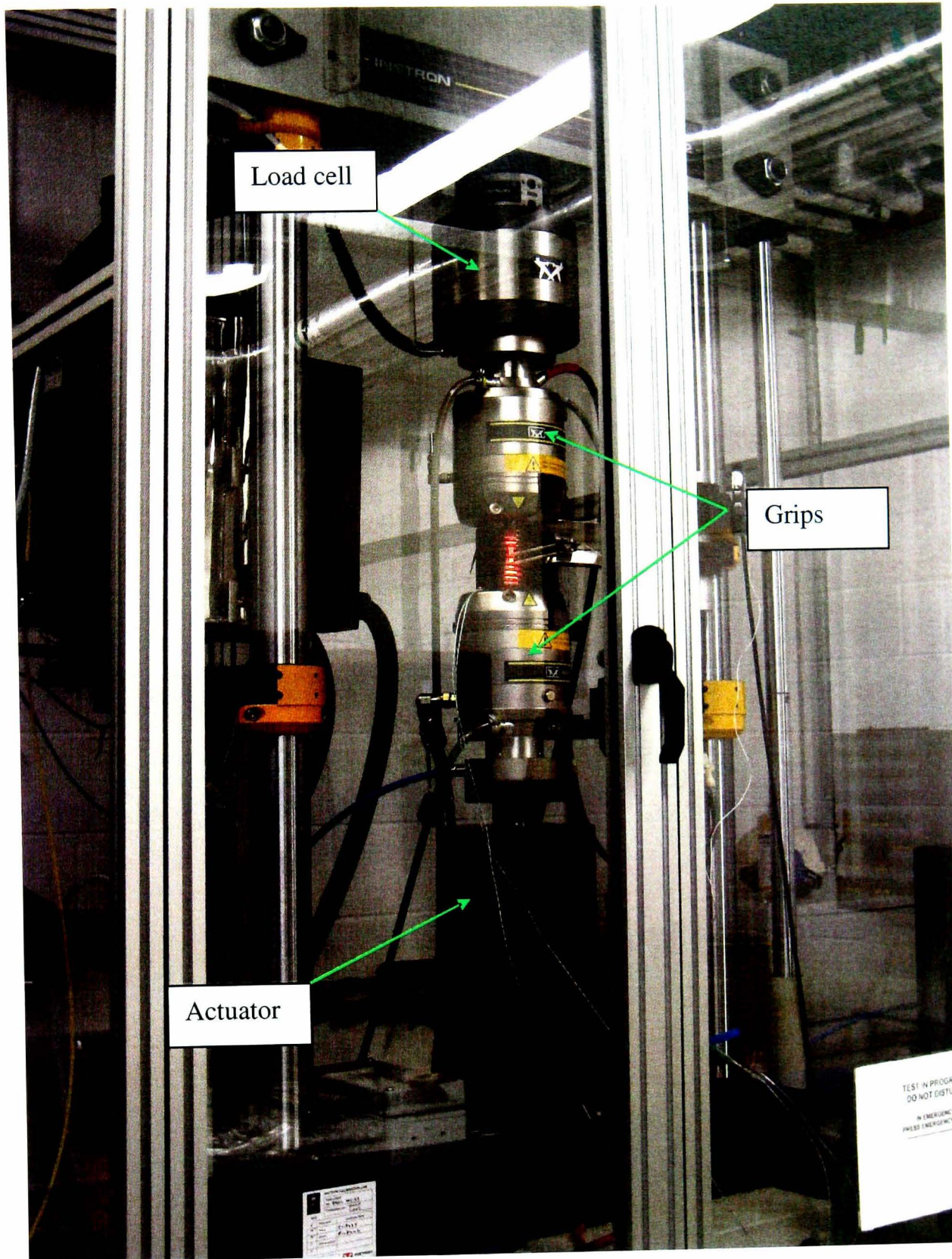
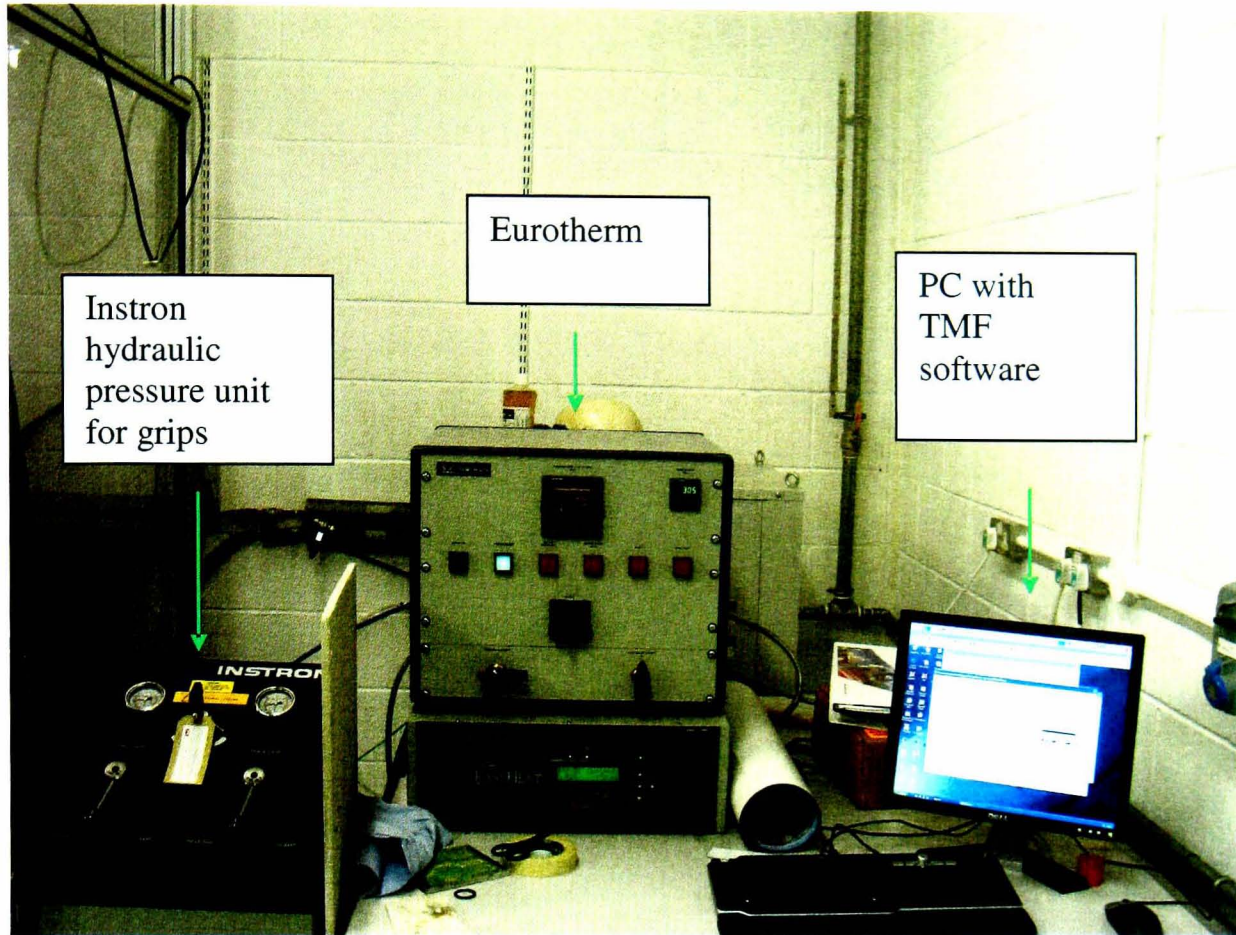


Figure 3.1 Out of phase and in phase TMF cycles [97].



(a)

Figure 3.2 TMF test rig; (a) Machine set-up, (b) Accessories



(b)

Figure 3.2 (Contd.) TMF test rig; (a) Machine set-up, (b) Accessories

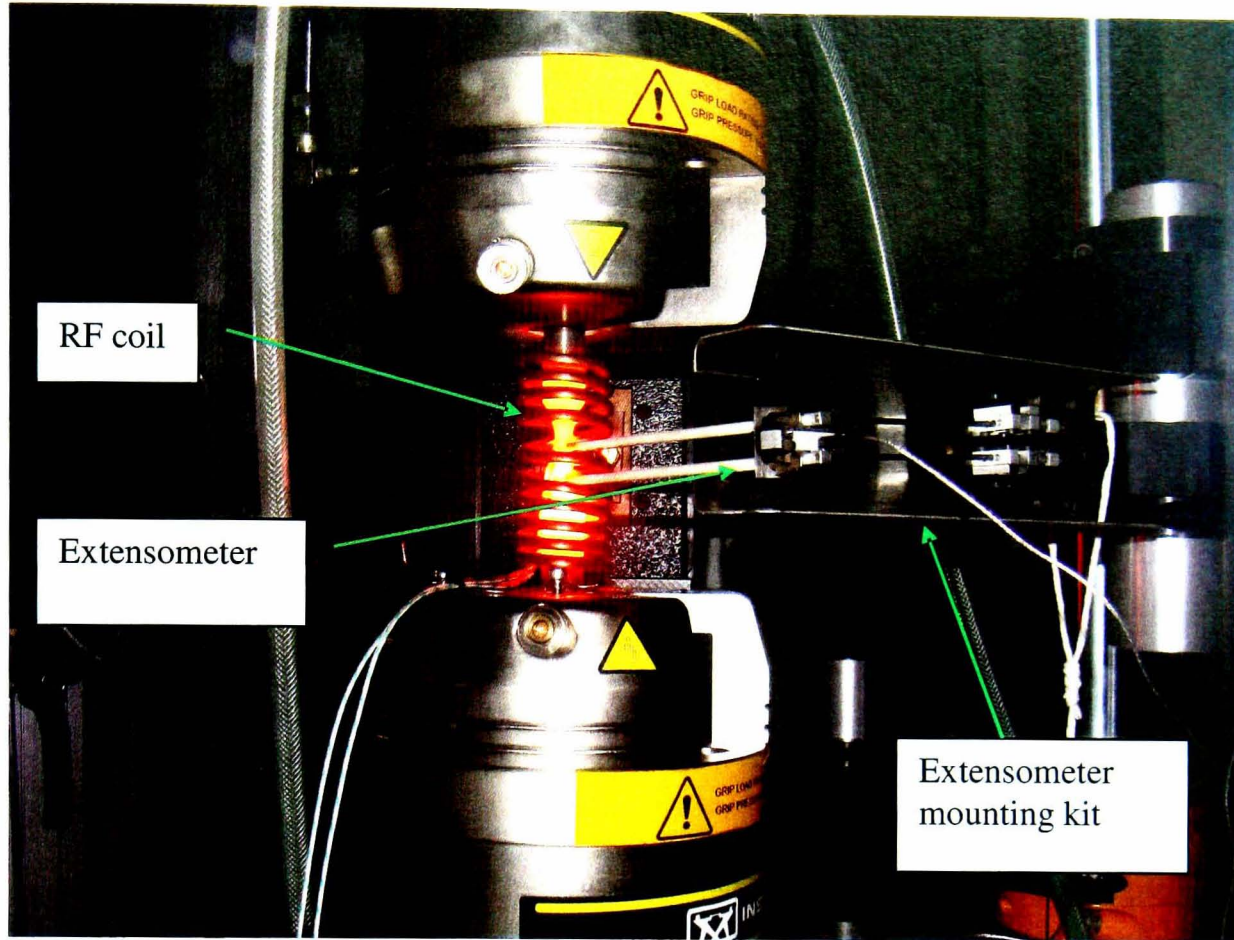


Figure 3.3 Extensometer mount kit and RF coil of TMF test rig.

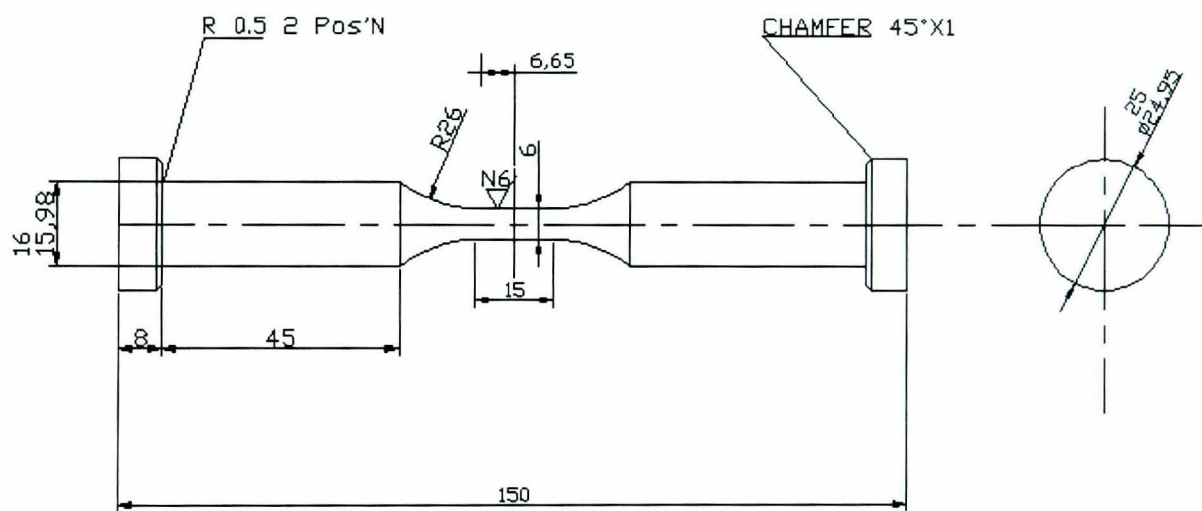


Figure 3.4 TMF specimen

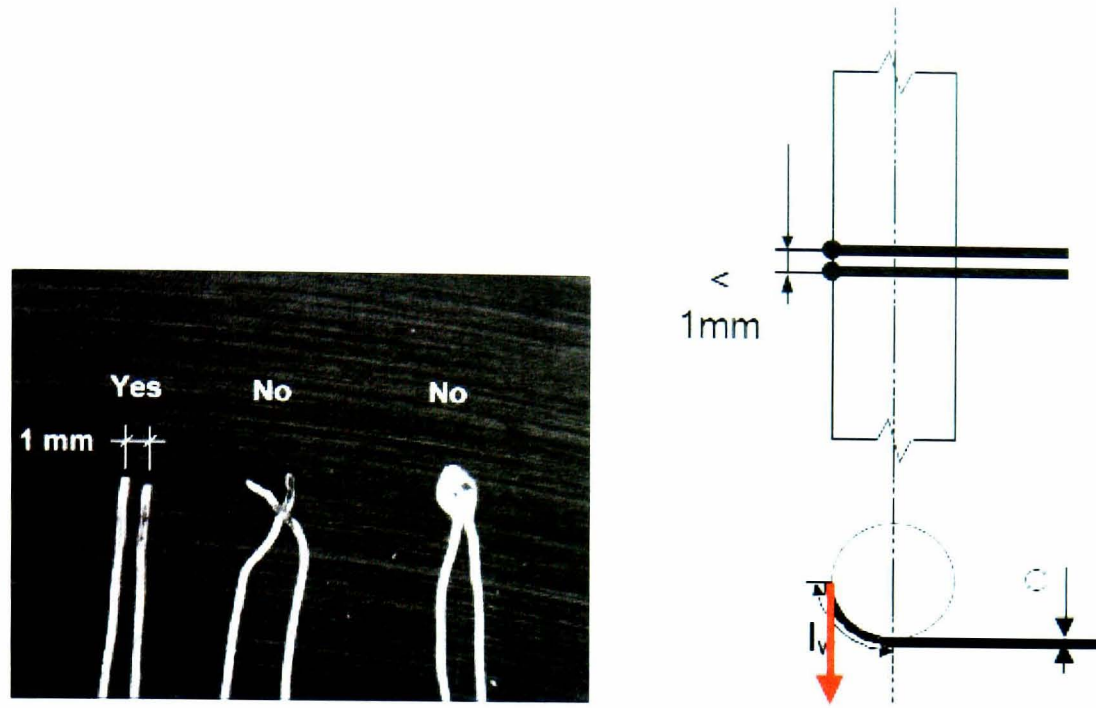


Figure 3.5 Standard practice of thermocouple welding [97].

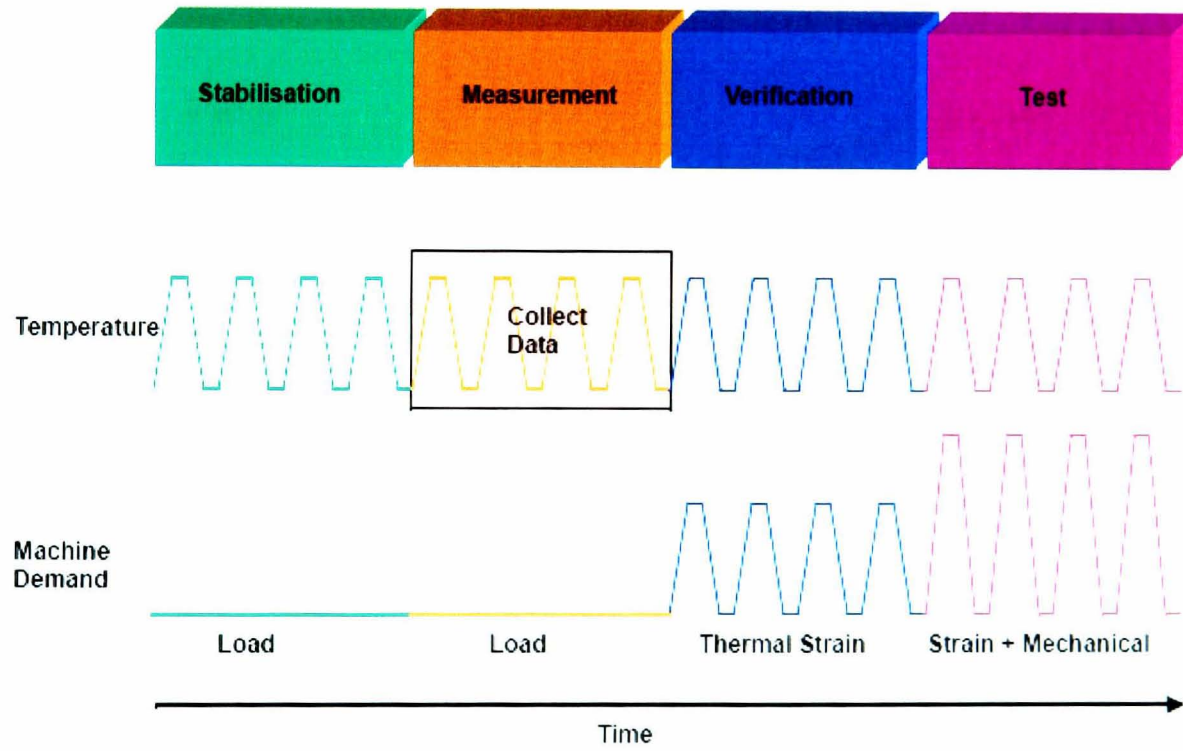


Figure 3.6 Schematic diagram of TMF test stages [99]

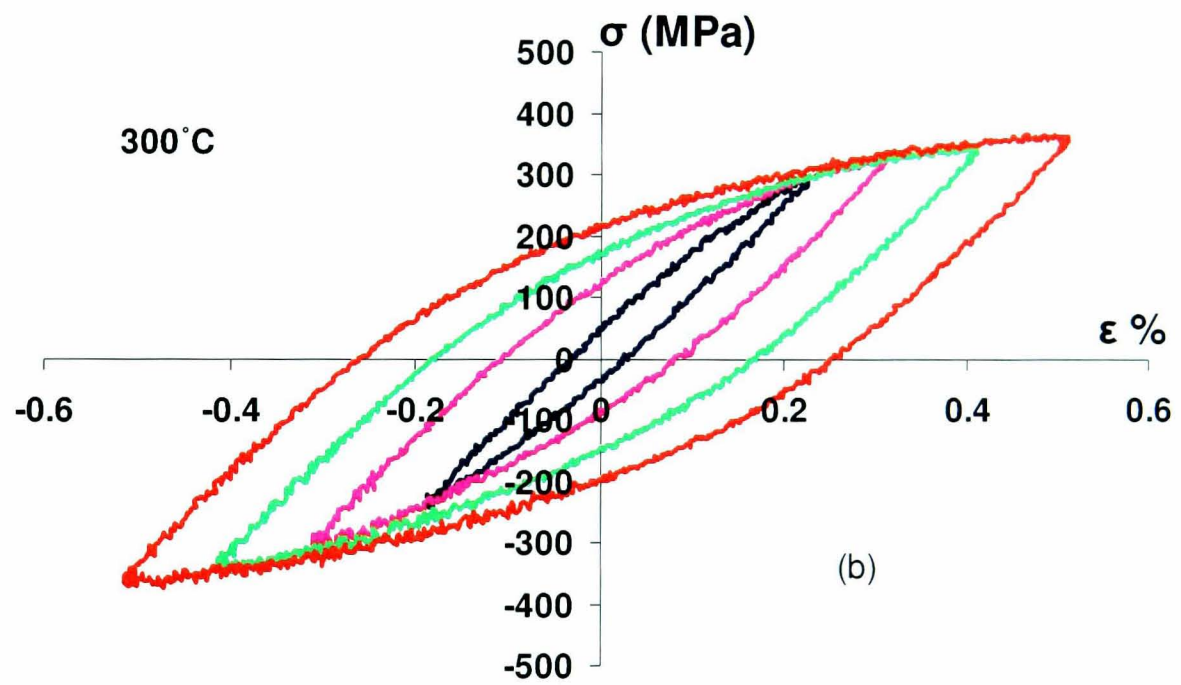
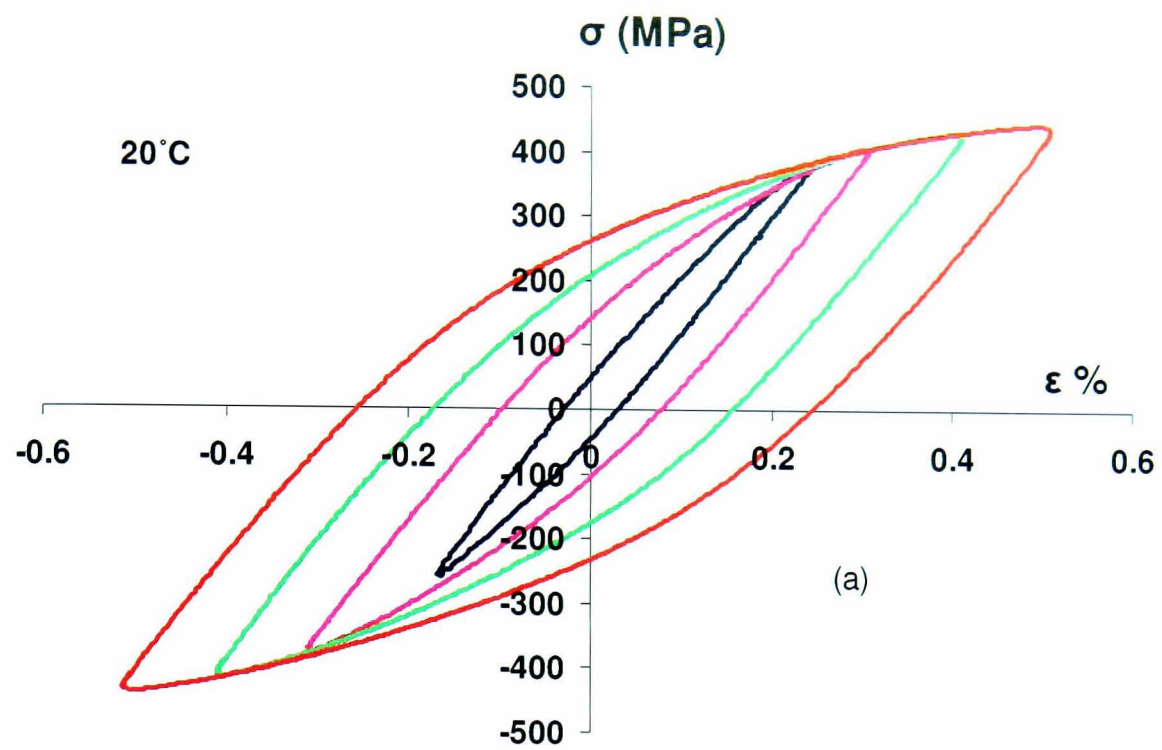


Figure 3.7 Measured stabilized stress-strain loops of SS-316 stainless steel from the multi strain range strain controlled LCF tests carried out at a strain rate of  $2 \times 10^{-4} \text{ s}^{-1}$ ; (a) 20°C, (b) 300°C and (c) 600°C

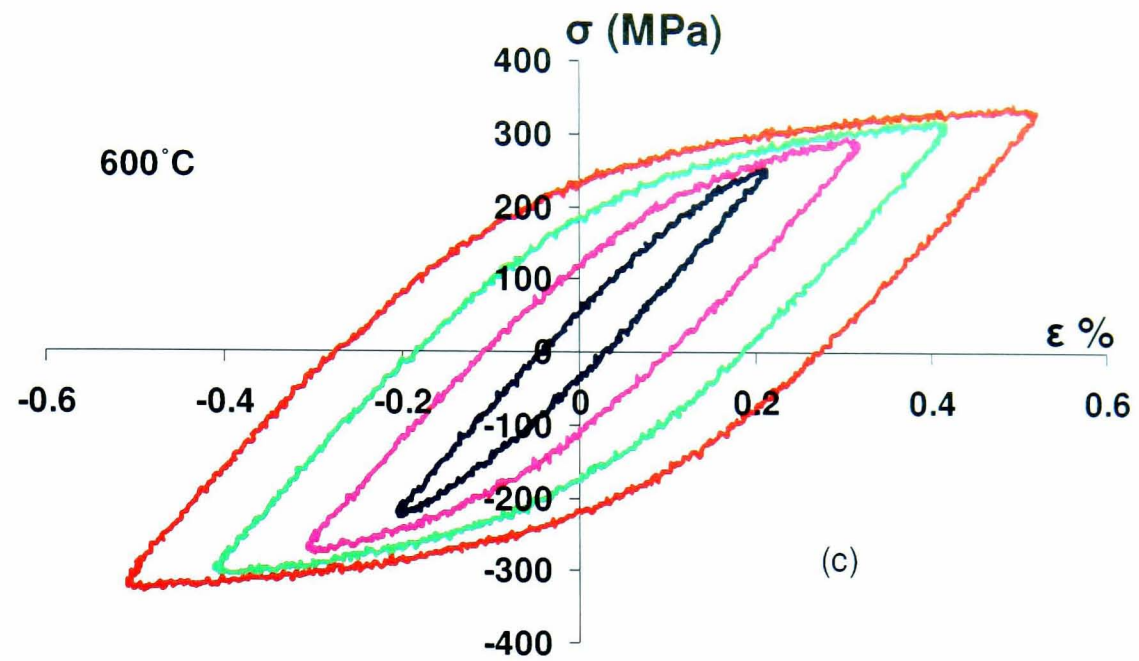


Figure 3.7 (Contd.) Measured stabilized stress-strain loops of SS-316 stainless steel from the multi strain range strain controlled LCF tests carried out at a strain rate of  $2 \times 10^{-4} \text{ s}^{-1}$ ; (a)  $20^\circ\text{C}$ , (b)  $300^\circ\text{C}$  and (c)  $600^\circ\text{C}$

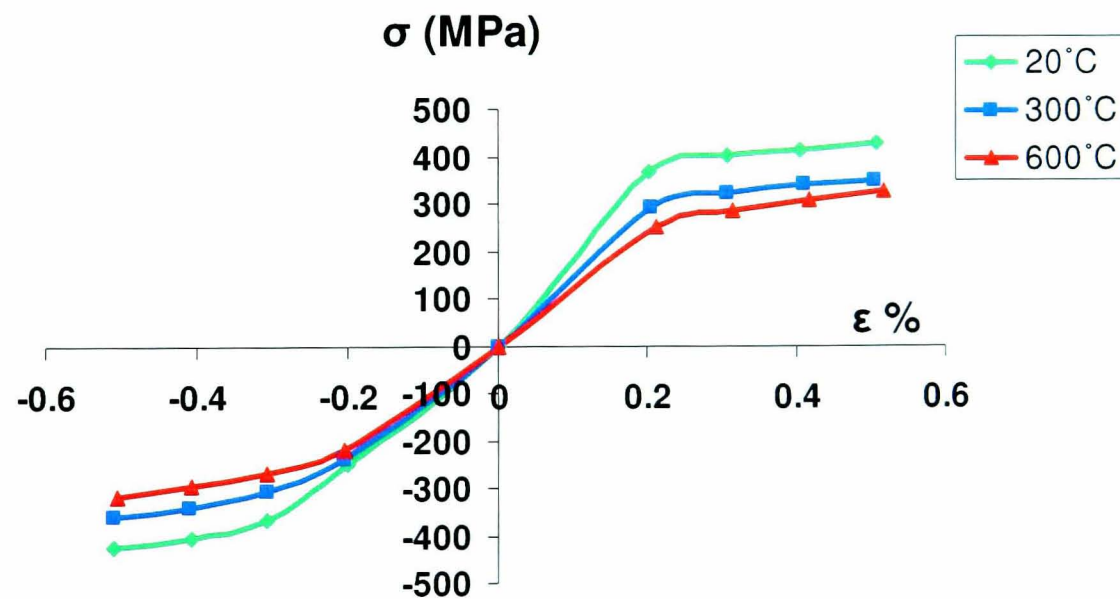


Figure 3.8 Backbone curve plotted from stabilized stress-strain loops of SS-316 stainless steel of the multi strain range strain controlled LCF tests carried out at a strain rate of  $2 \times 10^{-4} \text{ s}^{-1}$  for three different temperatures

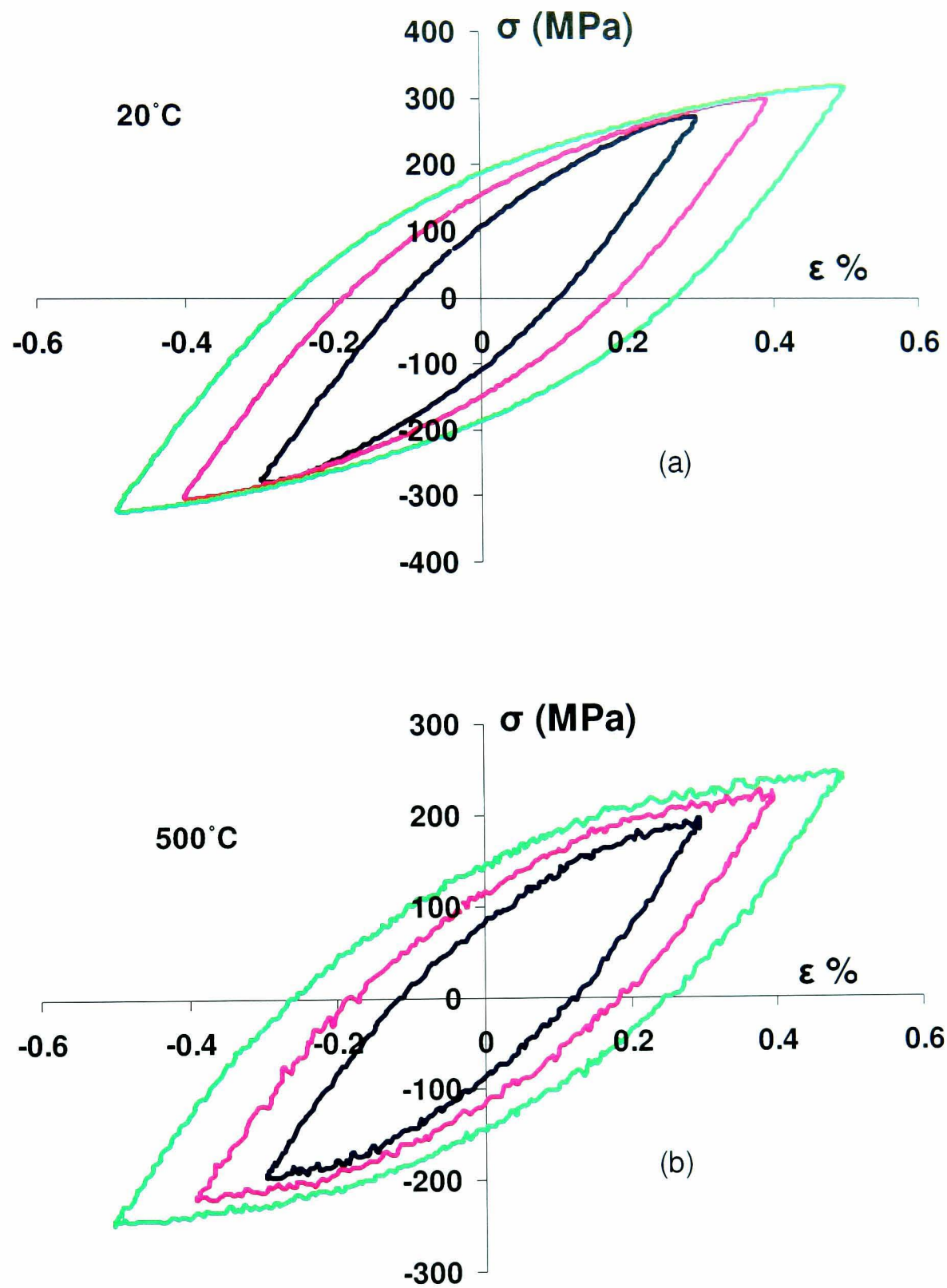


Figure 3.9 Measured stabilized stress-strain loops of XN40F alloy from the multi strain range strain controlled LCF tests carried out at a strain rate of  $5 \times 10^{-3} \text{ s}^{-1}$ ; (a) 20°C, (b) 500°C, (c) 700°C, (d) 900°C

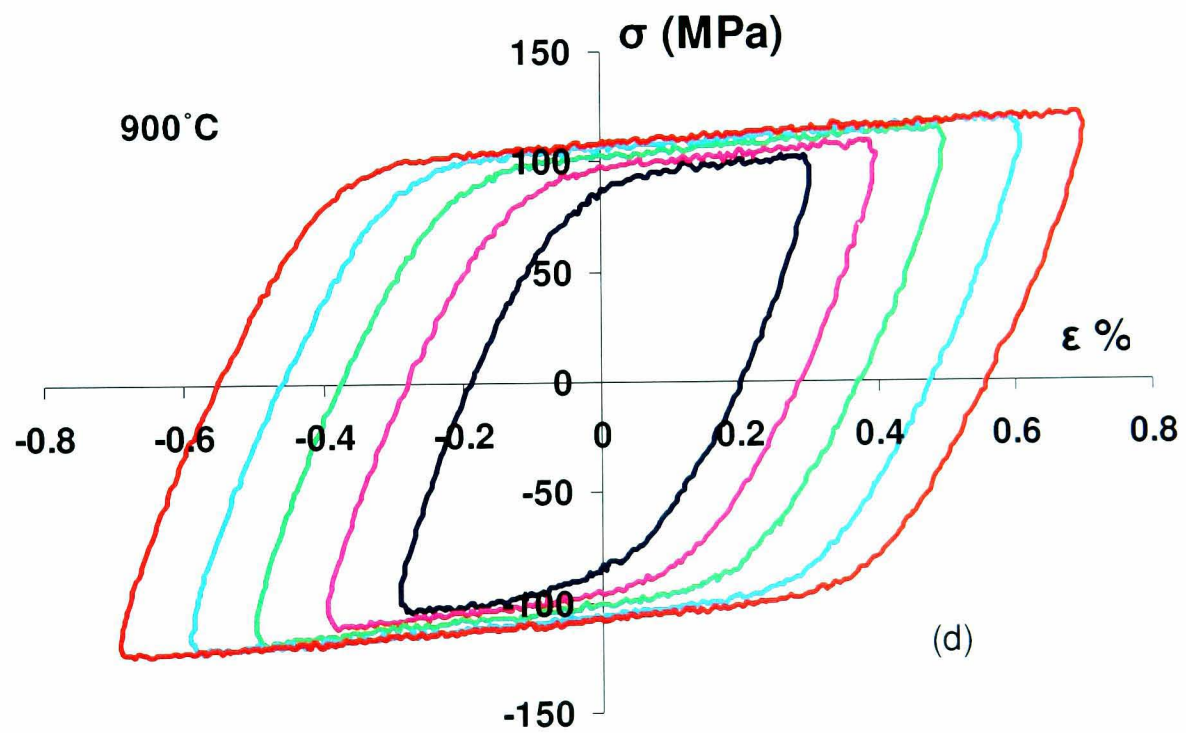
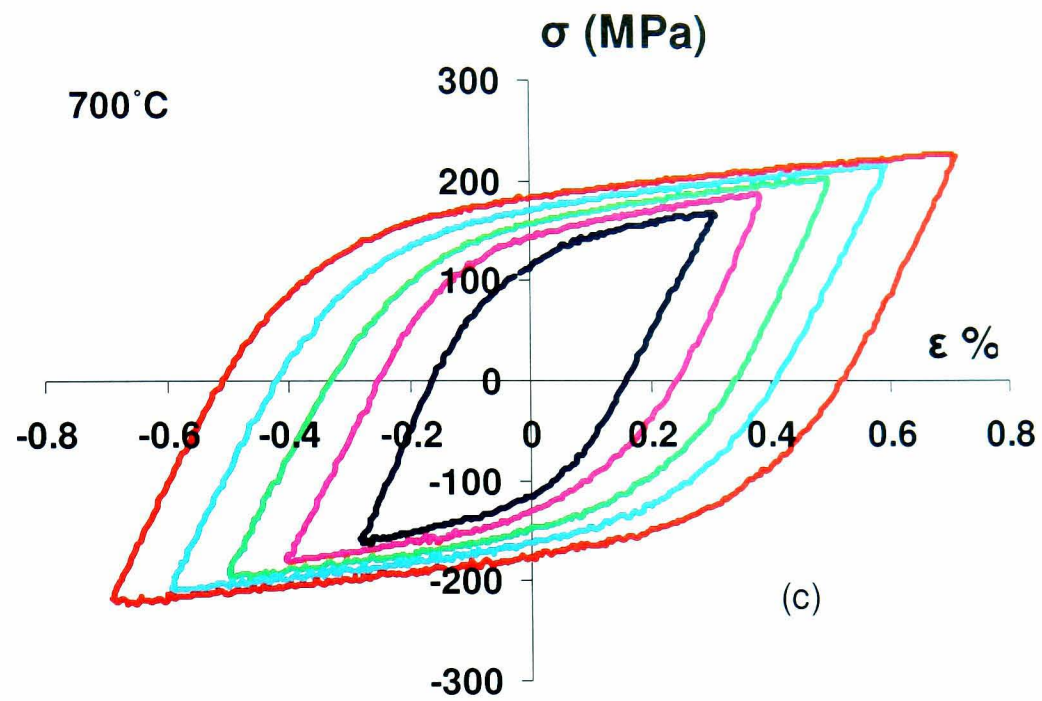


Figure 3.9 (Contd.) Measured stabilized stress-strain loops of XN40F alloy from the multi strain range strain controlled LCF tests carried out at a strain rate of  $5 \times 10^{-3} \text{ s}^{-1}$ ; (a) 20°C, (b) 500°C, (c) 700°C, (d) 900°C

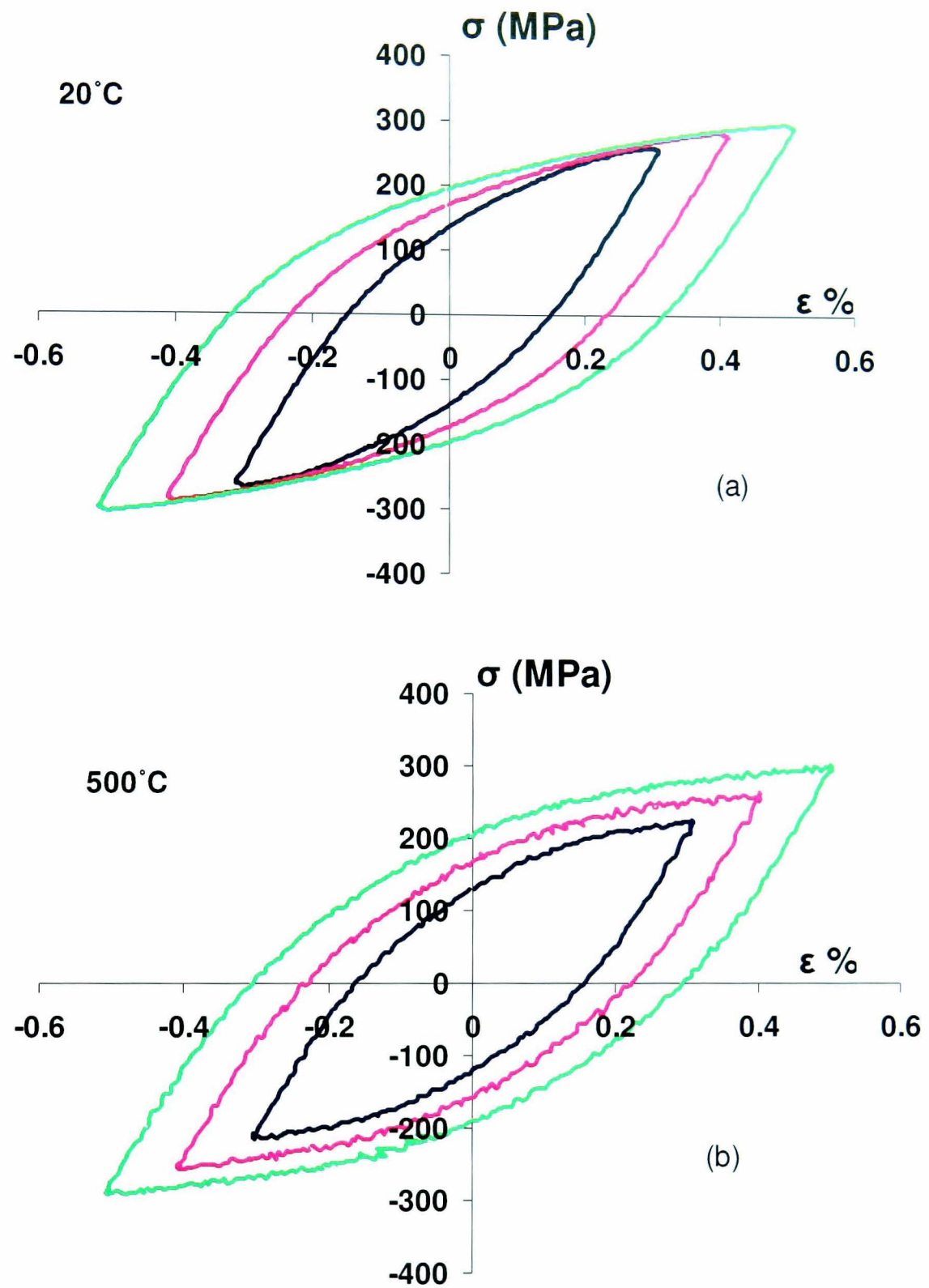


Figure 3.10 Measured stabilized stress-strain loops of XN40F alloy from the multi strain range strain controlled LCF tests carried out at a strain rate of  $5 \times 10^{-4} \text{ s}^{-1}$ ; (a) 20°C, (b) 500°C, (c) 700°C, (d) 900°C

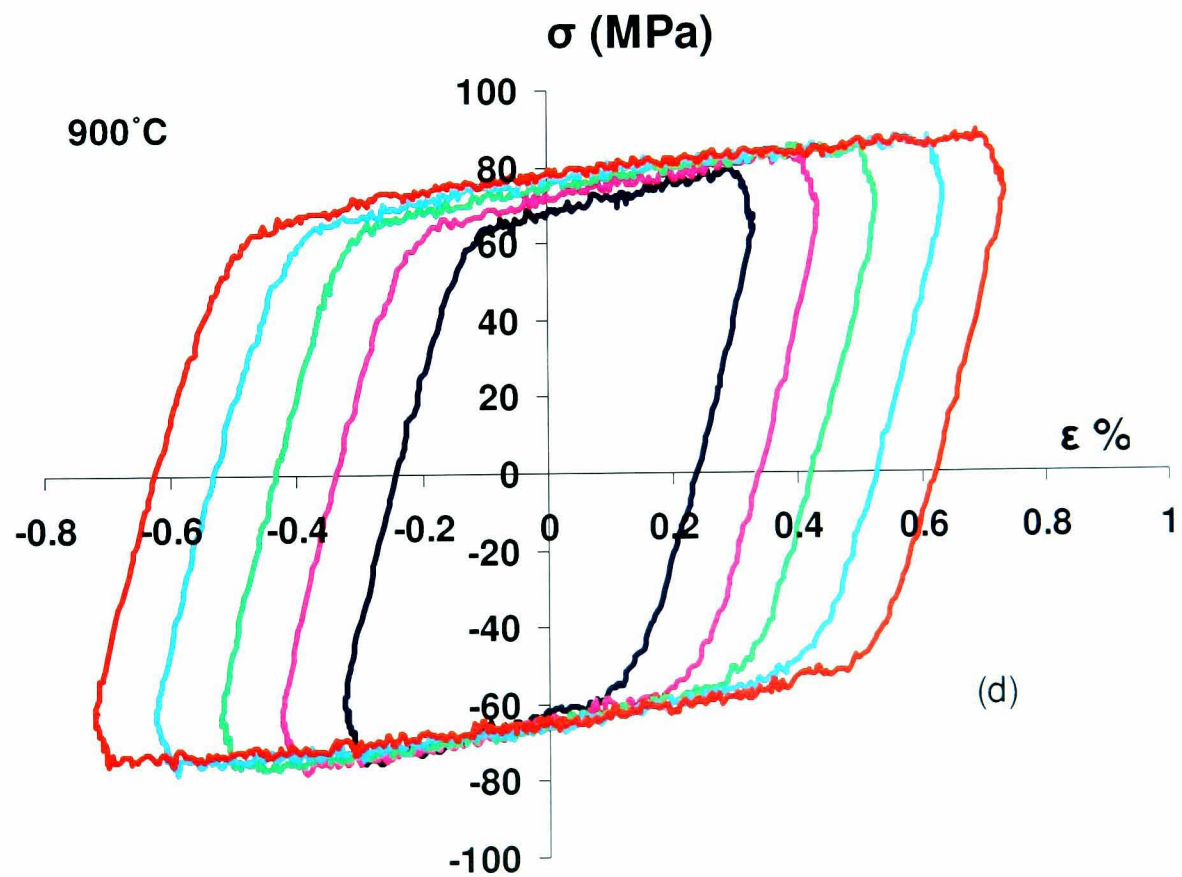
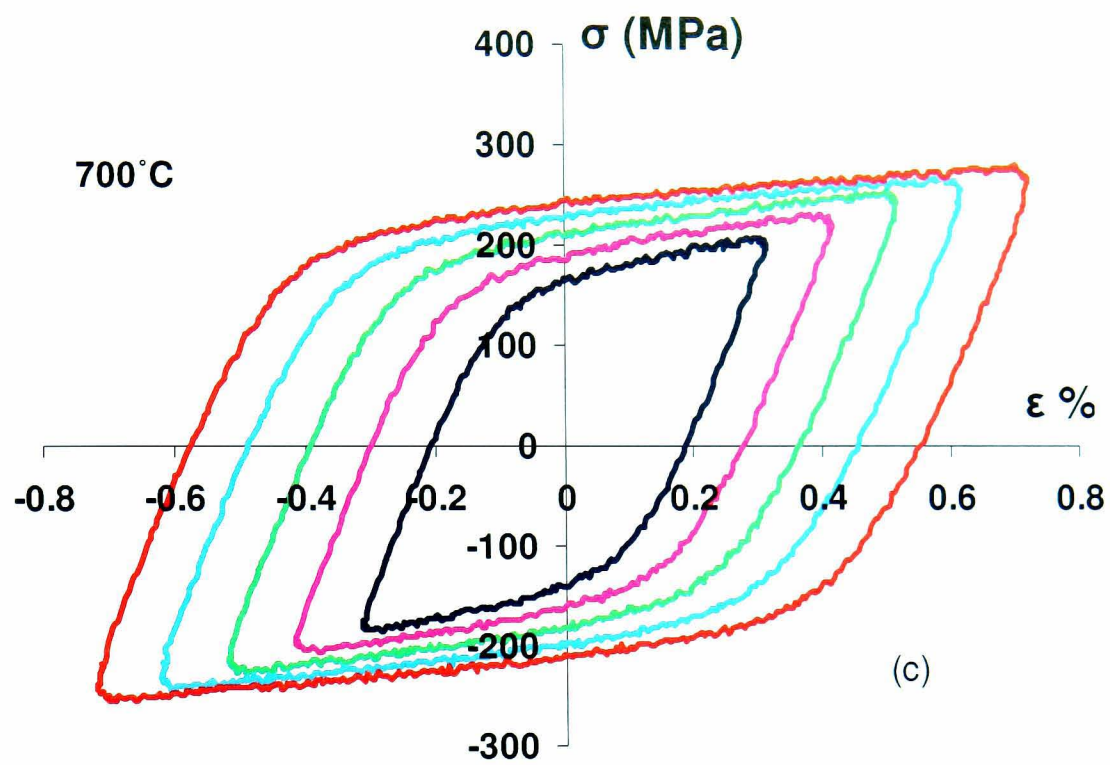


Figure 3.10 (Contd.) Measured stabilized stress-strain loops of XN40F alloy from the multi strain range strain controlled LCF tests carried out at a strain rate of  $5 \times 10^{-4} \text{ s}^{-1}$ ; (a) 20°C, (b) 500°C, (c) 700°C, (d) 900°C

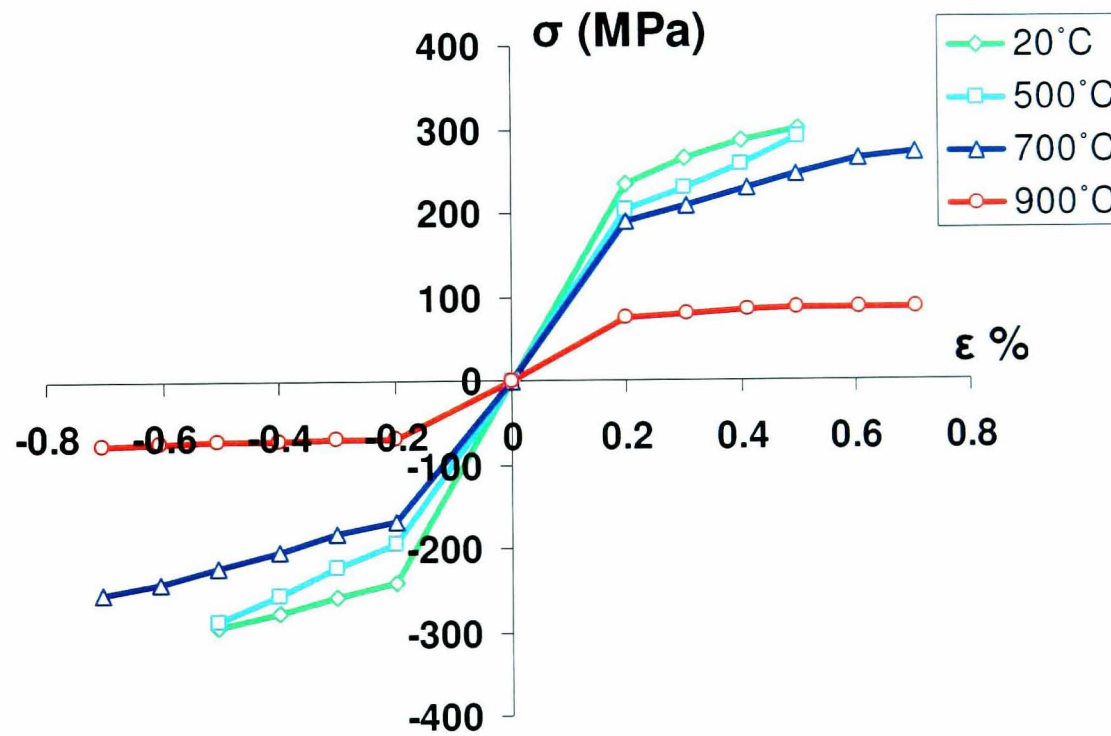
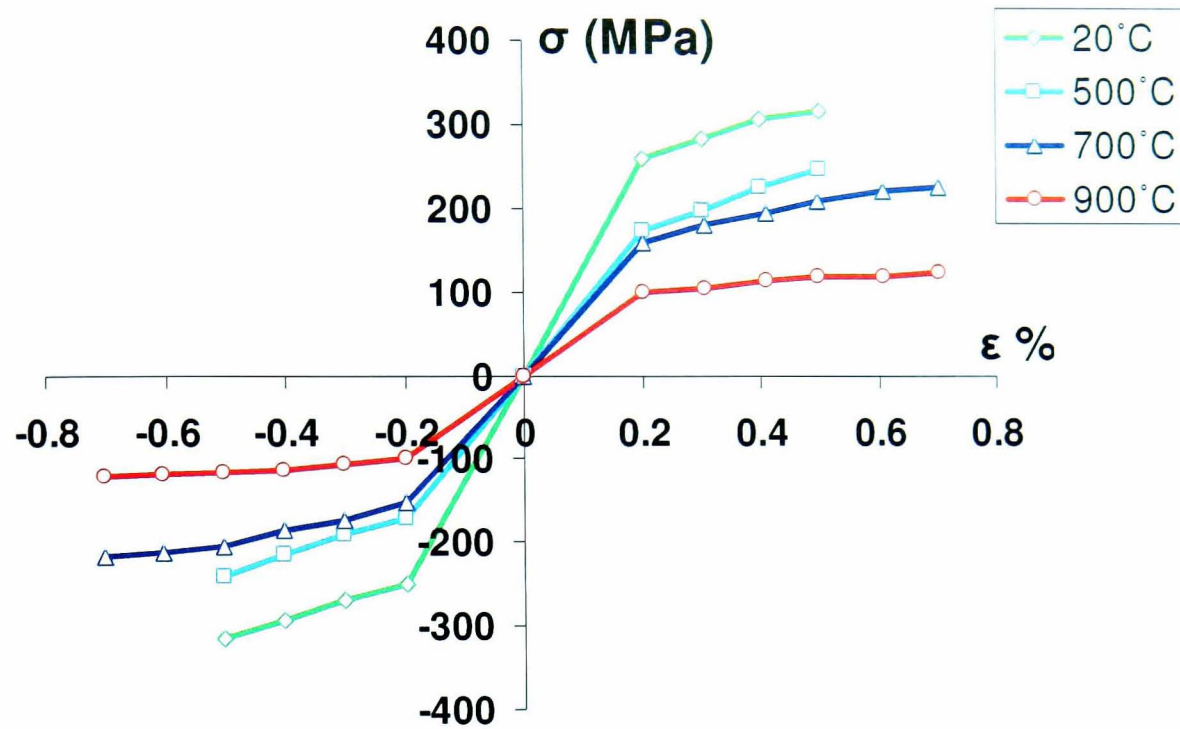


Figure 3.11 Backbone curve plotted from stabilized stress-strain loops of the multi strain range strain controlled LCF tests of XN40F alloy ; (a)  $5 \times 10^{-3} \text{ s}^{-1}$ , (b)  $5 \times 10^{-4} \text{ s}^{-1}$

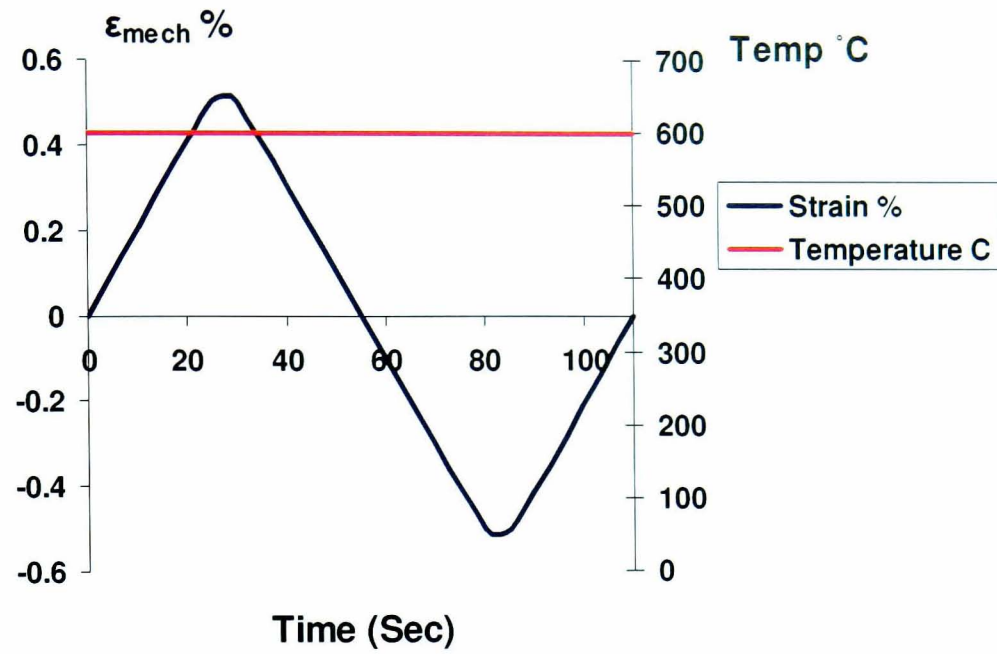


Figure 3.12 Mechanical strain and temperature waveform for IF testing of SS-316 stainless steel: IF  $\Delta\epsilon_{\text{mech}}=1.0\%$

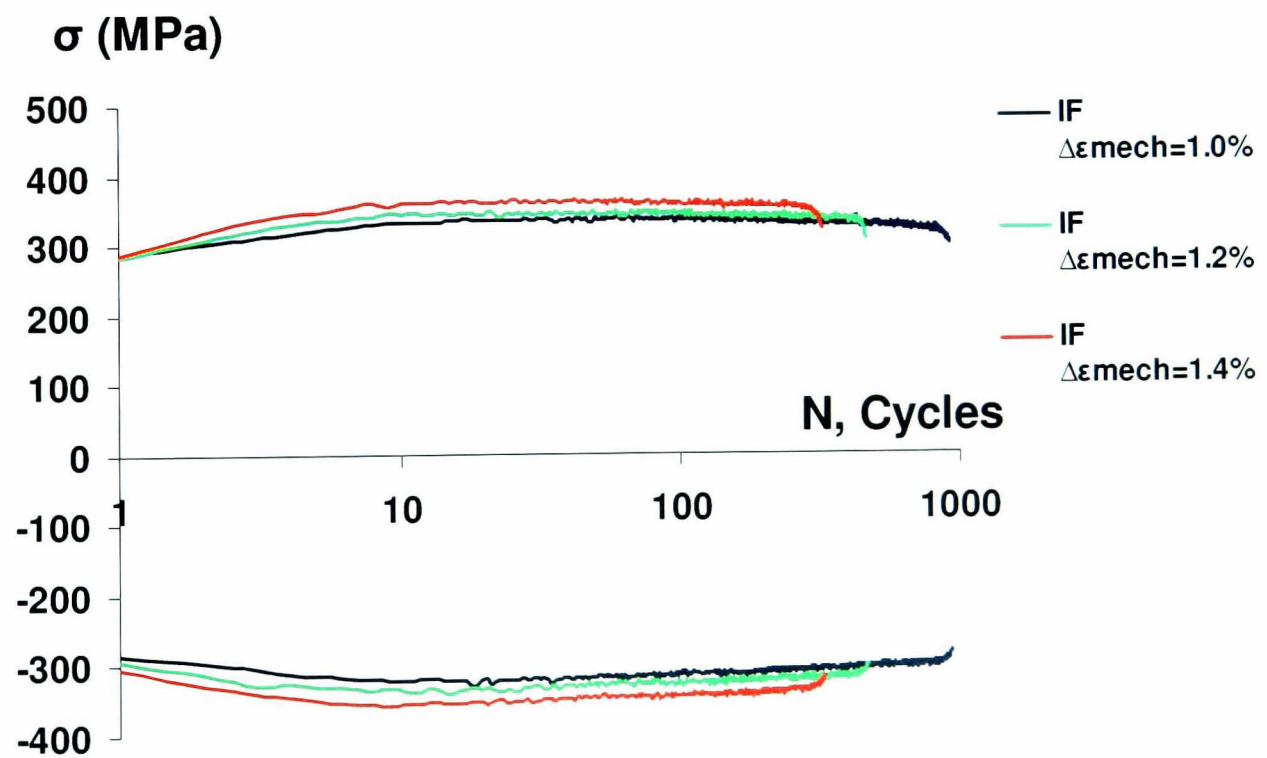


Figure 3.13 Cyclic stress response curves from IF tests for SS-316 stainless steel

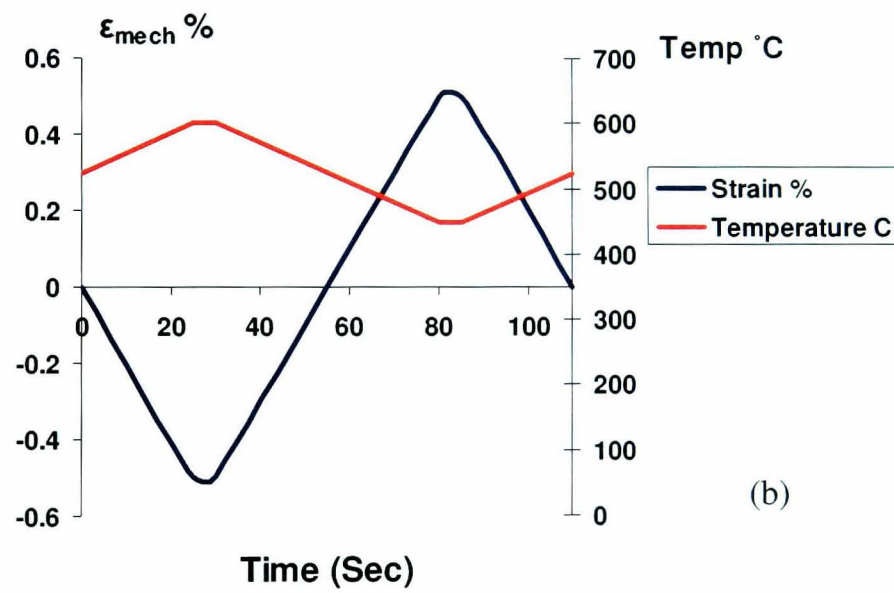
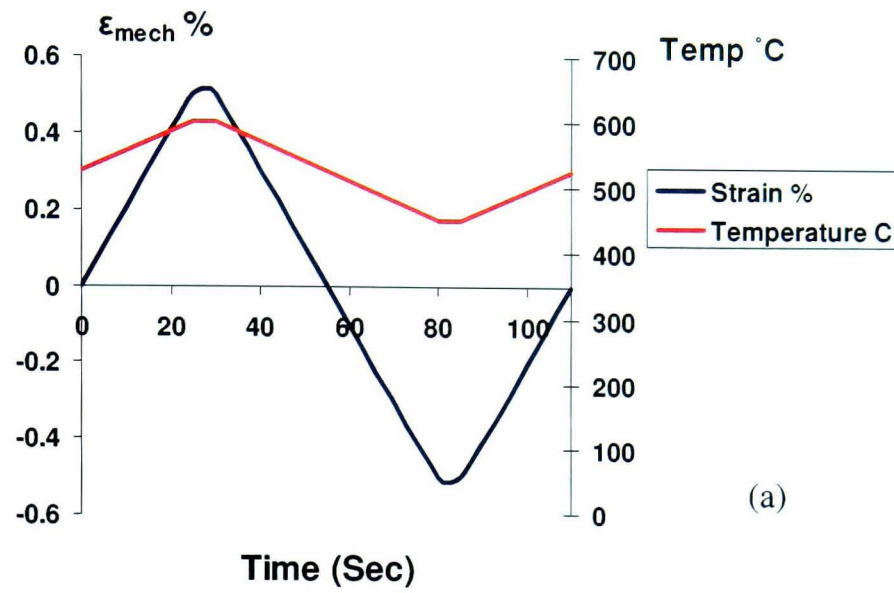


Figure 3.14 Mechanical strain and temperature waveform for TMF testing of SS-316 stainless steel: (a) TMF IP  $\Delta\epsilon_{\text{mech}}=1.0\%$  (b) TMF OP  $\Delta\epsilon_{\text{mech}}=1.0\%$

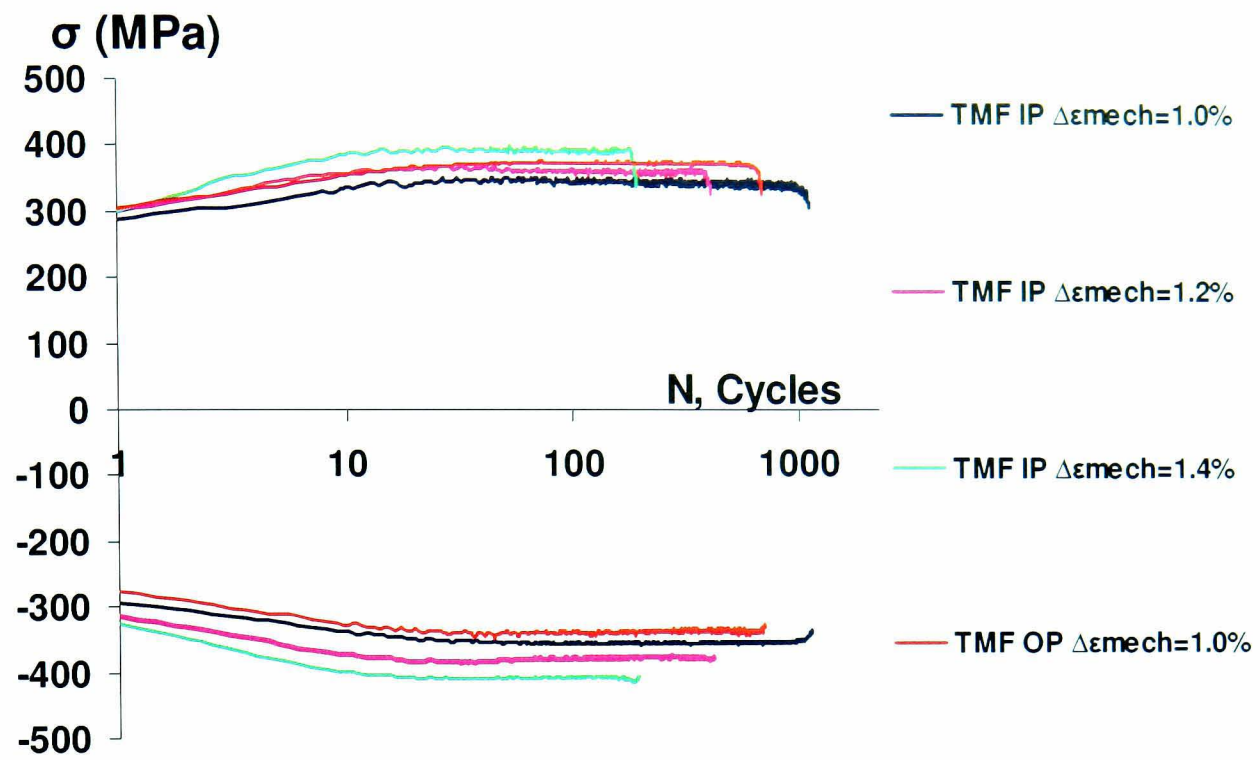


Figure 3.15 Cyclic stress response curves from TMF tests for SS-316 stainless steel

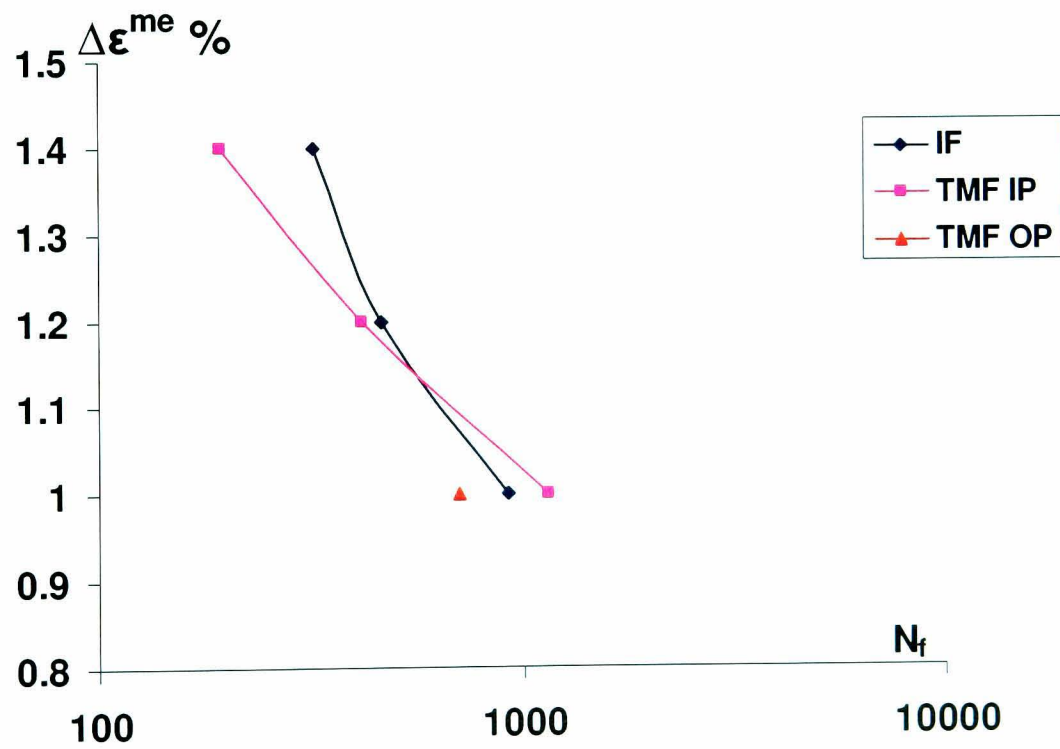


Figure 3.16 Mechanical strain ranges versus number of cycles to failure for SS-316 stainless steel

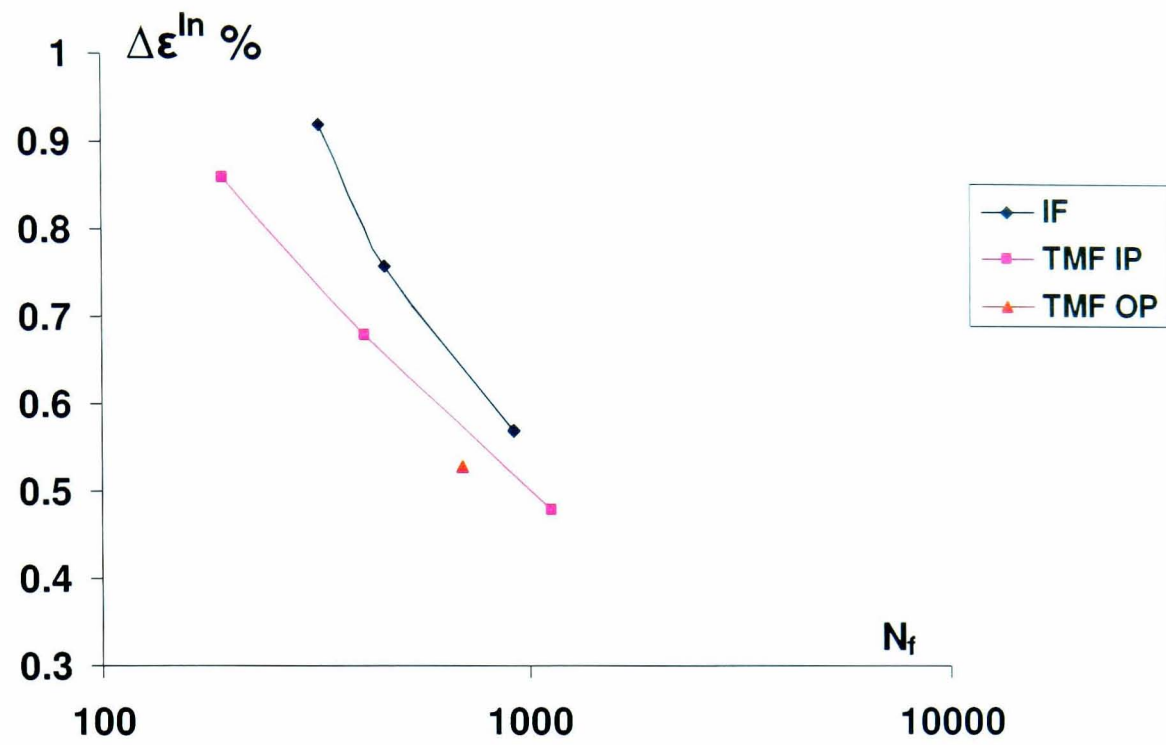


Figure 3.17 Inelastic strain ranges versus number of cycles to failure for SS-316 stainless steel.

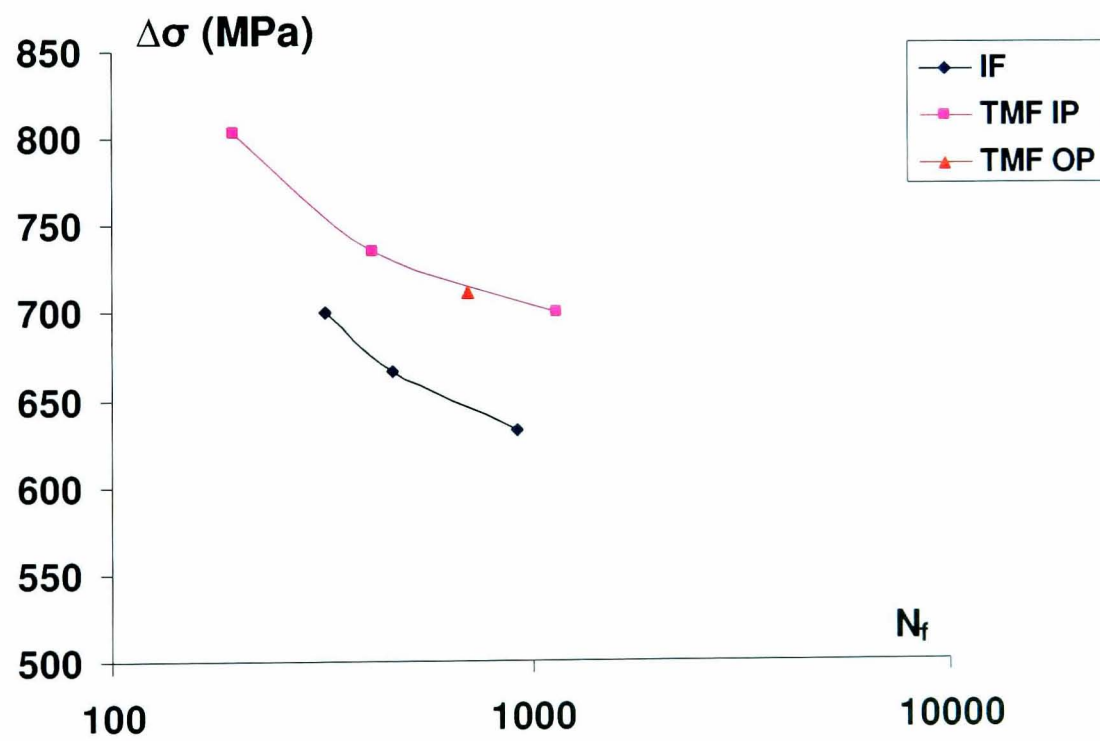


Figure 3.18 Stress ranges versus number of cycles to failure for SS-316 stainless steel.

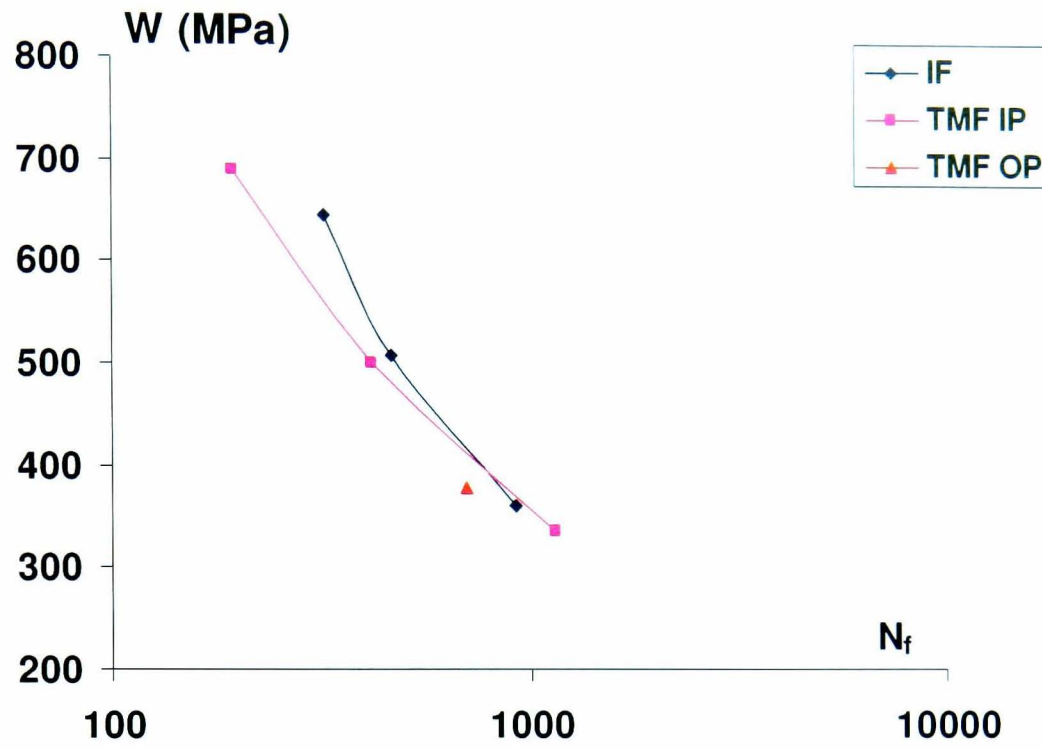


Figure 3.19 Total energy versus number of cycles to failure for SS-316 stainless steel

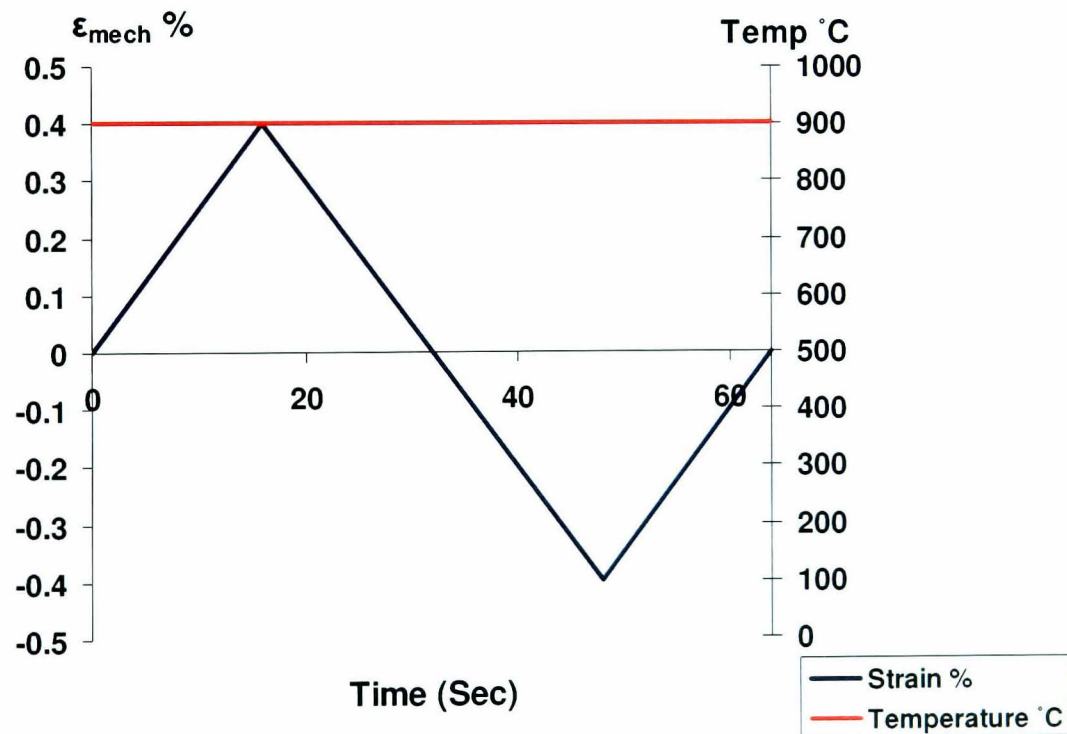


Figure 3.20 Mechanical strain and temperature waveform for IF testing of XN40F alloy:  $\Delta\epsilon_{\text{mech}}=0.8\%$

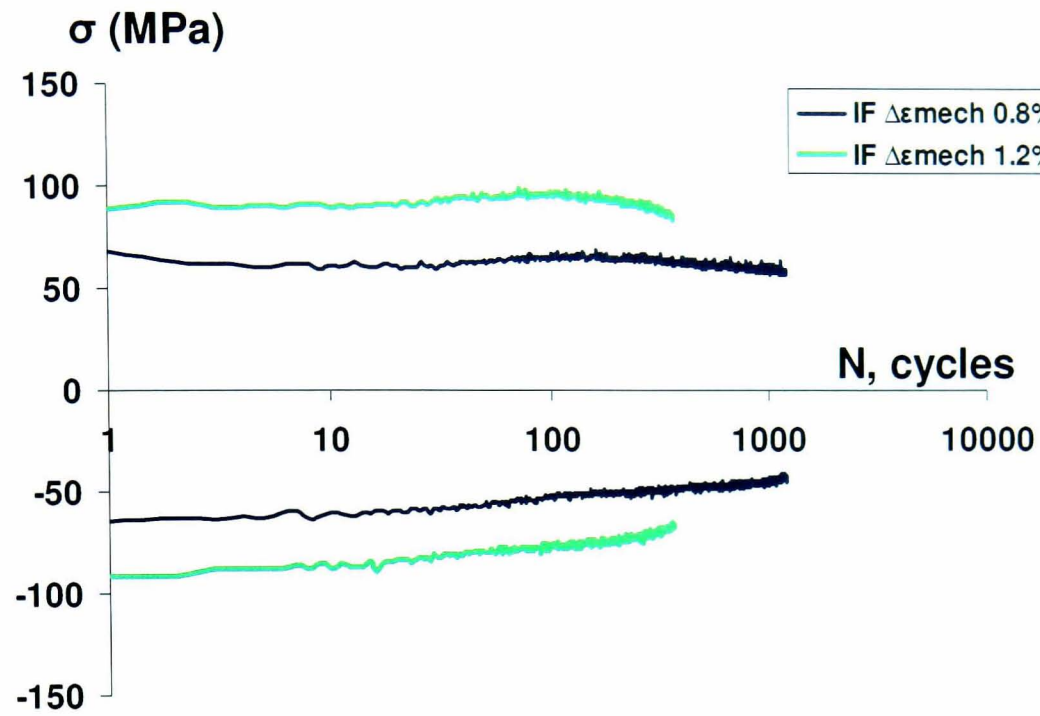


Figure 3.21 Cyclic stress response curves from IF tests for XN40F alloy

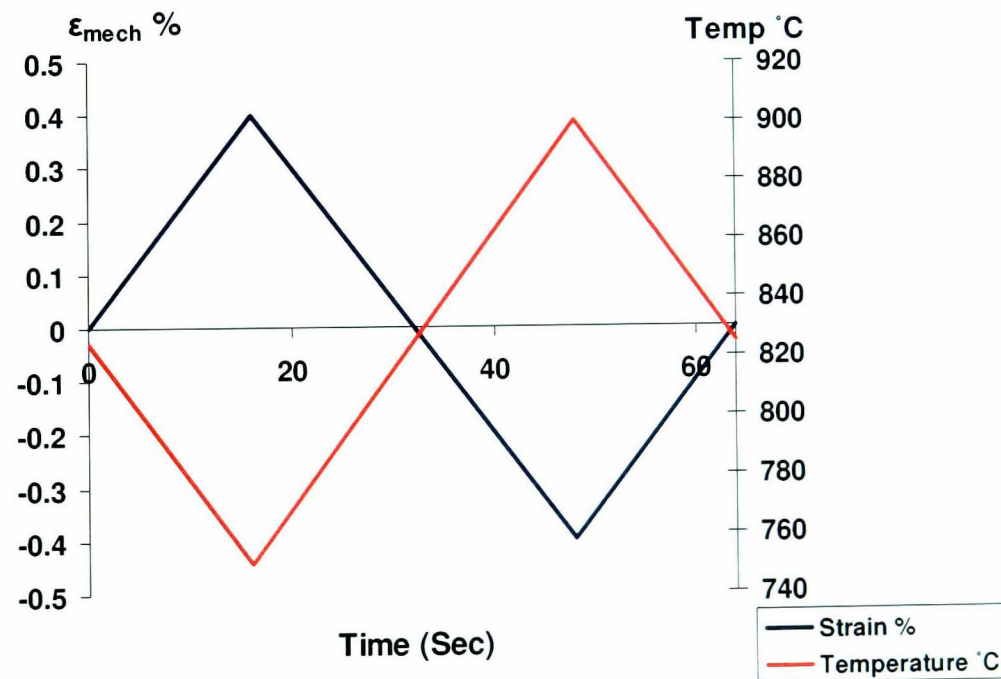


Figure 3.22 Mechanical strain and temperature waveform for TMF testing of XN40F alloy: TMF OP  $\Delta\epsilon_{\text{mech}}=0.8\%$

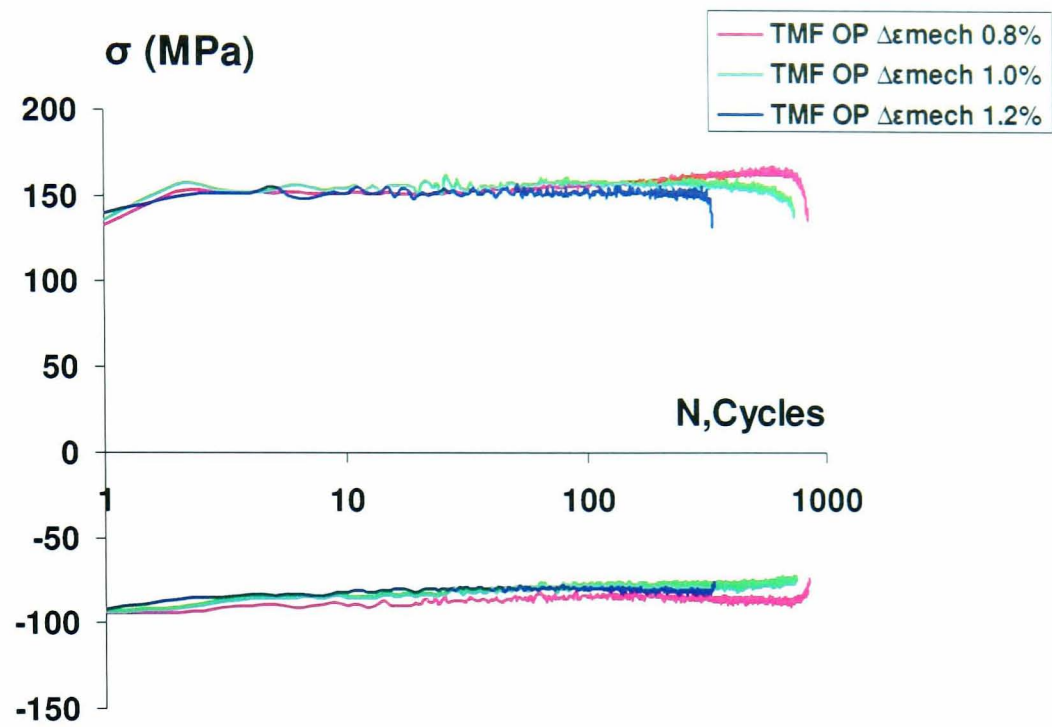


Figure 3.23 Cyclic stress response curves from TMF OP tests for XN40F alloy

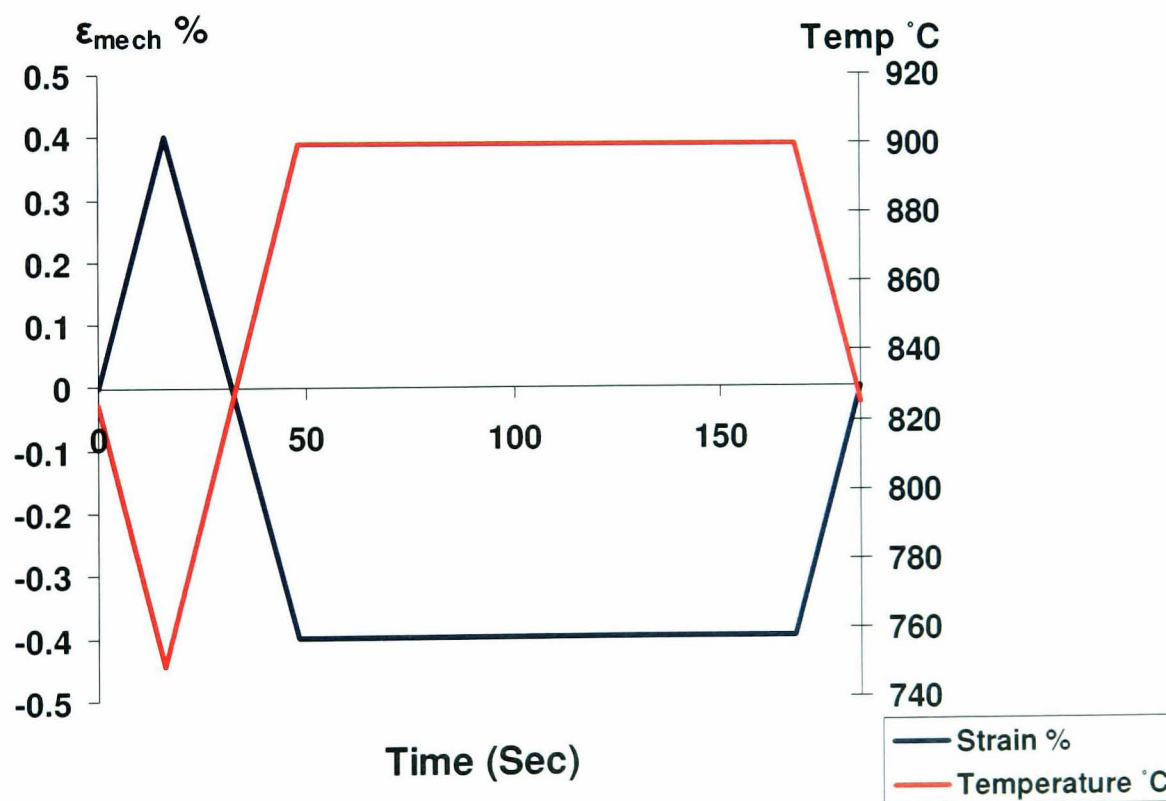


Figure 3.24 Mechanical strain and temperature waveform of TMF OP testing with strain hold for XN40F alloy with  $\Delta\epsilon_{\text{mech}}=0.8\%$

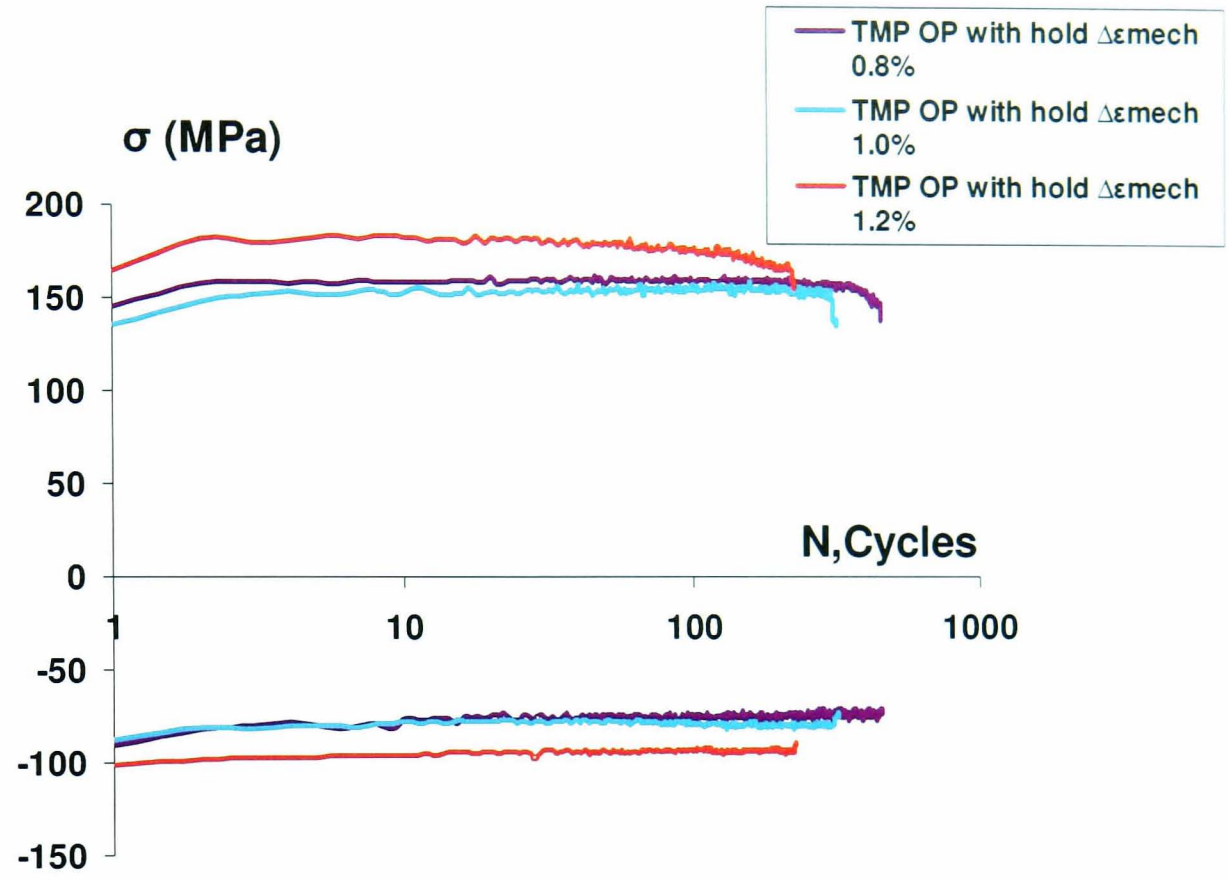


Figure 3.25 Cyclic stress response curves from TMF OP tests with strain hold period for XN40F alloy

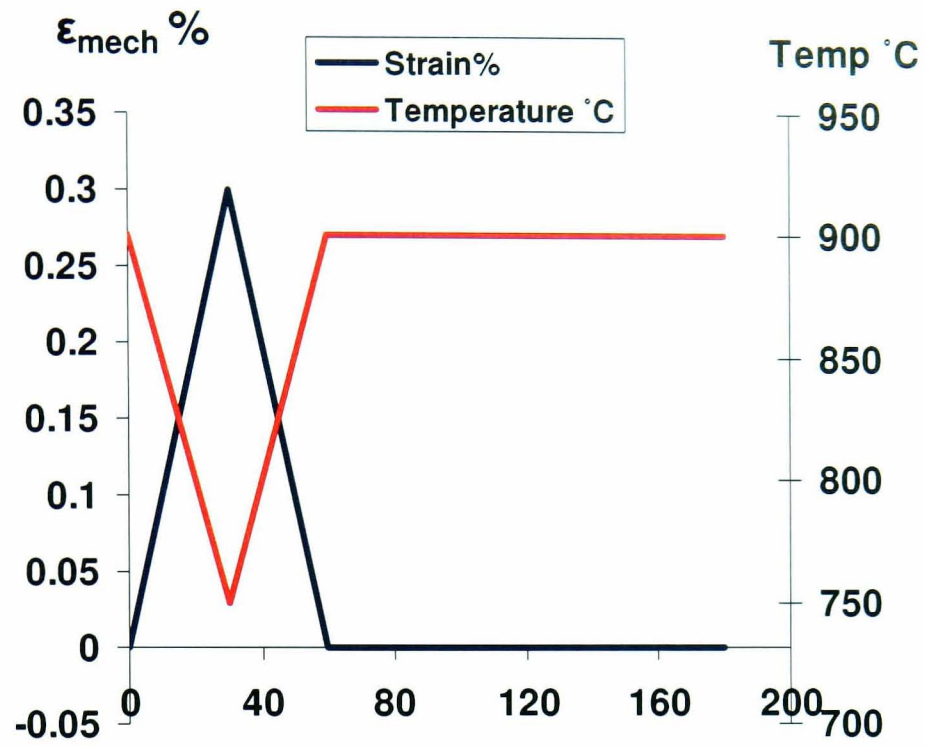


Figure 3.26 Mechanical strain and temperature waveform of representative SPF tool test on XN40F alloy using strain control.

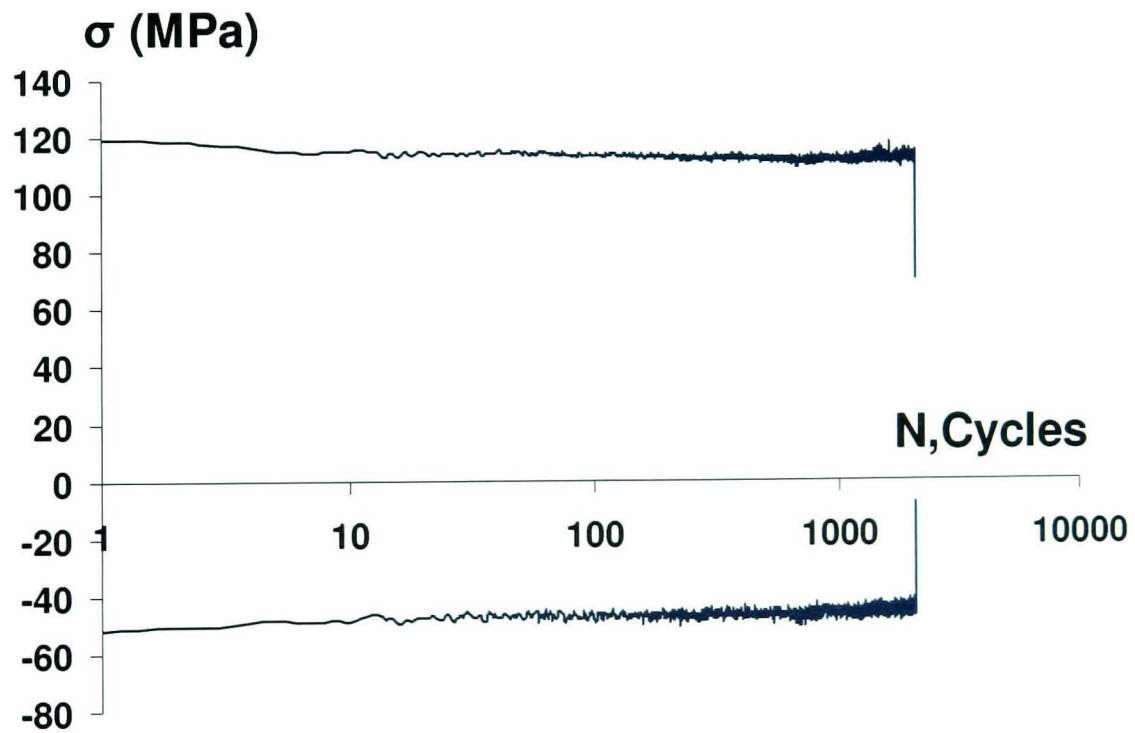


Figure 3.27 Cyclic stress response curves from representative tool test on XN40F alloy using strain control



Fig. 3.28 Fractured specimen of the representative strain controlled TMF test.

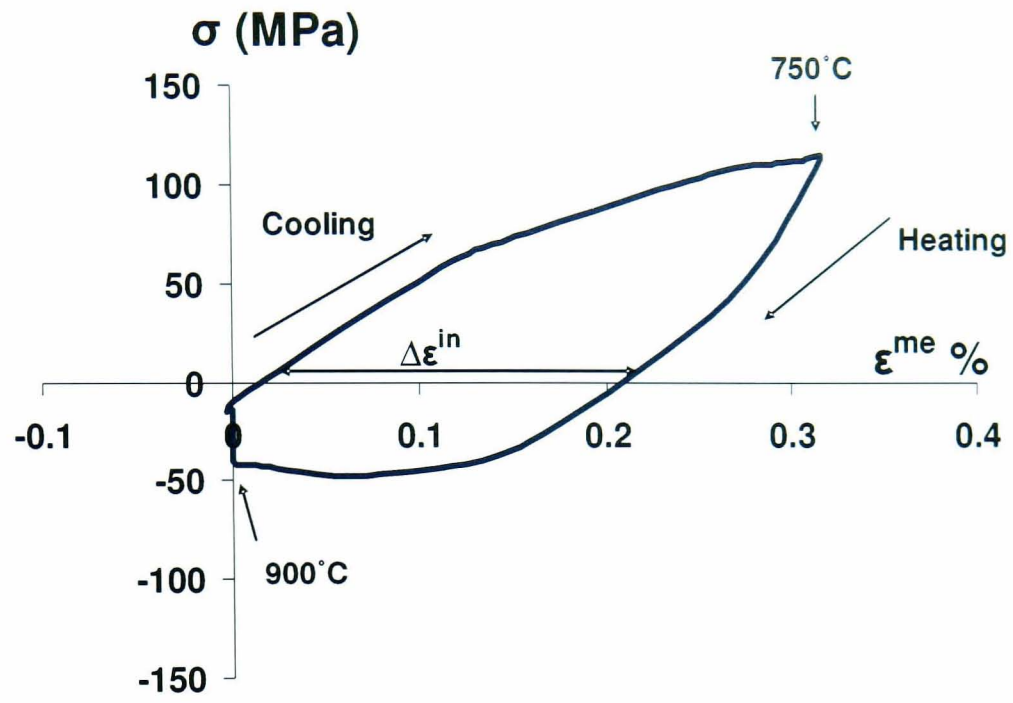


Figure 3.29 Measured stabilized stress-strain loop from representative SPF tool test using strain control

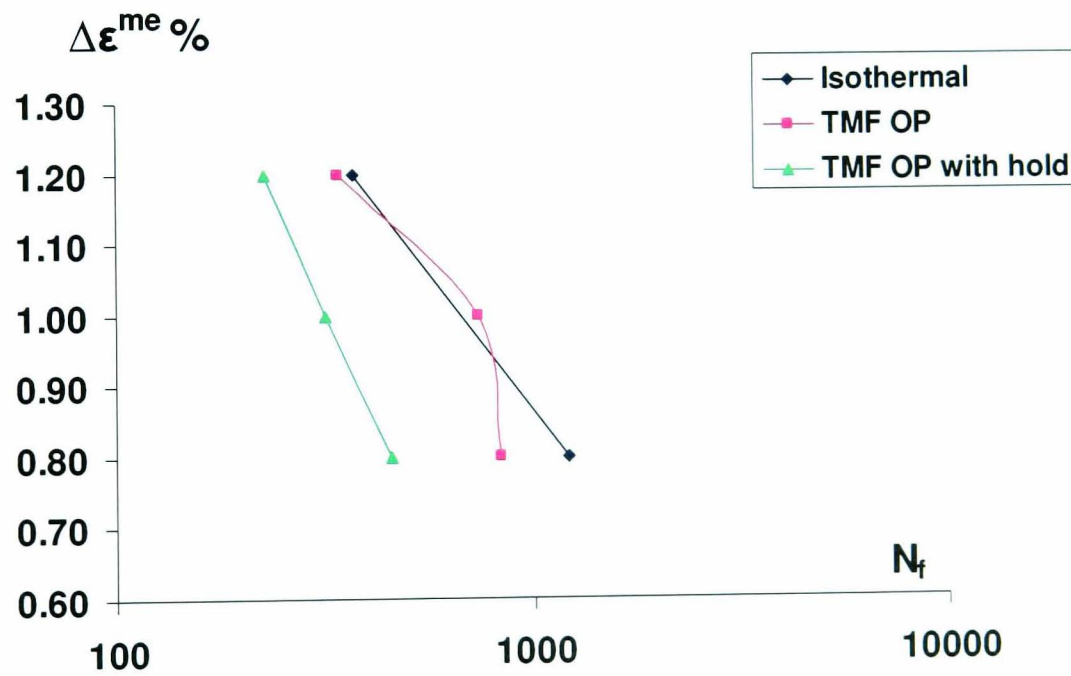


Figure 3.30 Mechanical strain ranges versus number of cycles to failure for XN40F alloy

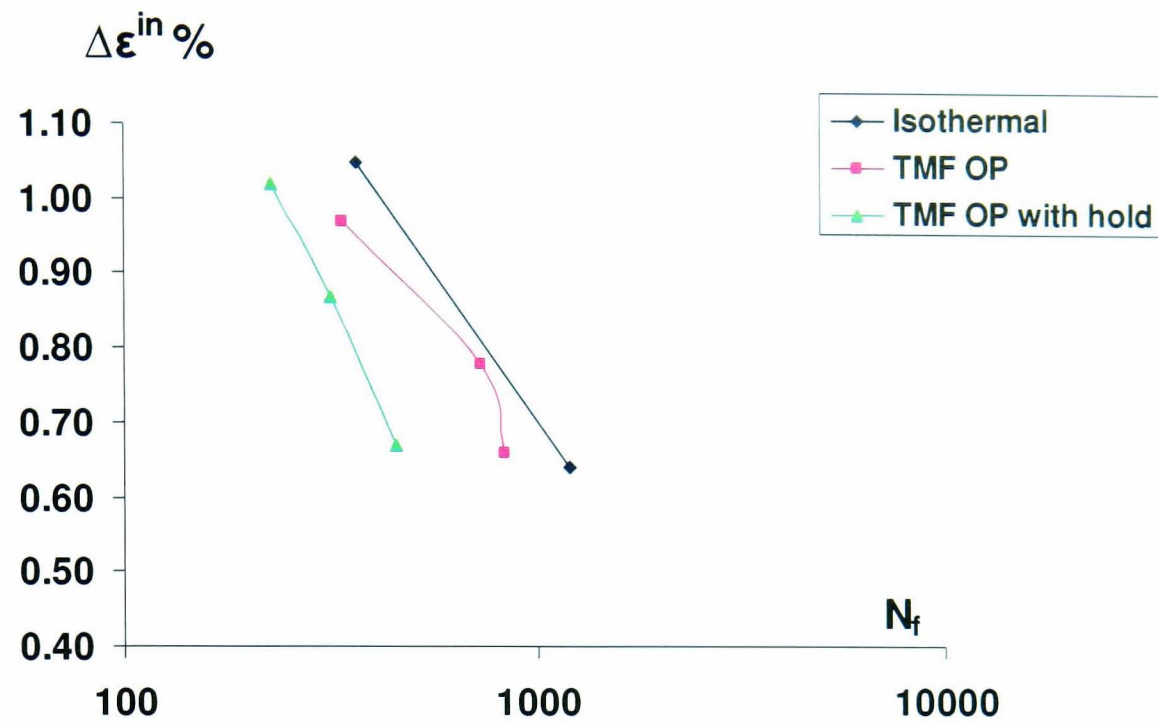


Figure 3.31 Inelastic strain ranges versus number of cycles to failure for XN40F alloy

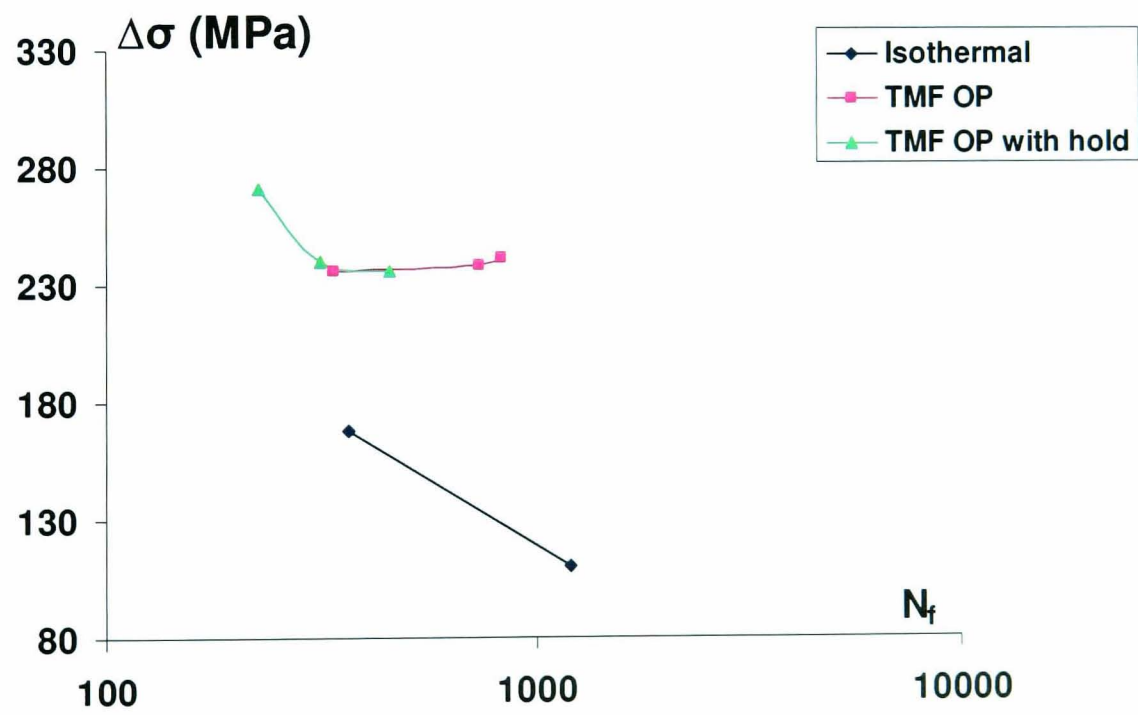


Figure 3.32 Stress ranges versus number of cycles to failure for XN40F alloy

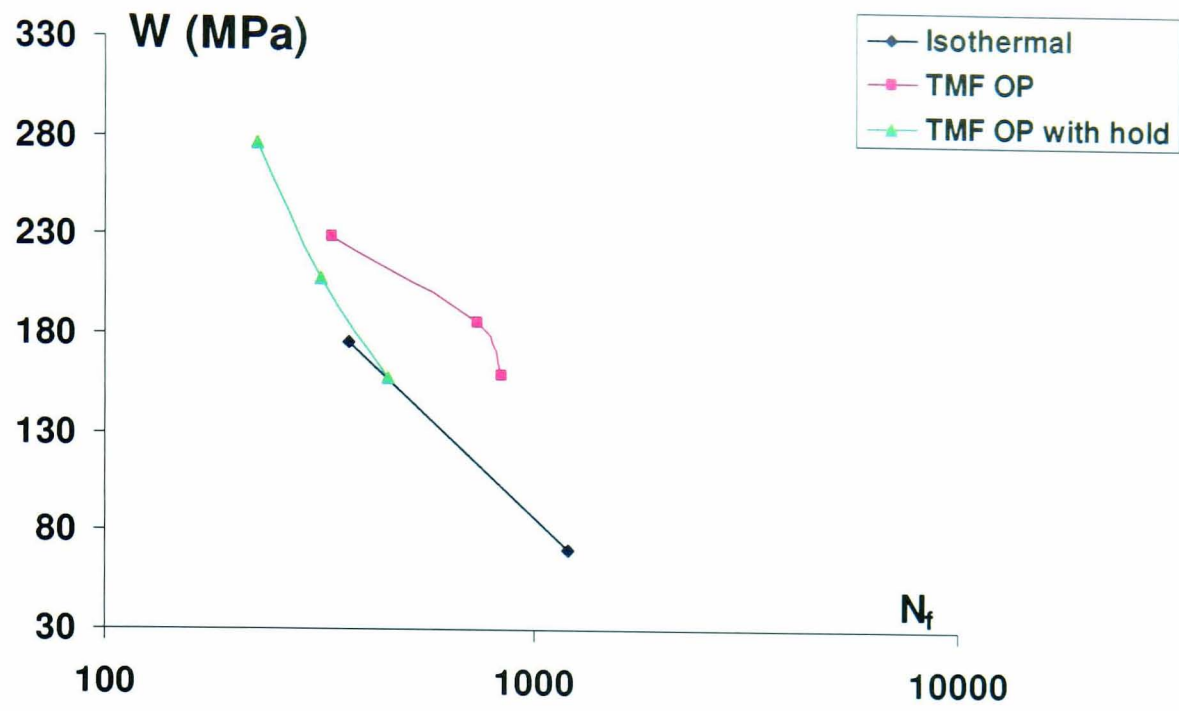


Figure 3.33 Total energy versus number of cycles to failure for XN40F alloy

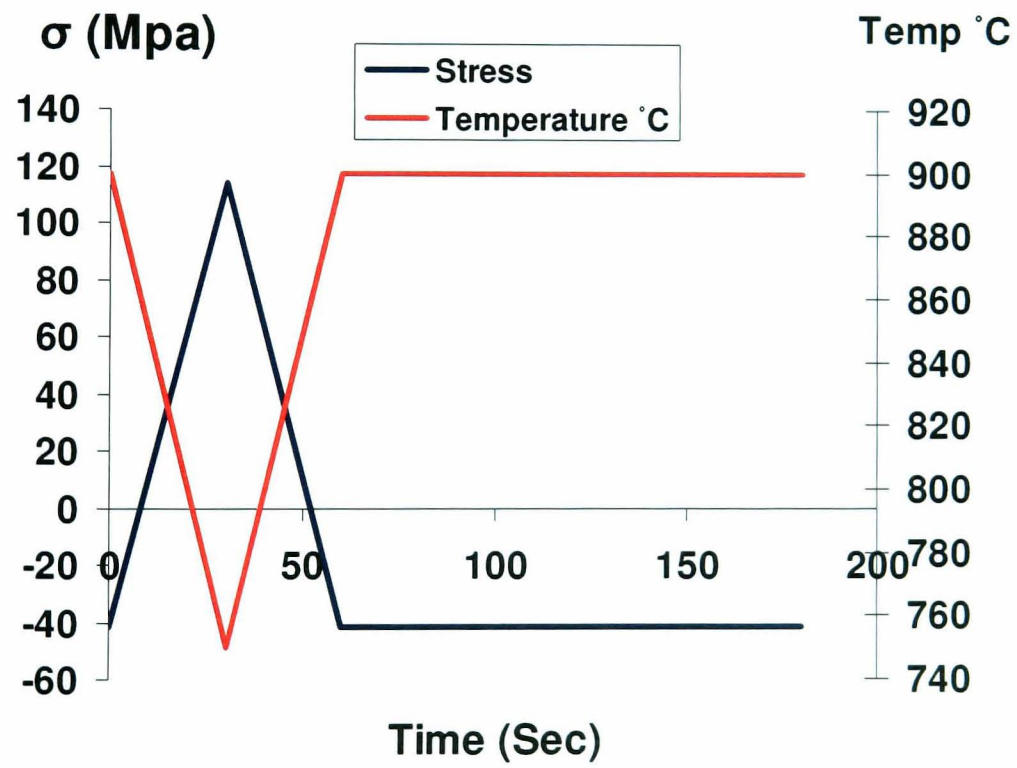


Figure 3.34 Mechanical and temperature waveform of a representative SPF tool test on XN40F alloy using stress control.

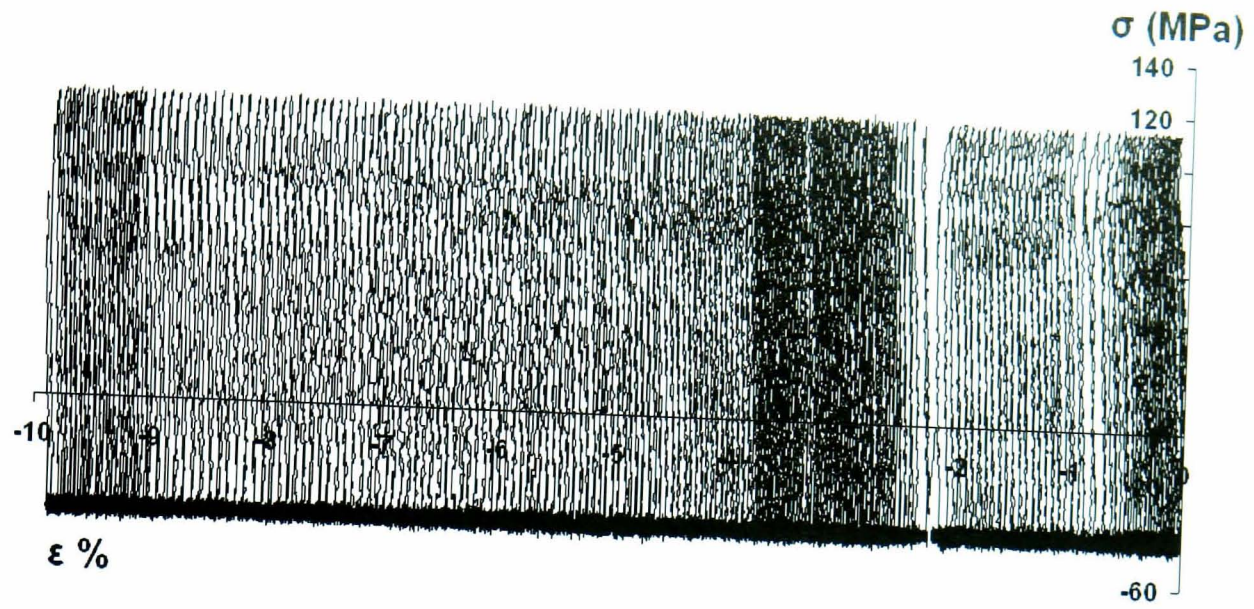


Figure 3.35 Measured stress-strain loops from a stress control representative SPF tool test on XN40F alloy

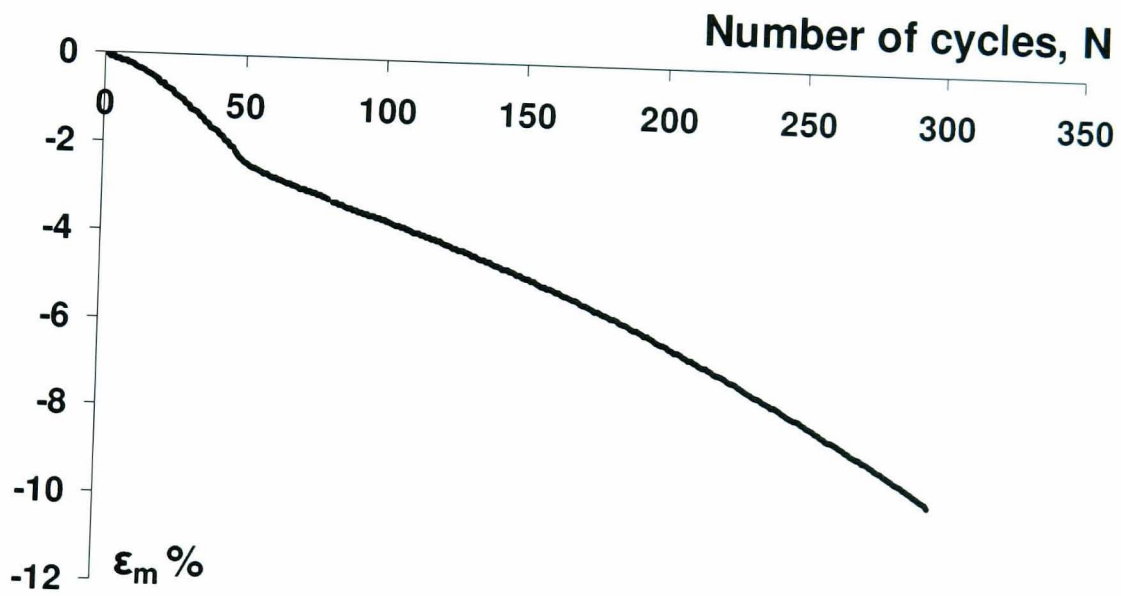


Figure 3.36 Mean strain versus number of cycles measured from a stress control representative SPF tool test (Fig 3.33) on XN40F alloy

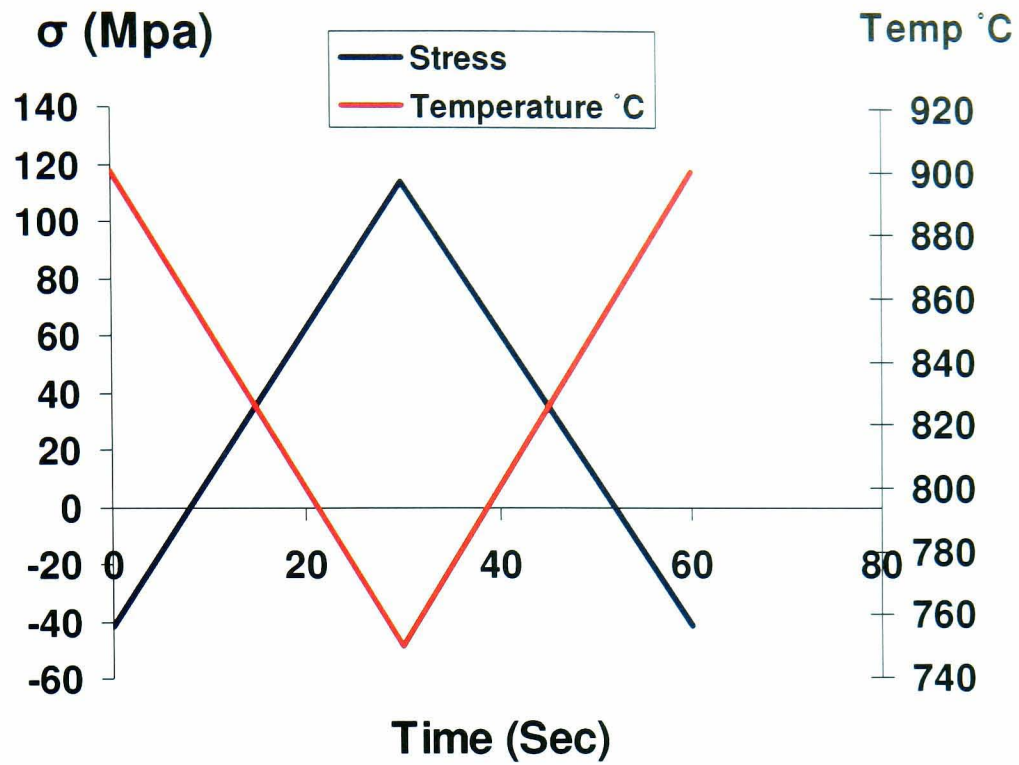


Figure 3.37 Mechanical and temperature waveform of a stress control TMF OP test on XN40F alloy

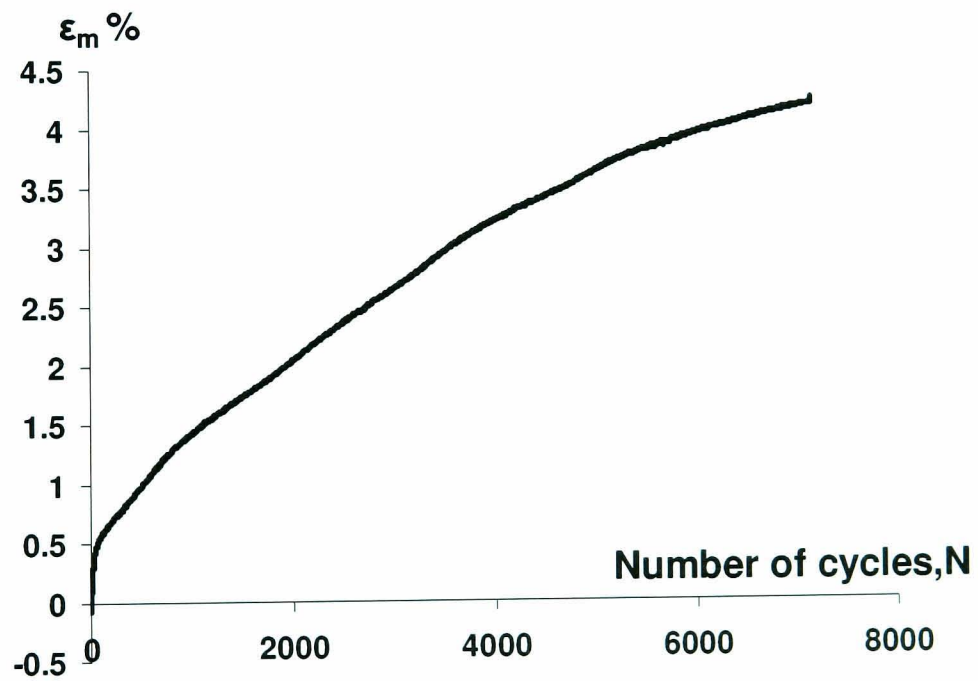


Figure 3.38 Mean strain versus number of cycles measured from a stress control TMF OP test (Fig 3.36) on XN40F alloy

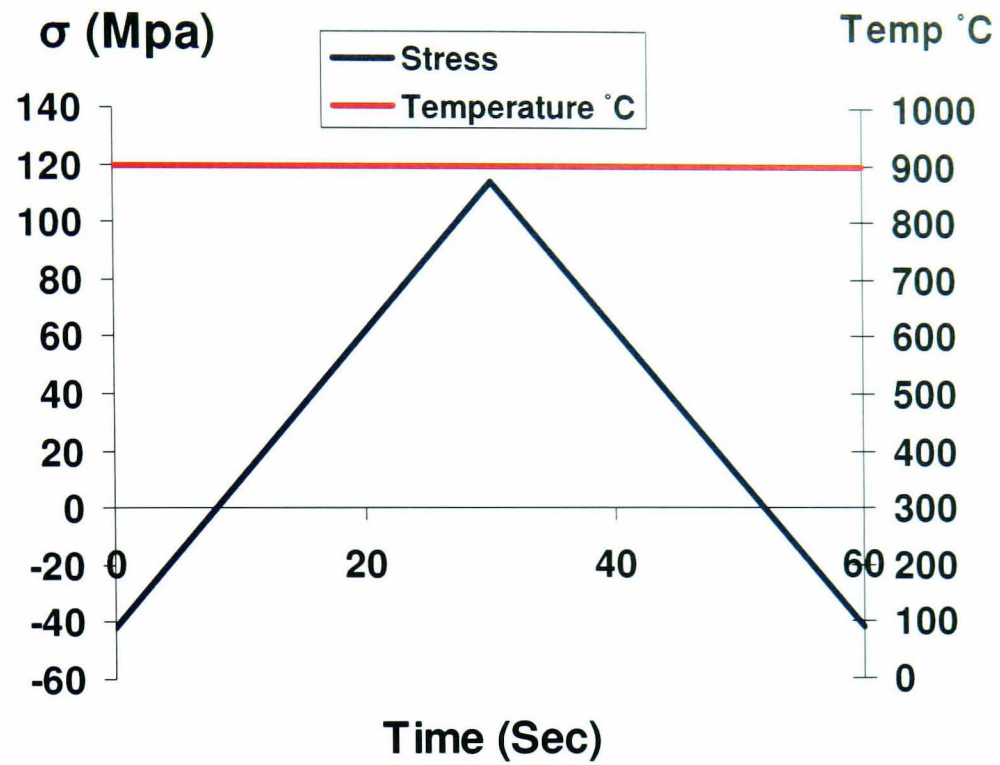


Figure 3.39 Mechanical and temperature waveform of a stress control Isothermal test at 900°C for XN40F alloy

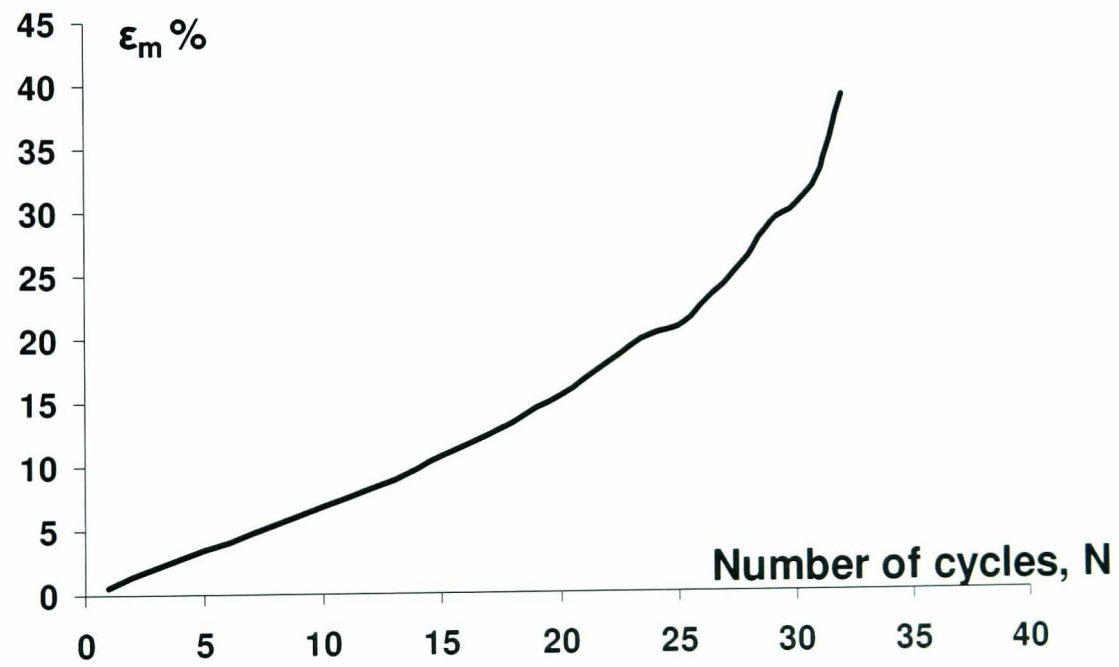


Figure 3.40 Mean strain versus number of cycles from a stress control Isothermal test (Fig 3.39) at 900°C for XN40F alloy



Figure 3.41 A fractured specimen from a stress controlled isothermal test at 900°C.

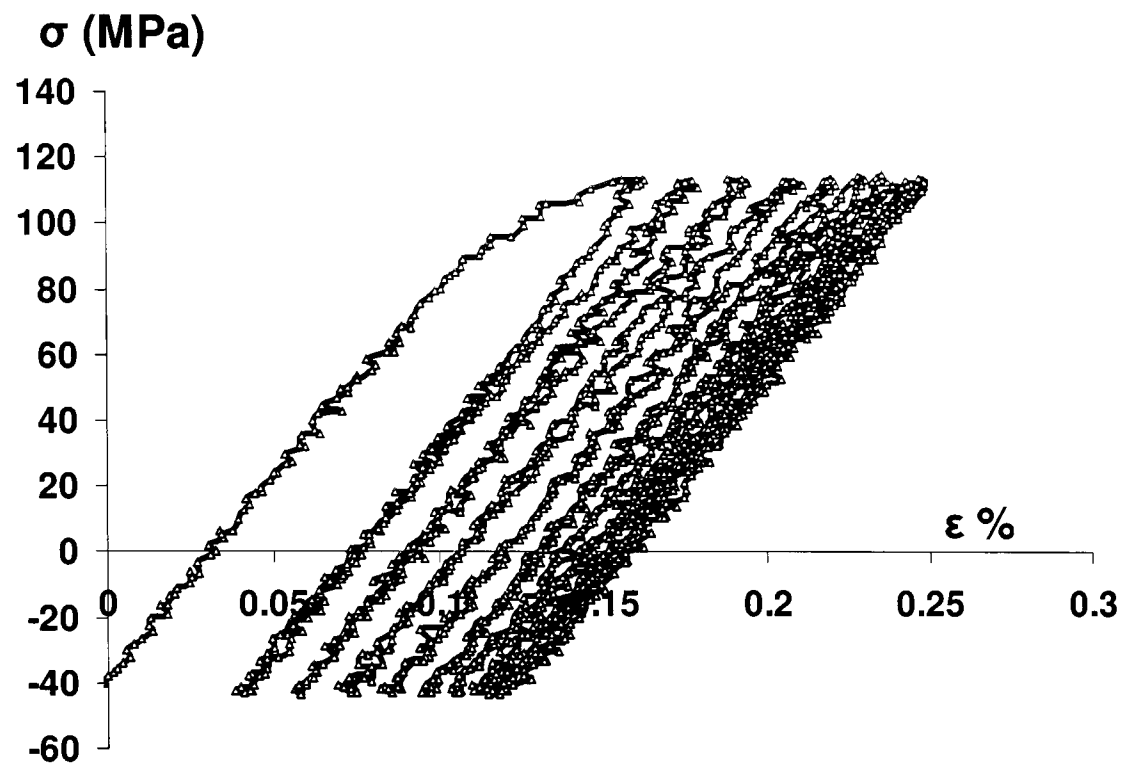


Figure 3.42 Measured stress-strain loops from a stress controlled isothermal test at 700°C using the stress waveform from Figure 3.39

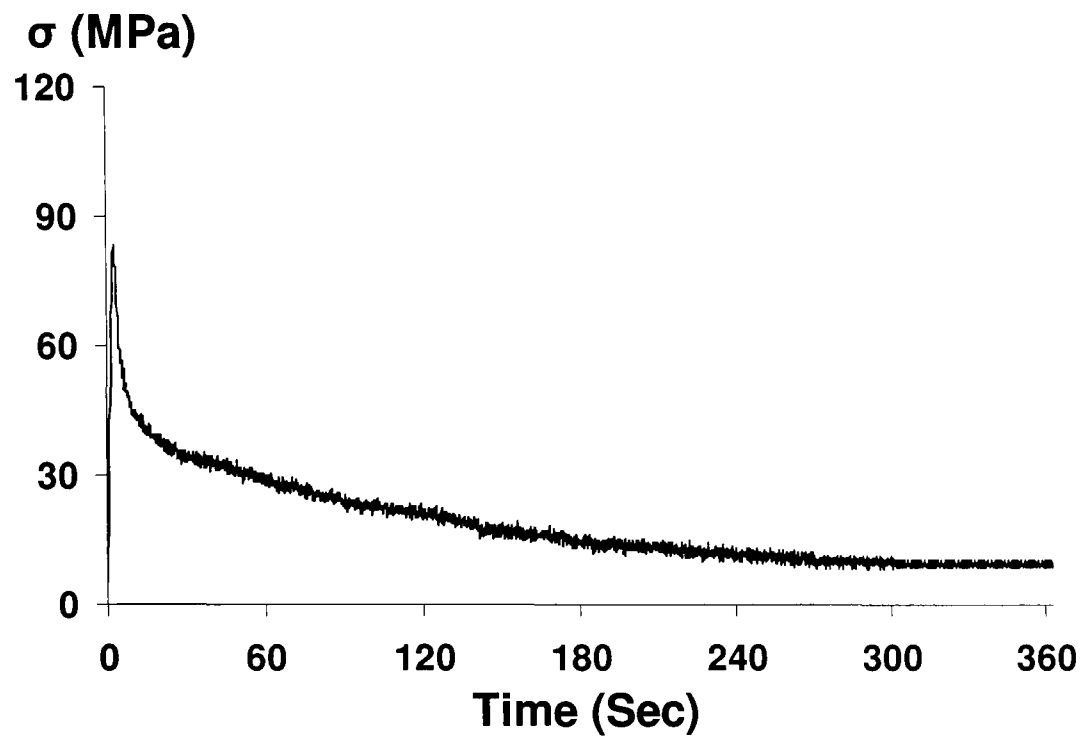


Figure 3.43 Stress history from a stress relaxation test carried out at 900°C on XN40F alloy by holding 0.15% strain in tension for 360 seconds

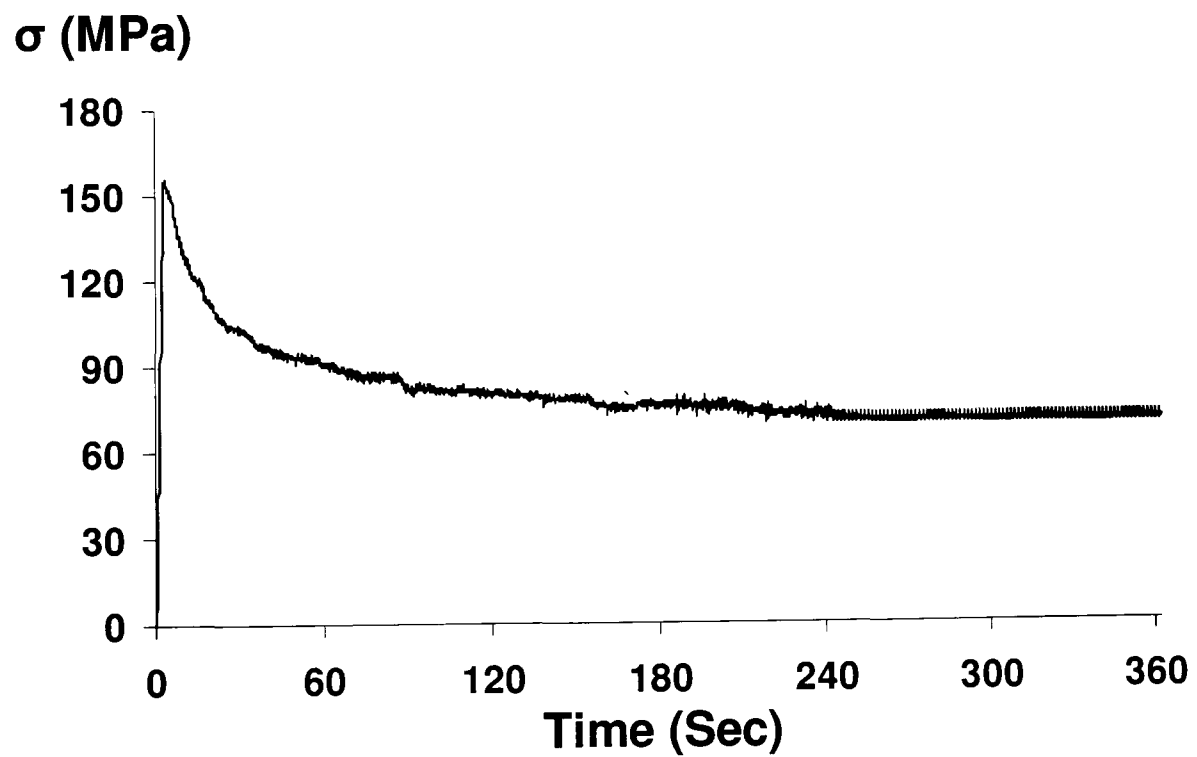


Figure 3.44 Stress history from a stress relaxation test carried out at 700°C on XN40F alloy by holding 0.15% strain in tension for 360 seconds

## Chapter 4

# MATERIAL CHARACTERISATION AND MODELLING

### 4.1 Introduction

This chapter focuses on identifying material parameters for different material models and validating them against experimental results discussed in Chapter 3. Finite element (FE) based simulation is an effective method for analysing thermo-mechanical behaviour of a realistic large SPF tool. However accurate material models are crucial for the credibility of FE predictions. Therefore the choice of a suitable material model and an accurate identification of material parameters are important in FE based simulations.

Two phenomenological material behaviour models were applied and analysed in this project to model SPF tool thermo-mechanical behaviour. An uncoupled plasticity-creep model was used where the cyclic plasticity during temperature transients was simulated using Chaboche (i) non-linear kinematic hardening and (ii) combined non-linear kinematic/isotropic hardening. In both cases power law (Norton) creep was used to model the creep deformation during the dwell period of each forming cycle. The other model applied is the so-called two layer viscoplasticity where the stress is partitioned into elastic-viscous and elastic-plastic components and the two components are in parallel with each other. The performance of these two models were compared and analysed in the context of the experimental results.

The material parameters for the non-linear-kinematic and the combined kinematic/isotropic hardening models were identified using stress-strain loops

obtained from multi-strain range cyclic tests. The Power law (Norton) creep constants representing steady state secondary creep were determined using stress relaxation tests. The material models and identified material constants were validated against the experimental results.

## 4.2 Material models

### 4.2.1 Isotropic hardening model

Isotropic hardening has been widely used due to its ease in implementation. It depicts very well the behaviour of proportionally loaded structures where the principal stresses do not rotate at any point of a structure. Isotropic hardening implies that the yield surface increases in size with increasing plastic strain without changing its original shape.

In isotropic hardening, the evolution of the loading surface is identified by isotropic hardening variable  $R$  which is the function of accumulated plastic strain  $p$ . Fig. 4.1 shows the schematic diagram of isotropic hardening in 3D stress space and in tension and compression where  $\sigma_y$ , the initial yield stress in tension defines the initial yield surface size. It also shows the uniform expansion of the initial yield surface and justifies the application of accumulated plastic strain as a variable of isotropic hardening as the points M and M' in Fig. 4.1 have the same accumulated plastic strain.

The isotropic hardening is expressed as

$$f = f(\sigma, R) \quad (4.1)$$

It can also be expressed in the form as

$$f = f_Y(\sigma) - \Gamma(R) \quad (4.2)$$

where the function  $f_Y$  signifies the form of yield criterion and the function  $\Gamma$  establishes hardening through the relation between isotropic hardening variable  $R$  and the accumulated plastic strain  $p$ .

#### 4.2.2 Linear kinematic hardening model

In reality, the hardening is mainly anisotropic and this hardening aspect of plasticity must be taken into account when the loading is no longer proportional. In the case of cyclic loadings, most metals and alloys experience anisotropic hardening behaviour. Prager developed a simple formulation of anisotropy called kinematic hardening, on which the most of the present theories are formed to simulate inelastic behaviour of materials subjected to cyclic loading.

Linear kinematic hardening assumes that the original yield surface retains its size but translates in stress space. In this model the yield surface moves in stress space and causes straining in one direction that reduces the yield stress in the opposite direction (Fig. 4.2). This phenomenon is called the Bauschinger effect.

Two kinematic hardening rules are described below.

##### a) Prager's kinematic hardening rule

Prager's rule is the generalised form of kinematic hardening which corresponds to the translation of the loading surface.

The kinematic hardening loading function is expressed as

$$f = f_y(\sigma - X) - k \quad (4.3)$$

where  $X$  is the kinematic hardening variable called as the back stress which indicates the present position of the centre of the loading surface and  $k$  is the cyclic yield

stress. Fig. 4.2 shows the linear kinematic hardening in three dimensional stress space and in tension and compression.

The Prager kinematic hardening rule is based on the following form,

$$d\mathbf{X} = \frac{2}{3} C d\boldsymbol{\varepsilon}^p \quad (4.4)$$

where  $C$  is the hardening modulus and  $d\boldsymbol{\varepsilon}^p$  is the incremental plastic strain .

b) Ziegler's kinematic hardening rule

The Ziegler's kinematic hardening rule is described as,

$$d\mathbf{X} = (\boldsymbol{\sigma} - \mathbf{X})d\mu \quad (4.5)$$

where  $d\mu$  is a constant determined from the hardening curve as  $d\mu = \frac{C}{\sigma^0} d\boldsymbol{\varepsilon}^p$ .

The anisothermal (Ziegler) linear kinematic hardening model can be expressed as follows

$$d\mathbf{X} = C \frac{1}{\sigma^0} (\boldsymbol{\sigma} - \mathbf{X}) d\bar{\boldsymbol{\varepsilon}}^{pl} + \frac{1}{C} \mathbf{X} \dot{C} \quad (4.6)$$

where  $C$  is the kinematic hardening modulus,  $d\bar{\boldsymbol{\varepsilon}}^{pl}$  is the equivalent plastic strain rate and  $\mathbf{X}$  is the translation of the yield surface in the stress space called the back stress. In this model  $\sigma^0(T)$ , can be a function of temperature, and remains constant,  $\sigma^0 = \sigma_b$ , as  $\sigma_b$  is the equivalent stress defining the size of the yield surface at zero plastic strain.  $\dot{C}$  is the rate of change of hardening modulus with respect to temperature.

### 4.2.3 Nonlinear isotropic/kinematic hardening model

The combined isotropic/kinematic hardening model provides a better approximation of the stress-strain relation than the linear kinematic hardening model. This model also depicts different material phenomena such as ratchetting, mean stress relaxation and cyclic hardening [62]. The evolution rule of the model consists of two components; 1) Non-linear kinematic hardening 2) Isotropic hardening. A schematic representation of the combined isotropic/kinematic hardening model is shown in Fig. 4.3 and 4.4.

A non-linear kinematic hardening component defines the translation of the yield surface in stress space through the back stress  $X$ . Fig. 4.3 shows the schematic diagram of non-linear kinematic hardening in three dimensional stress space and in tension and compression loading.

The temperature dependent Ziegler evolution law for back stress is expressed as

$$dX = C \frac{1}{\sigma^0} (\sigma - X) d\bar{\epsilon}^{pl} - \gamma X d\bar{\epsilon}^{pl} + \frac{1}{C} X \dot{C} \quad (4.7)$$

where  $\gamma$  is the relaxation term which decides the rate at which the kinematic hardening modulus decreases with increasing plastic deformation. This relaxation term introduces non-linearity to the linear Ziegler hardening law.

The isotropic hardening component expresses the change of the equivalent stress defining the size of the yield surface,  $\sigma^0(\bar{\epsilon}^{pl}, T, f_i)$ , which is a function of equivalent plastic strain,  $\bar{\epsilon}^{pl}$ ; temperature,  $T$  and field variable  $f_i$  [100].

$$\sigma^0 = k + Q_\infty (1 - e^{-b\bar{\epsilon}^{pl}}) \quad (4.8)$$

where  $k$  is the yield surface size at zero plastic strain, and  $Q_\infty$  and  $b$  are isotropic hardening material parameters. Furthermore  $Q_\infty$  is the asymptotic value from stabilized cycles defining the maximum change in the size of the yield surface and  $b$  indicates the rate at which the size of the yield surface changes as plastic straining develops.

#### 4.2.4 Power law creep model

This is mainly used to model the steady state secondary creep as shown in Fig. 4.5. Power law creep model is popular for its simplicity in use but has limitations in its range of applications. This steady accumulation of strain with time is usually considered in many engineering problems of designing against creep.

In the case of steady state creep, the creep strain rate is a function of only temperature and stress. Power law creep for the uniaxial loading is expressed as

$$\dot{\epsilon}_{ss}^{cr}(\sigma, T) = A(T)\sigma^n \quad (4.9)$$

There are two hardening rules associated with the power law creep model to take into account the state of stress.

a) Time hardening

$$\dot{\epsilon}^{cr} = A\bar{q}^n t^m \quad (4.10)$$

b) Strain hardening

The strain hardening form of the power law is generally used when the stress state varies during the analysis.

$$\dot{\bar{\epsilon}}^{cr} = \left( A \bar{q}^n \left[ (m+1) \bar{\epsilon}^{cr} \right]^m \right)^{\frac{1}{m+1}} \quad (4.11)$$

where  $\bar{q}$  is the equivalent uniaxial stress,  $\dot{\bar{\epsilon}}^{cr}$  is the equivalent creep strain rate and  $t$  is the total time.  $A$ ,  $n$  and  $m$  are temperature dependent material constants.  $A$  and  $n$  must be positive for physically reasonable behaviour and  $m$  should be in a range of  $-1 < m \leq 0$ .

#### 4.2.5 Two-layer viscoplastic model

Two-layer viscoplastic model is anticipated for modelling materials in which significant time dependent as well as time independent behaviour is observed which is generally occurred at high temperature applications. Therefore this model is intended for modelling the material behaviour under fluctuation loading over a wide range of temperatures. The model comprises of an elastic –plastic network in parallel with elastic –viscous network (Maxwell model). A one dimensional rheological depiction of the model is shown in Fig. 4.6. Charkaluk [101] first applied this model in the case of cast-iron exhaust manifolds. The multiaxial equations for the two-layer viscoplastic model are defined as follows:

$$\boldsymbol{\epsilon}_v^{el} = \frac{1+\nu}{K_v} \boldsymbol{\sigma}_v - \frac{\nu}{K_v} \text{tr}(\boldsymbol{\sigma}_v) \mathbf{I} \quad (4.12)$$

$$\boldsymbol{\epsilon}_p^{el} = \frac{1+\nu}{K_p} \boldsymbol{\sigma}_p - \frac{\nu}{K_p} \text{tr}(\boldsymbol{\sigma}_p) \mathbf{I} \quad (4.13)$$

$$\sigma_v = K_v : (\varepsilon - \varepsilon_v) \quad (4.14)$$

$$\sigma_p = K_p : (\varepsilon - \varepsilon_p) \quad (4.15)$$

$$\sigma = \sigma_p + \sigma_v \quad (4.16)$$

with the yield surface defined by:

$$f(\sigma_p - X) = \sigma^0 \quad (4.17)$$

where  $\sigma^0$  is the current size of the yield surface and  $f(\sigma_p - X)$  is the equivalent (von

Mises) stress with the back stress  $X$  defined as:

$$f(\sigma_p - X) = \sqrt{\frac{3}{2} (\mathbf{S}_p - \mathbf{X}^{dev}) : (\mathbf{S}_p - \mathbf{X}^{dev})} \quad (4.18)$$

where  $\mathbf{X}^{dev}$  is the deviatoric part of the back stress and  $\mathbf{S}_p$  is the deviatoric (plastic)

stress tensor. The plastic flow-rule is:

$$\dot{\varepsilon}_p = \frac{\partial f(\sigma_p - X)}{\partial \sigma_p} p \quad (4.19)$$

where  $p$  is the equivalent plastic strain rate defined as follows

$$p = \sqrt{\frac{2}{3} \dot{\varepsilon}_p : \dot{\varepsilon}_p} \quad (4.20)$$

The steady state (secondary) creep behaviour is modelled using the Norton power-law as follows:

$$\dot{\varepsilon}_v = \frac{3}{2} A [f(\sigma_v)]^n \frac{\mathbf{S}_v}{f(\sigma_v)} \quad (4.21)$$

where  $A$  and  $n$  are temperature-dependent material constants,  $\dot{\varepsilon}_v$  is the viscous creep strain rate and  $\mathbf{S}_v$  is the deviatoric viscous stress tensor.

The elastoplastic network predicts the time independent behaviour of the material whereas elastic viscous network predicts the time dependent behaviour of the material. The uniaxial elastoplastic mechanism with a linear kinematic hardening is expressed as

$$\sigma_p = K_p \varepsilon \quad \text{if} \quad \sigma_p < \sigma_y \quad (4.22)$$

$$\sigma_p = K_p \varepsilon + C \left( \varepsilon - \frac{\sigma_y}{K_p} \right) \quad \text{if} \quad \sigma_p \geq \sigma_y \quad (4.23)$$

where  $K_p$  is the long term modulus of elastic-plastic network,  $\sigma_y$  is the initial yield stress and  $C$  is the hardening modulus.

Viscous behaviour of the material is assumed to be governed by the Norton-Hoff rate law which is described as

$$\sigma_v = A \dot{\varepsilon}^n \quad (4.24)$$

Any of the forms of power law described earlier can be chosen in this model.

Here the value of  $n$  is assumed to be zero by choosing a time hardening of the power law for illustration.

$$\dot{\varepsilon} = A \sigma_v^n t^m \quad (4.25)$$

$\sigma_v$  is the viscous stress in the visco-elastic network and  $A$  and  $n$  are Norton-Hoff material constants.

The ratio of the elastic modulus of elastic-viscous network;  $K_v$  to the total instantaneous modulus;  $K_p + K_v$  is given as

$$f = \frac{K_v}{(K_p + K_v)} \quad (4.26)$$

This user specified ratio  $f$  divides up the total moduli specified for the elastic behaviour among elastic-viscous and elastic-plastic networks. The parameters that require to be identified for this model are the elastic properties of two networks,  $K_p$  and  $K_v$ ; the initial yield stress  $\sigma_y$ ; the hardening modulus  $C$  and the Norton-Hoff rate constants,  $A$  and  $n$ . A static (effectively zero strain rate) uniaxial tension test

determines the long term modulus,  $K_p$ ; the initial yield stress  $\sigma_y$ ; and the hardening modulus  $C$ . A linear kinematic hardening described here is for illustration and any other general plasticity model such as non-linear kinematic or combined isotropic/kinematic models can be used to define the time independent network. In the case of the combined non-linear kinematic/isotropic hardening model employed for elastic-plastic network, additional parameters such as  $\gamma$ ,  $Q_\infty$  and  $b$  are required. The instantaneous elastic modulus  $K = K_p + K_v$  can be identified by measuring the initial elastic response of the material under non zero and relatively high strain rates. A number of such measurements at different applied strain rates should be compared until the instantaneous moduli does not change with change in applied strain rate [100]. The difference between  $K$  and  $K_p$  determines the elastic modulus of elastic-viscous network,  $K_v$ . However in this thesis the ratio  $f$  is identified by fitting the two-layer model with the stress relaxation test data using the identified creep constants from the relaxation tests.

### **4.3 Identification of material constitutive constants**

#### **4.3.1 Non-linear kinematic hardening model**

The material constants for non-linear kinematic hardening (NLKH) were identified from the stabilized hysteresis loops corresponding to different strain amplitudes of the multi-strain range isothermal cyclic tests carried out on SS-316 stainless steel as well as XN40F alloy. The constant  $k$  for a particular temperature was determined as the mean of the individual  $k$  values for each strain range, which were readily

estimated from the stabilised stress-strain loops. The ratio  $\frac{C}{\gamma}$  was determined as the asymptotic value of  $\frac{\Delta\sigma}{2} - k$  plotted against  $\frac{\Delta\varepsilon_p}{2}$ , corresponding to the saturated value of back stress. The coefficients  $C$  and  $\gamma$  were identified by fitting the following equation (4.27) [62], which represents the NLKH relationship between the cyclic stress and strain to the measured stabilized cyclic stress-strain data

$$\frac{\Delta\sigma}{2} - k = \frac{C}{\gamma} \tanh\left(\gamma \frac{\Delta\varepsilon_p}{2}\right) \quad (4.27)$$

Fig. 4.7 shows the identification of coefficients  $C$  and  $\gamma$  for the SS-316 stainless steel material at 20°C, 300°C and 600°C and the strain rate of  $2 \times 10^{-4} \text{ s}^{-1}$ . The identified material constants for SS-316 steel are summarised in Table 4.1. Fig. 4.8 shows the comparison of the NLKH material model predictions using the identified constants (Table 4.1) with the experimental stabilized loops over the range of temperatures and the two representative strain ranges of  $\Delta\varepsilon = 0.8\% \text{ \& } 1.0\%$  for SS-316 steel. The correlation for other strain ranges is of equivalent quality. Similarly Fig. 4.9 shows the identification of the coefficients  $C$  and  $\gamma$  for the XN40F tool material at 20°C, 500°C, 700°C and 900°C for the strain rate of  $5 \times 10^{-4} \text{ s}^{-1}$ . The material constants were also identified for the strain rate of  $5 \times 10^{-3} \text{ s}^{-1}$  in similar fashion. The identified material constants are summarised in Table 4.2. Fig. 4.10 and 4.11 show the comparison of the NLKH material model predictions using the identified constants (Table 4.2) with the experimental stabilized loops over the range of temperatures and strain-ranges for the  $5 \times 10^{-4} \text{ s}^{-1}$  case.

The correlation for the  $5 \times 10^{-3} \text{ s}^{-1}$  case is of equivalent quality (see Appendix A)

### 4.3.2 Combined isotropic/kinematic hardening model

Superposition of isotropic hardening on a non-linear kinematic hardening, results in a modification of the elastic domain by translation and uniform expansion [62]. The variables applied in expressing the isotropic hardening are the accumulated plastic strain  $p$  and the associated isotropic hardening variable  $R$  which represents the change in size of elastic domain. This domain can be given as

$$f = J_2(\boldsymbol{\sigma} - \boldsymbol{X}) - R - k \leq 0 \quad (4.28)$$

Here the  $k$  parameter represents the initial elastic limit in tension.

The evolution of  $R$  as a function of  $p$  represents the progression of hardening and the evolution of  $R$  can be expressed as

$$dR = b(Q_\infty - R)dp \quad (4.29)$$

The integration of this equation and the application of the given criterion to every uniaxial cycle give [62]

$$\sigma_{Max} = X_{Max} + k + Q_\infty[1 - \exp(-bp)] \quad (4.30)$$

$X_{Max}$  is assumed to be a constant along with the plastic strain range  $\Delta\varepsilon_p$  and the relationship representing isotropic hardening is obtained for the  $N^{\text{th}}$  cycle [62].

$$\frac{\sigma_{Max} - \sigma_{Max0}}{\sigma_{Maxs} - \sigma_{Max0}} = 1 - \exp(-2b\Delta\varepsilon_p N) \quad (4.31)$$

where  $\sigma_{Maxs}$  and  $\sigma_{Max0}$  are respectively the maximum stress of the stabilized cycle and that of the first cycle. This evolution rule represents cyclic hardening effects. The combined isotropic/kinematic hardening model was considered only for XN40F alloy. The isotropic hardening parameters of the combined model for XN40F alloy were identified from cyclic stress-strain loops corresponding to strain range of 0.6% and the strain rate of  $5 \times 10^{-4} \text{ s}^{-1}$  at 20, 500 and 700°C. Fig. 4.12 shows the stress-strain loops at 20, 500, 700 and 900°C representing cyclic hardening and stabilization

behaviour of XN40F alloy. However negligible or no cyclic hardening was observed at 900°C. The material parameter  $Q_\infty$  was determined as the difference between  $\sigma_{Maxs}$  and  $\sigma_{Max0}$ . The parameter  $b$  was identified by fitting equation (4.31) which represents the cyclic hardening relationship between cyclic stress and strain to the measured cyclic stress-strain data (Fig. 4.13). Following the method described by Lemaitre and Chaboche (1990), the  $k$  (elastic domain) value for non-linear kinematic hardening model determined from stabilized stress-strain loops was modified by subtracting  $Q_\infty$  from it. The identified material constants are summarised in Table 4.3. Fig. 4.14 and 4.15 show the comparison of the combined material model and experiment using the identified constants at 20°C, 500°C and 700°C.

### 4.3.3 Power law creep model

Steady state (secondary) creep defined by Norton's power law is a practical and effective approximation of the creep problem. The power law creep constants for steady state (secondary) creep were identified here from stress relaxation tests carried out on XN40F alloy at 700 and 900°C.

Creep causes stresses to relax with time at high temperature when the strain is held constant. Fig. 4.16 shows the stress relaxation behaviour where the elastic strain is replaced by creep strain. The relaxation time can be calculated from the power law creep data as follows:

At any time

$$\varepsilon^{tot} = \varepsilon^{el} + \varepsilon^{cr} \quad (4.32)$$

$$\varepsilon^{el} = \frac{\sigma}{E} \quad (4.33)$$

Power law creep at constant temperature is given.

$$\dot{\varepsilon}^{cr} = A\sigma^n \quad (4.34)$$

As the total strain  $\varepsilon^{tot}$  is constant, differentiating equation 4.32 with respect to time and substituting equations 4.33 and 4.34 gives

$$\frac{1}{E} \frac{d\sigma}{dt} = -A\sigma^n \quad (4.35)$$

Integrating equation 4.35 from  $\sigma = \sigma_i$  at  $t=0$  to  $\sigma = \sigma$  at  $t=t$ , gives

$$t = \frac{1}{AE(n-1)} \left[ \frac{1}{\sigma^{n-1}} - \frac{1}{\sigma_i^{n-1}} \right] \quad (4.36)$$

An initial set of values for A and n were identified by plotting the experimental data as  $\text{Log}(\dot{\sigma})$  versus  $\text{Log} \sigma$  (Fig. 4.17). These initial set of creep constants was optimised by fitting equation (4.36) to the measured stress relaxation data. Fig. 4.18 shows the comparison of the analytical equation (4.36) and the experimental stress relaxation at 700 and 900°C. The power law creep constants for 700 and 900°C are summarised in Table 4.4.

#### 4.3.4 Two-layer viscoplastic model

The elastic-plastic component of the model can be defined by any of the plasticity models such as non-linear kinematic or combined isotropic/kinematic model. Here a non-linear kinematic hardening was used for the elastic-plastic network. The elastic-viscous component was defined by the power law creep. The identification of the material parameters required for this model such as  $k$ ,  $C$ ,  $\gamma$ ,  $A$  and  $n$  were described earlier. The ratio  $f$  from equation (4.26) which apportions the total moduli specified

for the elastic behaviour among elastic-viscous and elastic-plastic networks was identified by fitting the model with the experimental stress relaxation results. Fig. 4.19 shows the comparison of the two-layer model and experimental stress relaxation at 700 and 900°C. Material parameters for the two-layer viscoplastic model are listed in Table 4.2 and 4.4. The two-layer model was applied to model multi strain-range isothermal tests at 700°C and 900°C for the strain rates of  $5 \times 10^{-3} \text{ s}^{-1}$  and  $5 \times 10^{-4} \text{ s}^{-1}$ . FE analyses for both the strain rates were performed using the cyclic plasticity material constants identified for  $5 \times 10^{-4} \text{ s}^{-1}$  strain rate (Table 4.2) and the same set of material constants showed a good agreement with experimental results for both the strain rates. Fig. 4.20 and 4.21 show the comparison of the two-layer viscoplasticity model predictions using the identified constants with the experimental stabilized loops at 700°C and 900°C. Fig. 4.22 shows the strain rate effect captured by the two-layer viscoplastic model for 900°C.

#### **4.4 Validation of material models**

Two material models, the uncoupled plasticity-creep and the two-layer viscoplasticity models were compared against the stress-strain loops of thermo-mechanical fatigue tests carried out on XN40F alloy. Uniaxial thermo-mechanical fatigue tests were simulated using a single element FE analyses. The non-linear kinematic hardening parameters (Table 4.2) for the strain rate of  $5 \times 10^{-4} \text{ s}^{-1}$  were used in all analyses to model the cyclic plasticity whereas creep deformation was simulated using power law creep constants summarised in Table 4.4. All the material parameters identified from isothermal tests are assumed to vary linearly between the TMF test temperatures.

In case of the uncoupled plasticity-creep model, the transient temperature part of the cycle is modelled by a temperature dependent non-linear kinematic hardening and the constant temperature dwell period was represented by Norton's power law for creep.

For the two layer viscoplasticity model, the additional parameter  $f$  was defined. Fig. 4.23 shows the comparison of these two models against the experimental stabilised stress-strain loops of TMF OP test with strain holds. For both the models, a reasonable correlation is observed with experimental loops. However the two-layer viscoplasticity model was more accurate than the uncoupled plasticity-creep model. This is due to the ability of two-layer model to capture the strain rate effects.

A strain controlled representative SPF tool test carried out at a strain rate of  $1 \times 10^{-4} \text{ s}^{-1}$  was also replicated using the two-layer model and depicted a reasonably accurate correlation with the experimental stabilised stress-strain loop as shown in Fig. 4.24.

## 4.5 Summary and conclusions

Material parameters were successfully identified for non-linear kinematic and combined isotropic/kinematic hardening models using cyclic stress-strain loops obtained from multi-strain range isothermal fatigue tests. These material parameters were employed in FE analyses and compared with the experimental cyclic stress-strain results.

The non-linear kinematic hardening model for SS-316 steel showed a reasonably accurate correlation with the experimental stabilised stress-strain loops for all temperatures; 20, 300 and 600°C, shown in Fig. 4.8. Similarly for XN40F alloy, the non-linear kinematic hardening showed a good agreement with experimental results (Fig. 4.10-4.11). However, a largest discrepancy was seen for 700 and 900°C due to the creep deformation occurring at high temperature. The combined isotropic/kinematic hardening model was also explored for XN40F alloy and the identified material parameters were verified by comparing FE results with experimental loops. The cyclic hardening behaviour was successfully reproduced in the FE analysis using the identified material constants (Fig. 4.14& 415).

Norton power law creep constants were determined initially from the stress relaxation tests and tuned by fitting the analytical expression for relaxation time to the experimental stress relaxation results. The material constant  $f$  for the two-layer model was identified by fitting the model with the experimental stress relaxation results. Unlike non-linear kinematic hardening, the two-layer viscoplasticity model gave a better correlation with experimental stabilised loops at high temperature.

All these temperature dependent material constants were used in describing two material modeling phenomena; uncoupled plasticity-creep and two-layer viscoplasticity. These models are phenomenological and capture only the macroscopic behaviour of the material. They were used to simulate thermo-mechanical fatigue tests carried out on XN40F alloy. For the uncoupled plasticity-creep model, the strain rate dependent creep is defined during the strain hold period of TMF tests where as the strain rate independent non-linear kinematic hardening

model is used to model transient temperature portion of the cycle. However in the case of the two-layer model, the specified ratio  $f$  incorporates the strain rate dependency not only during the strain hold period but also during the transient temperature cycle by parting of elastic-plastic and elastic-viscous components in the analysis. The strain rate dependency of the model depends on the contribution of elastic-viscous network at that temperature. Therefore the two-layer viscoplastic model showed more accurate correlation with the experimental loops than the uncoupled plasticity-creep model (Fig. 4.23).

Table 4.1 Nonlinear kinematic hardening parameters for SS-316 stainless steel for a strain rate of  $2 \times 10^{-4} \text{ s}^{-1}$

| Temperature °C | k (MPa) | C (MPa) | $\Gamma$ |
|----------------|---------|---------|----------|
| 20             | 255     | 150000  | 810      |
| 300            | 202     | 130000  | 812.5    |
| 600            | 195     | 110000  | 815      |

Table 4.2 Nonlinear kinematic hardening parameters for XN40F alloy

| Strain rate= $5 \times 10^{-4} \text{ s}^{-1}$ |         |         |          |
|--|---------|---------|----------|
| Temperature °C                                 | k (MPa) | C (MPa) | $\Gamma$ |
| 20   | 175     | 82000   | 656      |
| 500  | 154     | 55000   | 393      |
| 700  | 151     | 32000   | 267      |
| 900  | 60      | 8000    | 320      |
| Strain rate= $5 \times 10^{-3} \text{ s}^{-1}$ |         |         |          |
| Temperature °C                                 | k (MPa) | C (MPa) | $\Gamma$ |
| 20   | 183     | 125000  | 892      |
| 500  | 160     | 38000   | 422      |
| 700  | 155     | 21000   | 300      |
| 900  | 90      | 9000    | 250      |

Table 4.3 Combined nonlinear/isotropic hardening parameters for XN40F alloy for a strain rate of  $5 \times 10^{-4} \text{ s}^{-1}$

| Temperature °C | k (MPa) | $Q_{\infty}$ (MPa) | b  | C (MPa) | $\gamma$ |
|----------------|---------|--------------------|----|---------|----------|
| 20             | 125     | 50                 | 35 | 82000   | 656      |
| 500            | 104     | 50                 | 20 | 55000   | 393      |
| 700            | 101     | 50                 | 24 | 32000   | 267      |
| 900            | 60      | 0                  | -  | 8000    | 320      |

Table 4.4 Power law creep and two-layer viscoplasticity constants for XN40F alloy

| Temperature °C | A [ $\text{MPa}^{-n} \text{ s}^{-1}$ ] | n    | F    |
|----------------|--|------|------|
| 700            | $2.68 \times 10^{-15}$                 | 4.68 | 0.92 |
| 900            | $3.48 \times 10^{-14}$                 | 5.5  | 0.99 |

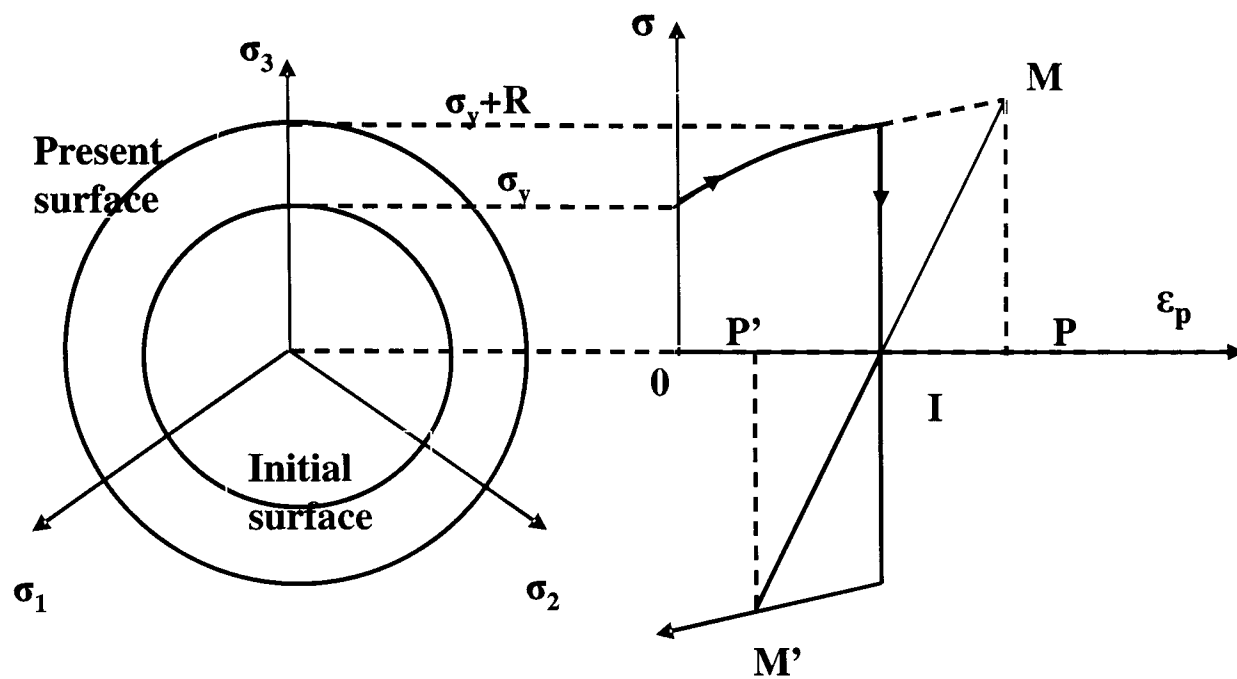


Figure 4.1 Schematic representation of isotropic hardening in three-dimensional stress space in tension and compression.

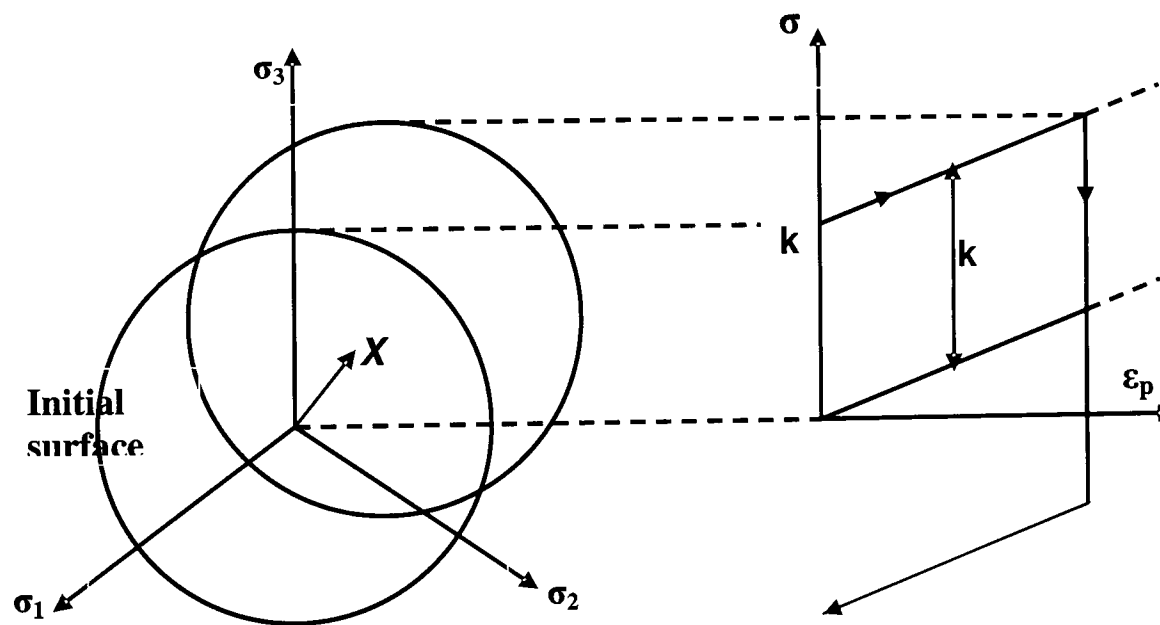


Figure 4.2 Schematic representation of linear kinematic hardening in three-dimensional stress space in tension and compression.

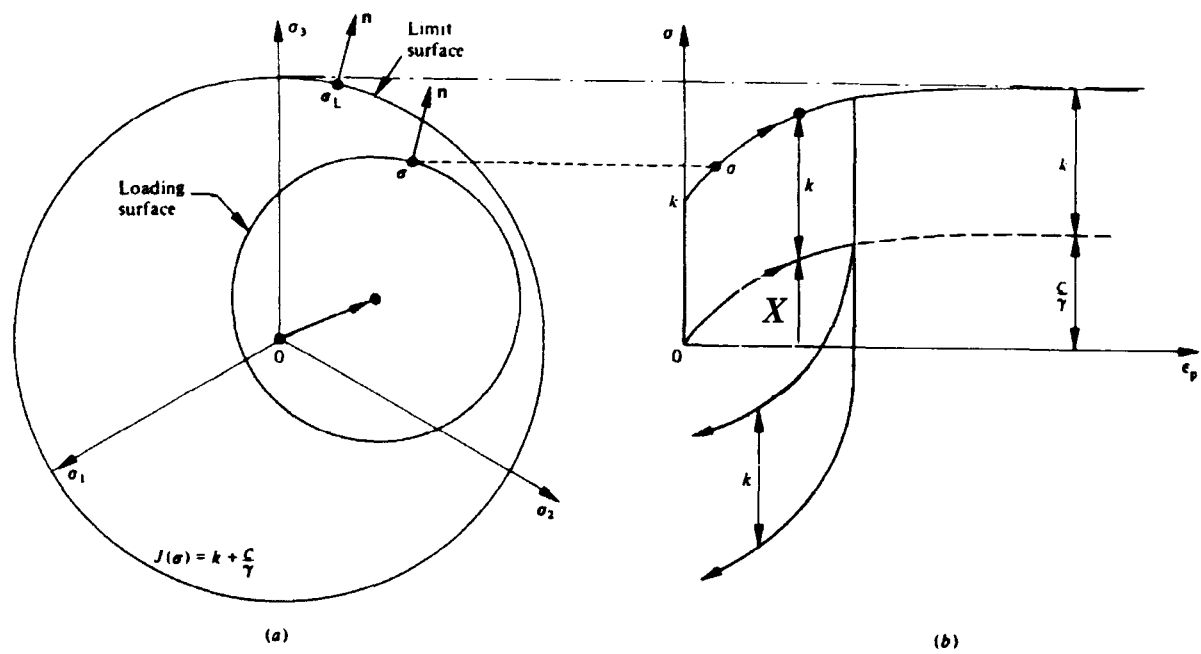


Figure 4.3 Schematic representation of nonlinear kinematic hardening model: (a) three dimensional, (b) tension-compression [62].

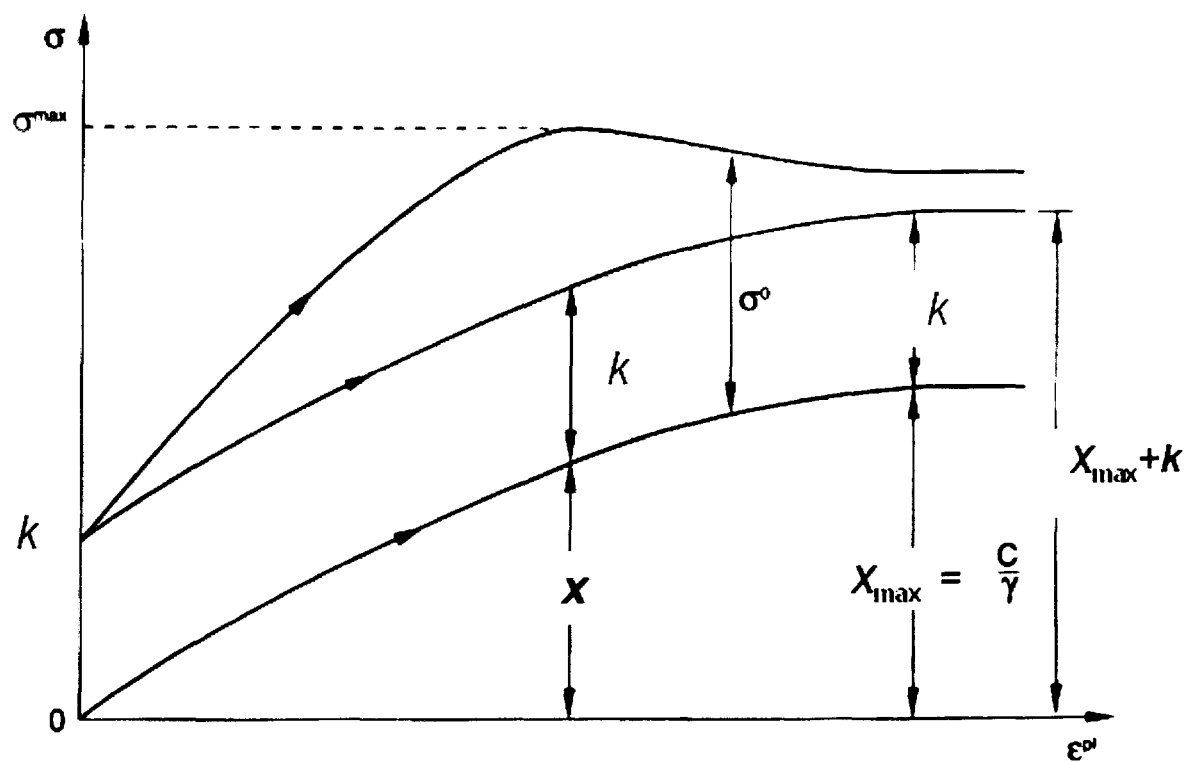


Figure 4.4 Schematic one dimensional representation of combined nonlinear kinematic/isotropic hardening model [100].

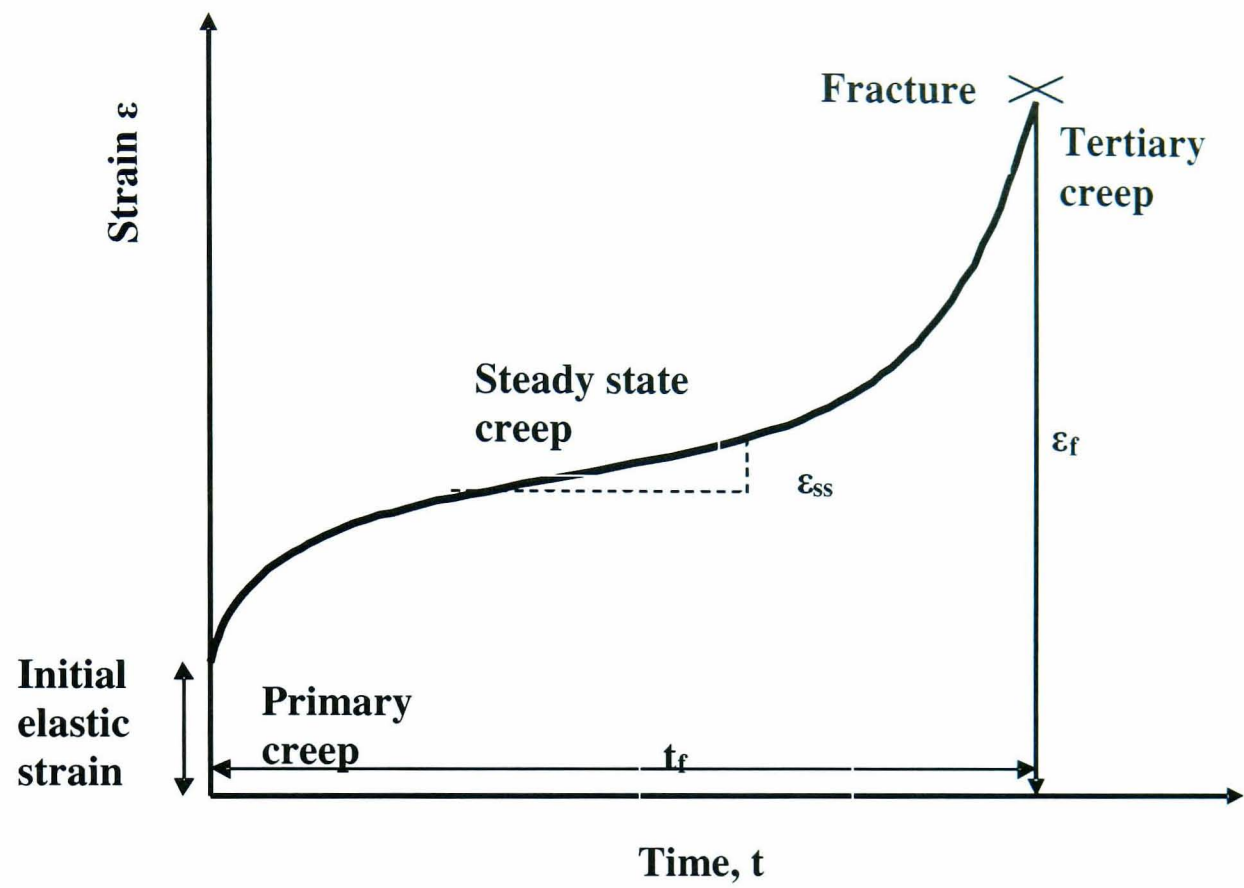


Figure 4.5 Schematic diagram of creep strain versus representing primary, secondary and tertiary creep.

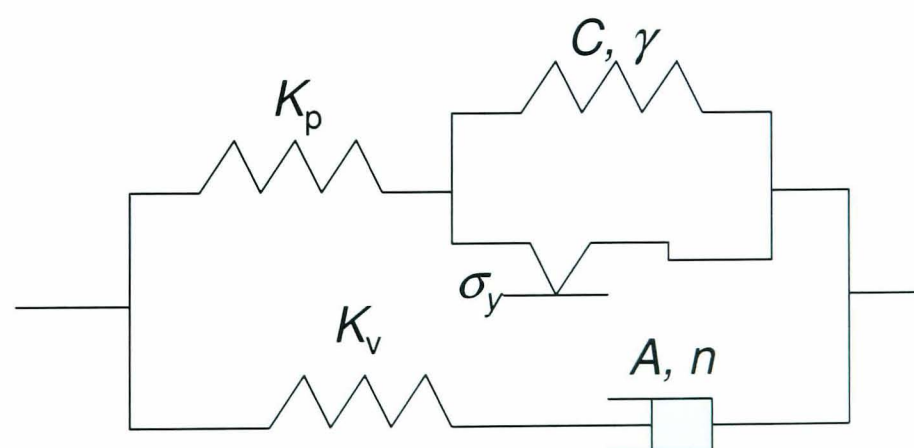
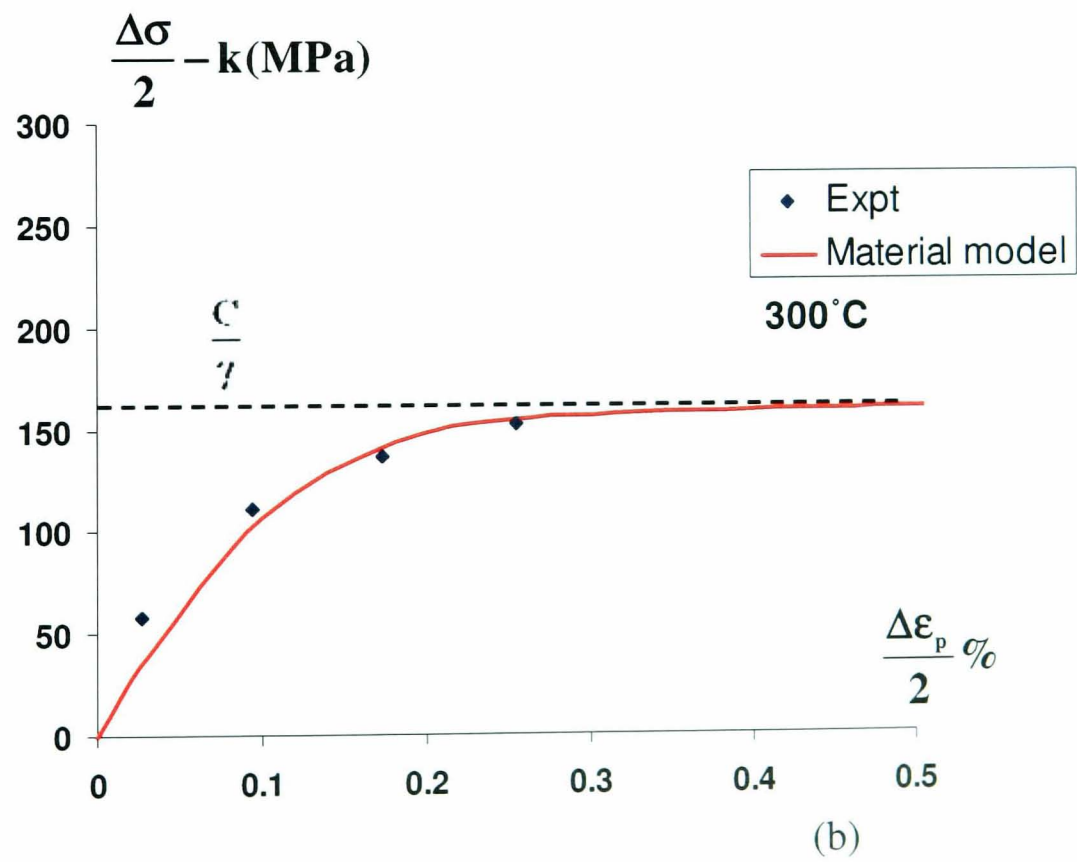
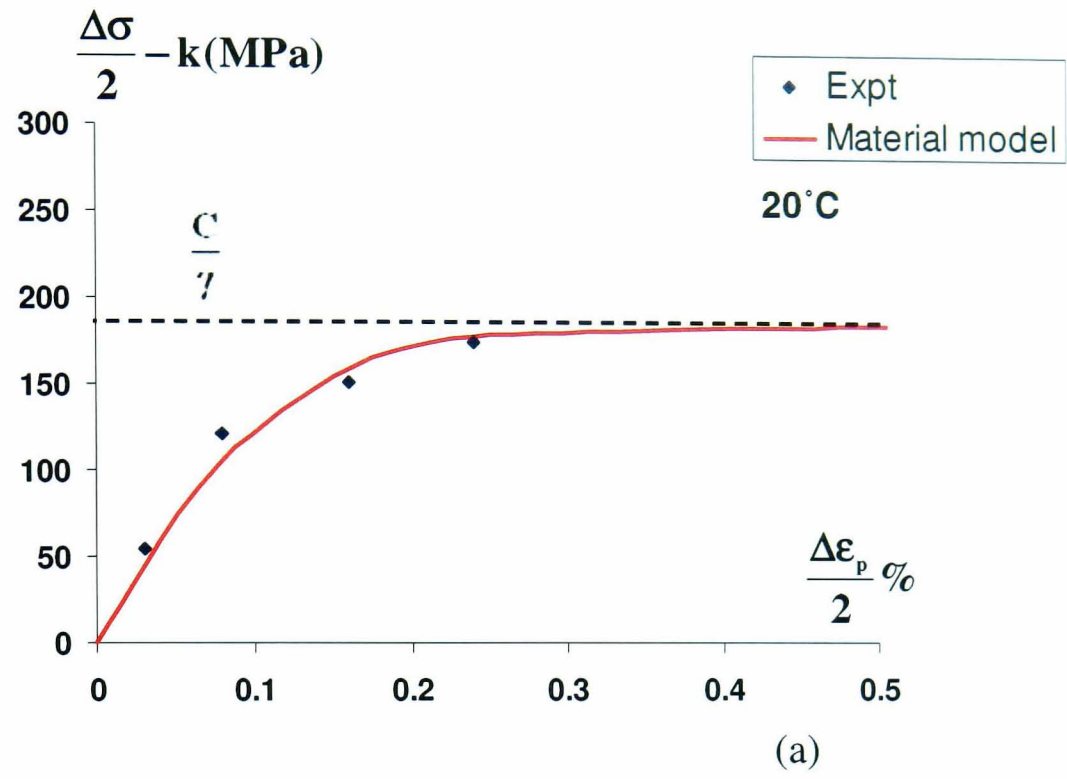


Figure 4.6 One dimensional rheological representation of two-layer viscoplastic model [100].



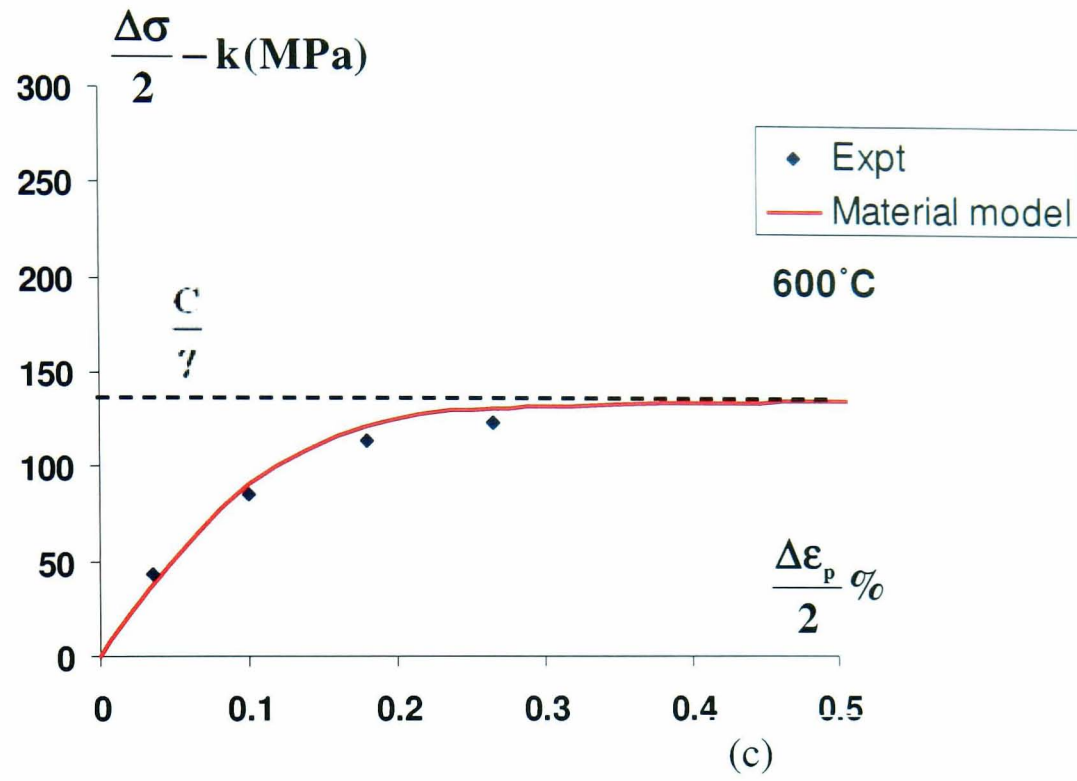


Figure 4.7 Identification of coefficients  $C$  and  $\gamma$  for SS-316 stainless steel for the strain rate  $2 \times 10^{-4} \text{ s}^{-1}$ : (a) 20°C, (b) 300°C and (c) 600°C.

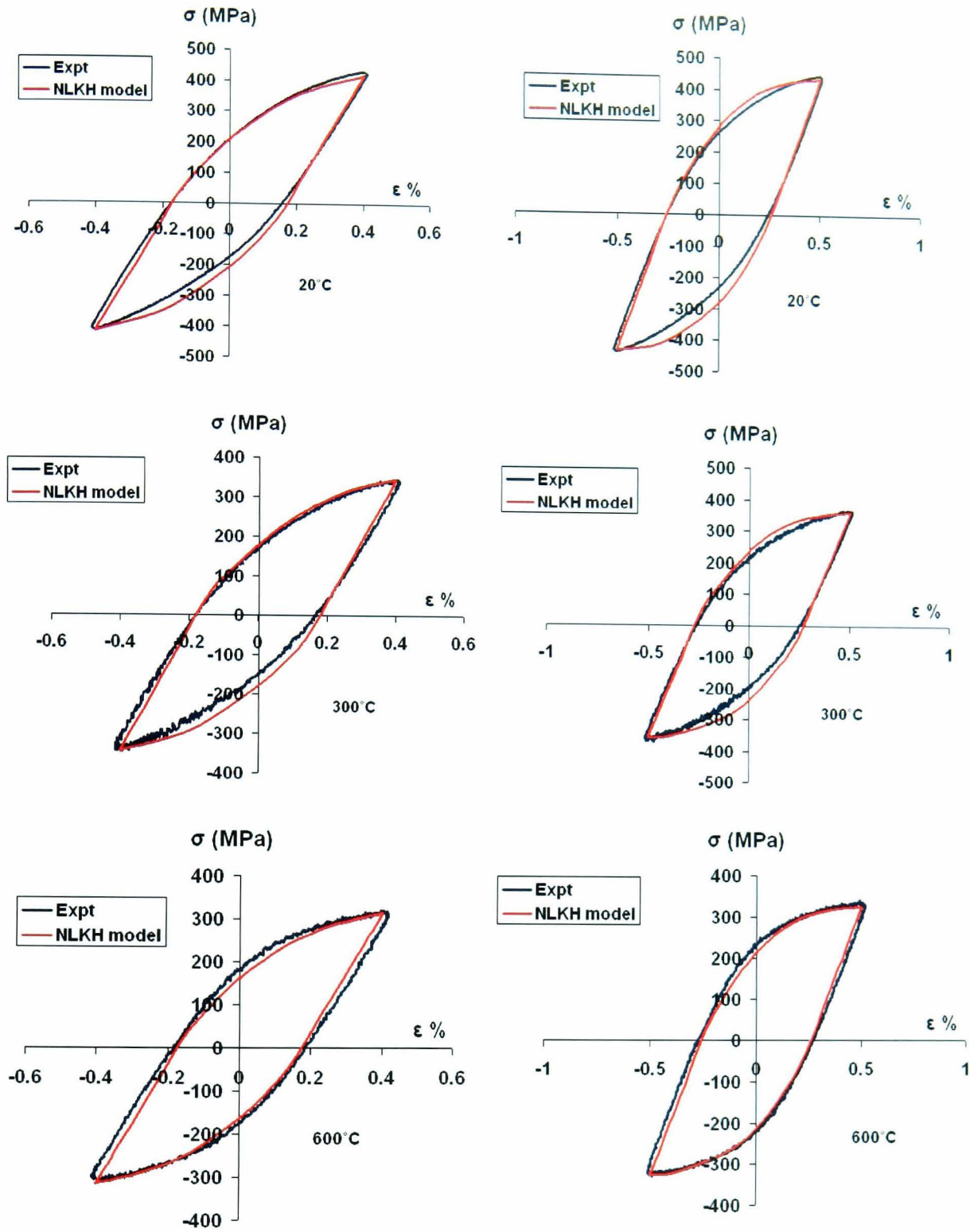
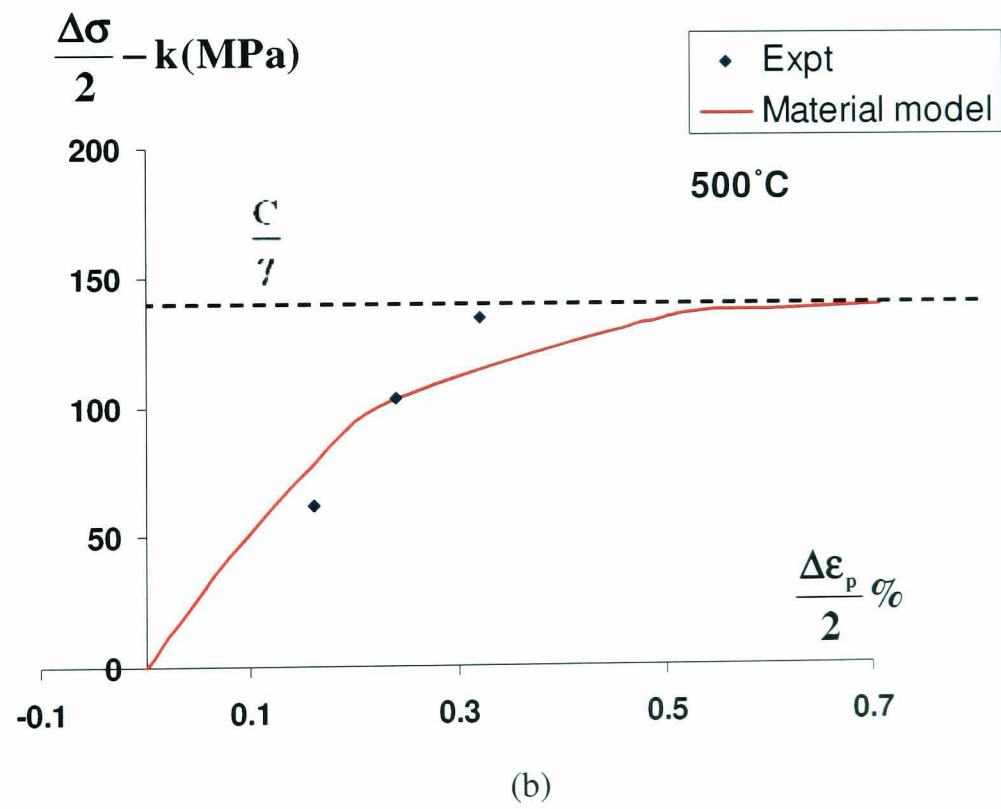
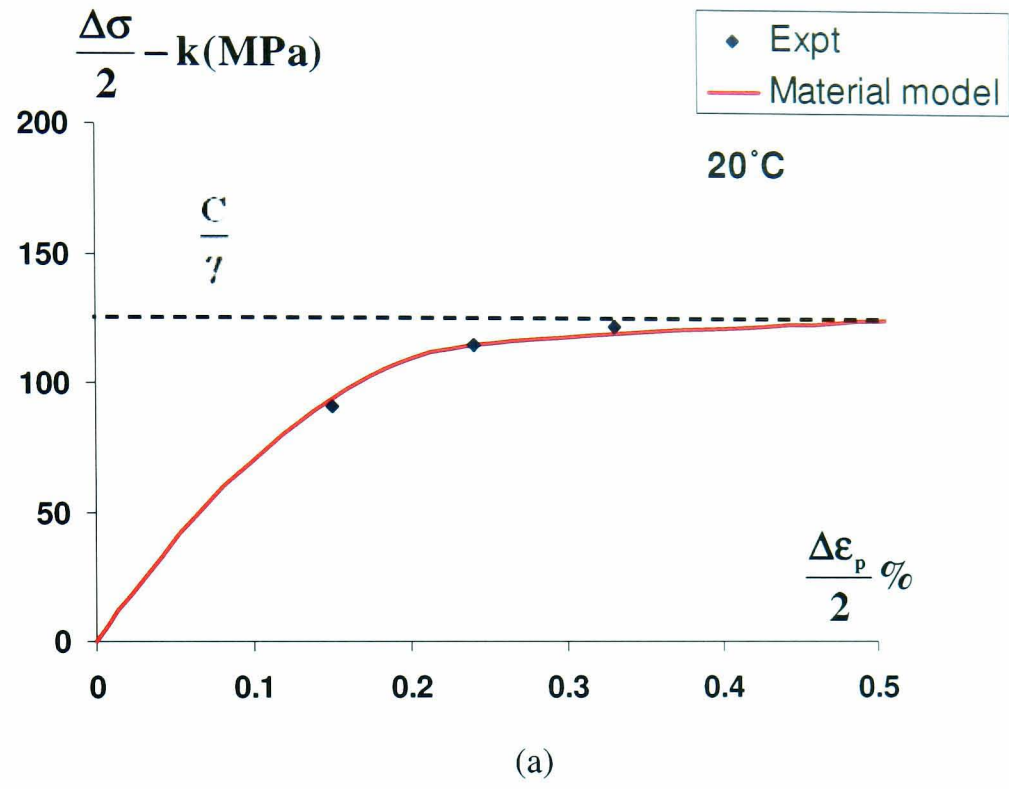


Figure 4.8 Validation of identified non-linear kinematic hardening constitutive constants of SS-316 stainless steel for different strain ranges with a strain rate of  $2 \times 10^{-4} \text{ s}^{-1}$  at 20, 300 and 600°C.



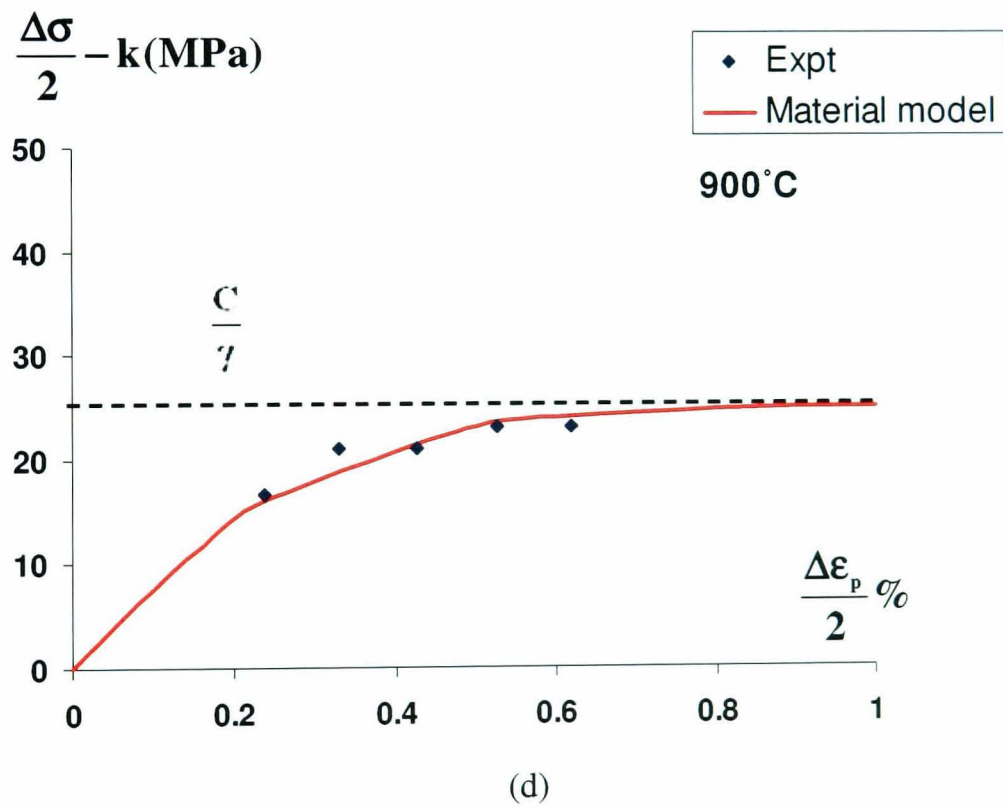
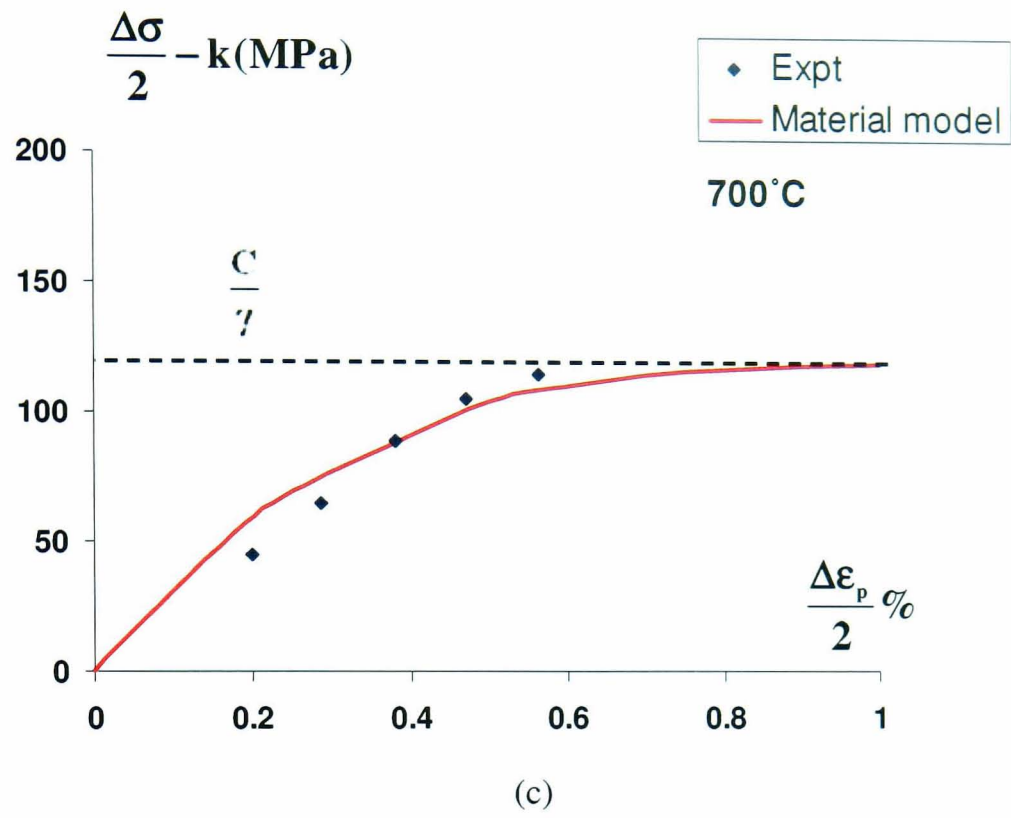


Figure 4.9 Identification of coefficients  $C$  and  $\gamma$  for XN40F alloy for the strain rate  $5 \times 10^{-4} \text{ s}^{-1}$  at: (a)  $20^\circ\text{C}$ , (b)  $500^\circ\text{C}$  and (c)  $700^\circ\text{C}$  and (d)  $900^\circ\text{C}$ .

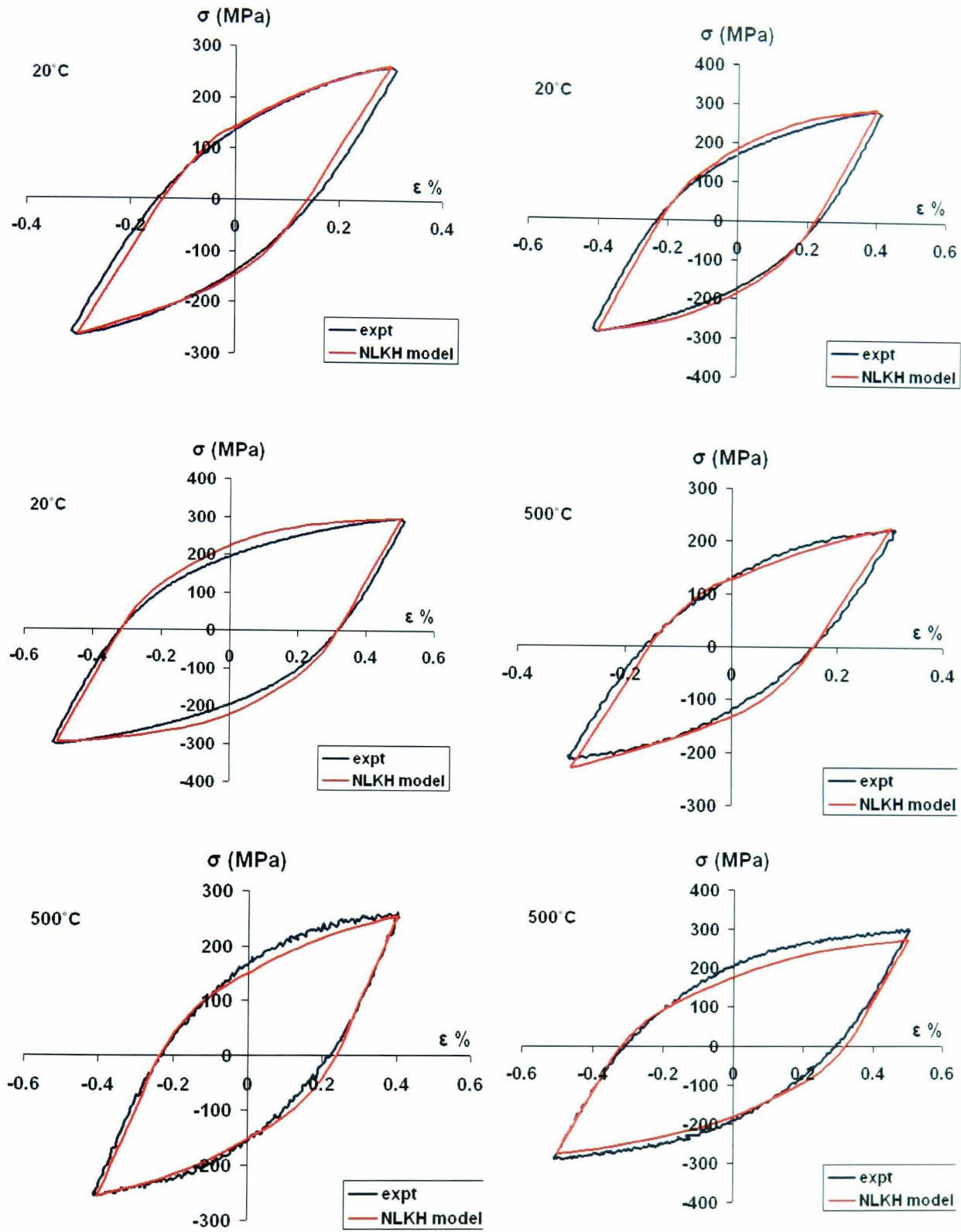


Figure 4.10 Validation of identified non-linear kinematic hardening constitutive constants of XN40F alloy for different strain ranges at 20 and 500°C for  $5 \times 10^{-4} \text{ s}^{-1}$ .

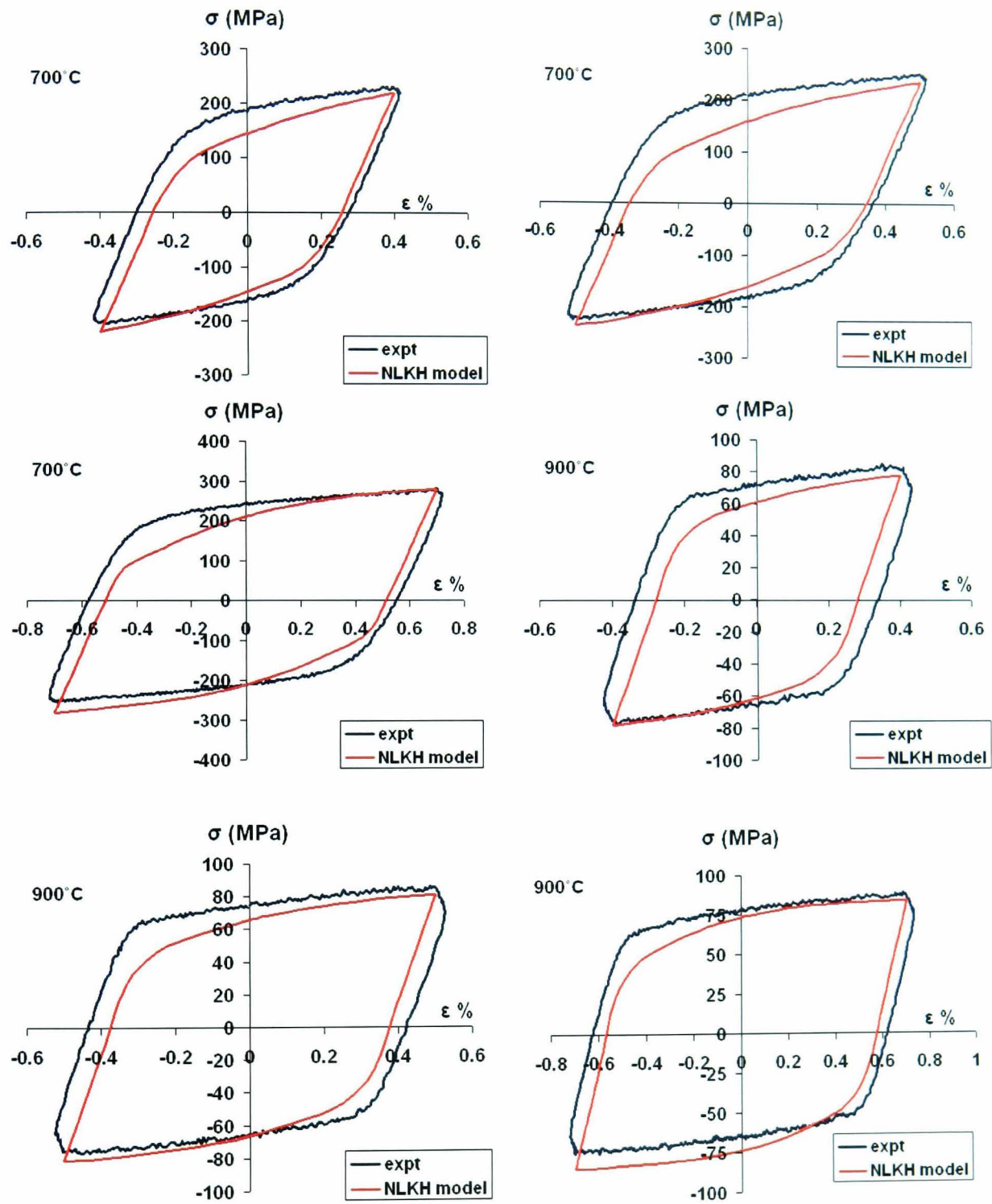
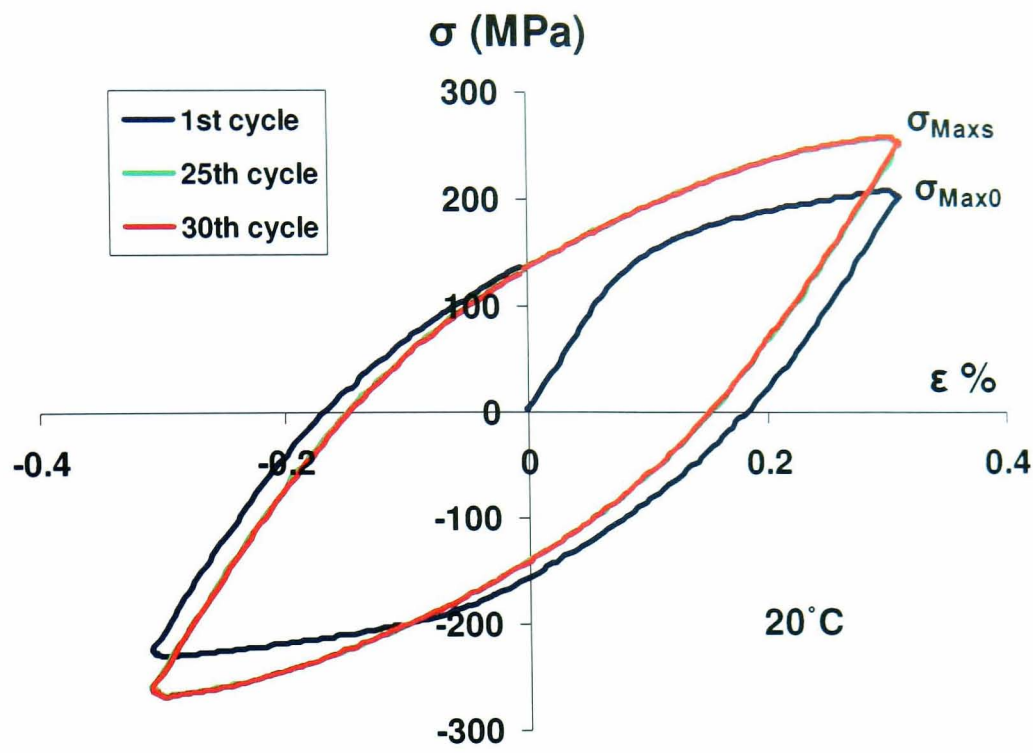
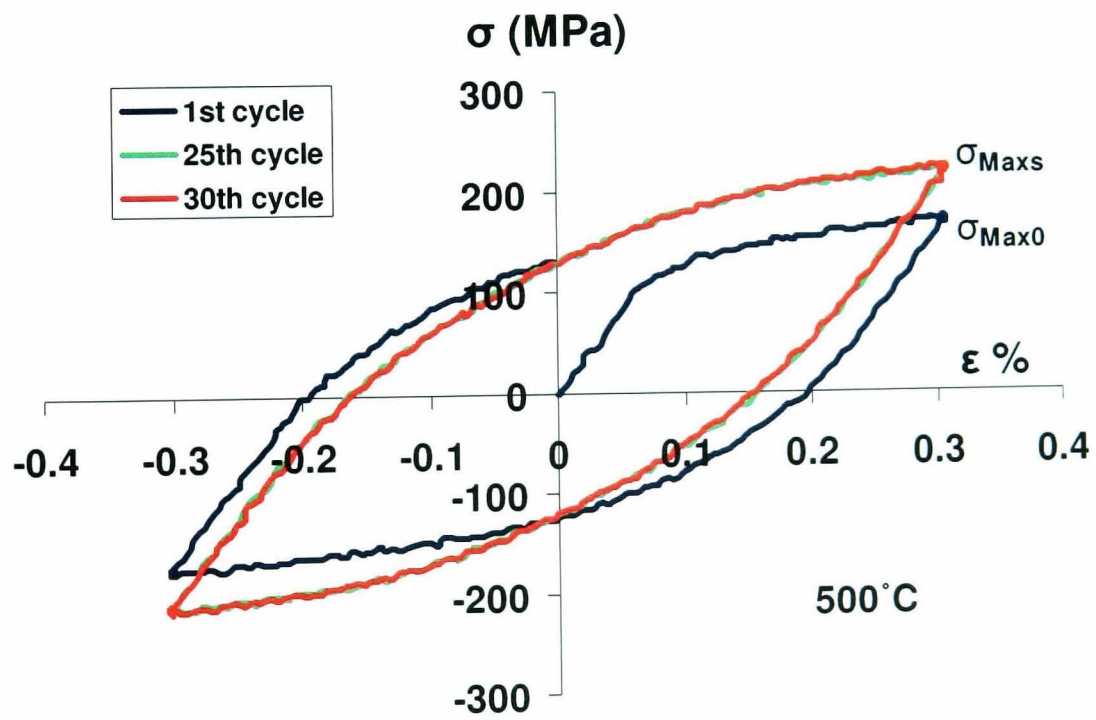


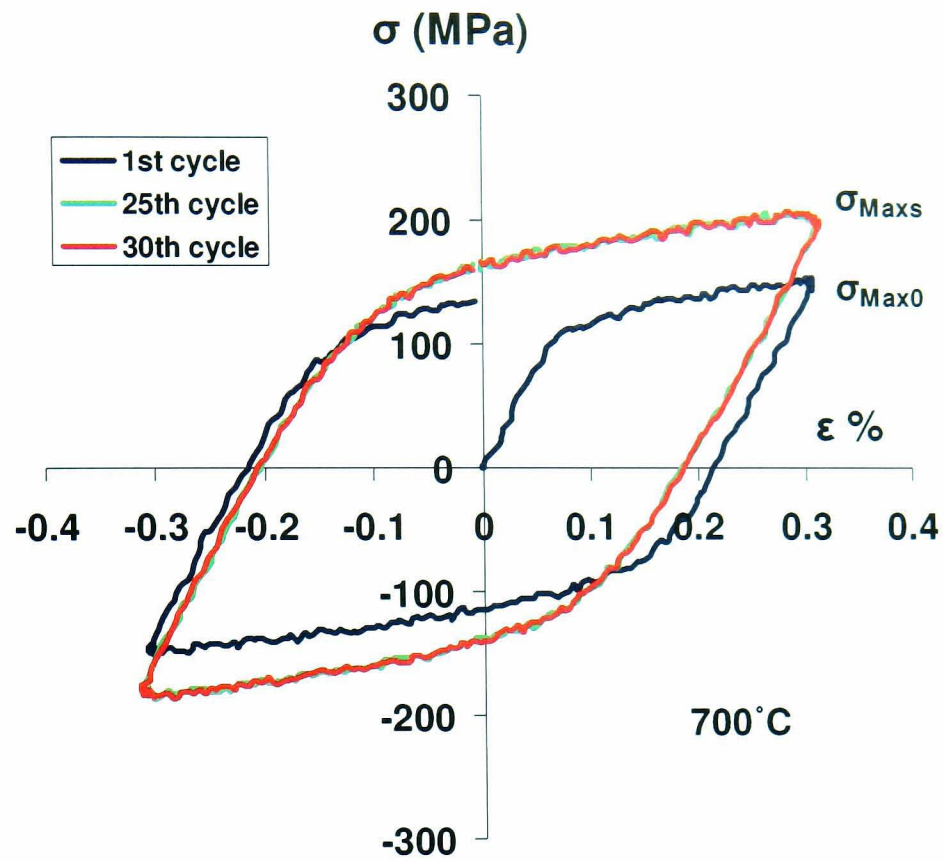
Figure 4.11 Validation of identified non-linear kinematic hardening constitutive constants of XN40F alloy for different strain ranges at 700 and 900°C for  $5 \times 10^{-4} \text{ s}^{-1}$ .



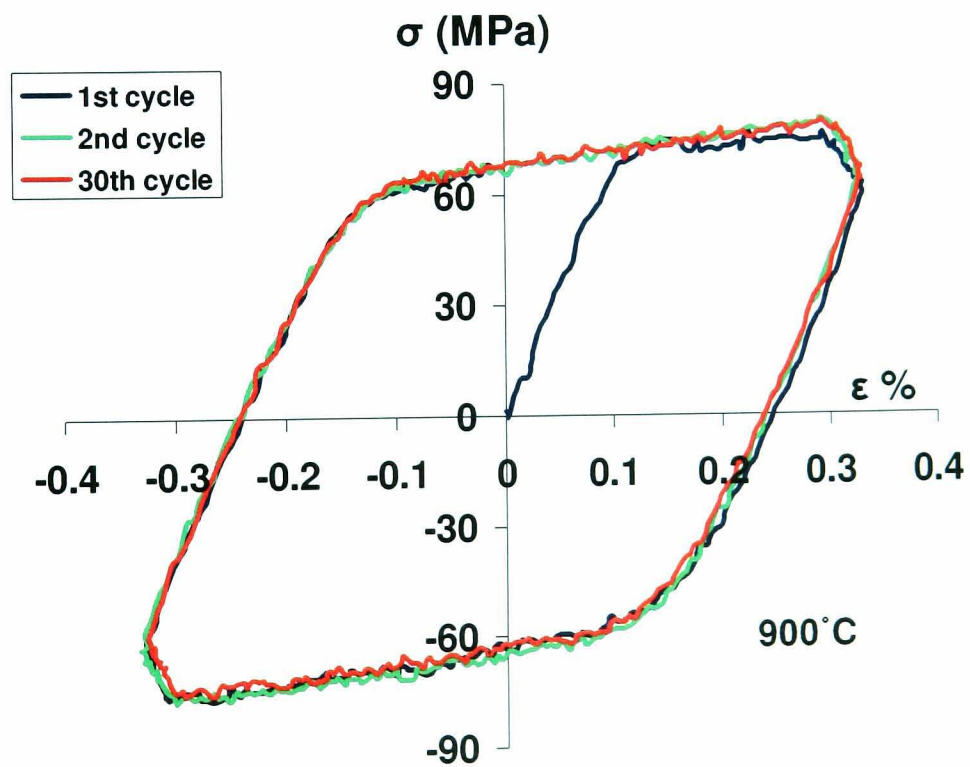
(a)



(b)

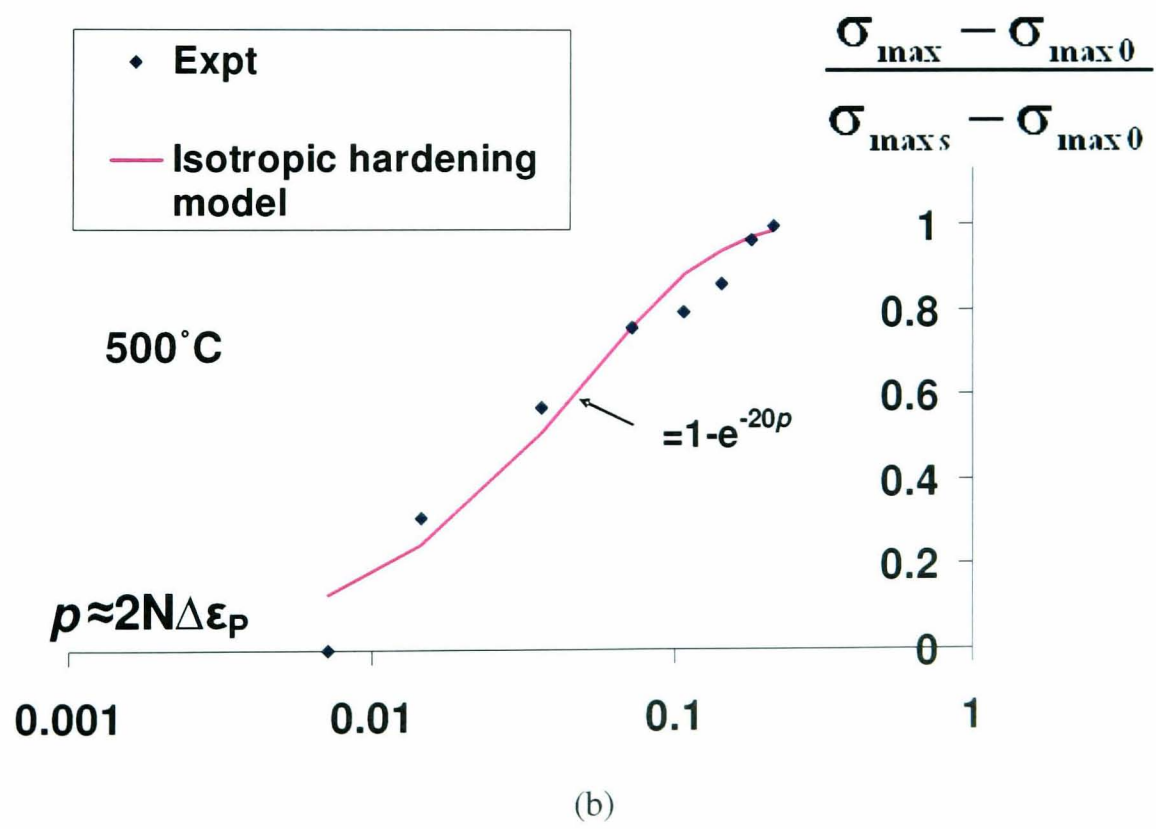
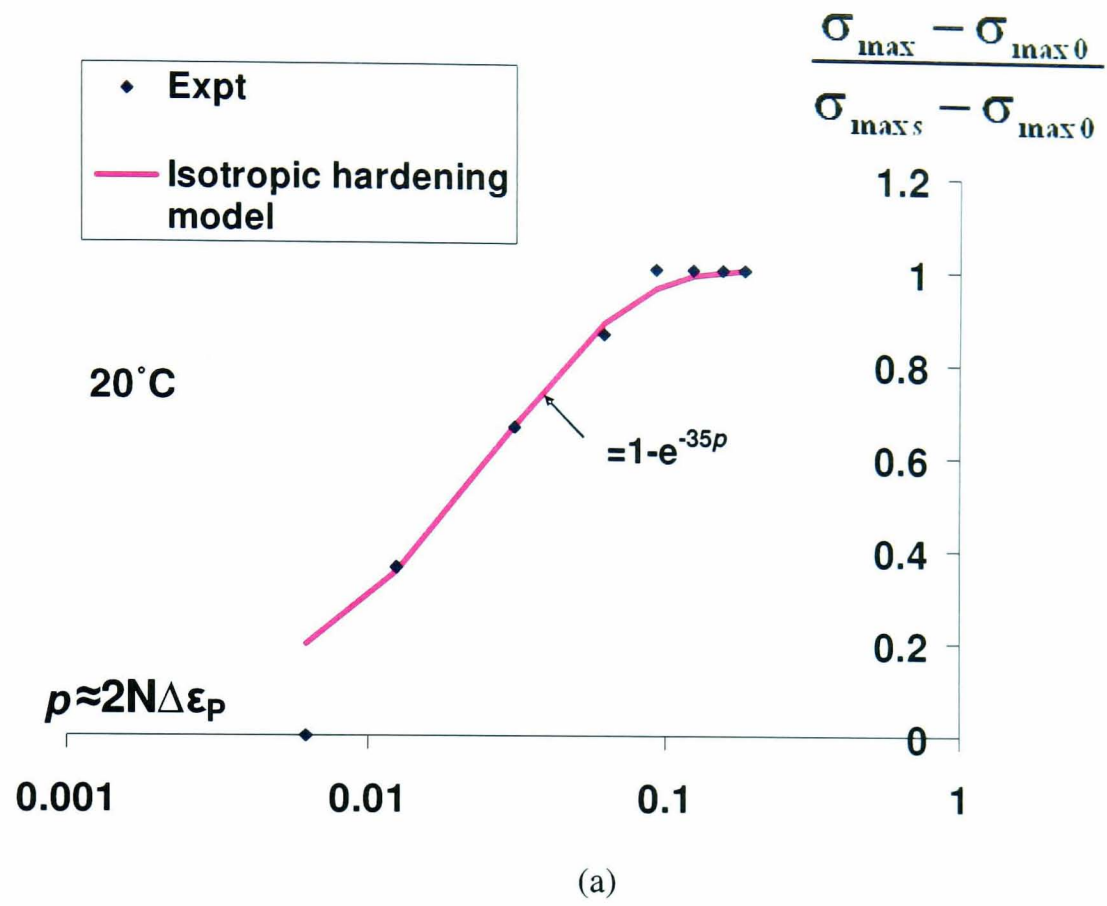


(c)



(d)

Figure 4.12 Experimental cyclic stress-strain loops representing cyclic hardening behaviour of XN40F alloy for 0.6% strain range and  $5 \times 10^{-4} \text{ s}^{-1}$  strain rate at: (a) 20°C, (b) 500°C, (c) 700°C and (d) 900°C.



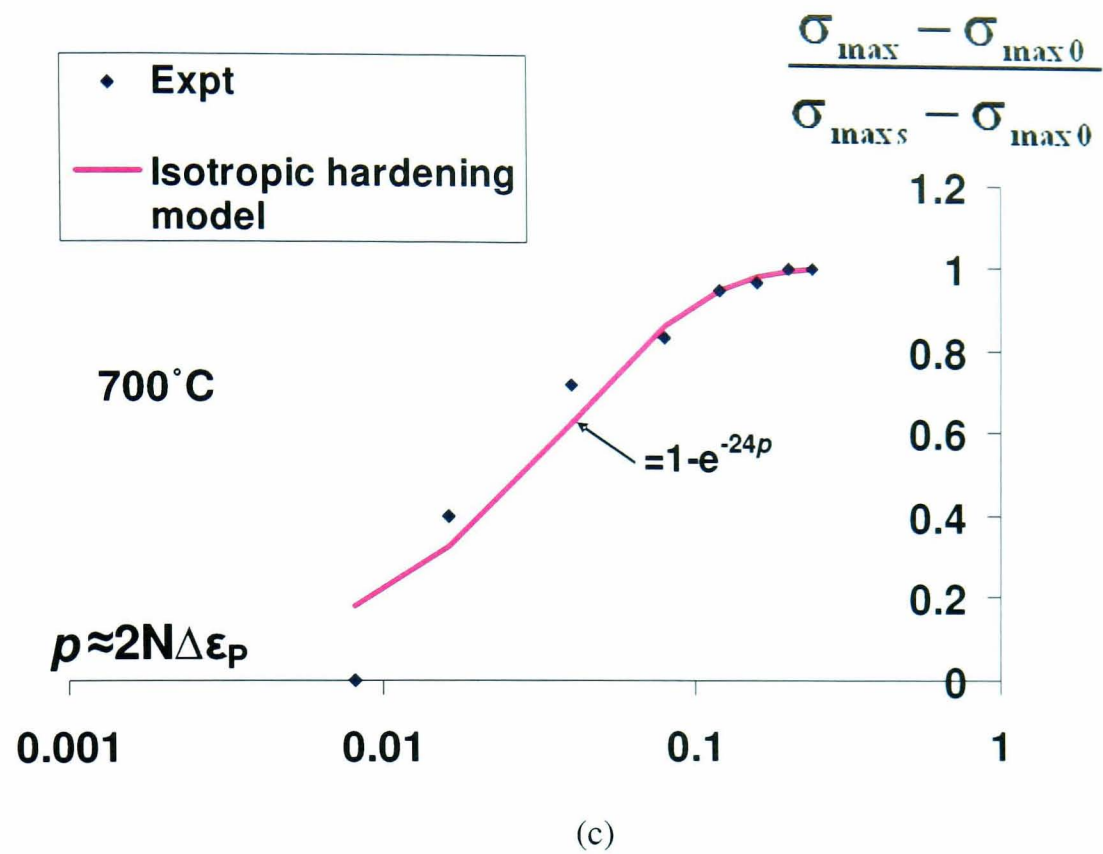


Figure 4.13 Identification of isotropic hardening parameter  $b$  for XN40F alloy for  $5 \times 10^{-4} \text{ s}^{-1}$  strain rate and 0.6% strain range at: (a) 20°C, (b) 500°C and (c) 700°C.

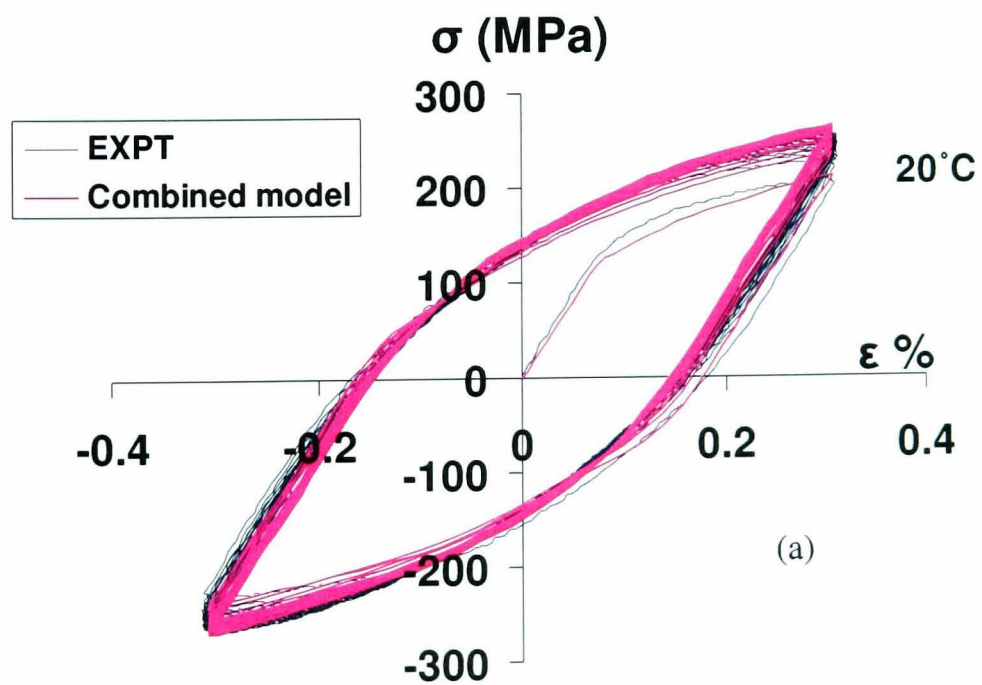


Figure 4.14 Comparison of combined kinematic-isotropic hardening model with tests at (a) 20°C for  $5 \times 10^{-4} \text{ s}^{-1}$ .

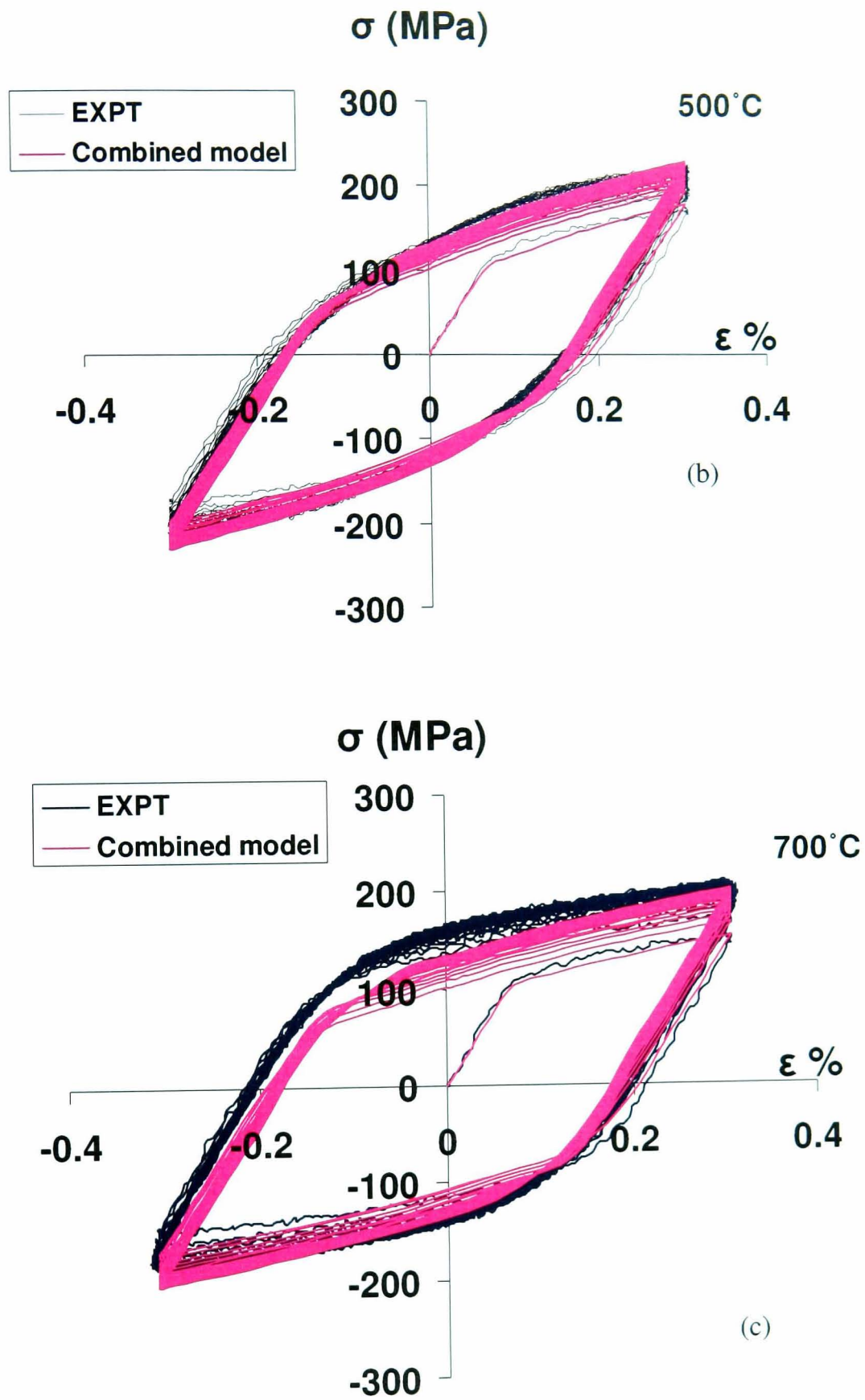


Figure 4.14 Comparison of combined kinematic-isotropic hardening model with tests at (b) 500°C and (c) 700°C for  $5 \times 10^{-4} \text{ s}^{-1}$ .

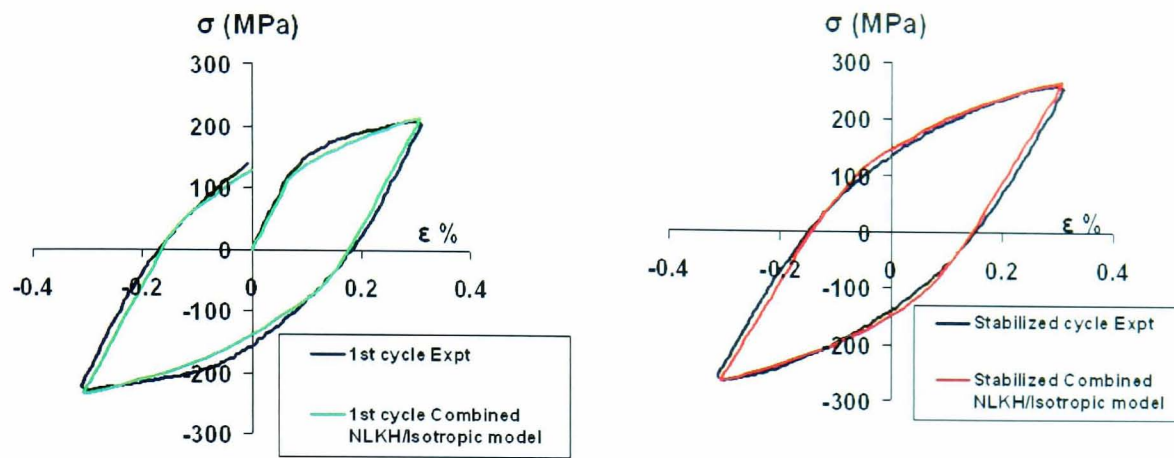


Figure 4.15 Validation of identified constants of combined kinematic-isotropic hardening model at 20°C for  $5 \times 10^{-4} \text{ s}^{-1}$ .

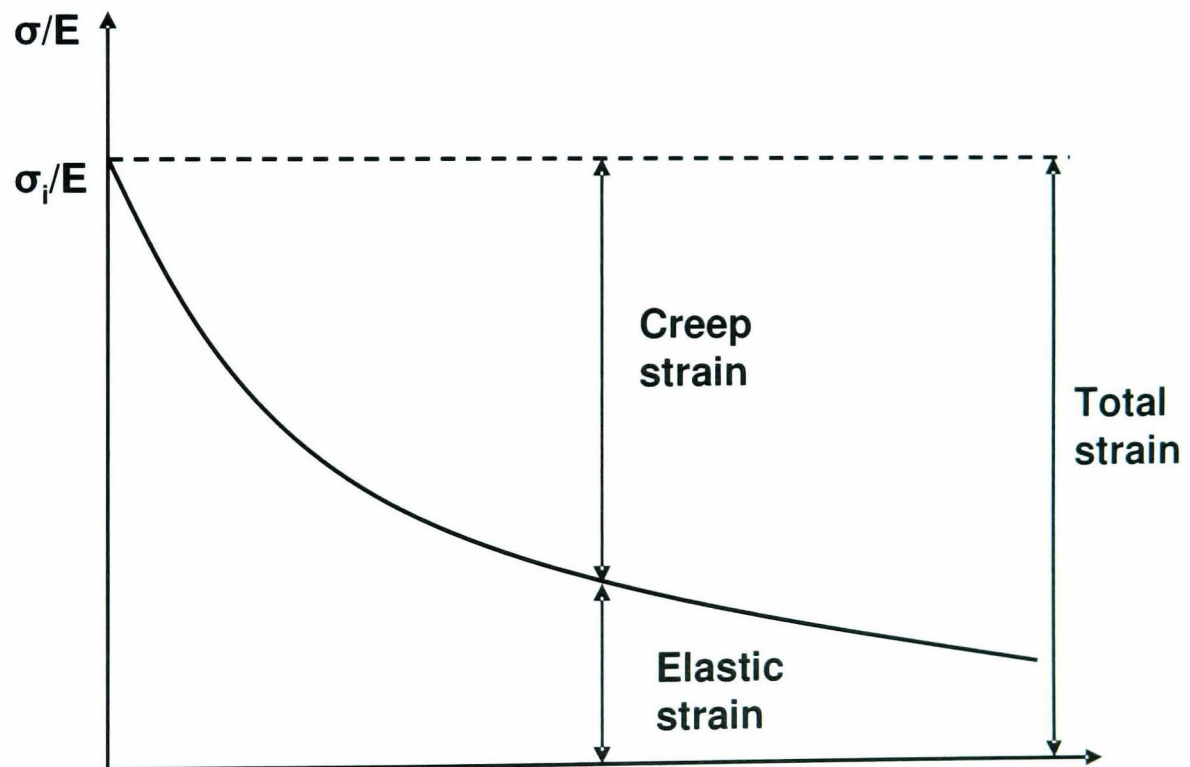


Figure 4.16 Replacement of elastic strain by creep strain with time at high temperature.

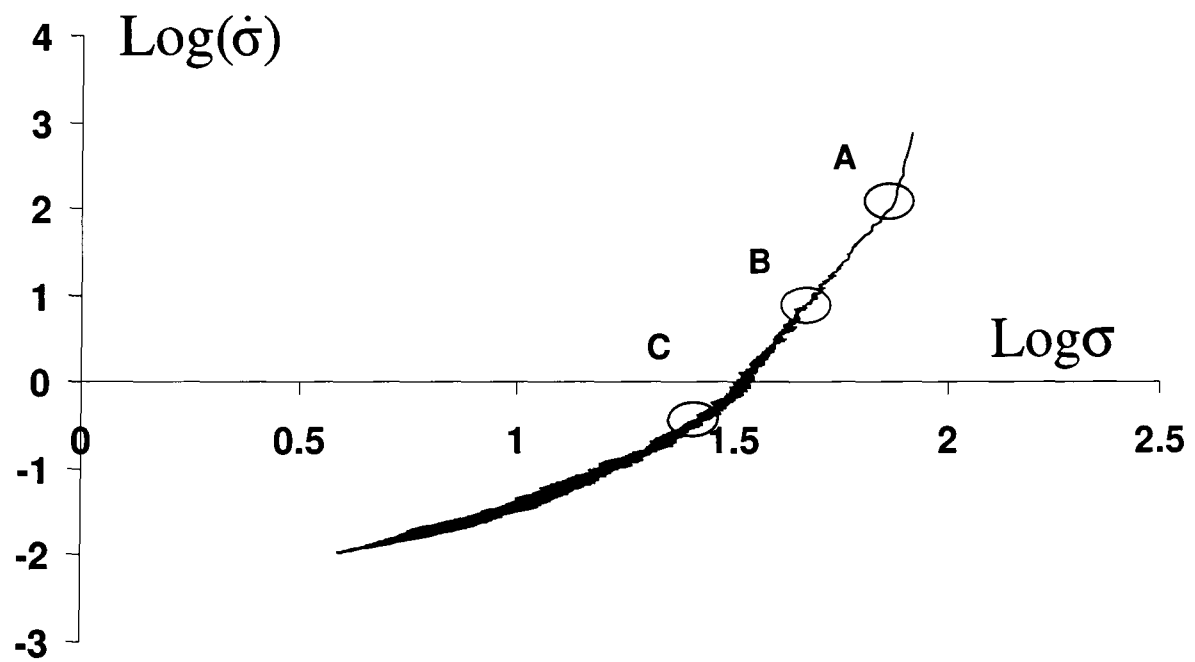
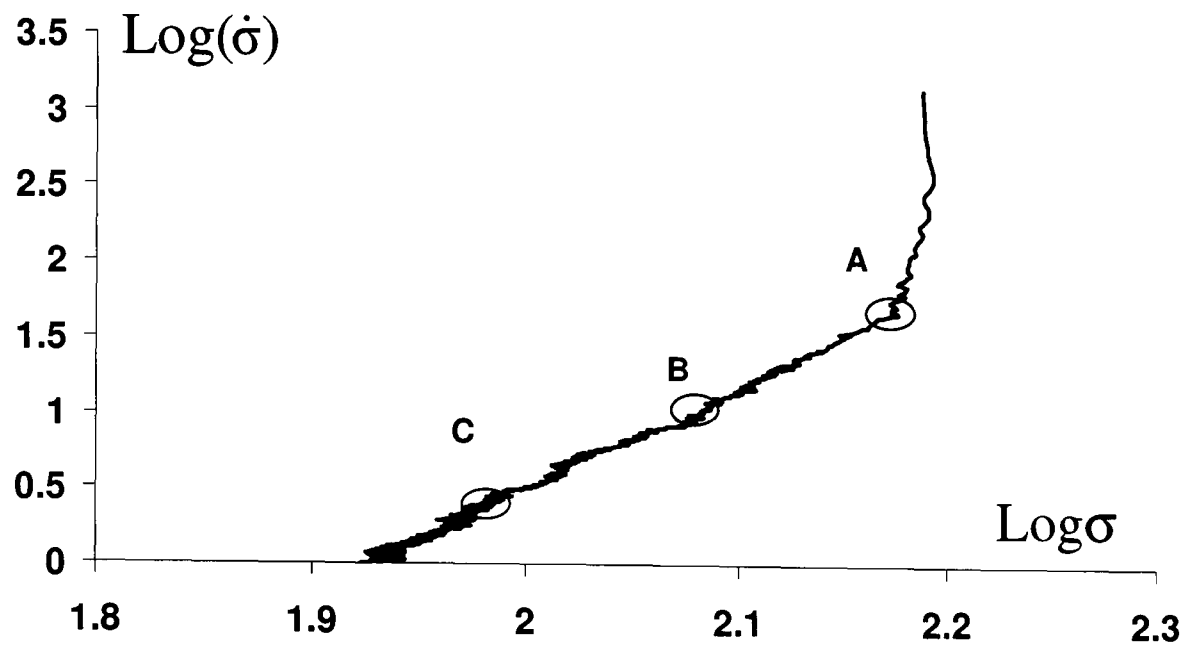


Figure 4.17 Identification of creep constants from stress relaxation test: (a) 700°C, (b) 900°C.

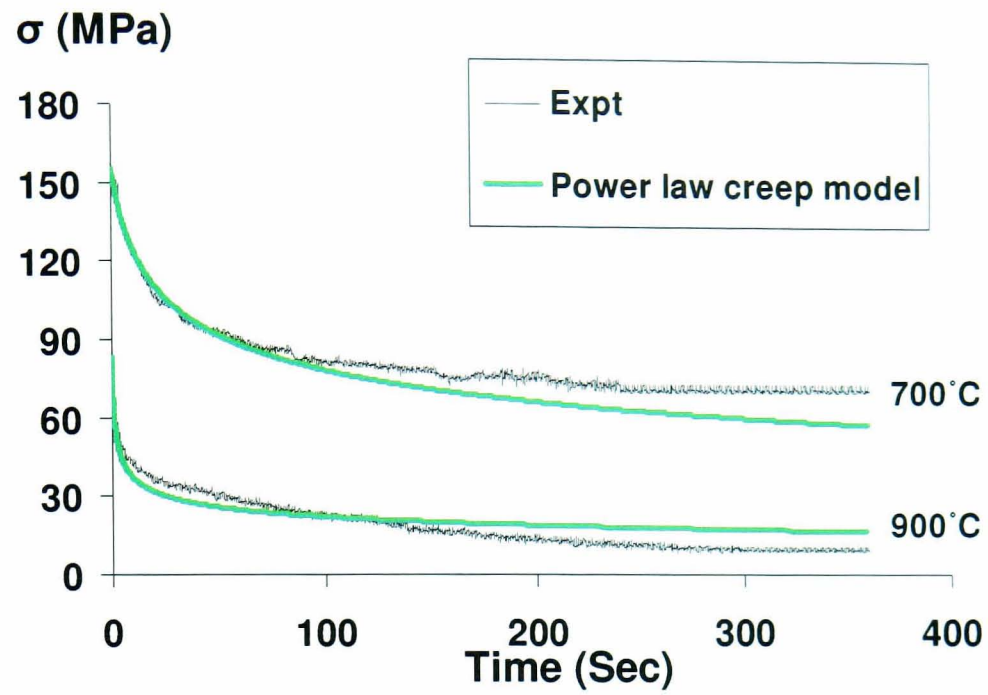


Figure 4.18 Validation of power law creep constants  $A$  and  $n$  for XN40F alloy at 700 and 900°C.

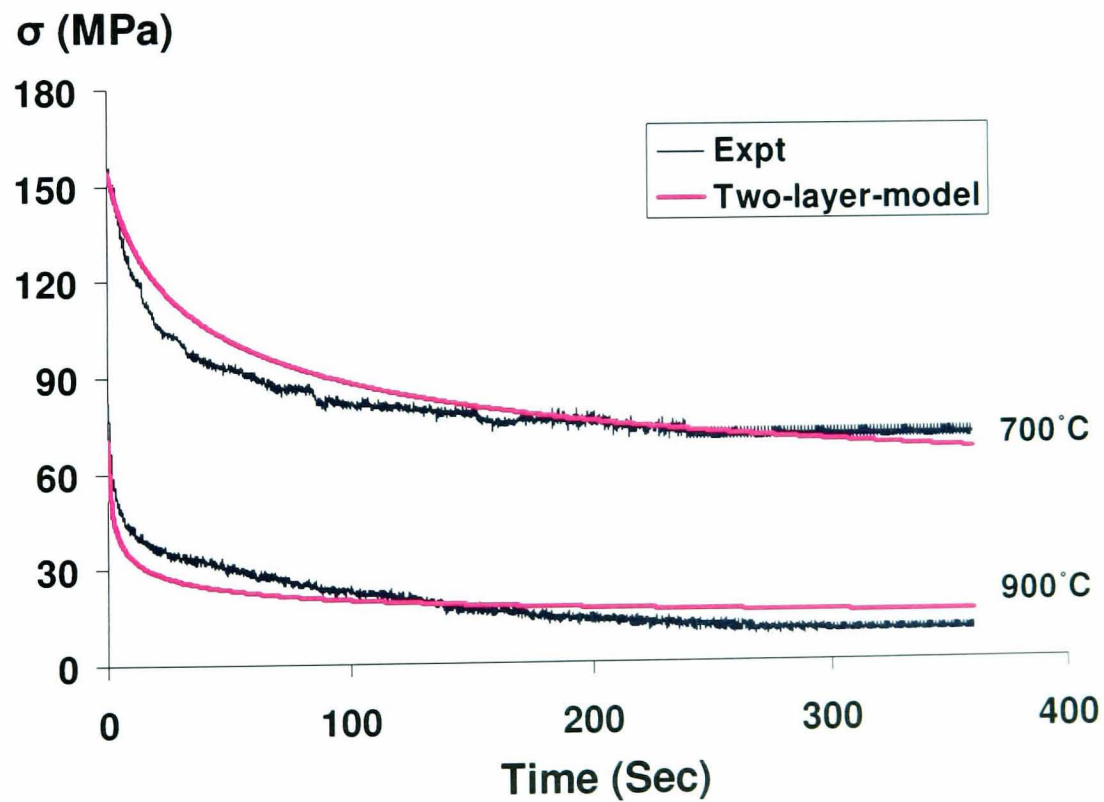


Figure 4.19 Validation of two-layer viscoplasticity constant  $f$  for XN40F alloy at 700 and 900°C.

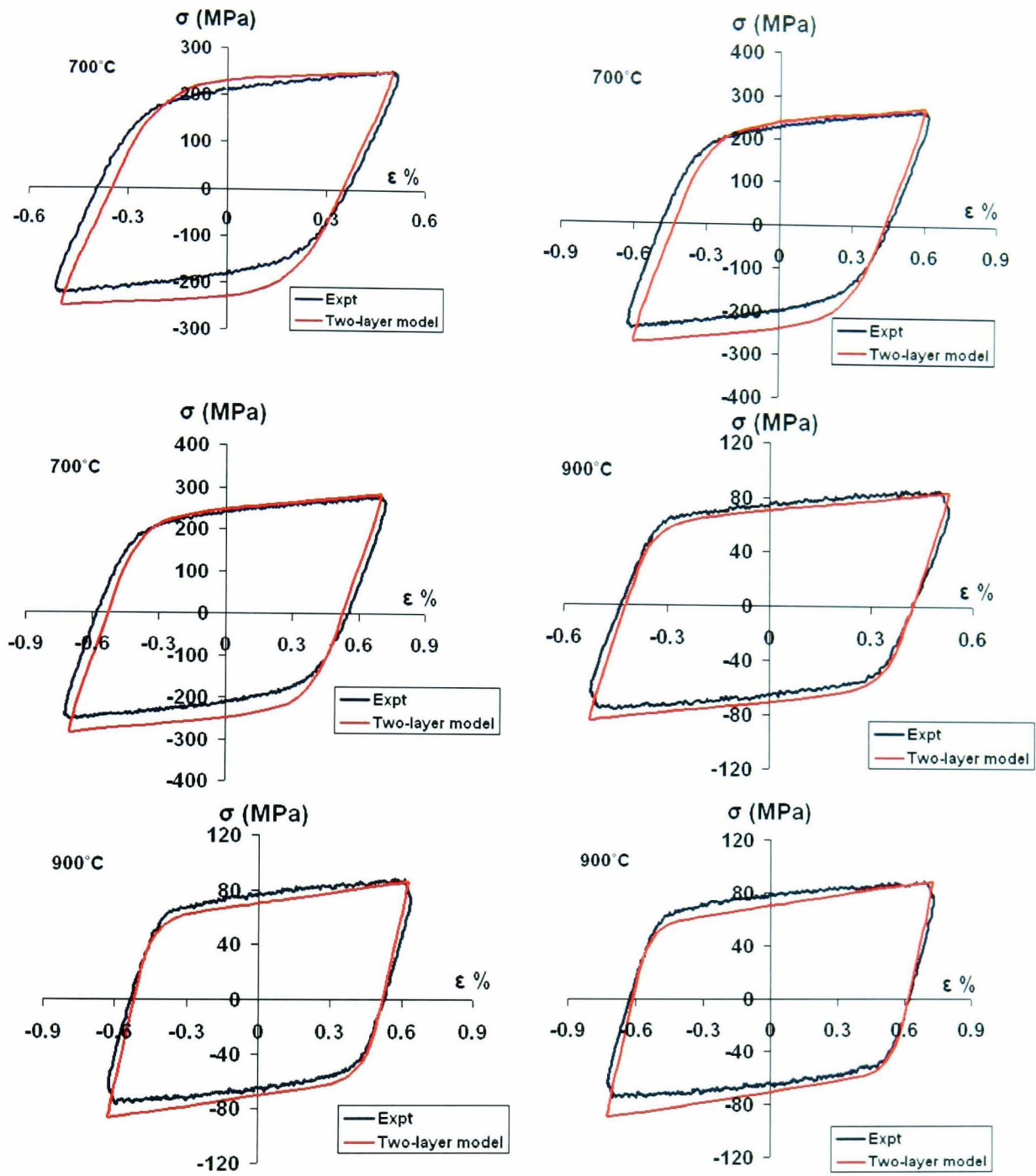


Figure 4.20 Validation of two-layer viscoplasticity model for different strain-ranges at 700°C and 900°C for a strain-rate of  $5 \times 10^{-4} \text{ s}^{-1}$ .

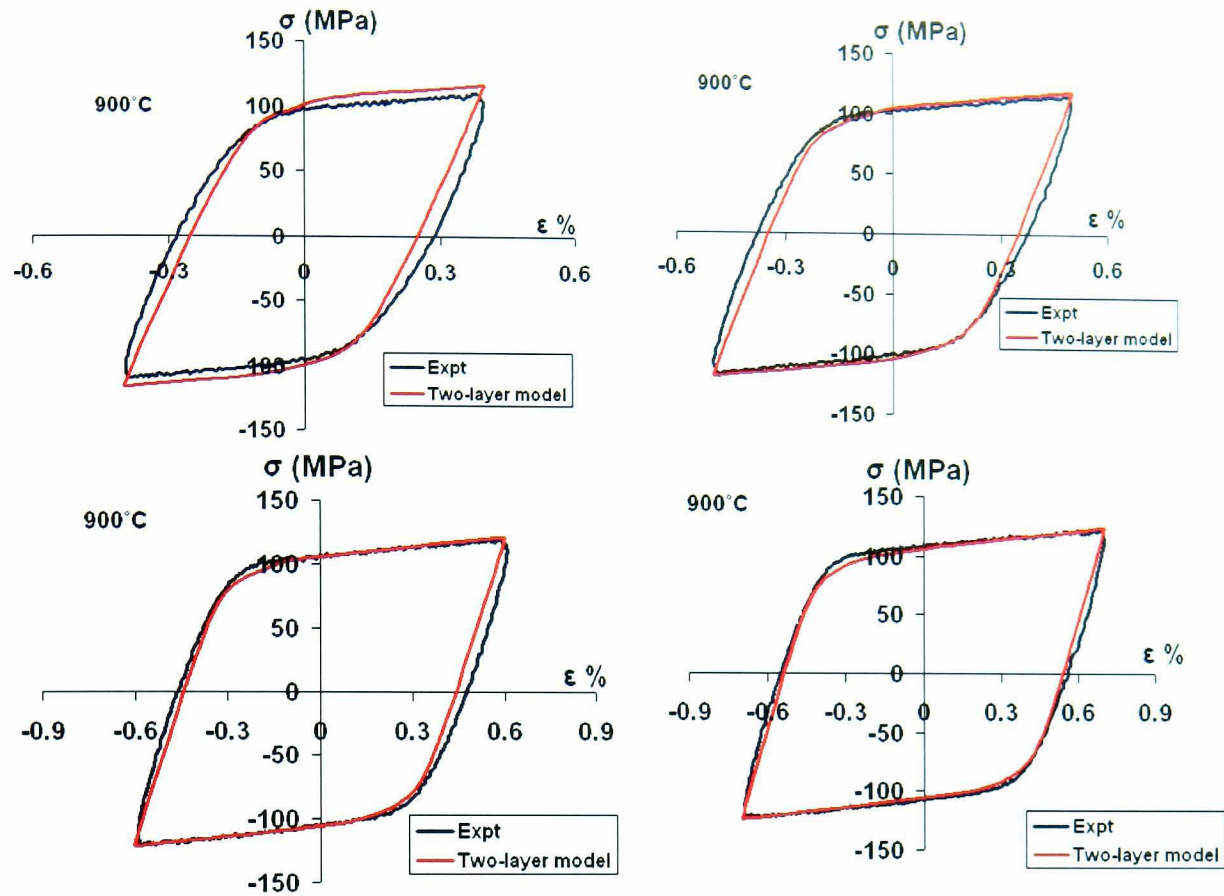


Figure 4.21 Validation of two-layer viscoplasticity model for different strain-ranges at 900°C for a strain-rate of  $5 \times 10^{-3} \text{ s}^{-1}$ .

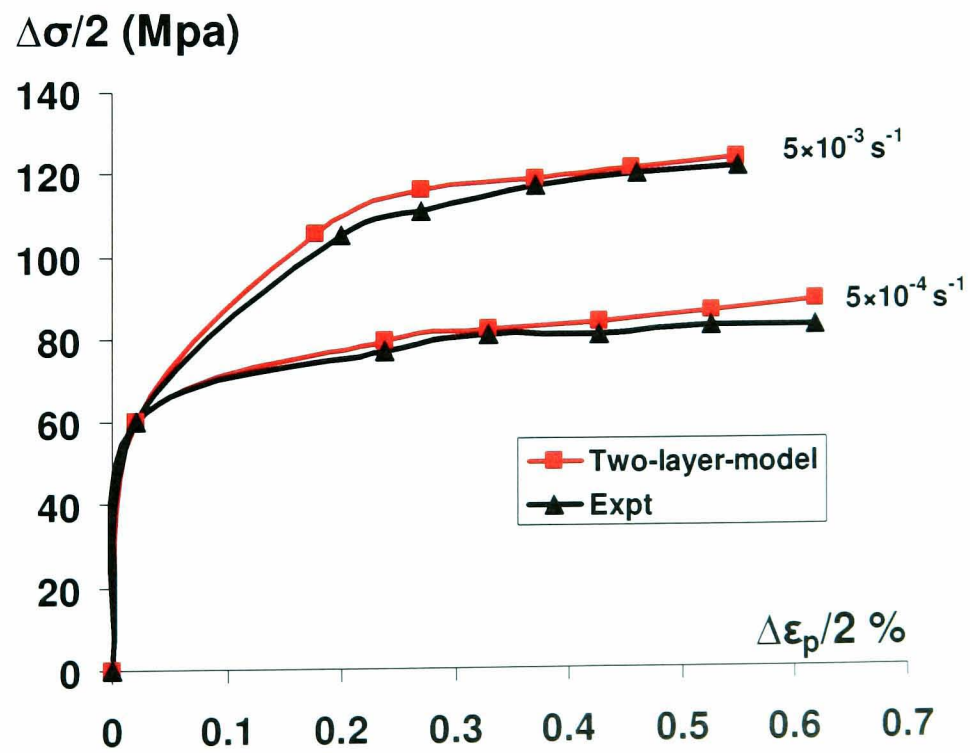


Figure 4.22 Measured and predicted (two-layer model) strain-rate effect on cyclic stress-strain curve at 900°C.

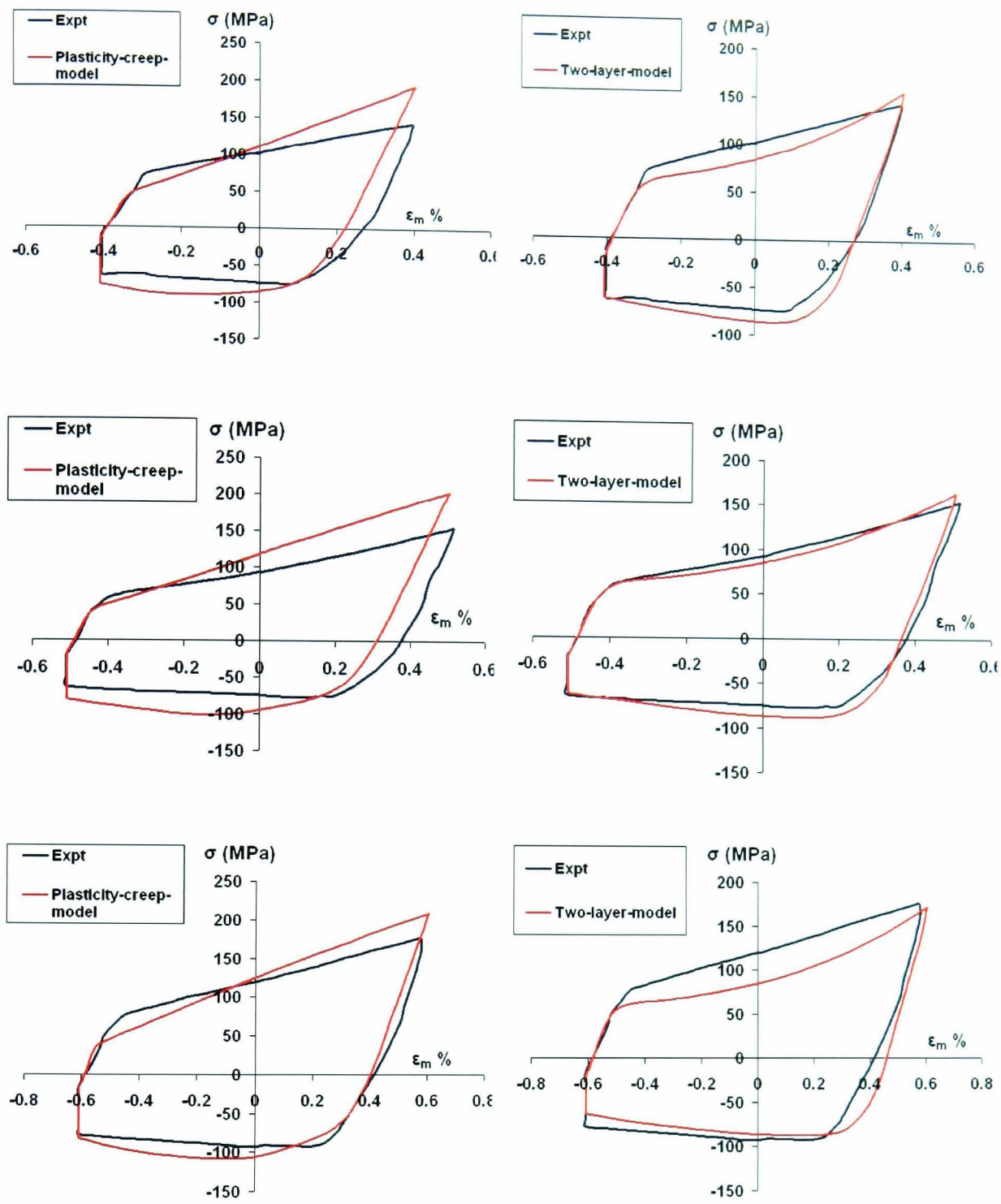


Figure 4.23 Comparison and validation of uncoupled plasticity-creep and two-layer-viscoplasticity models against experimental stabilized loops of TMF OP tests with a strain hold carried out for strain ranges; 0.8%, 1.0% and 1.2% with a strain rate of  $2.5 \times 10^{-4} \text{ s}^{-1}$ .

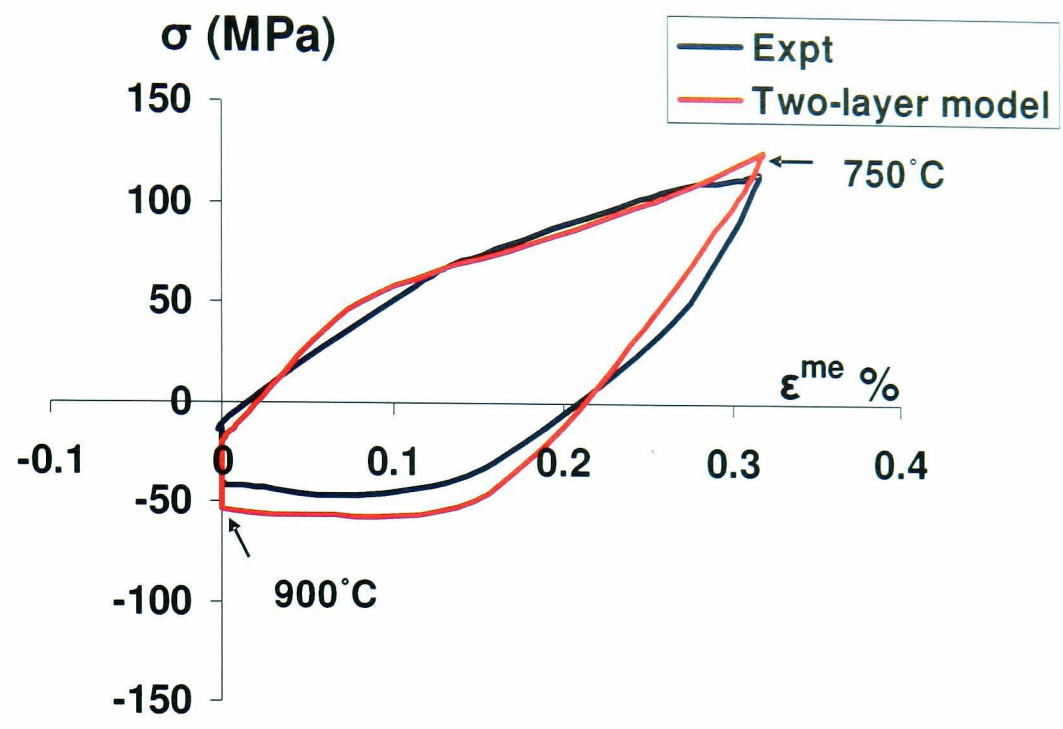


Figure 4.24 Validation of two-layer-viscoplastic model against the strain controlled representative SPF tool (TMF OP) test carried out for  $1 \times 10^{-4} \text{ s}^{-1}$  strain rate.

## Chapter 5

# LIFE PREDICTION METHODOLOGY

### 5.1 Introduction

The chapter presents thermo-mechanical fatigue life prediction methodologies for predicting the life of SS-316 stainless steel and XN40F alloy specimens for various TMF tests using isothermal test data (See Chapter 3). The predicted lives are compared with the corresponding actual lives from TMF experiments. The predictions generally use strain range and strain energy methods. Strain-life and strain energy-life equations are determined using methods such as Coffin-Manson [38] , Ostergren [83], and Zamrik [102]. Moreover, ductility exhaustion, based on predicted ratchet strain and measured ductility limit, is also explored to predict the ratchetting life for stress controlled ratchetting test. These methodologies are subsequently used in Chapter 7 for SPF tool life predictions using the FE predicted stress-strain-temperature data.

Thermo-mechanical fatigue is a complex damage process caused by mechanical and cyclic thermal loading. TMF life prediction becomes more complex at high temperature due to the occurrence of creep-fatigue interaction. The life of components under TMF loading is observed to be significantly different from isothermal low cycle fatigue tests [76]. Therefore TMF life prediction for high temperature components needs advanced life modelling techniques. TMF life prediction can be carried out using crack initiation as well as crack propagation models. In this chapter crack initiation methods are applied and verified against TMF experimental results. The advanced models require numerous variables such as

elastic, inelastic, and total strain ranges, dissipated energy, frequency, hold time, mean stress and strain rate along with associated parameters in the life equations. These variables are generally identified from stabilized cycles and used in life equations.

## 5.2 Review of TMF life prediction models

Life prediction models such as damage summation, frequency separation, ductility exhaustion, strain range partitioning and strain energy partitioning are popular and widely used by many researchers.

### 5.2.1 Linear Damage summation model

This is the simplest model for predicting creep-fatigue life. In this case the total damage is calculated as the summation of individually calculated fatigue and creep damage. Therefore

$$D_f + D_c = D_t \quad (5.1)$$

where  $D_f$  and  $D_c$  are the fractional damages due to fatigue and cyclic creep mechanisms respectively and  $D_t$  is the total damage. Using Miner's rule for fatigue damage [103] and Robinson's rule [104] for creep damage, the damage expression is written as

$$N_f \left( \frac{1}{N_p} + \frac{\tau_h}{\tau_r} \right) = D_t \quad (5.2)$$

where  $N_f$  is the number of cycles to failure at a given strain range,  $N_p$  is the number of fatigue cycles at that strain range and  $\frac{\tau_h}{\tau_r}$  is the creep damage fraction in

which  $\tau_h$  is a hold time at a given stress in a cycle and  $\tau_r$  is the creep rupture time at that stress.

For strain controlled cycles, creep damage comprises of loading cycle creep strain and dwell period (strain hold) creep strain. During strain hold, stress is relaxed due to creep. Ellison and Zamily [113] developed a new fraction rule considering the changing strain during loading which is given as

$$\left(\frac{\tau_h}{\tau_r}\right)_t = \sum \left(\frac{\tau_{hj}}{\tau_{rj}}\right)_{load} + \sum \left(\frac{\tau_{hj}}{\tau_{rj}}\right)_{dwell} \quad (5.3)$$

From equation 5.2 and 5.3, the total damage is expressed as

$$\sum \left(\frac{N_j}{N_{pj}}\right) + \sum \left(\frac{\tau_{hj}}{\tau_{rj}}\right) = D_t \quad (5.4)$$

This model is widely used because of its simplicity. However the model does not take into account the sequence effect on creep-fatigue life where creep and fatigue damage are treated independently. Also creep rupture properties identified from monotonic tests used in the model do not consider cyclic hardening and softening of materials.

### 5.2.2 Ductility exhaustion model

This model is evolved from the Coffin-Manson relationship between the inelastic strain range and number of cycles to failure which is expressed as

$$\Delta \epsilon^{in} N_f^\beta = D \quad (5.5)$$

The  $D$  is commonly taken as tensile ductility and  $\beta$  is a material constant which is approximately 0.5 at ambient temperature and increases to near unity, at elevated temperatures for many materials.

Priest and Ellison [105] derived new equations to predict creep-fatigue life by calculating the total damage as a summation of creep damage and fatigue damage. Creep damage and fatigue damage are individually calculated from equations (5.6) and (5.7)

$$\Delta\epsilon^{cr} N_c = D_{cr} \quad (5.6)$$

where  $D_{cr}$  is the creep ductility which is an accumulated creep strain in a dwell period,  $\Delta\epsilon^{cr}$  is the tensile creep strain per cycle.

$$\Delta\epsilon^{pl} N_p = D_{pl} \quad (5.7)$$

Similarly  $D_{pl}$  is the fatigue ductility and  $\Delta\epsilon^{pl}$  is the effective plastic strain.  $\Delta\epsilon^{pl}$  and  $\Delta\epsilon^{cr}$  are generally determined from stabilized stress-strain loops of creep-fatigue interaction tests.  $D_{pl}$  is obtained from a fatigue test carried out for the plastic strain range  $\Delta\epsilon^{pl}$ . However  $D_{cr}$  must be identified after stress relaxation of a creep-fatigue test. By using a simple creep-fatigue damage summation rule, the creep-fatigue life can be expressed as

$$\frac{1}{N_f} = \frac{1}{N_p} + \frac{1}{N_c} \quad (5.8)$$

This model is also simple to use. However conducting tests required for creep ductility is not so straightforward and the creep-fatigue life predicted by this model is normally conservative.

### 5.2.3 Frequency separation model

In this model, Coffin [79] modified the simple Coffin-Manson law while incorporating the effect of cyclic frequency on creep-fatigue life which is expressed as

$$N_f = C \Delta \epsilon_{in}^\alpha v_t^n \left( \frac{v_c}{v_t} \right)^k \quad (5.9)$$

where  $\Delta \epsilon_{in}$  is the inelastic strain range and  $v_t$  and  $v_c$  are tension and compression pseudo frequencies which are calculated as reciprocals of tension and compression times of a cycle.  $\alpha$ ,  $n$ ,  $C$  and  $k$  are material constants influenced by the environment and temperature. They are determined by a number of slow-fast and fast-slow strain rate tests. This model was derived to deal with complex cycle shapes by considering tension and compression damages separately. However the model requires significant experimental work to evaluate four or more constants for every temperature of interest. This model has been proposed in different forms such as frequency modified model [79] and Ostergren models [83].

### 5.2.4 Strain range partitioning model

This model separates the stress-strain cycle into plastic and creep components. The total inelastic strain range is assumed to be constant with no ratcheting occurs. Therefore total inelastic strain range can be divided into four basic cycles as shown in Fig 5.1

$$\Delta \epsilon_{in} = \Delta \epsilon_{pp} + \Delta \epsilon_{pc} + [\Delta \epsilon_{cp}] + \Delta \epsilon_{cc} \quad (5.10)$$

where  $\Delta \epsilon_{pp}$  indicates tensile plastic strain reversed by compressive plastic strain,  $\Delta \epsilon_{cp}$  indicates tensile creep reversed by compressive plastic deformation if the

compressive plastic strain is greater than the tensile plastic strain. Therefore a cycle contain either  $\Delta\epsilon_{cp}$  or  $\Delta\epsilon_{pc}$ .  $\Delta\epsilon_{cc}$  corresponds to tensile creep strain reversed by compressive creep strain.

The cyclic endurance using Coffin-Manson equations is

$$\frac{\Delta\epsilon_{pp}^{\alpha_1}}{C_{pp}} = N_{pp}, \frac{\Delta\epsilon_{pc}^{\alpha_2}}{C_{pc}} = N_{pc}, \frac{\Delta\epsilon_{cp}^{\alpha_3}}{C_{cp}} = N_{cp} \text{ and } \frac{\Delta\epsilon_{cc}^{\alpha_4}}{C_{cc}} = N_{cc} \quad (5.11)$$

The total fatigue life damage is given by the summation of individual damage contributions from each of  $\Delta\epsilon_{pp}$ ,  $\Delta\epsilon_{pc}$ ,  $\Delta\epsilon_{cp}$  and  $\Delta\epsilon_{cc}$

$$D_T = \frac{N_f}{N_{pp}} + \frac{N_f}{N_{cp}} + \frac{N_f}{N_{pc}} + \frac{N_f}{N_{cc}} \quad (5.12)$$

where  $N_f$  is the number of cycles to failure under the combined creep-fatigue damage condition and  $D_T$  is the damage level corresponding to failure and is assumed to be 1 in the linear damage summation approach. Therefore the number of cycles to failure for the creep-fatigue cycles is given by [28]

$$\frac{1}{N_f} = \frac{1}{N_{pp}} + \frac{1}{N_{cp}} + \frac{1}{N_{pc}} + \frac{1}{N_{cc}} \quad (5.13)$$

To identify four different partitioned strain range-cyclic life relations, four separate fatigue and fatigue-creep tests are required. Thus this model requires a special extensive experimental work to implement. This model is not suitable for brittle materials due to the small inelastic strain ranges and hence difficult to partition. Although the SRP model works very well for ductile materials, according to Nitta et al (1983) the predictions are not very satisfactory for nickel base alloys. Furthermore it is difficult to partition inelastic strain range experimentally.

### 5.2.5 Ostergren strain energy model

Ostergren strain energy model [83] employs the product of plastic strain range and maximum tensile stress of the stabilized stress-strain loop as a damage parameter.

Ostergren strain life equation is expressed as

$$C_1 = N_f^\beta \Delta \epsilon_p \sigma_t \quad (5.14)$$

where  $C_1$  and  $\beta$  are material constants and  $N_f$  is number of cycles to failure for the product of  $\Delta \epsilon_p$ ; plastic strain range and  $\sigma_t$ ; maximum tensile stress.

### 5.2.6 Zamrik strain energy model

Zamrik and Renuald [102] developed a new energy based life prediction model based on the Ostergren model for out of phase TMF loading. Unlike Ostergren model, Zamrik model considers additional, tensile elastic strain range, material ductility limit and ultimate tensile strength of the material. The energy-life equation for the Zamrik model is given as

$$N_f = A(\Delta E)^B \quad (5.15)$$

$$\Delta E \approx \frac{\sigma_t \epsilon_t}{\sigma_u \epsilon_f} \quad (5.16)$$

where  $A$  and  $B$  are the constants;  $\sigma_t$  and  $\epsilon_t$  are the maximum tensile stress and tensile strain range at the mid life, respectively, whereas  $\sigma_u$  and  $\epsilon_f$  are the ultimate tensile strength and the ductility to failure, respectively, obtained from monotonic tensile testing at the minimum temperature of TMF OP condition.

### 5.2.7 Strain energy partitioning model

He et al (1983) combined strain range partitioning and the Ostergren damage function model to develop a strain-energy partitioning model where both stress and strain are considered to identify the damage. Similar to strain range partitioning, the strain energy method has four partitioned strain energy- life equations as follows

$$\frac{\Delta E_{pp}^{\beta_1}}{C_{pp}} = N_{pp}, \frac{\Delta E_{pc}^{\beta_2}}{C_{pc}} = N_{pc}, \frac{\Delta E_{cp}^{\beta_3}}{C_{cp}} = N_{cp} \text{ and } \frac{\Delta E_{cc}^{\beta_4}}{C_{cc}} = N_{cc} \quad (5.17)$$

where the partitioned strain energy is  $\Delta E_{ij}$  which is given by  $\sigma_t \Delta \epsilon_{ij}$ ,  $\sigma_t$  is the tensile peak stress, and  $\beta$  and  $C$  are material constants. Since this model considers inelastic strain range and tensile stress, it is capable of giving better life predictions for both brittle and ductile materials.

### 5.3 TMF life prediction

Strain-life and strain energy-life constants are obtained from stabilized stress-strain loops of IF tests carried out at maximum temperature of TMF tests (Chapter 3). However the ductility exhaustion method is also explored here for isothermal stress controlled ratchetting test for XN40F alloy due to the prediction of a ratchetting phenomenon in the SPF tool analysis as shown later.

The Coffin-Manson strain-life equation is expressed as

$$C = N_f^\alpha \Delta \epsilon_p \quad (5.18)$$

where  $C$  and  $\alpha$  are Coffin-Manson constants and  $N_f$  is number of cycles to failure for a plastic strain range  $\Delta \epsilon_p$ . The Coffin-Manson constants are identified from IF data at the maximum temperature of TMF tests (Chapter 3) as shown in Fig. 5.2. The

constants for stainless steel (SS-316) and XN40F alloy are given in equations 5.19 and 5.20 respectively.

$$0.1354 = N_f^{0.466} \Delta \epsilon_p \quad (5.19)$$

$$0.1225 = N_f^{0.416} \Delta \epsilon_p \quad (5.20)$$

The Ostergren strain energy approach is also explored to predict TMF lives. The model constants are obtained from IF test data as shown in Fig. 5.3. The Ostergren constants for stainless-steel and XN40F alloy are given in equations 5.21 and 5.22 respectively.

$$83.92 = N_f^{0.558} \Delta \epsilon_p \sigma_t \quad (5.21)$$

$$72.84 = N_f^{0.719} \Delta \epsilon_p \sigma_t \quad (5.22)$$

The Zamrik model is only applied for XN40F alloy since the required test data is not available for stainless steel. The material constants for Zamrik model obtained from the IF data presented in Chapter 3 and shown in Fig. 5.4 are given in the following expression:

$$N_f = 0.4337(\Delta E)^{-1.551} \quad (5.23)$$

Note that for the XN40F alloy,  $\sigma_u$  and  $\epsilon_f$  at 700°C are taken as 286 MPa and 16% respectively[16].

The predicted lives from the Coffin-Manson and Ostergren approaches are plotted against actual lives for all of the TMF tests performed on stainless steel (Chapter 3) in Fig. 5.5 and 5.6, respectively. For the Coffin-Manson approach all points lie within a factor of two of the unit correlation line whereas for the Ostergren approach points lie within a factor of about 1.5.

Similarly the predicted and observed lives are plotted for all strain controlled TMF tests on XN40F (Chapter 3) using the Coffin-Manson and Ostergren approaches. In the case of the Coffin-Manson approach, (Fig. 5.4) all points except the representative test (see Fig. 3.26) lie within a factor of two. The predicted life based on the Coffin-Manson approach for a representative test is ten times higher than the actual life. However for the Ostergren approach (Fig. 5.5), all points including representative test lie within a factor of 2.

For the Zamrik model applied to XN40F, the majority of points lie approximately within a factor of 2 (Fig. 5.6). The Zamrik model predictions which consider the elastic and plastic strain together as a damage parameter, give conservative results.

The simple ductility exhaustion method is also explored for predicting the life of stress- controlled ratchetting test carried out on XN40F alloy at constant 900°C (see Fig. 3.39 and 3.40 of chapter 3). In this approach, failure is assumed to occur when the accumulated strain due to ratchetting reaches the uniaxial failure strain (ductility). It is expressed as

$$N_f = \frac{\varepsilon_f}{\Delta \varepsilon_r} \quad (5.24)$$

$$\Delta \varepsilon_r = \varepsilon_m(k) - \varepsilon_m(k-1) \quad (5.25)$$

where  $\varepsilon_m(k)$  is the mean strain corresponding to the  $k^{\text{th}}$  cycle and  $k^{\text{th}}$  cycle is the cycle at the mid life of the test. The ductility limit  $\varepsilon_f$  of XN40F alloy at 900°C is 37% and the ratchet strain  $\Delta \varepsilon_r$  at the mid life is 0.89% (See Fig. 3.40 from Chapter 3). From Table 5.3, the predicted ratchetting life is thus 41 cycles while the actual life is 32 cycles.

## 5.4 Summary and conclusion

Simple strain and strain energy life prediction models are chosen here on the basis of experimental work carried out in this project. The Coffin-Manson approach, based on inelastic strain range showed reasonable correlation (within a factor 2) with observed life for stainless steel. However for XN40F, it could not provide a correlation within a factor of 10 for the representative TMF test and the predicted lives for other TMF tests were consistently non-conservative. The Ostergren strain energy approach gave more accurate TMF life prediction for stainless steel than Coffin-Manson approach (within a factor of 1.5). The Ostergren approach which considers the effect of stress and inelastic strain range also provided a better life prediction for XN40F (within a factor of 2 for all TMF tests) and was conservative for all but the representative TMF test. The Zamrik model which takes into account elastic and plastic strain along with the stress, provided a slightly less accurate life prediction than the Ostergren approach. However it was consistently conservative and therefore is a safe prediction method. From Tables 5.1 and 5.2, it can be concluded that the Ostergren approach gives better correlation of predicted and actual life than the Coffin-Manson and Zamrik approaches for different TMF loading conditions.

Table 5.1 Summary of predicted TMF lives for stainless steel (SS-316).

| Test Specifications                                    | Actual Life ( $N_f$ ) | Predicted Life ( $N_f$ ) |           |
|--|-----------------------|--------------------------|-----------|
|  |                       | Coffin-Manson            | Ostergren |
| TMF IP test<br>450-600 °C<br>$\Delta\varepsilon=1.0\%$ | 1136                  | 1285                     | 1096      |
| TMF IP test<br>450-600 °C<br>$\Delta\varepsilon=1.2\%$ | 414                   | 609                      | 535       |
| TMF IP test<br>450-600 °C<br>$\Delta\varepsilon=1.4\%$ | 193                   | 368                      | 306       |
| TMF IP test<br>450-600 °C<br>$\Delta\varepsilon=1.0\%$ | 700                   | 1039                     | 811       |

Table 5.2 Summary of predicted TMF lives for XN40F alloy.

| Test Specifications   | Actual Life ( $N_f$ ) | Predicted Life ( $N_f$ ) |           |        |
|---|-----------------------|--------------------------|-----------|--------|
|   |                       | Coffin-Manson            | Ostergren | Zamrik |
| TMF OP<br>750-900 °C<br>$\Delta\varepsilon=0.8\%$             | 833                   | 1116                     | 391       | 360    |
| TMF OP<br>750-900 °C<br>$\Delta\varepsilon=1.0\%$             | 733                   | 747                      | 302       | 186    |
| TMF OP<br>750-900 °C<br>$\Delta\varepsilon=1.2\%$             | 337                   | 442                      | 219       | 143    |
| TMF OP with hold<br>750-900 °C<br>$\Delta\varepsilon=0.8\%$   | 453                   | 1076                     | 360       | 335    |
| TMF OP with hold<br>750-900 °C<br>$\Delta\varepsilon=1.0\%$   | 315                   | 575                      | 248       | 177    |
| TMF OP with hold<br>750-900 °C<br>$\Delta\varepsilon=1.2\%$   | 226                   | 392                      | 166       | 114    |
| Representative TMF<br>750-900 °C<br>$\Delta\varepsilon=0.3\%$ | 2086                  | 21666                    | 3186      | 861    |

Table 5.3 Summary of predicted ratchetting life for stress controlled isothermal test (900°C) for XN40F alloy.

| <b>Ratchet Strain <math>\epsilon^r</math></b> | <b>Ductility limit <math>\epsilon_f</math></b> | <b>Actual Life</b>     | <b>Predicted Life</b>  |
|---|--|------------------------|------------------------|
| <b>%</b>                                      | <b>%</b>                                       | <b>(N<sub>f</sub>)</b> | <b>(N<sub>f</sub>)</b> |
| 0.89  | 37   | 32                     | 41                     |

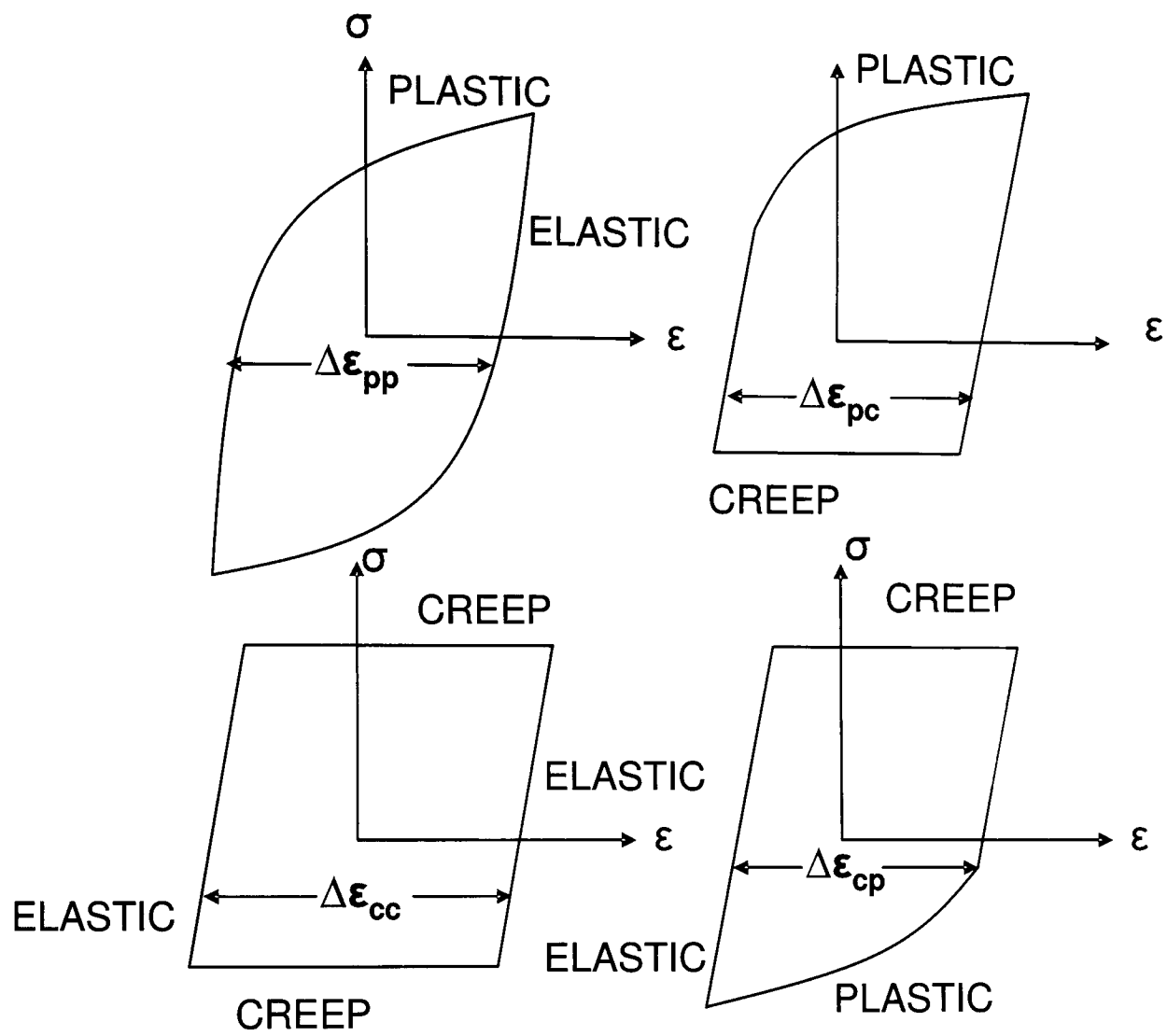


Figure 5.1 Ideal hysteresis loops for the four basic types of inelastic strain ranges in strain range partitioning [106].

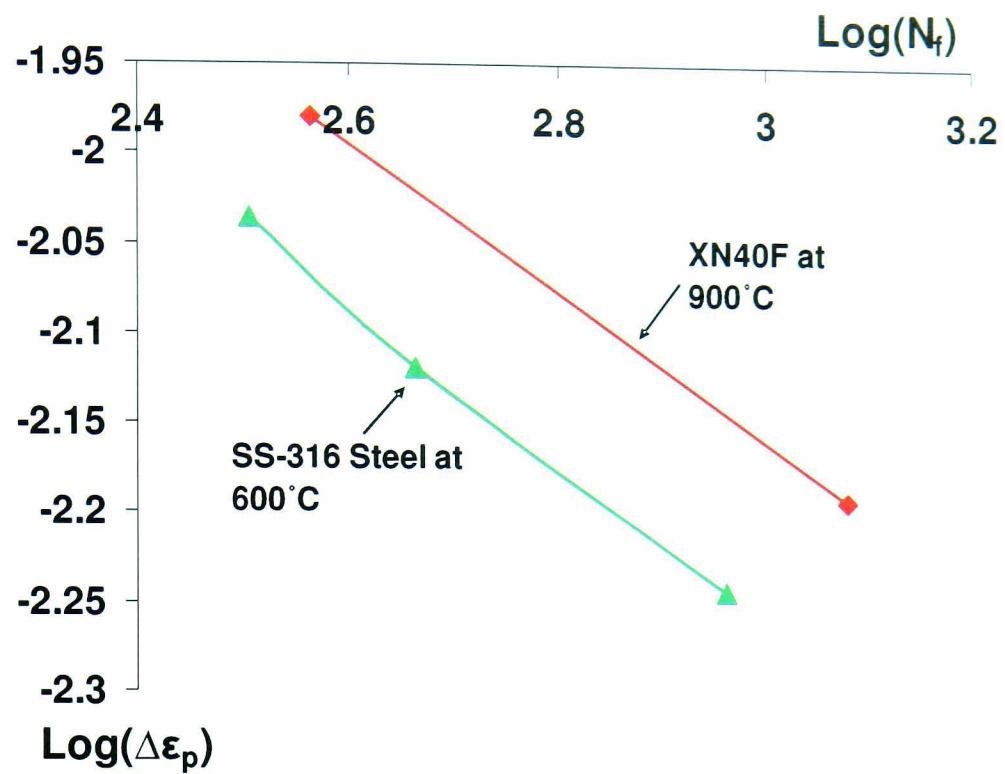


Figure 5.2 Logarithmic plastic strain ranges versus logarithmic life from isothermal fatigue tests for stainless steel (SS-316) and XN40F alloy

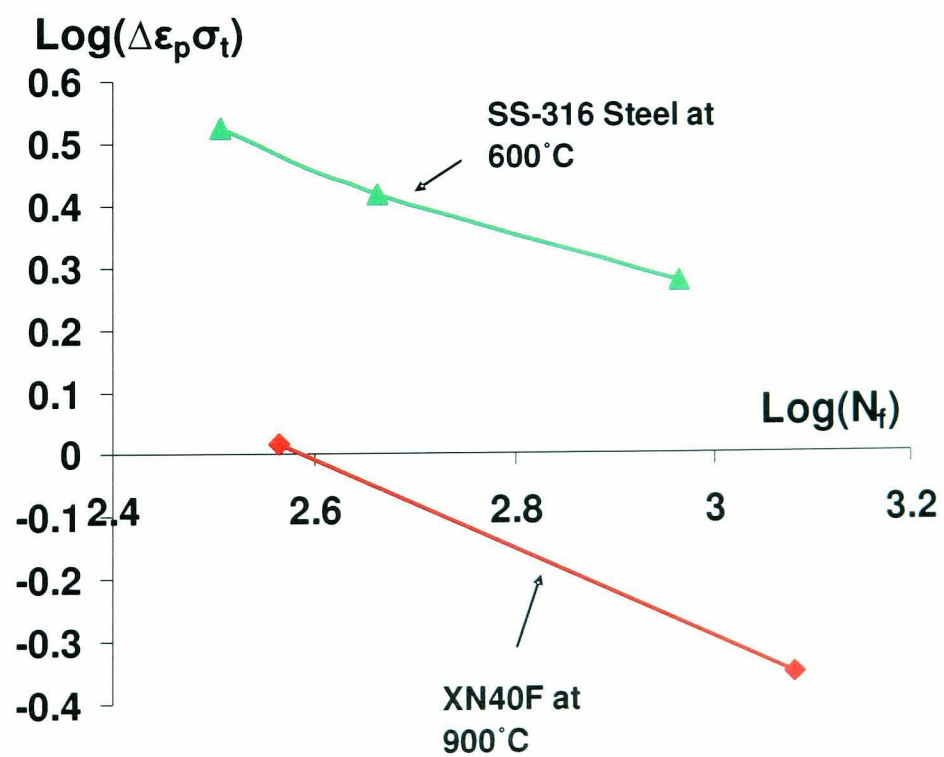


Figure 5.3 Logarithmic stain energy (based on the Ostergren model) versus logarithmic life from isothermal fatigue tests for stainless steel (SS-316) and XN40F alloy

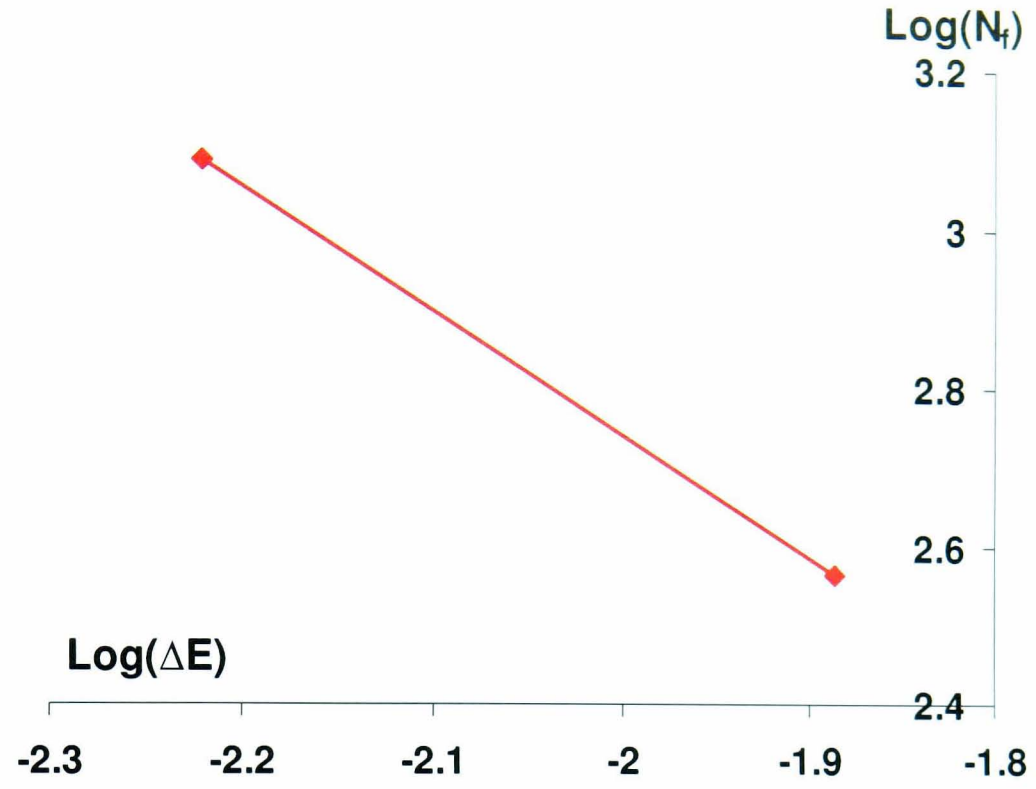


Figure 5.4 Logarithmic life versus logarithmic stain energy (based on the Zamrik model) from isothermal fatigue tests for stainless steel (SS-316) and XN40F alloy

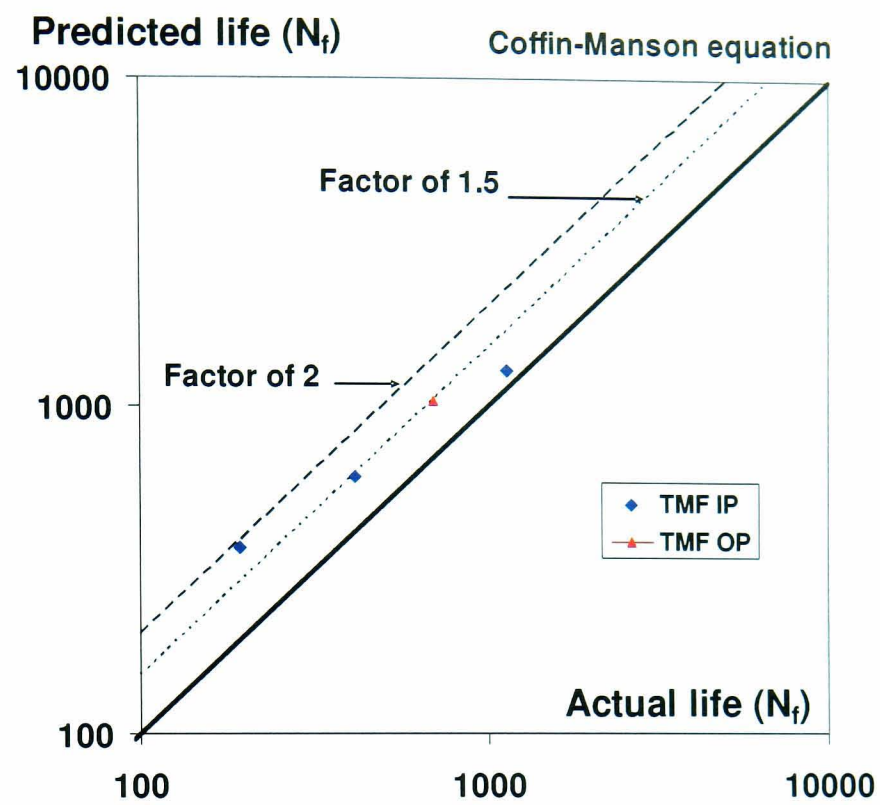


Figure 5.5 Predicted life versus actual life under TMF conditions for stainless steel (SS-316) by Coffin-Manson approach

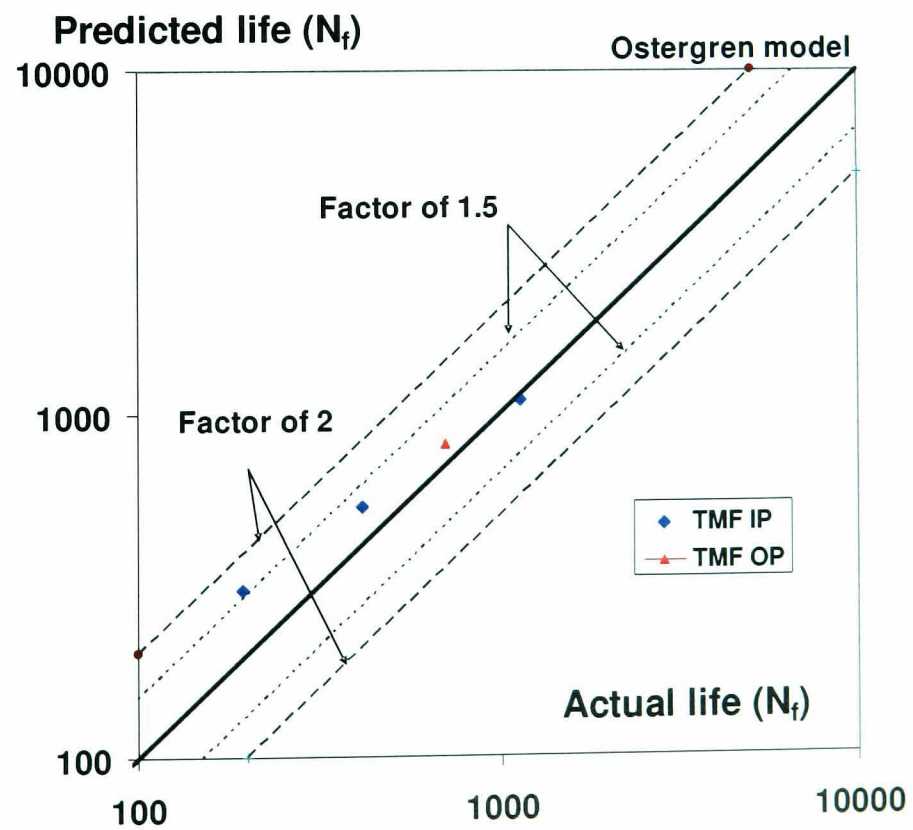


Figure 5.6 Predicted life versus actual life under TMF conditions for stainless steel (SS-316) by Ostergren approach

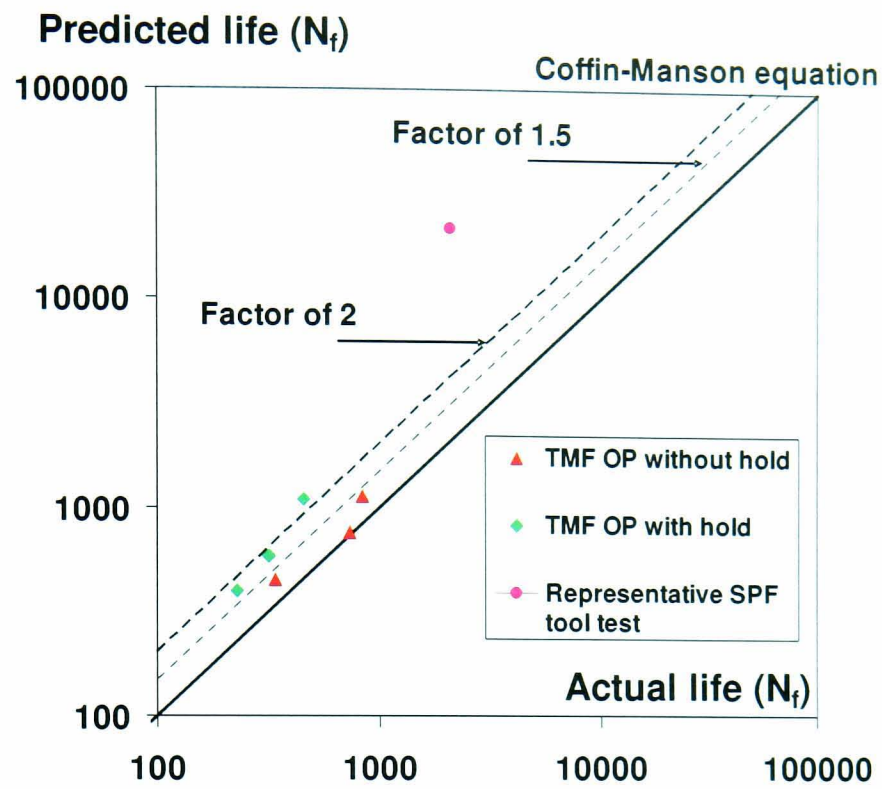


Figure 5.7 Predicted life versus actual life under TMF conditions for XN40F alloy by Coffin-Manson approach

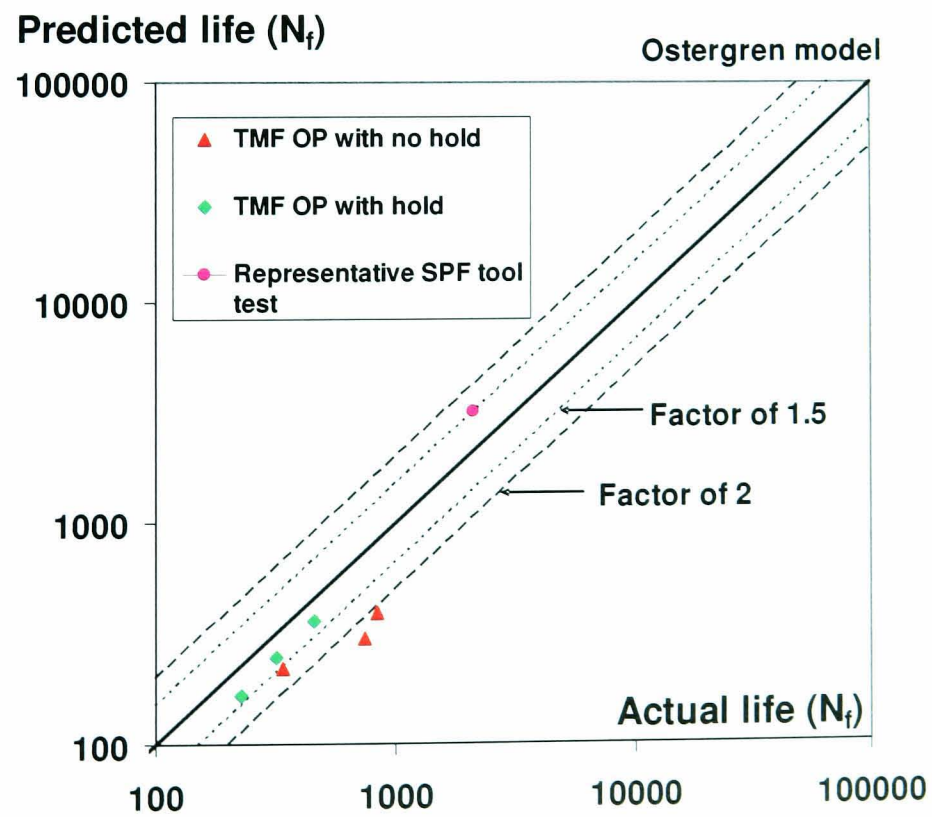


Figure 5.8 Predicted life versus actual life under TMF conditions for XN40F alloy by Ostergren approach

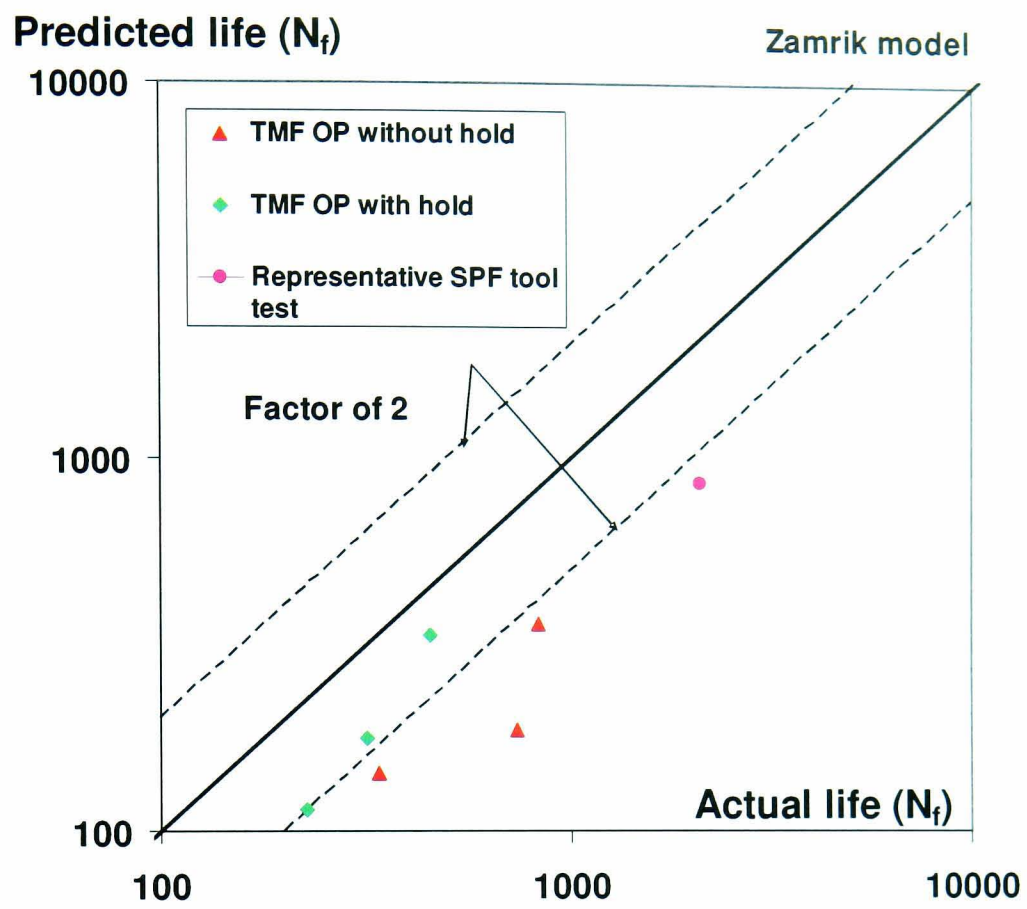


Figure 5.9 Predicted life versus actual life under TMF conditions for XN40F alloy by Zamrik model

## Chapter 6

# FINITE ELEMENT MODELLING

### 6.1 Introduction

Finite element (FE) based simulation of realistic thermo-mechanical conditions is an effective and arguably the only full-field method for analysing realistic large SPF tool behaviour to predict the complex temperature-stress-strain cycles and hence the damage and deformation for identifying SPF tool failure mechanisms.

Sequentially coupled thermo-mechanical analyses are performed to simulate the thermo-mechanical behaviour of the SPF tool. The time-dependent temperature distribution from a transient heat transfer analysis is employed in a subsequent thermo-mechanical analysis, where thermal stresses and strains are calculated using temperature-dependent thermal expansion coefficients and the applied non-linear elastic-plastic-creep material models. The realistic industrial SPF tool shown in Fig. 6.1 is represented in a geometrically simplified form, as shown in Fig. 6.2 to reduce the computational expense and complexities in the FE model. The main simplifications relate to the omission of local features, such as hangings and alignment lugs, so that the dominant deformation mechanisms are still captured, since the objective here is to address the major cracks observed in real tools. However the effect of local features is also analysed as a case study and this is described in the Appendix C. A lower half of the SPF tool is modelled assuming symmetry between the upper and lower tool. The platen-tool frictional contact is defined as a mechanical boundary condition in the FE model. The effect of the upper tool is modelled via a clamping pressure applied along the top edge of the lower tool

during the dwell time i.e. when the two halves are clamped together for forming. The gas pressure during forming is not modelled as the stresses induced by the forming pressure are considered to be negligible [4]. Tool gravity is modelled along with frictional contact between the tool bottom surface and the platen.

The transient heat transfer methodology employed to model thermal histories of SPF tool is validated against thermal experiments carried out on a rectangular block of XN40F material at the University of Nottingham. Convective heat transfer coefficients are identified using empirical equations for dimensionless numbers. The emissivity value for radiation is employed from a previously calibrated heat transfer methodology [107]. Table 6.1 shows the thermal properties of the tool material such as conductivity and specific heat. These thermal properties are applied in the FE model along with convective heat transfer coefficients and emissivity. Uncoupled heat transfer analyses, in which the temperature field does not depend on the stress field, are carried out in the commercial, general-purpose, non-linear FE code, ABAQUS, using conduction, convection and open radiation mechanisms and the predicted results are compared against the measured thermal histories.

The SPF tool thermal cycles are modelled using the validated heat transfer methodology. Unlike Shang et al. [107], free convection and open radiation mechanisms are modelled during transient heating of the tool since the industrial SPF press is large in volume and the heat transfer through circulation of hot air and radiations from press walls is extremely possible.

## 6.2 Tool geometries and material

Three tool geometries are explored in this project: a realistic industrial SPF tool with local features, a simplified SPF tool without local features and a rectangular block of XN40F material. The geometry of the realistic SPF tool is shown in Fig. 6.1. Side A is approximately 2000 mm long, side B is approximately 800 mm long and the nominal thickness of the tool is 200 mm. The bottom side of the tool has eleven cavities of 100 mm depth, for casting purposes. Fig. 6.1 also shows the forming surface of the tool and other features such as alignment lugs and hangers. Major cracks tend to occur along the top edges of the two longer sides while smaller cracks tend to occur at stress concentration features, such as alignment lugs, hangings and corner cavities.

In this thesis, primarily the simplified SPF tool (Fig.6.2) is used in FE analyses. The simplified SPF tool resembles the shape of the forming surface of the realistic industrial SPF tool and the key dimensions of the simplified tool are similar to the industrial tool. Local features such as hangings and alignment lugs and forming cavities are removed in the simplified tool. Fig. 6.3 defines the key dimensions of the simplified SPF tool with 5 cavities of 100 mm depth, at the underside of the tool. However a realistic industrial SPF tool (Fig. 6.1) is also explored briefly (Appendix B) to investigate the effect of local features on tool damage. Fig. 6.4 shows the key dimensions of XN40F block which is used to perform heat transfer tests to validate the heat transfer modelling methodology for the SPF tool.

## 6.3 Theory of heat transfer

### 6.3.1 Introduction

Uncoupled heat transfer analysis is conducted using solid body heat conduction, temperature dependent conductivity, internal energy and convection and radiation boundary conditions. The heat transfer problems can be non-linear because of the temperature dependent material properties but the non-linearity is not severe as material properties do not change rapidly with temperature. Time dependent thermal behaviour of SPF tools is simulated using uncoupled heat transfer analysis. Transient heat transfer analysis is employed and time increments are automatically calculated by ABAQUS with initial time and total time defined in the model using ABAQUS CAE [100].

The basic energy balance equation for heat transfer analysis is given as [100]

$$\int_V \rho \dot{U} dV = \int_S q dS + \int_V r dV \quad (6.1)$$

where  $V$  is a volume of solid material, with surface area  $S$ ,  $\rho$  is the density of the material,  $\dot{U}$  is the time rate internal energy,  $q$  is the heat flux per unit area of the body, and  $r$  is the heat entered into the body per unit volume.

### 6.3.2 Heat transfer mechanisms

There are three basic mechanisms of heat transfer; (i) Conduction (ii) Convection (iii) Radiation. The basic equation of heat conduction is governed by Fourier's law based on experimental observations is given as [108]:

$$q_x'' = -k \frac{\partial T}{\partial x}, q_y'' = -k \frac{\partial T}{\partial y}, q_z'' = -k \frac{\partial T}{\partial z} \quad (6.2)$$

where  $q_x''$  is the heat transfer rate in the x direction, directly proportional to temperature gradient  $\frac{\partial T}{\partial x}$  and thermal conductivity k.

Convection is the heat transfer process that is executed by the flow of fluid. The fluid acts as a carrier for the energy that it draws from a solid wall [8]

The thermal balance equation for convection where fluid is flowing with a velocity v is [108]:

$$\int \left[ \rho c \left\{ \frac{\partial T}{\partial t} + v \cdot \frac{\partial T}{\partial x} \right\} - \frac{\partial}{\partial x} \cdot \left( k \cdot \frac{\partial T}{\partial x} \right) - q \right] dV + \int \left[ n \cdot k \cdot \frac{\partial T}{\partial x} - q_s \right] dS = 0 \quad (6.3)$$

where  $T$  is the temperature at  $x$  spatial position,  $\rho$  is the temperature-dependent fluid density,  $c$  is the temperature dependent specific heat of the fluid,  $k$  is the temperature dependent conductivity of the fluid,  $q$  is the energy per unit volume,  $q_s$  is the heat energy across the surface,  $n$  is the outward normal to the surface and  $t$  is time.

The boundary conditions are that  $T(x)$  is specified on some part of the surface, and  $q_s(x)$  is the heat flux per unit area entered across the surface. The boundary condition in the thermal balance equation is:

$$q_s = -n \cdot k \cdot \frac{\partial T}{\partial x} \quad (6.4)$$

Thermal radiation is the stream of electromagnetic radiation emitted by a material entity on account of its finite absolute temperature [108]. The radiation boundary condition can be defined using two mechanisms; cavity radiation and open radiation.

Cavity radiation occurs when the surfaces within a cavity, exchange heat through electromagnetic waves as shown in Fig. 6.5.

A cavity is formed by closed surfaces which are composed of facets. In the case of 2D or axisymmetric problems, a facet is a line and for 3D problems facet is a solid element. Each of the facets is assumed to have uniform emissivity. Cavity radiation is based on gray body radiation theory where the emissivity of the body is independent of the wavelength of radiation propagation. The radiation energy per unit area into a cavity facet is described as [100]

$$q_i^c = \frac{C_{SB}e_i}{A_i} \sum e_j \sum F_{ik} C_{kj}^{-1} \left( (T_j - T^Z)^4 - (T_i - T^Z)^4 \right) \quad (6.5)$$

where  $C_{ij} = \delta_{ij} - \frac{(1-\epsilon_i)}{A_i} F_{ij}$ , and  $A_i$  is the area of facet  $i$ ,  $e_i$  and  $e_j$  are the emissivities of facets  $i$  and  $j$ ;  $C_{SB}$  is the Stefan-Boltzmann constant;  $F_{ij}$  is the geometrical viewfactor matrix;  $T_i$  and  $T_j$  are the temperatures of facets  $i$  and  $j$ ;  $T^Z$  is the absolute zero on the temperature; and  $\delta_{ij}$  is the Kronecker delta. Heat exchange depends on viewfactors which measure the relative interaction between the surfaces in the cavity. The viewfactor between two elementary areas,  $A_i$  and  $A_j$  can be generally written as

$$F_{ij} = \int_{A_i} \int_{A_j} \frac{\cos \phi_i \cos \phi_j}{\pi S^2} dA_i dA_j \quad (6.6)$$

where  $S$  is the distance between the two facets, and  $\phi_i$ ,  $\phi_j$  are the angles between  $S$  and the normal to the surfaces of the areas, as shown in Fig. 6.6.

In practice not all facets from a surface radiates energy to another surface facets. This is called radiation blocking. ABAQUS checks for all possible radiation path blocks occurring in a cavity. The program checks the radiation ray in each pair of facets intersected by any other facets. Cavities with large number of facets increase the computational time significantly and make the thermal modelling expensive particularly for time dependent problems. As cavity radiation is computationally very expensive, an open radiation mechanism can be used to define the radiation boundary condition where the heat flux due to radiation is defined on element faces, surfaces or at nodes.

The heat flux on a surface due to open radiation to the ambient is given as

$$q = A \left[ (T - T^z)^4 - (T^0 - T^z)^4 \right] \quad (6.7)$$

where  $q$  is the heat flux across the surface,  $A$  is the radiation constant, defined as the product of emissivity of the surface and Stefan-Boltzmann constant;  $A = eC_{SB}$ ,  $T$  is the temperature at this point on the surface and  $T^0$  is the ambient temperature. The ambient temperature and emissivity value of the surface are required to define the open radiation mechanism in ABAQUS.

## 6.4 Heat transfer test on XN40F block

### 6.4.1 Introduction

Heat transfer tests were carried out to validate the heat transfer FE model with assumed boundary conditions and the applied thermal properties. The SPF press with ceramic platens (Fig. 6.7) is used to perform simple heat transfer tests of heating and cooling of the XN40F block. A rectangular block of XN40F material is positioned on

the lower platen and sealed in the furnace using fire brick walls as shown in Figs 6.7 and 6.8. The lower platen is brought closer to the upper platen up to the level of bricks placed on the lower platen. Since the height of the XN40F block is lower than the brick, there is a gap between the upper platen and the block. The XN40F block representing as SPF tool is heated up to 830°C and then cooled down to 100°C by shutting down the SPF press. During the SPF process the tool is heated to the forming temperature (900°C for the titanium SPF process) and then cooled back to ambient after finishing the forming campaign. The cooling process varies from company to company where in some companies the cooling is carried out within the furnace itself whereas in others the tool is removed from the furnace and allowed to cool on an open pallet at the end of the SPF process. Here the cooling of the XN40F block is carried out within the furnace. Temperatures are measured and monitored at three different positions of the block (Fig 6.7). Thermocouples are firmly positioned in the holes drilled on the block (see Fig. 6.4). The platens are resistance-heated with resistance wires circulated horizontally through the platens. The upper and lower platen wires are built in series, which may develop a temperature gradient within the press cavity. The efficiency of the heating system and the heat loss from the platens may influence the test results. Thermal histories at different positions of the block are measured and transferred to the computer using K type thermocouples and a computer interface.

Thermal histories are measured for three positions as shown in Fig 6.7; where one thermocouple is fixed at the interface of the bottom surface of the block and the lower platen referred to as position 'B', which corresponds to the lower platen temperature; another is fixed at the longer side of the block which is 5 mm from the

top surface, referred to as position 'L' and the third one is positioned on the small side surface which is again 5 mm from the top, referred to as position 'S' (see Fig. 6.4).

### **6.4.2 Test results**

The test is divided into two regimes: heating and cooling. Fig. 6.9a shows that during the heating phase, a slow heating rate of 105°C/hr is observed up to 60°C and between 400 to 800°C; however a higher heating rate of 210°C/hr is observed between 60 and 400°C. The temperatures at position B are higher than the temperatures at positions S and L for most of the heating phase. However the difference in temperatures between the position B and S is smaller at lower temperatures and increases with increasing temperature. A very small difference of 2°C is observed between the position B and L at the end of the heating phase, but a larger temperature difference of 31°C is observed between the positions B and S at the end of the heating phase. During the cooling phase, a large temperature gradient is observed initially whereas a negligible gradient is measured by the end of the cooling regime (Fig. 6.9b).

## **6.5 Validation of heat transfer model**

### **6.5.1 Thermal properties**

Thermal conductivity is a thermo physical property of material which is a function of temperature and position, i.e.  $k = k(T, x, y, z)$  [108]. In the present work, since the tool is assumed to be homogeneous and isotropic, it is assumed that  $k = k(T)$  only.

The temperature-dependent conductivity data from Table 6.1 is employed in the FE modelling of heat transfer test as well as of the realistic SPF thermal cycles.

Newton's law of cooling which gives the relation between convective heat transfer rate and temperature difference between the surface  $T_s$  and ambient  $T_\infty$  is used to model convective heat transfer [108], as follows

$$q'' = h(T_s - T_\infty) \quad (6.8)$$

where  $h$  is the convective heat transfer coefficient and  $q''$  is the convective heat flux. SPF tools are commonly (or at least partially) cooled with a natural flow of air, so that the natural convection mechanism is assumed for calculating convective heat transfer coefficients. Convective heat transfer coefficients are commonly expressed using the Nusselt non-dimensional number which is defined as

$$Nu_L = \frac{hL}{k} = CRa_L^n \quad (6.9)$$

where  $L$  is the characteristic length of the geometry (Table 6.3),  $k$  is the conductivity of air, and  $Ra_L$  is the Rayleigh number, given by:

$$Ra_L = \frac{g\beta(T_s - T_\infty)L^3}{\nu\alpha} \quad (6.10)$$

where  $g$  is the local acceleration due to gravity,  $\beta$  is the volumetric thermal expansion coefficient, defined as  $\beta = \frac{1}{T}$  for an ideal gas,  $\nu$  is kinematic viscosity ( $\text{m}^2/\text{s}$ ), and  $\alpha$  is thermal diffusivity ( $\text{m}^2/\text{s}$ ). The convective heat transfer coefficient changes depending on the surface orientation.

For a vertical surface, which is parallel with the gravitational vector; the buoyancy force causes fluid motion in the upward or downward direction and the following empirical formula is used to calculate h for vertical surfaces [108]:

$$\overline{Nu}_L = 0.68 + \frac{0.670Ra_L^{1/4}}{[1 + (0.492\alpha/\nu)^{9/16}]^{4/9}} \quad Ra_L \leq 10^9 \quad (6.11)$$

Alternatively, for a horizontal surface, the buoyancy force is normal to the surface and the recommended correlations [8] for the average Nusselt number are given as follows.

(a) For the upper surface of a heated plate or the lower surface of cooled plate [108]:

$$\overline{Nu}_L = 0.54Ra_L^{1/4} \quad (10^4 \leq Ra_L \leq 10^7) \quad (6.12)$$

$$\overline{Nu}_L = 0.15Ra_L^{1/3} \quad (10^7 \leq Ra_L \leq 10^{11}) \quad (6.13)$$

(b) For the lower surface of a heated plate or the upper surface of cooled plate:

$$\overline{Nu}_L = 0.27Ra_L^{1/4} \quad (10^5 \leq Ra_L \leq 10^{10}) \quad (6.14)$$

These equations are employed to calculate the film coefficients for modelling of convective heat transfer of the SPF tool and XN40F block. The identified convective heat transfer coefficients are listed in Table 6.4 and 6.5 respectively for the XN40F block and SPF tool.

The ratio of radiation emitted by a surface to the radiation emitted by a black body is called the emissivity [108]. The emissivity of a black body is assumed equal to 1 and no surface can emit more radiation than a black body. The radiative heat transfer is defined here via the following equation [108]:

$$q = eC_{SB}T^4 \quad (6.15)$$

where  $e$  is the radiation emissivity of the surface,  $q$  is the surface emissive power ( $\text{W}/\text{m}^2$ ),  $T$  is the absolute temperature of the surface and  $C_{sb}$  is the Stefan-Boltzmann constant, which is equal to  $C_{SB} = 5.67 \times 10^{-8} \text{W}/\text{m}^2\text{K}$ .

Previous calibration of the present heat transfer methodology [107] against the measured transient temperature history of a representative tool made of Cronite HR6 has shown that a value of  $e = 0.9$  is appropriate for accurate prediction of the cooling and heating cycles of SPF tool. The same value of emissivity is also used here for modeling the heat transfer test carried out on the XN40F block as well as for the SPF tool thermal cycles.

### **6.5.2 Validation of heat transfer model**

The transient heat transfer analysis is carried out using the conduction, convection and open radiation mechanisms. Thermal properties such as temperature dependent conductivity, convective heat transfer coefficients and emissivity, summarised in Tables 6.1 and 6.4 are employed in the FE model to simulate thermal histories of the XN40F block. Thermal history measured at position B is used in the FE model as a temperature boundary condition, applied to the bottom surface nodes. The contact with the platen is assumed to be adiabatic. Surface ambient temperatures for modelling open radiation and free convection mechanisms are varied according to the changing temperatures at position B. Fig. 6.10 shows different heat transfer mechanisms employed at different surfaces of the block for modelling the heating and cooling experiments. The nodal temperatures of the bottom surface are controlled using the measured thermal history at position B. Temperatures of all the

nodes were set to 28°C at the beginning of the heating phase. An automatic time incrementation is used in the FE analyses with a maximum allowable temperature change of 50°C per increment. The eight node linear heat transfer brick elements are used to mesh the XN40F block. The mesh sensitivity study is carried out to assess the effect of mesh size on the predicted temperatures. A uniformly distributed mesh is employed with three different sizes of 10 mm, 5 mm and 2.5 mm and the heating phase is modelled using the above three mesh sizes. Fig. 6.11 shows a negligible discrepancy in the predicted temperatures among all three mesh sizes. A mesh with a size of 5 mm is employed in further analyses and the results are compared against the experiments. The FE predicted thermal histories at position L and S are compared with the experimental thermal histories for the corresponding positions. Fig. 6.12 shows the FE model of XN40F block with nodal temperature contours at the end of the heating and cooling phase.

During the heating phase, a maximum of 24°C difference is observed between the FE and experiment at position L (Fig. 6.13a). Alternatively a temperature difference of 31°C occurs at position S at the end of heating phase (Fig.6.13b). For a cooling phase at position L, virtually negligible difference is observed between the FE and experimental thermal histories (Fig.6.14a). However a temperature difference of 31°C is identified for position S at the beginning of the cooling phase which is later on disappeared with decrease in temperature (Fig 6.14b).

From Fig. 6.13 and 6.14, it can be concluded that the applied heat transfer methodology and the identified convective heat transfer coefficients depicted a reasonably accurate prediction of thermal histories of the XN40F block. The

validated heat transfer methodology is further employed for modelling the SPF tool thermal cycles. However the Nottingham university SPF press used in the experimental work is much smaller than the BAE systems SPF press. Moreover, BAE systems press has heating elements on the side walls and press doors in addition to the heating elements underneath of platens; whereas, the university press has heating elements only inside the platens. Therefore the open radiation and free convection mechanisms are more important for modelling thermal cycles of the BAE SPF tool.

## **6.6 FE modeling of SPF thermal cycles**

### **6.6.1 Description of SPF thermal cycles**

The SPF tool temperature cycling is complex and is therefore divided into two types. The two types are (i) lower frequency cycles, referred here as major cycles, broadly associated with heating and cooling from ambient, and (ii) higher frequency cycles, referred to here as minor cycles, which are associated with opening and closing of the press doors for blank inserting and removal of formed parts. In reality these cycles are not easy to standardize since they are not automated and are carried out by manual operation. Therefore there can be significant variations in the time periods, in particular, associated with these idealised cycles. However the time periods specified below are given as typical by the sponsoring industry, BAE systems. Nonetheless, for the purposes of analyses they are specified as follows and as shown in Fig. 6.15.

## **Major cycle**

### **Step 1:**

The tool is heated in a pre-heat furnace to 500°C at a controlled rate of 50°C/hr and then allowed to reach steady state by soaking at 500°C in the pre-heat furnace. The heating process is mainly controlled by conduction with the temperature boundary condition applied to the bottom surface of the tool. The open radiation and free convection mechanisms are also applied to remaining surfaces using the same temperature-time curve employed for the bottom surface of the tool. The temperature of the tool bottom surface is maintained constant (here 500°C) during the soaking period. Furthermore the surface ambient temperature for convection and open radiation is also held constant during the soak time.

### **Step 2:**

The tool is transferred to the SPF press in 3 minutes. During this time-period all external surfaces except the top surface of the tool (due to presence of upper tool) are exposed to the ambient; this is modelled via open radiation and free convection mechanisms.

### **Step 3:**

The tool arrives in the SPF press and is heated to 900°C, again at 50°C/hr, until a uniform temperature is achieved. This process is again controlled through conductive heating of the tool via temperature control of the bottom surface nodes. Free convection and open radiation are also applied by varying surface temperature according to the heating rate.

**Step 4:**

The tool is control-cooled to 500°C at 50°C/hr in the SPF press again by controlling the temperature of the bottom surface nodes of the tool and using free convection and open radiation; and then removed from the press to cool to ambient temperature via free convection and open radiation.

Commonly in industry, heating to the forming temperature is carried out by heating directly from room temperature to forming temperature without any pre-heating. Also the cooling to ambient temperature is commonly performed directly by removing the tool from SPF press and allowing it to cool in free air. In that case Steps 1 and 4 are carried out without pre-heating in the preheat oven and without controlled cooling in the SPF press respectively. Hence there is no tool transfer from pre-heat oven to SPF press. One of the objectives of the present thesis, from the industrial point of view, is to assess the likely significance of these different protocols for heating and cooling of the tool.

**Minor cycle****Step 1:**

The SPF press is opened to unload the formed component. This consists of allowing the two longest sides of the tool (facing the press doors) to cool via free convection and open radiation with the ambient for a period of 5 minutes.

**Step 2:**

The press is closed again and the tool is heated back to 900°C.

**Step 3:**

The press is opened again to load the new blank. This again allows the two longest sides to cool via free convection and open radiation for 5 minutes.

**Step 4:**

The press is closed again and the tool is heated back to 900°C along with the new blank sheet.

**Step 5:**

The tool and the blank temperature is maintained at a constant temperature of 900°C for 7 hours corresponding to the forming cycle of one component.

**6.6.2 Boundary conditions**

The transient heating and controlled cooling processes of the tool are modelled using the controlled time dependent temperature variation of the tool bottom surface nodes. Moreover the open radiation and free convection mechanisms are also employed on other surfaces using the same temperature-time history employed to the bottom surface of the tool. The tool contact with the platen is assumed to be adiabatic. During the soak time periods and 7 hours forming cycle (Dwell period), the temperature of the tool bottom surface for conduction and surface ambient temperature for convection and open radiation is maintained constant. The tool bottom surface is also held at 900°C during the blank insertion and heating back to 900°C processes of the minor cycle. However, during the blank insertion and part unloading, the surfaces across the two long sides of the SPF tool facing press doors are exposed to ambient air outside the press which is modelled via free convection and open radiation. The temperature boundary condition of the tool bottom surface is deactivated when the tool is removed from the press and allowed to cool via free convection and open radiation mechanisms only. Similar to the XN40F block, an automatic incrementation with a maximum allowable temperature change per increment of 50°C is employed. Eight node heat transfer brick elements are used to

mesh the simplified SPF tool using 8160 elements in total with a mesh size of 25 mm along the thickness of the tool.

### **6.6.3 FE predicted SPF thermal cycles**

Uncoupled transient heat transfer analyses are performed to simulate the SPF thermal cycles using thermal properties from Tables 6.1 and 6.5. The two different SPF thermal cycles based on different heating and cooling protocols are: Thermal cycle A- without pre-heating and without controlled cooling and Thermal cycle B-, with pre-heating in a pre-heat oven and controlled cooling in the SPF press

Fig. 6.16 shows the FE model of the simplified SPF tool depicting the temperature contour plots at various stages of the thermal cycle. From Fig. 6.16a, it can be seen that a uniform temperature with a very small temperature gradient of 2°C is predicted at the end of heating to forming temperature 900°C. Fig. 6.16b shows the effect of opening of the press doors on the temperature distribution in the tool. A significant temperature gradient is predicted at the end of blank insertion and part unloading operations where the temperature across the two long sides of the SPF tool facing the press doors drops by approximately 150°C. However the middle portion of the SPF tool is predicted to be at 900°C as the bottom surface of the tool is still controlled to be at 900°C. Fig 6.16c shows the temperature contour plot at the end of ambient cooling where the temperature of the tool is the same as the atmospheric air. As mentioned earlier, two thermal cycles, thermal cycle A and thermal cycle B are simulated. The predicted thermal histories at EL C are shown in Fig. 6.17. Fig. 6.17a shows the predicted temperature history for thermal cycle-A and Fig. 6.17b shows the predicted temperature history for thermal cycle-B, where the tool is heated to

500°C in the pre-heat oven and control-cooled in the SPF press to 500°C before removal from the press for ambient cooling. The minor cycles comprising of opening and closing of press doors followed by 7 hours forming cycle are common to both thermal cycles A and B.

The predicted thermal cycles are compared with industrial observations and the measured BAE SPF tool thermal history of ambient cooling (after a forming campaign) by Kelly and Leen [114] (see Appendix B). The FE predicted thermal cycle results have shown reasonable agreement with industrial observation and the measured thermal history.

## **6.7 FE modeling of thermo-mechanical analyses of SPF tool**

### **6.7.1 Introduction**

Sequentially-coupled thermo-mechanical analyses are performed to simulate the thermo-mechanical behaviour of the SPF tool. The nodal temperatures from the transient heat transfer analysis are applied in the thermo-mechanical analysis with the same mesh and compatible element type used in the heat transfer analysis. Thermal stresses and strains are calculated via temperature-dependent thermal expansion coefficients. Fig 6.18 shows the FE model of the simplified SPF tool and the analytically rigid platen with applied tool gravity represented by yellow arrows on the SPF tool.

## 6.7.2 Contact modeling

In FE analysis, contact is classified as a discontinuous constraint which allows forces to be transmitted from one part to another. The constraint is only applied when the two surfaces are in contact and hence the algorithm has to be able to detect when the two surfaces are in contact and apply the constraint accordingly.

Contact problems are difficult to converge and must be addressed properly. The contact between the two surfaces is defined using the slave-master algorithm in ABAQUS. The platen is defined as an analytically rigid surface and is assigned to be the master surface. The bottom surface of the tool is defined as a slave surface. The platen (master surface) is extended well enough beyond the bottom surface (slave) of the tool to avoid slave surface nodes 'falling off the edge' of the master surface. The interaction between the contacting surfaces consists of normal and tangential components. When two surfaces are in contact with each other, the force normal to the contacting surfaces acts on the two bodies. The surfaces separate when the contact pressure between them becomes zero or negative and the constraint is removed. This surface interaction is referred to as hard contact (Fig. 6.19) and is used to model the normal behaviour between the platen and the tool. In the presence of friction, shear forces are created between the contacting surfaces, which resist the tangential motion of the bodies. The Coulomb friction model is used here to describe this interaction between the platen and the tool (Fig. 6.20). The frictional behaviour is defined using a coefficient of friction  $\mu$  which is equal to 0.2 in the tool-platen contact. Contact with friction is difficult to converge due to the discontinuity between the two states of sticking or slipping. A penalty friction formulation with an allowable elastic slip is employed here. The allowable elastic slip is a small amount

of relative motion permitted, when surfaces are formally under a stick state condition, to alleviate the numerical difficulties and facilitate convergence [100]. An allowable elastic slip value of 0.02 mm is used here.

The ABAQUS contact algorithm described in Fig. 6.21 always checks for changes in the contact conditions (closed or opened) before checking for equilibrium forces and moments. Iterations with contact state changes detected are called severe discontinuity iterations. In order to converge contact successfully, the maximum number of severe discontinuity iterations allowed is changed from default 12 to 30 in the current problem and the contact converges successfully in all thermo-mechanical analyses of the SPF tool.

### **6.7.3 Boundary conditions**

Apart from the tool-platen contact, two more boundary conditions are applied during thermo-mechanical analyses of the SPF tool. Out of which one is constraining the reference point of the platen in all six degrees of freedom throughout the analyses. Boundary conditions are also applied at nodes A and B (Fig. 6.22) in the beginning of the analysis to restrict the free body motion until the friction between the platen and the tool bottom surface is completely active i.e. only during the application of gravity of the tool. The boundary condition at nodes A and B is deactivated at the end of the gravity application step.

#### **6.7.4 Loading conditions**

The SPF tool is subjected to three different types of loading during the SPF process, namely thermal-mechanical loading, gravity loading and clamping pressure. Tool gravity is applied at the beginning of the analyses and remains active throughout. The clamping pressure of 4 MPa, comprising of 100 tonnes of clamping force applied by the press between the two halves and the additional force counteracting the forming gas pressure of 3.44 MPa is applied along the top surface (highlighted in Fig.6.22 with red) of the lower half of the SPF tool just before the forming cycle and remains active during the 7-hour forming period. The gas forming pressure is not modelled here as it is negligible and distributed over a large forming surface of the tool. The clamping pressure in real tools is commonly actively controlled, both spatially and temporally, but this aspect is not modelled here. Thermal-mechanical loading is applied through temperature gradients and mechanical restraints due to friction between the tool and the platen.

#### **6.7.5 Meshing**

First order elements are preferred for the slave surfaces over the second order elements [100]. For 3D second order elements, the equivalent nodal forces do not have the same sign for a constant pressure and hence it is difficult for the contact algorithm to run accurately, especially for the non-uniform contact. The first order elements are also recommended for the problems involving contact and large distortions. For the problems involving bending and large distortions, a fine mesh with a first order reduced integration elements are recommended. Moreover the reduced integration reduces the analysis running time significantly for three

dimensional problems [100]. Therefore 8 node linear brick elements with reduced integration and a finer mesh across the thickness and critical edges (sides facing press doors) of the SPF tool are used in the thermo-mechanical analyses of the simplified SPF tool.

In order to assess the effect of mesh size on the predicted stresses and strains, three different mesh sizes (coarse, medium and fine ) are employed in the thermo-mechanical analysis of a major cycle including a minor cycle. The uncoupled plasticity-creep material behaviour model (see Chapter 4) is employed for this mesh sensitivity study. A local co-ordinate system is defined in Fig. 6.23 where the  $X$  direction is parallel to the edge of the tool and the  $Y$  direction is parallel to the thickness of the tool. Fig. 6.23 shows the local inelastic strain distribution along  $X$  direction (also referred to as 1 direction) at the end of the part unload operation for the fine mesh (see Table 6.6). Fig. 6.24 shows the predicted local stress,  $\sigma_{11}$  versus local inelastic strain  $\epsilon_{11}^m$  at the critical element for three different mesh sizes employed. From Fig. 6.24 and Table 6.6, less than 5 % error is seen on the predicted stress range and less than 9 % error is observed on the predicted inelastic strain range from the medium to the fine mesh. However the total computational time for the fine mesh analysis is five times higher than for the medium mesh analysis. The medium mesh is employed in this thesis for all the analyses of the simplified SPF tool.

The results of various thermo-mechanical analyses of the simplified SPF tool are described in Chapter 7 using different material behaviour models discussed in Chapter 4.

## 6.8 Summary and conclusion

The heat transfer methodology employed for the SPF tool thermal cycle simulation is validated against the measured thermal histories of XN40F block in the University of Nottingham SPF press. Free convection heat transfer coefficients for different surface orientations are determined using empirical equations for dimensionless numbers. The emissivity value is chosen from a previously calibrated heat transfer methodology. The identified convective heat transfer coefficients, chosen emissivity value and other thermal properties such as temperature dependent conductivity and specific heat are used in the uncoupled heat transfer analyses of XN40F block to verify them against the measured thermal histories. The FE predicted results are observed to be reasonably accurate with experimental thermal histories. The validated heat transfer methodology is further employed to model the SPF tool thermal cycles. The predicted SPF thermal cycles are found to be in reasonable correlation with industrial observations and the measured BAE SPF tool thermal histories by Kelly and Leen [114].

Table 6.1 Thermal properties of BAE systems SPF tool material XN40F [109]

| Thermal conductivity<br>$\lambda$ |       | Thermal expansion<br>$\alpha$ |                  | Specific heat<br>$c_p$ |        |
|-----------------------------------|-------|-------------------------------|------------------|------------------------|--------|
| Temperature<br>°C                 | W/m/K | Temperature<br>°C             | $\times 10^{-6}$ | Temperature<br>°C      | J/kg/K |
| 20                                | 11    | 20-100                        |                  | 0                      | 437    |
| 500                               | 20    | 20-500                        | 15.8             | 500                    | 536    |
| 850                               | 26    | 20-850                        | 17.35            | 850                    | 603    |
| 950                               | 28    | 20-950                        | 17.7             | 950                    | 618    |

Table 6.2 Thermo-physical Properties of air at Atmospheric Pressure [110]

| Temperature<br>K | Conductivity<br>$k \cdot 10^3$<br>W/mK | Kinematic<br>viscosity<br>$\nu \cdot 10^6$<br>$m^2/s$ | Thermal<br>diffusivity<br>$\alpha \cdot 10^6$<br>$m^2/s$ |
|------------------|--|---|--|
| 500              | 40.7                                   | 38.79   | 56.7   |
| 800              | 57.3                                   | 84.93   | 120  |
| 1100             | 71.5                                   | 141.8   | 195  |
| 1200             | 76.3                                   | 162.9   | 224  |

Table 6.3 The characteristic length  $L$  of the horizontal surface for different tools.

| Model Name              | The characteristic length $L$ (m) |
|-------------------------|-----------------------------------|
| XN40F rectangular block | 0.03148                           |
| Simplified BAE SPF tool | 0.328                             |

Table 6.4 Film coefficients at different temperatures for XN40F block.

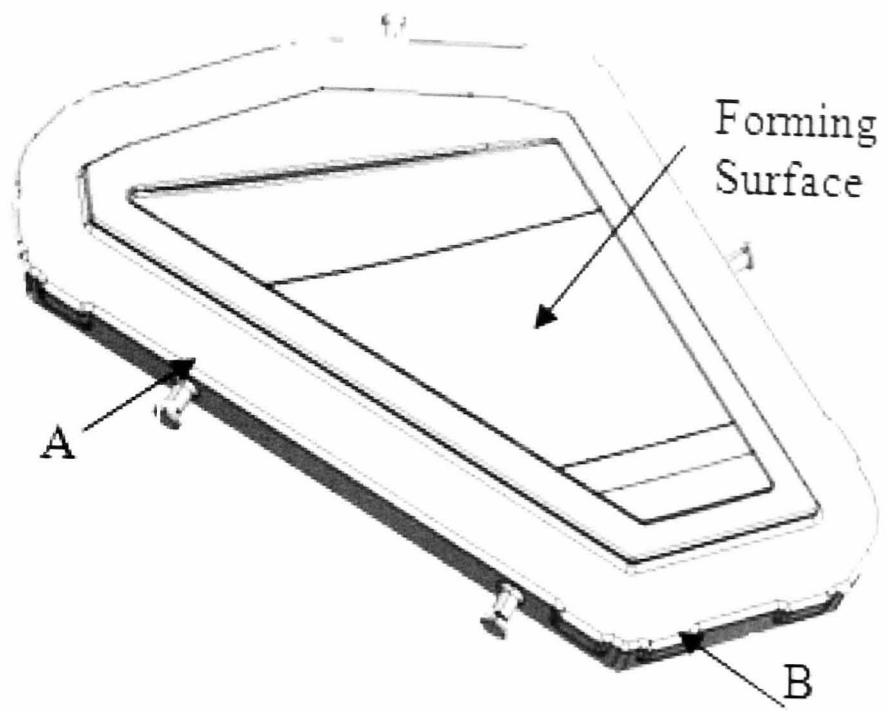
|                  | Temperature<br>K | Rayleigh<br>number<br>$Ra_L$ | Nusselt<br>number<br>$\overline{Nu}_L$ | Convection<br>coefficient<br>h<br>W/m <sup>2</sup> K |
|------------------|------------------|------------------------------|--|--|
| Vertical surface | 500              | 2.31E5                       | 11.90                                  | 9.69   |
|                  | 800              | 7.63E4                       | 9.22                                   | 10.56  |
|                  | 1100             | 3.25E4                       | 7.60                                   | 10.87  |
|                  | 1200             | 2.54E4                       | 7.18                                   | 10.97  |
| <b>Average</b>   |                  |                              |  | <b>10.52</b>   |
| Upper surface    | 500              | 5.76E4                       | 8.36                                   | 10.81  |
|                  | 800              | 1.90E4                       | 6.34                                   | 11.54  |
|                  | 1100             | 8.12E3                       | 5.12                                   | 11.6426  |
|                  | 1200             | 6.34E3                       | 4.81                                   | 11.67  |
| <b>Average</b>   |                  |                              |  | <b>11.44</b>   |
| Lower surface    | 500              | 5.76E4                       | 4.18                                   | 5.40   |
|                  | 800              | 1.90E4                       | 3.17                                   | 5.77   |
|                  | 1100             | 8.12E3                       | 2.56                                   | 5.82   |
|                  | 1200             | 6.34E3                       | 2.40                                   | 5.83   |
| <b>Average</b>   |                  |                              |  | <b>5.71</b>  |

Table 6.5 Film coefficients at different temperatures for simplified BAE tool [111]

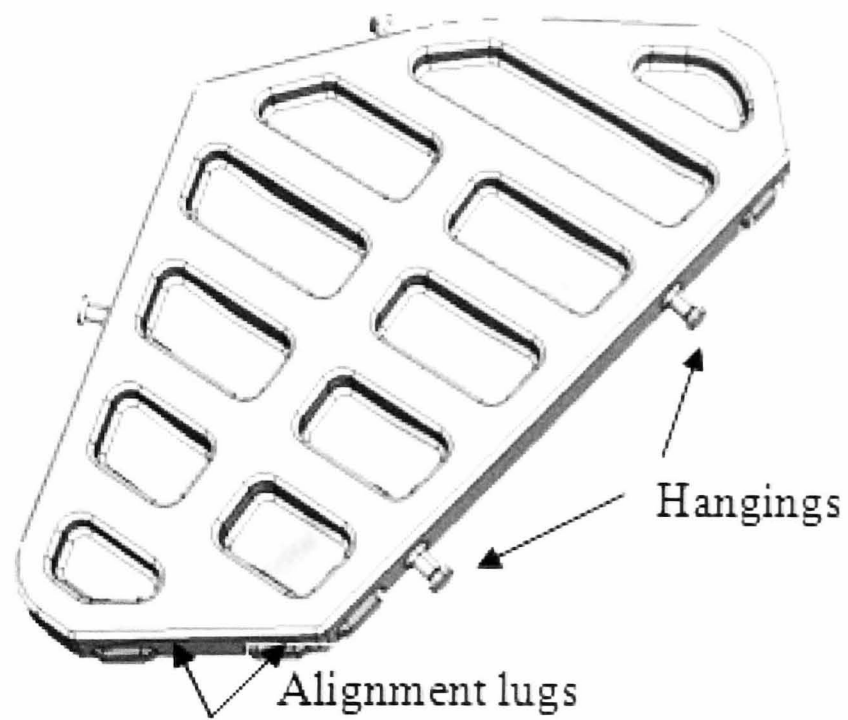
|                  | Temperature<br>K | Rayleigh<br>number<br>$Ra_L$ | Nusselt<br>number<br>$\overline{Nu}_L$ | Convection<br>coefficient<br>h<br>W/m <sup>2</sup> K |
|------------------|------------------|------------------------------|--|--|
| Vertical surface | 500              | 1.4E7                        | 32.95                                  | 6.71   |
|                  | 800              | 4.8E6                        | 25.37                                  | 7.27   |
|                  | 1100             | 2.0E6                        | 20.48                                  | 7.32   |
|                  | 1200             | 1.6E6                        | 19.5                                   | 7.44   |
| <b>Average</b>   |                  |                              |  | <b>7.13</b>  |
| Upper surface    | 500              | 5.5E7                        | 46.5                                   | 5.8  |
|                  | 800              | 2.0E7                        | 36.11                                  | 6.3  |
|                  | 1100             | 8.8E6                        | 29.41                                  | 6.4  |
|                  | 1200             | 6.9E6                        | 27.7                                   | 6.4  |
| <b>Average</b>   |                  |                              |  | <b>6.22</b>  |
| Lower surface    | 500              | 5.5E7                        | 23.3                                   | 2.9  |
|                  | 800              | 2.0E7                        | 18.5                                   | 3.2  |
|                  | 1100             | 8.8E6                        | 14.7                                   | 3.2  |
|                  | 1200             | 6.9E6                        | 13.9                                   | 3.2  |
| <b>Average</b>   |                  |                              |  | <b>3.12</b>  |

Table 6.6 Effect of mesh size on FE analysis (a major cycle including a minor cycle) of simplified SPF tool

| Mesh                                   | Mesh size (mm)       | Total CPU time (Sec) | $\Delta\sigma/2$ (MPa) | $\sigma_{\text{mean}}$ (MPa) | $\Delta\varepsilon^{\text{in}}$ % |
|--|----------------------|----------------------|------------------------|------------------------------|-----------------------------------|
| Coarse<br>(Total no. of elements-6411) | X=52<br>Y=25<br>Z=62 | 4042                 | 97                     | 30.31                        | 0.15                              |
| Medium<br>(Total no. of elements-8160) | X=40<br>Y=25<br>Z=40 | 5374                 | 100                    | 31.5                         | 0.171                             |
| Fine<br>(Total no. of elements-20880)  | X=30<br>Y=20<br>Z=30 | 26827                | 104                    | 33                           | 0.186                             |

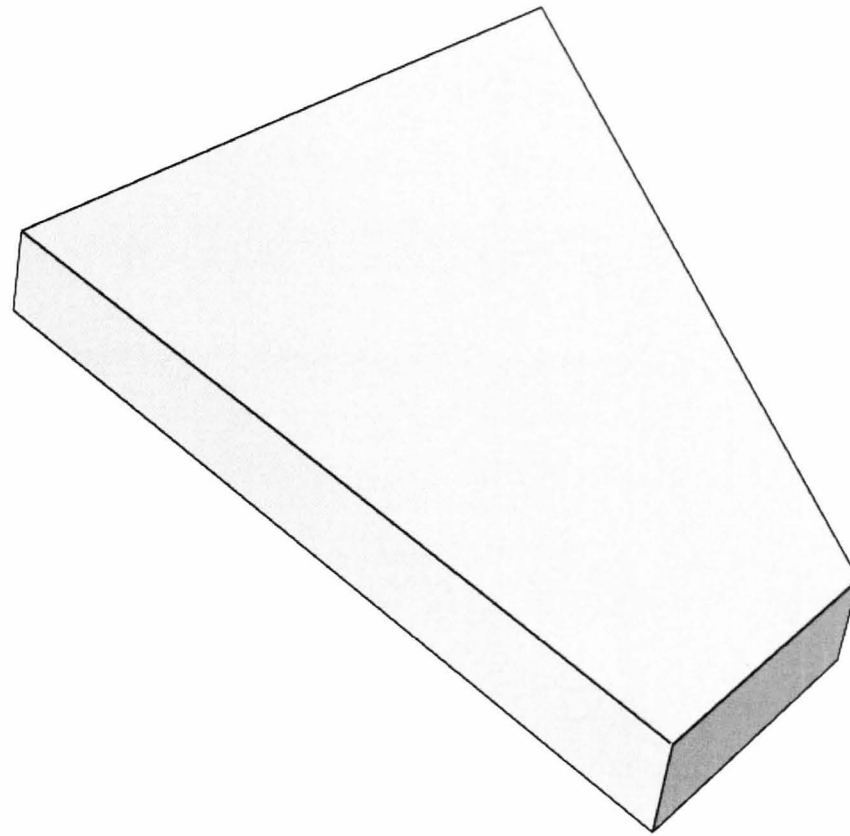


(a)

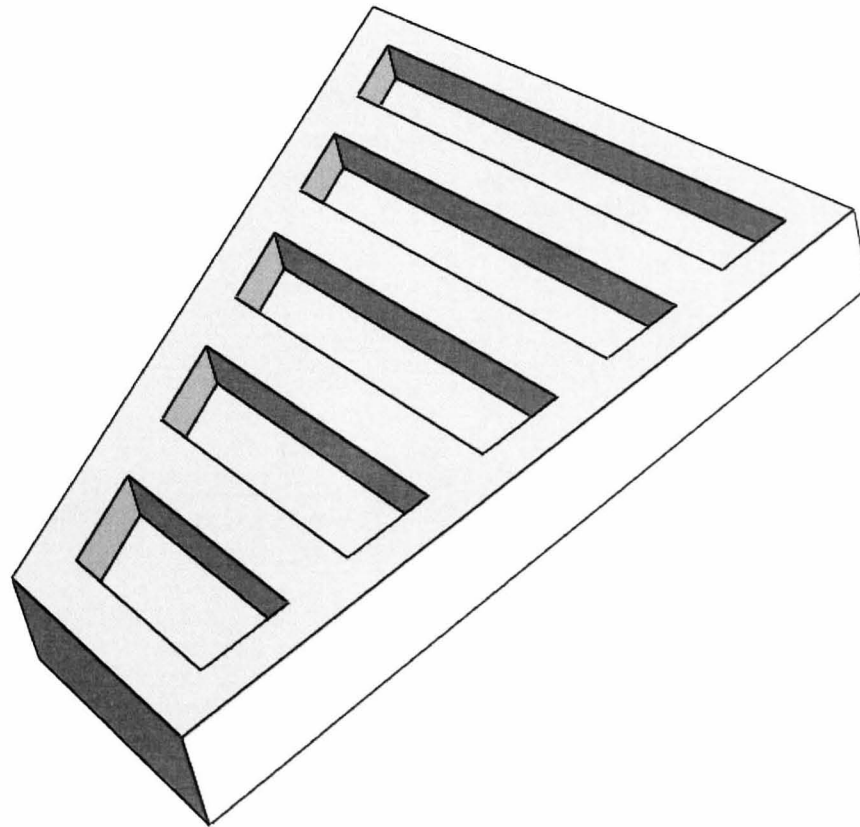


(b)

Figure 6.1 Lower half of a realistic industrial SPF tool; (a) Top view, (b) bottom view



(a)



(b)

Figure 6.2 Lower half of a Simplified SPF tool; (a) Top view, (b) bottom view

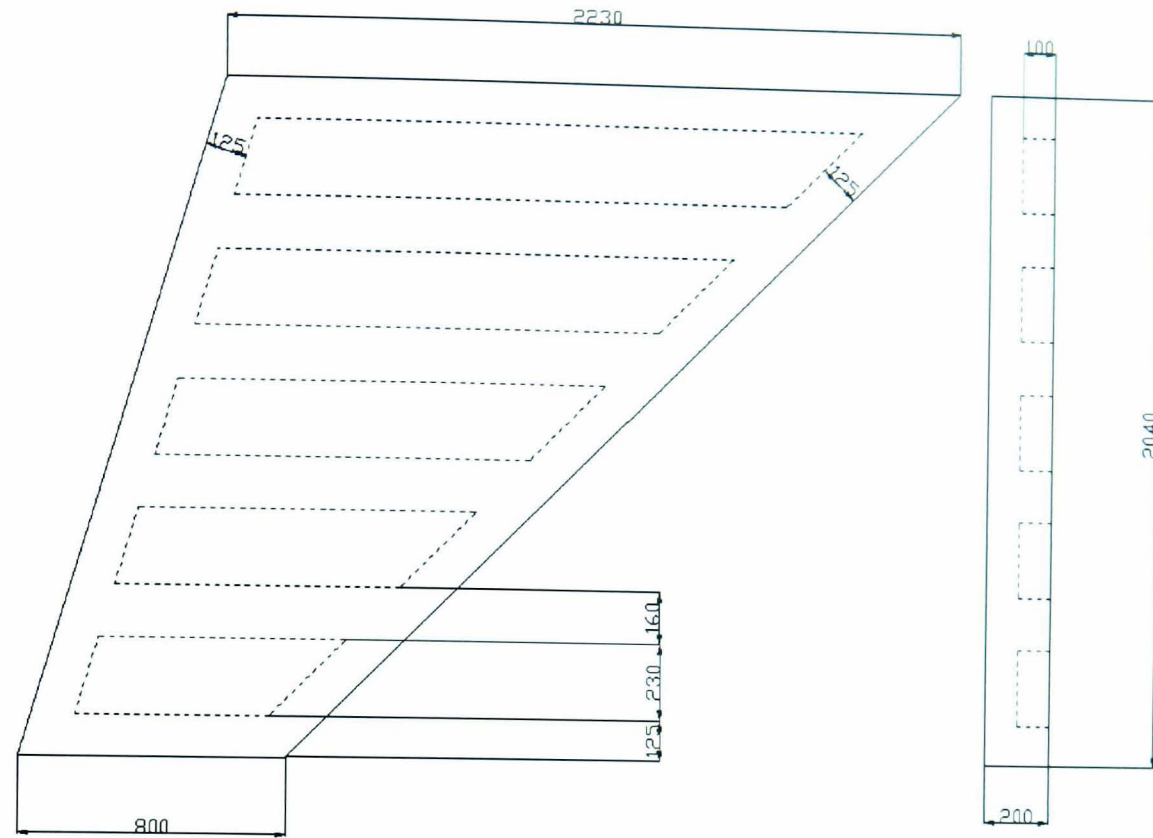


Figure 6.3 Orthographic drawing of a lower half of the simplified SPF tool (all dimensions are in mm)

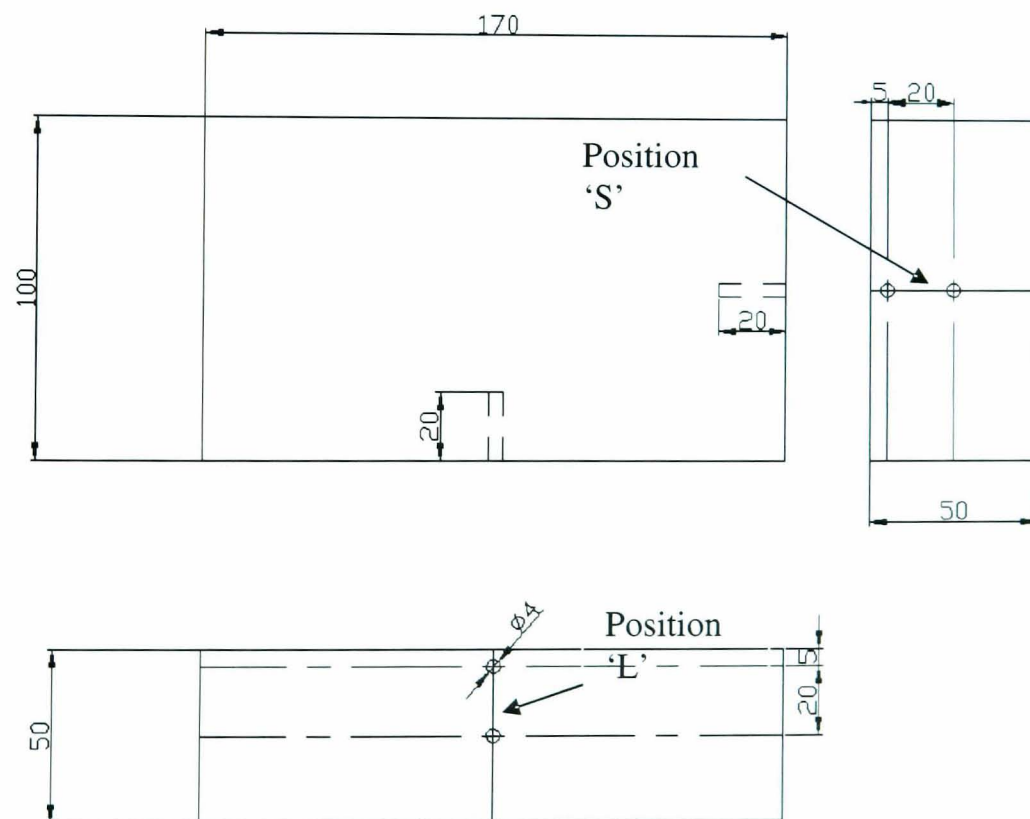


Figure 6.4 Orthographic drawing of the XN40F block (all dimensions are in mm)

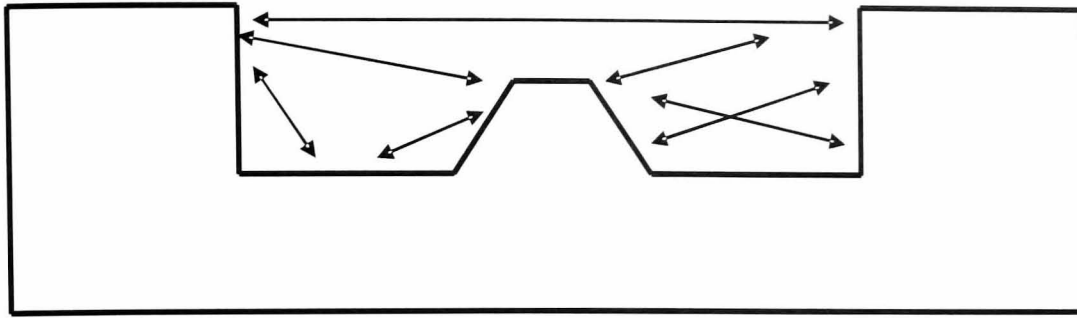


Figure 6.5 Schematic diagram of heat exchange between surfaces by radiation

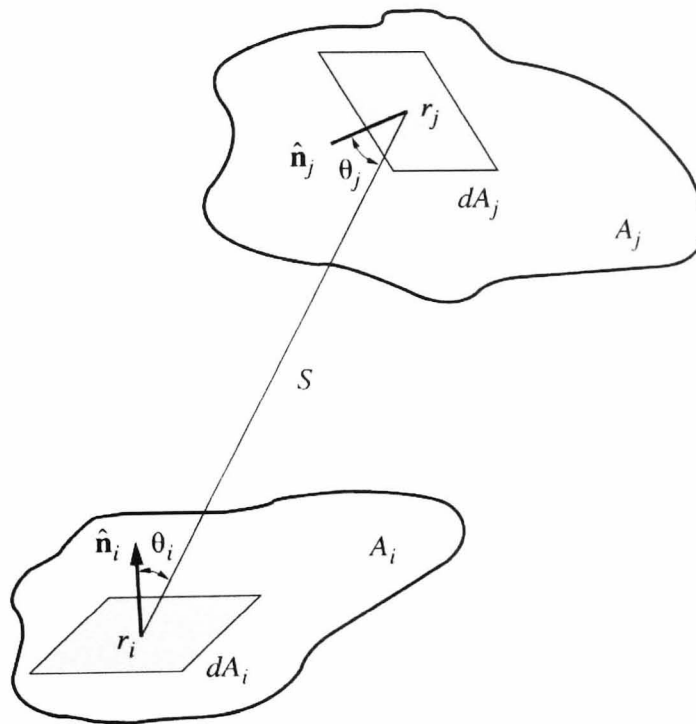


Figure 6.6 Schematic of viewfactor calculation between two elementary areas [108].

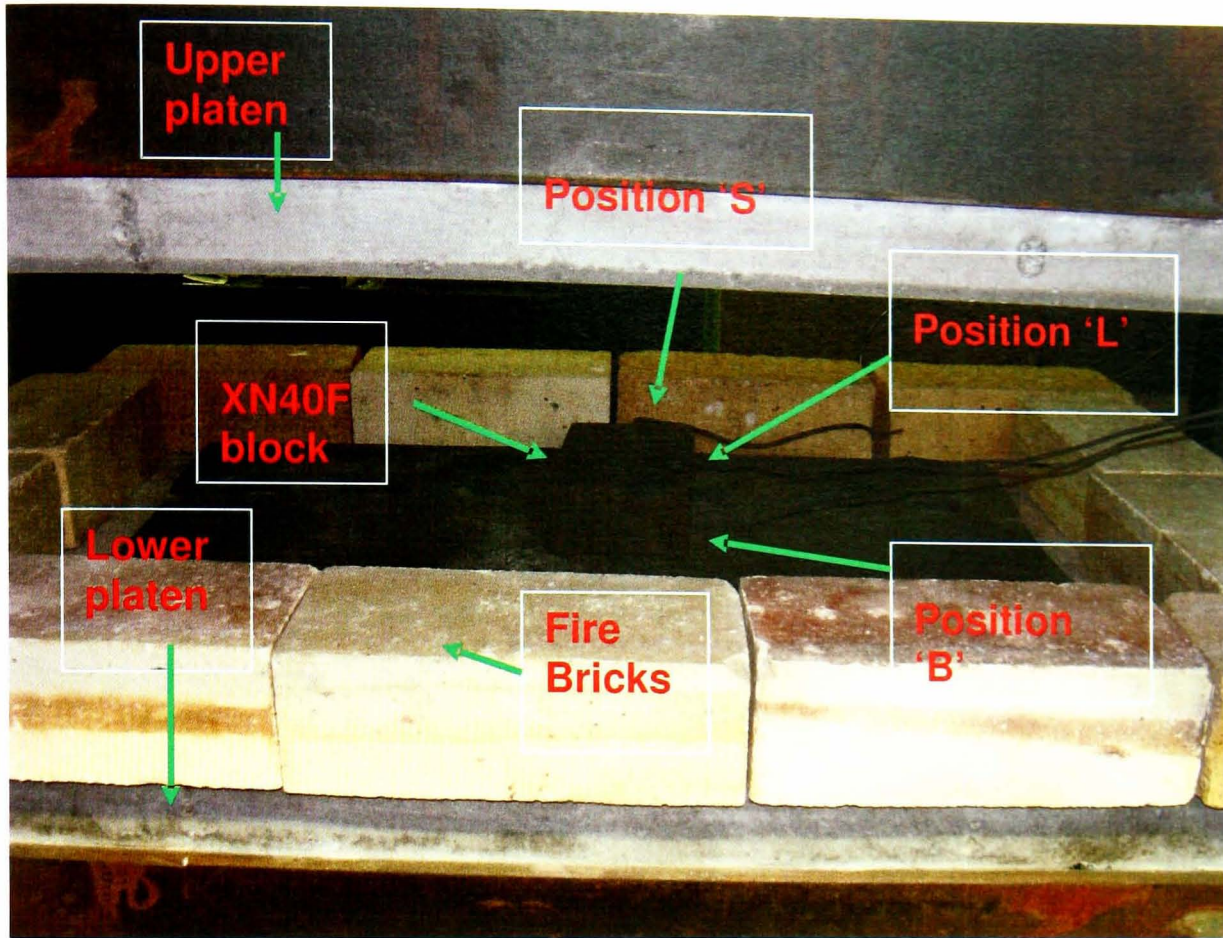
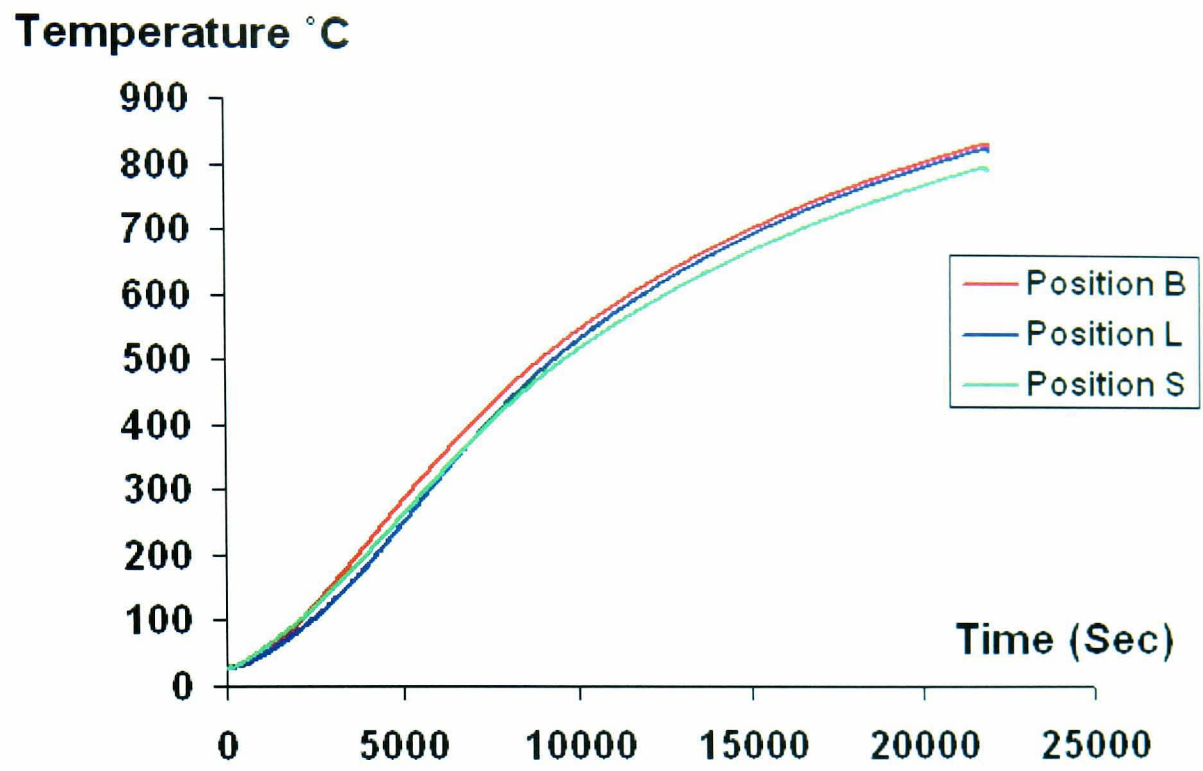


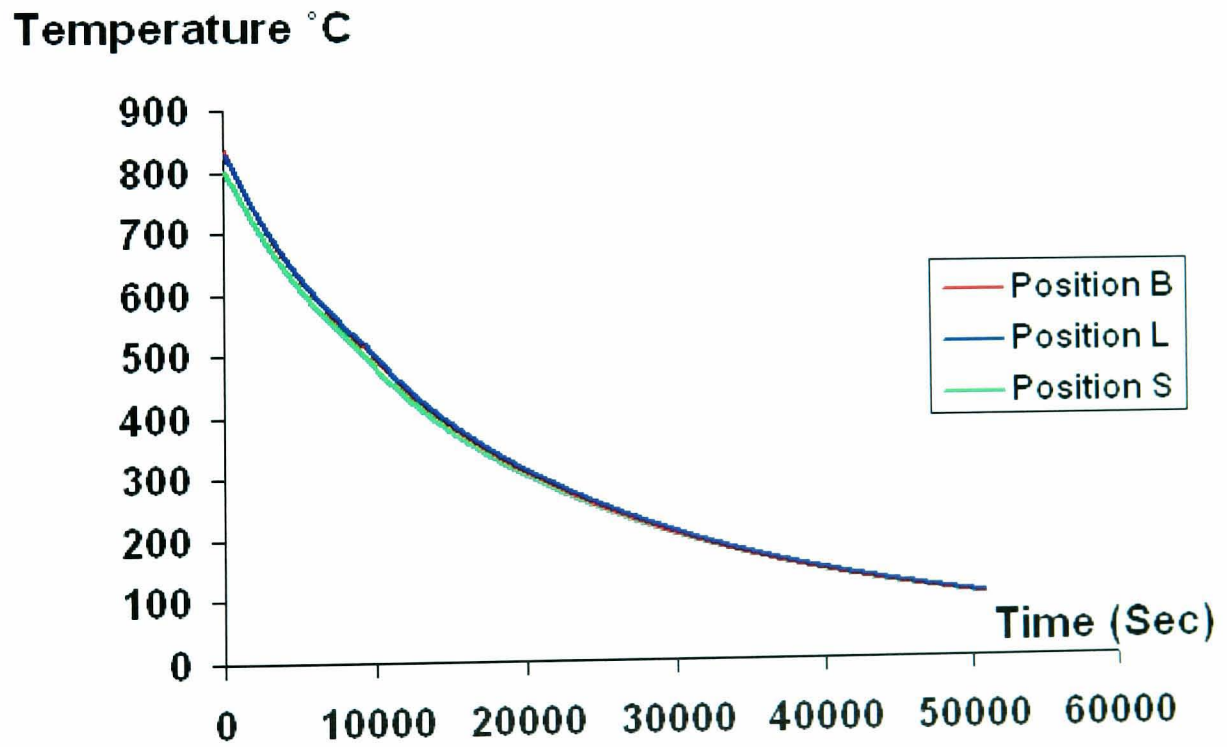
Figure 6.7 XN40F block heat transfer test set-up



Figure 6.8 University SPF press used for heat transfer test carried out on XN40F block.

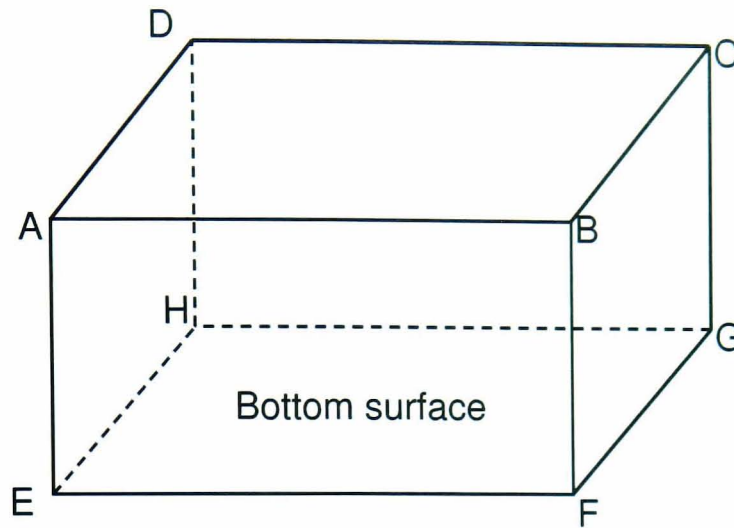


(a)



(b)

Figure 6.9 Measured thermal histories at various positions of the XN40F block; (a) heating phase, (b) cooling phase



EFGH- Conduction

ABFE and DCGH - Free convection and open radiation

ADHE and BCGF - Free convection and open radiation

Figure 6.10 Applied heat transfer mechanisms to different surfaces of the XN40F block

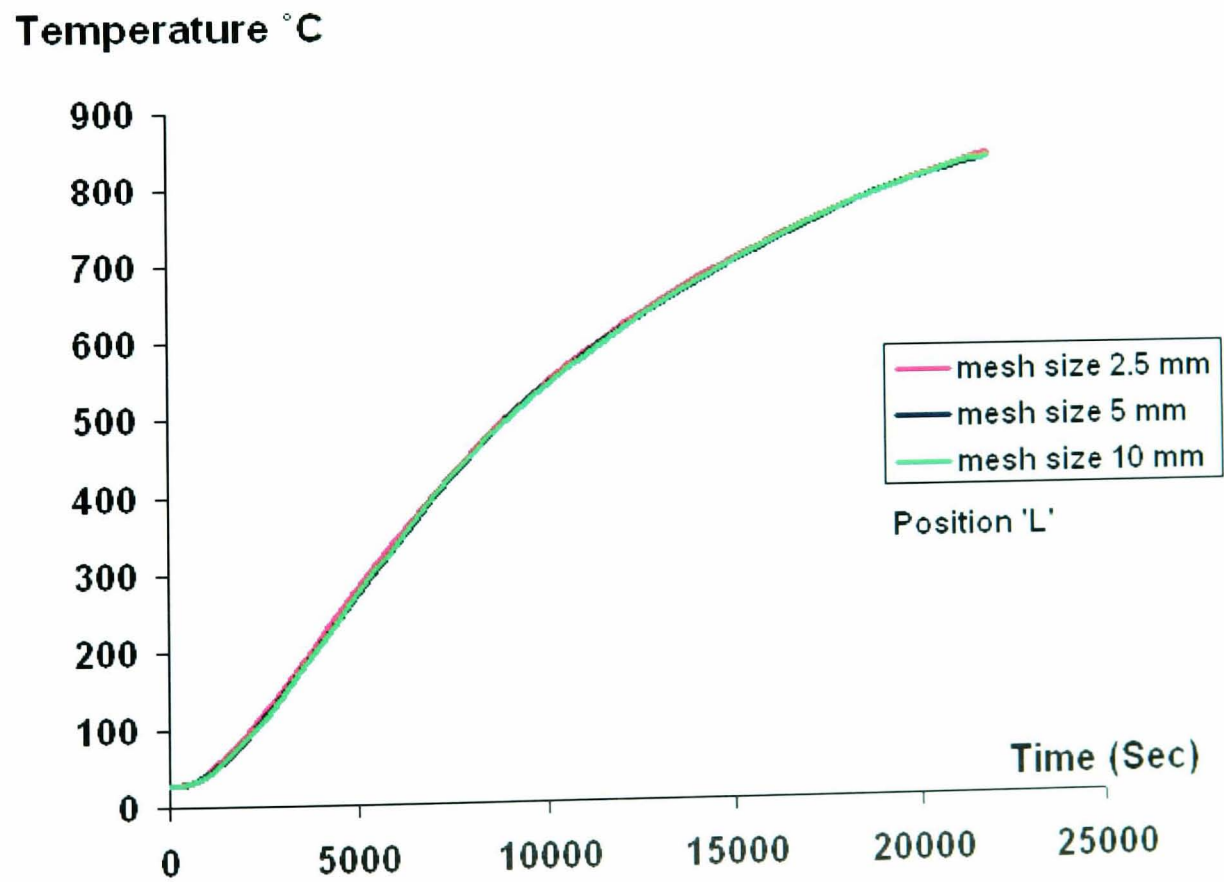


Figure 6.11 FE predicted thermal history of the XN40F block at position 'L' using different mesh sizes

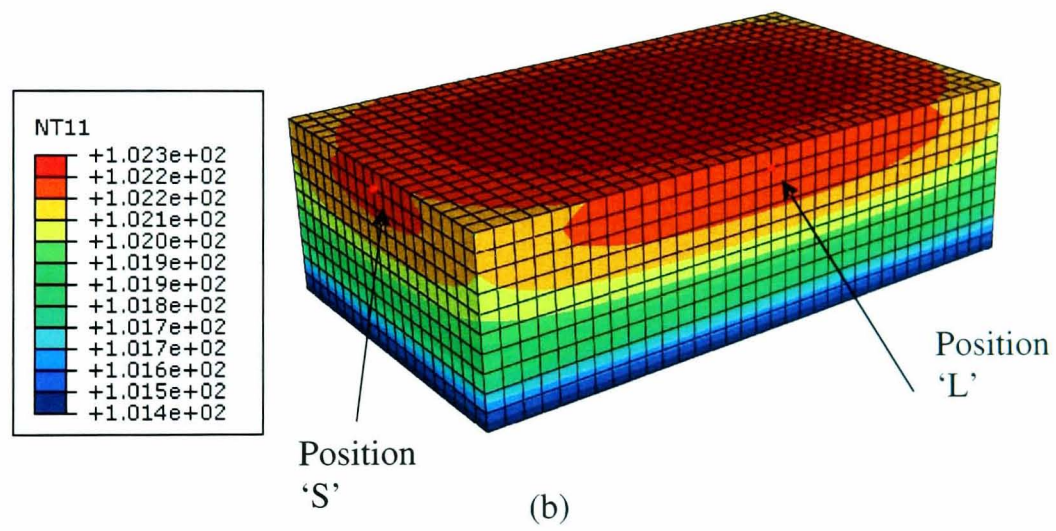
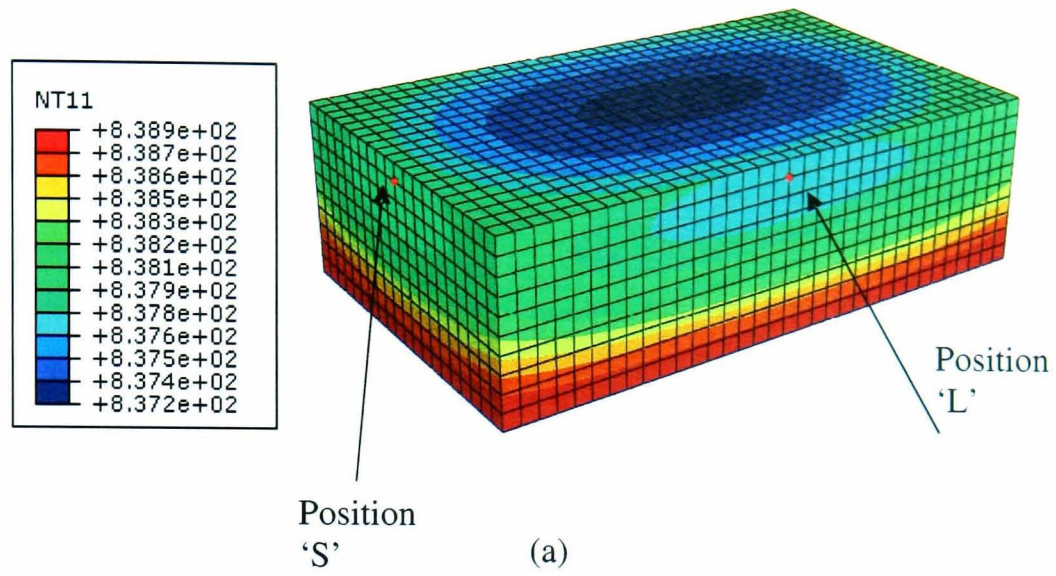
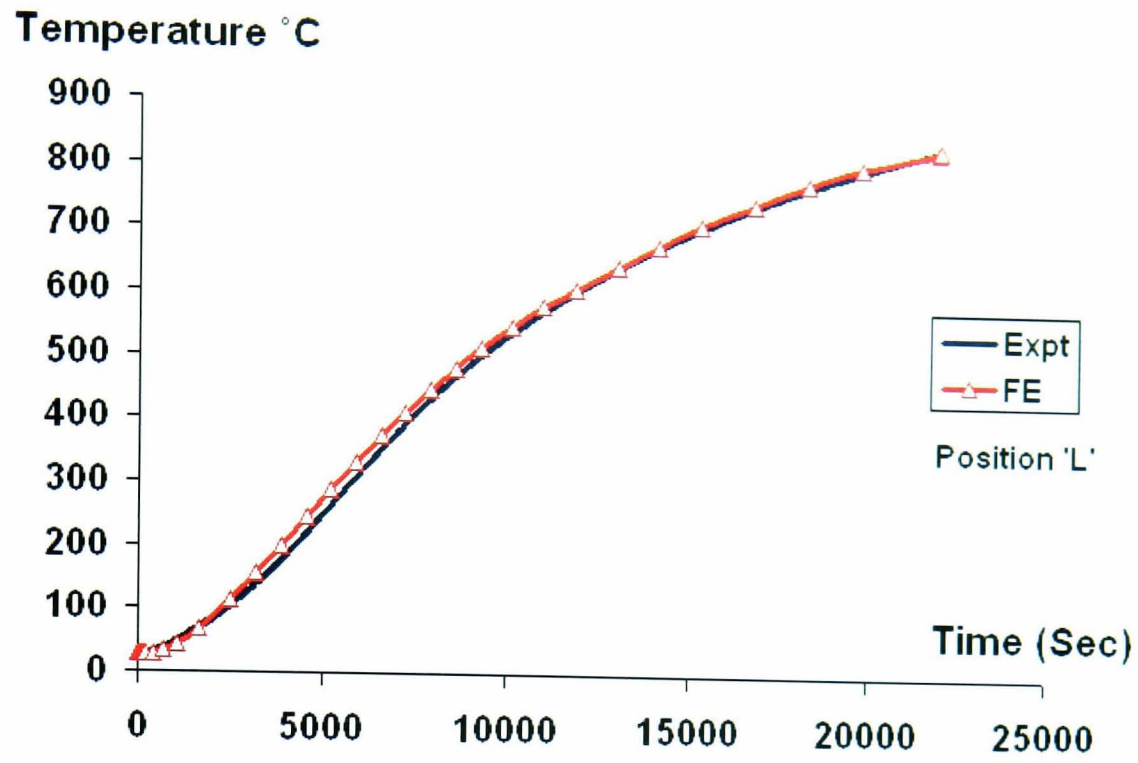
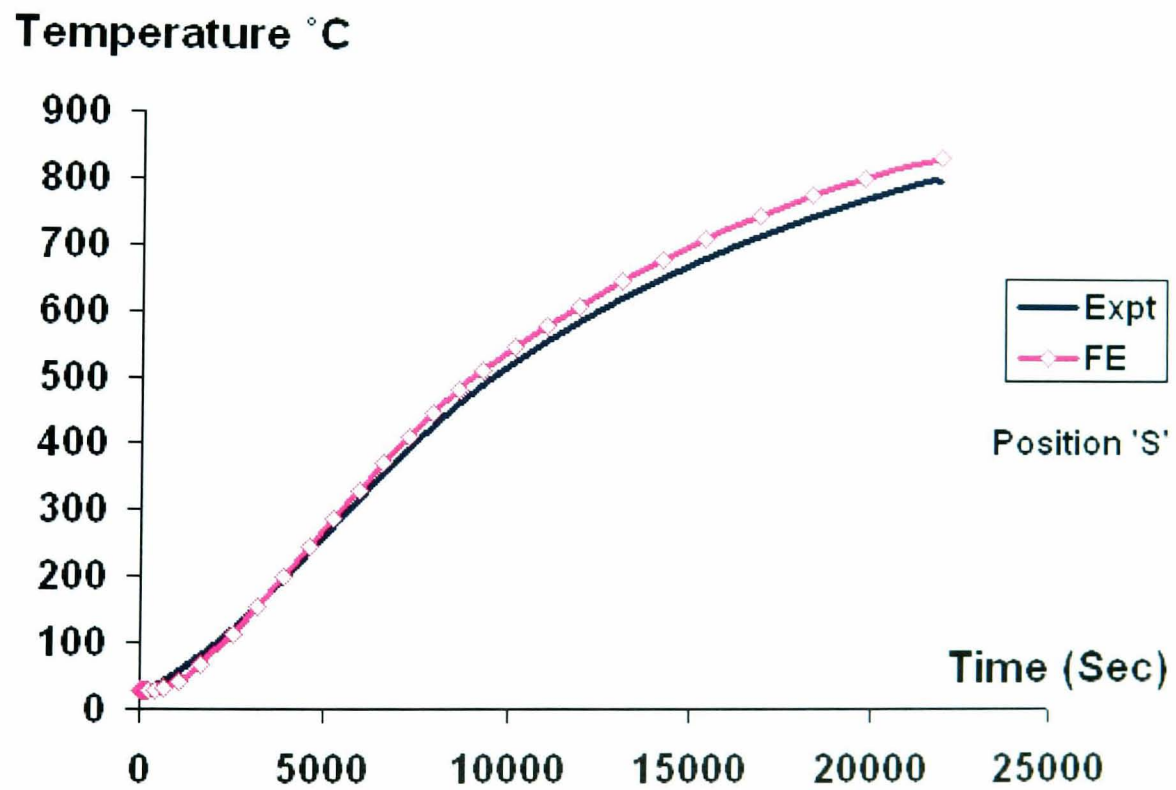


Figure 6.12 FE predicted nodal temperature contours of XN40F block at ; (a) end of heating phase, (b) end of cooling phase

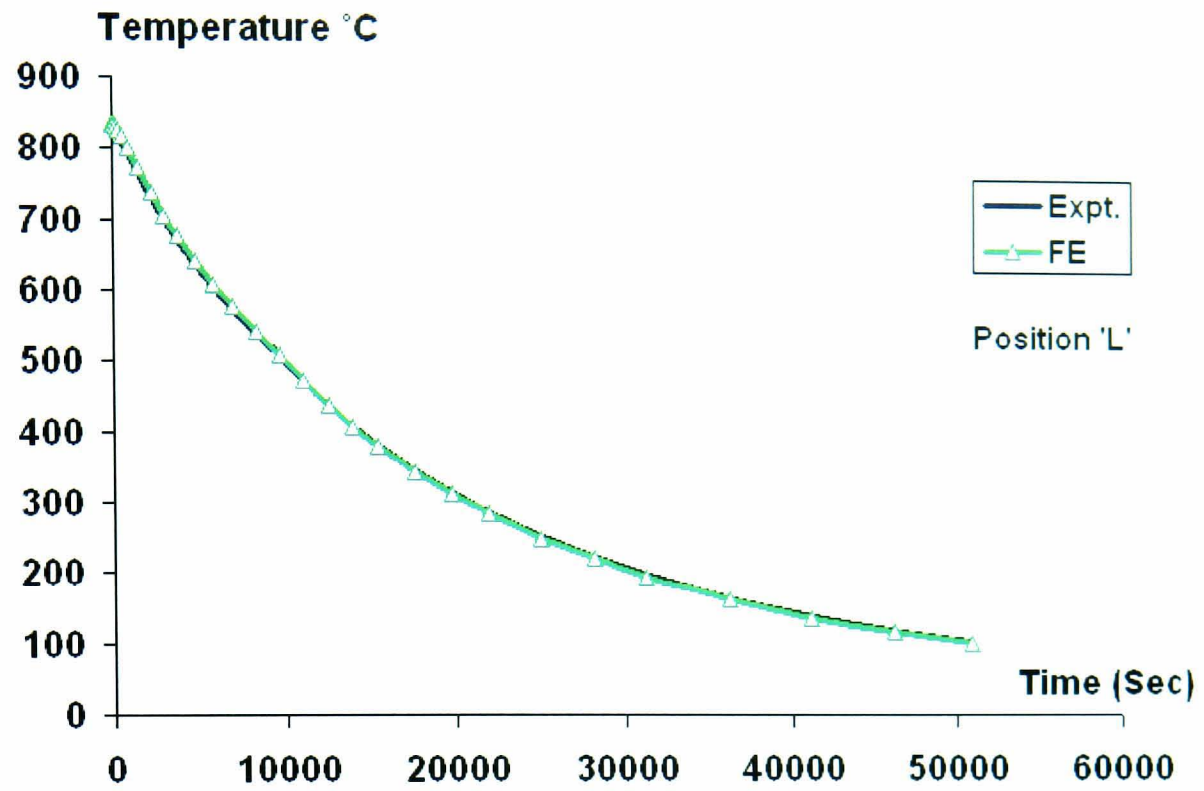


(a)

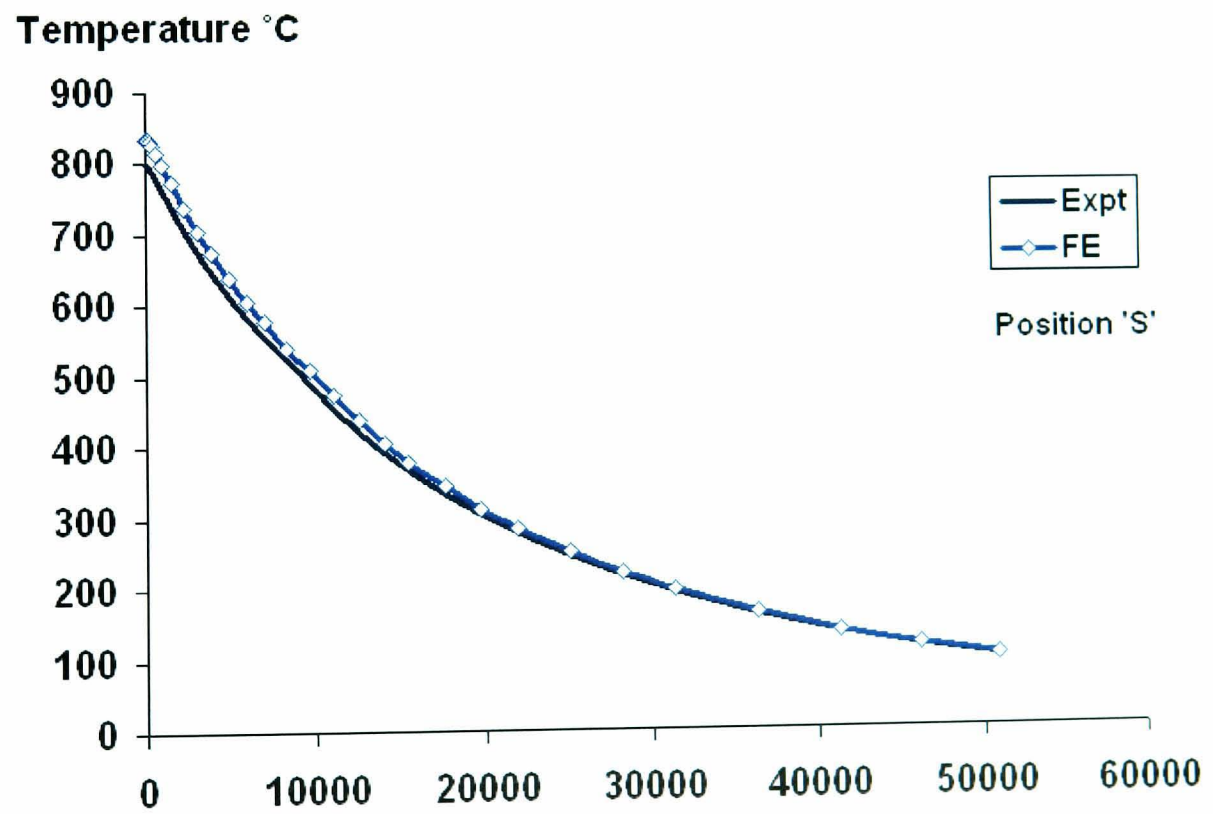


(b)

Figure 6.13 Comparison of FE versus measured thermal histories of XN40F block for heating phase; (a) position 'L', (b) position 'S'



(a)



(b)

Figure 6.14 Comparison of FE versus measured thermal histories of XN40F block for cooling phase; (a) position 'L', (b) position 'S'

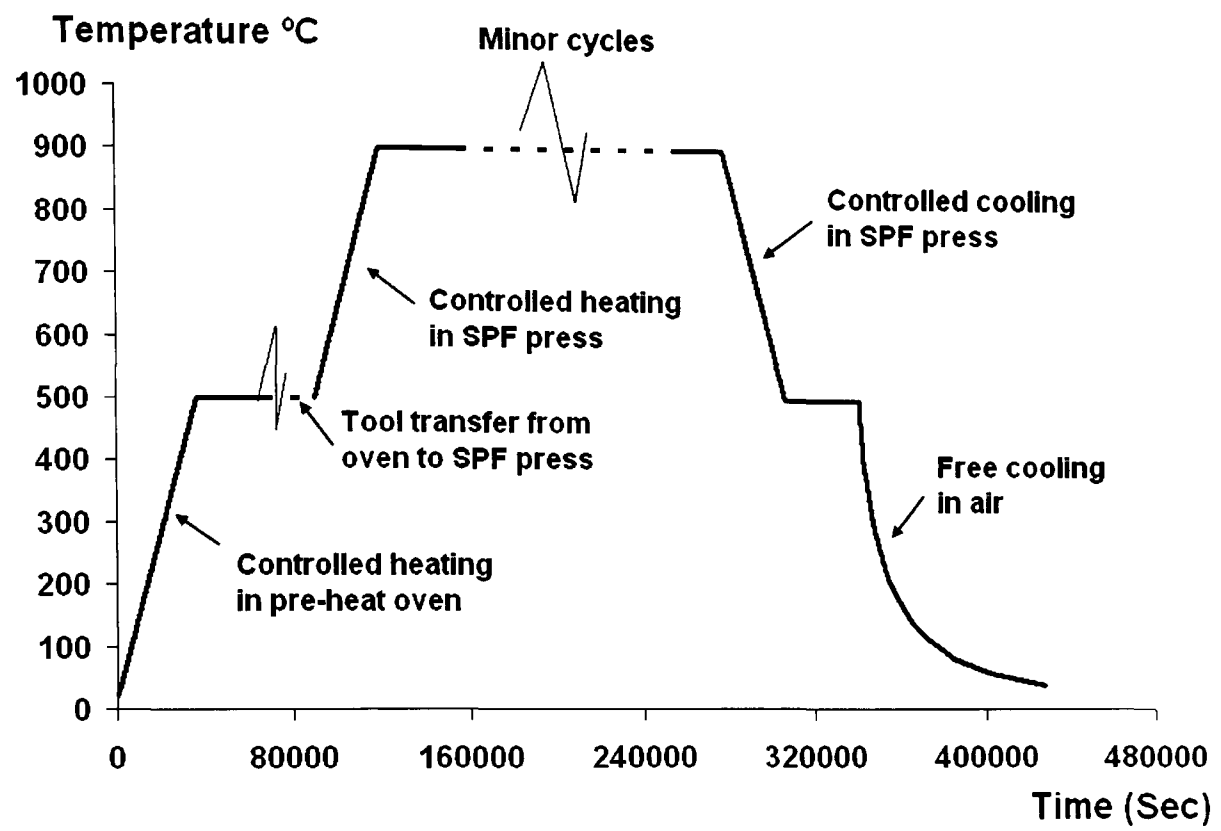
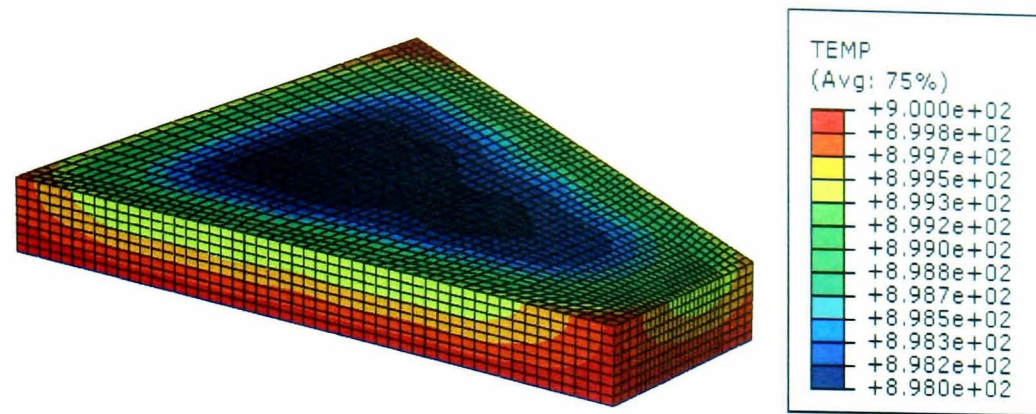
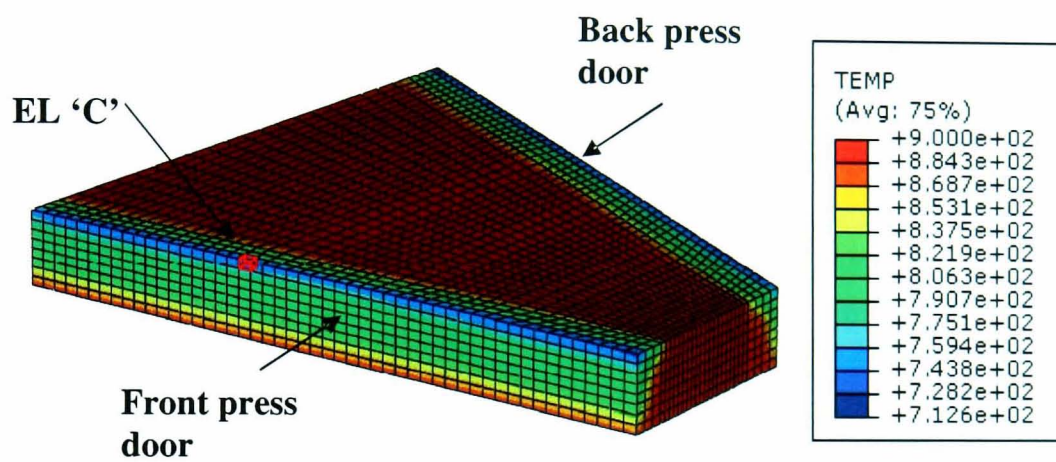


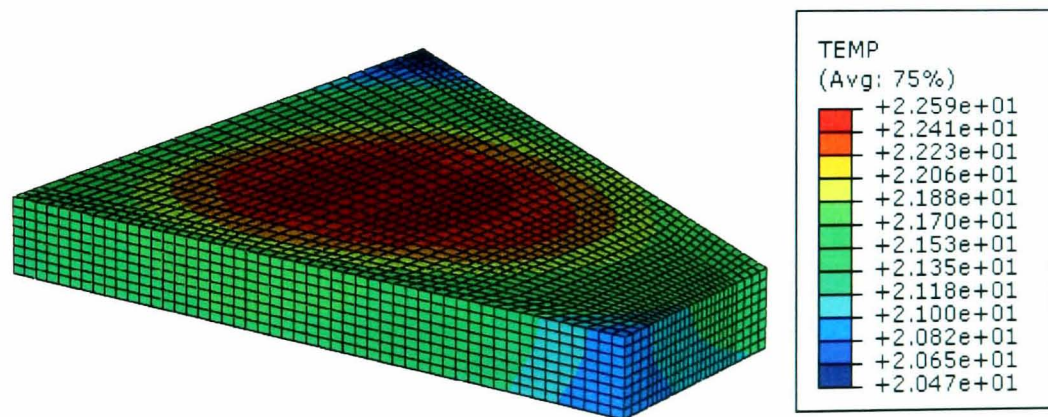
Figure 6.15 Specified temperature history of SPF tool



(a)

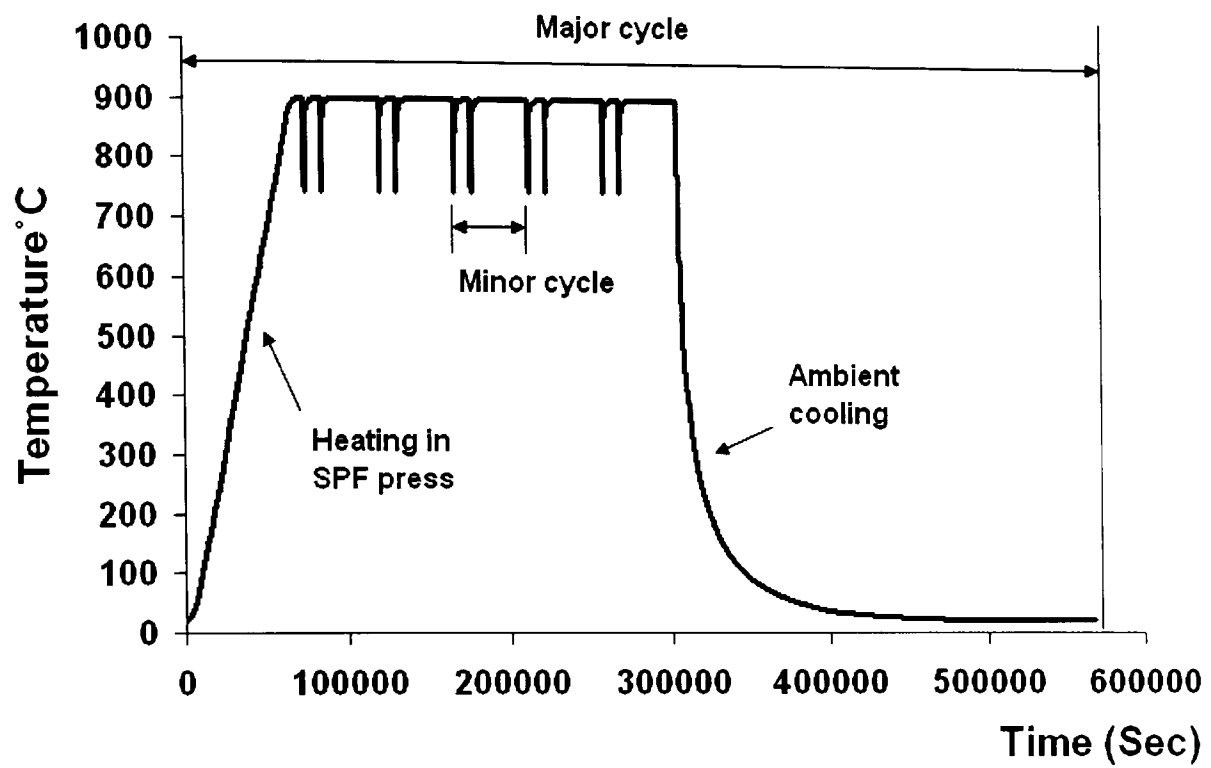


(b)

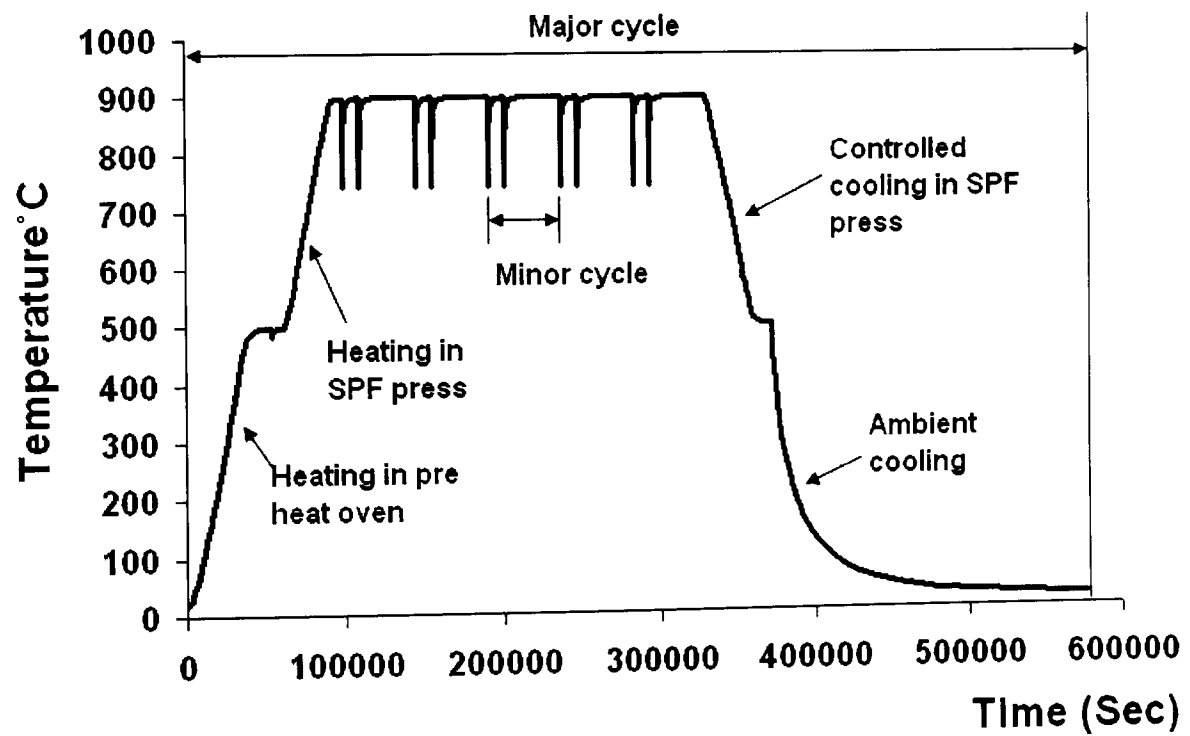


(c)

Figure 6.16 FE predicted temperature contours of lower half of simplified SPF tool ;  
 (a) end of heating to forming temperature, (b) end of blank inserts or part unload, (c)  
 end of ambient cooling



(a)



(b)

Figure 6.17 FE-predicted SPF tool thermal cycles at EL C; (a) thermal cycle-A, (b) thermal cycle-B

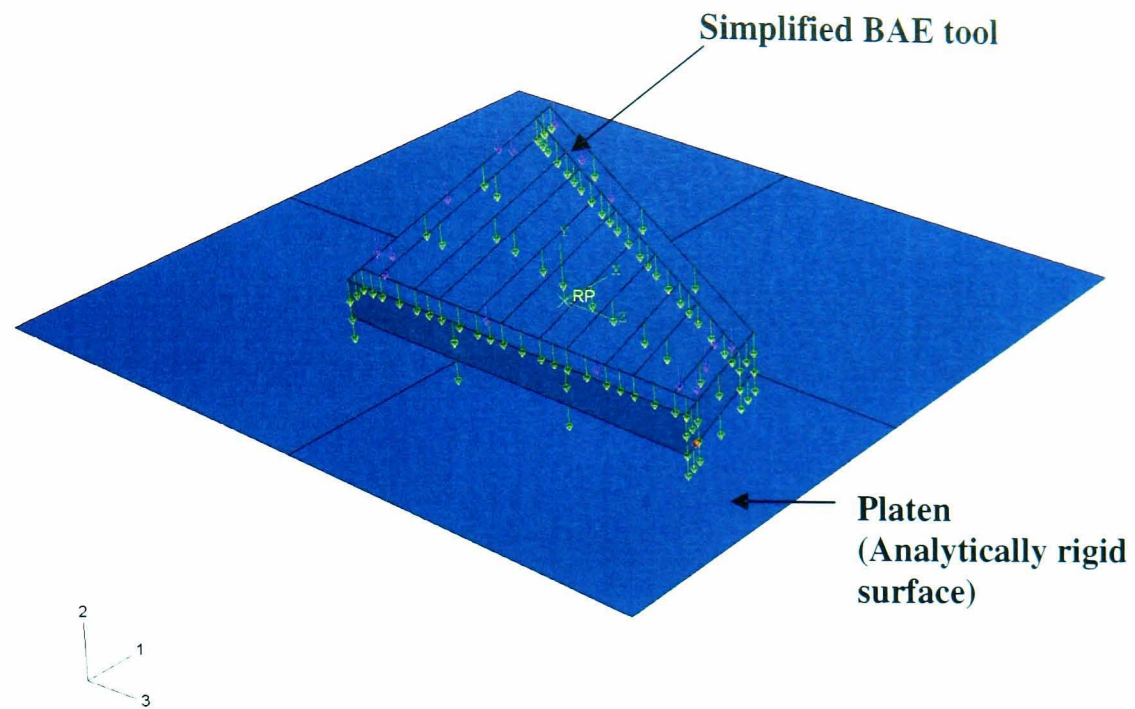


Figure 6.18 Lower half of Simplified SPF tool resting on platen with gravity and clamping pressure applied.

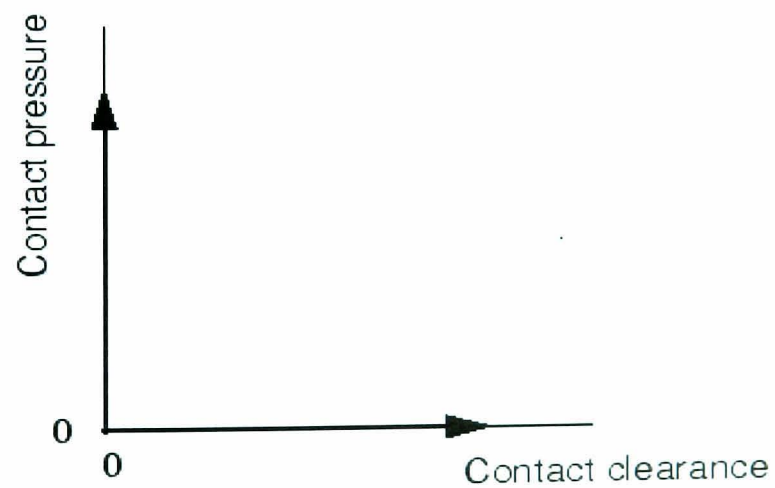


Figure 6.19 Contact pressure-clearance relationship for hard contact [100]

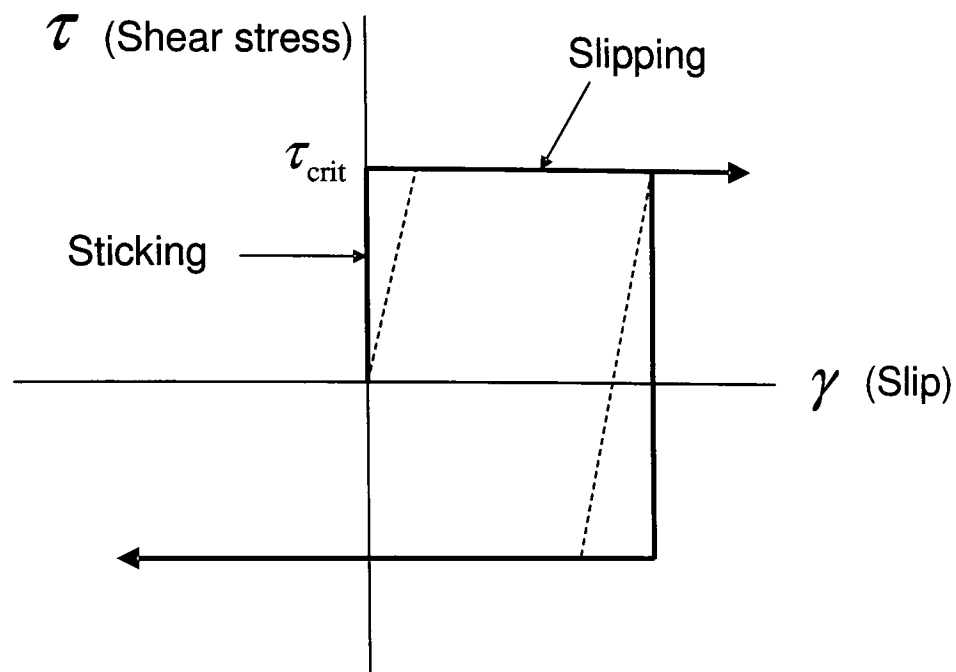


Figure 6.20 Frictional behaviour of contacting surfaces [100]

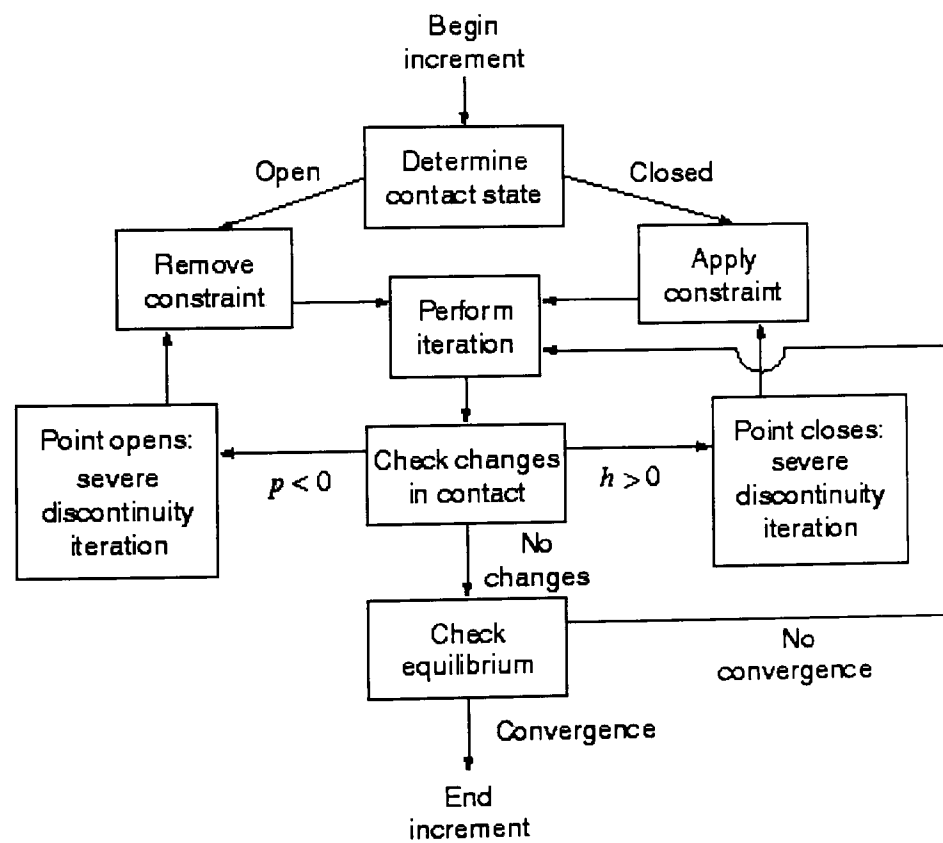


Figure 6.21 Contact algorithm [100]

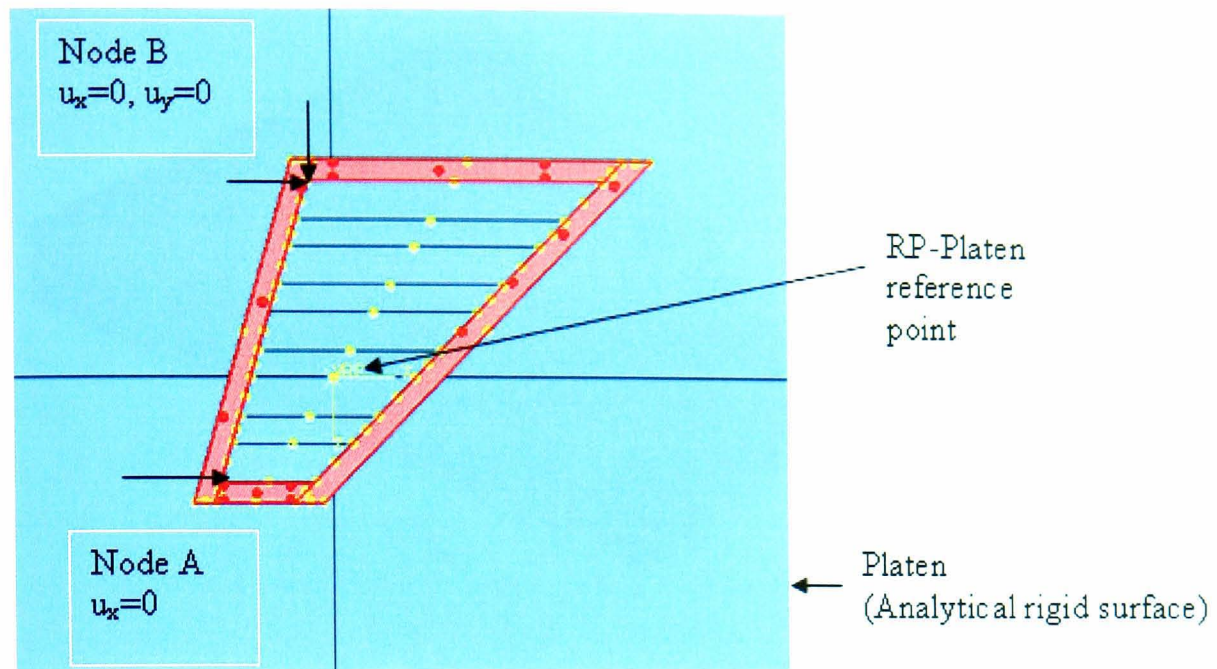


Figure 6.22 Mechanical boundary conditions and clamping pressure for FE model of SPF tool and platen.

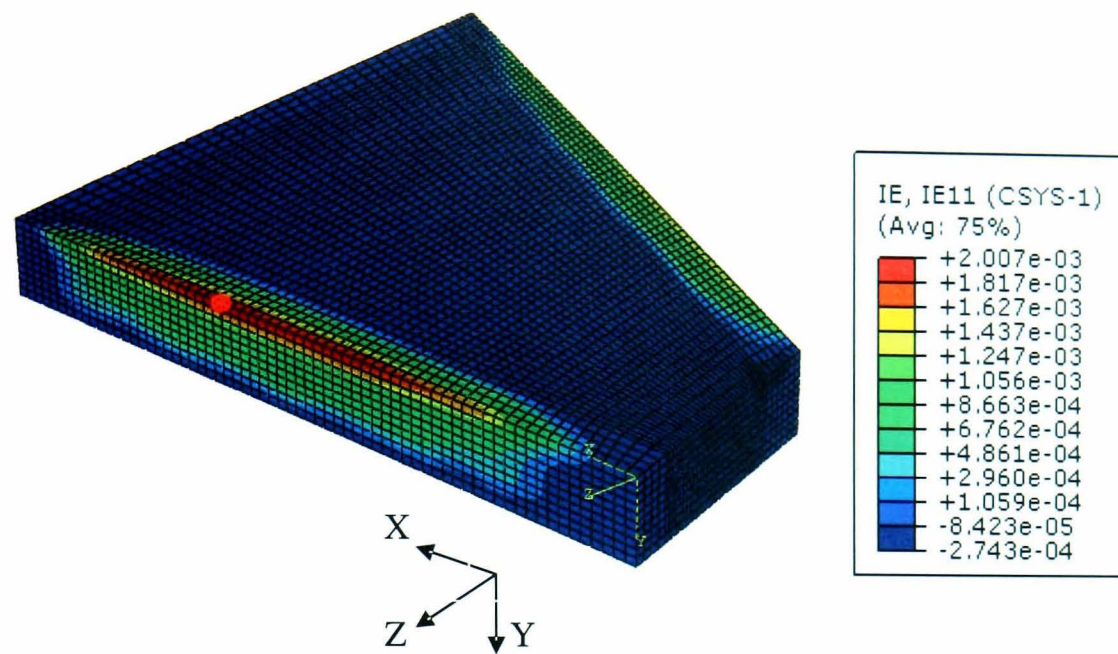


Figure 6.23 Inelastic strain distributions along local X-X direction at the end of part unload operation using fine mesh (see Table 6.6 for mesh size)

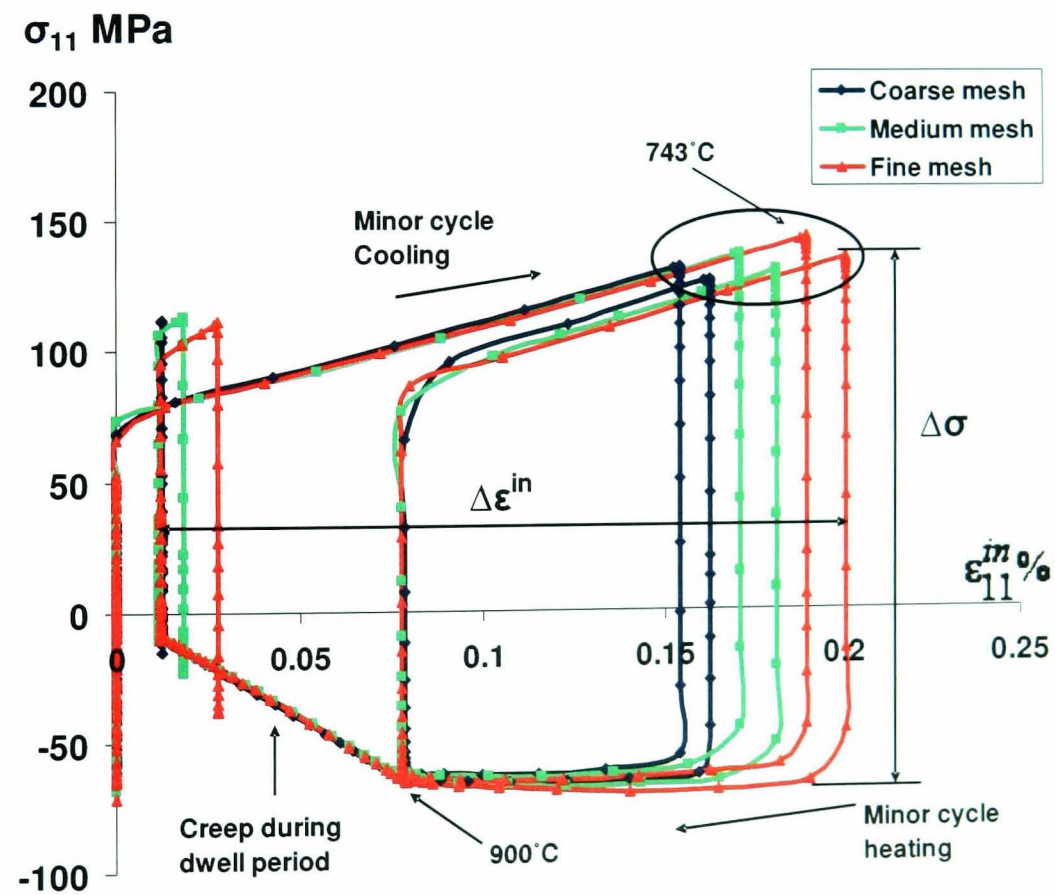


Figure 6.24 Predicted local stress (X-X) versus local inelastic strain (X-X) of a major cycle including a minor cycle at the critical element for three different mesh sizes (see Table 6.6 for mesh sizes).

## Chapter 7

### THERMO-MECHANICAL ANALYSES OF SPF TOOL

#### 7.1 Introduction

The chapter describes the results of various thermo-mechanical analyses carried out on a representative simplified SPF tool. Thermo-mechanical analyses were performed to analyse the effect of major and minor cycles, using identified XN40F material parameters and material behaviour models discussed in Chapter 4. Major cycles were further studied for analysing the effect of heating and cooling rates of the controlled heating and cooling phases of SPF tool thermal cycle. Minor cycles were also analysed to understand the effect of batch size i.e. number of components formed in a forming campaign (major cycle). SPF tool life predictions were also performed using different life prediction methodologies explained in Chapter 5.

Initially major (low frequency) cycles alone without any minor (high frequency) cycles were investigated to understand the effect of thermal cycles 'A' (Fig. 6.17a) and 'B' (Fig. 6.17b) described in Chapter 6. The combined nonlinear kinematic/isotropic hardening model was applied for analyses of major cycles alone. The results of thermal cycles 'A' and 'B' were compared and it was found that cycle 'A' is extremely detrimental to the SPF tool in comparison with cycle 'B'. Therefore thermal cycle 'B' with pre-heating and controlled cooling was considered for further investigation. The effects of heating and cooling rates were analysed for thermal cycle 'B'. Three different rates of 25°C/hr, 40°C/hr and 80°C/hr were studied and compared along with the general rate of 50°C/hr. Stress-strain loops and residual

nodal displacements for critical locations in the tool were plotted to analyse the effects of thermal cycles and controlled heating/cooling rates on tool damage.

Minor cycles representing blank insertion and formed part unloading along with a 7 hours forming period were analysed by performing thermomechanical analyses comprising of these higher frequency cycles within a major cycle. Two material models; an uncoupled cyclic plasticity-creep and a two-layer viscoplasticity model were implemented and the results were studied and compared. In the beginning, analyses for 3 major cycles each including 5 minor cycles were carried out using each of the above material models. The results were analysed and compared by plotting the stress-strain loops of critical elements. The distortion behaviour of the SPF the tool was also analysed by plotting residual nodal displacements, since the geometrical distortion can impair the dimension precision of formed components. The distortion behaviour was further studied by performing thermomechanical analyses of a major cycle with three different batch sizes (minor cycles) of 20, 30 and 40.

SPF tool life predictions were carried out using different life prediction methodologies such as the strain and strain energy methods. The ductility exhaustion method was also applied to predict the ratchetting life of the SPF tool. Predicted tool lives were analysed and compared with industrial observations and a representative TMF test carried out on the XN40F material (Chapter 3).

## 7.2 Effect of major cycles without minor cycles

A major cycle alone comprises heating of the SPF tool to the forming temperature of 900°C and cooling back down to ambient. Thermo-mechanical analyses of five major cycles without any minor cycles were carried out for thermal cycles A and B with a general heating and cooling rate of 50°C/hr. The combined non-linear kinematic/isotropic hardening material behaviour model with the material parameters identified in Chapter 4 was applied for those major cycle analyses. The creep deformation is not considered for these analyses since there is no dwell period at high temperatures. However the inclusion of creep may increase the predicted inelastic strain for the analyses of major cycles alone.

### 7.2.1 Effect of thermal cycle 'A'

Figure 7.1a and b show the FE-predicted von-Mises stress and accumulated equivalent plastic strain at the end of the five major cycles. Plasticity is predicted to occur mainly along the top free edges of the tool. A local co-ordinate system is defined in Fig. 7.1 where the  $X$  direction (also referred to as 1 direction) is parallel to the edge of the tool and the  $Y$ -direction (also referred to as 2-direction) is parallel to the thickness of the tool. A maximum of 144 MPa equivalent residual stress is predicted to occur at the end of 5<sup>th</sup> major cycle (Fig.7.1a). Fig 7.1b also shows the critical element C with maximum equivalent plastic strain along the top surface edge of the tool.

Fig 7.2 shows the predicted local stress,  $\sigma_{11}$  versus local inelastic strain  $\epsilon_{11}^{in}$  ( $\epsilon_{11}^{in} = \epsilon_{11}^p + \epsilon_{11}^{cr}$ ) for critical element EL 'C' shown in Fig. 7.1b. From Fig.7.2.

plasticity is predicted to occur during the cooling phase when thermal stresses exceed the temperature dependent yield stresses. The first yield is predicted during the cooling phase of 1<sup>st</sup> major cycle at 862°C and 0.17% inelastic strain is accumulated during the temperature drop from 862°C to 662°C. Compressive stresses are predicted for EL C primarily during the heating phase as the tool bottom surface is heated faster than the top surface, whereas tensile stresses are predicted during the part of the cooling phase where the tool bottom surface is cooled faster than the top surface considering the presence of the upper tool sitting on the lower tool. Plastic shakedown is predicted to occur after an initial transient ratchetting response for first three cycles. Therefore low cycle fatigue is likely to be a failure mode in this local direction which represents the uniaxial stress-strain behaviour along the top surface edge of the long side of the SPF tool.

A residual geometrical distortion of the tool is predicted at the end of ambient cooling. This is an important quantity for manufacturing tolerance on the formed components. SPF tool distortion behaviour is studied by plotting residual vertical nodal displacements along three different paths; 'P', 'Q' and 'R' defined in Fig.7.3. Paths P and R are defined along the top surface edges of the two long sides of the tool where path 'R' is the longest between the two. Path 'Q' is in the middle of the SPF tool forming surface. Fig 7.4 shows the predicted residual vertical ('Y' direction of local co-ordinate system) nodal displacement along paths 'P', 'Q' and 'R'. From Fig 7.4, progressive distortion behaviour is predicted where the rate of progression decreases with number of major cycles. For all three paths, residual displacement increases with distance from the end points and reaches a maximum towards the

middle portion. Maximum residual displacements of 0.92 mm for path 'R', 0.33 mm for path 'P' and 0.66 mm for path 'Q' are predicted at the end of 5<sup>th</sup> major cycle.

### 7.2.2 Effect of thermal cycle 'B'

For thermal cycle 'B', Fig. 7.5 shows the final predicted von-Mises stress and the accumulated equivalent plastic strain for this cycle. The local stress  $\sigma_{11}$  versus local inelastic strain  $\epsilon_{11}^{in}$  is plotted for a critical element EL D, in Fig. 7.5b. Similar to cycle 'A', plasticity is predicted across the top free edges. However elastic shakedown is predicted to occur for EL D as shown in Fig. 7.6. A maximum of 22 MPa equivalent residual stress is predicted to occur at the end of 5<sup>th</sup> major cycle (Fig. 7.5a). From Fig. 7.6, EL D is predicted to yield during the cooling phase of the 1<sup>st</sup> major cycle at 460°C. Furthermore a plastic strain of 0.017% is accumulated during cooling from 460°C to 370°C. From 2<sup>nd</sup> major cycle, EL D is predicted to have shaken down elastically for local X direction and the SPF tool failure is more likely to be due to high cycle fatigue which corresponds to significantly higher life than for cycle 'A'.

SPF tool distortion behaviour is also analysed in a similar fashion to that of cycle 'A'. The same three paths defined in Fig. 7.3 are employed to analyse vertical residual nodal displacement. The results are shown in Fig. 7.7. The key point is that the displacements are significantly smaller than for cycle 'A'. In contrast to cycle 'A', a maximum distortion is predicted at the end of the 1<sup>st</sup> major cycle and a small reduction in distortion is observed from the 2<sup>nd</sup> major cycle onwards. The same deformed shape is predicted for all three paths. Again a maximum residual

displacement is predicted in the middle part of all three paths with maximum predicted displacements of 0.03 mm, 0.045 mm and 0.05 mm for paths 'P', 'Q' and 'R'.

### **7.2.3 Comparison of thermal cycle 'A' and 'B'**

From the results described above, clearly, thermal cycle 'A' is more damaging than thermal cycle 'B'. At the end of the 5<sup>th</sup> major cycle, a maximum residual von-Mises stress predicted for thermal cycle 'A' is six times higher than for thermal cycle 'B' and the maximum inelastic strain for cycle 'A' is ten times higher than for cycle 'B'. Cycle 'A' has predicted plastic shakedown behaviour whereas cycle 'B' has predicted elastic shakedown. In comparison to cycle 'A' a negligible residual distortion is predicted for cycle 'B'. This demonstrates that the preheating and controlled cooling are always advisable over direct heating and cooling of cycle 'A'. Thermal cycle 'B' is considered below for further investigations of SPF tool damage mechanisms by analysing damaging factors such as heating and cooling rates and minor cycles.

## **7.3 Effect of heating and cooling rates**

The effect of heating and cooling rates is analysed by performing thermo-mechanical analyses for major cycle (cycle 'B') alone. In addition to the general rate of 50°C/hr, three different heating /cooling rates are explored. Thermo-mechanical analyses for five major cycles without any minor cycles are carried out for heating and cooling rates of 25°C/hr, 40°C/hr and 80°C/hr. Rates lower than the general rate are employed to investigate the possibility of improving the tool life. However the higher

rate of 80°C/hr is explored to analyse the option of improving productivity of the process by evaluating its effect on tool damage.

A local stress  $\sigma_{11}$  versus local inelastic strain  $\epsilon_{11}^{in}$  is plotted for all three rates at critical element EL D (Fig. 7.5). Figs 7.8, 7.9 and 7.10 respectively show the predicted local stress-strain loops of five major cycles for each of, 25°C/hr, 40°C/hr and 80°C/hr, heating and cooling rates. For 25°C/hr (Fig.7.8) and 40°C/hr (Fig.7.9), elastic shakedown is predicted to occur from 2<sup>nd</sup> major cycle which is significantly similar to the results of 50°C/hr (Fig.7.6).

From Fig.7.10 for 80°C/hr, plastic shakedown is predicted where compressive inelastic strain is also predicted during the heating phase. This leads to a tension-compression stress-strain loop. Fig 7.10 shows that during heating to 500°C in the pre-heat oven, the critical element yields in compression at 264°C and compressive inelastic strain of 0.017% is accumulated at 367°C. Furthermore while heating in the SPF press from 500°C to 900°C, EL D goes plastic at 753°C and further compressive inelastic strain of 0.044% is accumulated at 808°C. A high temperature gradient occurs between the bottom and the top surface of the tool due to the faster heating rate, which leads to inelastic compressive strain across the top surface edges of the tool. During controlled cooling to 500°C in the SPF press, tensile stresses are predicted across the top edges where EL D again yields at 848°C. Moreover an inelastic tensile strain of 0.02% is accumulated at 613°C.

Residual vertical nodal displacements for paths, 'P', 'Q' and 'R' are plotted for each of 25°C/hr, 40°C/hr and 50°C/hr at the end of 5<sup>th</sup> major cycle, as shown in Fig 7.11.

Fig. 7.11 shows that the predicted residual displacements for these rates are nearly the same for all three paths. Therefore lowering of the heating and cooling rate from a general rate of 50°C/hr is not predicted to be very useful. The distortion behaviour for 80°C/hr is separately studied in Fig. 7.12. The predicted distorted shape is opposite to that for the lower heating and cooling rates. Unlike the lower rates, the maximum distortion is predicted at the ends of the three paths. In terms of cycle to cycle changes, the maximum distortion for all three paths is predicted at the end of the 1st major cycle; this is predicted to decrease further with every major cycle. The predicted residual distortion at the end of the 5<sup>th</sup> major cycle for 80°C/hr is four times higher than for the lower rates of 25°C/hr, 40°C/hr and 50°C/hr and is up to ten times for fewer major cycles.

Residual stress is an alternative representation of thermally induced damage which occurs mostly when a structure is restrained to prevent distortion. These stresses result from change of shape of the tool due to plastic deformation and / or non uniform heating and cooling. Therefore the maximum residual tensile principal (S<sub>max</sub>), compressive principal (S<sub>min</sub>) and von Mises (S<sub>Mises</sub>) stresses predicted at the end of 5<sup>th</sup> major cycle are plotted and compared for the four different heating or cooling rates explored in Fig 7.13. The residual stresses for 25°C/hr, 40°C/hr and 50°C/hr are identical; however the stresses for 80°C/hr are much higher. The predicted tensile principal stress for 80°C/hr is 14 times higher than the respective predicted stresses for lower rates, while the compressive and von Mises stresses for 80°C/hr are predicted to be twice the respective values of lower rates. These results suggest that the higher heating rate of 80°C/hr is significantly more damaging than the lower rates. Therefore improving productivity of the process by faster heating or

cooling rates can damage the tool and also diminish the quality of formed products due to excessive distortion. Furthermore, lower rates such as 25°C/hr, 40°C/hr are not so useful in terms of improving the tool life. Therefore a general rate of 50°C/hr is considered optimum for further investigations of minor cycles.

## **7.4 Effect of minor cycles**

The effect of minor cycles on tool damage is analysed by performing thermo-mechanical analysis of three major cycles each including five minor cycles. A general heating and cooling rate of 50°C/hr is used for controlled heating and cooling of a major cycle. Two material models, the uncoupled plasticity-creep and the two layer viscoplasticity were employed in separate analysis for modeling the material behaviour of XN40F and the predicted results are analysed and compared.

### **7.4.1 Uncoupled plasticity-creep model**

In the case of the uncoupled plasticity-creep model, the cyclic plasticity during temperature transients is simulated using Chaboche combined non-linear kinematic/isotropic hardening model and the power law (Norton) creep is used to model the creep deformation at 900°C dwell period during which actual forming of component takes place.

Fig. 7.14 shows the FE-predicted accumulated equivalent plastic strain at the end of three major cycles, each including five minor cycles. Clearly, plasticity is predicted to occur along the top interface edges of the two sides of the tool facing the press doors. The temperature drops along these edges during part unloading and blank

inserts (from 900°C to 743°C), leading to large temperature gradients. Fig. 7.15 shows the predicted von-Mises stress history for EL 'E' (see Fig. 7.14) for the first major cycle, (including five minor cycles). A maximum of 66 MPa von-Mises stress is predicted to occur during transient heating in the preheat oven at 308°C, due to the temperature gradient between the bottom and the top surfaces as well as the core and the outer surfaces of the tool. The stress is predicted to be approximately zero at the end of the soaking period at 500°C, due to the uniform temperature in the tool. The stress is again predicted to increase during tool transfer from the preheat oven to the SPF press at 483°C, due to the temperature gradient developed during transfer. Similar to heating in the pre-heat oven, a maximum of 40 MPa stress is predicted to occur during transient heating to 900°C in the SPF press. Stress is again predicted to drop down to approximately zero during soaking at 900°C. Furthermore, a very high stress is predicted at the end of part unload and blank insert. This is due to the large temperature gradient of 157°C occurring between the two long exposed side edges and rest of the tool. A maximum of 130 MPa stress is predicted to occur at 743°C for part unload of the 1<sup>st</sup> minor cycle which is further predicted to increase slowly with number of minor cycles. The stress is again predicted to drop back to 60 MPa when the tool is heated back to 900°C after every part unload and blank insert operation. This is followed by stress relaxation due to creep from 60 MPa to 7 MPa in seven hours dwell period (forming cycle) at 900°C. After five minor cycles the tool is cooled down to ambient in two stages: controlled cooling in the SPF press to 500°C and cooling to ambient in free air by removing the tool from the SPF press. A maximum of 35 MPa equivalent stress is predicted during controlled cooling at 528°C whereas 119 MPa stress is predicted during open air cooling at 369°C.

Local stress-strain loops along  $X$  direction are plotted for the critical element 'E' where the  $X$  direction (also referred to as 1 direction) is parallel to the edge of the tool on which EL E is present (see Fig. 7.14). Fig. 7.16 shows the predicted local stress  $\sigma_{11}$  versus local mechanical strain  $\epsilon_{11}^{me} (\epsilon_{11}^{tot} - \epsilon_{11}^{th})$  for three major cycles (each including five minor cycles) while Fig. 7.17 shows the predicted local  $\sigma_{11}$  stress versus inelastic strain,  $\epsilon_{11}^{in}$ . The temperature drop to 743°C along the top interface edges of the two sides of the tool facing the press doors, leads to plasticity deformation, as shown in Figs 7.16 and 7.17, due to the thermal stresses exceeding the temperature-dependent yield stress. The local tensile stress  $\sigma_{11}$  at the end of part unloading and blank inserting is predicted to drop back to compressive 60 MPa during re-heat back to 900°C. The stress is seen to relax from 60 MPa to 7 MPa during the dwell time at 900°C, due to creep deformation. The constant clamping pressure of 4 MPa across the edges of the top four sides of the tool is also introduced during the dwell time at 900°C. Plastic shakedown is predicted to occur for this combination of stress-strain components, which essentially represents the normal stress-inelastic strain response parallel to the long side of the tool. This suggests that low cycle fatigue is a likely failure mode for this direction.

To understand the minor cycle and anisothermal stress-strain response, the local stress-strain response is plotted for the first minor cycle of the first major cycle in Fig. 7.18, for EL E. The compressive stresses are mainly predicted during the heating-up process to 900°C, because EL E is on the top surface of the tool and heats up slower than the bottom surface of the tool. During tool transfer from the pre-heat oven to the SPF press, tensile stress is predicted due to the bottom surface cooling faster than the top surface, which is modelled by assuming the lower half of the tool

is being in contact with the upper half of the tool (via an adiabatic boundary condition). During part unloading and blank inserting, a tensile stress is predicted due to the temperature dropping to 743°C whereas the bulk of the tool (i.e. away from the press doors) remains at 900°C. A plastic strain of 0.18% is predicted at the end of the blank insert operation (see Fig. 7.21). The elastic recovery followed by the compressive plastic strain is predicted during re-heat back to 900°C after every part unload and blank insertion operation. The compressive creep is predicted to follow the compressive plasticity during the dwell time along with stress relaxation. Hence, the analyses predict low cycle fatigue and fatigue-creep interaction damage across the local  $X$  direction. Fig. 7.18 also shows the inelastic strain ranges  $\Delta\epsilon_{pp}$  and  $\Delta\epsilon_{pc}$  for minor cycles, where  $\Delta\epsilon_{pp}$  corresponds to tensile plasticity reversed by compressive plasticity and  $\Delta\epsilon_{pc}$  corresponds to tensile plasticity reversed by compressive creep.

In addition to the cyclic plasticity and plasticity reversed by creep cycles, a progressive deformation or ratchetting phenomenon is also predicted along the top edges of the tool. This phenomenon results from the fact that the reversed creep strain accrued during the dwell time of the minor cycles does not completely reverse the plastic deformation accrued (due to thermal gradients) during the part unload and blank insertion processes. This phenomenon is illustrated in Fig.7.19, for EL E. Fig.7.19a, b and c respectively show the predicted temperature versus strain responses of local inelastic strains;  $\epsilon_{22}^{in}$ ,  $\epsilon_{23}^{in}$  and  $\epsilon_{33}^{in}$ . These plots clearly illustrate the progressive strain accumulation. Tensile ratchetting strain is predicted for the  $Z$ -direction while compressive ratchetting strain is predicted for the  $Y$ -direction

(vertical), leading to an effectively shear-driven ratchetting process (the local strain components correspond to principal strain directions), where the shear is approximately transverse to the  $X$ -direction and the shear strain  $\epsilon_{23}^{in}$  is approximately equal in magnitude to the average of  $\epsilon_{22}^{in}$  and  $\epsilon_{33}^{in}$ . The inelastic strain accumulation is predicted to increase approximately linearly in the  $Y$  ( $\epsilon_{22}^{in}$ ) and  $Z$  ( $\epsilon_{33}^{in}$ ) direction. Fig. 7.19 shows that the predicted ratchetting is restricted to the temperature range of 743°C to 900°C which corresponds to the minor cycles. Therefore ratchetting is predicted to occur during minor cycles in the plane transverse to the local  $X$  direction.

#### **7.4.2 Two-layer viscoplasticity model**

In this model the stress is partitioned into elastic-viscous and elastic-plastic components and the two components are in parallel with each other. The details of the material model are described in Chapter 4.

The elastoplastic network is defined by the combined non-linear kinematic/isotropic hardening whereas elasto viscous network is defined by the power law creep. The ratio  $f$  (equation 4.26) decides the contribution of elastic-plastic and elastic viscous components by apportioning the total moduli specified for the elastic behaviour between elastic-viscous and elastic-plastic networks. The identified  $f$  value for XN40F alloy at 700°C and 900°C (Chapter 4, Table 4.4) is applied in thermo-mechanical analyses with linear interpolation. No time dependent deformation is assumed below 600°C and therefore  $f$  value at 600°C is assumed to be zero.

Thermomechanical analysis for three major cycles each comprising five minor cycles is carried out using the two-layer viscoplasticity model. Similar to uncoupled-plasticity-creep model results, inelasticity is predicted to occur along the top interface edges of the two long sides of the SPF tool due to time dependent as well as time independent deformation occurring majorly during minor cycles. The results are again focused on EL 'E' which is one of the predicted critical locations of the SPF tool (see Fig. 7.14). Figs. 7.20 to 7.22 show the corresponding predicted results for the two-layer viscoplasticity model. Fig.7.20 shows the predicted von-Mises stress history for EL 'E' in the first major cycle. From Fig. 7.20, the predicted stresses occurring during heating phases to forming temperature and cooling down to ambient are approximately the same as for the uncoupled-plasticity-creep model. However the magnitude of stresses at the end of part unloading and blank insert operation is predicted to be 89 MPa which is significantly lower than the uncoupled model. This is due to the time dependent deformation occurring above 600°C. The stress is predicted to decrease to 10 MPa when the tool is heated back to 900°C after every part unload and blank insert operation. This is followed by seven hours dwell period where the stress is merely relaxed from 10 MPa to 7MPa.

Figs. 7.21 and 7.22 respectively show the local stress  $\sigma_{11}$  versus local mechanical strain  $\epsilon_{11}^{me}$  and local inelastic strain  $\epsilon_{11}^{in}$ , loops. Unlike the uncoupled model, some inelastic deformation is predicted to occur at 710°C during heating to forming temperature, due to viscoplastic deformation. The temperature drop to 743°C along the top interface edges during part unload and blank insertion, leads to inelastic deformation, as shown in Figs 7.21 and 7.22. This inelastic deformation comprises of time independent as well as time dependent deformation. The local tensile stress  $\sigma_{11}$

occurred at the end of minor cooling processes is predicted to change to compressive 39MPa at 815°C during re-heat back to 900°C, which relaxes to 10 MPa compressive at 900°C with a full recovery of the tensile inelastic strain by the end of part unload and blank insert phase. This is largely due to time dependent deformation at high temperature. The predicted stress then relaxed from 10 MPa to 7 MPa during the dwell time at 900°C. Plastic shakedown or reversed inelasticity is predicted to occur along local X direction.

Similar to Fig. 7.18 for the uncoupled model, the local stress-strain response is plotted for the first minor cycle of the first major cycle in Fig. 7.23. The compressive stresses are mainly predicted during the heating-up process to 900°C leading to compressive inelastic strain occurring at 710°C. Tensile stress is predicted due to the temperature dropping to 743°C along the sides during minor cooling processes. An inelastic tensile strain of 0.25% is predicted to occur at the end of the minor cooling. Elastic recovery followed by reversed inelastic strain is predicted during the re-heat back to 900°C after every minor cooling operation. Inelastic strain is fully reversed at the end of re-heating to 900°C. This is largely due to viscoplastic deformation occurring between 815°C to 900°C. Unlike the uncoupled model the dwell period creep is predicted to be negligible in the case of two-layer viscoplasticity model. Again the predicted stress-strain loops (along local X direction) show plastic shakedown behaviour with a higher inelastic strain range and a lower stress range than the uncoupled model mainly due to time dependent deformation predicted during minor cycles. However no progressive deformation or ratchetting phenomenon is predicted by the two-layer viscoplasticity model since the inelastic

strain after every minor cooling is predicted to be fully reversed during re-heating to 900°C.

## 7.5 Effect of batch size

In the present work of SPF tool analyses, batch size means the number of parts formed in a single forming campaign, i.e. number of minor cycles per major cycle. The effect of batch size is mainly analysed in terms of predicted progressive deformation behaviour. Thermo-mechanical analyses are carried out for four different batch sizes; 5, 20, 30 and 40. The uncoupled plasticity-creep model is primarily used in analysing the effect of batch size since the minor cycle ratchetting behaviour is predicted by this model. However a representative thermo-mechanical analysis for a batch size of 40 is also performed using the two-layer viscoplasticity model.

Thermo-mechanical analyses for a major cycle which includes 40 minor cycles are carried out. Fig. 7.24 shows the evolution of the mean local inelastic strains,  $\epsilon_{11,m}^{in}$ ,  $\epsilon_{22,m}^{in}$  and  $\epsilon_{33,m}^{in}$ , with number of minor cycles using the uncoupled plasticity creep-model. Tensile incremental growth is predicted in the Z-direction with approximately 0.4% mean inelastic strain accumulated over 40 minor cycles, while compressive incremental deformation is predicted in the Y-direction with approximately 0.5% mean inelastic strain accumulated over 40 minor cycles. No ratchetting is predicted in the X-direction where a constant mean strain  $\epsilon_{11,m}^{in}$  of 0.085% is predicted over 40 minor cycles as shown in Fig. 7.24.

In the case of the two-layer viscoplasticity model, no minor cycle ratchetting is predicted for any of the local directions as shown in Fig. 7.25. The mean local inelastic strains versus number of minor cycles for two-layer viscoplasticity model is shown in Fig. 7.25. For the local X direction, a constant tensile mean strain  $\epsilon_{11,m}^{in}$  of 0.125% is predicted over 40 minor cycles. However an approximately constant compressive mean strain,  $\epsilon_{22,m}^{in}$  of 0.08% and  $\epsilon_{33,m}^{in}$  of 0.044% is predicted over 40 minor cycles. Therefore no progressive deformation is predicted for the two-layer viscoplasticity model and hence the uncoupled plasticity-creep model is employed to analyse batch size effect on tool damage by plotting residual deformation and residual stresses for different batch sizes at the end of a major cycle.

Initially, residual deformation is studied by plotting residual nodal vertical displacements (Y direction) along paths 'P', 'Q', and 'R', for 3 major cycles with batch sizes of five and twenty each as shown in Fig. 7.26. Progressive distortion behaviour is predicted for Path 'P' (Fig. 7.26a) and 'R' (Fig. 7.26b) where the distortion is predicted to progress in compressive direction. Distortion along paths 'P' and 'R' for a batch size of twenty is predicted to be approximately four times higher than for a batch size of five. This is primarily due to accumulation of inelastic strains occurring along these edges during minor cycles. Significantly smaller distortion is predicted along Path 'Q' for both the batch sizes, yet the distortion predicted for a batch size of twenty is higher in magnitude than the batch size of five. No progressive deformation is predicted along Path 'Q' (Fig.7.26c) for a batch size of five as the residual displacements are predicted to stabilise after the first major cycle. However a progressive deformation with a decreasing rate is predicted along path 'Q' for a batch size of twenty.

A broader study on the effect of batch size on tool damage is evaluated by comparing residual vertical nodal displacements for batch sizes of 0, 5, 20, 30 and 40. Residual stresses are also compared. Fig. 7.27 shows the predicted results along paths 'P', 'Q' and 'R'. For paths 'P' and 'R', a positive vertical residual displacement is predicted for zero batch size (without minor cycles) and this is predicted to evade into a negative direction with increasing batch size (Figs 7.27a and 7.27b). For path 'Q', shown in Fig. 7.27c, the residual displacement is predicted to increase from low values at the end nodes to the middle portion, for batch sizes of 0 and 5; however for batch sizes 20, 30 and 40, the larger magnitudes are predicted at the end nodes with a minimum value towards middle portion of the path. From batch sizes of 20, 30 and 40 the distortion is predicted to increase rapidly with increasing batch size of the ends of the path 'Q'. From Figs. 7.26 and 7.27, residual distortion is predicted to increase linearly with increasing batch size along paths 'P' and 'R', mainly due to the predicted local ratchetting. For path 'Q', the distortion is predicted to increase non-linearly with increasing batch size.

Fig. 7.28 shows the predicted maximum residual (tensile) principal stress ( $S_{max}$ ), (compressive) principal stress ( $S_{min}$ ) and von-Mises (equivalent stress) ( $S_{Mises}$ ) for different batch sizes. The residual compressive stresses remain approximately constant for all the batch sizes however the tensile residual stresses are predicted to increase with increasing batch size. Increasing tensile residual stresses may cause detrimental effects on tool life as they may add to the applied stresses to propagate on earlier cracking or to increase in plastic deformation. Therefore the bath size needs to be chosen carefully to balance between the productivity and tool damage.

## 7.6 Tool life predictions

The SPF tool life is predicted using the Zamrik and Ductility exhaustion methods described in Chapter 5. The Coffin-Manson and Ostergren models are not employed as the Zamrik model gave consistently conservative life predictions. In addition a bilinear strain range partitioning method developed by Shang [111] (see Chapter 2) is also explored to predict the tool life. The FE predicted stress-strain data is used in stress-strain-life equations for XN40F alloy described in Chapter 5. The tool life is predicted using stress-strain data obtained from both the uncoupled plasticity-creep and two-layer-viscoplasticity models. The tool life is predicted assuming a batch size of twenty; i.e. twenty parts formed per forming campaign. Equation 5.21 is employed to predict the tool life using the Zamrik model. Table 7.1 shows the life predictions using the Zamrik model.

Shang [5] proposed a bi-linear creep-fatigue interaction approach for the present XN40F tool material described in Chapter 2. Based on the uncoupled plasticity-creep model predictions, SPF tool experience cyclic inelastic strain ranges of  $(\Delta\epsilon_{pp})$  plastic strain reversed by plastic strain and  $(\Delta\epsilon_{pc})$  plastic strain reversed by creep strain. A schematic plot of the bi-linear damage summation approach is shown in Fig. 2.39. Strain controlled fatigue and fatigue-creep interaction tests on XN40F material were carried out at 900°C by Shang [5] and the resulting cyclic strain-life equation for  $\Delta\epsilon_{pc}$  is used here since the test for  $\Delta\epsilon_{pc}$  is not carried out in this project, however the cyclic strain life equation for  $\Delta\epsilon_{pp}$  is employed from isothermal fatigue tests performed at 900°C (see Chapters 3 and 5). The strain-life equations are as follows:

$$N_{pp}(\Delta\varepsilon_{pp})^{2.4} = 0.00645 \quad (7.1)$$

$$N_{pp}(\Delta\varepsilon_{pc})^{1.518} = 0.462 \quad (7.2)$$

The bi-linear strain range partitioning equations from Shang's work are modified here in the present work. Since the major cycles alone predicted elastic shakedown, only minor cycle strain ranges are employed to predict the fatigue-creep life. The modified equation is expressed as

$$N_f \left[ \alpha \left( \frac{n}{N_{pp}} \right) + \left( \frac{n}{N_{pc}} \right) \right] = 1 \quad (7.3)$$

where  $n$  is the number of minor cycles per major cycle ( $n = 20$ ). Additional tests at 900°C, devised to simulate the interaction between  $\Delta\varepsilon_{pp}$  and  $\Delta\varepsilon_{pc}$  strain ranges for

the tool, were employed by Shang [5], to show that  $\frac{N_f}{N_{pp}} < \frac{N_f}{N_{pc}}$  for the tool material

and to identify the relevant value of  $\alpha$  for equation 7.3. The inelastic strain ranges from the uncoupled-plasticity-creep model (Fig. 7.18) are used to predict the tool life using equation 7.3; the results are given in Table 7.2.

A local ratchetting phenomenon is predicted along the two long edges of the tool using the uncoupled plasticity-creep model. The significance of this ratchetting behaviour is assessed here via a simple life (crack initiation) prediction approach, based on the work of Kapoor [39], whereby failure is assumed to occur when the accumulated strain due to ratchetting reaches the uniaxial failure strain (ductility), i.e. a ductility exhaustion approach. Thus, the predicted number of cycles to ratchetting failure,  $N_r^f$  defined here as the occurrence of ductility exhaustion over a volume of approximately 25 mm (typical element size at ratchetting location, with one integration point per element) is given by:

$$N_r^f = \left( \frac{\varepsilon_f}{n\Delta\varepsilon_{eq}^r} \right) \quad (7.4)$$

where  $\varepsilon_f$  is the ductility limit; as determined from tensile tests,  $n=20$  (batch size) and  $\Delta\varepsilon_{eq}^r$  is an equivalent ratchet strain, defined in a manner akin to the definition of equivalent plastic strain, as follows:

$$\Delta\varepsilon_{eq}^r = \sqrt{(2/3)\Delta\varepsilon_{ij}^r\Delta\varepsilon_{ij}^r} \quad (7.5)$$

where  $\Delta\varepsilon_{ij}^r$  are the tensorial ratchet strain components, calculated from the time histories of each individual strain component, as follows:

$$\Delta\varepsilon_{ij}^r(k) = \varepsilon_{ij}^{in,m}(k) - \varepsilon_{ij}^{in,m}(k-1) \quad (7.6)$$

where  $\varepsilon_{ij}^{in,m}(k)$  is the mean inelastic strain corresponding to the  $k^{\text{th}}$  minor cycle since the ratchetting phenomenon is associated with the minor cycle creep-plastic deformation. Equation 7.5 is applied to each minor cycle to obtain a  $\Delta\varepsilon_{eq}^r$  value for every minor cycle and an average  $\Delta\varepsilon_{eq}^r$  value over all of minor cycles is then employed in Equation 7.4. The average equivalent ratchet strain  $\Delta\varepsilon_r^{eq}$  over 40 minor cycles (Fig. 7.24) is considered for the ratchet life prediction. Since the ratchetting is accumulated between 743°C and 900°C [16] the isothermal ductility data for both 700°C and 900°C is used individually to predict ratchetting life as shown in Table 7.3. The life predicted using 700°C data is lower than using the 900°C data.

The predicted SPF tool lives and the thermo-mechanical behaviour are compared with industrial observations and the representative TMF test performed on the XN40F material (Chapter 3, Figs. 3.26 to 3.29). The representative TMF test results are given in Table 7.4. The representative TMF test showed specimen failure after

2086 minor cycles, i.e. 104 major cycles with a batch size of twenty. According to industry, XN40F tools have not failed due to cracking yet. However, based on industrial experience, the approximate estimated life for these tools is 30 to 40 major cycles.

From industrial experience, progressive distortion (Ratchetting) is a key failure mechanism prior to cracking, which leads to frequent machining of the tool to produce components within required dimensional tolerances. The surface tolerance on the formed component of the XN40F tool is  $\pm 0.5$  mm [25]. Assuming symmetry between the two halves of the tool, the surface tolerance on the lower half of the tool is considered to be  $\pm 0.25$  mm. From Fig 7.26c for path Q (which is in the middle of the forming surface), the time to re-machining of the tool can be approximately estimated. The distortion behaviour for a batch size of 20 is assumed to stabilise from 2<sup>nd</sup> major cycle and the increase of 0.034 mm predicted from 2<sup>nd</sup> to 3<sup>rd</sup> major cycle, for the end node of Path 'Q' is considered to remain constant for further major cycles. The maximum distortion predicted at the end of 3<sup>rd</sup> major cycle (60 parts formed) is 0.124 mm (Fig. 7.26c). Thus the time to re-machine the tool is approximately estimated to be 134 components formed. The progressive distortion behaviour along paths 'P' and 'R' is also accountable for the overall deformed shape (twist and bow) of the tool. According to industrial tool history, XN40F tools have undergone re-machining after approximately every 120 to 140 components formed.

## 7.7 Summary and conclusion

This chapter presents thermo-mechanical analyses of a simplified representative SPF tool under different loading conditions. Controlled heat-up with dwell at 500°C and controlled cooling was found to be less damaging than direct heating to 900°C and uncontrolled cooling. The effect of different heating and cooling rates was also explored. The 25°C/hr and 40°C/hr rates, which are lower than the nominal (current) rate of 50°C/hr, did not show significant improvement in tool life. However a higher rate of 80°C/hr was found to be more damaging. Hence the general rate of 50°C/hr is recommended taking into consideration the productivity of the process and tool damage.

The effect of minor cycles associated within major cycles were analysed to understand the effect of intermittent press opening and closing during blank insert and part unload operations along with seven hours dwell period (forming cycle) at 900°C. Both the material models; uncoupled plasticity-creep and two-layer viscoplasticity, were employed to analyse their effect on the behaviour of SPF tool. The uncoupled plasticity-creep model predicted plastic shakedown for the critical element 'E' in the local  $X$  direction parallel to the top surface edge of the tool whereas ratchetting was predicted in a plane transverse to the  $X$  direction, associated with minor cycles. Therefore two failure mechanisms, namely low cycle fatigue-creep and ratchetting, were predicted by the uncoupled plasticity-creep model. The two-layer viscoplastic model also predicted plastic shakedown for the critical element. The inelastic strain range predicted by the two-layer model was larger than that predicted by the uncoupled plasticity-creep model. However no ratchetting was predicted by the two-layer viscoplasticity model under the same loading conditions.

The effect of batch size was studied using the uncoupled plasticity-creep model. Progressive residual distortion was predicted mainly along the top surface edges of the two long sides of the SPF tool facing the press doors. Residual vertical distortion and tensile residual stresses were predicted to increase with increasing batch size. Therefore the selection of batch size is important. From Figs. 7.26 and 7.27, a batch size of twenty (as opposed to thirty and forty) can be recommended, taking into consideration the productivity and tool life.

The SPF tool life was predicted using the Zamrik and ductility exhaustion methods. Previously developed bi-linear strain range partitioning method [94] was also explored. Industrial experience with such tools suggests that the failure through cracking can occur at around 30 to 40 major cycles [25]. The Zamrik model predicted TMF tool failure at 24 major cycles using the uncoupled plasticity-creep model and at 58 cycles using the two layer viscoplasticity model. However a bi-linear strain range method predicted 260 major cycles. The Zamrik model was found to be superior over other crack initiation models explored in this project. A simplified ratchetting life calculation based on ductility exhaustion, predicted cracking at 47 cycles using the ductility limit at 700°C and at 110 cycles using the limit at 900°C. A representative uniaxial strain controlled TMF-creep test predicted tool failure at 104 major cycles.

In addition to crack initiation, the time to re-machine the SPF tool forming surfaces was approximately estimated based on the predicted progressive distortion behaviour, which is equal to 134 formed components. The ratchetting (shear)

mechanism with progressive distortion behaviour of the tool was found to be a key mode of failure.

Table 7.1 Predicted SPF tool life using Zamrik strain energy model.

| Material model             | $\epsilon_t$ % | $\sigma_t$ (MPa) | $\Delta E$ | $N_f$ (minor cycles) | $N_f$ (major cycles) |
|----------------------------|----------------|------------------|------------|----------------------|----------------------|
| Uncoupled plasticity-creep | 0.3            | 165              | 0.010817   | 485                  | 24                   |
| Two-layer viscoplasticity  | 0.316          | 89               | 0.006146   | 1167                 | 58                   |

Table 7.2 Predicted SPF tool life using Bi-linear strain range partitioning method.

| Parameter     | $\Delta\epsilon_{pp}$ % | $\Delta\epsilon_{pc}$ % | $N_f$ (minor cycles) | $N_f$ (Major cycles) |
|---------------|-------------------------|-------------------------|----------------------|----------------------|
| $\alpha=4.53$ | 0.1036                  | 0.0657                  | 5200                 | 260                  |

Table 7.3 Predicted SPF tool ratchetting life using ductility exhaustion method.

| $\Delta\epsilon_r^{eq}$ average % | Parameter            | $N_r^f$ (minor cycles) | $N_r^f$ (major cycles) |
|-----------------------------------|----------------------|------------------------|------------------------|
| 0.0168                            | $\epsilon_f$ @ 900°C | 2202                   | 110                    |
|                                   | $\epsilon_f$ @ 700°C | 952                    | 47                     |

Table 7.4 Representative strain controlled TMF test life results of XN40F alloy specimen.

| $\Delta\epsilon^{in}$ % | $\sigma_t$ (MPa) | $N_f$ (minor cycles) | $N_f$ (major cycles) |
|-------------------------|------------------|----------------------|----------------------|
| 0.192                   | 114              | 2086                 | 104                  |

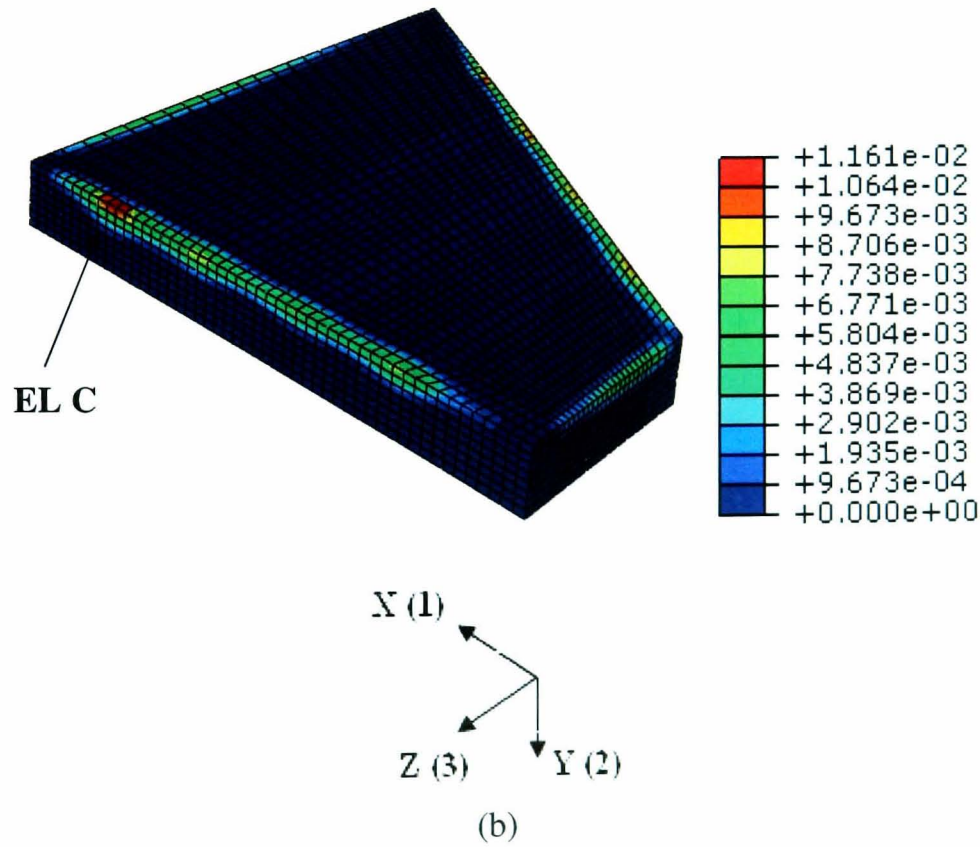
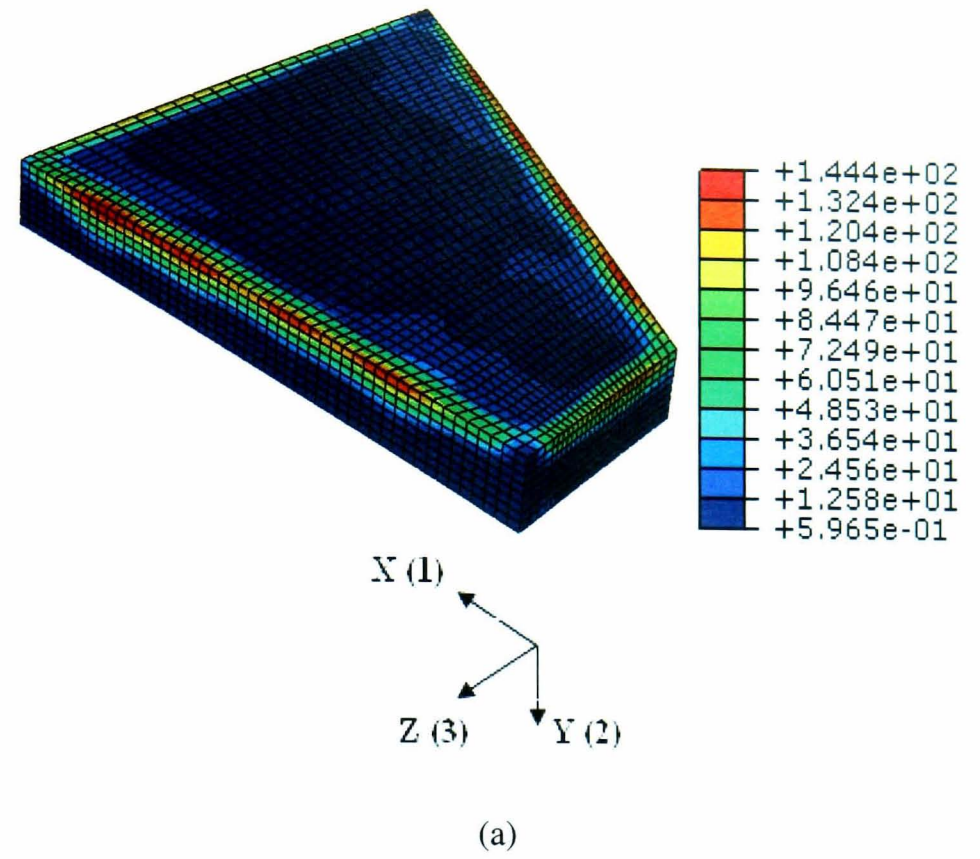


Figure 7.1 FE predicted equivalent stress and equivalent plastic strain distribution at the end of 5<sup>th</sup> major cycle for thermal cycle 'A': (a) Von-Mises equivalent stress (b) Equivalent plastic strain

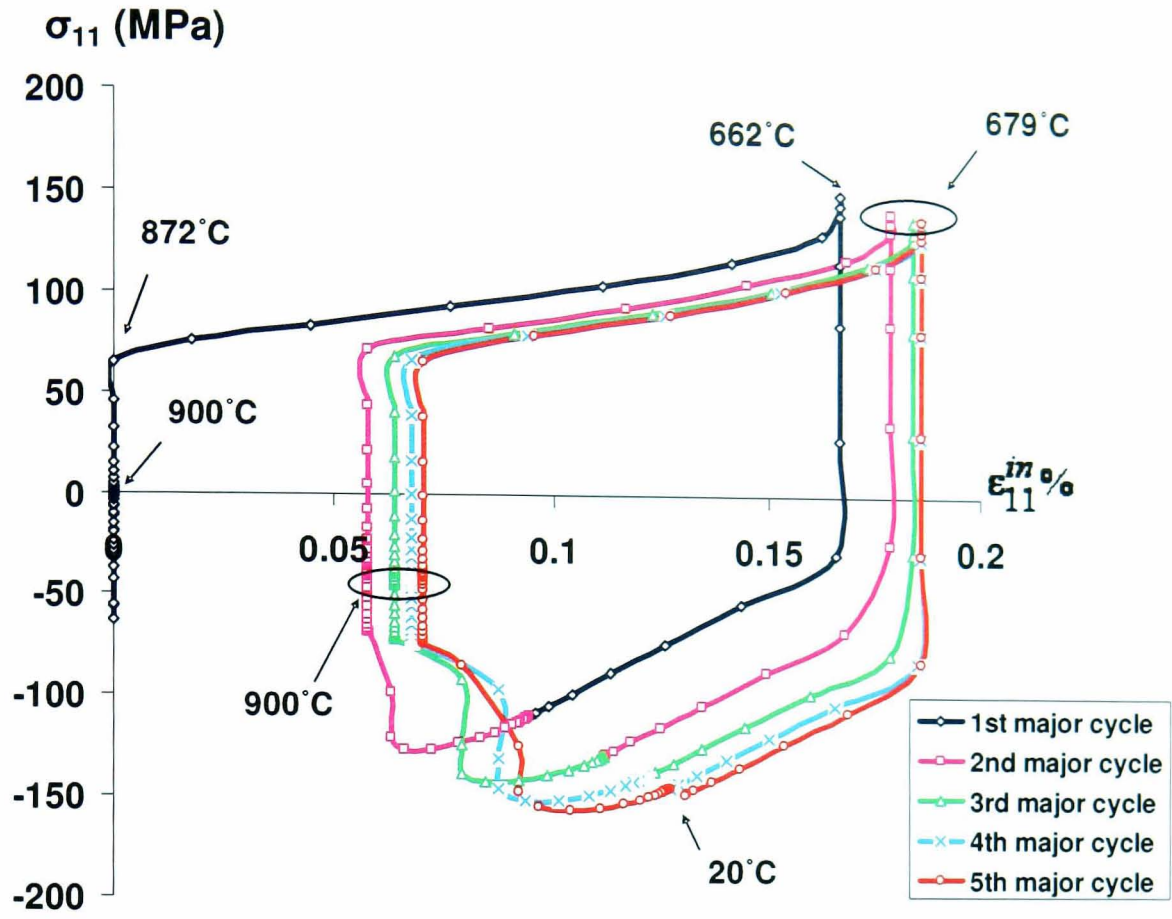


Figure 7.2 Local stress versus local inelastic strain for five major cycles of thermal cycle 'A'.

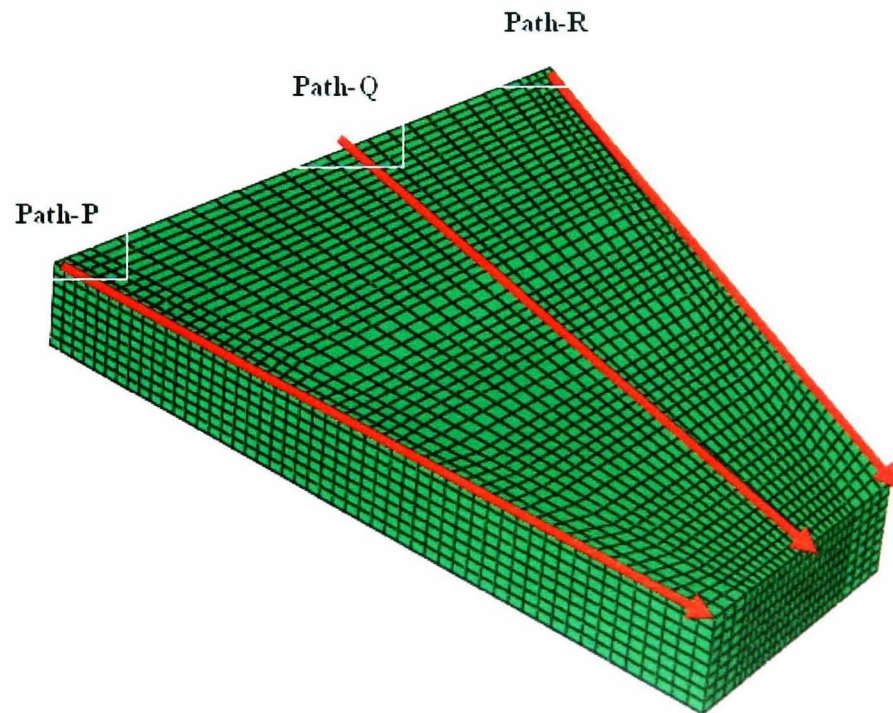
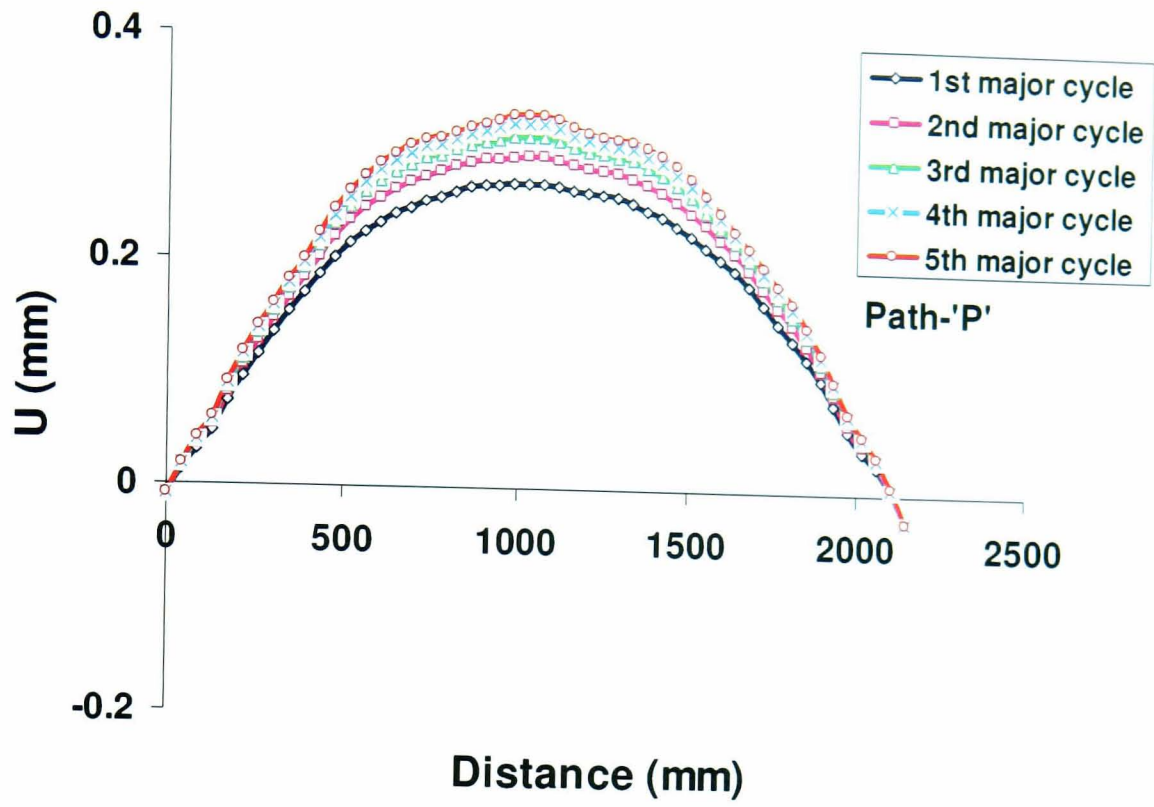
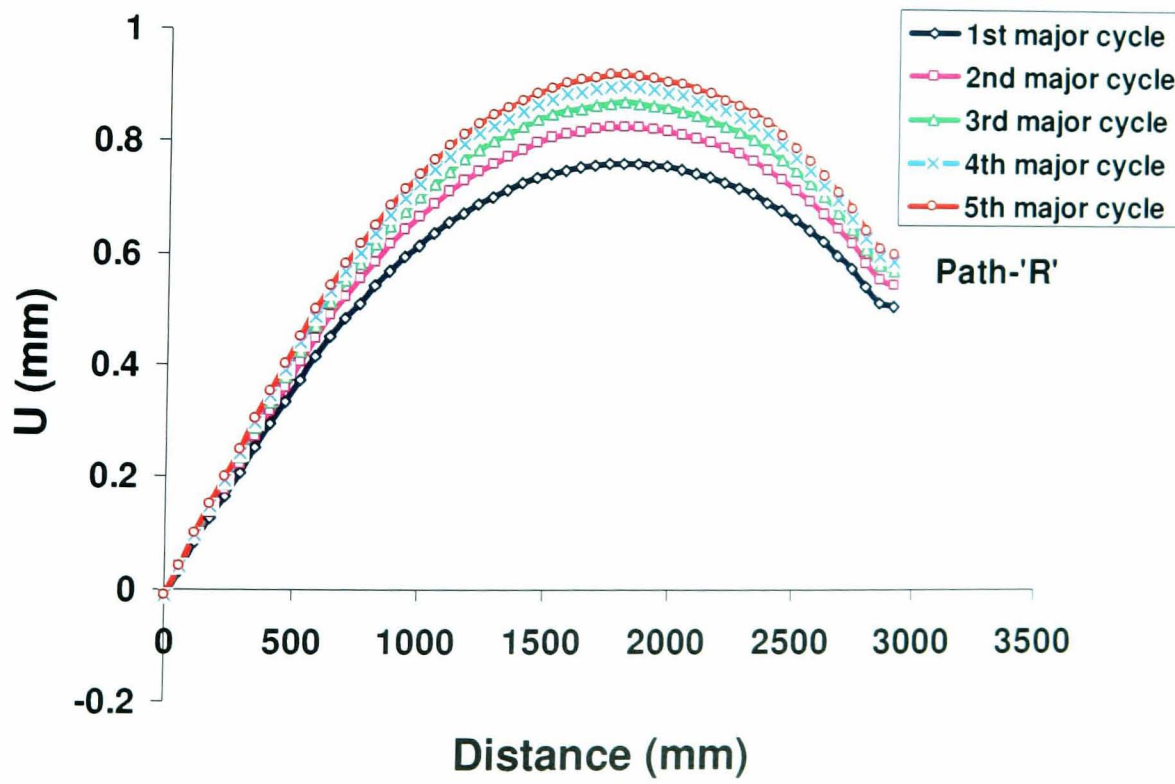


Figure 7.3 Nodal path definitions; 'P', 'Q' and 'R' for analysing residual distortions of SPF tool.

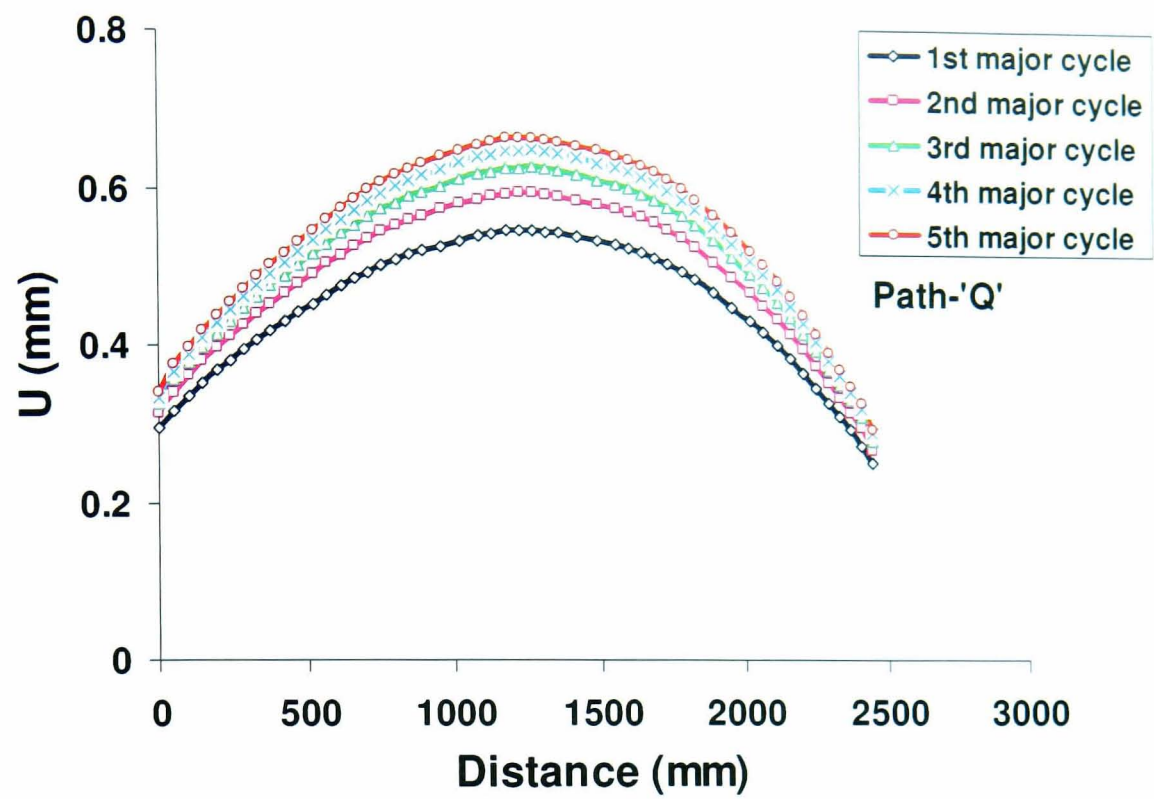


(a)



(b)

Figure 7.4 Predicted vertical nodal residual distortions at the end of ambient cooling of thermal cycle 'A' along paths; (a) Path 'P' (b) Path 'R'



(c)

Figure 7.4c Predicted vertical nodal residual distortions at the end of ambient cooling of thermal cycle 'A' along path 'Q'.

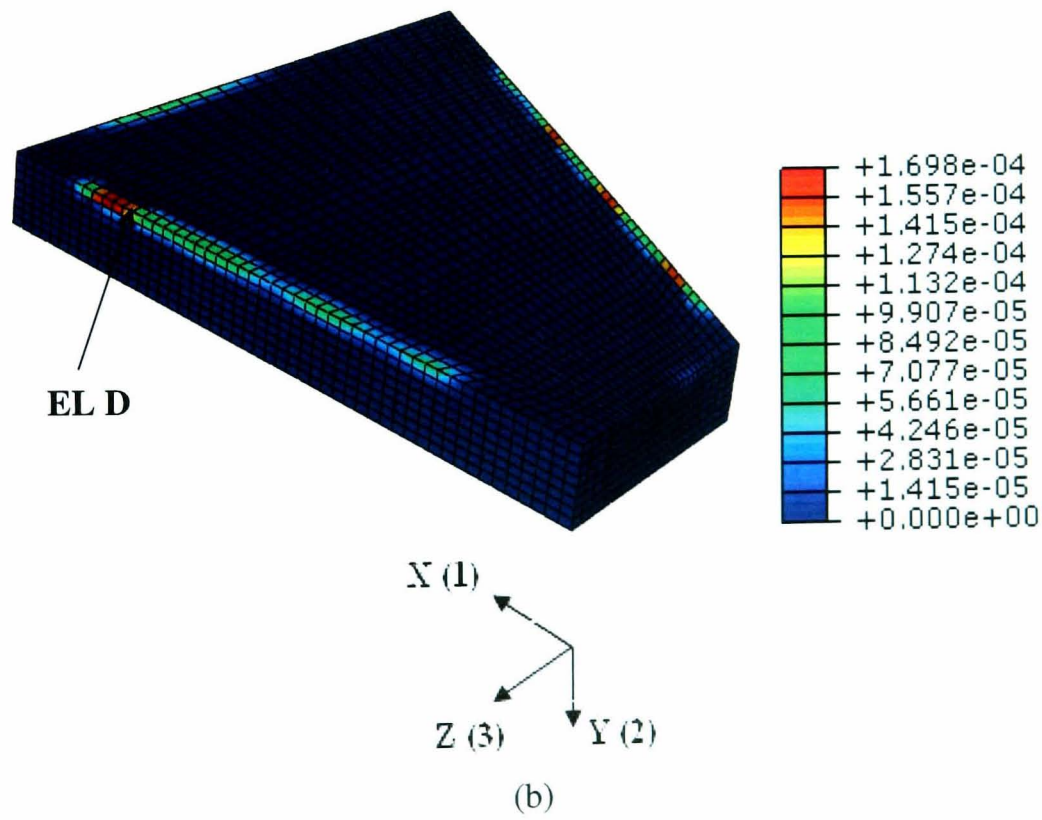
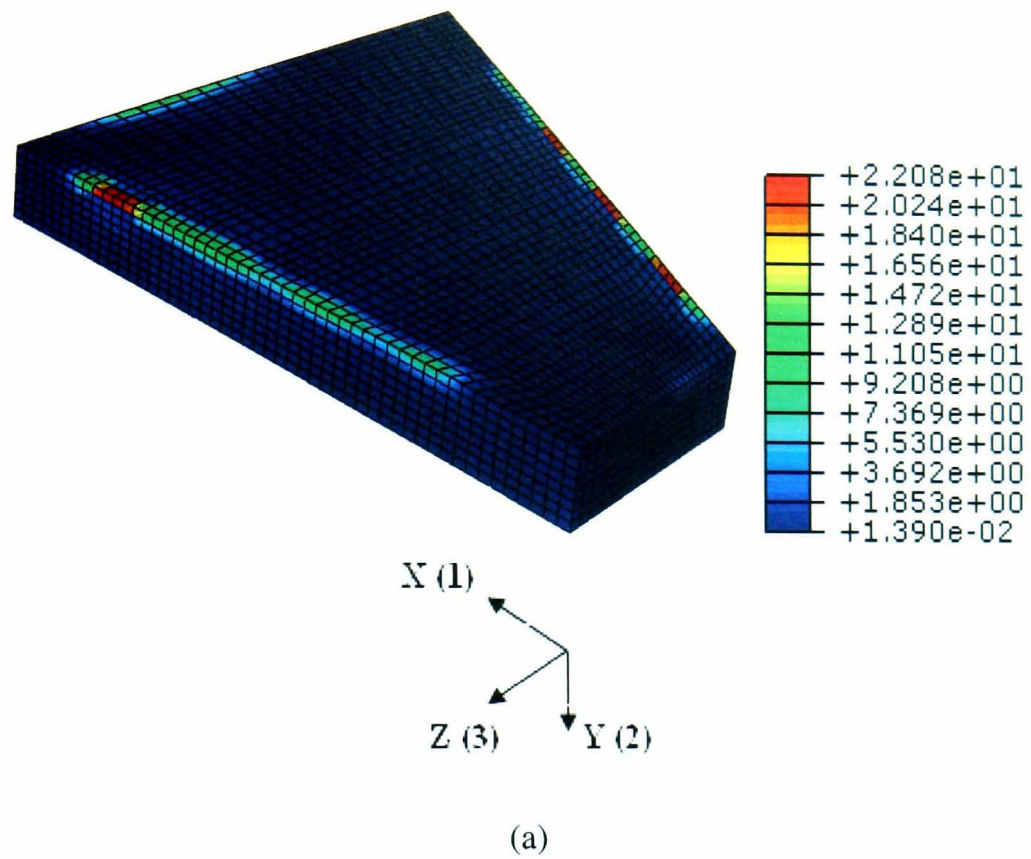


Figure 7.5 FE predicted equivalent stress and equivalent plastic strain distribution at the end of 5<sup>th</sup> major cycle for thermal cycle 'B': (a) Von-Mises equivalent stress (b) Equivalent plastic strain

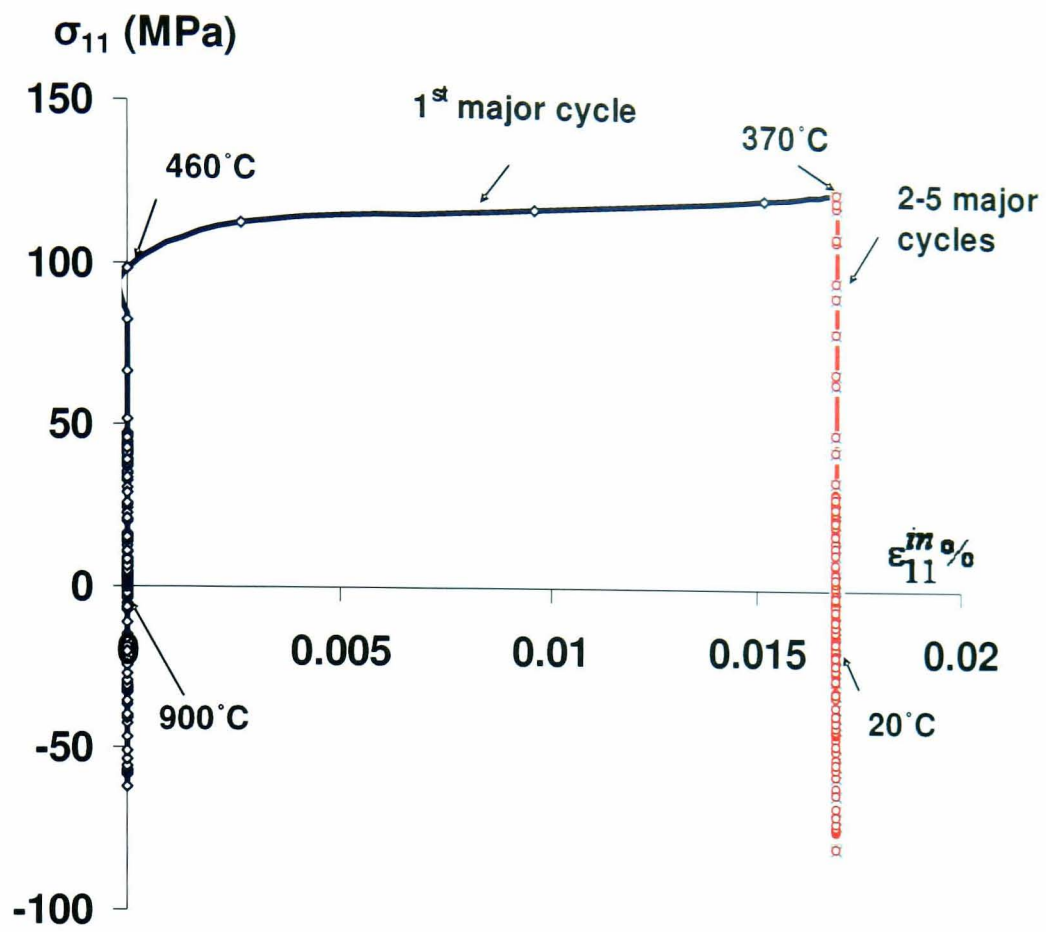
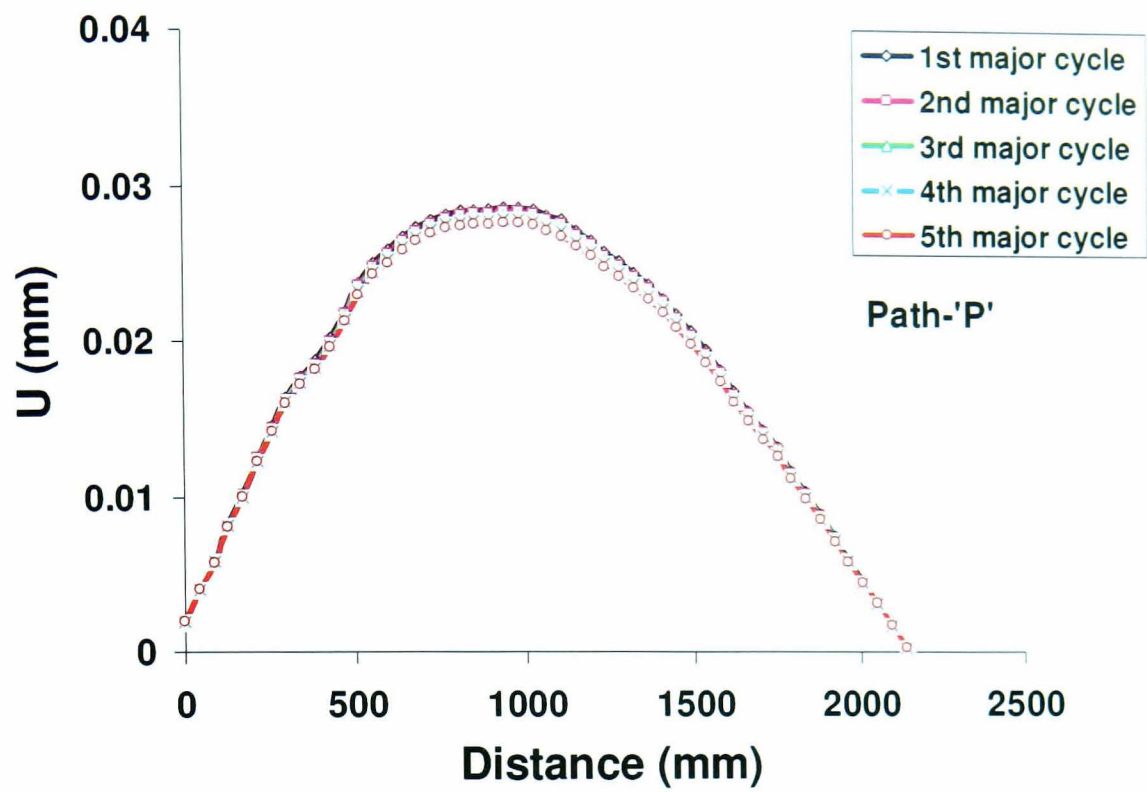
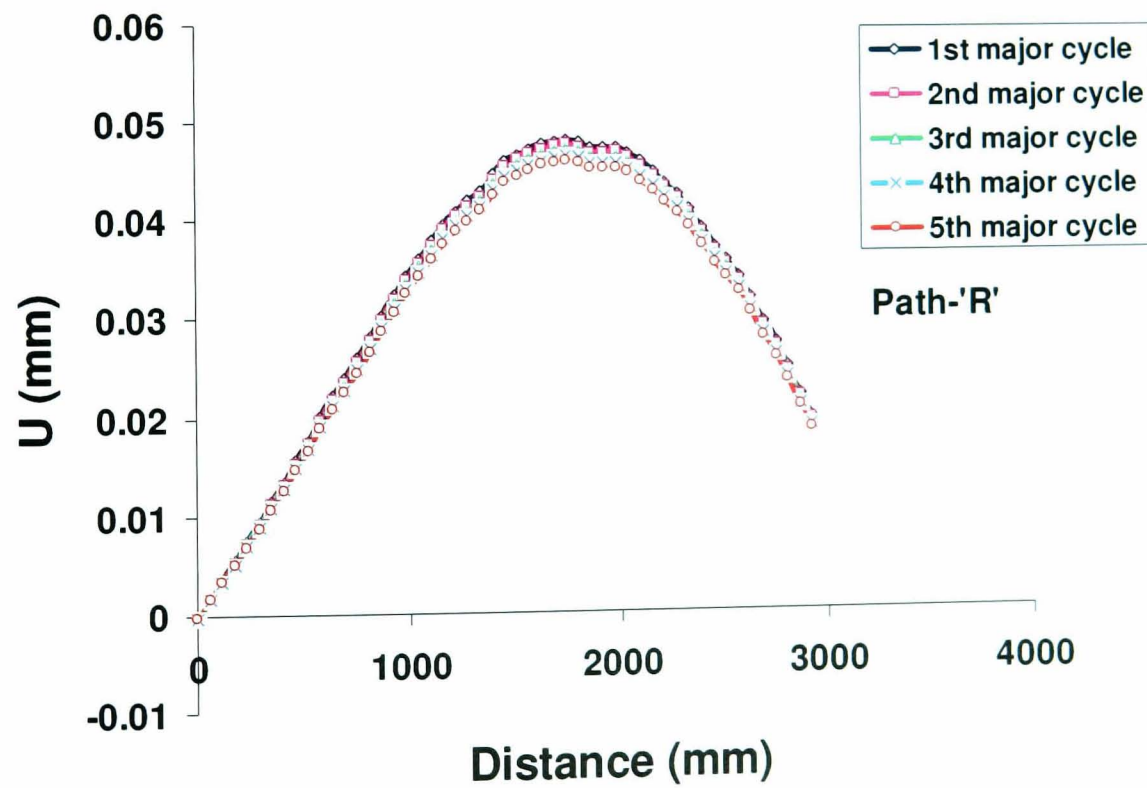


Figure 7.6 Local stress versus local inelastic strain for five major cycles of thermal cycle 'B' at EL 'D' shown in Fig. 7.5b.

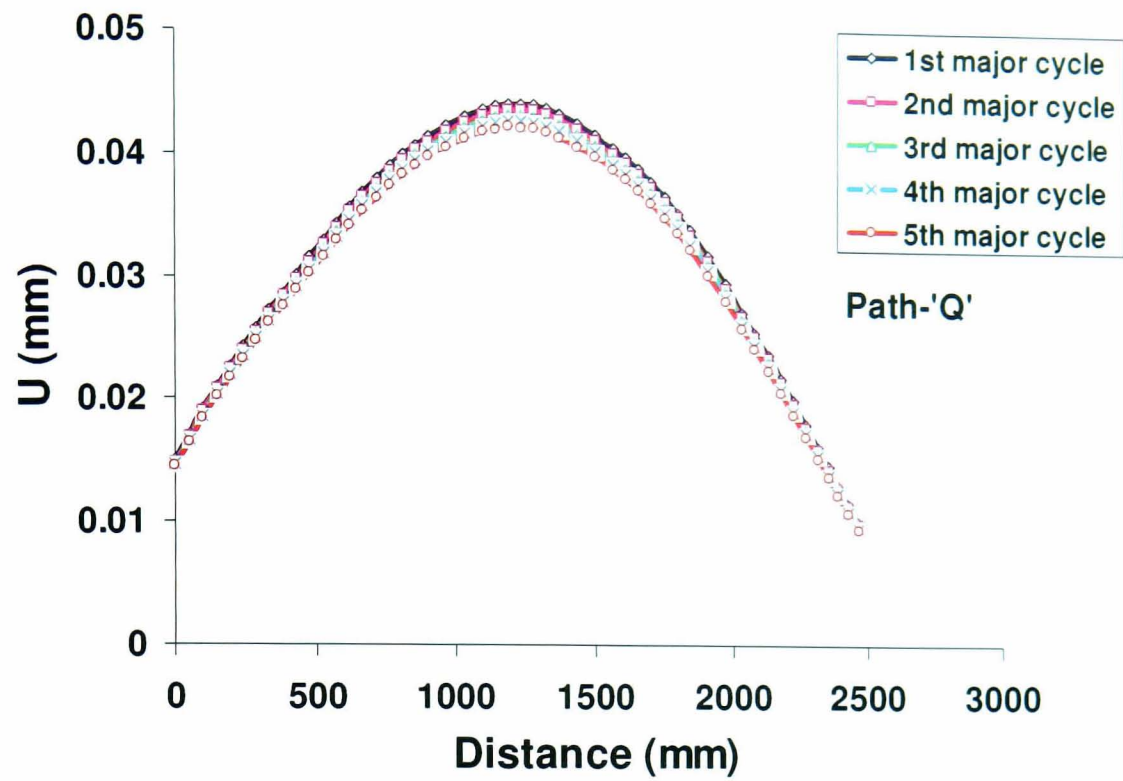


(a)



(b)

Figure 7.7 Predicted vertical nodal residual distortions at the end of ambient cooling of thermal cycle 'B' along paths; (a) Path 'P' (b) Path 'R' (c) path 'Q'



(c)

Figure 7.7 (Contd.) Predicted vertical nodal residual distortions at the end of ambient cooling of thermal cycle 'B' along paths; (a) Path 'P' (b) Path 'R' (c) path 'Q'

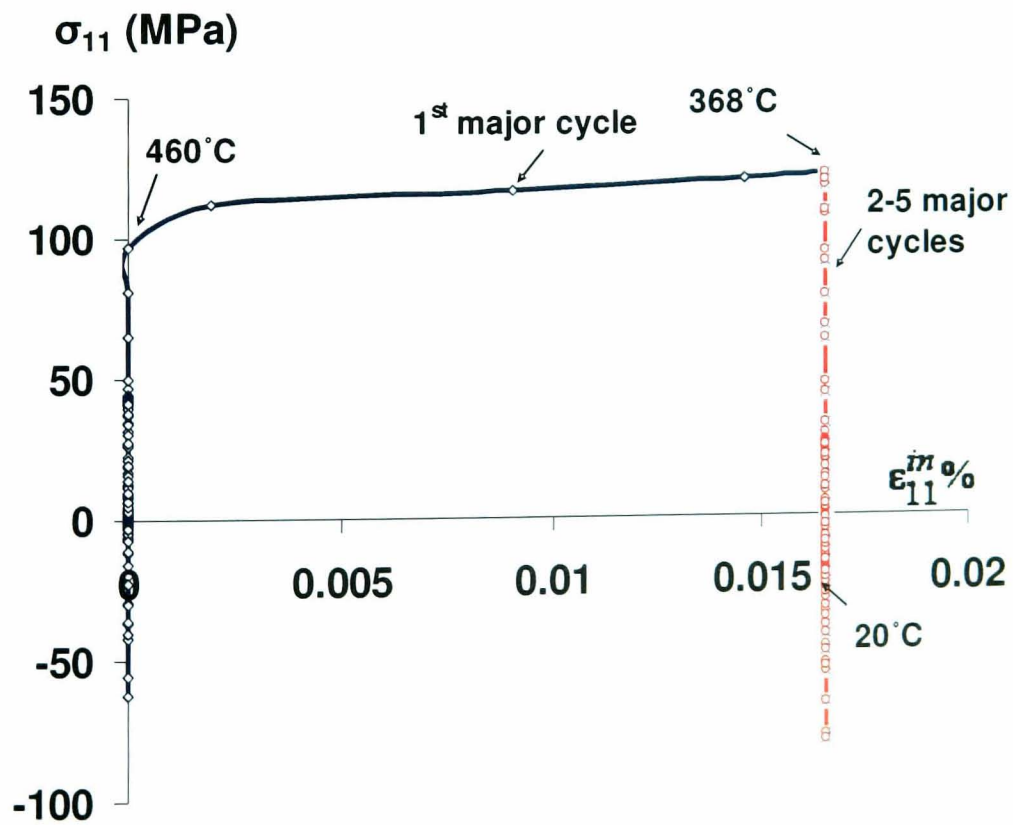


Figure 7.8 Local stress versus local inelastic strain for five major cycles of thermal cycle 'B' with 25°C/hr controlled heating and controlled cooling rate at EL 'D'.

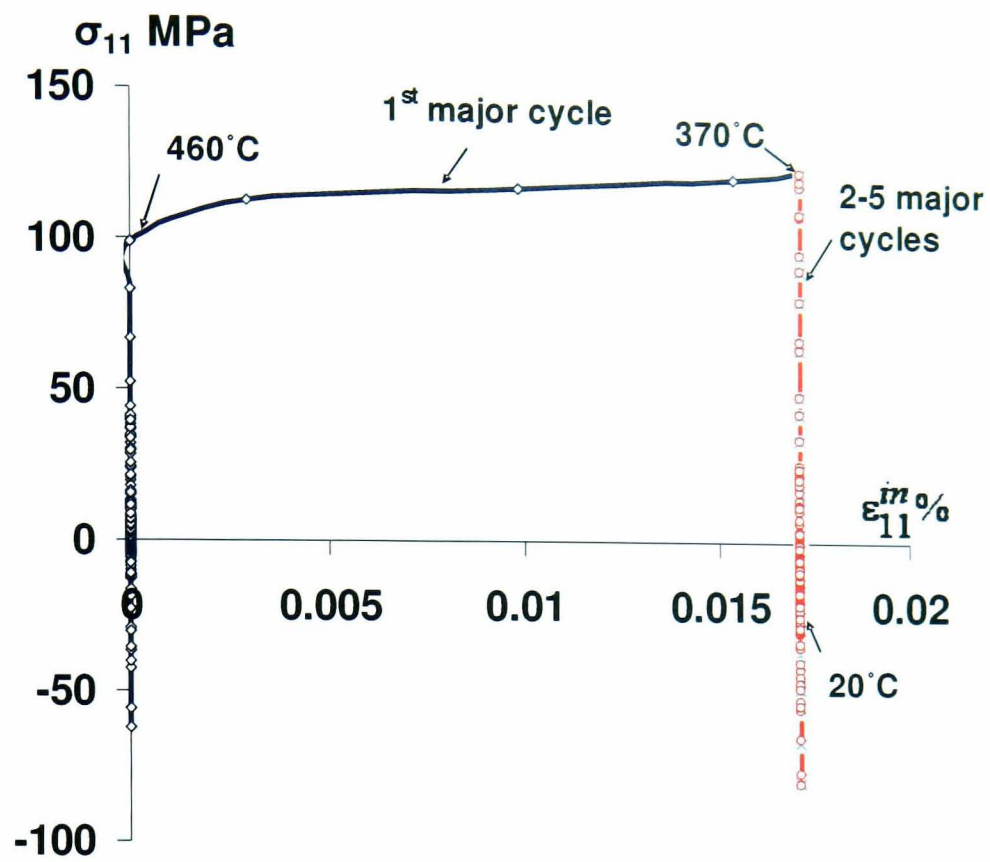


Figure 7.9 Local stress versus local inelastic strain for five major cycles of thermal cycle 'B' with 40°C/hr controlled heating and controlled cooling rate at EL 'D'.

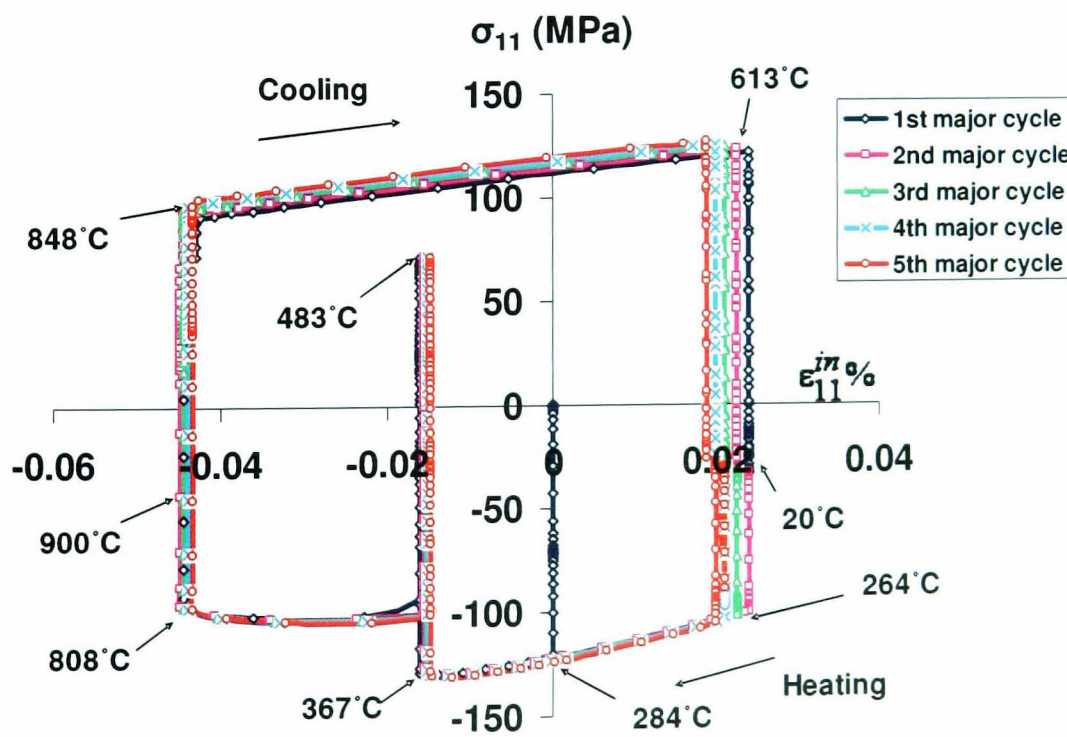
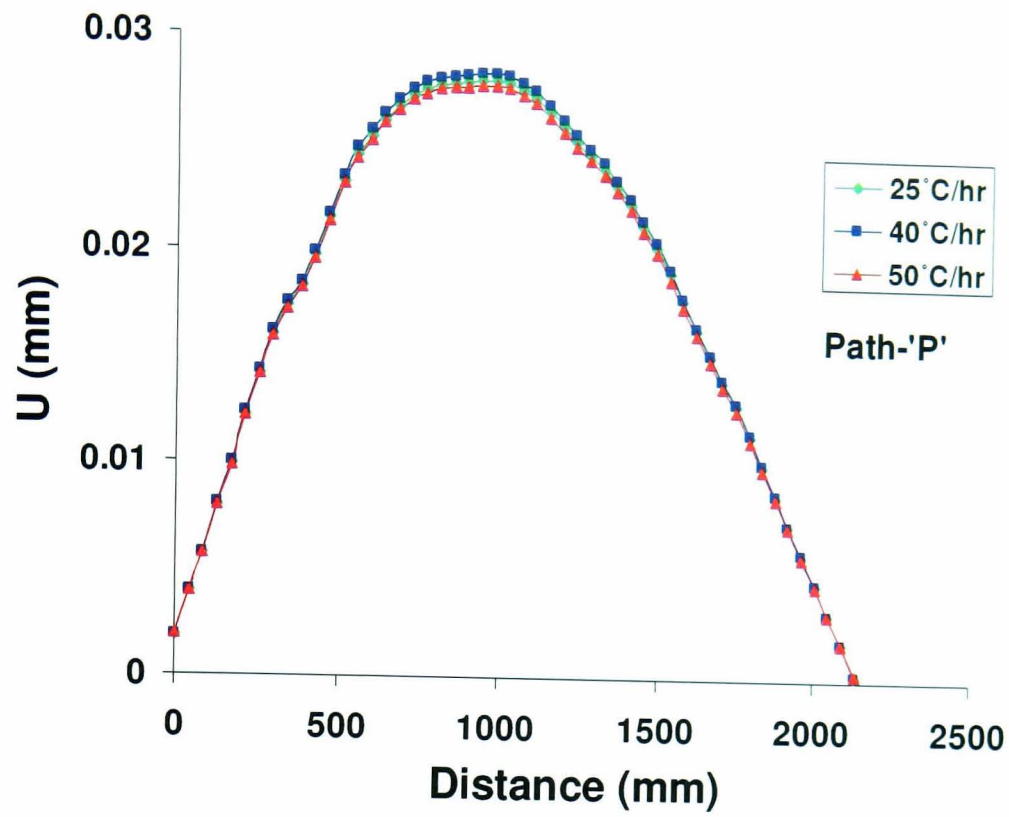
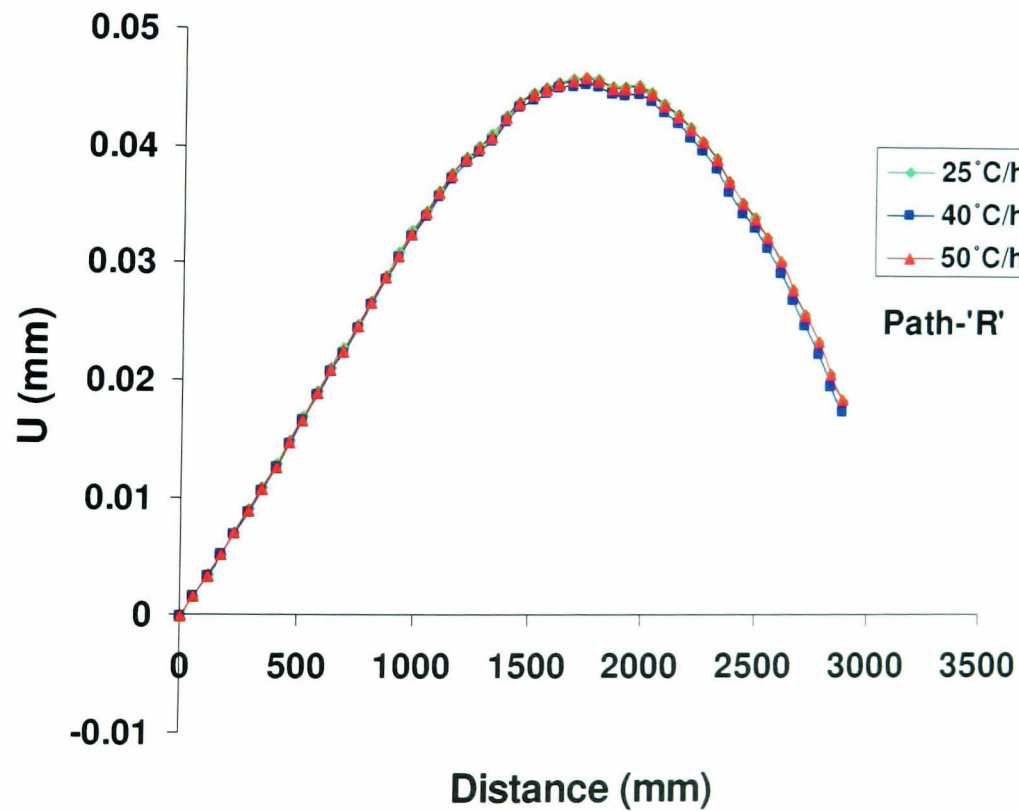


Figure 7.10 Local stress versus local inelastic strain for five major cycles of thermal cycle 'B' with 80°C/hr controlled heating and controlled cooling rate at EL 'D'.

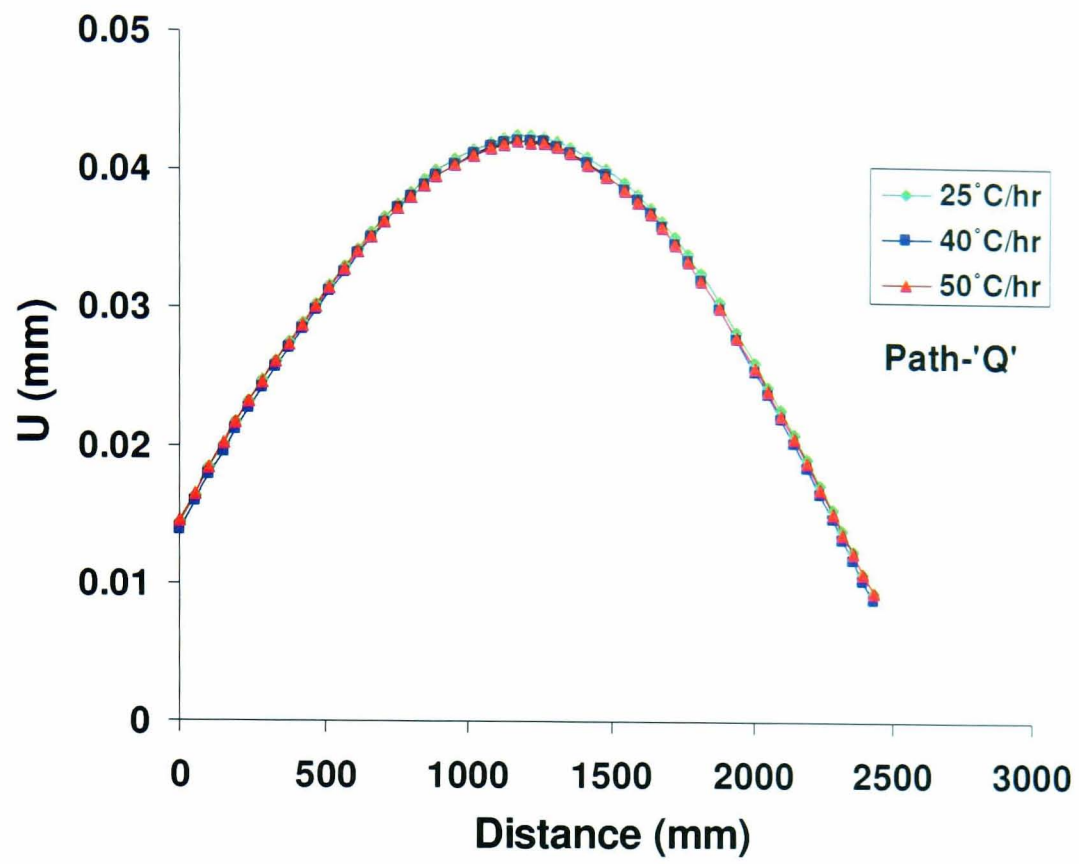


(a)



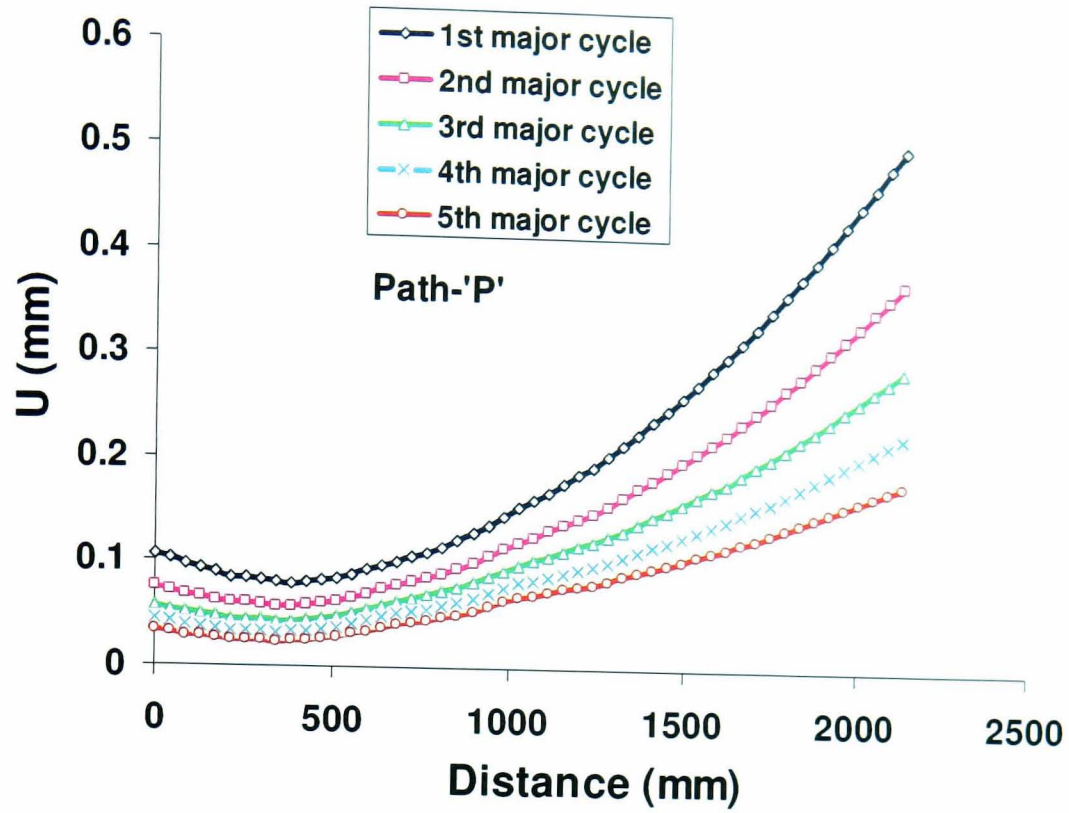
(b)

Figure 7.11 Predicted vertical nodal residual distortions of thermal cycle 'B' for 25°C/hr, 40°C/hr and general rate of 50°C/hr heating and cooling rates at the end of 5<sup>th</sup> major cycle along paths; (a) Path 'P' (b) Path 'R' (c) path 'Q'.

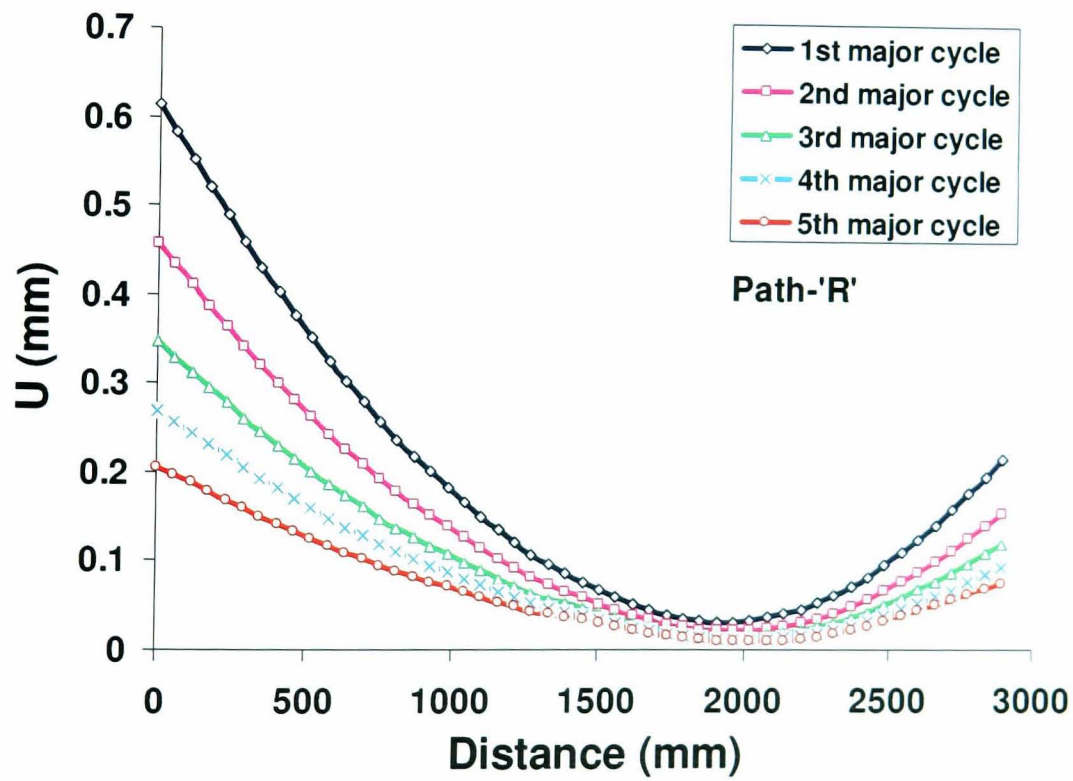


(c)

Figure 7.11 (Contd.) Predicted vertical nodal residual distortions of thermal cycle 'B' for 25 °C/hr, 40°C/hr and general rate of 50°C/hr heating and cooling rates at the end of 5<sup>th</sup> major cycle along paths; (a) Path 'P' (b) Path 'R'(c) path 'Q'.



(a)



(b)

Figure 7.12 Predicted vertical nodal residual distortions at the end of ambient cooling of thermal cycle 'B' for 80°C/hr heating and cooling rate along paths; (a) Path 'P' (b) Path 'R' (c) path 'Q'.

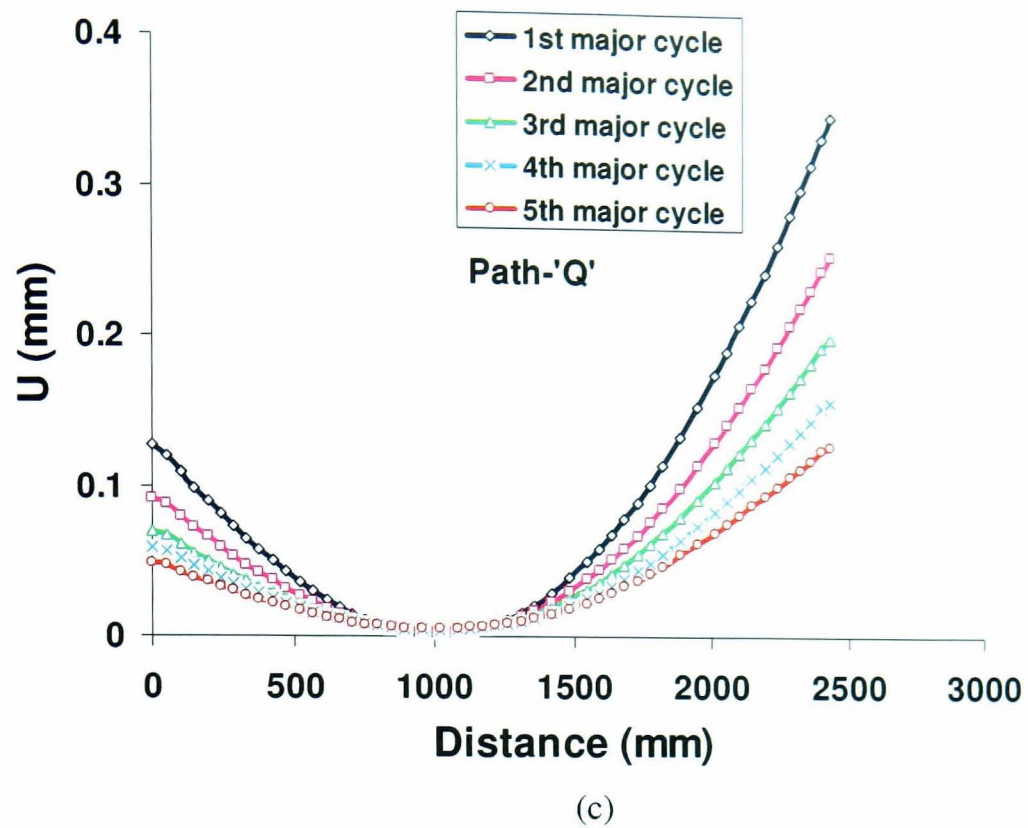


Figure 7.12 Predicted vertical nodal residual distortions at the end of ambient cooling of thermal cycle 'B' for 80°C/hr heating and cooling rate along paths; (a) Path 'P' (b) Path 'R' (c) path 'Q'.

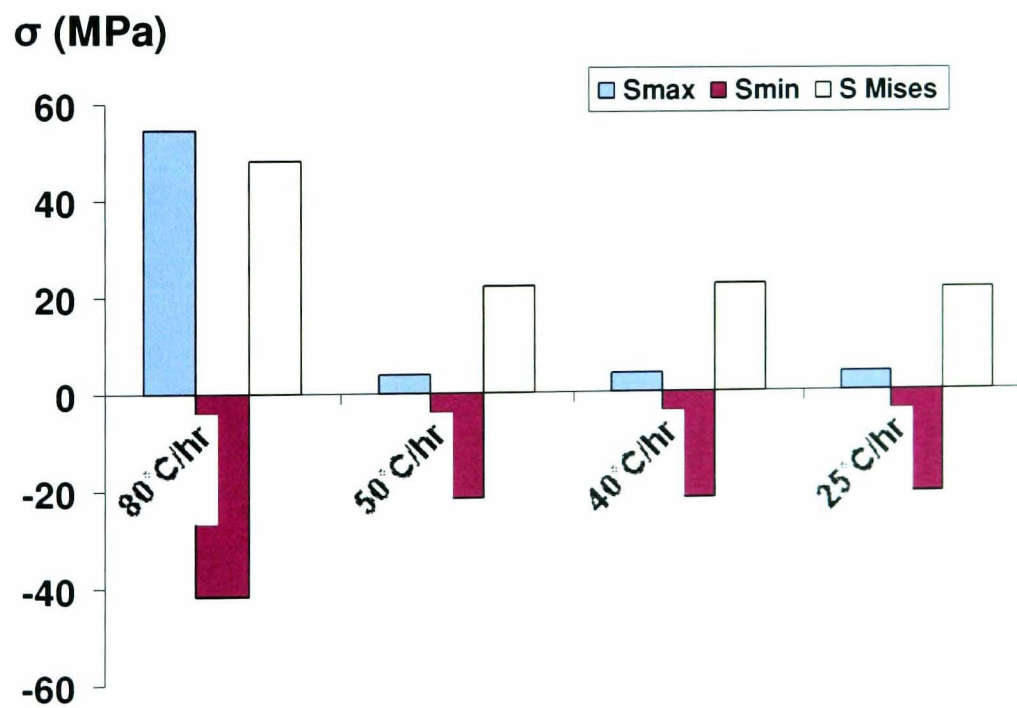


Figure 7.13 Maximum predicted residual tensile principal (Smax), compressive principal (Smin) and Equivalent (S Mises) stresses in the tool at the end of 5<sup>th</sup> major cycle for thermal cycle 'B' with different heating/cooling rates.

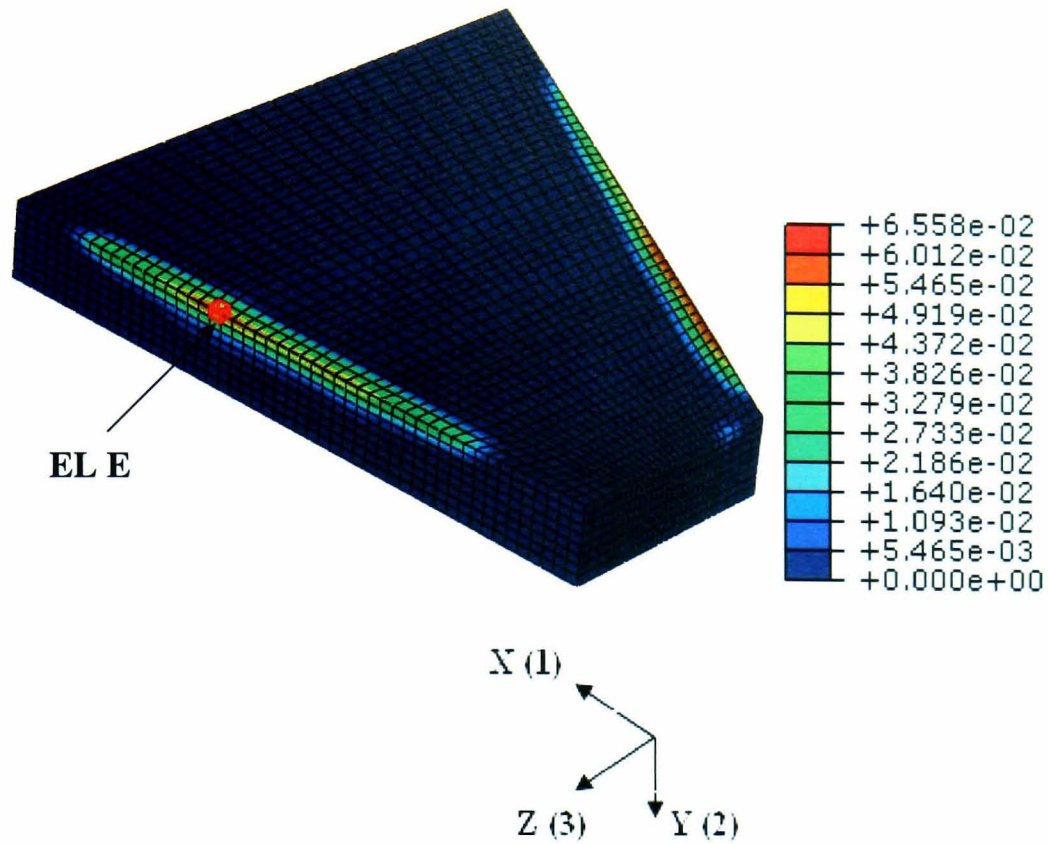


Figure 7.14 Equivalent plastic strain distributions at the end of third major cycle including five minor cycles per major cycle, employing uncoupled plasticity-creep material behaviour model.

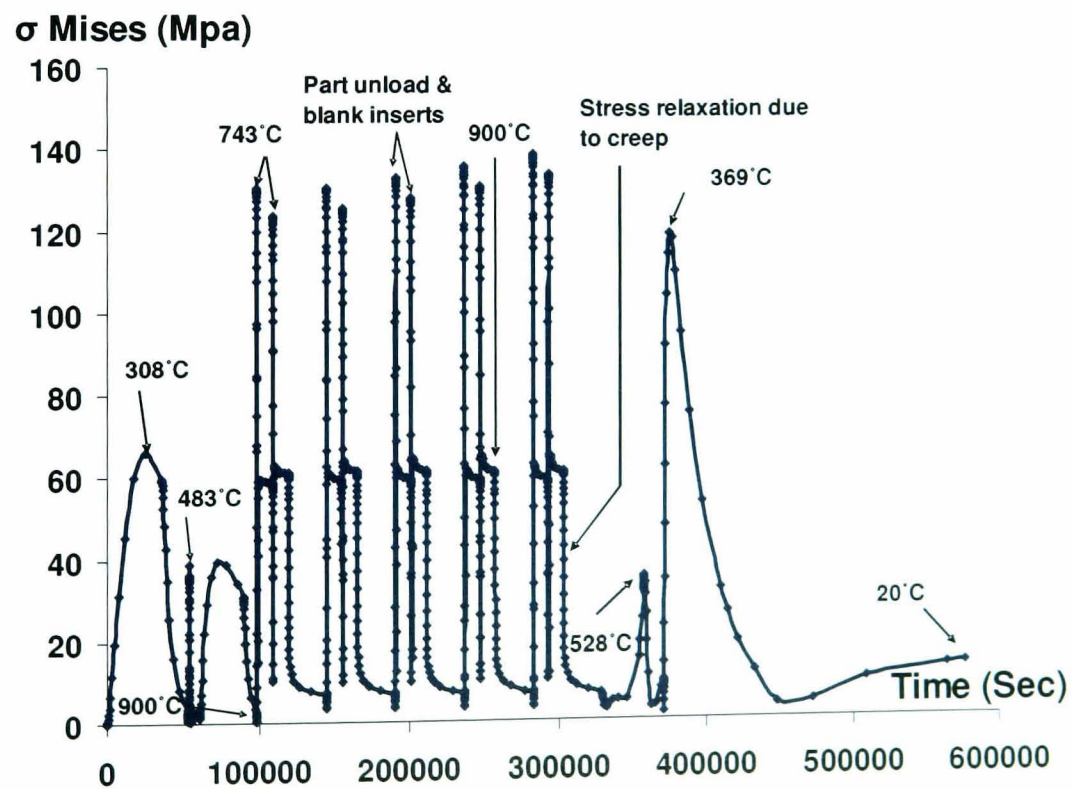


Figure 7.15 Predicted equivalent (Von-Mises) stress history of 1<sup>st</sup> major cycle including five minor cycles for critical element 'E' shown in Figure 7.15, employing uncoupled plasticity-creep material behaviour model

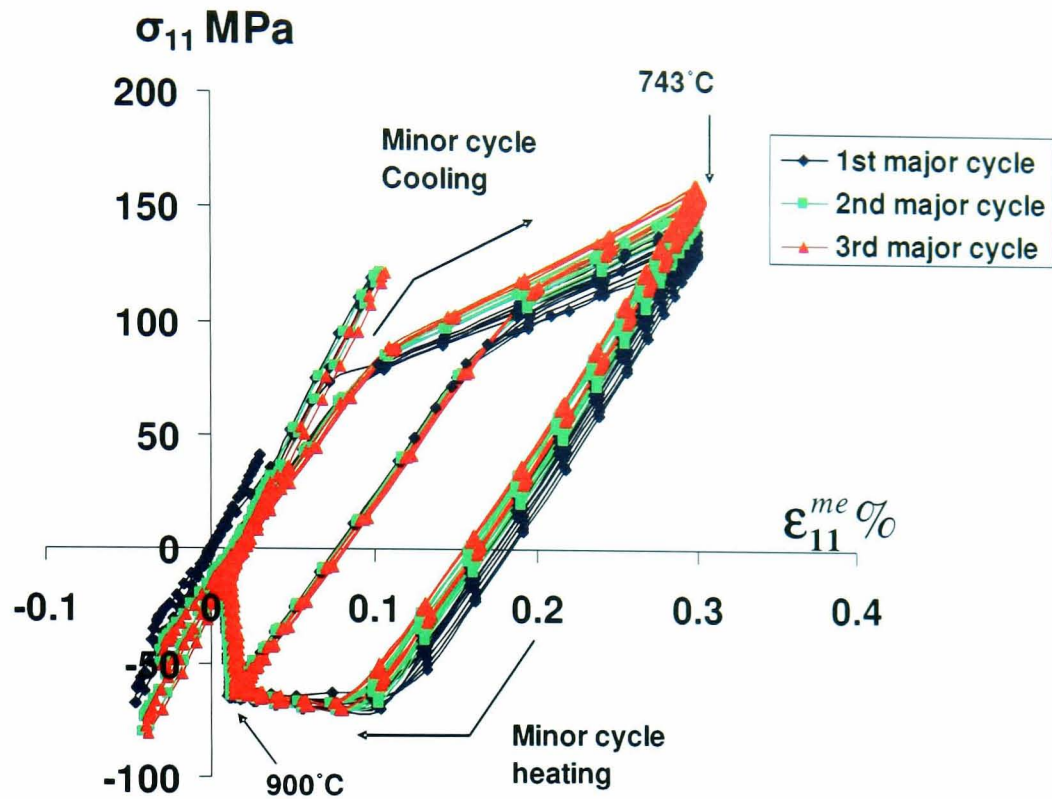


Figure 7.16 Predicted local stress versus local mechanical strain for three major cycles each including five minor cycles at element 'E' (uncoupled plasticity-creep material behaviour model)

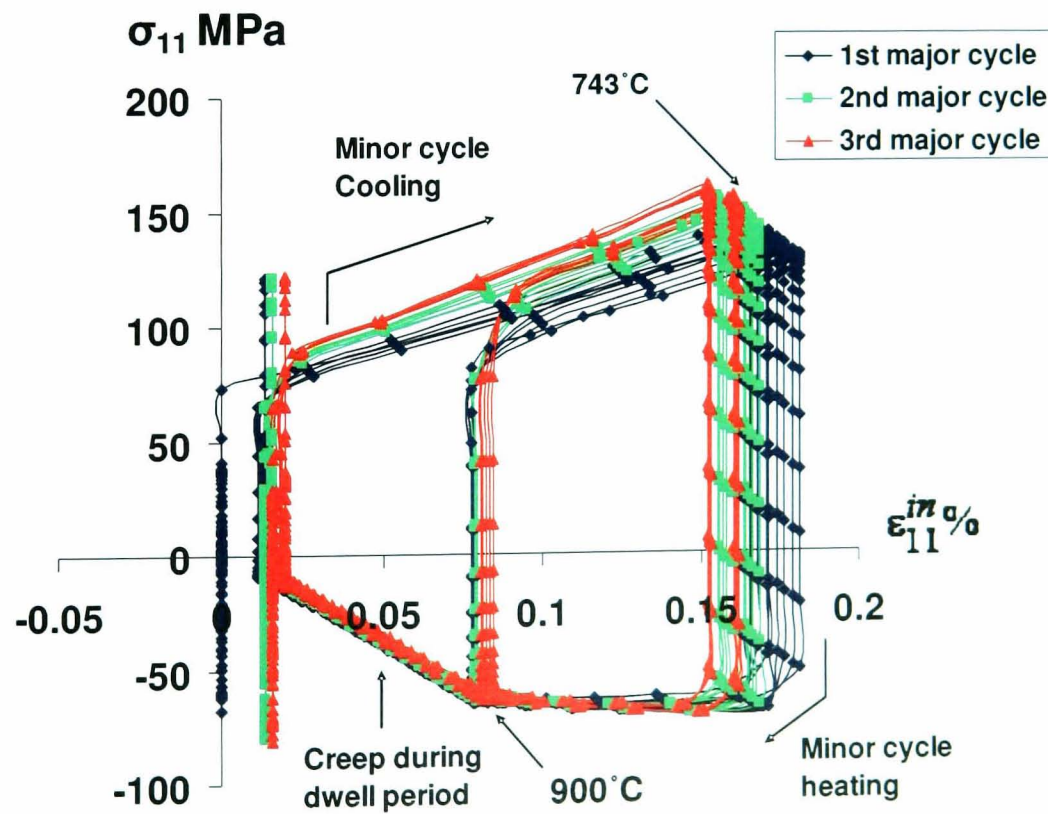


Figure 7.17 Predicted local stress versus local inelastic strain for three major cycles each including five minor cycles at element 'E' (uncoupled plasticity-creep material behaviour model)

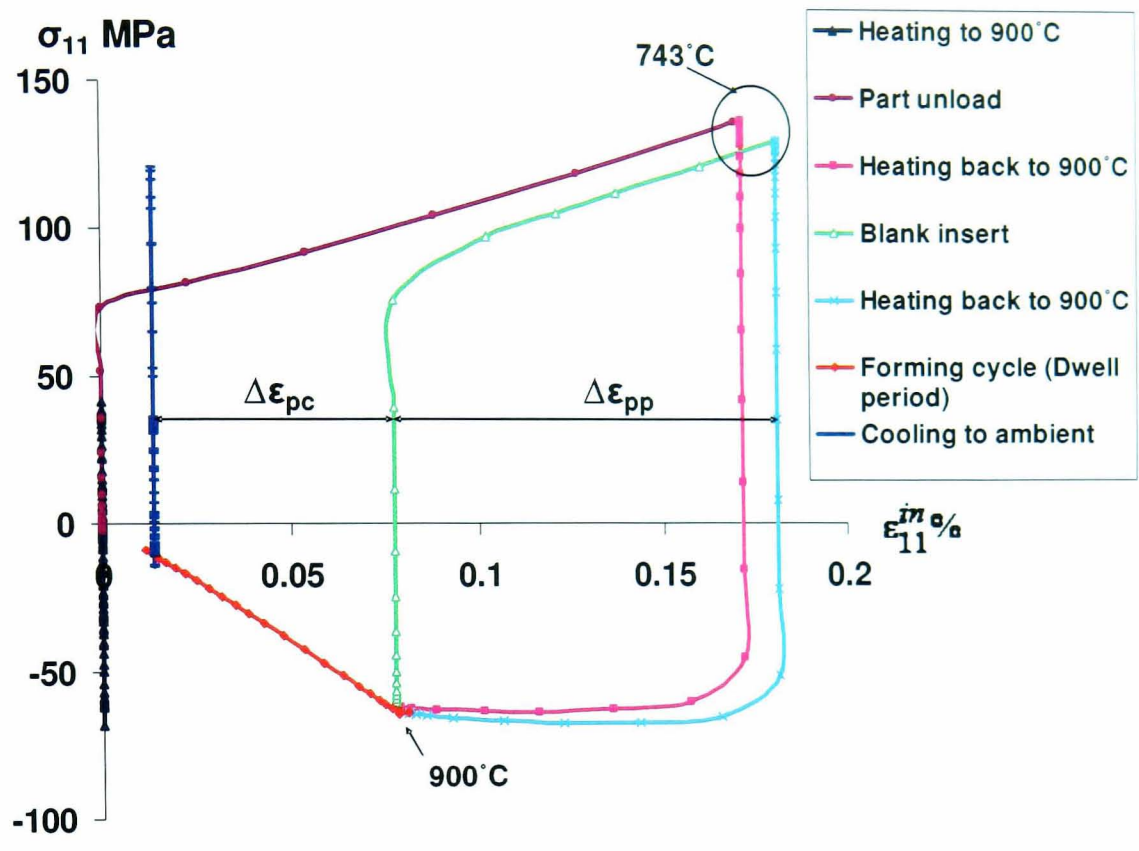
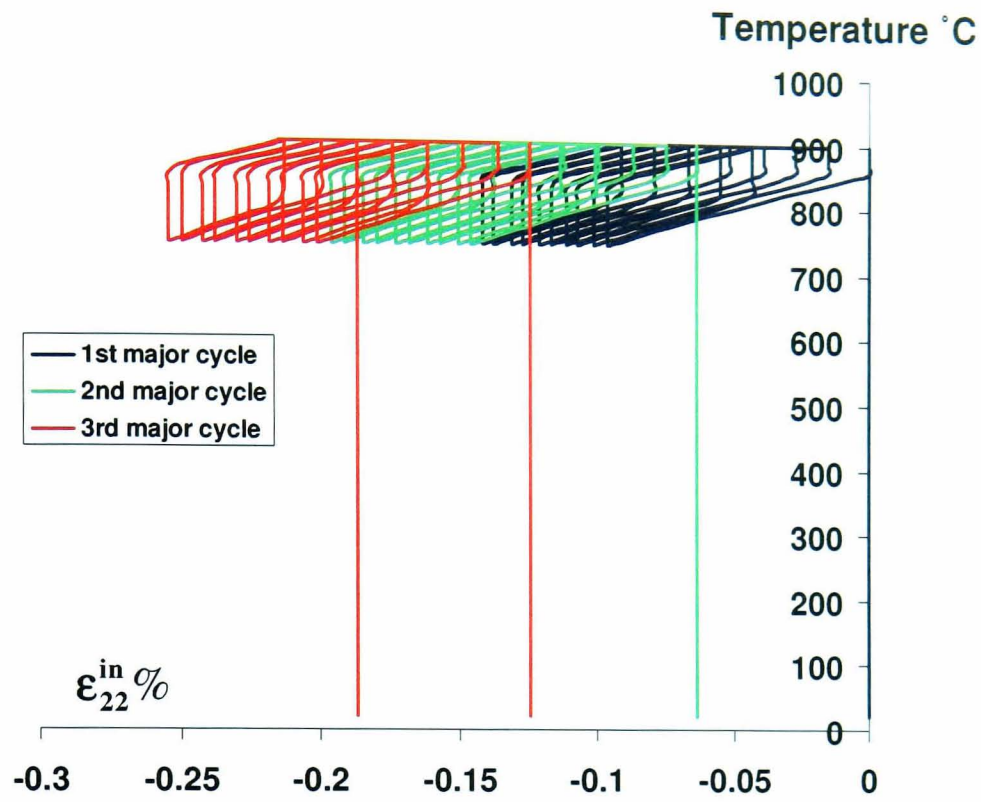
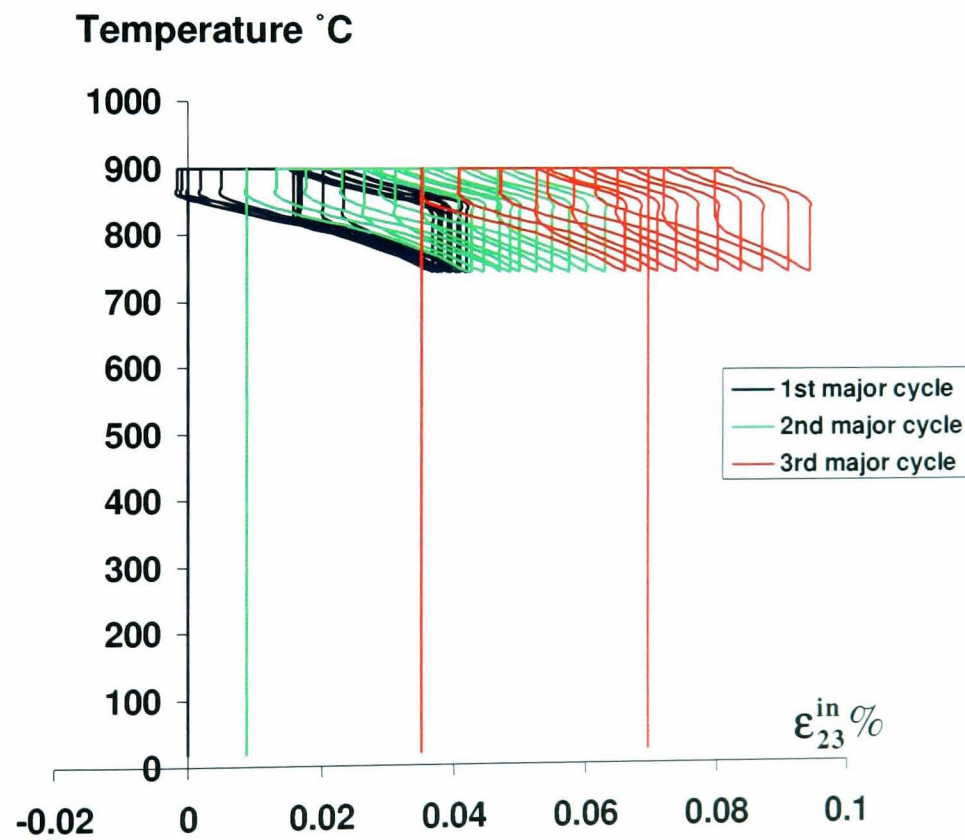


Figure 7.18 Predicted local stress versus local inelastic strain for the 1<sup>st</sup> minor cycle of the 1<sup>st</sup> major cycle at element 'E' (uncoupled plasticity-creep material behaviour model)



(a)



(b)

Figure 7.19 Predicted temperature versus local inelastic strain components for three major cycles each including five minor cycles at element 'E' from analysis employing uncoupled-plasticity creep model: (a) inelastic strain  $\epsilon_{22}^{in} \%$  (b) inelastic strain  $\epsilon_{23}^{in} \%$  (c) inelastic strain  $\epsilon_{33}^{in} \%$

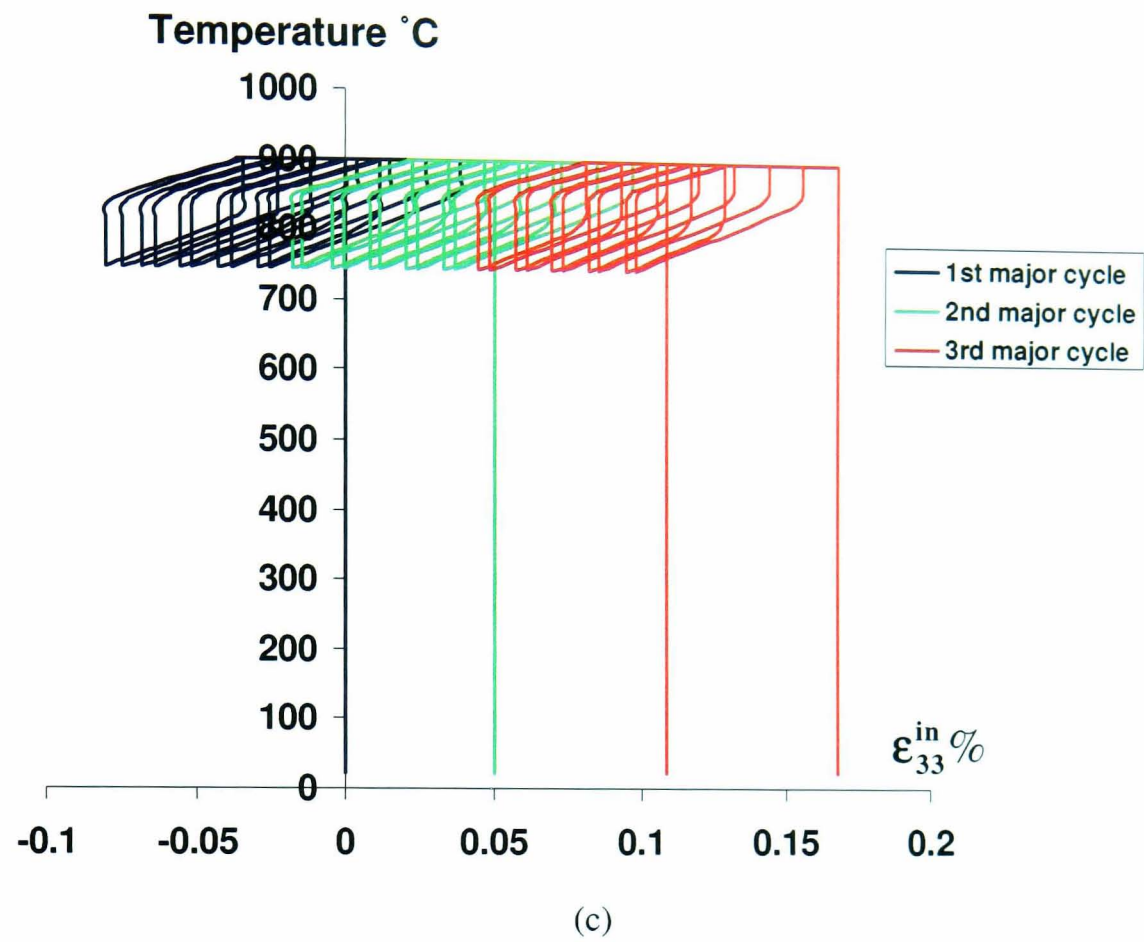


Figure 7.19 (Contd.) Predicted Temperature versus local inelastic strain components for three major cycles each including five minor cycles at element 'E' from analysis employing uncoupled-plasticity creep model: (c) inelastic strain  $\epsilon_{33}^{in} \%$

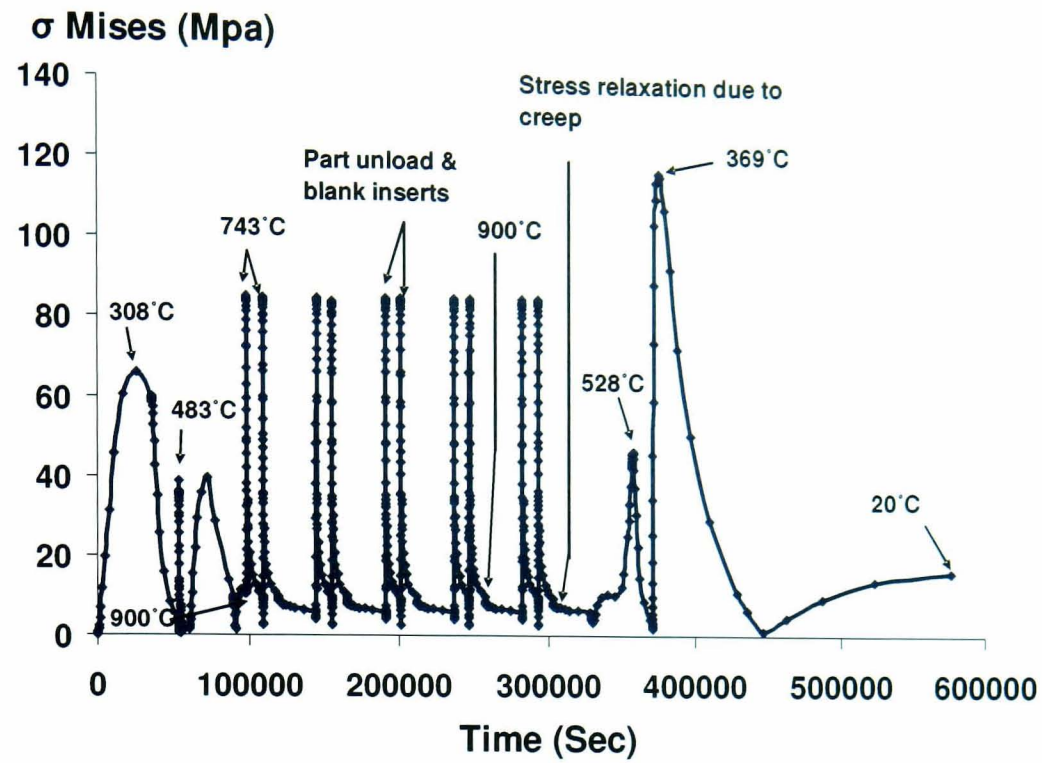


Figure 7.20 Equivalent (Von-Mises) stress history of 1<sup>st</sup> major cycle including five minor cycles for critical element 'E' shown in Figure 7.15, employing two-layer viscoplasticity material behaviour model

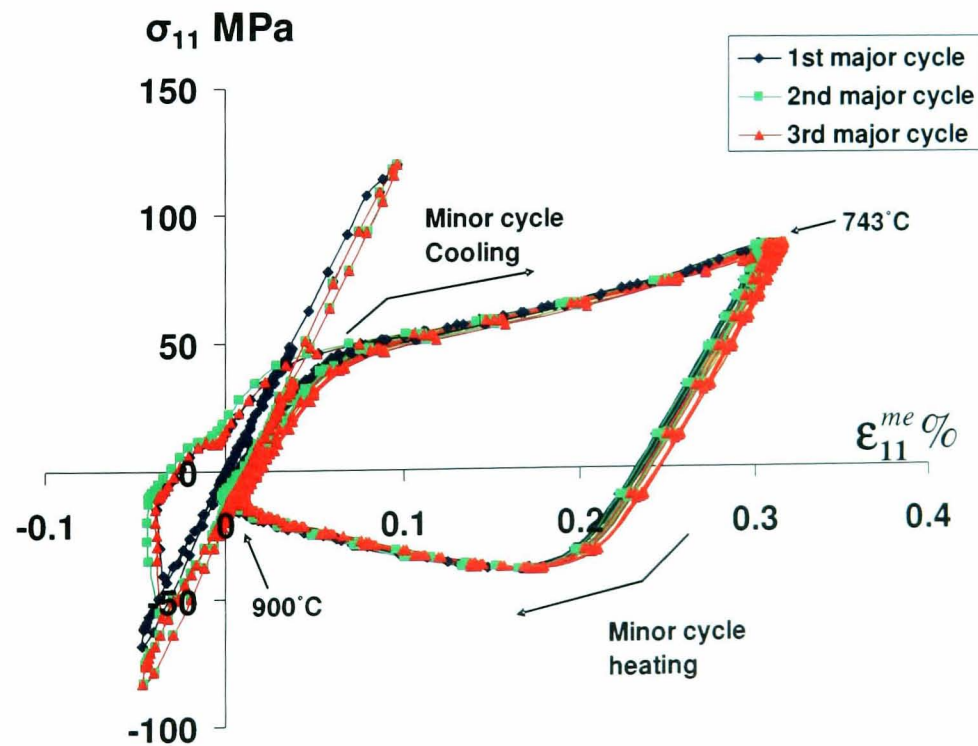


Figure 7.21 Predicted local stress versus local mechanical strain for three major cycles each including five minor cycles at element 'E' (two-layer viscoplasticity material behaviour model).

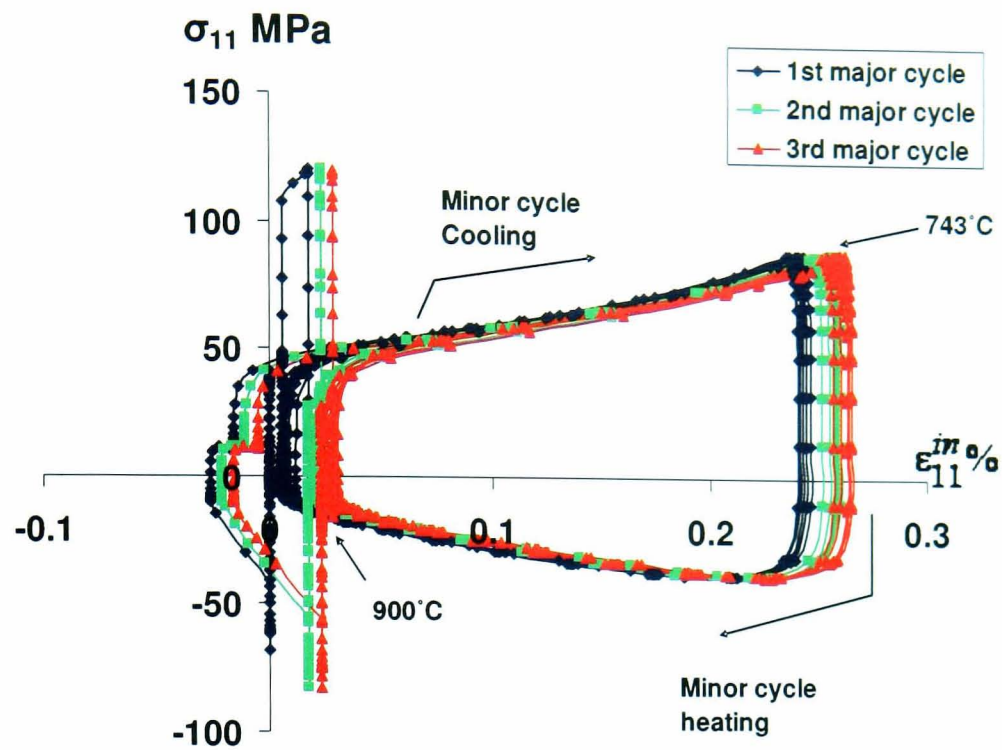


Figure 7.22 Predicted local stress versus local inelastic strain for three major cycles each including five minor cycles at element 'E' (two-layer viscoplasticity material behaviour model).

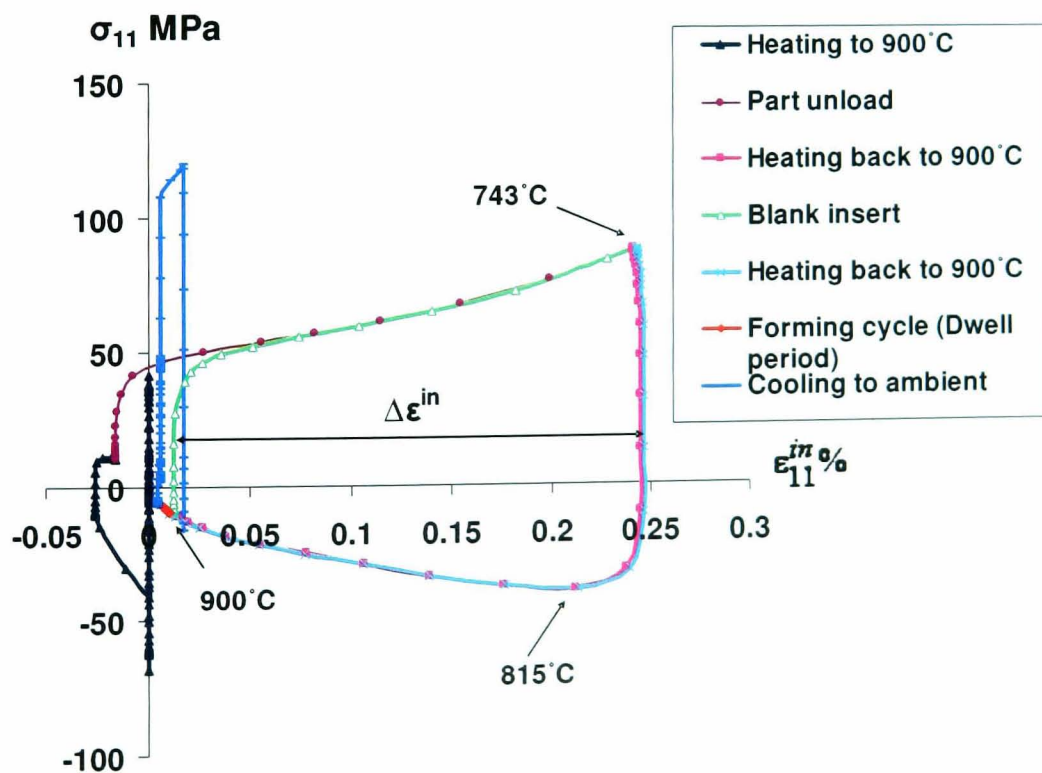


Figure 7.23 Predicted local stress versus local inelastic strain for the 1<sup>st</sup> minor cycle of the 1<sup>st</sup> major cycle at element 'E' (two-layer viscoplasticity material behaviour model).

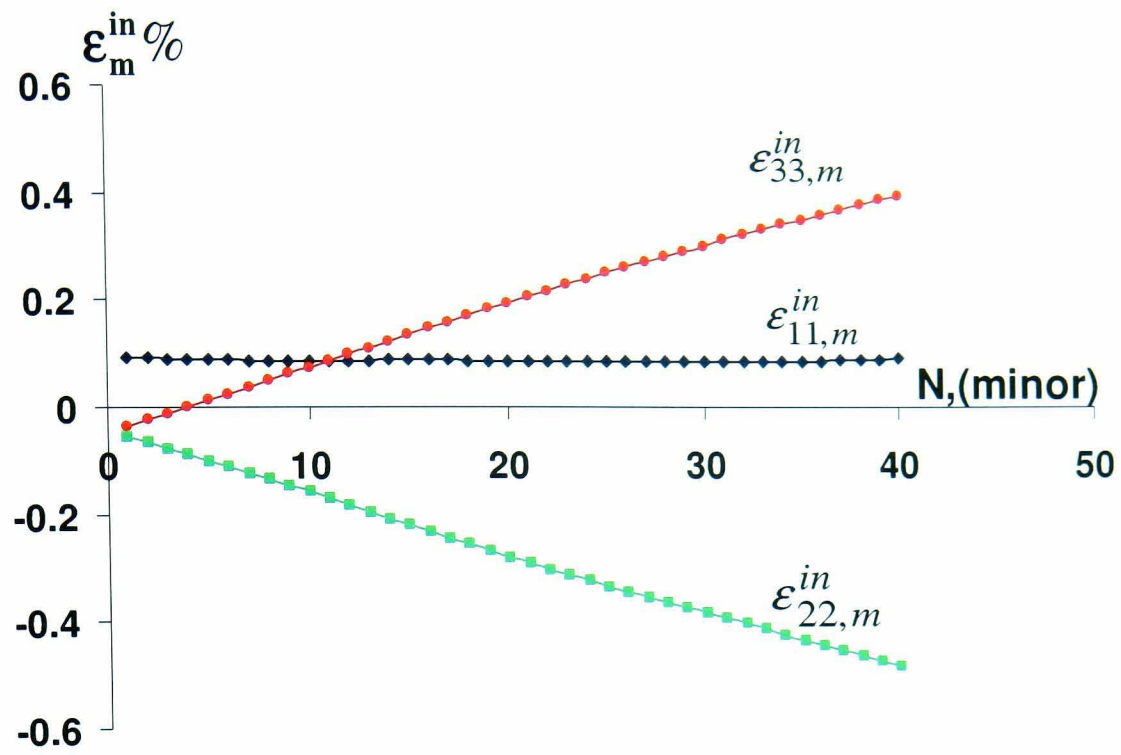


Figure 7.24 Predicted mean inelastic strain components versus number of minor cycles (uncoupled plasticity-creep model).

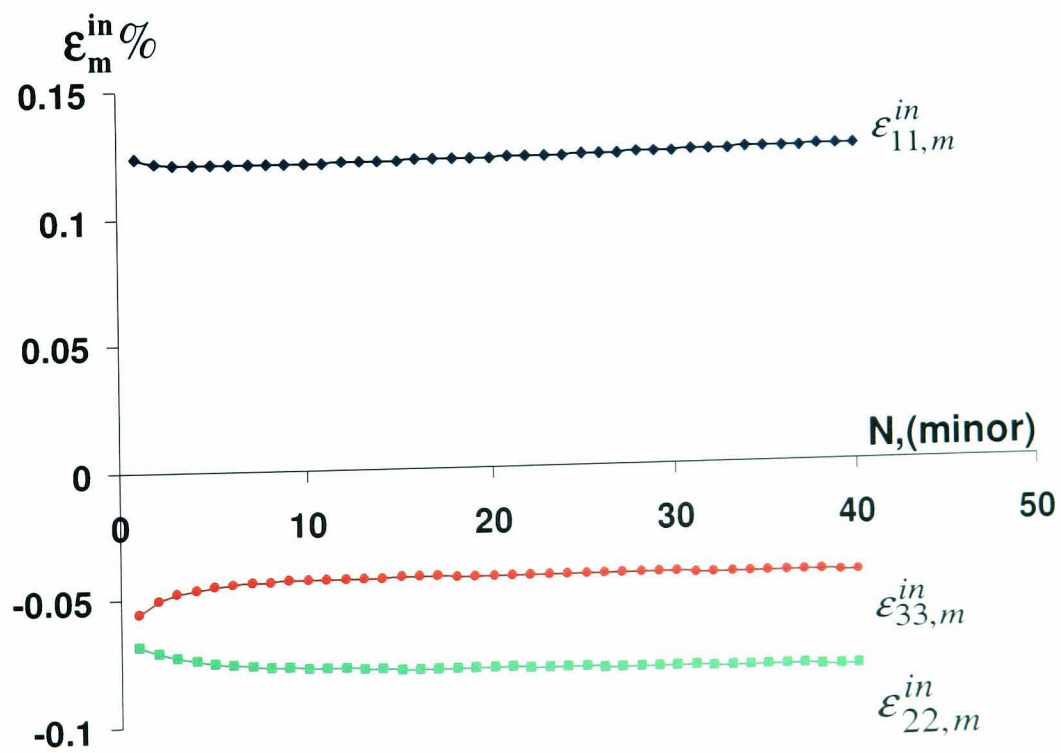
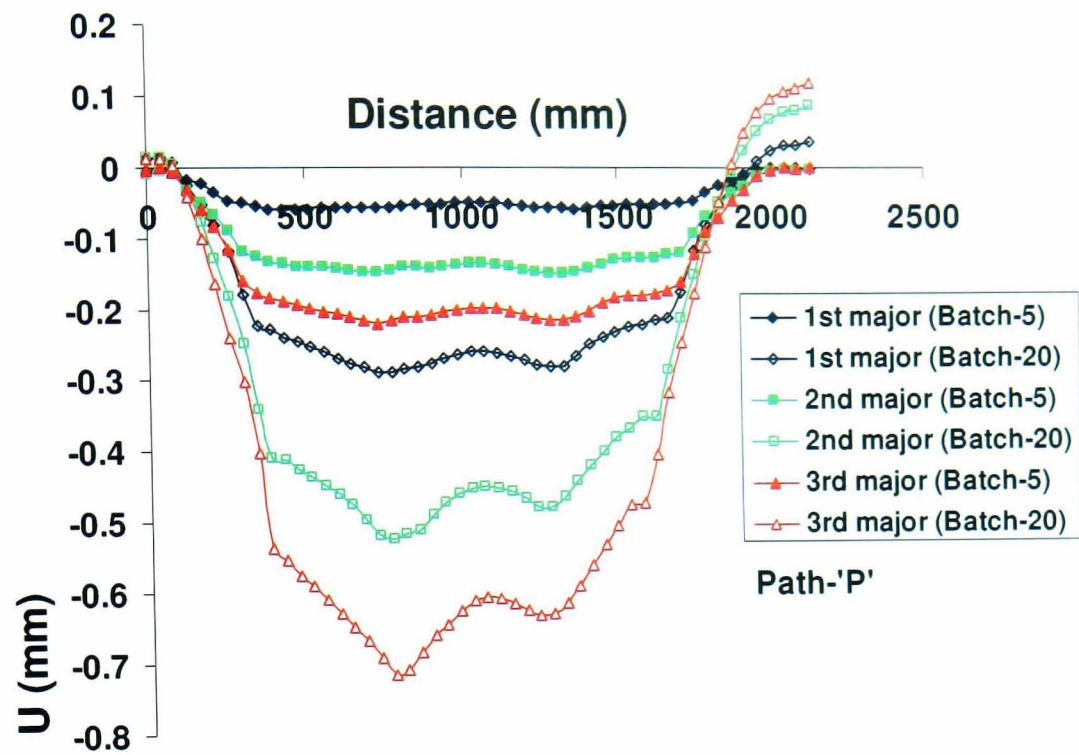
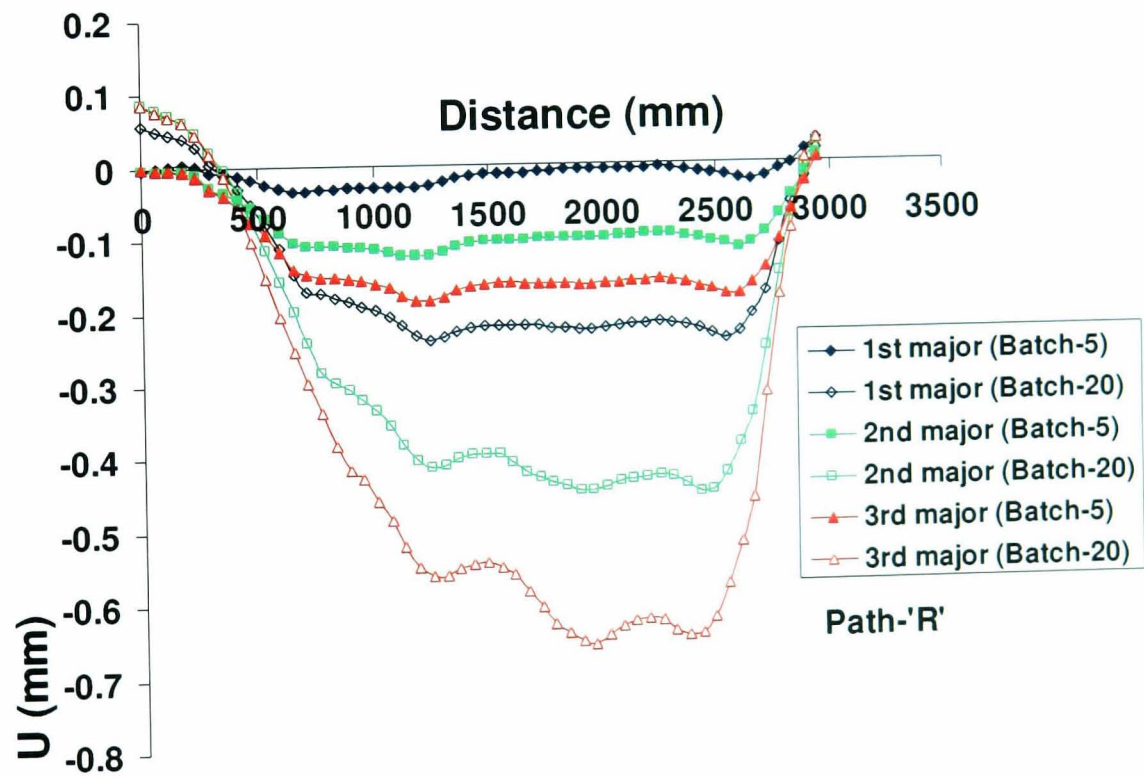


Figure 7.25 Predicted mean inelastic strain components versus number of minor cycles (two-layer viscoplasticity model)

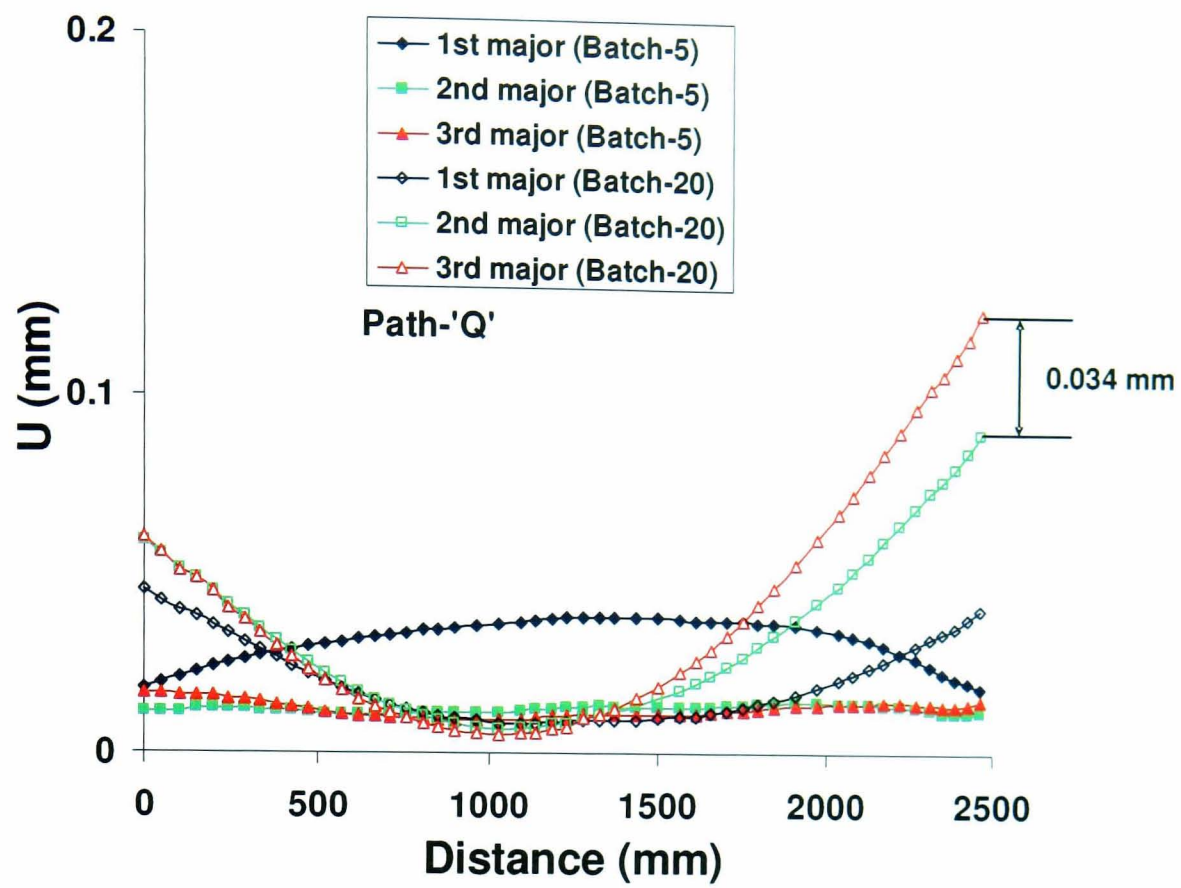


(a)



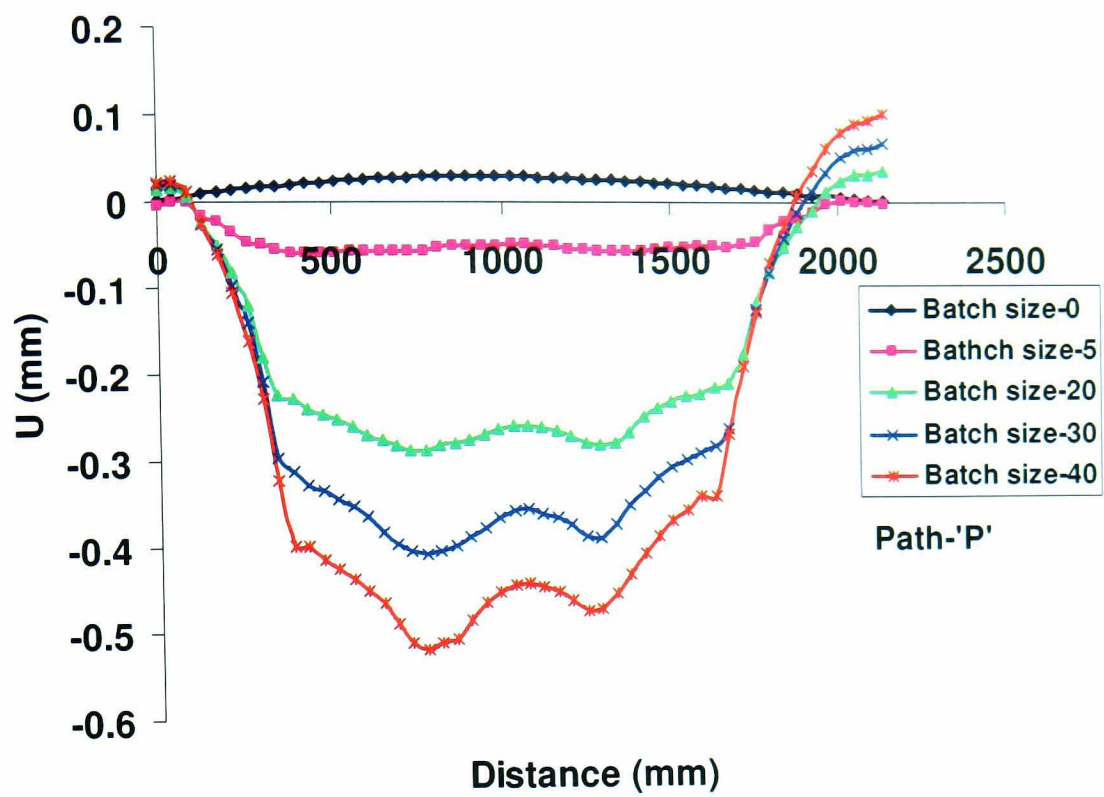
(b)

Figure 7.26 Predicted vertical nodal residual distortions for three major cycles of batch sizes five and twenty along paths; (a) Path 'P' (b) Path 'R' (c) Path 'Q'

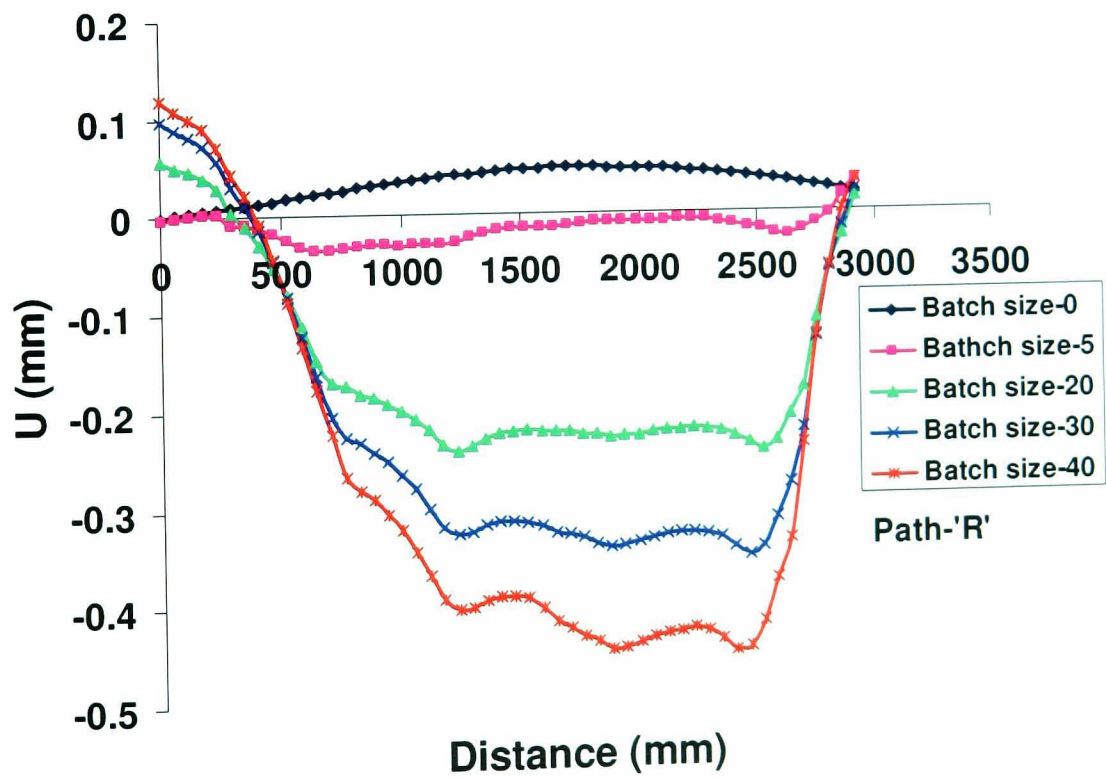


(c)

Figure 7.26 (Contd.) Predicted vertical nodal residual distortions for three major cycles of batch sizes five and twenty along path; ((a) Path 'P' (b) Path 'R' (c) Path 'Q')

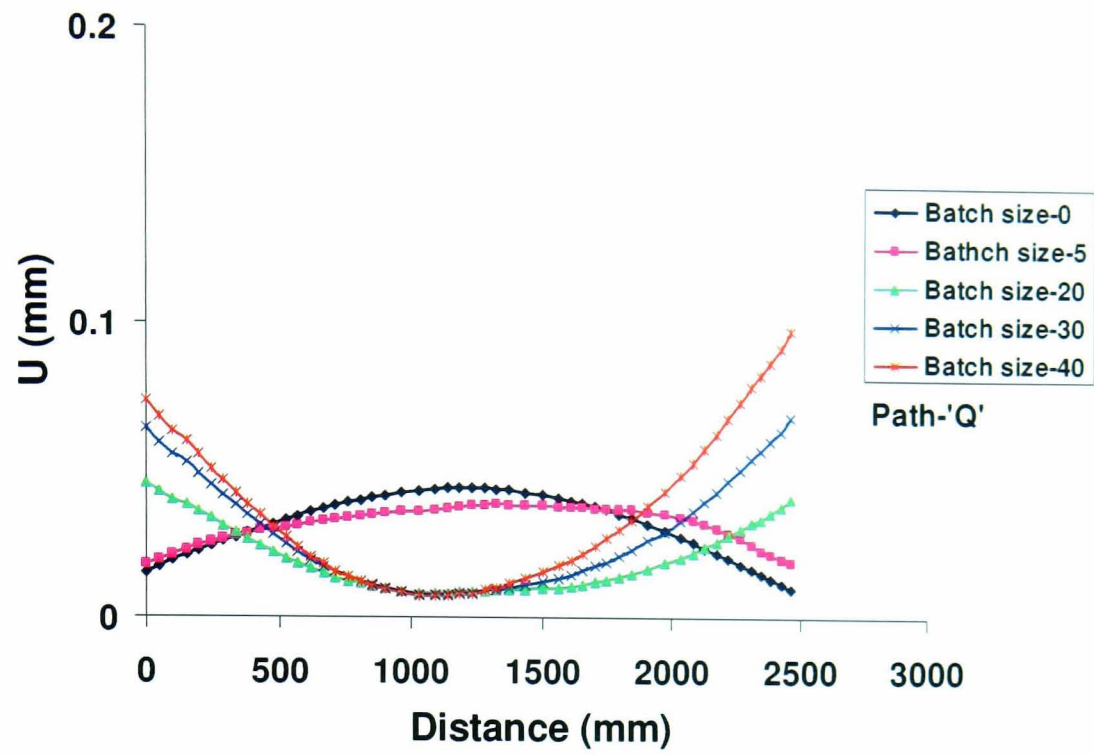


(a)



(b)

Figure 7.27 Predicted vertical nodal residual distortions for a major cycle of different batch sizes along paths; (a) Path 'P' (b) Path 'R' (c) Path 'Q'.



(c)

Figure 7.27 (Contd.) Predicted vertical nodal residual distortions for a major cycle of different batch sizes along path; (a) Path 'P' (b) Path 'R' (c) Path 'Q'

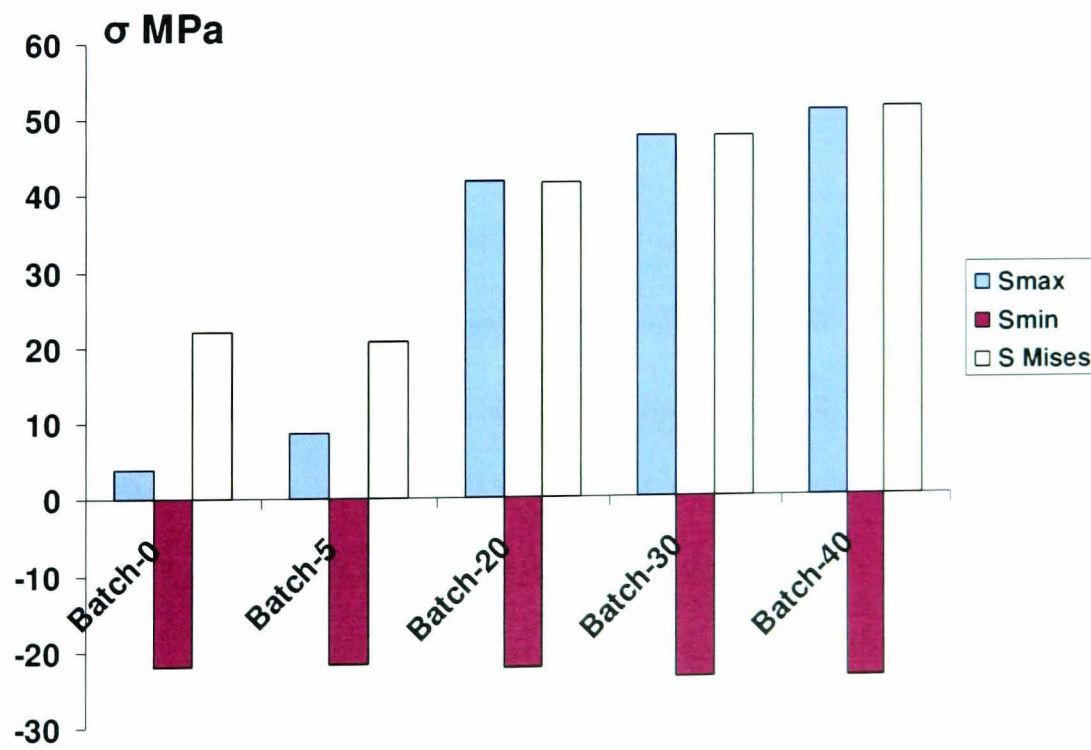


Figure 7.28 Maximum predicted residual tensile principal (Smax), compressive principal (Smin) and Equivalent (S Mises) stresses in the tool of a major cycle of different batch sizes.

## Chapter 8

### CONCLUSIONS AND FUTURE WORK

#### 8.1 Introduction

The high temperature cyclic and stress relaxation testing and modelling of XN40F alloy was carried out successfully to model the thermo-mechanical behaviour of a representative BAE SPF tool. The temperature dependent material constants for the combined non-linear kinematic/isotropic hardening, Norton's power law for secondary creep and the two-layer-viscoplasticity models were identified and the constants were validated against the experimental stress-strain data. Thermo-mechanical fatigue-creep and ratchetting lifing tests were performed to analyse the thermo-mechanical behaviour of the tool material under the most damaging phase (minor cycle) of thermal cycle. Isothermal lifing tests were also carried out to identify stress-strain-life equations for different life prediction models to predict the TMF-Creep and ratchetting life.

To investigate the thermo-mechanical behaviour of the tool and the failure mechanisms, thermal-elastic-plastic-creep FE analyses of a 3D representative BAE SPF tool were performed. The developed heat transfer methodology to model the SPF thermal cycles was validated against the heat transfer tests performed on the XN40F block. Sequentially coupled thermo-mechanical analyses were performed for various different loading conditions. In addition to thermal loading, the tool gravity and the clamping pressure was also incorporated in the FE models. The tool-platen contact was also modelled to simulate the realistic boundary conditions. The two

phenomenological material behaviour models, the uncoupled plasticity-creep and the two-layer viscoplasticity, were employed in the FE analyses and their effect on the thermo-mechanical behaviour of the tool was investigated. Different damage influencing factors such as thermal cycles, heating and cooling rates and batch sizes were evaluated. Various life prediction methodologies such as Coffin-Manson, Ostergren and Zamrik strain energy, ductility exhaustion and bi-linear strain range partitioning were explored in this project. Of these, the Zamrik model was found to be superior for the TMF life prediction of the tool.

## **8.2 Material characterisation and modelling**

Cyclic plasticity material constants for stainless steel SS-316 and XN40F alloy were identified successfully from the multistrain range isothermal cyclic tests carried out for a range of temperatures. For stainless steel SS-316, the non-linear kinematic hardening model gave an excellent correlation with the stabilised experimental stress-strain loops across range of temperatures; 20°C, 300°C and 600°C. In the case of XN40F alloy, the identified isothermal constants for the combined non-linear kinematic-isotropic hardening showed reasonable correlation with the experimental stress-strain loops, showing the largest discrepancies at high temperatures; 700°C and 900°C, mainly due to the omission of rate-dependent effects. The cyclic hardening behaviour of the XN40F alloy was successfully captured by the combined non-linear kinematic/isotropic hardening model. The cyclic hardening was observed for cyclic tests at temperatures of 20°C, 500°C and 700°C. However, a negligible cyclic hardening was seen at 900°C. The power law creep constants for a steady state secondary creep were identified from stress relaxation tests carried out at 500°C, 700°C and 900°C; however a negligible stress relaxation occurred at 500°C.

A two-layer visco-plasticity model, available within the commercial FE code ABAQUS was investigated in this project to capture thermo-mechanical behaviour of the SPF tool. The two-layer viscoplastic model constant  $f$  was identified by fitting the two layer model with stress relaxation test data using the identified creep constants from relaxation tests. Unlike cyclic plasticity models, the two-layer viscoplasticity model gave an excellent correlation with stabilised stress-strain loops of the isothermal cyclic tests at 700°C and 900°C.

An uncoupled cyclic-plasticity-creep model was also applied where the creep deformation is only considered during the constant temperature strain holds of TMF-creep tests and dwell time of the SPF tool analyses. A two-layer viscoplasticity model showed a reasonable and more accurate correlation with the experimental stabilised stress-strain loops of TMF-creep tests than that of the uncoupled plasticity-creep model. This is mainly due to the ability of the two-layer-viscoplasticity model to capture the strain rate effects during temperature transients.

### **8.3 Isothermal and TMF-creep ratchetting lifing tests**

Strain controlled isothermal, TMF and TMF-creep lifing tests were carried out on materials, stainless steel SS-316 and XN40F. For stainless steel, the IF life (600°C) for the lowest strain range employed ( $\Delta\varepsilon=1.0\%$ ) was observed to be higher than the corresponding TMF IP (450-600°C) life. However, the TMF OP life for the same strain range was seen to be lower than the TMF IP and IF lives. Moreover, for higher strain ranges, the TMF IP lives were observed to be lower than the corresponding IF lives.

In the case of XN40F alloy, the IF lives at 900°C tested for two strain ranges ( $\Delta\varepsilon=0.8\%$ ,  $1.2\%$ ) were observed to be smaller than the corresponding TMF OP (750-900°C) lives. The TMF OP tests with a strain hold showed shorter lives in relation to the corresponding lives of the IF and TMF OP tests without hold. The stress relaxation due to creep reduces life approximately by half from the TMF OP tests without a strain hold.

From all the above lifing tests, it can be concluded that the estimation of TMF and TMF-creep life based on the IF testing is not advisable especially for critical components working at high temperatures. It was also observed that for most lifing tests performed in this project, TMF lives were shorter than the corresponding IF lives. However this relationship can not be generalised as the TMF life changes with the material, strain rates, strain ranges and temperatures.

A representative strain controlled TMF test was designed and performed to capture the critical phase of blank insert and part removal along with a forming cycle dwell period based on preliminary FE analyses of SPF tool. A brittle fracture was observed at 2086<sup>th</sup> cycle and the representative SPF tool life was obtained. Stress controlled thermo-mechanical and isothermal ratchetting tests were also carried out to understand the material ratchetting behaviour of the XN40F alloy. The maximum and minimum stresses from the strain controlled representative test were applied in stress controlled ratchetting tests using the same cycle times.

In the representative stress controlled thermo-mechanical ratchetting test where the temperature is cycled between 750 to 900°C, the strain progresses in compression mainly due to the compressive stress hold period (120 seconds) at 900°C. The mean compressive strain of 9.91% was accumulated in 297 cycles before the test was stopped due to buckling of the specimen. A stress controlled thermo-mechanical ratchetting test without a stress hold showed the progression of strain in the tensile direction which is the direction of the mean stress. A tensile mean strain of 4.25% was accumulated in 7151 cycles and the test was stopped. Two stress controlled isothermal tests without a stress hold period were performed at 900 and 700°C. For 900°C, a tensile mean strain of 39% was accumulated in 32 cycles and thus a ductile fracture was observed at the end of 32<sup>nd</sup> cycle. For 700°C, a plastic shakedown was seen after initial transient ratchetting for the first five cycles. From stress controlled cyclic tests, the uniaxial material ratchetting phenomenon was studied under the tensile mean stress of 36 MPa obtained from the representative strain controlled TMF test. The strain and stress hold period at 900°C representing dwell period (forming cycle) in the SPF process appears to be extremely damaging for the tool material due to occurrence of significant creep deformation.

#### **8.4 Thermo-mechanical analyses of SPF tool**

Sequentially coupled thermo-mechanical analyses were performed on a representative BAE SPF tool to analyse the effect of major cycles, minor cycles, heating and cooling rates and batch sizes. For all analyses, inelastic strains were predicted to occur along the top surface edges of the tool where its behaviour is approximately uniaxial.

From major cycle analyses, preheating in the pre-heat oven and controlled cooling in the SPF press (thermal cycle 'B') was predicted to be less damaging than the direct heating to forming temperature and free cooling to ambient (thermal cycle 'A'). The pre-heating and controlled cooling result in better uniform temperature in the tool and ultimately lower the thermal stresses. Therefore, thermal cycle 'B' is recommended over thermal cycle 'A'. The controlled heating and cooling rates below the rate of 50°C/hr did not predict the significant improvement in the tool life. A higher rate of 80°C/hr was predicted to be extremely damaging. Therefore, considering the tool damage and the productivity of the process, the controlled heating and cooling rate of 50°C/hr appears to be appropriate.

The effect of high frequency minor cycles associated within major cycles were analysed employing both the material models; the uncoupled plasticity-creep and the two-layer viscoplasticity. For both models, damage due to minor cooling was mainly predicted along the top surface edges of the two long sides of the tool facing the press doors. This is mainly due to a high temperature gradient of 157°C occurring between the sides facing the press doors while the rest of the tool is still being heated at 900°C. The middle edge of the two long sides of the tool was predicted to be a critical location for cracks to appear.

The general local stress-strain loops were plotted for a critical element along local X direction parallel to the edge of the tool on which the critical element is present. Both material models predicted a plastic shakedown (reverse plasticity) in the local X direction. However, the predicted inelastic strain range of the two-layer model was higher than the uncoupled plasticity-creep due to time dependent deformation of the

two-layer model above 600°C. Moreover, a minor cycle ratchetting phenomenon was predicted locally by the uncoupled plasticity-creep model in a plane transverse to the local *X* direction. Alternatively, no ratchetting was predicted by the two-layer viscoplastic model. This may be due to the inability of this model to simulate long term static responses such as seven hours dwell time period of the SPF forming. From various thermo-mechanical analyses, the minor cycles were predicted to be extremely damaging than the major cycles alone.

Due to predicted progressive deformation, the uncoupled plasticity-creep model was further explored to analyse the effect of batch sizes on the tool behaviour. Thermo-mechanical analyses for different batch sizes were performed. The residual distortion was predicted to increase linearly with the batch size along the two side edges of the tool facing the press doors (Paths 'P' and 'R'). This is mainly due to the minor cycle plasticity-creep ratchetting behaviour predicted locally along these edges. The residual distortion was predicted to increase non-linearly with batch size across the middle portion of the tool (see path 'Q'). This progressive distortion can directly impair the dimensions of the formed parts. Furthermore, the part to be formed by the present BAE SPF tool has a tight tolerance of  $\pm 0.5$  mm. The present BAE tool experiences progressive distortion behaviour and needs intermittent re-machining to produce good quality components within the tolerance limit. Moreover, increasing tensile residual stresses may add to applied stresses in the tool which may lead to fatigue-creep cracking. Therefore the selection of batch size is crucial for the tool life, the quality of formed parts and the productivity of the process. From the predicted residual distortions and stresses, a batch size of twenty can be chosen over thirty and forty, considering together the tool damage and productivity.

From various thermo-mechanical analyses performed, three potential tool failure mechanisms, thermo-mechanical fatigue cracking, fatigue-creep cracking and ratchetting (progressive distortion) were identified. However, progressive distortion appears to be the primary failure mechanism since it hinders the progress of producing parts within tolerance and leads to intermittent machining of the tool prior to cracking. The fatigue-creep interaction is the most important aspect in the tool damage as it leads to both LCF and ratchetting. The minor and major cooling phases were predicted to be more damaging than the heating phases and therefore the optimisation of cooling processes is highly recommended.

## **8.5 SPF tool life predictions**

Different strain and strain energy life prediction methods were explored in this project. The strain energy methods such as Ostergren and Zamrik were found to be superior than the strain methods such as Coffin-Manson and bilinear strain range partitioning. Among all, the Zamrik model was chosen to predict the thermo-mechanical fatigue life of the tool since it consistently gave a conservative life for TMF tests performed, which is safer than other models. The bi-linear strain range partitioning was also employed. However, it significantly over predicted the tool life. The simplified ductility exhaustion approach was also employed to predict the ratchetting life.

The predicted low cycle fatigue and ratchetting failure mechanisms were considered to be independent while predicting the tool life. The predicted tool lives were compared against the representative TMF-creep test and industrial experience. The representative test gave a representative tool life of 104 major cycles using 20 as batch size. The industrial experience suggests that such tools develop cracks

approximately after 30 to 40 major cycles. The XN40F tools are not cracked yet however undergone intermittent machining after approximately 120 to 140 components formed.

The Zamrik model predicted 24 major cycles using the uncoupled plasticity-creep model and 58 major cycles using the two-layer viscoplastic model based on crack initiation. The simple ductility exhaustion method predicted cracking after 47 major cycles using the ductility limit at 700°C whereas 110 cycles were predicted using the limit at 900°C. Based on the predicted distortion behaviour and the tolerance on the formed component, the time to re-machine the tool was estimated to be after every 134 components formed. It is to be noted that the predicted tool lives were based on the FE predicted stress-strain-distortion data obtained from the employed standard specified thermal cycle (times to load the blank sheet and unload the formed component are fixed). However in practice these times vary significantly due to a significant human involvement in the SPF process.

## **8.6 Future work recommendations**

The heat transfer methodology applied was validated against the heat transfer tests carried out on the XN40F block. However, no gap conductance and cavity radiation was employed in the validation process and the SPF tool analyses. Therefore it is recommended to model the SPF press details and the platen to develop a more accurate thermal analysis of the tool.

In thermo-mechanical analyses, the tool-platen contact was modelled by considering platen as an analytically rigid surface. From industrial observations, the metallic

platens also deform due to high temperature creep which results into the additional damage to the tool. It is strongly suggested to model the platen as a deformable body to analyse the effect of platen deformation on tool damage. Even though few analyses of industrial SPF tool with local features were performed and summarised in the Appendix C, a detailed study of local features is recommended using better element type and mesh to quantify accurately the effect of local features on the tool damage.

A temperature dependent material constant  $f$  of the two-layer viscoplasticity model was obtained by fitting the model with stress relaxation test data. Therefore it is suggested to identify this constant by determining the elastic modulus of elastic-plastic and elastic-viscous networks using the strain controlled tension tests described in Chapter 4. The cyclic plasticity models employed in this thesis do not consider the strain rate effect. Hence it is suggested to include the strain rate effect in the cyclic plasticity modelling. Ratchetting was predicted by the uncoupled plasticity-creep model, however to predict ratchetting accurately, more complex material behaviour models such as the unified viscoplastic model with added static recovery term applied by Kang [26, 112] can be considered. Ratchetting is a difficult phenomenon to capture accurately in the constitutive model and requires significant research time to develop such constitutive models which again need to be modified with change of material.

Due to the limited number of specimens, repeat tests were not performed. Therefore all tests should be repeated at least twice to see the repeatability of results. Additional TMF-creep tests can be performed with different strain hold periods to analyse the

effect of changing hold times. To understand the interaction of low cycle fatigue and ratchetting, bi-axial strain and stress controlled TMF-creep tests are recommended. It is also suggested to perform representative tests on a small scale XN40F tool to validate more accurately the predicted tool lives and distortion behaviour.

The tool life predictions in this thesis were based on distortion and crack initiation. Therefore, it is recommended to extend this to crack propagation predictions, applying the damage and fracture mechanics theory.

## REFERENCES

1. Hamilton, C.H. and Ghosh, A.K., Superplastic Sheet Forming, in ASM Materials handbook, , 2000. Vol 14B, p. 853-873.
2. Kim, Y.H., J.-M. Lee, and S.S. Hong, Optimal design of superplastic forming processes, Journal of Materials Processing Technology, 2001. 112(2-3): p. 166-173.
3. Lee, K.S. and H. Huh, Numerical simulation of the superplastic moving die forming process with a modified membrane finite element method, Journal of Materials Processing Technology, 2001. 113(1-3): p. 754-760.
4. Gao, C.Y., P. Lours, and G. Bernhart, Thermomechanical stress analysis of superplastic forming tools, Journal of Materials Processing Technology, 2005. 169(2): p. 281-291.
5. Grimes, R., Extended brief, Materials World Volume, (July 2005)
6. Sanders, D., Reinforced ceramic dies for superplastic forming operations, in The Third European conference on Superplastic Forming, EuroSPF04, Bernhart.G, T. Cutard, and P. Lours, Editors. July 2004, Ecole des Mines d'Albi-Camau: Albi, France. p. 109-115.
7. Barnes, A. J., Superplastic Forming 40 Years and Still Growing, Journal of Materials Engineering and Performance, 2007. 16(4): p. 440-454.
8. Barnes, A. J., Industrial application of superplastic forming: trends and prospects, Material Science Forum, 2001. 357-359: p. 3-16.
9. Koç, M. and M.A. Arslan, Design and finite element analysis of innovative tooling elements (stress pins) to prolong die life and improve dimensional tolerances in precision forming processes, Journal of Materials Processing Technology, 2003. 142(3): p. 773-785.

10. Lours, P., Baleix, and G. Bernhart, Investigation on the Damage of Superplastic Forming Tools, Journal of Material process technology. (CDROM special issue), T. Chandra, et al., Editors. 2001, Elsevier Science.
11. Baleix, S., G. Bernhart, and P. Lours, Oxidation and oxide spallation of heat resistant cast steels for superplastic forming dies, Materials Science and Engineering A, 2002. 327(2): p. 155-166.
12. Baleix, S., et al., Surface and image analysis of oxides grown and spalled on heat resistant cast steels exposed to thermal cycles, Journal of Materials Processing Technology, 2001. 118(1-3): p. 321-328.
13. Durbin, M., Mechanical and creep properties of XN40F alloy. 2002, Aubert & Duval Company.
14. Bernhart, G., V. Velej, and E. Jourdain, Thermomechanical simulation of NI-CR-FE heat resistant SPF dies, 4th European Conference EuroSPF, 2005, IOM: London.
15. Bernhart, G., et al., Design of SPF dies based on advanced material behaviour models Material Science Forum, 2004. 447-448: p. 123-130
16. Shang, J., S.B. Leen, and T.H. Hyde, Finite-element-based methodology for predicting the thermo-mechanical behaviour of superplastic forming tools, Proceedings of the Institution of Mechanical Engineers, Part L: Journal of Materials: Design and Applications, 2006. 220(3): p. 113-123.
17. Giuliano, G., Constitutive equation for superplastic Ti-6Al-4V alloy. Materials & Design, 2008. 29(7): p. 1330-1333.
18. Giuliano, G. and S. Franchitti, On the evaluation of superplastic characteristics using the finite element method, International Journal of Machine Tools and Manufacture, 2007. 47(3-4): p. 471-476.

19. Kim, Y.H., et al., Analysis of superplastic forming processes using a finite-element method, *Journal of Materials Processing Technology*, 1996. 62(1-3): p. 90-99.
20. Lee, K.S. and H. Huh, Simulation of superplastic forming/diffusion bonding with finite-element analysis using the convective coordinate system, *Journal of Materials Processing Technology*, 1999. 89-90: p. 92-98.
21. Tao, J. and M.A. Keavey, Finite element simulation for superplastic forming using a non-Newtonian viscous thick section element, *Journal of Materials Processing Technology*, 2004. 147(1): p. 111-120.
22. Wood, R.D. and J. Bonet, A review of the numerical analysis of superplastic forming. *Journal of Materials Processing Technology*, 1996. 60(1-4): p. 45-53.
23. Carrino, L., G. Giuliano, and C. Palmieri, On the optimisation of superplastic forming processes by the finite-element method. *Journal of Materials Processing Technology*, 2003. 143-144: p. 373-377.
24. Deshpande, A. A., Leen, S. B. and Hyde, T.H. High-Temperature Experimental Characterisation Of XN40F For Life Prediction Of SPF Tools. 2008, HAL - CCSD.
25. Chippendale, J. and Leaver, I., 2005, British Aerospace Systems UK.
26. Kang, G., et al., Time-dependent ratchetting experiments of SS304 stainless steel, *International Journal of Plasticity*, 2006. 22(5): p. 858-894.
27. Hertzberg, R.W., *Deformation and Fracture Mechanics of Engineering Materials*. 1996: John Wiley and Sons.
28. Wohler, A., *Zeitschrift fur Bauwesen* , 1860, 10. English summary: *Engineering*, 1860, 4, p.160-161.

29. Ashby, M.F. and Jones, D.R.H., *Engineering Materials 1, An introduction to their properties and applications*, 1996, Butterworth Heinemann.
30. Hardrath, H.F., Utley, E.C., Guthrie, D.E., in TN D-210, 1959, NASA.
31. Kraus, H., *Creep analysis*. 1980, Chichester: John Wiley.
32. Miller, D.R., *Thermal Stress Ratchet Mechanism in Pressure Vessels*, A.S.M.E., *J. Basic Eng.*, 1959. 81: p. 190-196.
33. Edmunds, H.G. and F.J. Beer, *Notes on Incremental Collapse in Pressure Vessels*, *J. Mech. Eng. Sci.*, 1961. 5: p. 187-199.
34. Burgreen, D., *Structural Growth Induced by Thermal cycling*, A.S.M.E., *J. Basic Eng.*, 1968. 90: p. 469-475.
35. Bree, J., *Elastic Plastic Behaviour of Thin Tubes Subjected to Internal Pressure and Intermittent High Heat Fluxes*, *J. Strain Analysis*, 1967. 2: p. 226-238.
36. Bree, J., *Incremental Growth Due to Creep and Plastic Yielding of Thin Tubes Subjected to Internal Pressure and Cyclic Thermal Stresses*, *J. Strain Analysis*, 1968. 3: p. 122-127.
37. Benham, P.P. and H. Ford, *Low endurance fatigue of a mild steel and an aluminium alloy*, *J. Mech. Eng. Sci.*, 1961. 3(2): p. 119-132.
38. Coffin, L.F., *The stability of metals under cyclic plastic strain*, *Trans. A.S.M.E., J. Basic Eng.*, 1960. 82D: p. 671-682.
39. Kapoor, A., *A Re-evaluation of the Life to Rupture of Ductile Metals by Cyclic Plastic Strain*, *Fatigue & Fracture of Engineering Materials Structures*, 1994. 17(2): p. 201-219.
40. Hübel, H., *Basic conditions for material and structural ratcheting*, *Nuclear Engineering and Design*, 1996. 162(1): p. 55-65.

41. Thomas, G., J. Bressers, and D. Raynor, Low-Cycle Fatigue and Life Prediction Methods, High Temperature Alloys for Gas Turbines. 1982. R.Brunetaud Ed., D. Riedel Publishing Co. Netherlands. p. 291-317.
42. Bill, R., M. Verrilli, and G. Halford, A Preliminary study of the Thermo-Mechanical Fatigue of Polycrystalline MAR M-200. 1984, NASA TP-2280.
43. Liu, F., et al., Thermal-mechanical fatigue behaviour of a cast K417 nickel-based superalloy, International Journal of Fatigue, 2002. 24(8): p. 841-846.
44. Shi, H.J., et al., High temperature fatigue behaviour of TZM molybdenum alloy under mechanical and thermomechanical cyclic loads, Journal of Nuclear Materials, 2000. 278(2-3): p. 328-333.
45. Roth, M. and H. Biermann, Thermo-mechanical fatigue behaviour of the [gamma]-TiAl alloy TNB-V5, Scripta Materialia, 2006. 54(2): p. 137-141.
46. Mannan, S.L. and M. Valsan, High-temperature low cycle fatigue, creep-fatigue and thermomechanical fatigue of steels and their welds, International Journal of Mechanical Sciences, 2006. 48(2): p. 160-175.
47. Zhou, H., et al., Investigations on the thermo-mechanical fatigue of two Ni-based single-crystal superalloys. Materials Science and Engineering A, 2005. 394(1-2): p. 161-167.
48. Park, S.J., K.S. Kim, and Kim, H.S., Ratchetting behaviour and mean stress considerations in uniaxial low-cycle fatigue of Inconel 718 at 649 C, Fatigue & Fracture of Engineering Materials & Structures, 2007. 30: p. 1076-1083.
49. Weiß, E., et al., Simulation of ratcheting and low cycle fatigue, International Journal of Pressure Vessels and Piping, 2004. 81(3): p. 235-242.
50. Rider, R.J., Harvey, S.J., and Chandler, H.D., Fatigue and ratcheting interactions, International Journal of Fatigue, 1995. 17(7): p. 507-511.

51. Kang, G. and Y. Liu, Uniaxial ratchetting and low-cycle fatigue failure of the steel with cyclic stabilizing or softening feature, *Materials Science and Engineering: A*, 2008. 472(1-2): p. 258-268.
52. Kang, G., Y. Liu, and J. Ding, Multiaxial ratchetting-fatigue interactions of annealed and tempered 42CrMo steels: Experimental observations, *International Journal of Fatigue*, 2008. 30(12): p. 2104-2118.
53. Satyadevi, A., Sivakumar, S.M. and Bhattacharya, S.S., A new failure criterion for materials exhibiting ratcheting during very low cycle fatigue, *Materials Science and Engineering: A*, 2007. 452-453: p. 380-385.
54. Ohno, N., Recent topics in constitutive modeling of cyclic plasticity and viscoplasticity, *Appl. Mech. Rev.*, 1990. 43(11): p. 283-295.
55. Chaboche, J., Constitutive equations for cyclic plasticity and cyclic viscoplasticity, *International Journal of Plasticity*, 1989. 5: p. 247-302.
56. McDowell, D.L., A bounding surface theory for cyclic thermo-plasticity, *Journal of Engineering Material. Technology*, 1992, 114: p. 297-303.
57. Ohno, N. and J. Wang, Nonisothermal constitutive modeling of inelasticity based on bounding surface, *Nuclear Engineering and Design*, 1992. 133: p. 369-381.
58. du Preez, R.J., Assessment of thermal stresses and ratchetting in reactor vessels, *International Journal of Pressure Vessels and Piping*, 1995. 61(2-3): p. 411-425.
59. Hyde, T.H., The Effect of Tranverse Pressure Loading on the Thermal Ratchetting of Circular Plates, *Journal of Strain Analysis*, 1980. 15(4): p. 217-223.

60. Velay, V., Bernhart, G., and Penazzi, L., Cyclic behaviour modeling of a tempered martensitic hot work tool steel, *International Journal of Plasticity*, 2006. 22(3): p. 459-496.
61. Bernhart, G., Moulinier, G., Brucelle O. and Delagnes, D., High temperature low cycle fatigue behaviour of a martensitic forging tool steel, *International Journal of Fatigue*, 1999. 21(2): p. 179-186.
62. Lemaitre, J. and Chaboche, J., *Mechanics of solid materials*, 1990: Cambridge university press.
63. Zhang, Z., Delagnes, D. and Bernhart, G., Anisothermal cyclic plasticity modelling of martensitic steels, *International Journal of Fatigue*, 2002. 24(6): p. 635-648.
64. Chaboche, J. L., On some modifications of kinematic hardening to improve the description of ratcheting effects, *International Journal of Plasticity*, 1991. 7(7): p. 661-678.
65. Ohno, N. and Wang, J. , Kinematic hardening rules with critical state of dynamic recovery: I. Formulation basic features for ratcheting behaviour, *International Journal of Plasticity*, 1993. 9(3): p. 375-389.
66. Ohno, N. and Wang, J. Kinematic hardening rules with critical state of dynamic recovery: II. Application to experiments of ratcheting behaviour, *International Journal of Plasticity*, 1993. 9(3): p. 390-403.
67. Bari, S. and Hassan, T., An advancement in cyclic plasticity modeling for multiaxial ratcheting simulation, *International Journal of Plasticity*, 2002. 18(7): p. 873-894.

68. Yaguchi, M. and Takahashi, Y. Ratcheting of viscoplastic material with cyclic softening, Part I: experiments on modified 9Cr-1Mo steel, *International Journal of Plasticity*, 2005. 21(1): p. 43-65.
69. Kan, Q.H., Kang, G.Z. and Zhang, J., Uniaxial time-dependent ratchetting: Visco-plastic model and finite element application, *Theoretical and Applied Fracture Mechanics*, 2007. 47(2): p. 133-144.
70. Lee, H.-Y., Kim, J.B., Lee, J-H. and Yoo, B., Prediction of Ratchetting Behaviour of 304 SS Cylindrical Shell using the Chaboche model, in *Creep-fatigue damage rules for advanced fast reactor design*, Technical committee meeting, 1996, International Atomic Energy Agency, Vienna (Austria) Manchester UK. p. pp:243-251
71. Krämer, D., Krolop, S., Scheffold, A. and Stegmeyer, R., Investigations into the ratchetting behaviour of austenitic pipes, *Nuclear Engineering and Design*, 1997. 171(1-3): p. 161-172.
72. Kulkarni, S.C., Desai, Y. M., Kant, T., Reddy, G. R., Prasad, P., Vaze, K. K. and Gupta, C., Uniaxial and biaxial ratchetting in piping materials--experiments and analysis, *International Journal of Pressure Vessels and Piping*, 2004. 81(7): p. 609-617.
73. Mahbadi, H. and Eslami, M.R., Elastic-plastic-creep Cyclic Loading of Thick Pressure Vessels based on the Frederick-Armstrong kinematic hardening model, *Structural Mechanics in Reactor Technology*. 2003: Prague, Czech Republic.
74. Kawashima, F., Ishikawa, A. and Asada, Y., Ratcheting deformation of advanced 316 steel under creep-plasticity condition, *Nuclear Engineering and Design*, 1999. 193(3): p. 327-336.

75. Solasi, R., Zou, Y., Huang, X. and Reifsnider, K., A time and hydration dependent viscoplastic model for polyelectrolyte membranes in fuel cells. *Mechanics of Time-Dependent Materials*, 2008. 12(1): p. 15-30.
76. Zhuang, W.Z. and Swansson, N.S., Thermo-Mechanical Fatigue Life Prediction: A Critical Review, A. Aeronautical and Maritime Research Laboratory, Editor, 1998, Defence Science and Technology Organisation.
77. Chaboche, J., Lifetime Predictions and Cumulative Damage under High Temperature Conditions, *Low-Cycle Fatigue and Life Prediction*, 1982, American Society for Testing and Materials. p. 81-104.
78. Taira, S., Lifetime of Structures Subjected to Varying Load and Temperature, *Creep in Structures*, Hoff, N.J., Editor, 1962, Springer-Verlag. p. 96-124.
79. Coffin, L.J., The Concept of Frequency Separation in Life Prediction for Time Dependent Fatigue, *ASME-MPC Symposium on Creep-Fatigue Interaction*, 1976. New York: American Society for Mechanical Engineers.
80. Ellison, E., A Review of the Interaction of Creep and Fatigue, *J. Mech. Eng. Sci.*, 1969. 11(3): p. 318-339.
81. Manson, S., G. Halford, and M. Hirschberg. Creep-Fatigue Analysis by Strain range Partitioning, *Symposium on Design for Elevated Temperature Environment*, 1971. New York: A.S.M.E.
82. He, et al. Strain Energy Partitioning and its Application to GH33A Nickel-base Superalloy and 1Cr-18Ni-9Ti Stainless Steel, *A.S.M.E international conference on advances in life prediction methods*, 1983. New York.
83. Ostergren, W., A damage function and associated failure equations for predicting hold time and frequency effects in elevated temperature, low cycle fatigue, *J. Test Eval.*, 1976. 4(5):327-39.

84. Suresh, S., *Fatigue of Materials*, 1998: Cambridge University Press.
85. Smith, R.N., Watson, P., and Topper, T.H., A stress strain function for the fatigue of metal, *J.Mater. JMLSA*, 1970. 5: p. 767-778.
86. Maier, H., R., Teteruk, and Christ, H.-J., Modelling thermomechanical fatigue life, *Mater. High Temp*, 2002. 19(1): p. 9-17.
87. Tomkins, B., Fatigue crack propagation-an analysis, *Philosophical Magazine*, 1968. 18(155): p. 1041 - 1066
88. Nagesha, A., et al., Thermomechanical fatigue evaluation and life prediction of 316L (N) stainless steel. *International Journal of Fatigue*, 2008. In Press, Corrected Proof.
89. Jeong, C.Y., et al., Normalized creep-fatigue life prediction model based on the energy dissipation during hold time, *Materials Science and Engineering: A*, 2007. 460-461: p. 195-203.
90. Yoon, Y.C. and S.W. Nam, A Correlation between Creep-Fatigue Life and Tensile Time for Austenitic Stainless Steels, *J.Mater. Sci*, 1994. 13: p. 1270-1271.
91. Feltham, P., *J. Inst. Met.*, 1961. 89: p. 210-214.
92. Goodman, J., *Mechanics Applied to Engineering*. 1919.
93. Walker, K., The effect of stress ratio during crack propagation for 2024-T3 and 7075-T6 aluminium, *Effects of Environment and Complex Load History on Fatigue Life*, 1970. Philadelphia: American Society for Testing Materials.
94. Shang, J., T.H. Hyde, and S.B. Leen, Finite element-based life prediction for high-temperature cyclic loading of a large superplastic forming die, *The Journal of Strain Analysis for Engineering Design*, 2006. 41(8): p. 539-559.

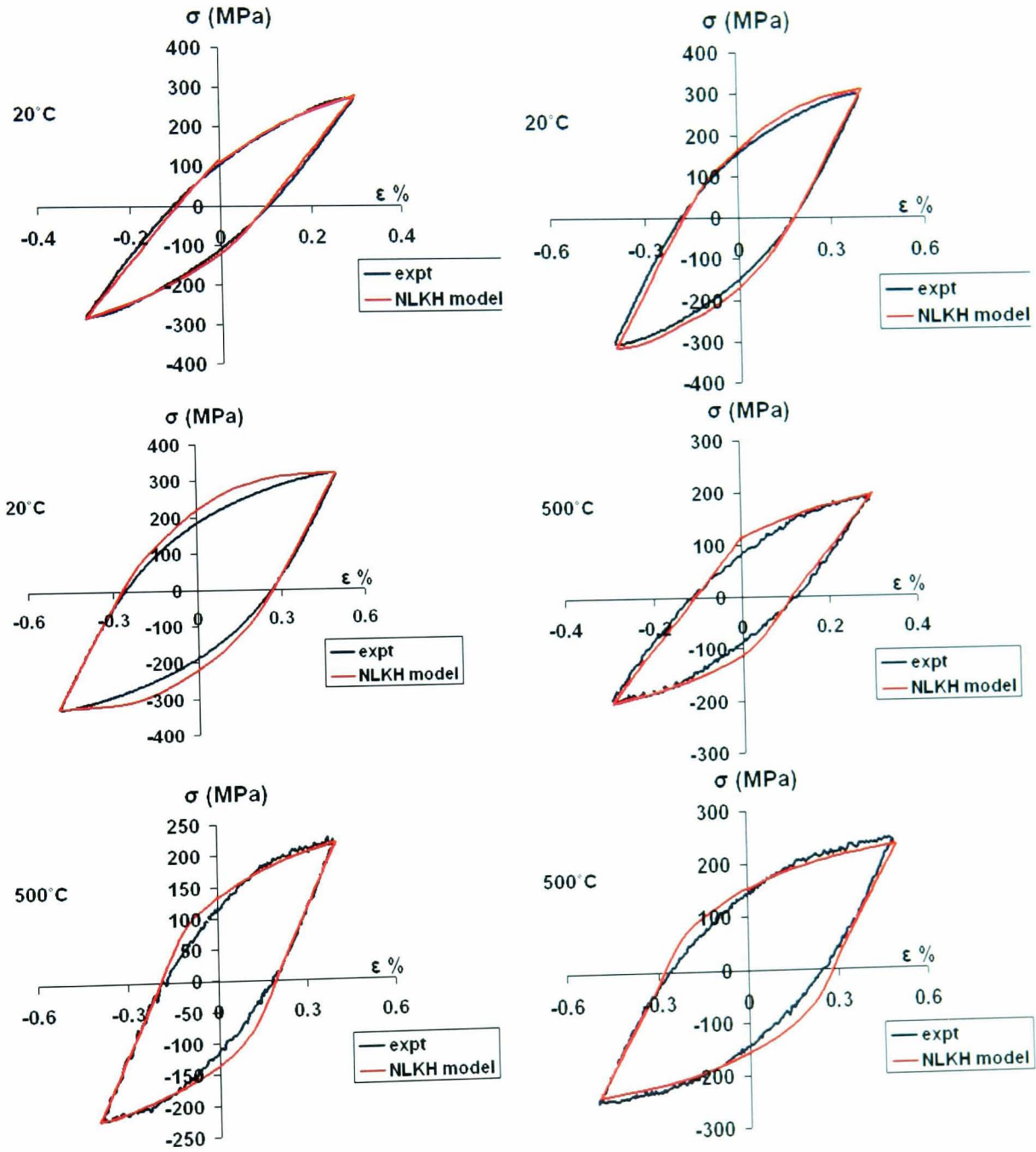
95. Jiang, Q.C., Fang, J.R. and Guan, Q.F., Thermomechanical fatigue behaviour of Cr-Ni-Mo cast hot work die steel, *Scripta Materialia*, 2001. 45(2): p. 199-204.
96. Liu, F., Wang, Z. G., Ai, S. H., Wang, Y. C., Sun, X. F., Jin, T. and Guan, H. R. , Thermo-mechanical fatigue of single crystal nickel-based superalloy DD8, *Scripta Materialia*, 2003. 48(9): p. 1265-1270.
97. Hahner, P., Affeldt, E, Beck, T, Klingelhoffer, H, Loveday, M and Rinaldi, C, Validated Code-of-Practice for Strain-Controlled Thermo-Mechanical Fatigue Testing, European Commission Joint Research Centre, 2006.
98. Hyde, C. J., Sun, W. and Leen, S.B., Cyclic thermo-mechanical material modelling and testing of 316 stainless steel, in *Creep and Fracture in High Temperature Components– Design and Life Assessment*. 2009: Zurich, Switzerland.
99. TMF Testing System manual. 2007, Instron Limited, UK.
100. ABAQUS User and Theory manual, Version 6.6, 2004, HKS inc, Rhode Is: US.
101. Charkaluk, E., et al., Fatigue design of structures under thermomechanical loadings, *Fatigue & Fracture of Engineering Materials & Structures*, 2003. 26(7): p. 661-661.
102. Zamrik. S.Y and Renauld, M.L., Thermo-mechanical Out-of-Phase Fatigue Life of Overlay Coated IN-738LC Gas Turbine Material, in *ASTM Special Technical Publication 2000*, ASTM, Conshohocken, PA, United States. p. 119-137.
103. Miner, M., Cumulative Damage in Fatigue, *Journal of Applied Mechanics*. 1952, Transactions A.S.M.E.

104. Robinson, E., Effect of Temperature Variation on the Long-Time Rupture Strength of Steels, Transactions A.S.M.E., 1952. 74(5): p. 777-780.
105. Priest, R. and E. Ellison, A Combined Deformation Map Ductility Exhaustion Approach to Creep-Fatigue Analysis, Material Science and Engineering, 1981. 49: p. 7-17.
106. Halford, G.R., Hirschberg, H.M. and Manson, S.S., Temperature Effects on the Strain range Partitioning Approach for Creep Fatigue Analysis, in Fatigue at Elevated Temperatures. 1973, American Society for Testing and Materials. p. 658-669.
107. Shang, J., et al., FE modelling of transient heat transfer in SPF dies, in Euro-SPF, Third European Conference on Super plastic forming, July 2004, Ecole des Mines d'Albi-Carmaux: France. p. 125-133.
108. Bejan, A., Heat Transfer. 1993: John Wiley and Sons.
109. Penny J, et al., Thermal properties of the alloys, A report for British Aerospace Systems plc. September 1995.
110. Incropera, F.P. and D.P. Dewitt, Introduction to Heat Transfer, 3 ed. 1996: John Wiley & Sons.
111. Shang, J., Thermo-mechanical life assessment of SPF tools. 2005, University of Nottingham, UK.
112. Kang, G., Ratchetting: Recent progresses in phenomenon observation, constitutive modeling and application, International Journal of Fatigue, 2008. 30(8): p. 1448-1472.
113. Ellison, E. and Zamily, A. Fracture and Life Prediction under Thermal-Mechanical Strain Cycling, Fatigue & Fracture of Engineering Materials & Structures, 1994. 17(1): p. 53-67.

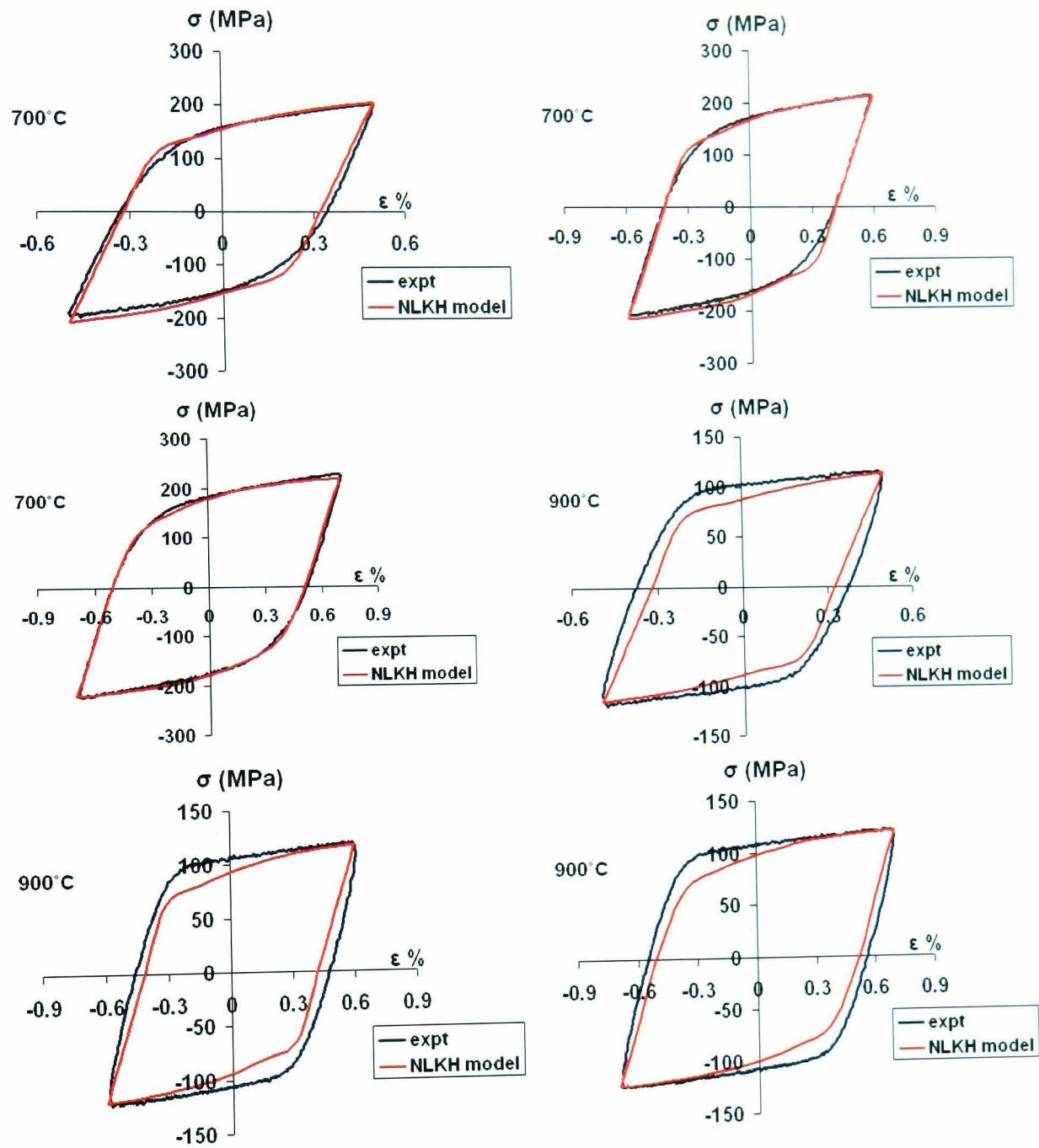
114. Kelly, R., Leen, S., A finite element investigation of the thermal stresses in SPF dies, MUTC report in the University of Nottingham, 2003
115. Kichenin, J., K. Dang, and K. Boytard, Finite-element simulation of a new two-dissipative mechanisms model for bulk medium-density polyethylene, *Journal of Materials Science*, 1996. 31(6): p. 1653-1661.

## APPENDIX A

A1] Validation of identified non-linear kinematic hardening constitutive constants of XN40F alloy for different strain ranges at 20 and 500°C for  $5 \times 10^{-3} \text{ S}^{-1}$ .



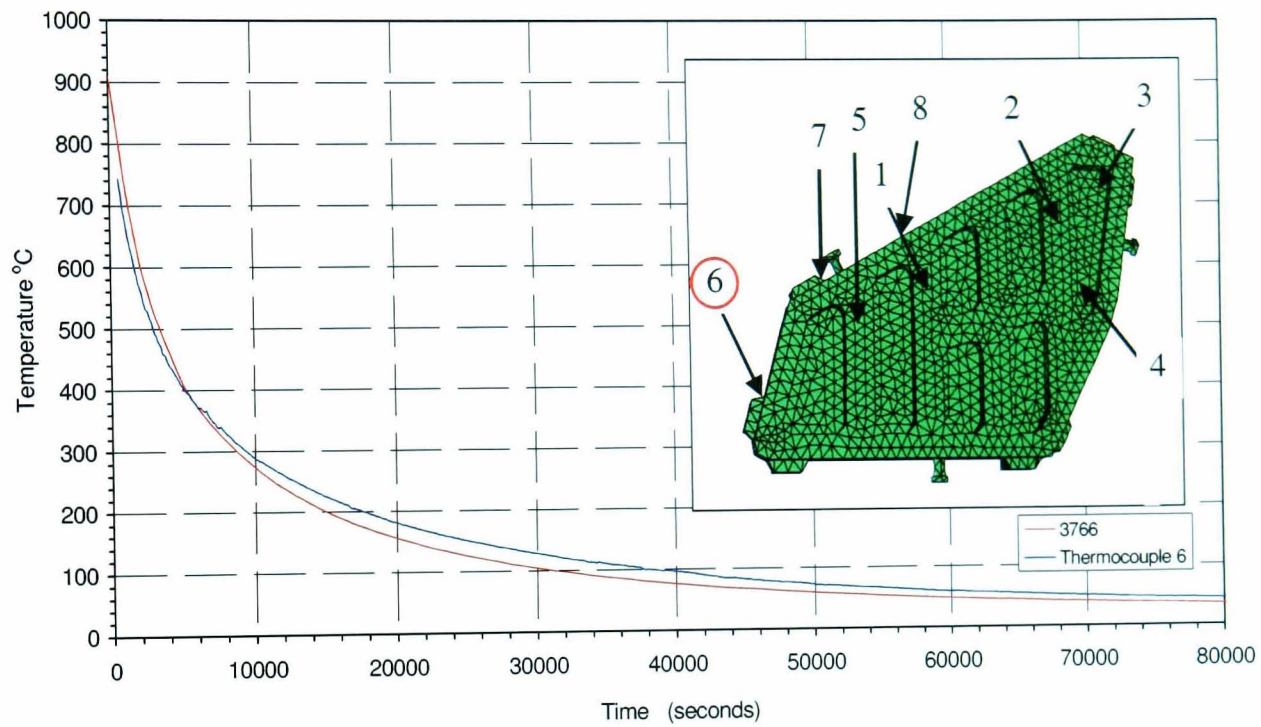
A2] Validation of identified non-linear kinematic hardening constitutive constants of XN40F alloy for different strain ranges at 700 and 900°C for  $5 \times 10^{-3} \text{ S}^{-1}$ .



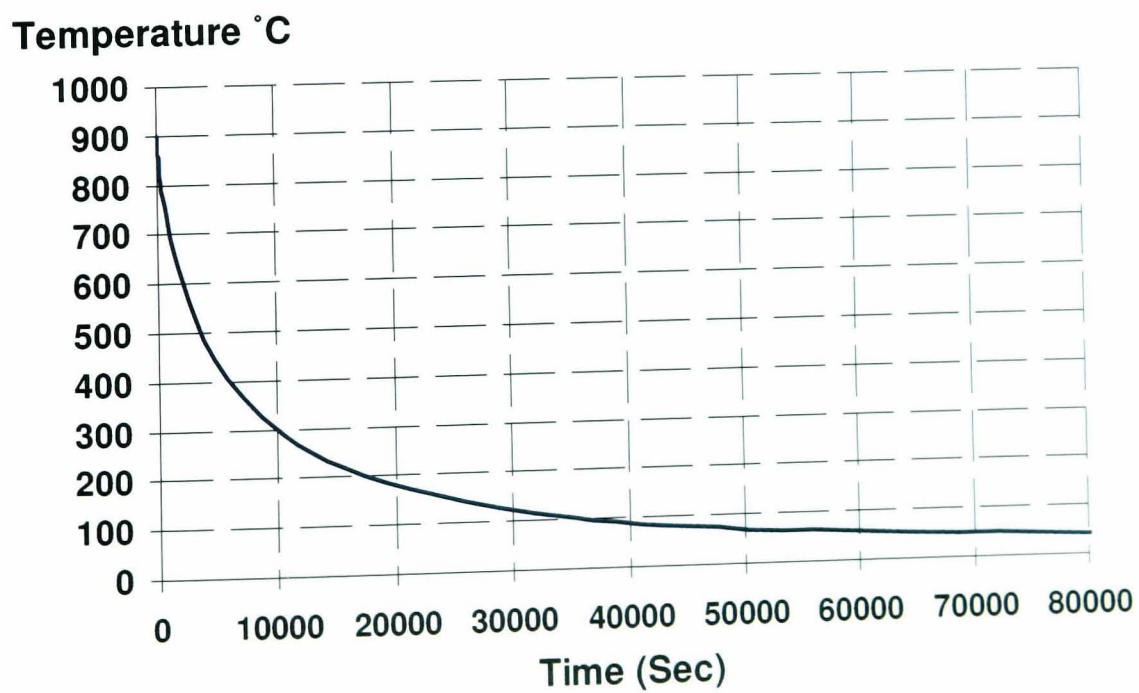
## APPENDIX B

This appendix shows the comparison of the FE predicted thermal history and the measured thermal history of a cooling cycle for the location 6.

B1] The measured thermal history (Cooling cycle) for the BAE SPF tool at location 6 by Kelly and Leen [114].



B2] The FE predicted thermal history (Cooling cycle) for the BAE SPF tool at location 6.



## APPENDIX C

The appendix shows the FE predicted results for the realistic industrial BAE SPF tool with local features using the same methodology employed for the representative simplified SPF tool. The results showed that the predicted inelastic strain ranges increased by 22% to that of the simplified BAE tool analyses mainly due to stress concentration at local features (see Chapter 7). However it is to be noted that the inferior element type (four node tetrahedral elements) with a reasonably fine mesh was used in the analysis of the industrial BAE SPF tool with local features.

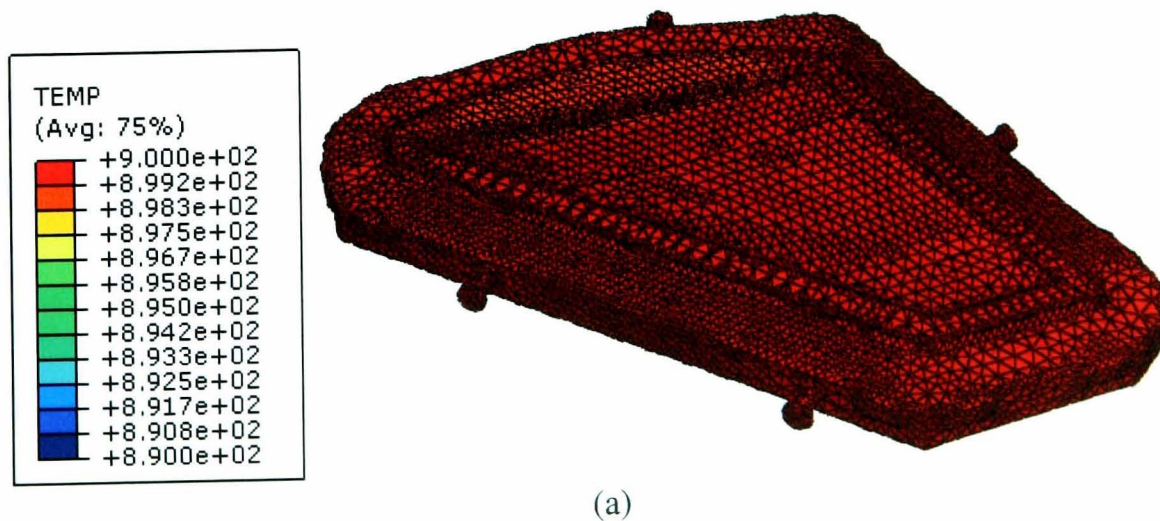
### Mesh Description

Element type - Four-node linear tetrahedral

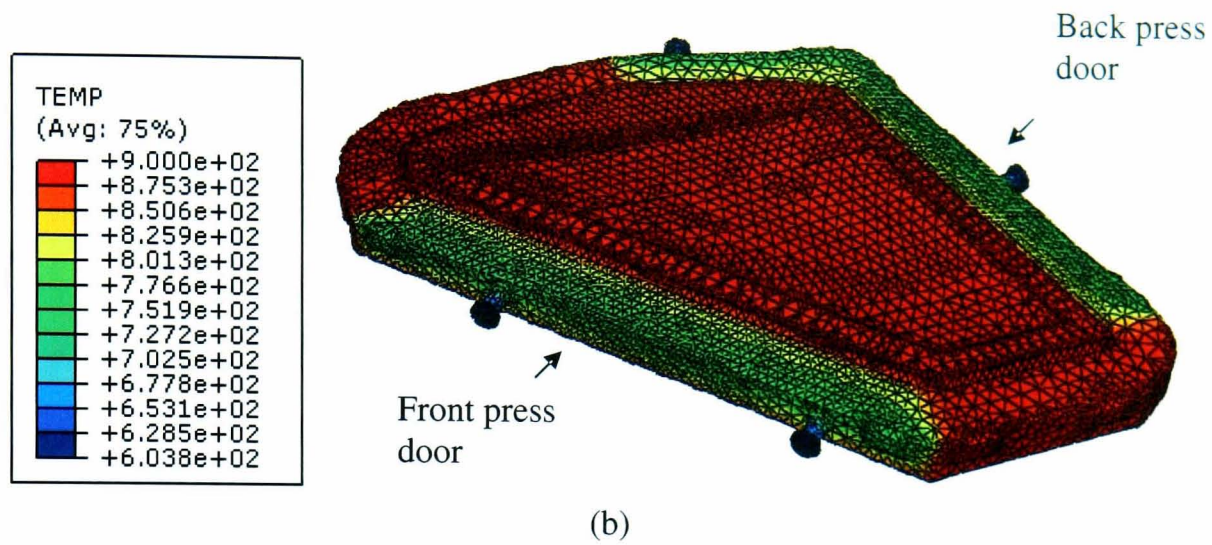
Number of elements- The whole model is meshed with 137725

The element characteristic length-40 mm

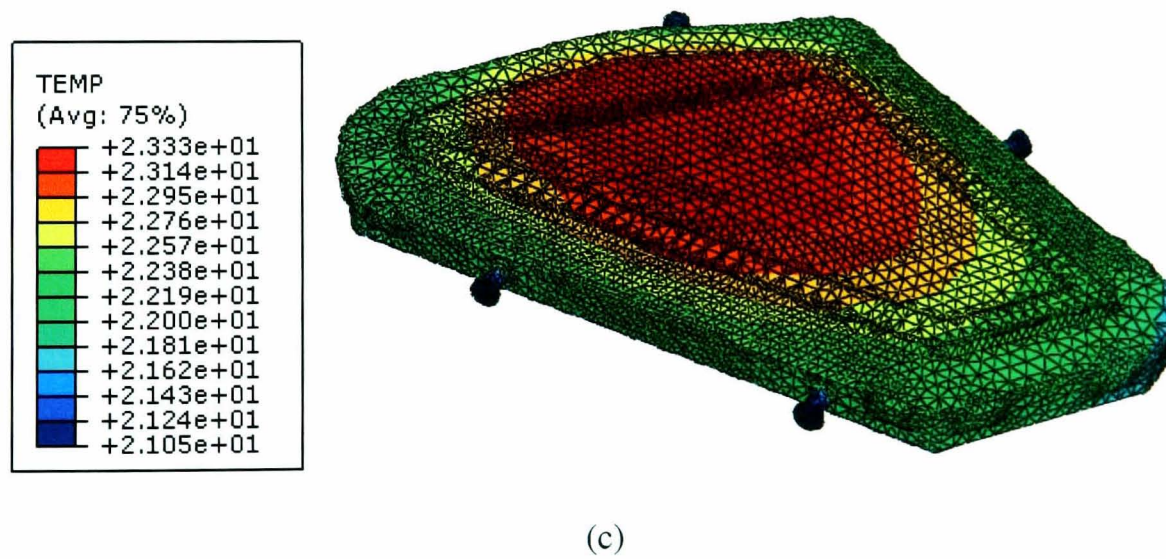
C1] FE predicted temperature contours of a realistic industrial SPF tool ; (a) end of heating to forming temperature 900°C, (b) end of blank inserts or part unload, (c) end of ambient cooling



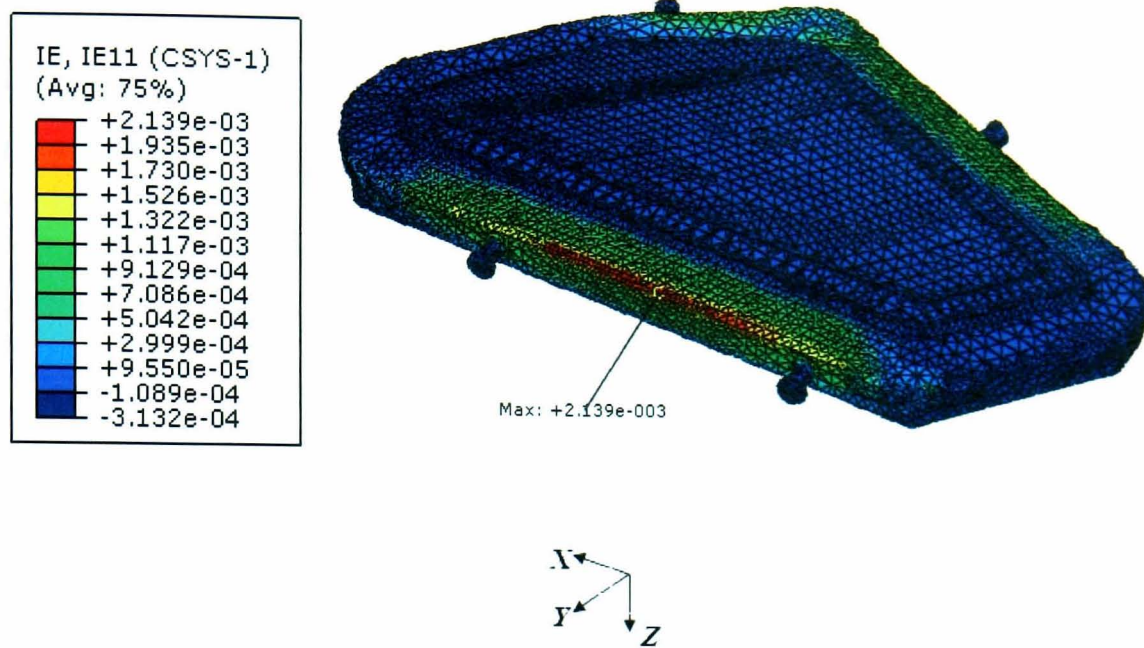
C1] (Contd.) FE predicted temperature contours of a realistic industrial SPF tool ;  
 (a) end of heating to forming temperature 900°C, (b) end of blank inserts or part unload,  
 (c) end of ambient cooling



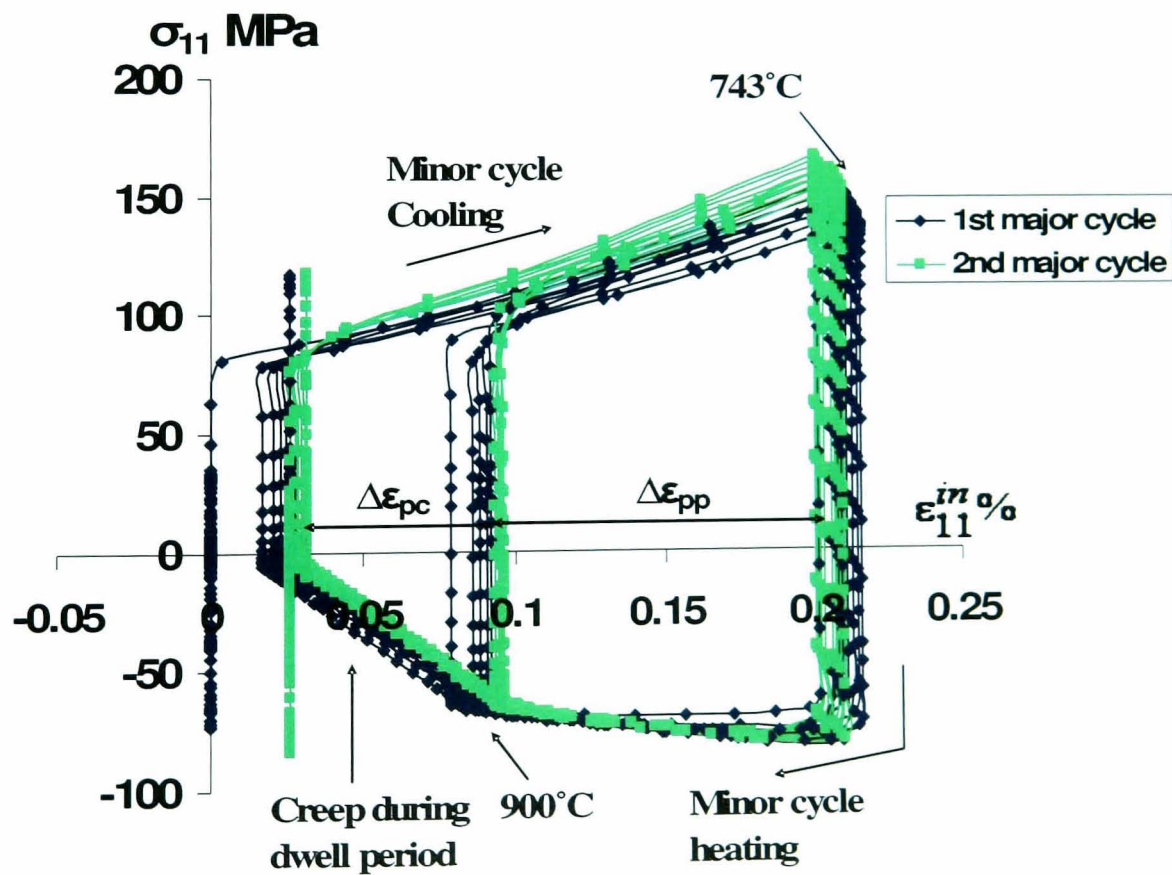
C1] (Contd.) FE predicted temperature contours of a realistic industrial SPF tool ;  
 (a) end of heating to forming temperature, (b) end of blank inserts or part unload, (c)  
 end of ambient cooling



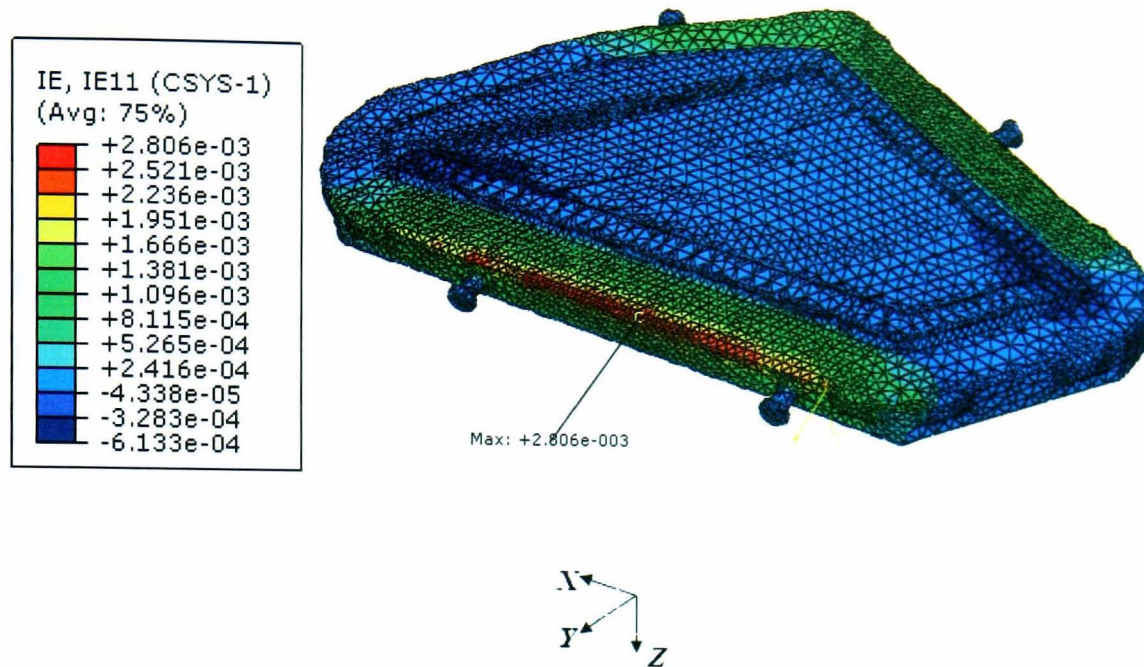
C2] Inelastic strain distribution along local X-X direction at the end of blank insertion or part unloading operations (Uncoupled plasticity-creep model)



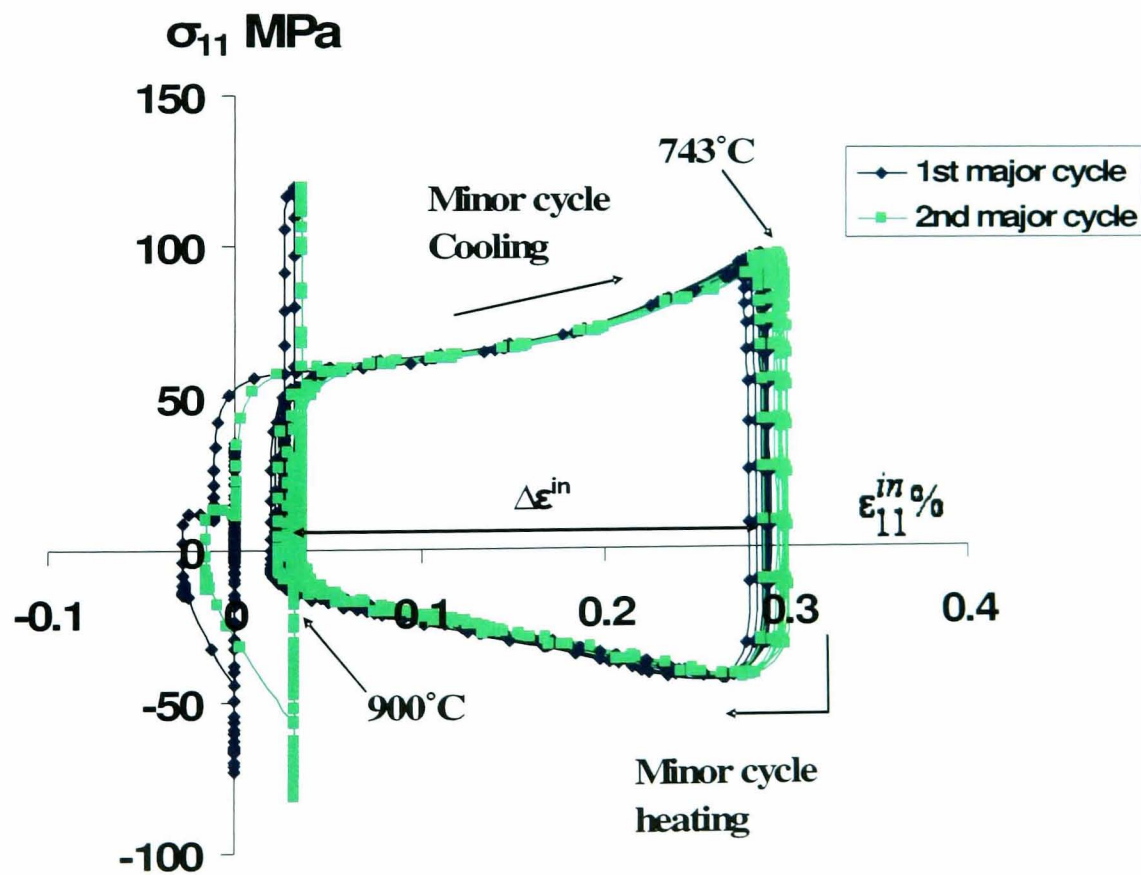
C3] Predicted local stress versus local inelastic strain for two major cycles each including five minor cycles for a critical element (Uncoupled plasticity-creep model)



C4] Inelastic strain distribution along local X-X direction at the end of blank insertion or part unloading operations (Two-layer viscoplastic model)



C5] Predicted local stress versus local inelastic strain for two major cycles each including five minor cycles for a critical element (Two-layer viscoplastic model)



## APPENDIX D

The appendix presents the SPF tool life predictions based on the Ostergren model with frequency term. The lifing tests performed in this thesis are accelerated tests since the actual heating and cooling rates of the SPF tool are very low and practically impossible to employ in uniaxial tests. Therefore the frequency term introduced by Maier et al. [86] is explored to predict the SPF tool life.

Ostergren model with frequency term presented by Maier et al. [86] is given below

$$N_f = L(\sigma_T \Delta \epsilon^{in})^n (V^*)^{(1-k)}$$

$$V^* = \frac{1}{\tau_0 + \tau_c}$$

$\sigma_T$  and  $\Delta \epsilon^{in}$  are peak tensile stress and inelastic strain range respectively.  $V^*$  is the effective frequency where  $\tau_0$  is the time spent in continuous cycling and  $\tau_c$  is the compression hold period.

Parameters  $n$  and  $L$  for XN40F alloy are identified from the isothermal low cycle fatigue data and the parameter  $k$  is approximately estimated from the available test data.

$$N_f = 386.23(\sigma_T \Delta \epsilon^{in})^{-1.3889} (v^*)^{(1-0.9)}$$

### **SPF tool life predictions**

| Material model                  | $\Delta \epsilon^{in}$ % | $\sigma_T$ (MPa) | $V^*$ S <sup>-1</sup> | $N_f$ (minor cycles) | $N_f$ (major cycles) |
|---------------------------------|--------------------------|------------------|-----------------------|----------------------|----------------------|
| Uncoupled plasticity-creep      | 0.1734                   | 165              | 0.00002808            | 1121                 | 56                   |
| Two-layer viscoplasticity model | 0.2452                   | 89               | 0.00002808            | 770                  | 38                   |